# NANOSTRUCTURES:
# PHYSICS AND TECHNOLOGY

6th International Symposium

St Petersburg, Russia, June 22–26, 1998

Co-Chairs
*Zh. Alferov*
*L. Esaki*

# PROCEEDINGS

Ioffe Institute
St Petersburg, 1998

# REPORT DOCUMENTATION PAGE

*Form Approved*
*OMB No. 074-0188*



| 1. AGENCY USE ONLY (Leave blank) | 2. REPORT DATE | 3. REPORT TYPE AND DATES COVERED |
|---|---|---|
| | 22 June 1998 | Conference Proceedings, 22-26 June 1998 |

**4. TITLE AND SUBTITLE**
Nanostructures: Physics and Technology. 6th International Symposium. St. Petersburg, Russia, 22-26 June 1998 Proceedings

**5. FUNDING NUMBERS**

**6. AUTHOR(S)**
Alferov, Ah.; Esaki, L.

**7. PERFORMING ORGANIZATION NAME(S) AND ADDRESS(ES)**

Ioffe Physico-Technical Institute
26 Poliekhnichesdkaya
St. Petersburg, Russia 194021

**8. PERFORMING ORGANIZATION REPORT NUMBER**

**9. SPONSORING / MONITORING AGENCY NAME(S) AND ADDRESS(ES)**

Office of Naval Research
European Office
PSC 802 Box 39
FPO AE 09499-0039

**10. SPONSORING / MONITORING AGENCY REPORT NUMBER**

**11. SUPPLEMENTARY NOTES**

**12a. DISTRIBUTION / AVAILABILITY STATEMENT**
Distribution A: Approved for public release; distribution unlimited

**12b. DISTRIBUTION CODE**
A

**13. ABSTRACT** ***(Maximum 200 Words)***
The International Symposium "Nanostructures: Physics and Technology" is held annually since 1993.

**14. SUBJECT TERMS**
ONRIFO; EOARD; Foreign reports; Conference proceedings; Symposia; Nanotechnology; Russia

**15. NUMBER OF PAGES**
552

**16. PRICE CODE**

| 17. SECURITY CLASSIFICATION OF REPORT | 18. SECURITY CLASSIFICATION OF THIS PAGE | 19. SECURITY CLASSIFICATION OF ABSTRACT | 20. LIMITATION OF ABSTRACT |
|---|---|---|---|
| Unclassified | Unclassified | Unclassified | Unlimited |

The International Symposium "Nanostructures: Physics and Technology" is held annually since 1993. The first Symposium was initiated by Prof. Zh. Alferov and Prof. L. Esaki who are its permanent co-chairs. By tradition the Proceedings of the Symposium is published before the beginning of the meeting.
More detailed information on the Symposium is presented on the World Wide Web **http://www.ioffe.rssi.ru/NANO-98/**.

This volume was composed at the Information Services and Publishing Department of the Ioffe Institute from electronic files submitted by the authors. When necessary these files were converted into the Symposium LaTeX2ε style without any text revisions. Only minor technical corrections were made by the composers.

ISBN 5-86763-120-6

Information Services and Publishing Department
Ioffe Physico-Technical Institute
26 Polytechnicheskaya, St Petersburg 194021, Russia
Phones: (812) 247 6805, 247 9932
Fax: (812) 247 2135, 247 1017
E-mail: vgrig@eo.ioffe.rssi.ru

Printed in Russian Federation

The Symposium is held under the auspices of
*the Russian Academy of Sciences*

## Organizers

*Ioffe Physico-Technical Institute*

*Scientific Engineering Center for Microelectronics at the Ioffe Institute*

in association with

*Research Council for the Project "Physics of Solid State Nanostructures" at the Ministry of Science and Technologies of Russia*

and

the institutions of the Russian Academy of Sciences

*Division of General Physics and Astronomy*

*St Petersburg Scientific Center*

## Acknowledgments

The Organizers of the Symposium gratefully acknowledge the following institutions for their financial support:

*Ministry of Science and Technologies of Russia*

*Russian Foundation for Basic Research*

*ONR International Field Office, Europe*

*European Office of Aerospace Research and Development, United Kingdom*

*European Research Office, US Army*

## Location and Date

The Symposium is held in St Petersburg's recreation area Repino on June 22–26, 1998.

## Programme Committee

R. Suris, Chair (*St Petersburg*)
Zh. Alferov (*St Petersburg*)
L. Asryan, Secretary (*St Petersburg*)
S. Gaponov (*Nizhnii Novgorod*)
A. Gippius (*Moscow*)
Yu. Gulyaev (*Moscow*)
S. Gurevich (*St Petersburg*)
L. Keldysh (*Moscow*)
Yu. Kopaev (*Moscow*)
P. Kop'ev (*St Petersburg*)
M. Kupriyanov (*Moscow*)
V. Mokerov (*Moscow*)
V. Panov (*Moscow*)
N. Samsonov (*Moscow*)
N. Sibel'din (*Moscow*)
V. Timofeev (*Chernogolovka*)
B. Zakharchenya (*St Petersburg*)

## Organizing Committee

M. Mizerov, Chair (*Center for Microelectronics*)
V. Grigor'yants, Secretary (*Ioffe Institute*)
L. Asryan (*Ioffe Institute*)
B. Egorov (*Ioffe Institute*)
P. Kop'ev (*Ioffe Institute*)
A. Prokhorenko (*St Petersburg Scientific Center*)
E. Solov'eva (*Ioffe Institute*)
V. Zayats (*Division of General Physics and Astronomy*)

# Contents

## Transport in Nanostructures



## Scanning Tunnelling Microscopy: Nanostructure Formation and Characterization

## 2D Electron Gas



## Far-Infrared Phenomena in Nanostructures

## Quantum Wires and Quantum Dots

## Single Electron Phenomena and Devices



## Self-Organization Phenomena in Nanostructures

## Nanostructure Technology

## General Properties of Low-Dimensional Structures



## Tunnelling Phenomena



## Excitons in Nanostructures

## Lasers and Optoelectronic Devices

## Nanostructure Characterization and Novel Atomic-Scale Probing Techniques

## Silicon Based Nanostructures



## Nanostructure Devices

## Closing Session



## Unprinted Papers

The papers listed below are included in the Symposium Programme, but not printed in the Proceedings, as the authors had not submitted electronic files in due time.

Ioffe Institute
6th Int. Symp. "Nanostructures: Physics and Technology"
St Petersburg, Russia, June 22–26, 1998.



# Master equations for the micro-states description of carrier relaxation and recombination in quantum dots

*D. Bimberg*, M. Grundmann and R. Heitz
Institut für Festkörperphysik, Technische Universität Berlin,
Hardenbergstr. 36, D-10623 Berlin, Germany

**Abstract.** Modeling of time resolved experiments on zero-dimensional quantum dots requires a conceptually different approach than for higher dimensional semiconductors. A description via master equations for the micro-states is necessary since quantum dots behave as independent objects. The impact of finite inter-level relaxation time is included in our model. Description via conventional rate equations for population probabilities averaged over the dot ensemble is inadequate. Two different time resolved luminescence experiments for quantum dot systems with fast and slow inter-level relaxation, respectively, are modeled to provide typical applications of our approach.

The energy relaxation and recombination of charge carriers in three-, two- and one-dimensional semiconductors has been investigated to great extent, e.g. Ref. [1–3]. Common to materials with these dimensionalities (bulk, quantum wells, quantum wires) is, that their properties can be adequately described by *continuous* charge carrier *densities* $n$ and $p$ for electrons and holes, respectively. The probabilities of events in the charge carrier gas are essentially dependent on the product of such densities, e.g. $np$ for inter-band recombination and $n^2p$ or $np^2$ for the Auger effect.

With the advent of semiconductor quantum dots (QDs) fabricated by self-organized growth [4–6] zero-dimensional electronic systems with well controlled properties and area densities of $10^9$ to $10^{11}$ $cm^{-2}$ became available. Such QD layers represent systems *qualitatively different from any higher dimensional semiconductor structure.* The carriers in individual QDs populate discrete levels and are described by *integer numbers.* The probability of events does not depend on the *average* carrier density but on the condition whether the event partners are simultaneously present in a particular QD. Despite this rather obvious fact, up to now only conventional rate equations (CRE) for the ensemble averaged level occupations, inspired by the description of bulk material or quantum wells, have been used to model carrier dynamics in QD ensembles [7–10]. The tremendous experimental interest in the carrier dynamics in quantum dots [7–16] is due to the concern about the general usefulness of QDs for high speed operation of devices, like lasers or light emitting diodes, because capture and inter-level relaxation processes might be slow.

In this work we will show that CRE fail for the description of QD systems. A conceptually fundamentally different model is presented, namely master equations for all micro-states (MEM) of the QD. A micro-state of the QD represents one particular occupation with carriers; the entirety of all micro-states represents the phase space. Such an approach has been used for the description of the Auger process for the spin-degenerate ground state of CdS micro-crystals in a glass matrix [17] and spin dynamics

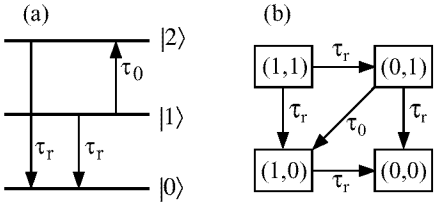


**Fig 1.** Schematic representation of the conventional rate equation model (CRE) and the master equation for the micro-states (MEM) for a two-level system.

of the ground state of (two-dimensional) excitons [18], both involving four micro-states. However, to the best of our knowledge, multi-level systems and inter-level relaxation have not been described using micro-states. An alternative approach are Monte-Carlo simulations [19] which are harder to implement, are much more time consuming and do not yield quasi analytical results. Using the MEM approach we will model actual time-resolved experiments on two fundament ally different QD systems: Small InAs/GaAs pyramids [6, 20] and strain induced quantum dots [10, 21], with fast and slow inter-level relaxation time constants, respectively.

In order to illustrate why CRE models fail in general to describe recombination from layers of decoupled QDs we compare the CRE and the MEM models for a simple two-level system. We assume two non-degenerate electron-hole pair (eh-pair) levels $|1>$ and $|2>$ which can both decay radiatively with the same time constant $\tau_r$ (Fig. 1). If in a dot level $|2>$ is occupied and level $|1>$ is empty, an inter-level relaxation process can occur with a time constant $\tau_0$. In the CRE model the system is described by population probabilities $f_1$ and $f_2$ for the levels, respectively, taking values $0 \leq f_i \leq 1$. The rate equations (after preparation of an initial non-equilibrium population and switch-off of any external excitation) are

$$\frac{df_1}{dt} = -\frac{f_1}{\tau_r} + \frac{f_2(1-f_1)}{\tau_0} \tag{1}$$

$$\frac{df_2}{dt} = -\frac{f_2}{\tau_r} - \frac{f_2(1-f_1)}{\tau_0} \tag{2}$$

The second term in both equations is used to model the inter-level scattering and contains a factor $1 - f_1$ for the available empty states to describe the "Pauli blocking". The final state population must be considered for quantum dots, while it is usually neglected in CRE models for quantum wells [22, 23].

A correct description of the QD ensemble is achieved using all micro-states. In our example these are dots with the two levels filled with $(n_1, n_2)$ eh-pairs, i.e. (0,0) for empty dots, (1,0) and (0,1) for dots where either the $|1>$ or the $|2>$ level is filled, and (1,1) for completely filled dots. The probabilities to find a dot with a specific micro-state in the ensemble shall be given by $w_{00}$, $w_{10}$, $w_{01}$, and $w_{11}$ with $w_{00}+w_{10}+w_{01}+w_{11} = 1$. The master equations for the possible transitions between the micro-states (Fig. 1) are

$$\frac{dw_{00}}{dt} = \frac{w_{10}}{\tau_r} + \frac{w_{01}}{\tau_r} \tag{3}$$

$$\frac{dw_{10}}{dt} = -\frac{w_{10}}{\tau_r} + \frac{w_{11}}{\tau_r} + \frac{w_{01}}{\tau_0} \tag{4}$$

$$\frac{dw_{01}}{dt} = -\frac{w_{01}}{\tau_r} + \frac{w_{11}}{\tau_r} - \frac{w_{01}}{\tau_0} \tag{5}$$

$$\frac{dw_{11}}{dt} = -2\frac{w_{11}}{\tau_r} \tag{6}$$

The term $w_{01}/\tau_0$ describes the inter-level relaxation. We note that "Pauli blocking" is not explicitly introduced; implicitly it is included by not considering "overfilled" microstates like (2,0). The issue of how to model finite state population does not arise in the MEM scheme.

The population probabilities $f_1$ and $f_2$ used in the conventional rate equation approach can be expressed as $f_1 = w_{10}+w_{11}$ and $f_2 = w_{01}+w_{11}$. The inter-level scattering term in the CRE description translates into

$$\frac{f_2(1-f_1)}{\tau_0} \rightarrow \frac{(w_{01}+w_{11})(w_{01}+w_{00})}{\tau_0} \tag{7}$$

which is obviously unreasonable. The term is quadratic in $w_{01}$ and includes, due to the ensemble averaging procedure, empty $(w_{00})$ and completely filled $(w_{11})$ dots which do not contribute to the inter-level scattering process at all.

For $\tau_0 = 0$ (and complete initial filling, i.e. $f_2(t=0) = f_1(t=0) = 1$ and $w_{11}(t=0) = 1$, respectively) the CRE model yields a non-exponential transient for the excited state and a kink at $t = \tau_r ln(2)$ in the transient of the ground state. The decay of the excited state occurs too fast in the CRE model for $\tau_0 < \tau_r$ and a false value $\tau_0 \approx \tau_r$ will be obtained from a fit with CRE. CRE models are in principle inadequate for the description of QDs. Their application for the determination of inter-level scattering times from time resolved luminescence experiments can lead to wrong results.

In our theoretical model we use the following assumptions, which are valid for strongly confined carriers: The single particle levels $n = 1, 2, \ldots$ of the QDs are populated with electrons and holes; $n = 1$ is also referred to as ground state, $n = 2$ as first excited state. The maximum number of carriers on a given level is determined by the degeneracy $g_n$ of the level. Electrons and holes recombine radiatively between single particle states, i.e. Coulomb correlation is neglected. However, also a representation in the exciton picture could be chosen. The transitions are denoted by the electron and hole levels involved, e.g. 1e-1h or 2e-2h. As a consequence, the lifetime of the biexciton (dot filled with two electrons and holes in their single particle ground state, $XX \rightarrow X + \gamma$) is given by $\tau_{XX} = \tau_X/2$, $\tau_X$ denoting the lifetime of a single eh-pair in the ground state. Two-photon processes $(XX \rightarrow 2\gamma)$ and Auger recombination are neglected. Throughout the paper the low temperature case is treated where excited states are not thermally populated.

The inter-level scattering is described by the time constant $\tau_0$ for one single relaxation process between any two non-degenerate levels. Thus the relaxation rate between microstates scales with the number of available initial and final states and becomes larger for higher excited states. The transition rate of an eh-pair in an excited state into the empty spin-degenerate ground state shall be $2/\tau_0$. If spin-conserving relaxation processes dominate, as suggested in Ref. [24] at least for moderate magnetic fields, the number of available final states would be only one; in this case $\tau_0/2$ must be interpreted as the inter-level scattering time. A more detailed model than presented here including detailed spin dynamics, also taking into account dark exciton states [24, 25], can be

derived on the basis of our multi-level MEM concept. It will be subject to subsequent work and needs additional experimental input on spin scattering rates in QDs.

First we predict the asymptotic decay constants (at long times after excitation) of QD excited state luminescence transients using the MEM model for the case that the ground state was initially filled. For $\tau_0 = 0$ the carriers populate always the energetically lowest possible states. The asymptotic transient of the first excited state is then governed by dots in the $(2, 1, \cdots)$ state. This micro-state obviously decays with the time constant $1/\tau_{(2,1)} = 1/\tau_r^2 + 2/\tau_r^1$, where $\tau_r^2$ ($\tau_r^1$) denotes the recombination time constant of the 2-2 (1-1) transition. For finite values of $\tau_0$, the asymptotic decay constant $\tau_\infty^2$ of the first excited state is given by eq. 8 in the MEM model:

$$\frac{1}{\tau_\infty^2} - \frac{1}{\tau_r^2} = \frac{2}{\tau_r^1} \quad \text{for} \quad \tau_0 < \tau_r^1, \quad \frac{2}{\tau_0} \quad \text{for} \quad \tau_0 \geq \tau_r^1 \tag{8}$$

A finite value of $\tau_0$ has only an impact on the asymptotic transient of the excited state for $\tau_0 > \tau_r$ (for CRE the lower formula is valid for all values of $\tau_0$). However, for $\tau_0/\tau_r \approx 1$ the true asymptotic values are only reached for large delay times; for the typical dynamic range $10^1 - 10^4$ of time resolved luminescence experiments numerical evaluation is needed.

The level structure of small pyramidal self-organized InAs/GaAs QDs has been analyzed [20, 26]. The multi-phonon relaxation mechanisms present in such dots have been discussed [27]. Here, we will analyze time resolved experiments where the hole ground and excited state become populated. The transitions with ground state electrons are labeled 1e-1h and 1e-2h. Both hole levels are spin-degenerate, thus $3 \times 3 = 9$ micro-states have to be included in the MEM. Our model shall contain only four physical parameters: the recombination time constants for both transitions $\tau_{1e-1h}$ and $\tau_{1e-2h}$ (the excited state is affected by a non-radiative recombination channel [27] and is thus expected to have the shorter time constant), the inter-level scattering time $\tau_0$ and the time constant $\tau_c$ describing the capture of carriers from the barrier into any level of the QD. We use $\tau_c/\tau_{1e-1h} = 0.01$ to generate transients with the experimental ly observed fast onset [15, 13]. Coulomb scattering is argued to shorten the capture process [12, 13].

Since the peaks of the two transitions overlap spectrally [20], at long delay time the temporal behavior of the luminescence detected at the energy of the excited state is given by that of the ground state. In Fig. 2 the measurement is shown together with several fits. In experiments with resonant excitation of the excited state [15], the (initially empty) ground state exhibits a rise time of 30 ps, which is a direct measurement of the fast inter-level relaxation constant. A fit of the transient for non-resonant excitation using $\tau_0 = 30$ ps yields a perfect fit of the transients for the MEM approach ($\tau_0/\tau_{1e-1h} = 0.04$). We note that the fit is practically identical for any value $\tau_0 < 100$ ps including $\tau_0 = 0$ ps. The decay of non-resonantly excited transients is found to be insensitive to the inter-level relaxation constant if it is small (as is clear from eq. 8) and thus unsuited for its determination. The (2,1) micro-sta te with a filled ground state governs the decay of the excited state in the InAs/GaAs pyramids. Using CRE an erroneous value of about $\tau_0 = 240$ ps is necessary in order to fit the experimental data for the excited state transition. The decay of the excited level in the CRE scheme is too fast for small values of $\tau_0$; a relatively sharp bend occurs in the transient, indicated by the arrow in Fig. 2.

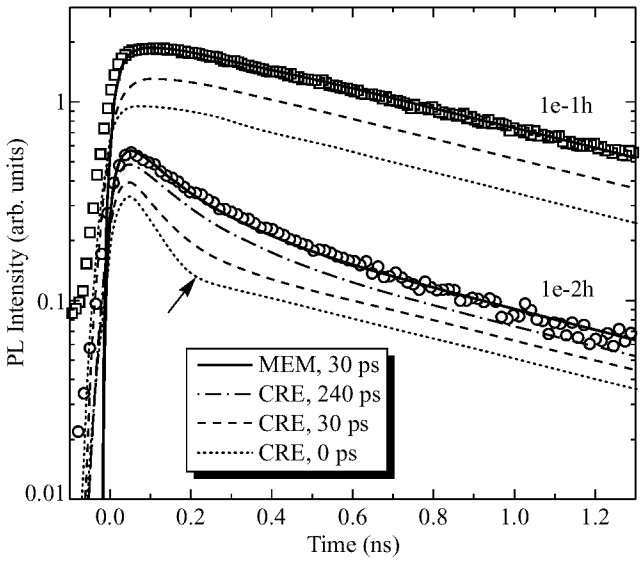


**Fig 2.** Experimental transients of the ground (1e-1h) and excited state (1e-2h) transition in InAs/GaAs quantum dots (symbols). Solid lines: Fit with MEM model, other lines (vertically shifted): fits with CRE model using different values for $\tau_0$ as given in the figure. For all transients $\tau_{1e-1h} = 0.85$ *ns* and $\tau_{1e-2h} = 0.24$ *ns* have been used. The arrow denotes the unrealistic sharp bend in CRE transient for small values of $\tau_0$.

Time resolved experiments on strain induced dots [21] have been reported in Ref. [10] (Fig. 3b). The electronic level structure of such dots is well described by a two-dimensional harmonic oscillator model, exhibiting $K = 5$ levels for electrons and holes with degeneracies $g_n = 2n$, $n = 1, \cdots, K$. Self-organized QDs, grown by a Stranski-Krastanov process, with similar five-level structure were reported [8]. The total number of states is $M = \sum_{n=1}^{K} g_n = 30$; the number of distinguishable micro-states is $\prod_{n=1}^{K}(g_n + 1) = 10395$. Each micro-state is unambiguously described by a quintuple $(n_1, n_2, n_3, n_4, n_5)$, $0 \leq n_i \leq g_i$. Radiative transitions are allowed between electrons and holes with the same quantum numbers, i.e. 1e-1h, 2e-2h. In the following we assume that the excess carriers have been deposited in the barrier via a short pulse at $t = 0$. The onset of the transients will be modeled with $\tau_c = 4$ ps as recently determined by up-conversion experiments using the same excitation intensity [28]. This onset is faster than the time resolution of the streak camera experiment shown in Fig. 3b and our simulations do not attempt to fit the onset. The saturation value of intensity from the four lines scales like 2:3.4:5.3:7.5 and is not exactly given by the degeneracies which would predict 2:4:6:8. We believe that this effect is caused by non-identical radiative lifetimes of eh-pairs on the different levels and include this fine-tuning for the quantitative fit by using recombination time constants $\tau_{ne-nh}$ which scale like 1:1.17:1.12:1.06. For the 5e-5h transition (not measured) we assume a factor of 1.1.

For finite $\tau_0$ the different inter-level scattering processes entering the model have to be distinguished. We will compare two "trickle down" models: "TDA": scattering processes are allowed to *all* lower levels $n \rightarrow n - 1, \cdots, 1$ and "TDN": scattering

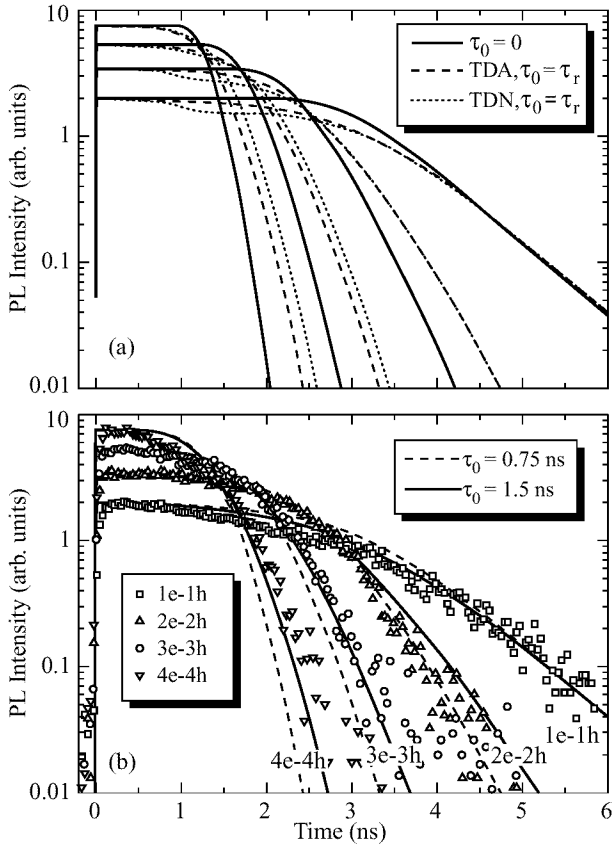


**Fig 3.** Transients for five-level quantum dots and master equation model. (a) Comparison of theoretical transients for instantaneous relaxation ($\tau_0 = 0$) and TDA and TDN model for $\tau_0 = \tau_{1e-1h}$. (b) Experimental data and fit with TDA model for two values of the inter-level scattering time, $\tau_0/\tau_{1e-1h} = 1$ and 2, $\tau_{1e-1h} = 0.75ns$.

processes are restricted to the *next* lower level $n \to n-1$. For $\tau_0 = 0$, the carriers are always in the energetically lowest states; thus the number of carriers describes the micro-state unambiguously. The number of micro-states is thus reduced to $M+1 = 31$ including the empty dot. The transients for this case are shown in Fig. 3a. The essential features of the experiments are already reproduced. While excited states are strongly populated, the lower levels exhibit a plateau region because they remain completely filled due to instantaneous carrier refill. Higher excited states exhibit increasingly faster asymptotic decay constants compared with that of the ground state ($\tau_{1e-1h}$).

For finite values of $\tau_0$ we consider first the TDA model, where relaxation processes into all lower levels are incorporated (Fig. 3a). The transients exhibit a significant difference from the case $\tau_0 = 0$ only for $\tau_0/\tau_{1e-1h} > 0.1$. The main effects are intensity from excited states remaining at larger delay times, an increase of the asymptotic decay constants of excited states and that the plateau region does not remain flat. It exhibits a slow decay while upper levels are still significantly filled because the refill rate decreases

with decreasing population of all excited states. Using the parameters $\tau_{1e-1h} = 0.75$ ns and $\tau_0 = 0.75$ ns a very good fit of the experimental data at large times (asymptotic slopes of the ground and excited state) is obtained (Fig. 3b). Using $\tau_0 = 1.5$ ns a better overall fit mimicking the decrease of plateau intensities is achieved; however, the decay of the 2e-2h transition comes out too slow.

We conclude for slow inter-level relaxation, $\tau_0/\tau_{1e-1h} \approx 1$. Therefore the asymptotic decay of the first excited state is governed by (0,1,0,0,0) QDs.

In the TDN model, considering only relaxation processes to the next lower level, the transients exhibit a concave bump (Fig. 3a) not observed in the experiment which yields convex transients. Thus the TDN model seems not appropriate, at least not in conjunction with initial complete filling of dots.

In Ref. [10] the experimental data had been fitted with a CRE model and TDN scheme; a value $\tau_0/\tau_{1e-1h} \approx 0.67$ was deducted. From our analysis it becomes clear that because the inter-level scattering time is large and close to the radiative lifetime, the CRE model was able to fit the experimental data with a reasonable value for $\tau_0$.

In summary we have applied a novel concept, master equations for the micro-states, to the description of time-resolved luminescence experiments on multi-level QDs with fast and slow inter-level relaxation. Conventional rate equation models for the ensemble averaged population probabilities are incorrect and largely overestimate the inter-level relaxation time constant if it is small compared to the recombination time constants. More complicated processes than discussed in this work, like Auger recombination, two photon processes, spin dynamics, and effects due to finite temperature (thermal population of excited states by phonon absorption) can be included.

*Acknowledgment*

We are indebted to J. H. H. Sandmann and J. Feldmann for fruitful discussion and experimental data. Part of this work has been funded by Deutsche Forschungsgemeinschaft in the framework of Sfb 296.

## References

[1] W. van Roosbroeck and W. Shockley, *Phys. Rev.* **94** 1558 (1954).
[2] G. Lasher and F. Stern, *Phys. Rev.* **133** A553 (1964).
[3] B. Deveaud, T.C. Damen, J. Shah, and C.W. Tu, *Appl. Phys. Lett.* **51** 828 (1987).
[4] L. Goldstein et al., *Appl. Phys. Lett.* **47** 1099 (1985).
[5] S. Guha, A. Madhukar, and K.C. Rajkumar, *Appl. Phys. Lett.* **57** 2110 (1990).
[6] M. Grundmann et al., *phys. stat. sol. (b)* **188** 249 (1995) *and references therein*, M. Grundmann et al., *Phys. Rev. Lett.* **47** 4043 (1995).
[7] G. Wang et al., *Appl. Phys. Lett.* **64** 2815 (1994).
[8] K. Mukai et al., *Appl. Phys. Lett.* **68** 3013 (1996).
[9] F. Adler et al., J. Appl. Phys. **80** 4019 (1996).
[10] S. Grosse et al., *Phys. Rev. B* **55** 4473 (1997).
[11] H. Yu et al., *Appl. Phys. Lett.* **69** 4087 (1996).
[12] U. Bockelmann et al., *Phys. Rev. Lett.* **76** 3623 (1996).
[13] B. Ohnesorge et al., *Phys. Rev. B* **54** 11532(1996).
[14] M. Vollmer et al., *Phys. Rev. B* **54** R17292 (1996).
[15] R. Heitz et al., *Phys. Rev. B* **56** 10435 (1997).
[16] D. Bimberg, N. Kirstaedter, N.N. Ledentsov, Zh.I. Alferov, P.S. Kop'ev, V.M. Ustinov, *IEEE J. Selected Topics in Quantum Electronics* **3** 1 (1997).

[17] D.I. Chepic et al., *J. Luminescence* **47** 113 (1990).
[18] M.Z. Maialle et al., *Phys. Rev. B* **47** 15776 (1993).
[19] M. Grundmann and D. Bimberg, *Phys. Rev. B* **55** 9740 (1997).
[20] M. Grundmann et al., *Appl. Phys. Lett.* **68** 979 (1996).
[21] H. Lipsanen, M. Sopanen, and J. Ahopelto, *Phys. Rev. B* **51** 13868 (1995).
[22] D. Bimberg et al., *J. Luminescence* **30** 562 (1985).
[23] G. Bastard "Wave mechanics applied to semiconductor heterostructures" (Les editions de physique, Les Ulis, 1988), p. 273.
[24] W. Heller and U. Bockelmann, *Phys. Rev. B* **55** R4871 (1997).
[25] M. Nirmal et al., *Phys. Rev. Lett.* **75** 3728 (1995).
[26] M. Grundmann, O. Stier, D. Bimberg, *Phys. Rev. B* **52** 11969 (1995).
[27] R. Heitz et al., *Appl. Phys. Lett.* **68** 361 (1996).
[28] J.H.H. Sandmann et al., *unpublished.*

Ioffe Institute
6th Int. Symp. "Nanostructures: Physics and Technology"
St Petersburg, Russia, June 22–26, 1998.



# Quantum-dot cellular automata devices and architectures

*Wolfgang Porod*
Department of Electrical Engineering, University of Notre Dame, IN, 46556

**Abstract.** We discuss novel nanoelectronic architecture paradigms based on cells composed of coupled quantum-dots. Boolean logic functions may be implemented in specific arrays of cells representing binary information, the so-called Quantum-Dot Cellular Automata (QCA). In addition, we discuss possible realizations of these structures in a variety of semiconductor systems (including GaAs/AlGaAs, Si/SiGe, and $Si/SiO_2$), rings of metallic tunnel junctions, and candidates for molecular implementations.

## 1 Introduction

Silicon technology has followed Moore's Law remarkably closely for more than three decades. However, there are indications now that this progress will slow, or even come to a standstill, as technological and fundamental limits are reached [1]. This slow-down of silicon ULSI technology may provide an opportunity for alternative device technologies. Among the chief technological limitations responsible for this expected slow-down of silicon technology are the interconnect problem and power dissipation [2]. However, these obstacles for silicon circuitry may present an opportunity for alternative device technologies which are designed for the nanometer regime and which are interconnected in an appropriate architecture.

In this paper, we describe our ideas of using nanostructures (more specifically, quantum dots) which are arranged in locally-interconnected cellular-automata-like arrays. We will demonstrate that suitably designed structures, the so-called "Quantum-Dot Cellular Automata" (QCA) [3], may be used for computation and signal processing. The fundamental idea for QCA operation is to encode information using the charge configuration in a cell, which is more naturally suited to nanostructures. This is an important break with the transistor paradigm, where binary information is encoded utilizing voltage-controlled current switches.

## 2 Quantum-dot cellular automata

Based upon the emerging technology of quantum-dot fabrication, the Notre Dame NanoDevices Group has developed the QCA scheme for computing with cells of coupled quantum dots [3], which will be reviewed below. To our knowledge, this is the first concrete proposal to utilize quantum dots for computing. There had been earlier suggestions that device-device coupling might be utilized in a cellular-automata scheme, alas, without an accompanying proposal for a specific implementation [4].

### *2.1 A quantum-dot cell*

The Quantum-Dot Cellular Automata (QCA) scheme is based on cells which contain quantum dots [3], as schematically shown in Fig. 1(a). The quantum dots are shown

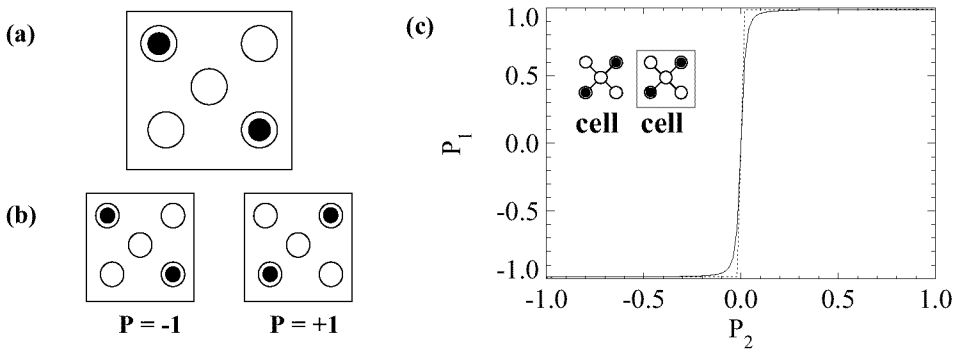


**Fig 1.** (a) A quantum-dot cell consisting of five dots is occupied by two electrons. (b) The two distinct ground-state configurations with their polarizations. (c) Cell-cell coupling characteristics.

as the open circles which represent the confining electronic potential. In the ideal case, each cell is occupied by two electrons, schematically shown as the solid dots, and each electron is allowed to tunnel between the individual quantum dots in a cell, but not between neighboring cells.

This quantum-dot cell represents an interesting dynamical system. The two electrons experience their mutual Coulombic repulsion, yet they are constrained to occupy the quantum dots. If left alone, they will seek, by tunneling between the dots, the configuration corresponding to the physical ground state of the cell. It is clear that the two electrons will tend to occupy different dots because of the Coulomb energy cost associated with bringing them together in close proximity on the same dot. It is easy to see that the ground state of the system will be an equal superposition of the two basic configurations with electrons at opposite corners, as shown in Fig. 1(b).

### *2.2 Cell-cell coupling*

The properties of an isolated cell were discussed above. The two polarization states of the cell will not be energetically equivalent if other cells are nearby. Here, we study the interactions between two cells, each occupied by two electrons. The electrons are allowed to tunnel between the dots in the same cell, but not between different cells. Coupling between the two cells is provided by the Coulomb interaction between electrons in different cells.

Figure 1(c) shows how one cell is influenced by the state of its neighbor. The inset shows two cells where the polarization of cell 1 (P1) is determined by the polarization of its neighbor (P2). Cell polarization P2 is presumed to be fixed at a given value, corresponding to a certain arrangement of charges in cell 2, and this charge distribution exerts its influence on cell 1, thus determining its polarization P1. The important finding here is the strongly non-linear nature of the cell-cell coupling. Cell 1 is almost completely polarized even though cell 2 might only be partially polarized.

### *2.3 QCA logic*

Based upon the bistable behavior of the cell-cell coupling, the cell polarization can be used to encode binary information. We have demonstrated that the physical interactions between cells may be used to realize elementary Boolean logic functions [5]. Figure 2

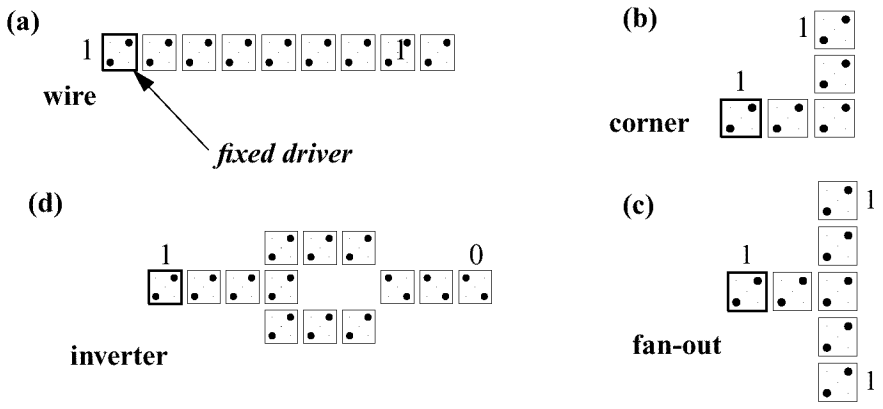


**Fig 2.** Examples of simple QCA arrays for Boolean logic.

shows examples of simple arrays of cells. In each case, the polarization of the cell at the edge of the array is kept fixed; this is the so-called driver cell and it is plotted with a thick border. We call it the driver since it determines the state of the whole array. Without a polarized driver, the cells in a given array would be unpolarized in the absence of a symmetry-breaking influence that would favor one of the basis states over the other. Each figure shows the cell polarizations corresponding to the physical ground state configuration of the whole array. Fig. 2(a) shows that a line of cells allows the propagation of information, thus realizing a binary wire. Note that only information but no electric current flows down the line, which results in low power dissipation. Information can also flow around corners, as shown in Fig. 2(b), and fan-out is possible, shown in Fig. 2(c). Cells which are positioned diagonally from each other tend to anti-align. This feature is employed to construct an inverter as shown in Fig. 2(d). In each case, electronic motion is confined to within a given cell, but not between different cells. Only information, and not charge, is allowed to propagate over the whole array.

These quantum-dot cells are an example of quantum-functional devices. Utilizing quantum-mechanical effects for device operation may give rise to new functionality. Figure 3 shows the fundamental QCA logical device, a three-input majority gate, from which more complex circuits can be built. The central cell, labeled the device cell, has three fixed inputs, labeled A, B, and C. The device cell has its lowest energy state if it assumes the polarization of the majority of the three input cells. The difference between input and outputs cells in this device, and in QCA arrays in general, is simply that inputs are fixed and outputs are free to change. The inputs to a particular device can come from previous calculations or be directly fed in from array edges. Using conventional circuitry, the design of a majority logic gate would be significantly more complicated, being composed of some 26 MOS transistors It is possible to "reduce" a majority logic gate by fixing one of its three inputs in the 1 or 0 state. In this way, a reduced majority logic gate can also serve as a programmable AND/OR gate. The new physics of quantum mechanics gives rise to new functionality, which allows a rather

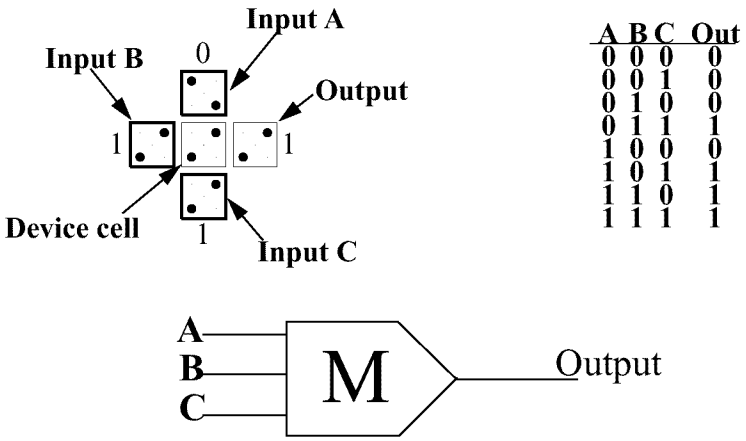


| A | B | C | Out |
|---|---|---|---|
| 0 | 0 | 0 | 0 |
| 0 | 0 | 1 | 0 |
| 0 | 1 | 0 | 0 |
| 0 | 1 | 1 | 1 |
| 1 | 0 | 0 | 0 |
| 1 | 0 | 1 | 1 |
| 1 | 1 | 0 | 1 |
| 1 | 1 | 1 | 1 |

**Fig 3.** QCA Majority Logic gate with its truth table and logic symbol.

compact realization of majority logic.

### *2.4 Quantum-dot cellular nonlinear networks*

In addition to employing QCA cells to encode binary information, these cells may also be used in an analog mode. Each cell interacts with its neighbors within a certain range, thus forming what we call a Quantum-Dot Cellular Nonlinear Network (Q-CNN) [6]. This way of viewing coupled cells as a nonlinear dynamical system is similar to Cellular Nonlinear (or, Neural) Networks (CNN), which are locally-interconnected structures implemented using conventional circuitry [7]. Each cell is described by appropriate state variables, and the dynamics of the whole array is given by the dynamical law for each cell, which includes the influence exerted by the neighbors on any given cell.

## 3 Possible quantum-dot cell implementations

### *3.1 Gate-controlled quantum dots*

The fabrication of a QCA cell by split-gate technology is a challenging problem, yet appears to be within reach of current lithographic capability [8]. Figure 4 shows a possible physical realization which is based on electrostatic confinement provided by a top metallic electrode. The key implementation challenges are (i) to gain sufficient gate control in order to define quantum dots in the few-electron regime, and (ii) to place these dots sufficiently close to each other in order to make coupling possible [9]. Using these techniques, it is conceivable that coupled-dot cells may be realized in a variety of materials systems, such as III-V compound semiconductors, Si/SiGe heterolayers, and $Si/SiO_2$ structures.

### *3.2 Rings of metallic tunnel junctions*

Single-electron tunneling phenomena may also be observed in metallic tunnel junctions, also schematically shown in Fig. 4. The tunnel junctions are represented by the capacitor symbols, indicating that they are characterized by their capacitance and tunnel resistance.

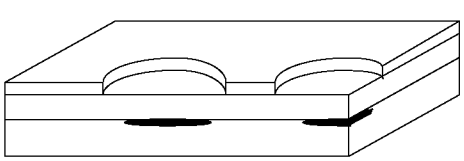

Semiconductor Heterostructures

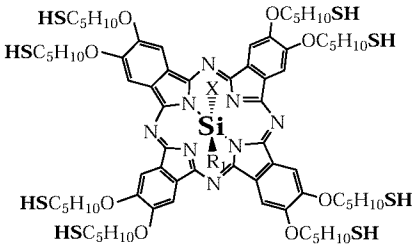


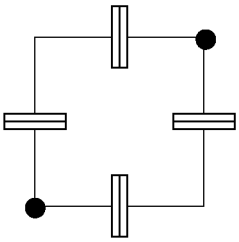

Rings of Metallic Tunnel Junctions

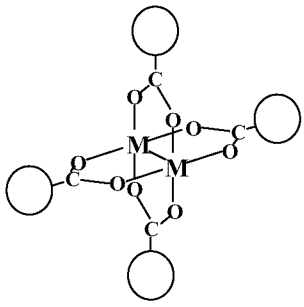

Molecular Structures

**Fig 4.** Possible QCA implementations using gate-confined quantum dots, rings of metallic tunnel junctions, and molecular structures.

The metallic droplets themselves are the "wires" between the tunnel junctions. Consider now that two extra electrons are added to such a cell, as schematically shown. This cell exhibits precisely the same two distinct ground state configurations as the semiconductor cell discussed above citelt:94. In addition, the cell-cell coupling, which is purely capacitive, also shows the same strongly non-linear saturating characteristic. The metallic tunnel-junction cell may be used as a building block for more complicated structures, in a fashion completely analogous to the semiconductor implementations. QCA behavior in such structures has been demonstrated in recent experiments [11].

### *3.3 Possible molecular implementation*

QCA room temperature operation would require molecular-scale implementations of the basic cell. In previous work by Fehlner and co-workers, a candidate for such a prototypical molecular cell has been synthesized and crystallographically characterized [12]. As schematically illustrated in Fig. 4 (bottom diagram), these molecular substances with the formula $M_2\{(CO)_9Co_3CCO_2\}_4$, where M = Mo, Mn, Fe, Co, Cu, consist of square arrays of transition metal clusters, each containing three cobalt atoms. Another candidate for QCA implementation are phthalocyanine molecules, also illustrated in Fig. 4 (top diagram), which have recently been synthesized and characterized [13].

## 4 Conclusion

We have developed a novel nanoelectronic scheme for computing with coupled quantum dots, where information is encoded by the arrangement of single electrons. We have shown that such structures, the so-called Quantum-Dot Cellular Automata, may used

for binary information processing. In addition, an analog version is also possible, the so-called Quantum-Dot Cellular Nonlinear Networks, which exhibit wave phenomena. We have discussed possible realizations of these structures in a variety of semiconductor systems (including GaAs/AlGaAs, Si/SiGe, and $Si/SiO_2$), rings of metallic tunnel junctions, and candidates for molecular implementations.

*Acknowledgments*

The work reviewed in this paper represents the collective effort of the *Notre Dame NanoDevices Group*, specifically Profs. Craig Lent, Gary Bernstein, Greg Snider, Jim Merz, and Jerry Iafrate. On the systems aspects of this work, I gratefully acknowledge my collaborators Profs. Árpád Csurgay, Yih-Fang Huang, and Ruey-Wen Liu.

## References

[1] Semiconductor Industry Association 1994 and 1997 *The National Technology Roadmap for Semiconductors* (Sematech, Austin TX).
[2] R. W. Keyes 1987 *The Physics of VLSI Systems* (Addison-Wesley).
[3] C. S. Lent, P. D. Tougaw, W. Porod, and G. H. Bernstein, *Nanotechnology* **4** 49–57 (1993).
[4] D. K. Ferry and W. Porod, *Superlatt. Microstruct.* **2** 41 (1986).
[5] C. S. Lent, P. D. Tougaw, and W. Porod, *Proc. Workshop on Physics and Computation, PhysComp94* (IEEE Computer Society Press) pp 1–9, 1994.
[6] W. Porod, C. S. Lent, G. Toth, H. Luo, Á. Csurgay, Y.-F. Huang, and R.-W. Liu, *Proceedings of the 1997 IEEE International Symposium on Circuits and Systems: Circuits and Systems in the Information Age* 1997.
[7] L. O. Chua and L. Yang, *IEEE Trans. Circuits Syst.* **CAS 35** pp 1257–1272; and *ibid.* pp 1273-1290 1988.
[8] G. H. Bernstein, G. Bazán, M. Chen, C. S. Lent, J. L. Merz, A. O. Orlov, W. Porod, G. L. Snider, and P. D. Tougaw, *Superlatt. Microstruct.* **20** 447–459 (1996).
[9] M. Chen and W. Porod, *J. Appl. Phys.* **78** 1050–1057 (1995).
[10] C. S. Lent and P. D. Tougaw, *J. Appl. Phys.* **75** 4077–4080 (1994).
[11] A. O. Orlov, I. Amlani, G. H. Bernstein, C. S. Lent, and G. L. Snider, *Science* **277** 928 (1997).
[12] W. Cen, P. Lindenfeld, and T. P. Fehlner, *J. Am. Chem. Soc.* **114** 5451–5452 (1992).
[13] M. Lieberman and Z. Li, submitted to *Supramolecular Science* (1998).

Ioffe Institute
6th Int. Symp. "Nanostructures: Physics and Technology"
St Petersburg, Russia, June 22–26, 1998.



# Generation and recombination in semimetallic heterostructures

A. Shik†, *M. Singh*‡ and W. Lau‡
† Ioffe Physico-Technical Institute, St.Petersburg, Russia
‡ Department of Physics, University of Western Ontario, London, Canada

Heterojunctions InAs-GaSb belong to the most interesting objects in the modern semiconductor physics [1]. Due to the partial overlapping of the InAs conduction band with the GaSb valence band, a semimetallic electron-hole system is formed at the interface. Contrary to ordinary semimetals (Bi), electron and hole systems in these heterostructures are spatially separated. That is why the current flow through single heterojunctions and multilayer heterostructures is governed by generation-recombination processes at the InAs-GaSb interface.

The aim of the present work is to calculate the interface generation-recombination (GR) rate. We considered the three-band Kane model Hamiltonaian [2] within the envelope-function approximation to calculate GR rate. We found that the generation-recombination processes in semimetallic heterojunctions are very different compared to those in ordinary semiconductors, p-n-junctions and other heterojunctions. In particular, the creation of electron-hole pairs requires no additional energy and, hence, the generation rate must have no activation temperature dependence. An electron of InAs reaching the interface can either reflect back or with some probability transmit into the valence band of GaSb. Such a transition is equivalent to a recombination of elelctron-hole pair. The process when electrons from the valence band of GaSb penetrate into InAs, is equivalent to the generation of an electron-hole pair at the interface. So, generation-recombination at the interface does not require the presence of any third body (photon, phonon, recombination center, etc.).

We applied the present theory to describe the conduction processes in heterojunctions n-InAs–p-GaSb. We found that the current-voltage characteristics of the junction n-InAs–p-GaSb have the properties of an Ohmic contact, in agreement with the experimental results [3]. As the applied voltage $U$ increases, the current-voltage characteristics become non-linear and finally saturate for $eU > \Delta$ at the value independent of the temperature. The results obtained above can also be applied to the InAs–GaSb superlattices. If the thickness of superlattice layers is of order of 100 Å or more, the superlattice is in a semimetallic state and contains alternating layers with high electron and hole concentration. It is usually assumed that the superlattice conductivity is provided by formation of electron and hole minibands. However, at large superlattice periods miniband conductivity will be very small. In this case we may expect that the conductivity in InAs layers will be provided by electrons, in GaSb – by holes and the total superlattice conductivity will be governed by generation-recombination processes at the interfaces. As a result the superlattice conductivity per unit area will be inversely proportional to the number of layers.

## References

[1] M. Altarelli, in: *Optical Properties of Narrow-Gap Low-Dimensional Structures*, edited by C. M. Sotomayor-Torres, et al. (Plenum Press, 1987), p. 15.
[2] P. Voisin, refeence 1, p. 85.
[3] H. Sakaki, et al. *Appl. Phys. Lett.* **31**, 211 (1977).

Ioffe Institute
6th Int. Symp. "Nanostructures: Physics and Technology"
St Petersburg, Russia, June 22–26, 1998.



# Spectral hole burning of $Eu^{2+}$ in selectively doped $CaF_2$:Eu/$CdF_2$ superlattices

*S. V. Gastev*†, A. Yu. Khilko†, N. S. Sokolov†, S. M. Suturin†
and R. S. Meltzer‡
† Ioffe Physico-Technical Institute, RAS, St. Petersburg, Russia
‡ University of Georgia, Athens, GA 30602, USA

## Introduction

It has been recently shown [1] that $Eu^{2+}$ $4f^6 5d \rightarrow 4f^7$ photoluminescence (PL) quenching in $CdF_2/CaF_2$:Eu superlattices (SL) grown on Si(111) [2] is due to the tunneling of electrons from $4f^6 5d$ excited state of $Eu^{2+}$ to the conduction band of the neighboring $CdF_2$ layer. The probability of tunneling for an electron from an $Eu^{2+}$ ion residing at $CaF_2/CdF_2$ interface at distance $z$, through a barrier $\Delta E$ is given by eq. (1):

$$W_t = \frac{2\Delta E}{\pi\hbar} \exp\left(-\frac{z}{z_0}\right), \qquad z_0 = \sqrt{\frac{\hbar}{8m\Delta E}} \tag{1}$$

where $\Delta E \sim 0.3$ eV [1] is the thermal ionization energy of the $Eu^{2+}$ $4f^6 5d$ excited state in $CaF_2$ and $z_0 \sim 0.2$ nm (supposing $m = m_0$). Using eq. (1) one can estimate that at a distance $z_{crit} \sim 3.2$ nm (10 monolayers (ML) of fluoride) the probability of tunneling $W_t$ equals the probability of radiative recombination $W_R \sim 2 \times 10^6$ $s^{-1}$ [3].

It is known that hole burning spectroscopy is very usefull for investigating dynamic processes in the excited state. However most of such experiments have been carried out in bulk crystalls. In this paper we investigate the burning of spectral holes in the $Eu^{2+}$ zero-phonon line in doped SLs, first observed in [4]. Two mechanisms of hole burning are considered: the tunneling-assisted and two-step photoionization processes. To separate these, both homogeniously and selectively doped SLs are studied. It is shown that relative contribution of the two processes depends strongly on the spatial distribution of $Eu^{2+}$ ions in the fluorite layer.

## Experiments and discussion

For our studies of hole burning three SLs were grown as described in [2]:

| | | | | | |
|---|---|---|---|---|---|
| SL #24 | [$CdF_2$ 60 ML \| | | \| $CaF_2$ : Eu 60 ML \| | | ]×8 \| Si(111) |
| SL #60 | [$CdF_2$ 60 ML \| | $CaF_2$ 10 ML | \| $CaF_2$ : Eu 40 ML \| | $CaF_2$ 10 ML | ]×8 \| Si(111) |
| SL #95 | [$CdF_2$ 20 ML \| | | \| $CaF_2$ : Eu 20 ML \| | | ]×8 \| Si(111) |

In structures #24 and #95, $CaF_2$ layers were uniformly doped with $Eu^{2+}$. In sample #60, a spacer of pure $CaF_2$ was introduced at each $CaF_2/CdF_2$ interface, so that only central part of each $CaF_2$ layer was doped. The concentration of $Eu^{2+}$ ions was $2 \times 10^{19}$ $cm^{-3}$ ($\sim 0.1$ mol.%). Band energy level diagrams of these SLs are presented in Fig. 1.

From eq. (1) it is seen that $W_t$ becomes considerably less than $W_R$ for ions located more than 10 ML from the interface. Taking into consideration the high excitation power (8 ns laser pulses each carrying 0.1 mJ focused in a spot 1mm in diameter) and the large cross-section of the $4f^6 5d \rightarrow CaF_2$ conduction band transition ($\sigma_{ex} \sim 10^{-19}$ $cm^{-2}$

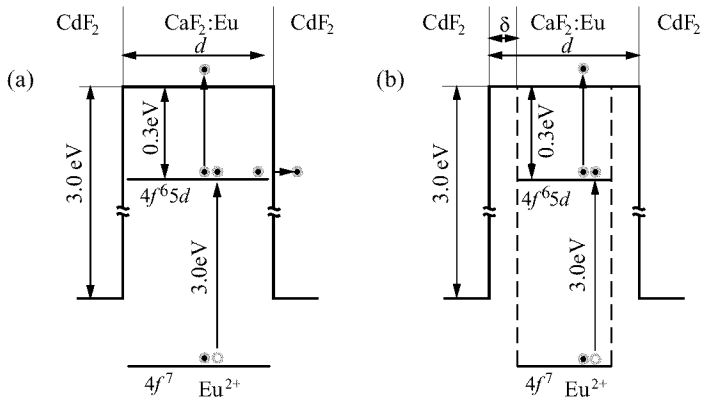


**Fig 1.** Energy levels of $Eu^{2+}$ in $CdF_2/CaF_2$:Eu superlattice (a) uniformly doped SLs #24 and #95, (b) selectively doped SL #60.

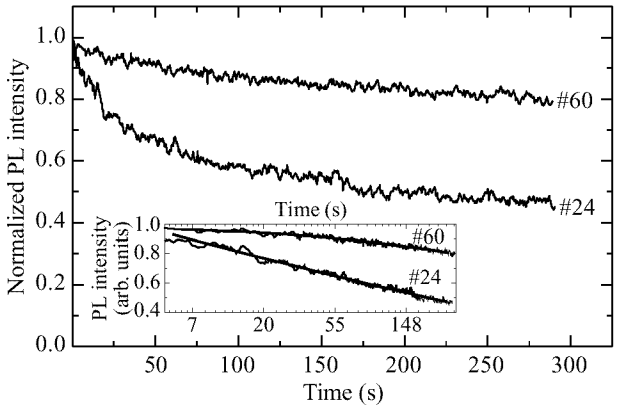


**Fig 2.** PL behavior in SLs #60 and #24 under continuos resonant excitation of the $4f^7 \rightarrow 4f^6 5d$ transition with a pulsed laser ($\lambda = 413.6$ nm) at $T = 2$ K. The inset represents the same dependences with a logarithmic scale.

if excited with $\lambda = 413$ nm photons), we suppose that a two-step photoionization process takes place with a probability for the second step of $W_{PI} \sim 10^5$ $s^{-1}$.

Both tunneling to the $CdF_2$ layers and two-step ionization with further thermalization of electrons from the $CaF_2$ conduction band to the $CdF_2$ wells will decrease the number of Eu ions in the divalent state. This will result in quenching of $Eu^{2+}$ PL (measured from its vibronic sideband luminescence) under resonant excitation of the f–d transition. Fig. 2 shows that under the same excitation conditions the quenching effect is considerably stronger in homogeneously doped sample #24 than in the selectively doped #60. The logarithmic behavior of the quenching for sample #24 (inset on Fig. 2) provides convincing evidence for the dominant role of the tunneling-assisted photoionization [1]. For sample #60, with no $Eu^{2+}$ ions residing near the interface, the tunneling process is less effective while the rate of two-step photoionization is the same as that in sample #24.

Excitation of the f–d transition was carried out with $\lambda = 413$ nm laser radiation having a spectral width of 0.2 $cm^{-1}$ (6 GHz) which is considerably less than the zero-

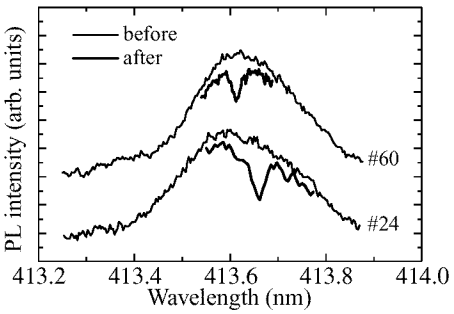


**Fig. 3.** PL excitation spectra of $4f^7 \rightarrow 4f^6 5d$ transition in SLs #24 and #60 before and after the hole burning. Laser irradiation is 5 times weaker than used for the hole burning. $T = 2$ K.

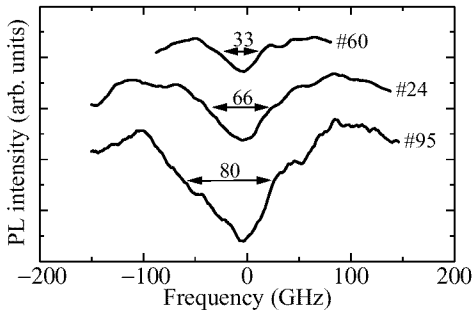


**Fig. 4.** The shape of spectral holes in the excitation spectra in SLs #60, #24, #90 after burning for 400 s.

phonon PL line width of $Eu^{2+}$ ($\sim$ 18 $cm^{-1}$ in the SLs studied). For this reason the PL quenching shown in Fig. 2 results in the burning of a hole in the $Eu^{2+}$ zero-phonon line (Fig. 3). Fig. 3 shows practically the same band shape for both SLs. The positions of their maxima demonstrate the coherentness of the SLs to their substrates while their relatively small width is evidence for the high degree of structural perfection of the $CaF_2$ layers [5]. The width of spectral holes varies for different SLs (Fig. 4): from 33 GHz in sample #60 to $\sim$ 80 GHz in #95 and greatly exceeds the value of 0.5 GHz obtained for persistent hole burning in bulk $CaF_2$:Eu [6].

To explain the broadening of the spectral holes, one must take into consideration specific features of SLs arising from the presence of the $CdF_2$ layers. Because the bottom of conduction band lies at $\sim$ 2.6 eV below the $4f^6 5d$ level of $Eu^{2+}$ (Fig. 1), the $CdF_2$ layers act as traps for both tunneling electrons and for electrons thermalized after a two-step photoionization process. The electron transfer results in the formation of a positively charged layer near the interface consisting of trivalent Eu ions and a negative charge of quasi-free electrons accumulated in $CdF_2$.

Narrow line laser radiation excites only those $Eu^{2+}$ ions whose f–d transition energy is exactly equal to that of the photons. However after a fraction of these ions become ionized the charge separation occurs near the interface inducing an internal electric field. A Stark-shift of the $Eu^{2+}$ f–d transition energy [7] may result in involvment of initially non-resonant Eu ions into the ionization process. To estimate the role of the Stark shift it seems reasonable to use the value of internal electric field $E_{int}$ at the interface. This can be obtained after calculating the number of ionized Eu ions obtained by comparing the area of the spectral hole with the area of the whole zero-phonon band (Fig. 3). Considering the interface area as a plane capacitor we obtain $E_{int} = 10^6$ V/cm. Using the value of $5 \times 10^{-13}$ $cm^{-1}(V/cm)^{-2}$ for the quadratic Stark shift of the $f-d$ transition energy of the centrosymmetric $Eu^{2+}$ cubic sites in $CaF_2$ [8], we estimate the shift in our SL to be about 0.5 $cm^{-1}$ ($\sim$ 15 GHz).

This shift allows us to explain 30 GHz wide spectral hole in sample #60 (Fig. 4). However, in order to explain the wider spectral hole widths in samples #24 and #95 (66 GHz and 80 GHz respectively) other processes must be considered. The remarkable feature of SLs #24 and #95 is that the ionization of Eu is mainly ascribed to tunneling which is known to be considerable in a 20 ML wide layer at each interface. The larger

fraction of Eu ions residing in those layers, the shorter will be the time for the PL intensity to decrease and come into saturation. Here we assume that there are two processes of Eu ionization taking place with different rates: fast tunneling from the interface region and two-step photoionization which is noticeably slower.

Excitation of those $Eu^{2+}$ ions whose zero-phonon f–d transition is resonant with the laser dominates. In addition, some less probable phonon assisted transitions may excite Eu ions whose zero-phonon line is not resonant with the laser. In spite of the relatively small rate, those transitions may result in some broadening due to additional hole burning on the both sides of the main spectral hole, provided we carry out the hole burning long enough to saturate the hole burning in the zero- phonon transitions. Then the slow phonon-assisted processes may become noticeable. The situation is similar to that which occurs for light detection by a photographic plate.

The fraction of Eu ions located in the vicinity of the interface increases considerably in the sequence of SLs #60, #24 and #95 leading to a corresponding reduction in the time for saturation of the ionization of the hole in the zero-phonon line. In this same sequence, the side band features become more pronounced as can be seen from the width of each spectral hole (Fig. 4).

## Conclusions

It is demonstrated that persistent hole burning in the zero-phonon line of $Eu^{2+}$ in SLs of $CaF_2$:Eu/$CdF_2$ with uniformly doped $CaF_2$ layers is mainly due to tunneling of electrons from the $4f^6 5d$ excited state of $Eu^{2+}$ to the conduction band of adjacent $CdF_2$ layer. However in selectively doped SLs, the two-step photoionization process dominates in the formation of spectral holes. Two mechanisms of spectral hole broadening were discussed. These are the Stark-shifting of the $Eu^{2+}$ f–d transition energy induced by internal electric field and phonon assisted transitions.

The authors appreciate valuable discussions with Dr. S. A. Basun and the assistance provided by Mr. K. Hong. This work was supported by grants from Russian Foundation for Basic Research, the Russian Ministry of Science and the U.S. National Science Foundation.

## References

[1] N. S. Sokolov, S. V. Gastev, A. Yu. Khilko, S. M. Suturin, I. N. Yassievich, J. M. Langer, A. Kozanecki, (to be published).
[2] R. N. Kyutt, A. Yu. Khilko, N. S. Sokolov, *Appl. Phys. Lett.* **70** 1563, (1997); A. Yu. Khilko, S. V. Gastev, R. N. Kyutt, M. V. Zamoryanskaya, N. S. Sokolov, *Appl. Surf. Sci.* **123/124** 595–598 (1998).
[3] J. F. Owen, P .B. Dorain, T. Kobayasi, *J. Appl. Phys.* **52** 1216–1223 (1981).
[4] D. M. Boye, Y. Sun, R. S. Meltzer, S. P. Feofilov, N. S. Sokolov, A. Yu. Khilko, J. C. Alvarez, *J. Lum.* **72-74** 290–291 (1997).
[5] N. S. Sokolov, E. Vihil, S. V. Gastev, S. V. Novikov, N. L. Yakovlev, *Fiz. Tverd. Tela* **31** 75 (1989).
[6] D. M. Boye, R. M. Macfarlane, Y. Sun, R. S. Meltzer, *Phys. Rev. B* **54** 6263 (1996).
[7] S. A. Basun, M. Raukas, U. Happek, A. A. Kaplyanskii, J. Rennie, J. C. Vial, W. M. Yen, R. S. Meltzer, *Phys. Rev. B* **56** 12992–12997 (1997).
[8] A. A. Kaplyanskii, V. N. Medvedev, *Pis'ma JETP*, **2** 209–212 (1965).

Ioffe Institute
6th Int. Symp. "Nanostructures: Physics and Technology"
St Petersburg, Russia, June 22–26, 1998.



# Details of valence band structure of p-GaAs/AlGaAs symmetric quantum wells unraveled by uniaxial compression

*O. P. Hansen*†, K. V. Pedersen†, A. M. Savin‡, and N. Ya. Minina‡
† Oersted Laboratory, Niels Bohr Institute for Astronomy, Physics and Geophysics, Universitetsparken 5, DK-2100 Copenhagen, Denmark
‡ Department of Low Temperature Physics, Moscow State University, 119899 Vorobyevy, Moscow, Russia

**Abstract.** Uniaxial compression has been applied to symmetrically grown quantum wells of GaAs with Be-modulation-doped barriers of AlGaAs. We demonstrate how the analysis of the influence of uniaxial compression on the Shubnikov–de Haas oscillations can unravel details of the valence band structure; e.g. the question of whether or not the ground state is doubly degenerate or is consisting of two slightly different bands. We find the latter to be the case, and that the carrier densities in both of the two bands decrease under the application of the uniaxial compression; however, with different pressure coefficients.

## Introduction

The spin-orbit coupling has important influence on the band structure of III–V semiconductors. Especially so, when the valence band is concerned. This applies to bulk materials as well as to heterostructures. For the latter, in the case of a single heterostructure (triangular quantum well) the interface electric field gives rise to a so-called *interface spin-orbit coupling* or *Rashba asymmetry* [1, 2], which causes a splitting of the $m_J$-degeneracy away from $k = 0$. Contrary to this, in the case of a double heterostructure (rectangular quantum well), there is no electric field in the well-provided it has a flat bottom — and the $m_J$-degeneracy remains. The problem with this nice picture is the lack of control of the potential shape details in actual samples. The only information which is usually accessible concerns the sequence of layers in the heterostructure samples. Thus, if there is just one interface, say GaAs/AlGaAs, the potential might coarsely be described as 'triangular', and — if there are two interfaces AlGaAs/GaAs/AlGaAs — as 'rectangular'. The first search to see the influence of the two potential types on the splitting of the $m_J$-degeneracy was made in magnetotransport, e.g.: Shubnikov–de Haas oscillations [3]. The feature looked for was a doubling of the frequency of $B^{-1}$-oscillations in fields strong enough to split the degeneracy expected for a rectangular well. The result was successful in the sense that a doubling was observed in rectangular wells, but not in triangular ones.

We have previously analysed our measurements of the influence of uniaxial compression on the Shubnikov–de Haas oscillations observed in rectangular quantum wells by looking at the ratio of $B^{-1}$-frequencies [4, 5]. Our conclusion was — with some reservations — that this influence was modest. By the present communication we want to present a new analysis, in which we give up the focus on the frequency ratio. By this new analysis we demonstrate how uniaxial compression can be used to unravel some finer details of the valence band ground state in rectangular quantum wells. Namely

that, instead of a doubly degenerate band, it has two closely lying bands which behave differently under uniaxial compression.

## 1 Samples and measurements

The wafer was grown by molecular beam epitaxy on a (100) semiinsulating GaAs substrate. The grown layer sequence was as follows: 0.5 $\mu$m GaAs, 0.2 $\mu$m $Al_{0.5}Ga_{0.5}$As, 5 nm $Al_{0.5}Ga_{0.5}$As:Be($2 \times 10^{18}$ cm$^{-3}$), 25 nm $Al_{0.5}Ga_{0.5}$As, 10 nm GaAs, 25 nm $Al_{0.5}Ga_{0.5}$As, 5 nm $Al_{0.5}Ga_{0.5}$As:Be($2 \times 10^{18}$ cm$^{-3}$), 0.1 $\mu$m $Al_{0.5}Ga_{0.5}$As, and 10 nm GaAs:Be($4 \times 10^{18}$ cm$^{-3}$), i. e.: A 10 nm GaAs layer is surrounded by layers of $Al_{0.5}Ga_{0.5}$As, which are doped by Be in 5 nm thick layers placed 25 nm away to both sides of the GaAs layer. This fully symmetric layer structure is identical to the one reported on in [4], and deviates slightly from the one in [5] which had one of the Be-doped layers placed 50 nm away from the GaAs layer. At ambient pressure the sample has $3.38 \times 10^{15}$m$^{-2}$ holes as determined from Hall measurements. Details of the experimental technique have been reported in [6]. The ranges of the experimental parameters are: 0–5 T, 0–3.4 kbar compression along (110), 1.45 K.

## 2 The Shubnikov–de Haas oscillations and the analysis

In Fig. 1 we show the Shubnikov–de Haas oscillations of the square resistance $R_{sq}$ with the reciprocal magnetic field as the horizontal variable, and with the uniaxial compression as parameter. We are obviously not dealing here with a single oscillation

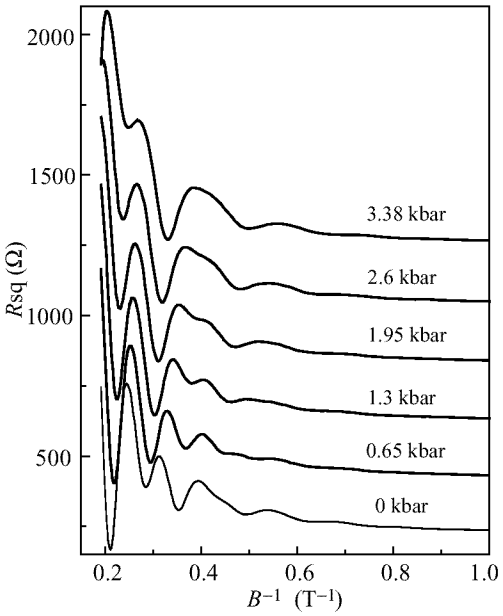


**Fig. 1.** Shubnikov–de Haas oscillations versus inverse magnetic field with the uniaxial (110) compression as parameter.

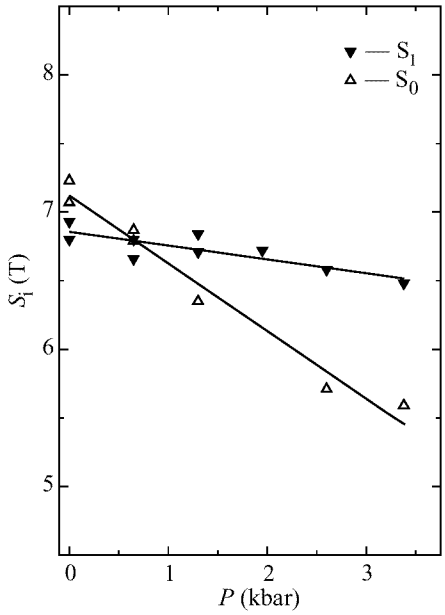


**Fig. 2.** SdH frequencies for the two bands versus uniaxial (110) compression. The straight lines present least-squares fits: $S_0 = 7.12 - 0.49P$ and $S_1 = 6.86 - 0.10P$, where S is in tesla and P in kbar.

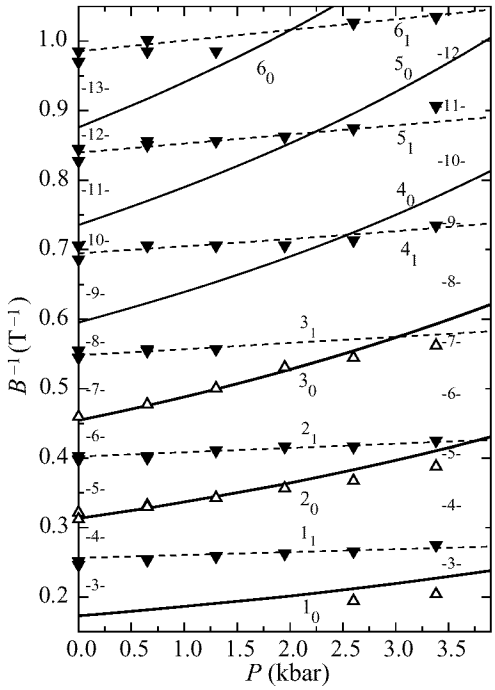


**Fig 3.** $B^{-1}$-positions of the SdH-maxima versus uniaxial (110) compression. The curves are calculated from the frequencies stated at Fig. 2 and the belonging phase factors, full: $B^{-1} = (n_0 + 1/2 - 0.263)/S_0$, dotted: $B^{-1} = (n_1 + 1/2 + 0.263)/S_1$. Filling factors at P = 0 and 3.38 kbar are shown as $-\nu-$; they are calculated from the Hall densities.

frequency. In the transition region from 0.4 to 0.5 $T^{-1}$ the oscillation pattern shifts to a higher frequency in the high-field range. In our previous analysis we found that the frequency ratio was close to 2, and was only modestly influenced by the uniaxial compression [5]. However, a strange feature was observed: The minima in the range of low fields are located at field values corresponding to *odd* filling factors, and these change to *even* at the maximal value of the uniaxial compression.

Now, having another look at the oscillation patterns, we note that the maxima moves differently under the application of the uniaxial compression: The maxima which at 0 kbar are located at 0.3 and 0.4 $T^{-1}$ move closer to each other, while those at 0.25 and 0.3 $T^{-1}$ move apart. With this observation as a guideline we then analysed the oscillations, assuming that they arise from two bands, each of which having a characteristic pressure dependence. The result is displayed in Fig. 2, where we show the Shubnikov–de Haas frequencies of the two bands as function of the uniaxial compression. As would be expected, the two frequencies are rather close to each other; but the dependence on pressure reveals a distinct difference. The carrier density calculated from the sum of the frequencies corresponds well to the Hall density.

In Fig. 3 we show the $B^{-1}$ — positions of the maxima versus pressure, $n_0$ and $n_1$ indicating the Landau level numbers of the two bands. Positions of minima calculated from the Hall densities at zero pressure and at maximum pressure are shown by symbols $-\nu-$, where $\nu$ indicates the filling factor. Comparing this figure with Fig. 1 we observe

the following features: Starting at the largest fields, the SdH-minimum corresponding to $\nu = 3$ falls between the maxima $n_0 = 1$ and $n_1 = 1$. The next minimum, $\nu = 4$, falls between $n_1 = 1$ and $n_0 = 2$, and like the $\nu = 3$ minimum it is clearly displayed at all pressures. The $\nu = 5$ falls between $n_0 = 2$ and $n_1 = 2$. On increasing pressure, these two maxima approach each other and the minimum becomes squeezed between them. The $\nu = 6$ minimum falls between the closely spaced $n_1 = 2$ and $n_0 = 3$ maxima at P = 0; however, as P increases, these two maxima go apart, and so the minimum becomes more pronounced on increasing P. Contrary to this, the $\nu = 7$ minimum at P = 0 falls between the maxima $n_0 = 3$ and $n_1 = 3$ and does show up; however, as P increases this minimum is squeezed between the two maxima, as was the case for $\nu = 5$. In this way we have reached an understanding of the *odd-even* problem mentioned above.

In conclusion, through investigation of SdH effect in symmetrically grown quantum wells under uniaxial compression we have demonstrated that the ground heavy hole state, instead of being doubly degenerate, consists of two slightly splitted bands.

*Acknowledgements*

This work was supported by grant 97-02-17685 from the Russian Foundation for Basic Research and by grants 9401081 and 9601512 from the Danish Research Council. MBE growth and sample processing was made by C.B. Soerensen, Oersted Laboratory.

## References

[1] Andrada e Silva E. A. de, La Rocca G. C. and Bassani F. *Phys. Rev. B* **50** 8523 (1994).
[2] Bychov Yu. A. and Rashba E. I. *J. Phys. C: Solid State Phys.* **17** 6039 (1984).
[3] Eisenstein J. P., Stoermer H. L., Narayanamurti V., Gossard A. C. and W. Wiegmann *Phys. Rev. Lett.* **53** 2579 (1984).
[4] Hansen O. P., Kraak W., Minina N., Pedersen K. V., Saffian B. and Savin A. M. in *Proceedings of the 21st International Conference on Low Temperature Physics, Prague, 1996, Czech. J. Phys.* **46** Suppl. **S5** 2517 (1996).
[5] Pedersen K. V., Savin A., Hansen O. P. and Minina N. Ya. in *Proceedings of the 10th International Conference on Superlattices, Microstructures, and Microdevices, Lincoln, 1997* to be published in *Phys. Low-Dim. Struct.*
[6] Hansen O. P., Olsen J. S., Kraak W., Saffian B., Minina N. Ya. and Savin A. M. *Phys. Rev. B* **54** 1533 (1996).

Ioffe Institute
6th Int. Symp. "Nanostructures: Physics and Technology"
St Petersburg, Russia, June 22–26, 1998.



# Giant drop of the lattice thermal conductivity due to confinement of acoustic phonons

*A. Balandin* and Kang L. Wang
Device Research Laboratory, Electrical Engineering Department,
University of California – Los Angeles
Los Angeles, California 90095-1594 U.S.A.

**Abstract.** Lattice thermal conductivity of a quantum well was investigated taking into account dispersion of confined acoustic phonon modes. We show that strong modification of phonon group velocities due to spatial confinement leads to significant increase in the phonon relaxation rates and corresponding drop in the the lattice thermal conductivity (13% of the bulk value for 10 nm well). Our theoretical results are consistent with the recent experimental investigations of the thermal conductivity of a 155 nm wide $Si_3N_4$(150 nm)/Si(155 nm)/$SiO_2$(300 nm) quantum well conducted in our group.

## 1 Introduction

Thermal properties of semiconductor nanostructures and superlattices have recently attracted a lot of attention. To a large degree, this is due to a rebirth of the field of thermoelectric materials which was brought about by the emergence of large numbers of new artificially synthesized materials, including those structured on an atomic scale [1]. Recent reports that predicted strong enhancement of the figure of merit [2-3] ZT for semiconductor superlattices and quantum wells treated rigorously only electronic contribution, $\kappa_e$, to the thermal conductivity while ignoring the effects of spatial confinement on lattice contribution $\kappa_l$. In this report, we address the issue of how *spatial confinement of acoustic phonon modes directly modifies the lattice thermal conductivity* in a free-standing quantum well.

## 2 Theory

It is well known that the normal three-phonon scattering processes in which the total momentum is conserved cannot by themselves lead to a finite thermal resistance [4]. Only processes which do not conserve crystal momentum contribute to the lattice thermal resistance. Such processes are boundary scattering, impurity scattering, and three-phonon Umklapp scattering process in which the sum of phonon wave vectors is not conserved but changes by a reciprocal-lattice vector. Due to this reason, we will be primarily interested in examining the effects produced by phonon confinement on the above mentioned resistive processes. The electronic contribution, $\kappa_e$, is assumed to be small in undoped fully depleted semiconductor structures. In order to calculate $\kappa_l$, we use Callaway's expression for the thermal conductivity under the assumption that the resistive processes are dominant. Limiting our consideration to the above mentioned major contributions to the resistive processes, we can write the following relation for the relaxation rate

$$\frac{1}{\tau_C} = \frac{1}{\tau_U} + \frac{1}{\tau_B} + \frac{1}{\tau_I}, \tag{1}$$

where $\tau_U$, $\tau_B$, and $\tau_I$ are the relaxation times due to the Umklapp processes (all allowed channels), boundary scattering, and impurity scattering, respectively. We find the relaxation rate of the U-process for a thermal mode from the first-order perturbation theory. The derivation is somewhat complex and is reported elsewhere. The impurity scattering mechanism, which is affected by spatial confinement the most through the group velocity, is so-called isotope scattering arising from the presence of atoms with different mass. The relaxation time for this type of impurity scattering can be written as

$$\frac{1}{\tau_I} = \frac{V_0\omega^4}{4\pi v_g^3}\sum_i f_i[1-(M_i/M)]^2, \tag{2}$$

where $V_0$ is the volume per atom, $M_i$ is the mass of an atom, $f_i$ is the fractional content of atoms with mass $M_i$ which is different from $M$. The relaxation time for the boundary

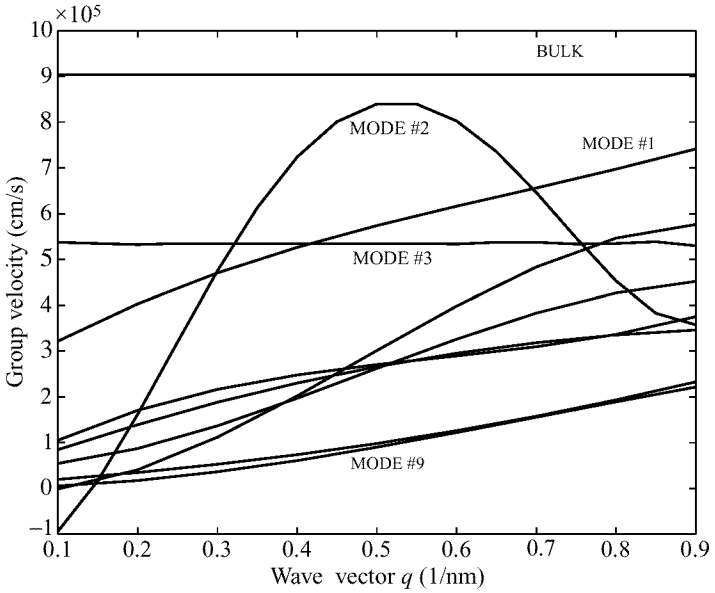


**Fig 1.** Group velocity as a function of the in-plane wave vector for the dilatational modes in a 10 nm wide Si quantum well. The dashed lines show the group velocity for bulk longitudinal acoustic phonon modes.

scattering can be evaluated from the semi-empirical relation $1/\tau_B = v_g/W$, where $W$ is some characteristic thickness of a bulk semiconductor or the width of a quantum well. In order to evaluate relaxation times, we should use the actual dispersion relations and group velocities $v_g \equiv v_g(\omega(q))$ for phonons in a quantum well, where $q$ is the wave vector. The modification of wave vector selection and frequency conservation rules due to the spatial confinement should also be taken into account.

We find confined phonon modes from the elastic continuum approximation [5]. The normal components of the stress tensor on the free-standing quantum well must vanish. These boundary conditions, substituted instead of *periodic boundary conditions* of the bulk material, bring about a significant change to the phonon dispersion and

group velocities. One should note here that a significant modification of phonon modes can be attained not only in a free-standing quantum well but also in a quantum well embedded in rigid material ($Si_3N_4$ for example) or in a heterostructure with relatively large difference of lattice constants. There are three different types of confined acoustic modes characterized by their distinctive symmetries: shear (S) waves, dilatational (D) waves, and flexural (F) waves, as compared to two types of the bulk modes: transverse (T) and longitudinal (L). The group velocities for the S and D modes in a 100 Å wide Si quantum well are shown on Fig. 1. It is easy to see that there are more dispersion and velocity branches for each polarization type as compared to the bulk, and group velocities of all branches decrease. The higher the mode number the smaller the group velocity. Since $\tau_I \propto v_G^3$, even a small decrease in the group velocity leads to a giant increase in phonon relaxation rates. The change of polarization types and the $\omega \equiv \omega(q)$ dependence brings also modifications of the energy and momentum conservation laws. It is known that for isotropic semiconductor only two general types of processes are allowed: $T + T \leftrightarrow L$, or $L + T \leftrightarrow L$. This restriction follows from the requirement that (i) all three interacting modes cannot belong to the same polarization branch, and (ii) the resultant mode should be above two initial (interacting) modes. It turns out that for confined acoustic phonons, the D mode is almost always above the S mode corresponding to the same branch $n$, and the processes $D_n + S_n \leftrightarrow D_n$ and $S_n + S_n \leftrightarrow D_n$ are *allowed* and can be treated by analogy with the bulk processes.

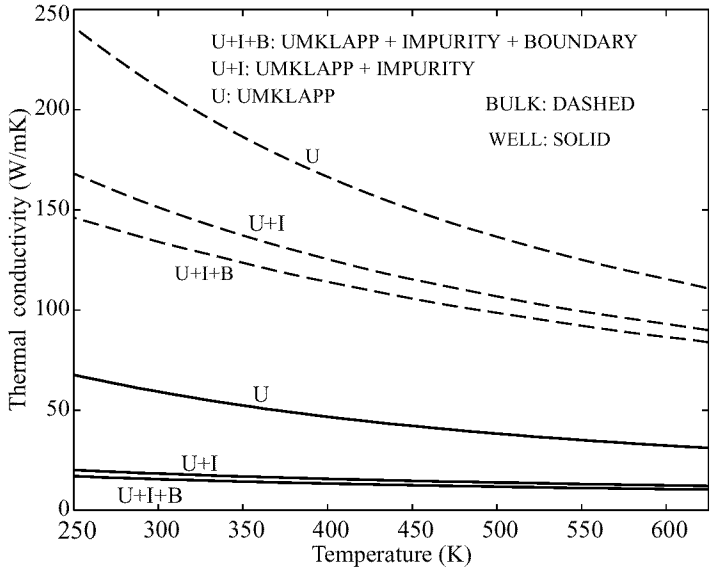


**Fig 2.** Lattice thermal conductivity as a function of temperature for bulk material (dashed) and the quantum well (solid).

## 3 Results and Discussion

We evaluate phonon scattering rates for a bulk Si 10 $\mu$m thick slab and Si 10 nm and 155 nm wide quantum wells. The material parameters used in simulation were the

following: $a = 5.45$ Å, $\rho = 2.42 \times 10^3$ kg/m$^3$, $M = 46.6 \times 10^{-27}$ kg, $n_a \approx 7.3$, $\gamma = 0.56$, and $\theta = 625$ K. Numerical results show that the overall scattering rate increases in a quantum well. This increase is a direct result of the modification of phonon dispersion due to spatial confinement of the phonon modes. The later leads to the reduction of the group velocity which strongly increases the impurity and Umklapp scattering. In Fig. 2 we show the lattice thermal conductivity as a function of the temperature for the quantum well and the bulk material. In order to illustrate the contribution of different scattering mechanisms to the thermal resistivity, the conductivities limited only by the Umklapp scattering and by the Umklapp and impurity scattering are also shown. The overall thermal conductivity of a quantum well at 300 K is about 13% of the bulk Si. The calculated value and temperature dependence of the thermal conductivity are consistent with the results of the experimental investigation recently reported by some of us [6]. The measurements were conducted with a suspended microstructure which served as a thermal bridge. These measurements have shown that the lateral thermal conductivity of a $Si_3N_4$ (150 nm) / monocrystalline Si(155 nm) / $SiO_2$ (300 nm) structure was about 1.5% of the conductivity of the bulk Si and was almost a constant in the temperature range from $T = 293$ K to $T = 413$ K. Although our model assumed a free-standing quantum well, the results can be extended to quantum wells with rigid boundaries by appropriate modification of the boundary conditions. Our model applied to a 155 nm wide Si well gives $k_l = 66.7$ W/m K. For comparison, experimentally measured thermal conductivity of bulk Si is 148 W/m K. This is a significant drop although much less then that observed in the experiment. The temperature dependence of the calculated $k_l$ is very close to the measured one. The discrepancy in the absolute value maybe due to (i) underestimated in our model boundary scattering, (ii) presence of other defect scattering processes [7], or (iii) crystal anisotropy, strain effects and related phonon focusing.

This work was supported by the DoD MURI-ONR program on Thermoelectrics and DoD MURI-ARO program on Low Power Electronics.

## References

[1] For a recent review see G. Mahan, B. Sales, J. Sharp, *Physics Today*, **50** No.3 42 (1997).
[2] L.D. Hicks, M.S. Dresselhaus, *Phys. Rev. B*, **47** 12727 (1993).
[3] L.D. Hicks, T.C. Harman, M.S. Dresselhaus, *Appl. Phys. Lett.*, **63** 3230 (1993).
[4] P.G. Klemens, in *Solid State Physics*, edited by F. Seitz and D. Turnbull (Academic, New York, 1958), Vol. 7, p. 1;
Y.-J. Han, P.G. Klemens, *Phys. Rev. B*, **48** 6033 (1993).
[5] A. Svizhenko, A. Balandin, S. Bandyopadhyay, M.A. Stroscio, *Phys. Rev. B*, Feb. 15, (1998).
[6] X.Y. Zheng, S.Z. Li, M.Chen, K.L. Wang, in Proceed. of IMEC'96, Atlanta, Georgia, Nov. 17-22, 1996.
[7] A. Balandin, K.L. Wang, in proceed. of *American Physical Society*, Los Angeles, CA, USA, March, 1998.

Ioffe Institute
6th Int. Symp. "Nanostructures: Physics and Technology"
St Petersburg, Russia, June 22–26, 1998.



# Linearly polarised photoluminescence in ZnSe/BeTe superlattices with no common atom at the interfaces

*A. V. Platonov*‡, V. P. Kochereshko‡, E. L. Ivchenko‡, D. R. Yakovlev§‡
S. V Ivanov‡, W. Ossau§, A. Waag§ and G. Landwehr§
‡ Ioffe Physico-Technical Institute RAS, St. Petersburg, Russia
§ Physikalisches Institut der Universität Würzburg, 97074 Wurzburg, Germany

**Abstract.** Photoluminescence spectra of type-II ZnSe/BeTe superlattices were studied. A linear polarised photoluminescence has been found in the spectral range of spatially indirect exciton transitions. This observation is interpreted in a model of optical anisotropy of heterostructures with no common atom at interfaces.

A number of publications have appeared recently devoted to studies of an optical anisotropy of heterostructures with no common atom at interfaces. This effect is attributed to the low local symmetry of the single interface between two different zinc-blend type materials. The interface has the $C_{2v}$ symmetry instead of the $D_{2d}$ in the bulk that allows to observe an optical anisotropy in the structure plane [1]. Microscopically the anisotropy can be treated in the terms of a heavy-light hole states mixing on the interface [2]. In a perfect quantum well the contribution from both QW interfaces to the anisotropy compensate each other and no resulting anisotropy can be found. One of the way to observe this anisotropy is to create non equal interfaces in quantum wells. This effect can be realised in heterostructures with no common atom at the interfaces, e.g. ZnSe/BeTe.

In present paper we use a type-II superlattices ZnSe/BeTe to study the in-plane anisotropy. An exciton photoluminescence (PL) of indirect transition between an electron from ZnSe and a hole from BeTe has been investigated.

The samples were grown by MBE on (100)-oriented GaAs substrates. During a growth the type of interfaces was controlled. Three type of ZnSe/BeTe (50/100 Å) × 20 periods samples were grown with BeSe... BeSe, ZnTe... ZnTe or BeSe... ZnTe interfaces.

PL measurements were performed in a temperature range 6–70 K. Photoluminescence was excited by 4416 Å He:Cd laser that is close to a direct exciton in ZnSe [3]. A linearly polarised excitation along [110], [1$\bar{1}$0] and [100] and a circulary polarised excitation were used.

We have found that independently of the polarisation of the excited light the resulting photoluminescence was polarised along [1$\bar{1}$0] direction (see Fig. 1). The degree of this polarisation was determined by the type of the interface. For the structures with nominally equal interfaces ZnTe... ZnTe the degree of polarisation was found to be of 30% and for BeSe... BeSe of 15% or even less. For the structures with non equal interfaces (BeSe... ZnTe) it was about 80%.

For spatially indirect excitons the hole wave function is strongly localised at the interface. This leads to increasing of a heavy-light holes mixing in comparison with type-I heterostructures.

A small value of the linear polarisation in the structures with nominally equal interfaces could be related with a different quality of the direct and indirect interfaces. This non-equality is due to the large difference of the chemical activity of Be to Zn and Se to Te. This leads also to the decreasing of the quality of the (ZnTe) as well as (BeSe) interfaces on the BeTe layer. At the same time on the ZnSe layer both interfaces can be grown of high quality.

A temperature dependence shows a fast suppression of the PL signal and a conservation of the polarisation.

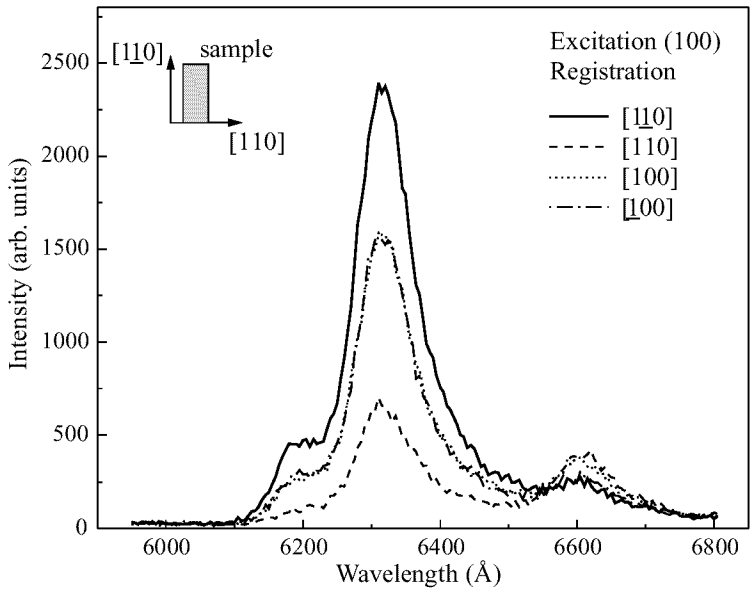


**Fig 1.** PL spectrum of ZnSe/BeTe superlattice with non-equal interfaces ZnTe...BeSe measured at $T = 6$ K.

*Acknowledgment*

The work was supported in part by RFBR grant No. 98-02-18234, the program "Nanostructures" of Russian Ministry of Sciences and by the Deutsche Forschungsgemeinschaft (SFB 410).

## References

[1] O. Krebs, P. Voisin *PRL* **77** 9 1829–1832 (1996).
[2] E. L. Ivchenko, A. A. Toropov *Heavy-Light Hole Mixing in Zinc-Blend Heterostructures with No-Common Atom* , preprint (1998).
[3] A. V. Platonov, D. R. Yakovlev, U. Zehnder, et al. *Acta Physica Polonica A* **92** 1063–1066 (1997).

Ioffe Institute
6th Int. Symp. "Nanostructures: Physics and Technology"
St Petersburg, Russia, June 22–26, 1998.



# Effect of lateral boundary conditions on electron states in tunnel-coupled quantum wells

O. E. Raichev and *F. T. Vasko*
Institute of Semiconductor Physics, NAS Ukraine, Pr.Nauki 45, Kiev, Ukraine

**Abstract.** The electron transport in tunnel-coupled, double-layer nanostructures of a finite size is studied theoretically. The boundary conditions for matrix distribution function of the electrons near edges and contacts are derived. The quantum size effects, associated with the tunnel coherence length, are demonstrated for several kinds of planar, laterally-restricted double-layer systems.

## Introduction

The fabrication of nanostructures based upon two-dimensional (2D) electron layers assumes lateral restriction of 2D electron gas as well as creation of contacts to it. Thus, two types of boundaries, the edges and the contacts, are present in a finite-size 2D system. An investigation of electrical properties of such a system requires a knowledge of boundary conditions for both kinds of boundaries and applications of the boundary conditions to description of the distribution function of the electrons.

In this paper we derive the boundary conditions for double-layer 2D electron systems [1]. A considerable experimental and theoretical interest to these systems is concerned with manifestations of an extra degree of freedom due to the tunnel coupling of electron states. Mathematically, it means that the Hamiltonian of the system is represented by $2 \times 2$ matrix in the left ($l$) and right ($r$) layer basis. As a consequence, the distribution function of the electrons is also a $2 \times 2$ matrix, and the boundary conditions for this function should be of a matrix form. Below we obtain the boundary conditions for columnar wave functions at contacts and edges. Then, we derive the boundary conditions for the matrix Wigner distribution function. Finally, we apply these boundary conditions to calculations of the electric current along a narrow strip [2] formed from a double-layer 2D system and across narrow double-layer regions formed by independently contacted 2D layers [3].

## 1 Wave functions of finite-size double-layer systems

Consider a double-layer system confined in $y$ direction. The free-particle Hamiltonian of the system is written as

$$-\frac{\hbar^2}{2m}\frac{\partial^2}{\partial y^2} + \frac{p_x^2}{2m} + \hat{h}. \tag{1}$$

Here $p_x$ is the electron momentum along $0X$, and $\hat{h} = (\Delta/2)\hat{\sigma}_z + T\hat{\sigma}_x$ is the potential energy matrix expressed through the Pauli matrices $\hat{\sigma}_i$, $\Delta$ is the splitting energy in the absence of tunnel coupling, and $T$ is the tunneling matrix element. The two-component wave function of the Hamiltonian (1) is given by

$$\Psi(y) = \mathcal{G}_+[A_1 e^{ik_+ y} + A_2 e^{-ik_+ y}] + \mathcal{G}_-[B_1 e^{ik_- y} + B_2 e^{-ik_- y}]. \tag{2}$$

Here $\mathcal{G}_\pm$ are the columns determined by parameters $\Delta$ and $T$, and $k_\pm^2 = [2m(\varepsilon \mp \Delta_T/2) - p_x^2]/\hbar^2$ ($\Delta_T = \sqrt{\Delta^2 + (2T)^2}$ is the splitting energy of the tunnel-coupled states). The columns $\mathcal{G}_\pm$ describe symmetrized $\mathcal{G}_+$ and antisymmetrized $\mathcal{G}_-$ electronic states, and $\Psi(y)$ contains a linear combination of these two states.

The coefficients $A_1$, $A_2$, $B_1$, and $B_2$ are to be found from boundary conditions. For a boundary at $y = y_0$ they are given by the matrix boundary condition of third kind:

$$\left[\frac{\partial}{\partial y} + \hat{\mathcal{P}}\right]\Psi(y)\Big|_{y=y_0} = 0. \tag{3}$$

Here $\hat{\mathcal{P}}$ is a diagonal matrix: $\hat{\mathcal{P}} = q_l\hat{P}_l + q_r\hat{P}_r$, where $\hat{P}_l = (1 + \hat{\sigma}_z)/2$ and $\hat{P}_r = (1 - \hat{\sigma}_z)/2$ are the projection matrices. The complex constants $q_l$ and $q_r$, characterizing the boundary, depend on the electron momentum. They are different from each other, because the boundary potentials for different layers are different. An explicit expression of $q_{l,r}$ for a model of hard-wall edge potentials is presented in [2]. According to Eq.(3), the total microscopic current through the boundary is equal to $(i\hbar/2m)\Psi^+(y_0)(\hat{\mathcal{P}} - \hat{\mathcal{P}}^+)\Psi(y_0)$. Therefore, if the boundary is an edge (no current through it), both $q_l$ and $q_r$ are real. If the boundary is a contact, $q_l$ and/or $q_r$ contain imaginary parts proportional to the microscopic currents injected in proper layer. In practice, the contact can be made independently to $l$ or $r$ layer. If only $l$ (or $r$) layer is contacted, we have $Im\ q_r = 0$ (or $Im\ q_l = 0$). Different kinds of structures can be realized experimentally by means of independent contacting [1,4]; two of them are shown in Fig. 1 (see also [3]).

## 2 Boundary conditions for Wigner distribution function

The density matrix of electrons obeys the quantum kinetic equation $\partial\hat{\rho}/\partial t + (i/\hbar)[\hat{H},\hat{\rho}] = 0$, where $\hat{H}$ is the Hamiltonian of the system. If one uses the two-coordinate representation of the density matrix, $\hat{\rho} = \hat{\rho}_{p_x}(y_1, y_2)$, the boundary conditions for it directly follow from Eq.(3), provided that the motion of electrons across the edge or contact area is nearly ballistic:

$$\begin{aligned}\left[\frac{\partial}{\partial y_1}\hat{\rho}_{p_x}(y_1,y_2) + \hat{\mathcal{P}}\hat{\rho}_{p_x}(y_1,y_2)\right]_{y_1=y_0} &= 0,\\ \left[\frac{\partial}{\partial y_2}\hat{\rho}_{p_x}(y_1,y_2) + \hat{\rho}_{p_x}(y_1,y_2)\hat{\mathcal{P}}^+\right]_{y_2=y_0} &= 0.\end{aligned} \tag{4}$$

For a finite-size system whose width is large in comparison with the quantum length (i.e. with the wavelength of an electron at the Fermi level), it is more convenient to introduce Wigner representation of the density matrix. Then, the quantum kinetic equation reduces to a quasi-classical kinetic equation for Wigner distribution function $\hat{f}_{p_xp_y}(y)$, provided that this function changes on the lengths larger then the quantum length. Such conditions are realized in a double-layer system when the splitting energy $\Delta_T$ is small in comparison with the Fermi energy $\varepsilon_F$. Assuming this, we derive the boundary condition for $\hat{f}_{p_xp_y}(y)$:

$$(ip_y + \hbar\hat{\mathcal{P}})\hat{f}_{p_xp_y}(y_0)(-ip_y + \hbar\hat{\mathcal{P}}^+) = (-ip_y + \hbar\hat{\mathcal{P}})\hat{f}_{p_x-p_y}(y_0)(ip_y + \hbar\hat{\mathcal{P}}^+), \tag{5}$$

where $p_y \simeq \hbar k_+ \simeq \hbar k_-$ is the absolute value of the electron momentum along $0Y$. For a non-contacted boundary (edge), the diagonal part $f^l_{p_xp_y}(y)\hat{P}_l + f^r_{p_xp_y}(y)\hat{P}_r$ of the

distribution function obeys the boundary conditions $f^{l,r}_{p_x p_y}(y_0) = f^{l,r}_{p_x - p_y}(y_0)$, which mean that both $l$-layer and $r$-layer currents through the edge are absent.

## 3 Some results and discussion

The boundary condition (5) can be applied to various problems of electron transport in double-layer nanostructures. To demonstrate the effect of the edges, we consider a symmetric, finite-width $(-L/2 < y < L/2)$, infinitely long $(-\infty < x < \infty)$ double-layer strip. If a weak electric field $E$ is directed along the strip, the linearized kinetic equation for nonequilibrium part $\delta\hat{f}_{p_x p_y}(y)$ of the distribution function is

$$\frac{p_y}{m}\frac{\partial}{\partial y}\delta\hat{f}_{p_x p_y}(y) + \frac{i}{\hbar}\left[\hat{h}, \delta\hat{f}_{p_x p_y}(y)\right]_- - eE\frac{p_x}{m}\delta\left(\varepsilon_F - (p_x^2 + p_y^2)/2m\right) = -\left[(1 + \mu\hat{\sigma}_z), \delta\hat{f}_{p_x p_y}(y)\right]_+ /2\tau \ , \qquad (6)$$

where the collision integral is expressed through the averaged scattering time $\tau$ and scattering asymmetry parameter $\mu$, and $[\ldots]_\pm$ denote the commutator $(-)$ and anti-commutator $(+)$. A solution of Eq.(6) together with the boundary condition (5) allows to find the resistivity of the system. The edge effects dramatically modify the resistivity of the strip in comparison with the resistivity of a double-layer plane [5], provided that the scattering in is non-symmetric $(\mu \neq 0)$, and $q_l \neq q_r$. The most important qualitative modifications, as they seen from Fig. 2, are: the overall suppression and asymmetry of the resistance resonance peak [5], and the oscillations of the resistivity upon the background of the peak. These phenomena can be considered as manifestations of the quantum size effect, which occurs in double-layer strips at $L \sim L_T = \hbar v_F/2T$ ($v_F$ is the Fermi velocity). The quantum size effect is suppressed when $L$ exceeds the mean free path length $v_F\tau$, and the resistance resonance peak becomes the same as for the double-layer plane.

To demonstrate the role of contacts, we consider the independently contacted double-layer systems shown in Fig. 1 (the layers are assumed to be infinite along $0X$). A solution of the kinetic equation together with the boundary conditions (5) with complex $q_l$ and $q_r$ allows to find the conductance associated with the double-layer region. The conductance for both the systems has oscillations as a function of $\Delta$, their period is determined by $\delta\Delta_T = 2\pi\hbar v_F/L$. These oscillations are of the same origin as those shown in Fig. 2, and they are suppressed at $L > v_F\tau$.

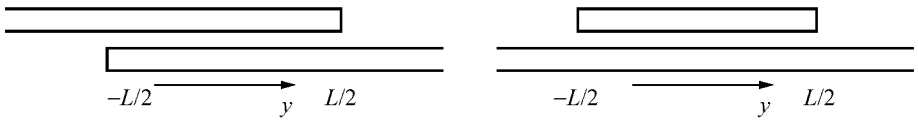


**Fig 1.** Two kinds of double-layer structures realized by independent contacting.

In conclusion, we have derived the matrix boundary conditions for Wigner distribution function of electrons in tunnel-coupled 2D layers, and demonstrated the quantum size effects occurring in double-layer nanostructures whose dimensions are comparable with tunnel coherence length $L_T = \hbar v_F/2T$. This length ($L_T \sim 100$ nm for typical parameters $2T \sim 1$ meV and $\varepsilon_F \sim 10$ meV) is large in comparison with the quantum

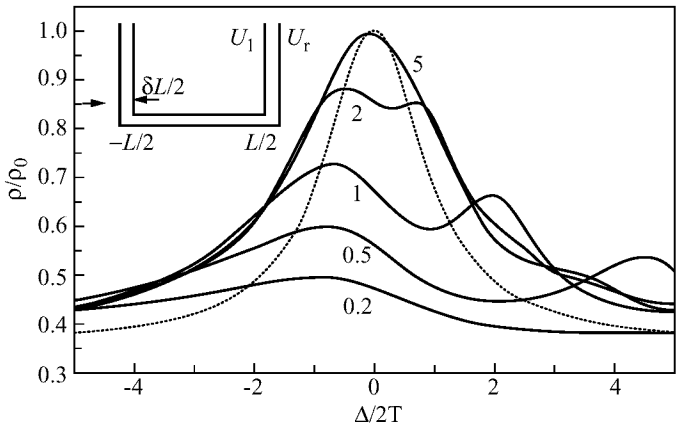


**Fig 2.** The shape of the resistance resonance for several values of $2TL/\hbar v_F$ (the values are shown near proper graphs) calculated in conditions $(2T\tau/\hbar)^2 \gg \mu^2$ and $v_F\tau \gg L$, at $\mu = 0.8$. The dashed line shows the same for an infinite double-layer plane. The inset shows the model of the boundaries used to estimate $q_l$ and $q_r$ (in the calculation we assumed that the Fermi momentum is equal to $4\hbar/\delta L$).

wavelengths of the electrons on the Fermi level. The effects could be observed experimentally in high-mobility samples at low temperatures, when the electron transport across the narrowest dimension is close to ballistic.

## References

[1] For a rewiew, see: J. P. Eisenstein, *Superlatt. Microstruct.* **12** 107 (1992); N.K. Patel *et. al.*, *Semicond. Sci. Technol.* **11** 703 (1996).
[2] O. E. Raichev and F. T. Vasko, *Phys. Rev. B* 1998 (to be published)
[3] F. T. Vasko, *Appl. Phys. Lett.* **68** 412 (1996); O. E. Raichev and F. T. Vasko, *Phys. Rev. B* **55** 2321 (1997); *Superlatt. Microstruct.* **22** N 8 (1997).
[4] N. K. Patel *et. al.*, *Appl. Phys. Lett.* **64** 3018 (1994).
[5] A. Palevski *et. al.*, *Phys. Rev. Lett.* **65** 1929 (1990); Y. Ohno *et. al.*, *Appl. Phys. Lett.* **62** 1952 (1993).

Ioffe Institute
6th Int. Symp. "Nanostructures: Physics and Technology"
St Petersburg, Russia, June 22–26, 1998.



# Electron saturated velocities in silicon carbide polytypes for drift direction along crystal axis

*V. I. Sankin* and A. A. Lepneva
Ioffe Physico-Technical Institute, Russian Academy of Sciences
26, Politekhnicheskaya, St.Petersburg, 194021, Russia
E-mail: sankin@widegap.ioffe.rssi.ru

## Introduction

The saturated drift velocity is a very important parameter of semiconductor crystals. It determines frequency limitation of semiconductor devices and consequently the range of the most effective application. Silicon carbide polytypes are not exclusion. Up to the present such velocities have been determined for two polytypes 4H and 6H SiC for direction perpendicular to crystal axis [1]. As it was shown these values were equal. But there is anisotropy of electrical properties in silicon carbide polytypes for the direction along and perpendicular to the axis. Besides the crystal axis is the axis of the natural superlattice (NSL) axis too. As well known the drift velocities in artificial SL depend very strong on parameters SL and change from $10^6$ cm/s for relatively wide [2] miniband to $10^4$ cm/s for narrow one [3]. Earlier we have shown that NSL creates such electron spectrum in silicon carbide polytypes that led to the existence such effects as Bloch oscillation, electro-phonon resonances, interminiband tunnelling and others. Evidently the saturated drift velocities have to experience an influence of NSL. But such data were absent in literature. Briefly some data on this question were given in [4]. A technical experimental difficulties did not allow to curry on such experiments. Usually used method of the current saturation was not used for geometry when a current was parallel to the axis because of unfavourable conditions of the Joule heat removing probably. But as far as a lot of devices including power high frequency devices are fabricated or will be fabricated for such geometry the determination of saturated drift velocities is an important problem both from fundamental and apply point of view.

## Experimental method

Our method is based on the following idea. When in an experimental structure with space charge limited current a drift current regime is realised the drift velocities may be obtained. This regime for one dimensional case may be described by two equations:

$$d^2V/dX^2 = \rho/\varepsilon_s \tag{1}$$

$$J = \rho v \tag{2}$$

where $V$, $X$, $\rho$, $\varepsilon_s$, $J$, $v$ the voltage on a specimen, the coordinator along a current, the space charge density, the dielectric constant of semiconductor, the current density, the drift velocity respectively. By some standard transformations we can show that a current–voltage characteristic consist of two regions: the first region where drift velocity is changed with changing of an electrical field and the second one where velocity is

saturated and is not changed with the field. If we consider the velocity equal to

$$v = \mu V / w \tag{3}$$

then I–V characteristic on the first region will be

$$J = 2\epsilon_s \mu V^2 / w^3. \tag{4}$$

Here $\mu$, $w$ are the mobility of carries, the length of the specimen respectively. It should take into account that in (4) may be a function of the field and then a real I–V characteristic will not correspond to (4).

On the second region where $v = \text{const}$ the I–V characteristic will be the following:

$$J = 2\varepsilon_s v_s V / w^2 \tag{5}$$

where $v_s$ is the saturated velocity. Thus, when the drift velocity is saturated, we have to observe the linear region on I–V characteristic.

## 1 Experimental structure

The original three-terminal $N^+$-p-$N^+$ structure will be used for this investigations. The structure consists of three regions, according to the transistor terminology base, collector and emitter. The middle region or base contains the silicon carbide polytype intended for investigations. It is doped by the deep acceptor impurity scandium for obtaining of the minimal free hole concentration about $10^{10}\,\text{cm}^{-3}$ for 300 K. The base is located between two n-regions, collector and emitter. The collector and emitter p-n junctions are the same, but they differ from the usual ones.

The forward biased junction is able to be opened only by a direct bias or by pulses with duration $\tau_p > 10^{-2}$ sec. Naturally for lowering of the potential barrier, it is necessary to deionize the deep acceptor impurity in the space charge region. The characteristic time of this process is more than $10^{-2}$ sec at a hole concentration about $10^{10}\,\text{cm}^{-3}$. But when the potential barrier is lowered, injection, which is an uninertial process, can be accomplished by pulses with $\tau_p \ll 10^{-2}$ sec.

There is the following situation in the reversal biased junction. At the reversal direct bias, the field in p-region is screened by ionised acceptor impurities with $N_a - N_d \sim 10^{17}\,\text{cm}^{-3}$. For voltage about several tens of volts, the length of screening is less than $10^{-4}$ cm and the field in the p-region is nonuniform. However the screening length is larger than $10^{-1}$ cm in accordance with the hole concentration of about $p < 10^{10}\,\text{cm}^{-3}$ at the reversal pulse bias with duration $\tau_p \ll \tau_i$. Here $\tau_i$ is the time of ionisation for the acceptor impurity. Therefore, the width of the p-region of about $(5-10) \times 10^{-4}$ cm allows to obtain a practically uniform electric field. The field has to be directed parallel to the superlattice axis.

The working principle of the structure is the following: the collector junction is reversal biased by the pulse voltage with $\tau_p \sim 10^{-7}$ sec. The emitter junction is forward biased by direct voltage which causes injection into the base. The electric scheme is analogous the transistor with common emitter. The pulse field spreading through the base reaches the open emitter junction and causes injection into the base. The injected current increases with the pulse voltage, but it is able to be limited by the decrease of the bias between emitter and base.

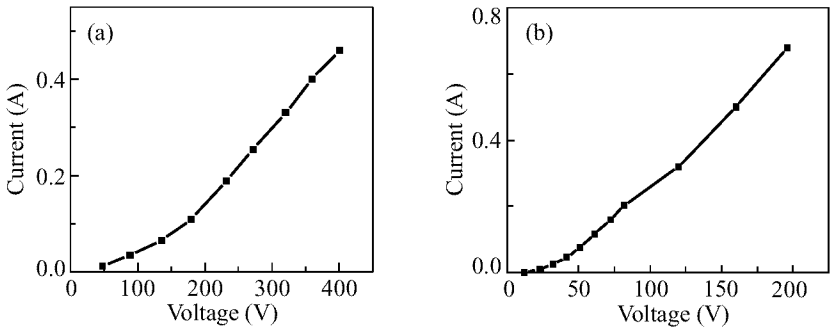


**Fig 1.** (a) I–V characteristic of the 4H-SiC tree terminal structure. (b) I–V characteristic of the 6H-SiC tree terminal structure.

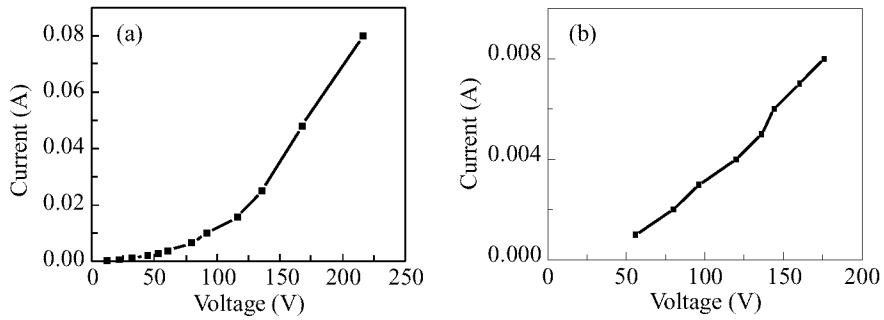


**Fig 2.** (a) I–V characteristic of the 8H-SiC tree terminal structure. (b) I–V characteristic of the 21R-SiC tree terminal structure.

Thus, there is the uniform electric field in the p-region and current intensity is controlled independently on the field in the base region. It is highly important that this experimental method allows to conduct measurements with the electron current only without the current associated with the holes.

## 2 Experimental results and discussion

The electronic transport in the experimental structure used for the measurements is determined by the transit time mechanism. It is known that the current-field characteristic inherent for the transit-time conduction mechanism includes the linear region associated with the space charge limited current. This region is observed when the concentration of the carriers injected is as large as an ionised impurity concentration in the base. In a usual situation such a condition is met at a very large current density and a strong electric field when the carriers drift velocity reaches its saturation value.

The feature of the experimental structure used for the study is an ionised impurity concentration so low that the space charge limitation of the current takes place at low current density when the electric field is insufficient for the carriers velocity saturation.

In this paper we present the data of I–V characteristics investigation for the polytypes 4H, 6H, 8H and 21R SiC. The current-field characteristic of the experimental structure may include the following regions connected with the space charge limitation of the

current injected: the region with $j \sim V^2$ (4) and the region with $j \sim V$ associated with electronic velocity saturation (5). These regions are identified in the experimental I–V characteristics clearly (Figs. 1-2). The values of high-field mobility obtained by the processing of the characteristic region with $j \sim V^2$ were found to be 3.1 $cm^2/Vs$, 4.5 $cm^2/Vs$ and 6.4 $cm^2/Vs$ for polytypes 8H, 6H and 4H respectively.

From the analysis of linear region of I–V characteristics the values of saturated electron drift velocities for 4H-, 6H-, 8H- and 21R-SiC were obtained which are approximately equal to $3.3 \times 10^6$, $2 \times 10^6$, $10^6$ and $4.4 \times 10^3$ cm/sec correspondingly. The low values of velocities, which are significantly smaller than the well known value $v_s = 2 \times 10^7$ cm/sec for F⊥C [1] are of special interest. But these values qualitatively correspond to the anological results for artificial SL's. Both for these SL and for the NSL of SiC polytypes the saturated drift velocity drops with decreasing of the miniband width.

Thus, the presented results are the new evidence of minizone structure of electron spectrum in SiC polytypes and the new basis of data for a device project. The partial financial support of Russian Foundation of Fundamental Research project 97-02-18295 and Russian Science Program "Physics of Solid State Nanostructures" project 97-1038 is gratefully acknowledged.

## References

[1] I. A. Khan and J. A. Cooper, Jr *Proceedings ICSCIII-N'97*, Stockholm, August 31–September 5, 1997, p. 57–58.

[2] A. Sibile, J. F. Palmier, and H. Wang, F. Mollot *Phys. Rev. Lett.* **6** 52–57 (1990).

[3] H. T. Grahn, K. von Klitzing, and K. Ploog, G. H. Doler *Phys. Rev. B* **43** 12094–12097 (1997).

[4] V. I. Sankin, A. A. Lepneva *Nanostructures: Physics and Technology 97* St Petersburg 23–27 June 1997 p. 155–158.

Ioffe Institute
6th Int. Symp. "Nanostructures: Physics and Technology"
St Petersburg, Russia, June 22–26, 1998.



# Activationless electron and hole recombination rate in semimetallic single and double quantum wells

*M. Singh*

In recent years, a tremendous amount of experimental and theoretical investigation has been done on intraband and interband transition diodes such as InAs/GaSb/InAs due to the possible device applications of these structures in optoelectronic devices of the future [1]. In this paper, we propose a theory for the electron-hole recombination and generation processes in these transition diodes in which a third particle is not involved. This type of recombination can occur in semimetallic quantum wells and heterostructures made from InAs and GaSb. The conduction band of an InAs semiconductor lies beneath the valence band of a GaSb semiconductor, and the separation between the conduction band and valence band is approximately 150 meV. This negative, or crossed-gap configuration of these quantum wells leads to a charge transfer between the semiconductor InAs and semiconductor GaSb generating intrinsic carriers, both electrons and holes, on either side of the interface. These quantum wells behave like semimetallic materials and they are called semimetallic quantum wells. Due to the overlapping conduction and valence band, there are activationless generation and recombination processes which do not require an extra excitation particle such as a phonon or photon. Therefore, we call these processes **acivationless recombination processes.** As we know that in direct semiconductors, an electron and a hole recombine via emitting a photon. This process is called **direct recombination**. But in case of indirect semiconductors, the conservation of the momentum cannot be satisfied in the electron-hole recombination. Generally in these semiconductors, electrons and holes recombine through recombination centers because they can take up any momentum difference between the electrons and holes. In this recombination process, the energy of the electron is usually lost to phonons. This process is called **indirect recombination process**. We have developed a theory for the conductance due the generation and recombination processes in semimetallic n-type and p-type single quantum wells (SQW) and double quantum wells (DQW). To calculate the generation and recombination rates we used an $8 \times 8\mathbf{k} \cdot \mathbf{p}$ matrix Hamiltonian. In this model, the effect of nonparabolicity and anisotropy are included. Using the transfered matrix method we have derived the expression of the tunneling coefficient and from the tunneling coefficient, the activationless recombination rate is obtained. Numerical calculations are performed for n- and p-type single and double quantum wells made from InAs and GaSb. We have considered the symmetric and asymmetric double quantum wells. We found that when we introduce the asymmetry due to different quantum well thicknesses or an external potential, the recombination rate decreases due to scattering for both n-type and p- type quantum wells. We also found that as the energies of the electrons and holes increase the recombination rates also increase for both types of SQWs.

## References

[1] R. Tsu and L. Esaki, *Appl. Phys. Lett.* **22**, 562 (1973); D. J Ting, *J. Appl. Phys. Lett.* **58**, 292 (91); J. C. Inkson, *Semicond. Sci. Technol.* **9**, 178 (1994); W. Lau and M. Singh, *J. Phys. C* (in press, 1998).

Ioffe Institute
6th Int. Symp. "Nanostructures: Physics and Technology"
St Petersburg, Russia, June 22–26, 1998.



# The thickness dependence of IR-reflectance from Al quantum wells

R. Villagomez†, O. Keller† and *F. Pudonin*
P. N. Lebedev Physical Institute, RAS, 117924 Moscow, Leninskii pr. 53, Russia
† Institute of Physics, Aalborg University, DK-9220 Aalborg Ost, Pontoppidancestrade 103, Denmark

The first report on the optical properties of metallic quantum wells (MQWs) in the IR-region appeared in 1991 [1]. The quantum sized effects (QSEs) in MQWs are usually studied in 0.1–4 nm thickness range due to small wavelength for electrons on Fermi surface for almost all metals. In this report the room temperature measurements on the IR (9.201 $\mu$m) linear p-polarized reflectivity ($R_p$) of Al-QWs deposited on $SiO_2$ and Si substrates are presented for thickness range from 0.5 nm to 112 nm [2]. Two type of ($R_p$) oscillations in depend from Al-layer thickness in two thickness range (0.5–3.4 nm and 6–11 nm) are observed.

All Al-QWs was prepared with the help of RF-sputtering. The crystalline Si and amorphous $SiO_2$ substrates were carefully selected to obtain a surface roughness as small as possible and symmetric QWs were made using barrier layers of $Al_2O_3$. The thickness of barrier layer was 2 nm for all structures. The change of Al thickness from sample to sample was made with step of near 1 monolayer. The Al-QWs on Si and $SiO_2$ substrates were prepared simultaneously in just the same technological process. Our experimental set-up allow us to make IR reflectance of He-Ne laser radiation on 9.201 $\mu$m wavelength with an accuracy better then 2%. The angle of incidence were fixed to 7°.

The dependence of $R_p$ from Al-thickness $d$ for Al-QWs is presented on Fig. 1, where the circles represent the date for $SiO_2$ substrates and the diamonds — for Si substrates.

Let us first consider the $R_p(d)$ for Al-QWs on $SiO_2$ substrates. For a small film thickness ($d$ less then 4–5 nm) it appears that $R_p$ decreases slightly and almost monotonously with $d$. Qualitatively, $R_p$ exhibits a parabolic dependence on $d$ in this region, see Fig. 2, instead of giving any quantitative correlation with an existing theory. We believe that this parabolic decreasing can be due to the kind of substrate and its crystallinity because all Al-QWs were prepared on both substrates simultaneously. When the Al-thickness is increased beyond $\approx 5$ nm, one still observed a slight decrease in the reflectivity before it finally passes through a flat minimum located in the region $d$ near 7–8 nm for our QW system. For some metallic films grown by sputtering technique there exist a critical thickness $d^*$ after which the mechanism of film grown is changed. The value of $d^*$ strongly depends on the substrate physical condition, i.e. its crystallinity, surface cleanness and technological condition during the sputtering process (substrate temperature, vacuum condition, metal rate deposition, etc.). For $d < d^*$ the metallic layer will be in amorphous state while for $d > d^*$ a crystalline layer begin to grow on the already amorphous layer giving as a result that the packing distance of the Al changes due to possible crystallites formation starting from this ($d^*$) thickness value. Although (quantum) oscillation are observed in $R_p$ in the range $d \sim 5$–$8.5$ nm and these are stronger than the weak oscillation appearing for $d$ approximately less than 5 nm (Fig. 2), the overall thickness dependence of $R_p$ is still rather smooth, but for film thiclness in the range

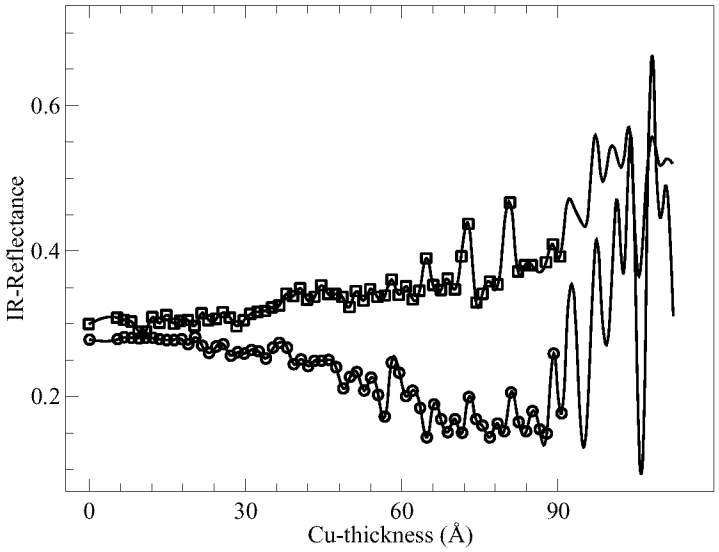


**Fig 1.**

$d \sim 8.5-11.2$ nm pronounced oscillations are observed in the thickness dependence of the reflectivity. In this range, the change $(\Delta R_p)$ in the reflectivity can be as much as $\Delta R_p \sim 0.4$ when $d$ is increased by just one monolayer. Smearing out the oscillations by averaging $R_p$ over a few monolayers, the overall tendency shows a significant increasing in $R_p$ with $d$ in the range $d \sim 8.5-11.2$ nm. At $d \sim 11.2$ nm the reflectivity is still far from the bulk value $(R_{bulk} \sim 0.98)$ for Al, and we expect that a thickness of at least $d \sim 15-20$ nm is needed before one would be able to characterize an Al film by its macroscopic (complex) refraction index. Though the physical nature why this oscillations appear is not clear by the moment, it is necessary to notice that for some metal films such as Al, Cu, Pb, In and other the existence of the critical thickness $d^*$ is a fact. On another hand, the strong oscillations observed in the thickness dependence of the p-polarized reflectivity cannot be explained on the basis of the simple quantum well picture even with interband and intrabend transitions in Al-QW taken into account. If one consider as a fact that formation of Al-crystalline layer is grown on the surface of an amorphous Al-Layer as the film grows and therefore we have a double metallic system consisting of a quantum crystalline Al-layer and an $\ll$ almost $\gg$ non-quantum amorphous layer, it is likely to think that these are responsible for a strong oscillations observed in the thicker films. We confident that the oscillations measured in the thickness dependence of $R_p$ for Al-QWs on $SiO_2$ substrate are due to electronic quantum confinement effects.

For Al-QWs on Si-substrates the measured thickness dependence of the reflectivity, to some extent, resembles that of the Al-QWs on $SiO_2$ substrates. Though the reflectivity shows an overall monotonous increasing and $R_p$ does not start with a $\ll$ parabolic $\gg$ decrease as it was the case for the Al-QWs on $SiO_2$ system, the oscillations are still present and more pronounced for the larger thickness. The reason why the reflectivity does not set-out with a $\ll$ parabolic $\gg$ decrease is not known at the moment. Although

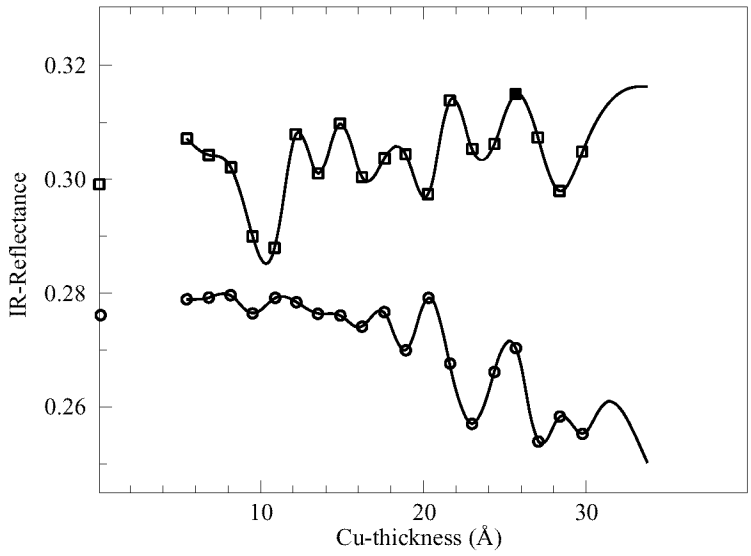


**Fig 2.**

we cannot predict the peak positions of such oscillations in Al-QWs on Si neither in Al-QWs on $SiO_2$ cases, it is worth noticing that a experimental correlation exists between the peak (or valley) position in both Al-QWs on $SiO_2$ and Al-QWs on Si, in our experimental measurements, as we can see in Fig. 1. A Fourier analysis of the experimental data gives a prominent spatial period of $\sim 2.6$ nm for range $d \sim 0.5-3.4$ nm and 3.4 nm for range $d \sim 3.4-11.2$ nm.

The authors (F.P.) are grateful to prof. V. Yakovlev, prof. Yu. E. Lozovik and Dr. L. Kuzik and (R.V.) Dr. D. Hotz for their useful discussions. We acknowledge the support received from the Institute of Physics in AAU under the Ph.D. program, the Mexican ministry of science and technology CONACyT (grant 40880.93.96), Program "Solid Nanostructures" (grant 97-10-50) and Russian Foundation for Fundamental Research (grant 97-02-17638) which made possible this work.

## References

[1] E. V. Alieva, E. I. Firsov, L. A. Kuzik, V. A. Yakovlev and F. A. Pudonin, *Phys. Lett. A* **152** 89 (1991).

[2] R. Villagomez, O. Keller, F. Pudonin, *Phys. Lett. A* (accepted for publication), (1998).

Ioffe Institute
6th Int. Symp. "Nanostructures: Physics and Technology"
St Petersburg, Russia, June 22–26, 1998.



# Hot electron birefringence and absorption in tunnel-coupled quantum wells due to real space transfer

L. E. Vorobjev†, V. L. Zerova†, I. E. Titkov†, D. A. Firsov†, *V. A. Shalygin*†, V. N. Tulupenko*, A. A. Toropov‡, T. V. Shubina‡ and E. Towe§

† St. Petersburg State Technical University, 195251 St. Petersburg, Russia
‡ Ioffe Physico-Technical Institute RAS, St. Petesburg, Russia
* Donbass State Engineering Academy, 343913, Kramatorsk,Ukraine
§ University of Virginia, Charlottesville, VA 22903-2442, USA

**Abstract.** Birefringence and absorption modulation under longitudinal electric field in the tunnel-coupled GaAs/AlGaAs quantum wells have been found and investigated in the spectral region corresponding to intersubband electron transitions. The observed phenomena are explained by electron heating in electric field and electron transfer in real space. The equilibrium absorption spectra at different lattice temperatures are analyzed too.

## Introduction

The radiation corresponding to intersubband transitions in quantum wells (QW) of semiconductor heterostructures usually lies in the mid and far infrared region ($\lambda > 5\ \mu$m). A lot of devices such as mid and far infrared photodetectors and modulators, cascade laser and fountain laser with optic pump [1, 2, 3, 4] are based on intersubband transitions of electrons. The physical processes leading to light modulation in simple rectangular QW under longitudinal electric field were investigated in [5, 6]. In this paper we study absorption and birefringence modulation under electron heating with longitudinal electric field in specially designed tunnel-coupled GaAs/AlGaAs quantum wells.

## 1 Samples

The investigated structure contained 150 pairs of GaAs/$Al_xGa_{1-x}As$ QW, separated by the wide barriers (20 nm). The surface concentration of electrons was $N_S = 5 \times 10^{11}$ cm$^{-2}$.

The states with the energies $\varepsilon_1 = 88$ meV and $\varepsilon_4 = 316$ meV are generated by the first (narrow) well and the states $\varepsilon_2 = 120$ meV and $\varepsilon_3 = 235$ meV by the second (wide) well. The energy interval $\varepsilon_3 - \varepsilon_2$ was about $CO_2$-laser quantum energy (117 meV) and the interval $\varepsilon_2 - \varepsilon_1$ was less then the optical phonon energy ($\hbar\omega_0 = 37$ meV). These conditions had to ensure electrooptical modulation of $CO_2$-laser radiation.

## 2 Equilibrium absorption spectra

The transitions between neighbor levels generated by the same QW give the most contribution to intersubband absorption. The optical matrix elements for such transitions are the greatest: $|M_{23}|^2 = 1$; $|M_{14}|^2 = 0.89$. For transitions between levels generated by

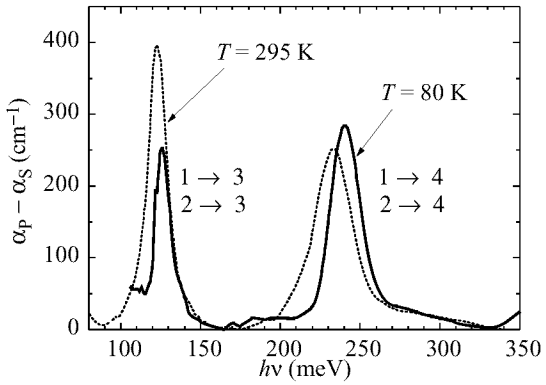


**Fig 1.** Equilibrium absorption spectra for two temperatures.

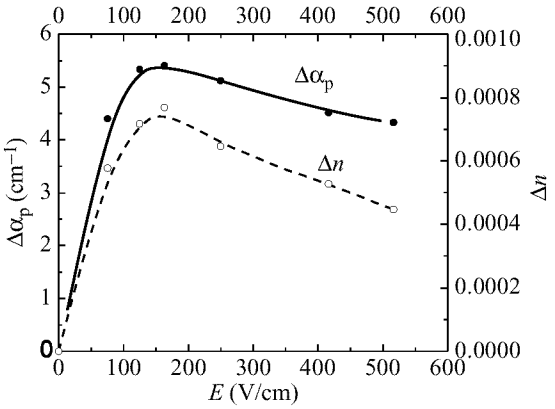


**Fig 2.** Absorption coefficient variation for p-polarized light and birefringence modulation versus longitudinal electric field.

different QW the optical matrix elements are less: $|M_{13}|^2 = 0.16$; $|M_{24}|^2 = 0.0062$ (in a.u.).

There are two absorption bands in equilibrium absorption spectra shown in Fig. 1. The longwavelength band corresponds to transitions $\varepsilon_1 \rightarrow \varepsilon_3$ and $\varepsilon_2 \rightarrow \varepsilon_3$, and the shortwavelength one is related to transitions $\varepsilon_1 \rightarrow \varepsilon_4$ and $\varepsilon_2 \rightarrow \varepsilon_4$.

## 3 Electrooptical investigations

This experiments were carried out with the help of $CO_2$-laser radiation at a lattice temperature $T_0 = 80$ K. The pulse electric field was applied parallel to plane of QW. Multipass waveguide geometry of the samples was used for input of radiation. The absorption coefficient variation dependence upon longitudinal electric field intensity is presented in Fig. 2. Modulation of absorption coefficient $\alpha$ was found only for light of $p$-polarization and there was no modulation for light of $s$-polarization. It corresponds to selection rules for intersubband transitions.

Due to these selection rules QW have a strong optical anisotropy: refractive index

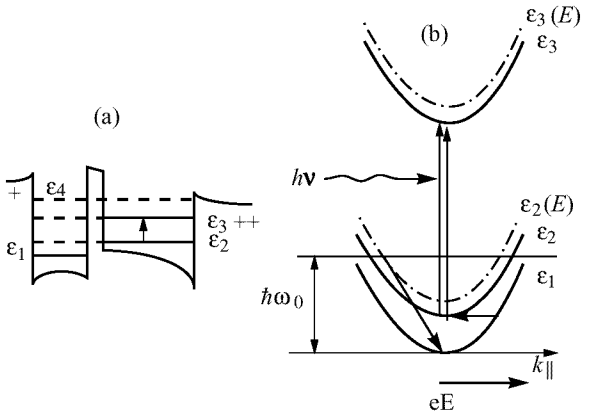


**Fig 3.** Potential relief with considering of the space charge (a); heating and redistribution of the electrons between subbands $\varepsilon_1$ and $\varepsilon_2$ under electric field $E$ (b).

$n$ is different for waves of $p$- and $s$-polarization. This difference is changed in electric field. Values of $\Delta\alpha_p$ and $\Delta n = \Delta\,|n_p - n_s|$ are connected by Kramers–Kronig relations. Dependence $\Delta n$ upon electric field determined experimentally is shown in Fig. 2 too. It is similar to dependence $\Delta\alpha_p(E)$. Let us discuss these results. The potential of QW is distorted due to space charge of electrons located in the wells and space charge of impurity ions situated in the barriers. The approximate potential relief of our QW with considering such distortion is shown in Fig. 3. The potential deformation results in shifting down levels $\varepsilon_2$ and $\varepsilon_3$ and decreasing difference $\varepsilon_2 - \varepsilon_1$. Without external electric field the electrons are in the first subband and are located in the narrow well. Under effect of external longitudinal electric field the average electron energy increases due to electron heating. The electrons transit to the second subband on account of scattering and it leads to increasing absorption connected with the transitions $\varepsilon_2 \rightarrow \varepsilon_3$. The region of increasing absorption in Fig. 2 is explained with a filling the second subband. Again the other factors appear in strong electric fields. The electrons occupying subband $\varepsilon_2$ are mostly located in the wide well while the electrons of subband $\varepsilon_1$ belong to the narrow well. So with intersubband transitions the redistribution of electrons happens in the real space and levels $\varepsilon_2$ and $\varepsilon_1$ shift. Therefore the part of electrons in the subband $\varepsilon_2$ causing absorption decreases. Due to strong scattering by optic phonons, the number of electrons with the energy $\varepsilon > \hbar\omega_0$ is small. All this leads to decreasing electroabsorption with a field. Besides more strong heating of the electrons in the subband $\varepsilon_2$ leads to intensive scattering with optical phonon emission and their returning to the first subband. So in strong electric fields electroabsorption is saturated and then decreases.

The theoretical calculations are consistent with experimental data.

## Conclusion

Optical phenomena connected with intersubband electron transitions in tunnel coupled quantum wells have been investigated. The observed birefringence and absorption modulation under longitudinal electric field have been explained by electron heating and electron transfer in real space.

*Acknowledgments*

This work was supported by RFBR: grant 96-02-17404; INTAS-RFBR: grant 00615i96; MSTRF: grant 96-1029; State program "Integration": project 75; UFBR: grant 2.4/970; NATO: grant HTECH LG 960931.

## References

[1] B. F. Levine. *J. Appl. Phys.* **74** R1 (1993).
[2] J. Faist, F. Capasso, D. L. Sivco, C. Sirtori, A. L. Hutchinson, A. Y. Cho. *Science* **264** 553 (1994).
[3] O. Gauthier-Lafaye, S. Sauvage, P. Boucaud, F. H. Julien, R. Prazeres, F. Glotin, J.-M. Ortega, V. Thierry-Mieg, R. Planel, J.-P. Leburton, V. Berger. *Appl. Phys. Lett.* **70** 3197 (1997).
[4] E. Dupont, D. Delacourt, V. Berger, N. Vodjdani, M. Papuchon. *Appl. Phys. Lett.* **62** 1907 (1992).
[5] L. E. Vorobjev, E. A. Zibik, Yu. V. Kochegarov, S. N. Danilov, D. A. Firsov, A. A. Toropov, T. V. Shubina, E. Towe, D. Sun. *Semiconductors* **29** 588 (1995).
[6] L. E. Vorobjev, I. I. Saidashev, D. A. Firsov, V. A. Shalygin. *JETP Lett.* **65** 549 (1997).

Ioffe Institute
6th Int. Symp. "Nanostructures: Physics and Technology"
St Petersburg, Russia, June 22–26, 1998.



# Auger recombination in a quantum well in a quantizing magnetic field

*G. G. Zegrya*
Ioffe Physico-Technical Institute, St. Petersburg 194021, Russia

**Abstract.** Basic mechanisms of Auger recombination of non-equilibrium carriers in quantum wells in the presence of a longitudinal quantizing magnetic field are studied. It is shown that two different recombination mechanisms are present: (i) a resonant non-threshold mechanism, (ii) a quasithreshold mechanism. The rate of the resonant Auger process depends on the temperature slightly but on the magnetic field essentially. For the quasithreshold Auger recombination process, the threshold energy depends on both the quantum well width and magnetic field. It is shown that the resonant Auger process dominates at low temperatures.

## Introduction

In the homogenious semiconductors the mechanisms of Auger recombination in the presence of quantizing magnetic field have been studied by many authors [1-3]. At low temperatures the most probable phenomenon may be a resonant process of Auger recombination wherein two electrons and and a heavy hole (CHCC process) as well as an electron and two heavy holes (CHHS) participate. In the presence of of a strong magnetic field the electron spectrum is quantized [4]. As the result of Coulomb interaction, the Auger electron havind acquired the energy of the order of $E_g$ (the forbidden band gap) executes a vertical transfer to a high Landau level without a change in quasimomentum. A large quasimomentum transfer is not required bacause of the Coulomb collision of two electrons. Thus, the Auger process has a resonant character in a quantizing magnetic field. The rate of the Auger process oscillates as a function of magnetic field, and these oscillations give rize to a break-down of the resonance.

The aim of the present paper is to study theoretically basic Auger recombination mechanisms in quantum wells in the presence of longitudinal qiantizing magnetic field. It is shown that in the undeep quantum wells ($E_g > U$, where $U$ is the quantum well depth for electrons) there exist two different mechanisms of Auger recombination: (i) a resonant mechanism analogous to the Auger process in a homogenious semiconductor and (ii) a quasithreshold mechanism whose threshold energy depends on the quantum well width [5] and on the magnetic field. In the case of deep quantum wells ($E_g < U$) there exists only one mechanism of Auger recombination that is the resonant Auger process.

## 1 The rate of Auger recombination

The Auger transition rate for a two-dimensional carrier gas in the magnetic field is calculated in the framework of first-order perturbation theory in electron-electron interaction:

$$G = \frac{2\pi}{\hbar} \sum_{1,2,3,4} |M|^2 \delta(E_1 + E_2 - E_3 - E_4) f_1^c f_2^c f_4^v (1 - f_3^c). \quad (1)$$

Here $f^c$ and $f^v$ are the Fermi distribution functions for electrons and holes, $E_1$ and $E_2$ are the initial, and $E_3$ and $E_4$ final, electron energy states (the hole state is treated as final one for one of the electrons participating in the process), summation in (1) is performed over all initial and final particle states including spins ones, $M$ is the matrix element of Coulomb electron distribution, calculated with taking account for antisymmetrization of the electron wave functions in the initial and final states. The squared modulus of the matrix element is broken up into the sum of direct and exchange parts being equal to

$$|M|^2 = |M_I|^2 + |M_{II}|^2 - \{M_I M_{II}^* + M_I^* M_{II}\}, \tag{2}$$

$$M_I = \frac{e^2}{\kappa} \sum_{\sigma,\sigma'} \iint d^3r\, d^3r'\, \psi_1^*(\mathbf{r},\sigma)\psi_2^*(\mathbf{r}',\sigma') \frac{1}{|\mathbf{r}-\mathbf{r}'|} \psi_3(\mathbf{r},\sigma)\psi_4(\mathbf{r}',\sigma'), \tag{3}$$

$$M_{II} = \frac{4\pi e^2}{\kappa} \sum_{\sigma,\sigma'} \iint d^3r\, d^3r'\, \psi_1^*(\mathbf{r},\sigma)\psi_2^*(\mathbf{r}',\sigma') \frac{1}{|\mathbf{r}-\mathbf{r}'|} \psi_3(\mathbf{r}',\sigma')\psi_4(\mathbf{r},\sigma), \tag{4}$$

where $\kappa$ is the dielectric permeability constant, $e$ is the electron charge. In the scope of Kane's model that will be used below, the quasiparticle wave function may be superposition of $s$- and $p$-type band states. It is convenient to use the basis $u_i(\mathbf{r}')(i = 1, 2, 3, \ldots, 8)$, where the conduction-band wave functions are spherical $s$-type functions, and those of valence band are eigenfunctions of the operators $J^2$ and $J_z^2$ (where $J$ is the complete-moment operator). Then, using the Landau gauge ($A_x = -H_y, A_y = A_z = 0$ where $A$ is the vector potential, and $H = (0, 0, z)$ is the magnetic field intensity), complete coordinate wave functions have the form

$$\psi(\mathbf{r}) = \varphi(x,z) \sum_i C_i\, \chi_{n_i}(y)\, u_i(\mathbf{r}). \tag{5}$$

Here $\chi_{n_i}$ are the oscillation functions of the number $n_i$, $\varphi(x,z)$ is a smoothly varying envelope that depends on the coordinates $(x,z)$, the coefficients $C_i$ being functions of $n_i$ and $k_z$.

The highly excited Auger electrons and holes are not localized in the $Z$-axis direction. We have $\varphi(x,z) = \exp(ik_x x + ik_z z)$ for those. For the electrons inside the well, $\varphi(x,z) = \exp(ik_x x) \cdot \tilde{\varphi}(z)$ where the form of $\tilde{\varphi}(z)$ depends on the profile of two-dimensional-electron potential well. For a rectangular well, $\tilde{\varphi}(x)$ is a linear combination of the functions $\sin k_z z$ and $\cos k_z z$. In the region of underbarrier motion of two-dimensional electrons which is of basic importance for a given problem, we have $\tilde{\varphi}(z) = \exp(-\kappa z)$, where $\kappa = \sqrt{2m_e U}$ is the damping index of the wave function under the barrier, $m_e$ is the effective electron mass; and $U$ is the barrier height.

We thus consider the Coulomb collision process for two electrons 1 and 2 with subsequent recombination of one of them with a hole and with the passage of the second electron onto a highly excited Landau level $n_3$. Then one should integrate in (3) and (4) not only over the well region, but over that of the whole narrow-gap semiconductor, *i.e.* we need integrate between $-\infty$ and $+\infty$. Then we substitute the Coulomb potential in the form of Fourier integral, and, replacing (5) into (3), we find

$$|M_I|^2 = \tag{6}$$
$$= \frac{16\pi^2 e^4}{\kappa^2} \iint \frac{d^2q\, d^2q'\, \delta_{\sigma_1\sigma_2}\delta_{\sigma_2\sigma_4}}{(q^2 + k_{31x}^2 + \lambda^2)(q'^2 + k_{31x}^2 + \lambda^2)} \times$$

$$\times \delta(\mathcal{K}_x) q \mathcal{K}^{13}_{ii'}(\mathbf{q},\mathbf{q}') \mathcal{K}^{24}_{jj'}(\mathbf{q},\mathbf{q}'), \tag{7}$$

where

$$\delta(\mathcal{K}_x) = \delta(k_{1x} + k_{2x} - k_{3x} - k_{4x}),$$
$$\mathcal{K}^{13}_{ii'}(\mathbf{q},\mathbf{q}') = [C^{*(1)}_i C^{(3)}_i I^{13}_i(\mathbf{q})][C^{(1)}_{i'} C^{*(3)}_{i'} I^{13}_{i'}(-\mathbf{q}')],$$
$$\mathcal{K}^{24}_{jj'}(\mathbf{q},\mathbf{q}') = [C^{*(2)}_j C^{(4)}_j I^{24}_j(-\mathbf{q})][C^{(2)}_{j'} C^{*(4)}_{j'} I^{24}_{j'}(\mathbf{q}')],$$
$$k_{31x} = k_{3x} - k_{1x},$$
$$I^{\alpha\beta}_i(\mathbf{q}) = \int e^{iq_y y} \chi^{\alpha}_{n_i}(y)\, \alpha^{(\beta)}_{m_i}(y)\, dy \int e^{iq_z z} \varphi^{\alpha}(z)\, \varphi^{\beta}(z)\, dz,$$

$\lambda$ is the Debye screening radius, $\mathbf{q}$ is the transmitted momentum, $\alpha$ and $\beta$ denote particle state numbers ($\alpha, \beta = 1, 2, 3, 4$), $\delta_{\sigma_\alpha \sigma_\beta} = 1$ if $\sigma_\alpha = \sigma_\beta$, and $\delta_{\sigma_\alpha \sigma_\beta} = 0$ if $\sigma_\alpha \neq \sigma_\beta$. The remaining summands in (2) would be expressed in a similar way. Last, the matrix element $| M |^2$ should be substituted into (1) and summed over all particle states with regard to the energy conservation law, $E_1 + E_2 = E_3 + E_4$. Let the particles (electrons and holes) be at low Landau levels in their initial state. Then, their energies measured from the valence band top in Kane's model have the form

$$E_{1,2} = E_g + E_0 + \frac{4}{3}\frac{\gamma^2}{a_{\mathrm{H}}^2 E_g}\left(\frac{1}{2} \mp \frac{1}{4}\right),$$
$$E_4 \equiv E_{hl} = -\frac{2}{3}\frac{\gamma^2}{E_g}\left[k_z^2 + \frac{2}{a_{\mathrm{H}}^2}\left(\frac{1}{2} \mp \frac{1}{4}\right)\right].$$

Here $a_{\mathrm{H}} = [\hbar c/(eB)]^{1/2}$ is the magnetic length, $\gamma$ is Kane's matrix element, the signs "$\pm$" correspond to two spin directions. For simplicity, we consider recombination with light holes whose mass is $m_{hl} = m_e$. The Landau level $n_3 \gg 1$ corresponds to a highly excited electron, the spectrum of that electron is of the following nonparabolic form:

$$E_3(n_3) = E_g/2 + \left\{(E_g/2)^2 \frac{2}{3}\gamma^2\left[k_z^2 + \frac{2}{a_{\mathrm{H}}^2}\left(n_3 + \frac{1}{2} \mp \frac{1}{4}\right)\right]\right\}^{1/2}. \tag{8}$$

Substituting $E_2, E_2, E_3$, and $E_4$ into the energy conservation law, we find the minimum value $n_3^{min}$:

$$n_3^{min} \simeq \frac{2E_g}{\hbar\omega}, \tag{9}$$

where $\omega = \frac{eH}{m_e c}$. While deriving (9), we have taken into account $\gamma k_z \ll E_g$ and $n_3 \gg 1$. We have also expressed Kane's matrix element $\gamma$ through the effective electron mass: $\hbar^2/m_e = 4/3 \cdot \gamma^2/E_g$.

## 2 Results

Thus summing over the initial and final states in (1) with regard for the energy conservation law, we find the Auger-recombination time $\tau^A_{ee}$:

$$1/\tau^A_{ee} = G/N_e = \frac{8\sqrt{3}(2\pi)^5}{2^{n_3}}\frac{E_B}{\hbar}\left(\frac{\hbar\omega E_0}{E_g^2}\right)^{1/2} \times$$
$$\times \left(\frac{\lambda_{E_0}}{d}\right)^4 (\lambda_{E_0}\lambda_T)^{1/2} a_{\mathrm{H}}{}^4 N_e N_h \psi(T, n_3). \tag{10}$$

Here $N_e$ is the two-dimensional electron concentration, $N_h$ is the tridimensional hole concentration; $E_B = \frac{me^4}{2\hbar^2\kappa^2}$ is the Bohr electron energy; the characteristic lenghs $\lambda_{E_0}$, and $\lambda_T$ are equal to

$$\lambda_{E_0} = \left(\frac{\hbar^2}{2m_e E_0}\right)^{1/2}, \lambda_T = \left(\frac{\hbar^2}{2m_e T}\right)^{1/2}$$

respectively, $d$ is the characteristic quantum-well width corresponding to the dimensional quantization energy $E_0$, $\psi(T, n_3)$ is a dimensionless function of the temperature and magnetic field equal to unity when the transition is resonant, and $\exp(-\frac{\hbar\omega}{3T})$ outside the resonance.

The oscillating behaviour of $1/\tau_{ee}^A$ as a function of magnetic field is an apparent result. When two electrons compile as Coulombian ones at the lowest Landau level, one of these passes into the valence band, another, absorbing the transmitted energy, turns into a highly excited state. The rate of such process is maximum if the highly excited electron exactly arrives at the Landau level of the number $n_3$, fitted the energy conservation law (formula (9)) (resonance transition), and small (or equal to zero at $T = 0$) if the highly excited electron has fallen between two Landau levels (non-resonant transition).

The work was partially supported by the Russian Foundation of Fundamental Research (Projects 96-02-17952 and 97-02-18151) and Russian State Program "Physics of Solid State Nanostructure" (Grants 97-0003 and 97-1035).

## References

[1] C. R. Pidgeon, E. N. Brown. *Phys. Rev.* **146** 575 (1966).
[2] R. R. Gerhardts. *Sol. St. Comm.* **23** 137 (1977).
[3] A. D. Andreev, G. G. Zegrya. *JETP* **78(4)** 539 (1994).
[4] L. D. Landau, E. M. Lifshitz. *Quantum Mechanics: Non-Relativistic Theory*, 3rd ed., London: Pergamon, 1977.
[5] G. G. Zegrya, A. S. Polkovnikov. *JETP* **86(4)** (1998).

Ioffe Institute
6th Int. Symp. "Nanostructures: Physics and Technology"
St Petersburg, Russia, June 22–26, 1998.



# Electronic superstructures in doped semiconductor superlattices

*I. P. Zvyagin*
Faculty of Physics, Moscow State University,
119899, Moscow, Russia

**Abstract.** We show that in doped semiconductor superlattices with narrow quantum wells at low temperatures and at sufficiently low doping levels, the exchange-correlation contribution to the system energy can exceed the sum of the kinetic and Hartree energies. Under these conditions, the uniform distribution of electrons over the wells becomes unstable, and the ground state corresponds to inhomogeneous distribution (electronic superstructure). For GaAs/GaAlAs superlattices the estimate of the critical doping concentration at which the stability of the homogeneous state at $T = 0$ K is lost yields the value of about $10^{17}$ cm$^{-3}$. Inhomogeneous ground states are discussed.

## Introduction

The fact that the ground state of a system of interacting electrons can become inhomogeneous (Wigner crystallization [1]) has been widely discussed in the literature. However, the conditions for Wigner crystallization are very restrictive and, in the absence of magnetic field, it has only been observed in electron sheets over the surface of liquid helium. In semiconductor superlattices (SL), new possibilities for the formation of inhomogeneous states appear, in particular, related to inhomogeneous electron distribution over the wells of the SL. One of the mechanisms was discussed in [2], where the symmetry breaking resulted from the carrier delocalization in the second subband for some specific shapes of the SL profile. In [3], a different mechanism of symmetry breaking was suggested for doped SL with electrons in the lowest subband, related to the exchange-correlation contribution to the total energy of the system. In what follows, we present the analysis of the latter situation; we study the ground state at $T = 0$ K and the possibility of spontaneous symmetry breaking in a system of interacting electrons in doped compositional SL.

## Density functional

It is convenient to use the approach based on the density functional theory. An important feature of the electron gas in a SL is that the confinement potential is generally not weak and forms the electronic states. We consider the case in which the wells of the SL are sufficiently narrow so that only the lowest subband is occupied, and moreover, the overlap of the wave functions of neighboring wells which determines the miniband width is sufficiently small. In this case one can use the method analogous to the tight binding approach and explicitly write the energy as the functional of the electron density $n$, thus making a straightforward analysis of the spatial distribution of the electron density possible. We have

$$E[n] = T[n] + E_{\text{Hartree}}[n] + E_{\text{ext}}[n] + E_{\text{xc}}[n], \tag{1}$$

where $T[n]$ is the kinetic energy of noninteracting electron gas, $E_{\text{Hartree}}$ is the energy of electron-electron interaction calculated in the Hartree approximation (including the interaction with the positive background), $E_{\text{ext}}$ is the energy of interaction with external fields (if present), and $E_{\text{xc}}$ is the remaining part of the energy (the so called exchange-correlation energy). We write the functional (1) using the set of states in the confinement potential, so that the electron density is a function of $\{\rho, i\}$, where $\rho$ is a radius vector in the well plane and $i$ is the discreet well number.

In what follows we study distributions of electron density over the wells of the SL in the absence of external fields; we call a distribution inhomogeneous if it corresponds to different average in-plane concentrations for different wells. We shall see that the conditions for the transition to such inhomogeneous states are much less restrictive than conditions for Wigner crystallization for the two-dimensional electron gas in a well. For this reason, we can assume that the electron density is independent of $\rho$, $n = \sum_i \nu_i \delta(z - z_i)$, where $z$ is the coordinate along the SL axis, $z_i = i\,d$, $d$ is the SL period and $\nu_i$ is the two-dimensional density in the $i$ th well; hence the density functional becomes simply a function of many variables $\nu = \{\nu_i\}$. For a small overlap, we can explicitly write the terms in the energy functional (1). The kinetic energy is additive,

$$T[\nu] = \sum_i T(\nu_i), \tag{2}$$

where $T(\nu_i) = 2\nu_i^2/2\rho_0$ is the kinetic energy of two-dimensional electron gas in the $i$ th well and $\rho_0$ is the density of states in a well. For the Hartree contribution we have

$$E_{\text{Hartree}}[\nu] = \sum_{i,j} V_{ij}(\nu_i - \nu_0)(\nu_i - \nu_0), \tag{3}$$

where $V_{ij} = -(2\pi e^2 d/\epsilon)|i-j|$, $\epsilon$ is the dielectric constant, and $\nu_0$ is the average electron concentration per well per unit area; for uniform donor doping $\nu_0 = N_d d$. For weak overlap of the wave functions of adjacent wells the exchange energy is also additive,

$$E_{\text{xc}}[\nu] = \sum_i E_{\text{xc}}(\nu_i), \tag{4}$$

where $E_{\text{xc}}(\nu_i) = C_{\text{xc}}(e^2/\epsilon)\nu_i^{3/2}$ is the exchange energy for two-dimensional electron gas in the $i$ th well and $C_{\text{xc}} \approx 0.81$ [4, 5]. The correlation energy is additive, provided that the radius of the Coulomb hole is smaller than the distance between the wells, $\nu_0^{-1/2} << d$. At small concentrations, the additivity is no more valid; in this case, however, the correlation energy contribution plays minor role in the transition to inhomogeneous state, and for simplicity we restrict ourselves with the exchange contribution. It can be easily seen that the inclusion of correlation gives rise to a weakening (unessential for $\nu_0^{1/2} d << 1$ ) of the conditions for the transition to the inhomogeneous state.

**Instability of the homogeneous distribution**

Once the energy functional is explicitly known, we can study the stability of the homogeneous ground state with respect to small perturbations. It is known that both in three- and two-dimensional electron gas, the Wigner crystallization occurs via a spin-polarized

state [6, 7]. As follows from (1)–(4), the stability of the nonpolarized ground state in any of the layers with respect to transition to the spin-polarized state is lost if

$$\nu_0 < (3C_{xc}e^2\rho_0/2\epsilon)^2. \tag{5}$$

Taking account of the weak overlap of wave functions of adjacent wells, we can see that the lowest energy corresponds to the antiferromagnetic-type ordering of spin polarizations of adjacent layers.

The variation of (1)–(4) yields the following condition for the loss of stability of the spatially homogeneous state:

$$\frac{1}{\rho_0} + \frac{2\pi e^2 d}{\epsilon} - C_x \frac{3e^2}{4\epsilon\nu^{1/2}} < 0. \tag{6}$$

It is seen that condition (5) which determines the threshold impurity concentration $N_d^*$ for the transition to the spin-polarized state is less strict than the condition for the loss of spatial homogeneity (6), i.e. the transition to an inhomogeneous state occurs via the spin-polarized state. This is due to the Hartee contribution which impedes the appearance of the inhomogeneous distribution. At the threshold concentration where the stability of the homogeneous solution is lost, the "most dangerous" density fluctuations are those corresponding to the period doubling. One can show that an inhomogeneous solution (electronic superstructure) with the period $2d$, stable with respect to small fluctuations, can exist for impurity concentrations $N_d < N_{d1}^*$, where $N_{d1}^* > N_d^*$. For $N_{d2}^* < N_d < N_{d1}^*$ it exists as a metastable state and then (for $N_d < N_{d2}^*$) it becomes the ground state. At still lower concentrations solutions with greater commesurate periods are also possible. It should be noted that the energy gain when an inhomogeneous state is formed decreases rapidly with decreasing concentration; accordingly, the temperature stability of the superstructures is expected to decrease at lower doping levels, and the intermediate concentrations are optimal for their observation.

**Discussion**

Thus in doped short-period doped SL, electronic superstructures (electron distributions over the wells inhomogeneous in the direction of the SL axis) can exist. The mechanism of spontaneous symmetry breaking in our case is, however, different from that of Wigner crystallization. Although formally the problem is reduced to a one-dimensional one, the transition is actually due to exchange interaction in quasi-two-dimensional quantum wells. The substantial weakening of the conditions for the transition to inhomogeneous ground state is due to the following reasons. In the theory of Wigner crystallization, the local density approximation in the density functional theory is known to appreciably overestimate the threshold concentrations, as is seen, e.g., from Monte Carlo calculations [7, 8]. This reflects the important role of corrections in the gradient expansion of the density functional. In our case, the overlap integral plays the role similar to that of gradient corrections, the expression for the density functional is similar to that of the local density approximation and the role of overlap corrections is actually small.

One can estimate the concentration of the doping impurity corresponding to the creation of the superstructure at $T = 0$ K. Taking $\rho_0 = 3 \cdot 10^{13}$ eV$^{-2}$ cm$^{-2}$, $\epsilon = 12.7$, and $d = 9$ nm, we obtain for the critical donor concentration $N_{d2}^* \approx 8 \cdot 10^{16}$ cm$^{-3}$. This indicates the possibility of the existence of electronic superstructures in doped SL under

conditions essentially less restrictive than those for the Wigner crystal. The appearance of the superstructure is expected to have much more pronounced effect on vertical transport in SL than the transition to the spin-polarized state. In fact, it is accompanied by the shifts of the size quantization levels in adjacent wells and by the appearance the gap in the spectrum of elementary excitations related to charge transfer between the wells. These excitations actually determine the vertical (in the direction of the SL axis) conductivity of the structure at finite temperatures. Vertical conductivity anomalies observed in doped GaAs/GaAlAs SL [3] just at impurity concentration $10^{17}$ $cm^{-3}$ might be related to the emergence of the superstructure.

The work was supported by the Russian Foundation for Basic Research (grant 97-02-17334) and INTAS (grant 94-4435).

## References

[1] Wigner E. P. *Phys. Rev.* **46** 1002 (1934).
[2] Tugushev V. V. and Zhukovskii E. A. *Solid State Commun.* **96** 203 (1995).
[3] Richter G., Stolz W., Thomas P., Koch S., Maschke K. and Zvyagin I. P. *Superlattices and Microstructures* **22** 475 (1997).
[4] Isihara A. *Quantum Liquids*, New York, Springer, 1995.
[5] Koch W. and Haug H. *Quantum theory of the optical and electronic properties of semiconductors*, 2nd ed., Singapore, World Scientific, 1993.
[6] Ceperley D. M.. *Phys. Rev.* **B 18** 3126 (1980).
[7] Senatore G. and March N. H.. *Rev. Mod. Phys.* **66** 445 (1994).
[8] Ceperley D. M. and Adler B. J. *Phys. Rev. Lett.* **45** 567 (1980).

Ioffe Institute
6th Int. Symp. "Nanostructures: Physics and Technology"
St Petersburg, Russia, June 22–26, 1998.



# Nonharmonic Bloch oscillations in GaAs/AlGaAs superlattices

*K. L. Litvinenko*†, K. Kohler‡, K. Leo‡, F. Loser‡ and V. G. Lyssenko†
† Institute of Problems of Microelectronics Technology RAS,
142432, Chernogolovka, Russia
‡ Institute für Angewandte Photophysik, Technische Universität Dresden,
01062 Dresden, Germany

Bloch [1] and Zener [2] theoretically calculated that in the materials with a periodical potential in the case of applying the steady external electric field the electrons should move periodically. This periodical motion is called Bloch oscillations.

Bloch oscillation can be seen experimentally when the period of Bloch oscillation is longer enough than the relaxation time of electrons and holes. This condition may be made up in such structures as multiple quantum wells and superlattices. Four wave mixing (FWM) technique was used for investigation of Bloch oscillations in superlattices in [3]. It was shown that the resonant position of exciton lines in the spectrum of FWM signal displays the harmonic oscillation, which is caused by the changing of local internal electric field by the periodical motion of electron wave package. In [3] was also mentioned that the anticrossing of heavy hole and light hole excitons can lead to nonharmonic Bloch oscillation.

To investigate the nonharmonic Bloch oscillations we used spectrally resolved four

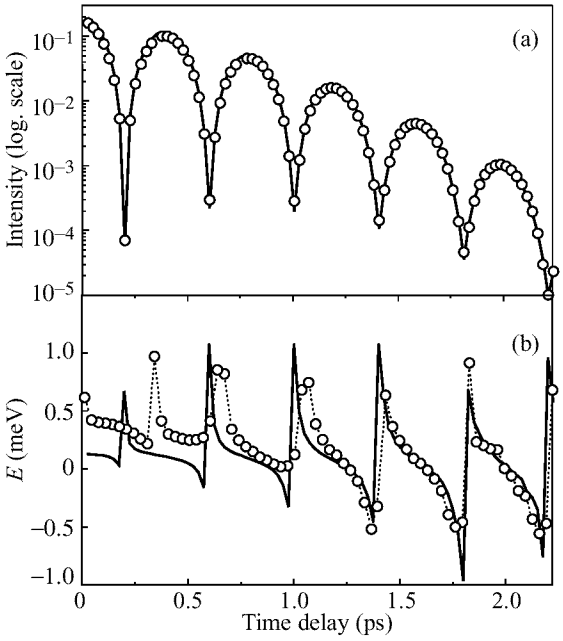


**Fig 1.** The experimental (open circles) and theoretical (solid line) dependencies of the intensity (a) and resonant position (b) of heavy hole exciton on the time delay

wave mixing technique. The superlattice with barriers of 17 Å and quantum wells of 97 Å was investigated. Our main experimental result is shown in Fig. 1 by opened circles. The nonharmonic Bloch oscillation (a) and beats of the intensity of heavy hole exciton line (b) we explained by the model of quantum beats of inhomogeneous exciton lines [4]. The results of our calculations are presented in Fig. 1 by solid lines. The very good agreement of theoretical calculation with experimental results proved the quite strong influence of inhomogeneous broadening on the Bloch oscillation of electron wave package.

## References

[1] F. Bloch *Z. Phys* **52** 555 (1928).
[2] C. Zener, *Proc. R. Soc. London Ser. A* **145** 523 (1932).
[3] V. Lyssenko, G. Valusis, F. Loser et al. *Phys. Rev. Lett* **79** 301 (1997).
[4] J. Erland, V. Lyssenko et al. *Phys. Rev. B.* **50** 15047 (1994).

Ioffe Institute
6th Int. Symp. "Nanostructures: Physics and Technology"
St Petersburg, Russia, June 22–26, 1998.



# Correlated dopant distributions in delta-doped layers

*P. M. Koenraad*
COBRA Inter-University Research Institute
Physics Department, Eindhoven University of Technology
P.O. Box 513, 5600 MB Eindhoven, The Netherlands

**Abstract.** In this paper we discuss the observation of correlations in the spatial distribution of Be atoms in delta doped layers. In Si delta doped samples we show that correlations in the charge distribution occur when DX centers are populated. The mobility enhancement we measure in our structures agrees with the calculated enhancement due to correlations effects.

## 1 Introduction

In most bulk-grown semiconductors ionized impurities dominate the scattering at low temperature. Modulation doping has been used successfully to suppress the scattering of free electrons on these ionized donor impurities. In this doping technique the ionized donor impurities are spatially separated from the free electron gas resulting in record mobilities of up to $2\times10^7$ cm$^2$/Vs. However in low-dimensional structures, like the well-known GaAs/AlGaAs heterostructures, ionized impurities still dominate the scattering of the electrons. However, in these heterostructures the maximum electron density is about $8\times10^{15}$ cm$^{-2}$. In many occasions one would like to have a much higher electron density. Delta doped layers are capable of delivering very high electron densities and have been studied in great detail. The delta doped layer has a thickness of typically 2 nm when the sample is grown at low growth temperature. Due to the high doping concentration the effective Bohr-radii of the doping atoms in the doping layer overlap and no freeze-out of the electrons occurs at low temperature. The thin layer of ionized impurity atoms forms a V-shaped Coulomb potential which has a thickness smaller than the de Broglie wavelength of the electrons and thus 2-D confined levels are formed. Normally a few levels are populated with electrons due to the high doping concentration. The strong overlap of the electron wavefunctions with the ionized impurities at the center of the well is reflected in the very low mobility of the electrons. In the lowest confined state we find electron mobility values of typically 1.000 cm$^{-2}$/Vs. In higher subbands the electron mobility can be quite different due to: (i) a smaller overlap between the electron wavefunction and the ionized impurity distribution (ii) a lower Fermi-velocity of the electron, (iii) a different screening.

A few decennia ago it has been proposed that the mobility in bulk doped samples might be enhanced due to ordering in the spatial distribution of the ionized impurities [1]. It is a well-known fact that ordered, or correlated, distributions of scatterers lead to a strong reduction of the scattering. For instance electrons in a semiconductor crystal are not scattered by the crystal itself but only by the imperfections in the crystal like: (neutral) impurities, growth defects, alloy fluctuations and phonons. In this paper we will discuss results we have obtained in delta doped layers where, due to the very high doping concentration, the ionized impurities interact with each other and thus give rise

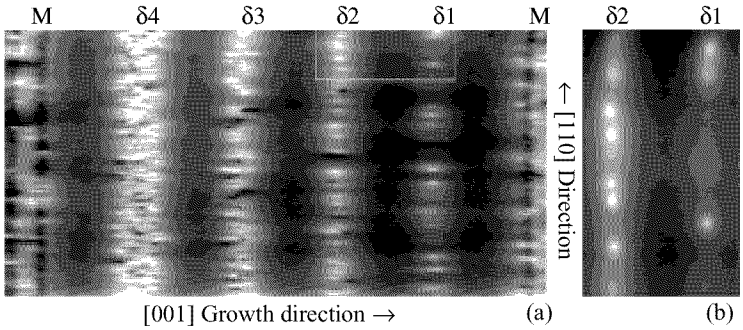


**Fig 1.** Filled state X-STM image (sample bias −1.0 V) of a structure containing several Be delta doped layers. (a) Large scale image (120 nm × 300 nm). The vertical scale (300 nm) is strongly compressed. The active Be atoms appear as white hillocks. (b) Enlarged view (31 nm × 54 nm) of the section containing the two doping layers with the lowest doping concentration. Atomic corrugation is observed in both directions allowing an exact position determination of the Be doping atoms.

to correlations in the distribution of ionized impurities. These correlations result in an enhanced mobility.

## 2 Correlations in the spatial distribution of Be-atoms studied by X-STM

With present day growth techniques like MBE, CBE etc. atomically sharp interfaces and doping profiles can be grown. The quality of the interfaces and their composition can be assessed at the atomic scale by cross-sectional Scanning Tunneling Microscopy (X-STM) [2]. In a X-STM setup the samples are cleaved under UHV conditions ($P < 10^{-11}$ torr) along either the (110) or the $(1\bar{1}0)$ plane. Because the two latter planes are parallel to the [001] growth direction we can image a cross-section of the grown layer structure. Several authors have recently reported that they were able to observe individual dopant atoms in semiconductor materials by X-STM [3, 4]. Therefore one can study both the thickness of a doping layer and the distribution of the dopant atoms within the dopant plane using X-STM.

The Be delta doped sample we have studied with X-STM was grown at 480°C on a (001) $p^+$ substrate with an alignment within 0.2° of the [001] direction. The growth rate was about 1 $\mu$m/h (1 monolayer/s). The doping layers where obtained by opening the shutter of the Be furnace during a growth interrupt lasting from 10 up to 360 s. During the growth interrupts the growth surface was kept under an As-flux. In this way a stack of four doping layers was produced with doping concentrations of $3 \times 10^{12}$, $10 \times 10^{12}$, $30 \times 10^{12}$, and $100 \times 10^{12}$ $cm^{-2}$ respectively. The highest doping concentration is equal to about 1/6 of a full monolayer. The doping layers were separated by 25 nm of undoped GaAs. The stack of four delta doping layers was repeated 3 times in the structure and the stacks were separated from each other by one or more 2.5 nm thick $Al_{0.2}Ga_{0.8}As$ layers which we used as marker layers. The intended doping concentrations was checked by SIMS measurements and the electrical activity of the dopant atoms was determined by etching CV profiling.

In Fig. 1 we show a large scale As-related image across a full stack of four delta

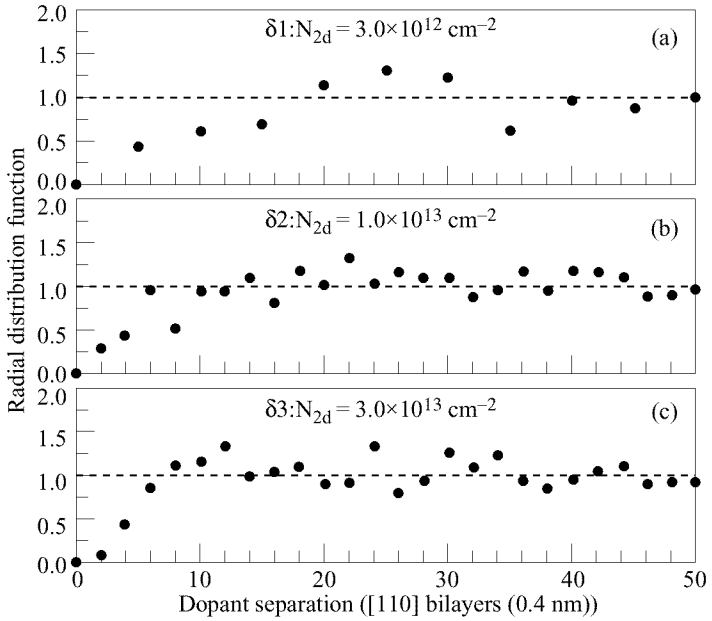


**Fig 2.** Radial distribution function for the three lowest-concentration doping layers as determined from our X-STM measurements. The dashed line represents the distribution function for a purely random separation.

doping layers. Clearly visible are the white hillocks which are due to individual Be doping atoms and the dark $Al_{0.2}Ga_{0.8}As$ marker layers. Note that the hillocks are absent between the delta doping layers. Each hillock extends over a few lattice sites because one does not observe the ionized Be atom itself but its Coulomb effect on the electrons tunneling in the immediate surrounding of the Be atom. The radius (2.5 nm) of each hillock is almost equal to the Bohr-radius of an ionized Be atom. The ionized Be atoms closest to the cleaved surface appear most strongest whereas the ones deeper below surface appear weaker. Roughly we are able to observe Be atoms up to a depth of about 1.5 nm below the cleaved surface. The original topographic images allow to determine the position of the Be atoms with atomic resolution. Thus histograms of the position of the dopants can be obtained.

The histograms demonstrate that the two lowest-concentration delta layers have a near atomic layer thickness of 1 nm. However in the layers with a higher doping concentration a considerable broadening of the layers has occurred. We think that the broadening of the doping layer observed in the layers with highest doping concentrations is due to a mutual Coulomb repulsion between the ionized doping atoms. If this argument holds one would expect an in-plane ordering of the dopant atoms as well. In Fig. 2 we show the radial distribution function (frequency plot of dopant separation of all pairs of dopants) for the three lowest-concentration delta layers. In the case of a purely random distribution we would expect the radial distribution to be equal to 1 for all dopant separations. The distribution functions of the delta layers show clearly that the occurrence of close-spaced neighbors is less probable. In these doping layers

with a correlated dopant distribution the mobility of the free holes must be enhanced. It is however rather difficult to prove this enhancement because one cannot easily prepare structures with either an uncorrelated or correlated doping layer. Furthermore accurate results concerning the mobility of the free holes can only be obtained if one can determine the hole mobility in the individual subbands. The subband mobility is obtained from the amplitude dependence of Shubnikov-de Haas oscillations. However, for p-type delta layers it is impossible to observe these SdH-oscillations because the mobility is extremely low, typically about 100 $cm^2/Vs$.

## 3 Effects of spatial correlations in the distribution of charged impurities on the electron mobility

We have shown that in n-type delta doped layers one can successfully obtain both the transport and the quantum mobility in the individual subbands [5]. The results showed that the mobility increases with the subband index. At first sight one would explain this by the stronger overlap of the electron wavefunction in lower subbands with the ionized Si dopant atoms compared to the wavefunctions in the higher subbands. This is however a crude simplification. We have shown that not only the overlap of the electron wavefunction with the ionized donors is important but also the Fermi velocity and, most important, a correct description of the screening [6].

In the case that DX centers saturate the electron density, correlation effects in charge distribution are expected to be present [7, 8]. Delta doped structures are ideal to study these correlation effects because there is strong interaction of the electrons with ionized impurities and there is also strong interaction between the ionized impurities themselves. In order that DX centers, and thus correlations in the charge distribution, have an influence on the electron mobility, the Fermi level has to be resonant with the DX level. It is a well established that DX centers in $Al_xGa_{1-x}As$ are resonant with the $\Gamma$ band at an Al fraction of approximately 0.25 or at a hydrostatic pressure of 20 kbar in GaAs [9]. In order to tune the position of the DX level relative to the Fermi level we have designed [10] and grown [11] delta doped GaAs/$Al_xGa_{1-x}As$/GaAs barrier structures. In these structures we need only modest hydrostatic pressures to populate the DX center effectively.

There is still some concern whether the DX centers traps only one electron ($DX^0$ model) or two electrons ($DX^-$ model). In either case a mixed valence system exists when a part of the free electrons is trapped by DX states, i.e. part of the Si atoms will have a positive charge (the normal shallow $d^+$ state) whereas the other part will have a neutral or negative charge (the deep $DX^0$ or $DX^-$ state). The spatial correlations in the charge distribution in a mixed valence system have a twofold effect [10, 11]: 1) the position of DX centers is lowered, and 2) the electron mobility increases. Lowering of the DX state means that a lower hydrostatic pressure, Al mole fraction or doping concentration is needed to populate this DX state. Spatial correlations in the charge distribution can be observed in the radial distribution function which was already discussed in the previous paragraph. In the case of the $DX^0$ model there is only one radial distribution function which gives the probability of finding a pair of two positively charged donors at a given separation. The distribution of the neutral donors is not important because the electrons are not scattered by them. In the case of the $DX^-$ model there will be three different radial distribution functions showing the probability of finding a pair of two

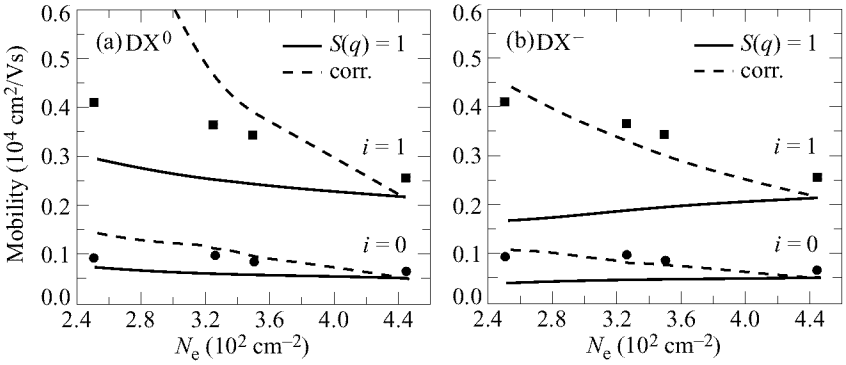


**Fig 3.** Quantum mobility as a function of the total free electron concentration in the structure doped at $4.4 \times 10^{12}\,\mathrm{cm}^{-2}$ and having a 4 nm thick $Al_{0.1}Ga_{0.9}As$ barrier. The experimental results (symbols) are compared with theory (lines). The theoretical results are shown without (guided by the dashed curves) and with (guided by the solid curves) inclusion of the correlation effects for the $d^+/DX^0$ (a) and $d^+/DX^-$ (b) models.

negative, two positive or one positive and one negative Si doping atoms respectively. These radial distribution functions are accounted for in the mobility calculations by the structure factor scaling the scattering rate [10, 11]. Because the spatial correlations have a short range character small scattering wave vectors are affected predominantly. Thus we expect that already small correlation effects have a strong influence on the mobility because ionized impurity scattering is most strongest for these small scattering wavevectors.

Applying hydrostatic pressure to the delta doped GaAs/$Al_{0.1}Ga_{0.9}As$/GaAs barrier structure having a doping concentration of $4.4 \times 10^{12}\,\mathrm{cm}^{-2}$ we are able to vary the total electron density and thus the population of the DX state. Our measurements show a reduction of the free electron density of approximately 30 percent at the maximum hydrostatic pressure of 10 kbar. In the case of that DX centers are negatively charged we find that the position of the DX level is at 320 meV above the $\Gamma$ conduction band. The observation of a mobility enhancement after the application of hydrostatic pressure does not prove that any spatial correlation in the charge distribution are present. We know from the normal delta doped structures and from the barrier doped structures as well that the mobility also increases when the doping concentration is lowered. If the $DX^0$ model applies then the number of scatterers is equal to the number of free electrons (the DX center becomes neutral after capturing an electron) whereas if the $DX^-$ model applies the number of scatterers remains equal to the total doping concentration (the DX center becomes negatively charged after the capture of two electrons). However when we compare the mobility in sample under pressure with samples at ambient pressure we clearly observe that for the structures with the same electron density, either at ambient pressure or under hydrostatic pressure, that the mobility is enhanced when $DX^-$ states are populated. This enhancement must be due to spatial correlations in the charge distribution of the mixed valence system.

Finally in Fig. 3 we show the quantum mobility measured in the structure under hydrostatic pressure as a function of the total free electron density together with the

calculated subband mobilities with and without the inclusion of spatial correlation effects. We show calculations for both the $d^+/DX^-$ (a) and $d^+/DX^0$ (b) models. The comparison between experiments and theory show that: correlations exist and can be correctly ac-counted for in the mobility calculations and 2) the DX center is negatively charged. Note also that the mobility enhancement is about a factor of two in the $i = 1$ subband and a factor of 1.5 in the $i = 0$ subband. From the Monte Carlo simulations we noted that the correlations are present up to distances of about 2 nm. In the STM results on the Be delta doped structures we observed correlations up to at least 4 nm. This means that a mobility enhancement in these structures is very plausible.

## 4 Conclusions

Our X-STM measurements on Be-delta doped GaAs samples have shown that spatial correlations in the position of the doping atoms occur up to distances of 4 nm. In Si delta doped GaAs/$Al_xGa_{1-x}$/GaAs barrier samples we find a clear mobility enhancement when correlations in the spatial charge distribution occur.

## References

[1] I. Y. Yanchev, B. G. Arnaudov, and S. K. Evtimova, *J. Phys. C* **12** L765 (1979).
[2] P. M. Koenraad, M. B. Johnson, and H. W. M. Salemink, *Materials Sci. For.* **196-201** 1471 (1996).
[3] M. B. Johnson, P. M. Koenraad, W. C. van der Vleuten, H. W. M. Salemink, and J. H. Wolter, *Phys. Rev. Lett.* **75** 1606 (1995).
[4] M. C. M. M. van der Wielen, A. J. A. van Roij, and H. van Kempen, *Phys. Rev. Lett.* **76** 1075 (1996).
[5] P. M. Koenraad, chapter 17 in the book *Delta-doping of Semiconductors*, ed by E. F. Schubert, Cambridge University Press, UK (1996).
[6] G. Q. Hai, N. Studart, F. M. Peeters, P. M. Koenraad, and J. H. Wolter, *J. App. Phys.* **80** 5809 (1996).
[7] E. Buks, M. Heiblum, and H. Shtrikman, *Phys. Rev. B* **49** 14790 (1994).
[8] Z. Wilamowski, J. Kossut, T. Suski, P. Wisniewski, and L. Dmowski, *Semicond. Sci. Technol.* **6** B34 (1991).
[9] P. M. Mooney, *J. Appl. Phys.* **67** R1 (1990).
[10] J. M. Shi, P. M. Koenraad, A. F. W. van de Stadt, F. M. Peeters, J. T. Devreese, and J. H. Wolter, *Phys. Rev. B* **54** 7996 (1996).
[11] P. Sobkowicz, Z. Wilamowski, and J. Kossut, *Semicond. Sci. Technol.* **7** 1155 (1992).

Ioffe Institute
6th Int. Symp. "Nanostructures: Physics and Technology"
St Petersburg, Russia, June 22–26, 1998.



# Room temperature ballistic transport in deeply etched cross-junctions

*Katharina Hieke* and Jan-Olof Wesström
Royal Institute of Technology, Dept. Electronics, Electrum 229,
S-164 40 Kista-Stockholm, Sweden, e-mail hieke@ele.kth.se

**Abstract.** We measured the transmission in nanoscopic cross-junctions at variable temperature. The devices were prepared by deep etching through a two-dimensional electron gas in InGaAs/InP samples. Our experiments show that the transmission characteristic is partly ballistic even at room temperature. The measurements are analysed in terms of an equivalent network, and the involved resistances are related to the electron mean free path.

## Introduction

Nanoscopic cross-junctions are examples for non-classical devices that might have potential for novel applications at the same time as they are subject to very basic research. In a cross-junction an injected electron from one terminal can propagate into each of the remaining three ports or be reflected back to the source. If the size of the junction is smaller or comparable to the electrons mean free path, the probability for straight propagation into the opposite port will be enhanced, i.e. the electrons will propagate ballistically. This leads to nonlinearities in the transmission behavior. In a four-terminal resistance measurement, using the terminals 1–2 for the current source and 3–4 for voltage measurement (see Fig. 1a), a negative differential resistance will be found [1]. The behavior of the junction can be described by means of the conductance matrix $\hat{G}$: $I = \hat{G}U$, where $I$ and $U$ are the column vectors of the incoming currents and the voltages at each terminal, respectively. The conductance matrix can be written down if we apply Kirchhoff's rules on the equivalent network of resistances in Fig. 1b. We suppose that the junction has perfect symmetry. Thus, the two conductances $G_i = 1/R_i$ and $G_o = 1/R_o$ (corresponding to the "inner" straight and the "outer" bend current

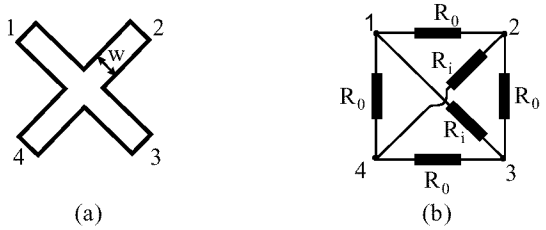


**Fig 1.** (a) symmetric cross-junction with width $w$, (b) corresponding network.

paths) can describe the junction. Then we can write:

$$I = \hat{G}U = \begin{pmatrix} 2G_o + G_i & -G_o & -G_i & -G_o \\ -G_o & 2G_o + G_i & -G_o & -G_i \\ -G_i & -G_o & 2G_o + G_i & -G_o \\ -G_o & -G_i & -G_o & 2G_o + G_i \end{pmatrix} U. \quad (1)$$

For the analysis of our measurements, we rewrite this equation to calculate $G_o$ and $G_i$ from the measured voltages and currents. The comparison between $G_o$ and $G_i$ lets us estimate the degree of ballistic transport in the junction.

## 1 Sample preparation and measurement details

We have prepared the devices by deep dry etching through a $In_{0.53}Ga_{0.47}As/InP$ two-dimensional electron gas (2DEG). The 2DEGs are grown by MOVPE on InP:Fe substrate. The active layer is a 12 nm thick $In_{0.53}Ga_{0.47}As$ layer, which by a 15 nm InP spacer is separated from the 10 nm thick n-InP doping layer ($1 \times 10^{18}$ $cm^{-3}$ Si). The carrier density in the active layer was determined in Hall measurements in macroscopic Hall bar samples. At $T = 23$ K we obtained a carrier density of $N_{2d} = 3 \times 10^{11}$ $cm^{-2}$ and electron mobility $\mu \approx 8$ $m^2/Vs$. The mean free path $L_0$ has been extracted from the Hall measurements. $L_0$ varies between 700 nm and 150 nm for temperature between 20 K and 293 K, respectively.

To fabricate nanostructures, the samples were patterned by electron beam lithography. We etched through the active layer with $CH_4/H_2$ reactive ion etching. Ohmic contacts were deposited on the capping InP layer and annealed at 425°C. Details of the sample fabrication are described in [2]. In that paper we demonstrated that this deep dry etching process allows fabrication of high-quality nanostructures, which exhibited quantized conductance at 20 K.

Electrical measurements (cw) have been done at variable temperature with Keithley K2400 source-meter units to source and measure voltages and currents. The contact resistance $R_c$ of our ohmic contacts was determined independently ($R_c$ varies between 1.8 kΩ and 9.5 kΩ when the temperature increases from 77 K to 293 K, respectively) and taken into account in the analysis of the measured data.

## 2 Results and discussion

The transmission characteristics of our devices were measured by supplying a voltage $V_{41}$ between the terminals 4 and 1 and measuring both the current $I_{41}$ and the voltage difference $V_{32}$ between terminals 3 and 2.

In Fig. 2, $V_{41}$ is plotted versus $V_{32}$ in a 320 nm wide cross-junction for 5 K and room temperature. The ballistic behavior at 5 K can be seen very clearly in the negative derivative $dV_{32}/dV_{41}$. With increasing magnitude of $V_{41}$ the number of electrons, which propagate ballistically, decreases, thus leading to decreasing magnitude of $dV_{32}/dV_{41}$. This is mainly due to increasing electron-electron and electron-LO-phonon scattering. For measurement at room temperature, we find that the magnitude of $dV_{32}/dV_{41}$ is strongly reduced and the sign is reversed. This corresponds to the potential difference between port 3 and port 2 created by electrons which underly drift-diffusion transport from port 4 to port 1.

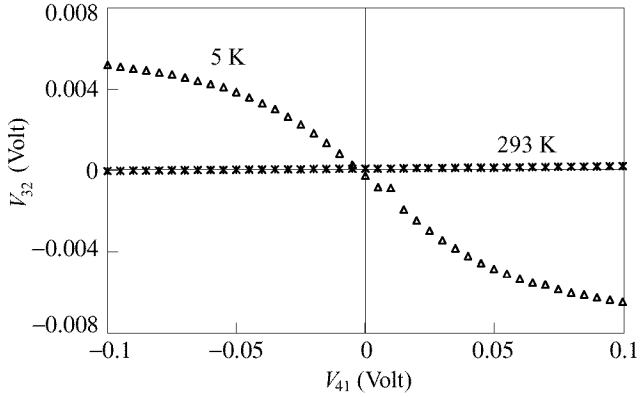


**Fig 2.** Dependence of $V_{32}$ on $V_{41}$ for a cross with $w = 320$ nm at 5 K and 293 K

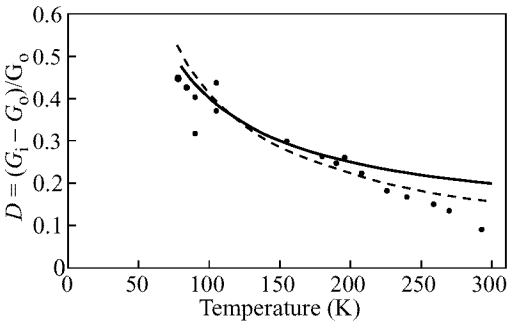


**Fig 3.** Degree of ballistic transport in a cross-junction with $w = 200$ nm versus temperature. Dots: extracted from the measurements; line: calculated using the model described in the text and the measured $L_0(T)$; dotted line: same as above, but modified with $G_o^c/G_i^c = 1.1$.

For a more detailed analysis we chose a 200 nm wide cross. We measured the dependence of $V_{23}$ and $I_{41}$ on $V_{41}$ between 77 K and 293 K. From the results, $G_o$ and $G_i$ were extracted as described above. Finally their normalized difference $D = (G_i - G_o)/G_o$ was plotted versus the temperature in Fig. 3. We used the values of $G_o$ and $G_i$ at $V_{41} = 0$, where electron-electron interaction should be neglegible.

Qualitatively, the decrease of $D$ with increasing temperature is expected, as higher temperature leads to increasing scattering and decreasing ballistic transport. It is remarkable that in the 200 nm wide cross-junction, even at room temperature a fraction of the electrons propagates ballistically ($D > 0$). This corresponds to the fact that the mean free path is comparable to the size of the cross.

For a first analysis of the experimental results we chose a purely phenomenological approach. The probability of scattering in a conductor with length $L$ is $P = L/(L + L_0)$ where $L_0$ is the mean free path of the electrons [3]. Now, we can suppose that we measure an ensemble average for all electrons passing through the cross-junction. Of all electrons injected in one port, we can expect the fractions $(1 - P)$ and $P$ to behave ballistically and as in classical (i.e. macroscopic) conductors, respectively. Let us idealize

the classical case with $G_o^c = G_i^c = G^c$ while in the strictly ballistic case $G_o^b = 0$, $G_i^b \equiv G^b$. We use $P$ as weight and get for the averaged $G_o^{ave}$, $G_i^{ave}$ the following equation:

$$D^{ave} = \frac{G_i^{ave} - G_o^{ave}}{G_o^{eff}} = \frac{1-P}{P}\frac{G^b}{G^c} = \frac{L_0}{L}\frac{G^b}{G^c}. \quad (2)$$

This relates our measured $D$ (identified with $D^{ave}$) to $L_0$. Using $G^b/G^c$ as adjustable parameter and the measured dependence $L_0(T)$, we get the solid curve in Fig. 3. In general, there is good agreement between both curves. However, at larger temperatures the measured $D$ drops faster than the calculated curve.

To understand this and to improve the agreement, a more detailed analysis is needed than what can be presented here [4]. In particular, a more thorough consideration of the scattering mechanism is required. The probability for an electron to be scattered into a port might not be the same for all ports. Instead, the scattering probability might be slightly larger for the side ports. This means that the calculation overestimates $G_i$ and underestimates $G_o$ with increasing number of scattering events (decreasing $L_0$ and $T$). This argument agrees with the observation of Fig. 2 ($dV_{32}/dV_{41} > 0$). The fit is getting much more satisfying if we suppose that $G_o^c = 1.1 \cdot G_i^c$ (dotted line in Fig. 3). However, more effort is needed to describe the behavior of the electrons in the cross in terms of a scattering matrix, which then can be related to the conductance matrix.

Furthermore, the electrically active width of the cross is likely to be smaller than the lithographically defined one. In a more detailed analysis one could determine the size of the depletion volume near the etched surfaces and estimate the actual size and shape of the confining potential, which probably deviates from the simple cross geometry.

## 3 Conclusions

To conclude, we presented experiments on the transmission characteristics of nanoscopic cross-junctions. Evidence for ballistic transport was found in a 320 nm wide cross at low temperature and in a 200 nm wide cross even at room temperature. The degree of ballistic transport, decreasing with increasing temperature, was related to the measured electron mean free paths by a simple model.

The authors thank B. Stålnacke (Semiconductor Laboratory, Royal Institute of Technology) for preparation of the 2DEG and B. Stoltz (Ericsson Components AB) for electron beam lithography.

## References

[1] Cumming D. R. S et al., *IEEE Transact. on Electron Devices* **43** 1754 (1996).
[2] Wesström J.-O. et al., *Appl. Phys. Lett.* **70** 1302 (1997).
[3] Datta S., *Electronic Transport in Mesoscopic Systems*, ch. 2, Cambridge 1997.
[4] Hieke K. et al., to be published.

Ioffe Institute
6th Int. Symp. "Nanostructures: Physics and Technology"
St Petersburg, Russia, June 22–26, 1998.



# On the applicability of miniband transport in semiconductor superlattices

*Andreas Wacker*† and Antti-Pekka Jauho‡
† Institut für Theoretische Physik, Technische Universität Berlin
‡ Mikroelektronik Centret, Danmarks Tekniske Universitet

**Abstract.** Electrical transport in semiconductor superlattices is often described by a miniband model, where the electrons perform a quasiclassical motion. Although this model is assumed to be valid in the limit of a large miniband width, some experiments indicate its validity for narrow minibands as well. By a comparison with a full calculation based on nonequilibrium Green functions we show, that this is the case if the width of the electronic distribution is larger than both the field drop per period and the scattering width. In addition we show that simplified expressions for miniband transport and sequential tunneling become identical in this regime.

The fabrication of semiconductor superlattices allows for the study of electric transport in an artificial band structure [1, 2, 3]. Spectacular effects like negative differential conductivity [4] and Bloch oscillations [5] have been observed experimentally. Recently, high frequency oscillations due to travelling field domains have been studied [6, 7] as well, see also Ref. [8] and references cited therein. For low electric fields (where higher subbands are not involved) the transport in superlattices is usually described by the semiclassical motion of electrons in the miniband [1]. This approach is assumed to be valid if the miniband width $\Delta$ is significantly larger than the scattering width $\Gamma$ [3]. Here we want to investigate its applicability by a direct comparison with a full quantum transport model.

We have recently proposed a transport model based on nonequilibrium Green functions in order to study transport in superlattices [9]. The current density is determined

$$J(F) = \frac{e}{2\pi^2} \int \mathrm{d}^2k \frac{2}{\hbar} \mathrm{Re} \left\{ \frac{\Delta}{4} G^<_{n+1,n}(t,t,\mathbf{k}) \right\} . \tag{1}$$

First we calculate the retarded and advanced Green functions $G^{\mathrm{ret}}_{m,n}$ and $G^{\mathrm{adv}}_{m,n}$ connecting different wells $n, m$. We use self energies $\Sigma^{\mathrm{ret}}$ and $\Sigma^{\mathrm{adv}}$ which include both the coupling between the wells (which is equal to $\Delta/4$) and scattering at $\delta$-potentials within the self-consistent Born approximation. Then we determine the lesser Green function between neighbored wells via the Keldysh equation

$$G^<_{m,n}(\mathcal{E},\mathbf{k}) = \sum_{m_1} G^{\mathrm{ret}}_{m,m_1} \Sigma^<_{m_1} G^{\mathrm{adv}}_{m_1,n} \tag{2}$$

where $\Sigma^<$ is obtained from a kind of relaxation time approximation. This approach allows the treatment of coupling and scattering on equal footing and therefore goes beyond the restrictions of standard transport models like miniband transport or sequential tunneling. Details of the calculation are given in Ref. [9]. The resulting current-field

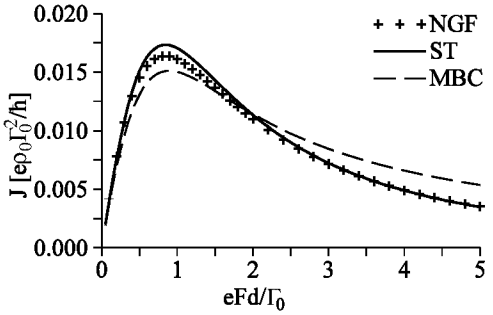


**Fig 1.** Current-field relation for three different approaches: sequential tunneling (full line), miniband conduction (dashed line), and our quantum transport theory (crosses). Parameters: $\Delta = 2\Gamma$, $k_B T = 3\Gamma$, $N_{2D} = 0.2\rho_0\Gamma$.

relations are found to be in good agreement with the results from the miniband conduction model if both $\Delta/2 \gg \Gamma$ and $\Delta/2 \gg eFd$ are fulfilled [9]. (Here $eFd$ denotes the potential drop per period.) Otherwise miniband conduction fails for a low electron concentration and a low temperature. In the opposite limit of small minibands ($\Delta/2 \ll \Gamma$) the results of our quantum transport model reproduce the results obtained from the sequential tunneling model described in Refs. [8].

Experiments [10, 11] indicate that miniband conduction holds for superlattices with relatively narrow miniband widths of $\Delta \approx 3-4$ meV as well, which are of the order typical scattering widths $\Gamma \sim 2-3$ meV [11]. These experiments have been performed at temperatures above 70 K, i.e. $k_B T > 6$ meV, which is larger than both $\Delta/2$ and $\Gamma$. Therefore we have performed several calculations within our full quantum transport theory for the experimental situation $k_B T \gg \Delta/2, eFd, \Gamma$ and compared the current field relations with the respective ones obtained from the miniband conduction model and sequential tunneling. As can be seen in Fig. 1 all three approaches give almost identical results in this regime.

In order to get more insight into these findings we want to consider the models for sequential tunneling and miniband conduction in detail. The miniband model is usually evaluated assuming a constant scattering time $\tau$ within the relaxation time approximation. In the nondegenerate limit one obtains the current density [3]

$$J_{\text{mini}}(F) = eN_{2D} \frac{I_1(\Delta/2k_B T)}{I_0(\Delta/2k_B T)} \frac{\Delta\tau}{2\hbar^2} \frac{eFd}{(eFd\tau/\hbar)^2 + 1} \tag{3}$$

where $N_{2D}$ is the electron density per period of the superlattice and $I_0$, $I_1$ are the modified Bessel functions. For $k_B T \gg \Delta/2$ the ratio between the Bessel functions becomes $\Delta/4k_B T$ and the current can be written as

$$J_{\text{mini}}(F) = eN_{2D} \frac{\Delta^2\tau}{8k_B T\hbar^2} \frac{eFd}{(eFd\tau/\hbar)^2 + 1} \quad \text{for} \quad k_B T \gg \Delta/2. \tag{4}$$

Now let us regard sequential tunneling between the wells. As the coupling between neighbored quantum wells is given by $\Delta/4$ the transition rate scales with $\Delta^2$. The current field relation is determined by a competition between the resonance condition and

the difference of chemical potentials between neighboring wells. Assuming a constant broadening $\Gamma$ of the states the current can be approximated by [8]

$$J_{\mathrm{seq}}(F) = e\rho_0 \frac{\Delta^2}{8\hbar} \frac{\Gamma}{(eFd)^2 + \Gamma^2} \int_0^\infty \mathrm{d}E \, [n_{\mathrm{F}}(E - \mu) - n_{\mathrm{F}}(E + eFd - \mu)] \qquad (5)$$

where $n_{\mathrm{F}}(x) = [\exp(x/k_{\mathrm{B}}T) + 1]^{-1}$ is the Fermi function, $\mu$ is the chemical potential with respect to the bottom of the well and $\rho_0 = m/(\pi\hbar^2)$ is the two-dimensional density of states. In the nondegenerate limit we have

$$[n_{\mathrm{F}}(E - \mu) - n_{\mathrm{F}}(E + eFd - \mu)] = \frac{N_{2D}}{\rho_0 k_{\mathrm{B}}T} \left[ \exp\left(-\frac{E}{k_{\mathrm{B}}T}\right) - \exp\left(-\frac{E + eFd}{k_{\mathrm{B}}T}\right) \right] \qquad (6)$$

and the integration yields

$$J_{\mathrm{seq}}(F) = eN_{2D} \frac{\Delta^2}{8k_{\mathrm{B}}T\hbar} \frac{\Gamma eFd}{(eFd)^2 + \Gamma^2} \quad \text{for} \quad k_{\mathrm{B}}T \gg eFd. \qquad (7)$$

Comparison between Eq. (4) and Eq. (7) exhibits that the expressions are identical if we set $\Gamma = \hbar/\tau$. Note that the origin of $\tau$ and $\Gamma$ is completely different: $\tau$ describes the relaxation time of electrons in the miniband while $\Gamma$ is the energy width of localized states in the wells. Nevertheless, both result from scattering processes and one can explicitly show the equality $\Gamma = \hbar/\tau$ for scattering at $\delta$-potentials [9]. From these observation we have found, that in the nondegenerate limit the simplified models for sequential tunneling and miniband conduction yield exactly the same relations if $k_{\mathrm{B}}T \gg \Delta/2, eFd$. In particular the current density scales with the square of the miniband width and is inversely proportional to the temperature as observed in Ref. [11] and Ref. [10], respectively. For a nondegenerate electron gas, one can similarly show that $J_{\mathrm{mini}} = J_{\mathrm{seq}}$ for $\mu \gg \Delta/2, eFd$ (see Refs. [8]). Again comparison with the full quantum model indicates that both approaches are valid for $\mu \gg \Delta/2, eFd, \Gamma$.

Note that all the approaches considered here treat scattering only in a phenomenological way and do not properly take into account energy relaxation processes. Therefore a full quantitative agreement with the experimental data can not be achieved. Nevertheless, we are convinced that the essential interplay between scattering and coupling is treated correctly and that we can draw conclusions concerning the applicability of the models. In particular we find that both miniband conduction and sequential tunneling are appropriate to describe the electric transport in superlattices if the energy width of the carrier distribution, $\mathrm{Max}(\mu, k_{\mathrm{B}}T)$, is large compared to the scattering width, the potential drop per period, and the miniband width.

## References

[1] L. Esaki and R. Tsu, *IBM J. Res. Develop.* **14** 61 (1970).
[2] R. F. Kazarinov and R. A. Suris, *Sov. Phys. Semicond.* **6** 120 (1972), [Fiz. Tekh. Poluprov. **6** 148 (1972)].
[3] A. Y. Shik, *Sov. Phys. Semicond.* **8** 1195 (1975), [Fiz. Tekh. Poluprov.**8** 1841 (1974)].
[4] A. Sibille, J. F. Palmier, H. Wang, and F. Mollot, *Phys. Rev. Lett.* **64** 52 (1990).
[5] C. Waschke, H. G. Roskos, K. Schwedler, K. Leo, H. Kurz, and K. Köhler, *Phys. Rev. Lett.* **70** 3319 (1993).

[6] J. Kastrup, R. Hey, K. H. Ploog, H. T. Grahn, L. L. Bonilla, M. Kindelan, M. Moscoso, A. Wacker, and J. Galán, *Phys. Rev. B* **55** 2476 (1997).
[7] E. Schombug, K. Hofbeck, J. Grenzer, T. Blomeier, A. A. Ignatov, K. F. Renk, D. G. Pavelev, Y. Koschurinov, V. Ustinov, A. Zhukov, S. Ivanov, and P. S. Kopev, *Appl. Phys. Lett.* **71** 401 (1997).
[8] A. Wacker, in *Theory of transport properties of semiconductor nanostructures*, edited by E. Schöll (Chapman and Hall, London, 1998).
[9] A. Wacker and A.-P. Jauho, *Phys. Rev. Lett.* **80** 369 (1998).
[10] G. Brozak, M. Helm, F. DeRosa, C. H. Perry, M. Koza, R. Bhat, and S. J. Allen, *Phys. Rev. Lett.* **64** 3163 (1990).
[11] A. Sibille, J. F. Palmier, M. Hadjazi, H. Wang, G. Etemadi, E. Dutisseuil, and F. Mollot, *Superlattices and Microstructures* **13** 247 (1993).

Ioffe Institute
6th Int. Symp. "Nanostructures: Physics and Technology"
St Petersburg, Russia, June 22–26, 1998.



# High frequency properties of electron waveguides, AC-admittance, scattering parameters, plasma oscillations

*Jan-Olof J. Wesström*
The Laboratory of Photonics and Microwave Engineering, Department of Electronics, Royal Institute of Technology, Electrum 229, S-164 40 Kista, Sweden

**Abstract.** The relation between the AC-admittance of single-mode electron waveguides is discussed in terms of the more complete scattering matrix of the same structure. For low frequencies, the admittance coincides with the series-inductance expressions in the literature. For higher frequencies the admittance shows resonances where it vanishes due to standing plasma waves.

## Introduction

Electron waveguide devices are a class of devices thought of as candidates for future high speed electronics. Therefore it is natural that the AC behavior of these structures has attracted increasing attention. In some low frequency calculations [1, 2] reflected and transmitted modes yield capacitive and inductive contributions respectively. For a long single-mode electron waveguide as in Fig. 1(a), where the inductive contribution is dominant, these calculations will typically yield an admittance built up of the usual DC-resistance $R_0 = h/2e^2 \approx 13$ kΩ in series with the kinetic inductance of the electrons in the waveguide yielding

$$Y(\omega) = 1/[R_0 + j\omega l R_0/(2v_F)], \tag{1}$$

where $l$ is the length of the electron waveguide and $v_F$ is the Fermi velocity.

Another manifestation of the dynamics in a single-mode electron waveguide or quantum wire are the plasma oscillations. These have been studied in for example [3, 4]. In contrast with the admittance calculations above most of these papers only consider infinitely long quantum wires, but on the other hand take the electrostatic environment of the structure into account (dielectric constant of the surrounding media, screening effects, etc).

In [5], quite a different microwave-engineering approach was applied to the plasma waves, thus describing the plasma waves as voltage and current waves traveling on transmission lines. This approach also allowed us to calculate the connection rules at the interfaces to the reservoirs forming part of ordinary microstrip transmission lines. These connection rules were formulated in terms of scattering-matrices.

The model developed in [5] also allows us to calculate the admittance. The object of the present paper is to do this and thus build a bridge between this microwave-engineering model and the concept of AC-admittance and thereby also relate the quantum inductance to the plasma waves. Apart from giving physical insight, this can also be used as a powerful tool for analyzing the hf-properties of electron waveguide devices. As an example we will use a long ideal single-mode electron waveguide at zero

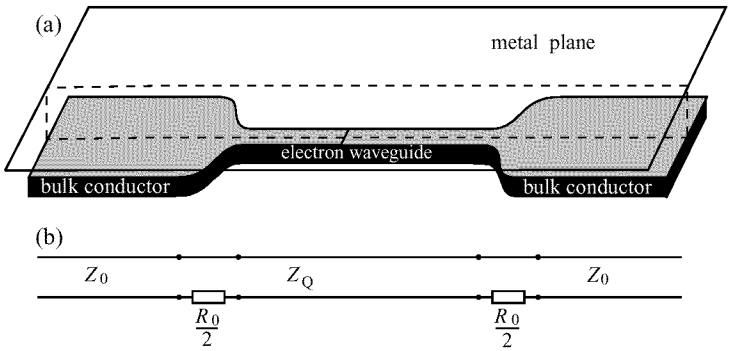


**Fig 1.** (a) Electron waveguide of length L between two reservoirs, (b) Transmission-line equivalent of the structure.

temperature. For low frequencies, the admittance obtained in this way is the same as the series quantum inductance formula. For higher frequencies, the expressions differ, yielding resonances where the admittance vanishes, since standing wave patterns form in the electron waveguide.

## 1 The voltage wave scattering matrix of an electron waveguide

We will now consider the electron waveguide as a micro-wave engineering 2-port where incoming voltage waves are partly reflected, partly transmitted to the other port. We will also derive the scattering matrix describing this. In the electron waveguide the signals propagate as plasma waves described in [5]. The propagation velocity of these waves was there found to be $v_p = \sqrt{1/(L_{tot}C_{tot})}$ where $L_{tot} = L_g + R_0/(2v_F)$ is the total inductance per unit length which is a sum of the ordinary magnetic inductance $L_g$ and the kinetic inductance $R_0/(2v_F)$ and $v_F$ is the Fermi velocity. In the same manner, the total capacitance per unit length is formed by the ordinary, electrostatic capacitance to the nearby conducting plane $C_g$ and the quantum capacitance due to the reduced density of states $C_{tot}^{-1} = C_g{}^{-1} + [2/(R_0 v_F)]^{-1}$. The boundary condition for the plasma wave at the interface between the electron waveguide and the reservoir (that forms the first part of the connecting microwave transmission line) was also derived. The result was a transmission-line equivalent where a characteristic impedance for the electron waveguide $Z_Q = \sqrt{(L_{tot}/C_{tot})}$ was introduced and a contact resistance of $R_0/2$ represented the junction. The total transmission-line equivalent for the electron waveguide connected between two microwave transmission lines then consists of a transmission line with $Z_Q$ representing the electron waveguide between the $R_0/2$ resistors connecting to the ordinary transmission lines. See Fig. 1(b). This model then gives the scattering matrix **S** relating ingoing and outgoing waves $\bar{V}^+$ and $\bar{V}^-$ at the structure:

$$\begin{pmatrix} V_1^- \\ V_2^- \end{pmatrix} = \begin{pmatrix} S_{11} & S_{12} \\ S_{21} & S_{22} \end{pmatrix} \begin{pmatrix} V_1^+ \\ V_2^+ \end{pmatrix}. \tag{2}$$

Using standard microwave-engineering analysis **S** is calculated from this model:

$$S_{11} = S_{22} = \frac{\left(\frac{R_0}{2} + Z_Q\right)^2 - Z_0^2 - \left[\left(\frac{R_0}{2} - Z_Q\right)^2 - Z_0^2\right] e^{-2jkl}}{A} \tag{3}$$

$$S_{12} = S_{21} = \frac{4e^{-jkl} Z_0 Z_Q}{A} \tag{4}$$

where

$$A = \left[ \left(1 + e^{-jkl}\right) \left( \frac{R_0}{2} + Z_0 \right) + \left(1 - e^{-jkl}\right) Z_Q \right] \times \left[ \left(1 - e^{-jkl}\right) \left( \frac{R_0}{2} + Z_0 \right) + \left(1 + e^{-jkl}\right) Z_Q \right]. \tag{5}$$

If we choose reasonable values [5] $Z_Q = 2R_0$, $Z_0 = 100\,\Omega$, the reflection $S_{11}$ stays within 1.5% from unity and that the transmission $|S_{12}|$ oscillates between 0.7% and 1.5%. The small transmission is due to the impedance mismatch between the ordinary transmission line and the electron waveguide. The corresponding measurement can be done with a microwave network analyzer. Measuring for example on a split gate structure, the ground of the hf-probes would be put in contact with the gate metal, while the signal leads would be put in contact with the ohmic contacts at the electron reservoirs.

## 2 Relation between the scattering matrix and the AC-admittance

The S-parameters relate incoming and outgoing voltage waves on the connecting transmission lines and since these waves are related to voltages and currents, we can use the S-parameters to calculate the admittance. Let waves with opposite signs impinge on the two ports $V_1^+ = -V_2^+$. Making use of the symmetry of the device we can calculate the voltage across the structure: $V = V_1 - V_2 = 2(V_1^+ + V_1^-) = 2V_1^+(1 + S_{11} - S_{12})$. In the same manner the current can be written as $I = I_1 = -I_2 = (V_1^+ - V_1^-)/Z_0 = V_1^+(1 - S_{11} + S_{12})/Z_0$. This yields the admittance

$$Y = \frac{I}{V} = \frac{1}{2Z_0} \frac{1 - S_{11} + S_{12}}{1 + S_{11} - S_{12}}. \tag{6}$$

This expression is the admittance in the sense that it relates voltage across the structure with the current into it. Also a measurement set-up with micro strips transmitting the micro-wave signal to the electron-waveguide contacts would yield such an odd excitation ($V_1^+ = -V_2^+$). There is however room for some discussion on the validity of this expression. Note that the net in Fig. 1(b) actually has 4 leads if we count the ground, and since there is a capacitive coupling to the ground it is not self-evident that the above expression is the correct one. Other excitations (e.g. $V_1^+ = V_2^+$) yield other result, but $V_1^+ = -V_2^+$ has the nice property of yielding the same current in port 1 as in port 2.

Inserting the expressions for the scattering parameters (3, 4) into (6) we obtain the admittance

$$Y(\omega) = \frac{1}{[R_0 + j2Z_Q \tan(kl/2)]}. \tag{7}$$

Note that the characteristic impedance $Z_0$ of the transmission lines used for the measurement cancels. Assuming a linear dispersion for the plasma waves $k = \omega/v_p$ the expression coincides with (1) for low frequencies since $(Z_Q l)/v_p = L_{tot} l \approx l R_0/(2v_F)$ since the magnetic inductance is negligible. Both expressions are illustrated in Fig. 2. We see that the expression derived in this paper oscillates due to the standing plasma

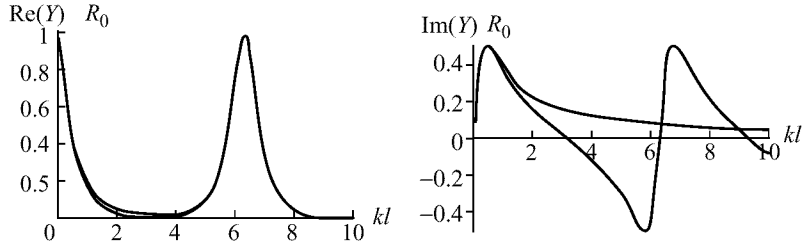


**Fig 2.** Real and imaginary part of the admittance of the structure in Fig. 1.

waves that form in the electron waveguide. At some frequencies both the real and the imaginary part of the admittance vanish. When $kl$ reaches $2\pi$ the curve repeats itself, again yielding a real admittance of $1/R_0$. For a $10\,\mu$ long electron waveguide with a plasma velocity $v_p$ as low as $10^5$ m/s the deviation from (1) would be seen already at a few GHz.

In conclusion, the relation between the admittance and the plasma oscillations, was investigated using a microwave-engineering approach where the voltage wave scattering matrix was used as an intermediate step. This approach proved to be a useful tool in finding the high frequency admittance of an electron-waveguide structure.

## References

[1] I. E. Aronov, G. P. Berman, D. K. Campbell, and S. V. Dudly. *J. Phys.: Cond. Mat.* **9** 5089 (1997).
[2] T. Christen and M. Büttiker. *Phys. Rev. Lett.* **77** 143 (1996).
[3] L. Wendler and G. Grigoryan, *Phys. Stat. Sol.* (b) **181** 133 (1994).
[4] M. Bonitz, R. Binder, D. C. Scott, S. W. Koch, and D. Kremp, *Phys. Rev. E* **49** 5535 (1994).
[5] J.-O. J. Wesström. *Phys. Rev. B* **54** 11484 (1996).

Ioffe Institute
6th Int. Symp. "Nanostructures: Physics and Technology"
St Petersburg, Russia, June 22–26, 1998.



# Phonon generation by current-carrying nanowires

*Y. M. Galperin*†‡, V. L. Gurevich‡ and H. Totland†
† Department of Physics, University of Oslo,
P. O. Box 1048 Blindern, N–0316 Oslo, Norway
‡ Solid State Physics Department, Ioffe Institute, 194021 St. Petersburg, Russia

**Abstract.** Spectral and spatial distributions of phonons generated in a quantum wire by a transport current are investigated as a function of the voltage across the nanostructure and the gate voltage. We start with consideration of the simplest case of a uniform nanowire which connects two thermal reservoirs. Then the role of the leads is discussed. It is shown that both spectral and angular distributions of emitted phonons depend significantly on the bias voltage. Studies of phonon generation allows one to determine the electron-phonon coupling constant in ballistic devices.

Electron-phonon interaction leads to absorption and emission of phonons by the electrons in quantum wires. In the equilibrium there is a detailed balance between the emitted and absorbed phonons. However, out of equilibrium, the distributions of electrons penetrating into a biased quantum wire from the leads are characterized by different chemical potentials. Therefore the phonon emission prevails over the absorption. The generation rate of the phonons at a given frequency $\omega$ propagating along a given direction is a specific function of the bias voltage. Knowing this function one can determine electron-phonon coupling constant, get information about the device shape, etc.

As we will see, at a small bias voltage only the transitions within one mode of transverse motion are allowed, while at large voltages the interband transitions are also possible. Consequently the voltage dependence of the generation rate is a step-like function. The threshold voltages are directly related to the band gaps between the modes of transverse quantization, while the generation rates at the plateaus are related to the electron-phonon coupling constant inside the nanowire. It is important to note that in this way one can study electron-phonon interaction in nanowires.

The edges of the channel play a specific role. Namely, if the channel's shape is smooth enough, one can describe the situation in terms of a position-dependent band structure [1]. We will show that the phonons with a given frequency and propagation direction can be generated only near specific points where the local energy and quasimomentum conservation laws are met. Consequently, the phonons emitted from the edges bear information about the position-dependent band gaps between the modes of transverse quantization.

## Uniform channel

In a *uniform* channel, the electron states are $\psi_{np}(\mathbf{r}) = L^{-1/2}\chi_n(\mathbf{r}_\perp)\exp(ipx/\hbar)$, where $L$ is a normalization length close to the physical length of the wire, $x$ is the longitudinal and $\mathbf{r}_\perp$ the transverse direction, $p$ is the $x$-component of the electron quasimomentum, and $\chi_n(\mathbf{r}_\perp)$ is the wave function of transverse quantization, the energy being $\epsilon_n(p) = \epsilon_n^0 + p^2/2m$. Here $m$ is the electron effective mass, and $\epsilon_n^0 \equiv \epsilon_n(p=0)$ is the

bottom of the $n$-th transverse band. The matrix element for phonon-induced transitions is $C_{nn'}(\mathbf{q}_\perp) = \langle\chi_{n'}|\exp(-i\mathbf{q}_\perp\mathbf{r}_\perp)|\chi_n\rangle$, where $\mathbf{q}$ is the phonon wave vector. For the phonon-electron collision operator one gets [2]

$$\left[\frac{\partial N_\mathbf{q}}{\partial t}\right]_{\text{coll}} = \frac{2}{\mathcal{A}}\sum_{nn'}\int d\xi_p\, W_\mathbf{q}\,|C_{nn'}(\mathbf{q}_\perp)|^2\,\left[f_{n,p+\hbar q_x}(1-f_{n'p})(N_\mathbf{q}+1)\right.$$
$$\left.-f_{n'p}(1-f_{n,p+\hbar q_x})N_\mathbf{q}\right]\,\delta[\epsilon_n(p+\hbar q_x)-\epsilon_{n'}(p)-\hbar\omega_\mathbf{q}]\,. \qquad (1)$$

Here $d\xi_p = dp/2\pi\hbar$, $\mathcal{A}$ is the cross section of the channel, while the factor 2 comes from the summation over electron spin (we assume all the transition probabilities to be spin-independent). The coupling coefficient $W$ for the piezoelectric coupling is $W_\mathbf{q} = (\pi/\rho\omega_\mathbf{q})[4\pi e\beta_{q,lq}\nu_l/\epsilon_{qq}]^2$. Here $e$ is the electron charge, $\beta_{i,ln}$ is the tensor of piezoelectric moduli (which is symmetric in the last two indices), $\epsilon_{il}$ is the tensor of dielectric susceptibility, and $\vec{\nu}$ is the polarization vector (that is the unit vector along the elastic displacement $\mathbf{u}$) of the phonon with the wave vector $\mathbf{q}$. The index $q$ indicates the projection of a tensor on the $\mathbf{q}$ direction, while $\rho$ is the mass density. For the deformation potential interaction we have $W = \pi\Lambda^2 q^2/\rho\omega_\mathbf{q}$, where $\Lambda$ is the deformational potential constant for the phonon branch under consideration.

Let us investigate the consequences of the energy and quasimomentum conservation $\epsilon_n(p+\hbar q_x) - \epsilon_{n'}(p) - \hbar\omega_\mathbf{q} = 0$. For the solution of this equation, $p_{nn'}$, one has

$$p_{nn'} = (m/\cos\theta)\,(s - \Delta_{nn'}/\hbar q) - (1/2)\hbar q\cos\theta\,, \qquad (2)$$

where $s = \omega/q$ is the sound velocity, $\theta$ is the angle between $\mathbf{q}$ and the $x$-axis, and $\Delta_{nn'} = \epsilon_n^0 - \epsilon_{n'}^0$. Consequently, the delta-function in Eq. (1) can be expressed as $(m/\hbar q|\cos\theta|)\,\delta(p-p_{nn'})$. Following Landauer-Büttiker-Imry (see e.g. [4]), we consider a semiconductor quantum channel connected to two reservoirs, each in independent equilibrium. Thus the equilibrium distribution functions are $f_n^{(0)}(p) = f^{(\mathrm{F})}[\epsilon_n(p) \pm eV/2 - \mu]$, where $f^{(\mathrm{F})}$ is the Fermi function.

Consider the transitions involving a phonon with a given $x$-component of the wave vector, $q_x > 0$. Such a phonon can be emitted by transition 1 from the state having positive initial momentum $p + \hbar q_x$ to the state with negative momentum $p$ (see Fig. 1, left). As is usually accepted [4], the initial and final states are determined by the Fermi functions with chemical potentials $\mu^{(\pm)} = \mu \pm eV/2$ and the same temperature $T$. For $n = n'$, the solution $p_{nn'}$ of Eq. (2) is $n$-independent and equal to $p_1 = ms/\cos\theta - (1/2)\hbar q\cos\theta$. So the $n = n'$ part of the collision term for $T = 0$ (or, to be more specific, $\hbar\omega_\mathbf{q} \gg k_\mathrm{B}T$) can be rewritten as

$$\left[\frac{\partial N_\mathbf{q}}{\partial t}\right]_{\text{coll}} = \frac{mW_\mathbf{q}}{\pi\mathcal{A}\hbar^2 q|\cos\theta|}\sum_n |C_{nn}(\mathbf{q}_\perp)|^2\,\theta[\mu^{(+)} - \epsilon_n(k_1)]\,\theta[\epsilon_n(p_1) - \mu^{(-)}]\,. \qquad (3)$$

where $k_1 = p_1 + hq_x = ms/\cos\theta + \hbar q_x/2$. One can easily see that a *current-carrying channel can generate phonons*, the phonon generation being restricted to the frequencies $2ms^2/\hbar \le \omega_\mathbf{q} \le eV/\hbar$. In the right panel of Fig. 1 the angular dependence of the phonon emission rate is shown for different bias voltages. The typical rate is $\mathcal{R} = W_\mathbf{q}/2\pi\mathcal{A}\hbar s$. Assuming $4\pi\beta^2/\epsilon\rho s^2 = 4\times10^{-4}$, $s = 3\times10^5$ cm/s, $\epsilon$=10, $\mathcal{A} = 10^{-12}$ cm$^2$, $q = 6ms/\hbar$, $m = 0.07m_0$, we get $\mathcal{R} \approx 5\times10^{11}$ s$^{-1}$. It is seen that the

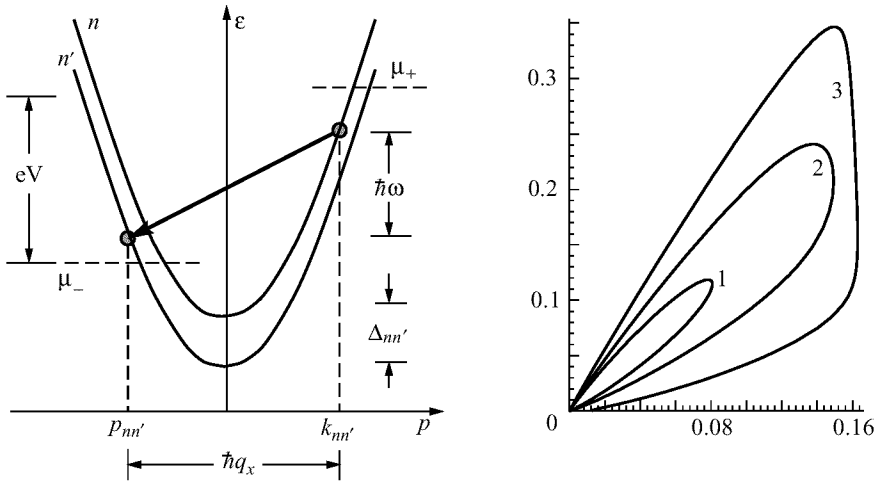


**Fig 1.** Left: Scheme of transitions. Right: Angular dependences of phonon generation rate near the threshold. $eV/k_BT$: 1 — 60, 2 — 65, 3 — 75.

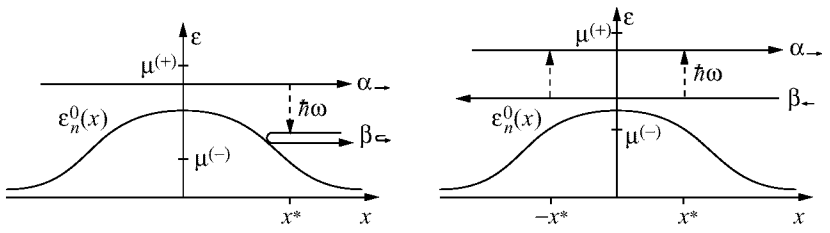


**Fig 2.** Left: Phonon emission in a nonuniform channel by a transition from a propagating to a reflected electron state. The transition is localized around the point $x^*$. Right: Phonon emission in a nonuniform channel by a transition between two oppositely directed propagating states. There are two transition points.

character of the angular dependence is changed at the threshold. The phonons can also be emitted by interband transitions. Qualitatively the angular dependences are similar to the case of intraband transitions, but the threshold values of voltage are shifted.

### Nonuniform channel

Now consider an adiabatic *nonuniform* quantum channel with the width depending on coordinate $x$. The electron wave functions for such channels can be subdivided into two categories – the propagating states and the reflected states on each side. An important simplification is that at $qL \gg 1$ one can employ the *stationary phase approximation* for estimation of the transition probabilities. As a result, it is the *local* conservation laws at the stationary phase points $x^*$ that enter transition probabilities. Let us again assume $T = 0$. Then the only possible phonon-generating processes are the ones shown in Fig. 2

For a transition of the kind in Fig. 2, right, there will in fact be *two* transition points,

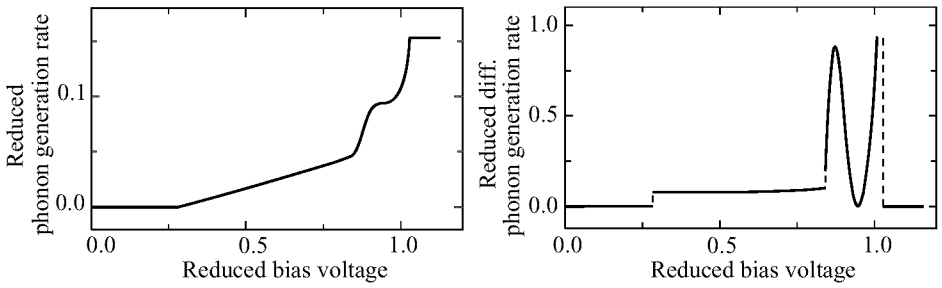


**Fig 3.** Dependence of the generation rate (left) and its voltage derivative (right) on bias voltage.

one on each side of the constriction The corresponding two parts of the transition amplitude give rise to the interference term $2\{1 + \sin[\varphi(x^*) - \varphi(-x^*)]\}$ where $\varphi$ is the phase of the transition amplitude. Fig. 3 shows the dependence of the generation rate on the bias voltage that results from such a term for a set of typical parameters. As $eV = \mu^{(+)} - \mu^{(-)}$ increases, more and more phonon emitting transitions become possible, and so the rate increases.

In conclusion, we have calculated the rate of phonon generation by a current-carrying quantum channel. It is shown that the spectral and spatial distributions of emitted phonons bear information both on electron-phonon coupling in the vicinity of the device and on characteristics of the electron spectrum.

V. L. Gurevich is grateful to the University of Oslo for hospitality and financial support of this work. His work was also partially supported by the Russian National Fund of Fundamental Research (Grant No. 97-02-18236-a). H. Totland is grateful to the Norwegian Research Council for financial support.

## References

[1] L. I. Glazman, G. B. Lesovik, D. E. Khmel'nitskii, and R. I. Shekhter, *Pis'ma Zh. Eksp. Teoret. Fiz.* **48** 218 (1988) [*Sov. Phys. — JETP Lett.* **48** 238 (1988)].
[2] V. L. Gurevich, *Phys. Rev. B* **55** 4522 (1997).
[3] V.L. Gurevich, V.B. Pevzner, G.J. Iafrate, *Phys. Rev. Lett.* **77** 3881 (1996).
[4] R. Landauer, *IRM J. Res. Dev.* **1** 233 (1957); **32** 306 (1989).

Ioffe Institute
6th Int. Symp. "Nanostructures: Physics and Technology"
St Petersburg, Russia, June 22–26, 1998.



# Electron velocity modulation under lateral transport in the weakly-coupled double quantum well structure

P. I. Birjulin, S. P. Grishechkina, I. P. Kazakov, Yu. V. Kopaev, S. S. Shmelev, *V. T. Trofimov*, M. V. Valeyko and N. A. Volchkov
P. N. Lebedev Physical Institute of RAS, Leninsky pr., 53, Moscow 117924, Russia

**Abstract.** Large electron velocity modulation was found under lateral transport in the GaAs/AlGaAs weakly coupled quantum well structure. It manifests in extremely strong dependence of the lateral conductance on the transverse electric field (gate voltage) as well as in the step-like shape of the lateral current on the lateral (source-drain) voltage.

## Introduction

The lateral transport properties of the coupled quantum wells are subject of wide investigation in connection with the search for the conductance modulation mechanisms that would not change the carrier concentration in the conducting channel. If the average number of carriers in the conducting channel of the structure remains constant the high-frequency limit of conductance modulation increases as the channel capacitance needn't be recharged.

## Structures and measurements

The structure consisted of two GaAs quantum wells separated by $Al_{0.3}Ga_{0.7}As$ barrier of 500 Å width. The lower non-doped quantum well QW1 of 200 Å width was combined by AlGaAs barrier layers, while upper triangle one QW2 was formed in Si-dopped GaAs cap layer near barrier interface. The electron mobilities at 300 K were about 8500 and 1500 $cm^2/Vs$ for the QW1 and QW2 respectively. Sheet carrier concentration in the conductive channel was about $10^{12}\,cm^{-2}$. Samples for measurements were prepared in the field effect transistor configuration with a Shottkey barrier gate, its length and width being 15 and 50 $\mu$m respectively. Ohmic contacts were formed by alloying of Au-Ge-Ni euthectics so that to provide reliable contact to both quantum wells. Normally open channel was driven by negative gate voltage. The lateral current dependences upon transverse electric field (gate voltage) and lateral potential difference (source-drain voltage) were measured at 77 and 300 K.

## Experimental results

Transistor channel conductivity dependence on the gate voltage was found to be non-monotonic for source-drain voltage higher than 0.6 V at room temperature (Fig. 1). Drain potentials are equal 0.1, 0.7, 1.25, 1.75, 2.25, 3.5, 4.5 V for curves 1–7, respectively. The transconductance increases up to extremely high value of 6 A/V at 4.5 V, and small auto-oscillations of lateral current are observed. The effect of the gate potential on the structure conductance significantly decreases as the temperature drops to 77 K. Figure 2 shows the dependences of the lateral current on the source-drain voltage,

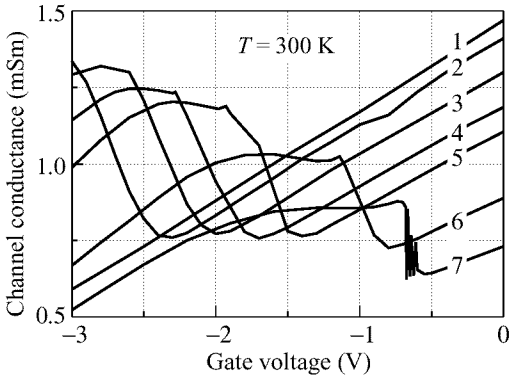


**Fig 1.** The channel conductance dependence on the gate voltage. The curves are plotted for the following source-drain voltages: (curve 1) 0.1 V; (curve 2) 0.7 V; (curve 3) 1.25 V; (curve 4) 1.75 V; (curve 5) 2.25 V; (curve 6) 3.5 V; (curve 7) 4.5 V.

the gate potential being 0, −0.8, −1, −1.2, −1.5 V for the curves 1–5, respectively. Sharp increase of the lateral current occures at the drain potential, corresponding to the transconductance sign inversion. Saturation of the current is observed at higher drain potential. At the highest source-drain voltage the current drops again for some samples (curves 2 and 3).

## Model

We explain the results by the electron tunneling between connected in parallel quantum wells with different saturation velocity of carriers in high electric field. Electron velocity saturates as a result of carrier heating, because lateral electric field magnitude exceeds 3 kV/cm. Field distribution along the structure differs for two quantum wells due to their different distance from the gate. Therefore, large potential difference between the wells occurs in the vicinity of positive electrode (drain), being comparable with lateral potential drop of the structure. The barrier between the wells becomes transparent for tunneling at high (up to $10^5$ V/cm) electric field, that leads to redistribution of the wells currents and to the modulation of the structure conductance. Figure 3 shows the result of calculations of the first quantum level and Fermi level positions along the structure in QW1 and QW2. They was obtained from simultaneous solution of 2D Poisson and drift-diffusion equations. The drain and gate potentials were taken to be 3 and −1 V respectively.

The main mechanism of the current leakage between the wells is supposed to be thermal excitation of the carriers to the higher quantum levels and their further tunneling, because drive effect significantly decreases as temperature drops to 77 K. Also, the transition from QW2 to QW1 through the AlGaAs barrier is caused by the carriers overheating by the lateral electric field. The potential difference between two wells can be increased by drain voltage increase or by gate voltage decrease. Electron transitions to the lower quantum well with higher saturation velocity lead to the increase of the channel conductance. It causes non-monotonic drain current dependency on the gate voltage (Fig. 1) and current jumps in I–V characteristics (Fig. 2) as well. The effect

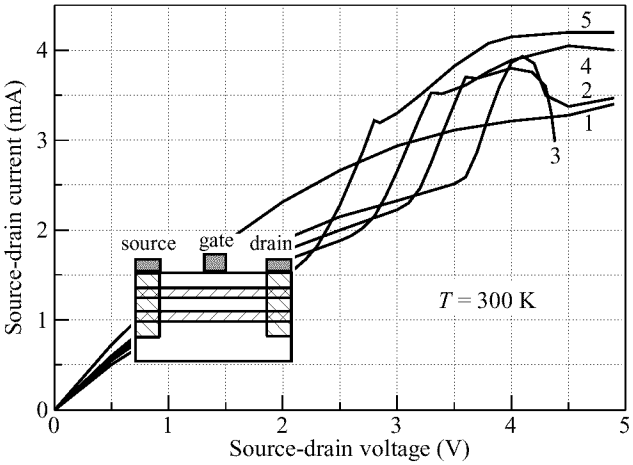


**Fig 2.** I-V characteristic of the channel. The curves are plotted for the following gate voltages: (curve 1) 0 V; (curve 2) −0.8 V; (curve 3) −1.0 V; (curve 4) −1.2 V; (curve 5) −1.5 V.

is amplified by the positive feedback between tunneling electric current and transverse potential difference.

Thus, conductance modulation of proposed GaAs/AlGaAs structure with two quantum wells is the result of coupling in high electric field, which is produced by drain voltage and controlled by a small change of gate voltage. The investigated phenomenon can be used for the development of p-type field effect transistor simulators (channel is opened by negative gate bias) with high transconductance, carriers being electrons instead of holes.

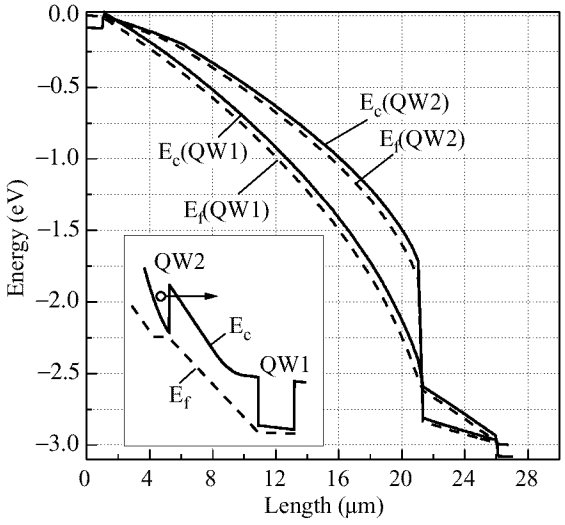


**Fig 3.** Calculated positions of the first quantum level and Fermi level along the structure in QW1 and QW2. The drain and gate potentials are 3 and −1 V respectively.

The work was finacially supported by the Russian Foundation of Basic Research.

## References

[1] A. Palevski, F. Beltran, F. Capasso, L. Pfeiffer, K. W. West. *Phys. Rev. Lett.* **65** 1929 (1990).
[2] A. Kurobe, I. M. Castleton, E. H. Linfield, M. P. Grimshaw, K. M. Brown, D. A. Ritchie, J. A. C. Jones, M. Pepper. *Semicond. Sci. Technol.* **9** 1744 (1994).
[3] P. I. Birjulin, S. P. Grishechkina, A. S. Ignatiev, Yu. V. Kopaev, S. S. Shmelev, V. T. Trofimov, N. A. Volchkov. *Semicond. Sci. Technol.* **12** 427 (1997).
[4] J. B. Bigelow, J. Laskar , J. Kolodzey, J. P. Leburton. *Semicond. Sci. Technol.* **6** 1096 (1991).

Ioffe Institute
6th Int. Symp. "Nanostructures: Physics and Technology"
St Petersburg, Russia, June 22–26, 1998.



# Fabrication and electron transport properties of superconducting–normal metal (ballistic) nanostructures

*G. M. Mikhailov* and I. V. Malikov
Institute of Microelectronics Technology & High Purity Materials of RAS,
142432, Chernogolovka, Moscow District, Russia

Experiments with ballistic weak link, where coherent Andreev's reflection may taken place, are of great interest. Recently, such type experiments were carried out using high electron mobility 2 DEG of semiconductor heterostructures contacted to the superconductors [1, 2]. Developing of monocrystalline metallic nanostructure fabrication capable ballistic electron transport [3] makes it possible to fabricate superconductor–normal metal (ballistic) structures, including also heteroepitaxial multilayered nanostructures. In this report we present for the first time the experimental realization of that and also the first results on electron transport investigation of S-N nanostructures fabricated.

Fabrication includes as a first step epitaxy of monocrystalline refractory metal films (5–200 nm thickness) on r-plane sapphire by Laser ablation deposition under UHV (Fig. 1). Process was also extended to the epitaxy of bilayered (Mo/Nb) films, grown by sequential deposition of the metal on substrate, kept at 700°C.

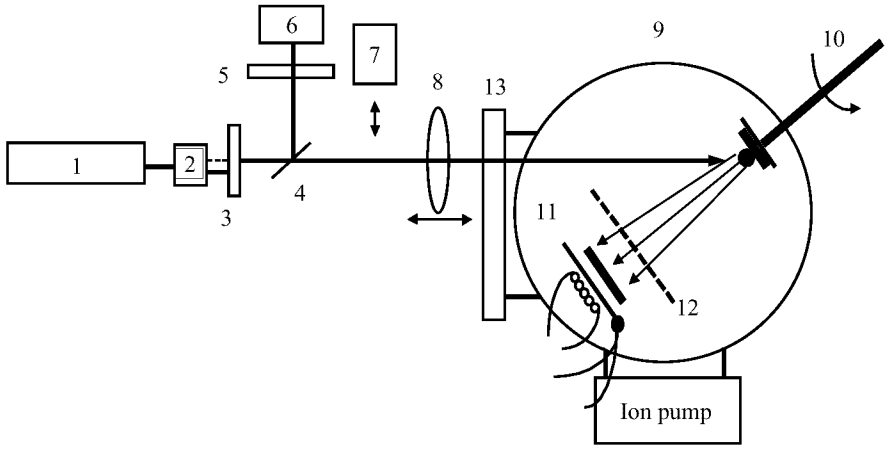


**Fig 1.** Equipment setup for metal film deposition. 1—s.s. pulse laser ($W = 0.16$ J, $f = 20$ Hz, $\tau = 15$ ns, $\lambda = 1.08\,\mu$m), 2—crystal KTP, 3—interference filter, 4—glass plate, 5—light filter, 6—mean power photometer, 7—pulse photometer, 8—focusing lens ($\phi = 0.9$ mm), 9—ultra high vacuum chamber ($P = 2 \times 10^{-9}$ Torr), 10—rotating target, 11—heating table ($T = 25$–$900$°C) for specimen with thermocouple, 12—shutter, 13—window.

Using the deposition method developed, high quality (001) monocrystalline films (Mo, Nb and Mo/Nb) were successfully grown. RHEED measurements for structural characterization, supported also by AFM experiments for film morphology investigation showed that the films grown have bcc crystal structure with low, about 1 monolayer,

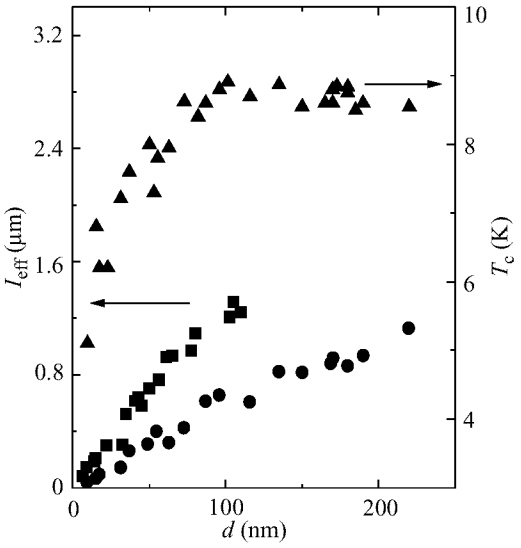


**Fig 2.** Thickness dependence of effective elastic EMFP in heteroepitaxial (001) Nb/Mo (circles) and Mo (squares) films. Superconducting transition temperature dependence on the thickness of bilayered Nb/Mo (001) films with equal thickness of the layers (triangles) is also shown. The Mo/Nb (001) films exhibit superconducting transition at $T_c = 8.7$ K, which is close to the $T_c = 9.2$ K of individual (001) Nb film. It decreases to 5 K for the film thickness low than 100 nm and is near a constant for higher thickness.

roughness of outer surface. They posses large enough elastic mean free path (EMFP), which exceeding the film thickness more than one order. Effective EMFP, estimated from experimentally found residual resistance ratio, is depicted in the Fig. 2 for Mo/Nb films with equal layer thickness, and also for Mo films as a function of the film thickness. As can be seen, EMFP for heteroepitaxial Mo/Nb films is comparable to that of the individual monocrystalline Mo films.

Fabrication of monocrystalline metallic nanostructures, including heteroepitaxial bilayered (Mo/Nb), was carried out using subtractive electron lithography and Al nanomask developing (Fig. 3). This approach helped to avoid the degradation of high electron mobility achieved in initial monocrystalline films due to its epitaxial growth. It was found that effective EMFP in nanostructures fabricated depends on the structure width and thickness and is ranged from 500 to 250 nm. It is only about 2 times lower than that of initial films with corresponding thickness. We believe that it is mainly due to the following reasons — small screening length in metals and also due to the grazing electrons, which defined electron conductivity [4]. It drastically differs from the case of semiconductor nanostructures, where during nanofabrication EMFP may be decreased in one-two orders in compare to initial 2DEG. As a result an effective EMFP in metallic monocrystalline nanostructures is only two-tree times lower than that in semiconductor nanostructures [1], also effective EMFP of metallic films grown is lower in one-two order than for 2 DEG of high quality. The other advantages of refractory metal nanostructures are in the property, that they keep thermal annealing up to 800°C or even

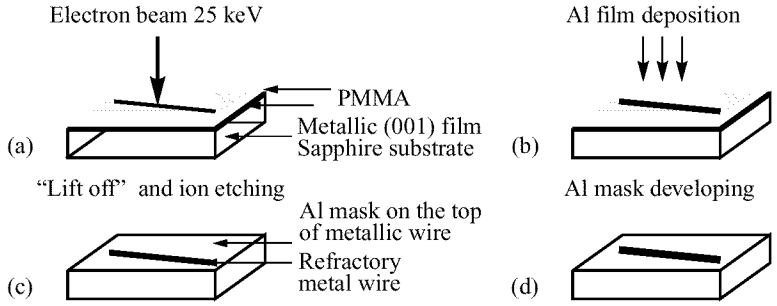


**Fig 3.** Electron lithography (a), resist developing and Al film deposition for fabrication of nanomask on the top of monocrystalline film (b), "lift off" and ion etching with energy 500 eV (c), developing of Al nanomask and nanostructure annealing at 400–800°C (d).

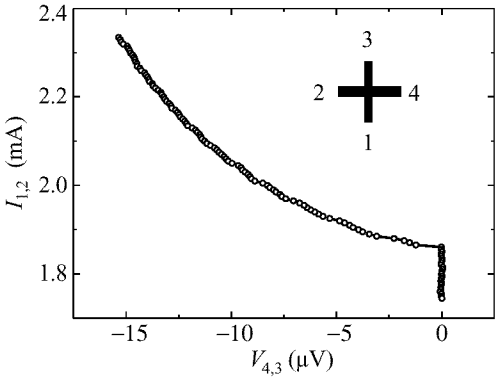


**Fig 4.** $I_{1,2}-V_{4,3}$ current-volt curve for cross-type heteroepitaxial Mo/Nb (001) nanostructure at $T = 8$ K. Schematic drawing and numbers of the terminals are shown in the inserting. The width of the structure is 300 nm and the thickness is 120 nm.

higher. It decreases concentration of radiating defects entered into the monocrystalline film during nanofabrication.

Within experimental approach monocrystalline heteroepitaxial nanostructures of bridge-, cross- and ring-type with spatial resolution down to 100 nm were fabricated, in which EMFP is compare to or exceeding of the structure length. In Fig. 4 volt-current curve of heteroepitaxial Mo/Nb (001) nanostructure is shown. At the current lower than 1.9 mA the nanostructure is in the superconducting state. For the current exceeding critical current the slope of the curve, which defined the bending resistance ($R_b = U_{4,3}/I_{1,2}$, where numbers of the terminals are shown in the inserting to the Fig. 4), is negative, proving realization of ballistic limit in electron transport [3]. Besides, the well seeing steps in I–V curve were also found. The critical current for nanostructure investigated is greater than 6 mA at 4.2 K. It corresponds to the current density exceeding $10^8$ A/cm$^2$.

To fabricate nonplanar S-N structures, the monocrystalline Mo (001) nanostructure with EMFP = 400 nm was fabricated by the method described above. After that,

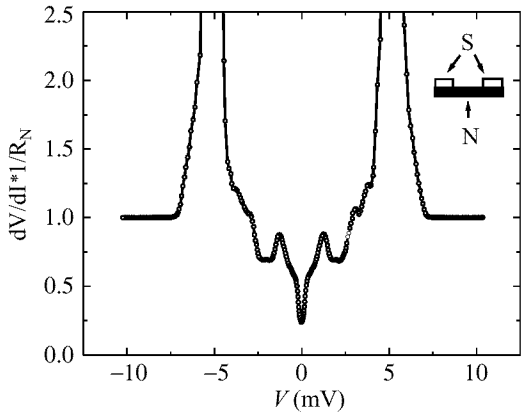


**Fig 5.** Differential resistance of the nanostructure, normalized by resistance in normal state, as a function of potential difference between Nb islands at $T = 4.2$ K. Schematic drawing of the structure is shown in the inserting.

additional lithography process and deposition of Nb islands at the distance of 400 nm were carried out. Since Nb was deposed after cutting of high vacuum there is oxide in the Nb-Mo interface. The structure fabricated is S-I-N (ballistic)-I-S type, where S — superconductor (Nb), I — insulator (oxide) and N — normal metal (Mo). Its electrical resistivity is shown in Fig. 5.

The large peaks at about 5 mV should be considered as quasiparticle injection [1], while the structure at potentials lower this value is due to Andreev's reflection of both ballistic and diffusion electrons [1, 2].

## References

[1] A. M. Marsh, D. A. Williams, H. Ahmed, *Phys. Rev. B* **50** (11) 8118–21 (1991).
[2] J. Kutchinsky, R. Taboryski, T. Clausen et al. *Phys. Rev. Lett.* **78**(5) 931–4 (1997).
[3] G. M. Mikhailov, L. I. Aparshina, S. V. Dubonos, et al. *Nanotechnology* **9**(1) 1–5 (1998).
[4] G. M. Mikhailov, I. V. Malikov, A. V. Chernykh, *Pis'ma JETP* (in Russian) **66** (11) 693–8 (1997).

Ioffe Institute
6th Int. Symp. "Nanostructures: Physics and Technology"
St Petersburg, Russia, June 22–26, 1998.



# One-dimensional miniband transport in doped GaAs/AlAs superlattices

*Yu. A. Pusep*, A. J. Chiquito, S. Mergulhão and J. C. Galzerani
Departamento de Física, Universidade Federal de São Carlos, 13565-905 São Carlos, SP, Brasil

Evidence of the crucial role of random fluctuations of the well size in vertical transport in doped GaAs/AlAs superlattices with broad minibands has been obtained by both Fourier-transform reflection spectroscopy and C–V measurements. The samples with different density of free electrons and, as a consequence, with different filling of the miniband were examined.

It turned out that even monolayer fluctuations of the periodicity, or random fluctuations of the impurity potentials, which are unavoidable, can cause a partial localization of electrons providing one-dimensional conducting channels where the periodicity is conserved, and through which the electron transport across the superlattice would occur.

This was found to be the reason why, instead of the constant vertical conductivity (independent of the electron density) predicted by the theory to occur when the Fermi energy exceeds the miniband width, a drop of the conductivity giving a metal-to-dielectric phase transition was observed.

The percentage of the electron states localized in the lowest miniband was determined in the superlattices with different electron concentrations and with different miniband widths. This showed the increase of a number of the localized states with increase of the electron concentration and with decrease of the miniband width.

Ioffe Institute
6th Int. Symp. "Nanostructures: Physics and Technology"
St Petersburg, Russia, June 22–26, 1998.



# Coulomb interaction and charging effects in conductance of mesoscopic quantum wire structures

*V. A. Sablikov*, S. V. Polyakov and B. S. Shchamkhalova
Institute of Radio Engineering and Electronics, Russian Academy of Sciences
Fryazino, Moscow district, 141120, Russia

**Abstract.** Electron transport in a quantum wire structure is investigated with comprehensive account of Coulomb interaction which includes both the direct interaction of electrons with each other and their interaction via the image charges induced on the leads. The Coulomb interaction is shown to change significantly the electron density distribution along the wire as compared with Luttinger liquid model. Under DC conditions, it causes the charge density to strongly increase near to the contacts with the leads. Together with a proximity effect, this may be a reason of nonuniversal conductance quantization. AC conductance shows a resonant behavior caused by charge waves. The charge wave velocity is renormalized due to the Coulomb interaction in a frequency-dependent manner: the velocity increases noticably with decreasing the frequency. In the nonlinear regime, the conductance is significantly affected by the charge stored in the wire.

## Introduction

Electron-electron (e-e) interaction becomes fundamentally important in one-dimensional structures. The interaction of 1D electrons turns out to be so significant that the Fermi liquid concept breaks down. More adequate becomes a strongly correlated state known as Luttinger liquid (LL) with boson-like excitations [1]. But there are important problems in application of this approach to actual quantum wire structures. First, the commonly used LL model treats the e-e interaction as a short-range one, though in reality the Coulomb interaction is essentially nonlocal. Second, the conductance of mesoscopic quantum wire structure is substantially determined by the wire contacts with leads, so the interaction of quantum wire electrons with leads is to be taken into consideration. Third, when applied voltage is compared with the Fermi energy, the balance of electron flows through the wire breaks down giving rise to a charging of the wire.

This paper aims to examine these problems and investigate phase coherent transport of electrons in a real situation of mesoscopic quantum wire structures with leads.

## 1 Electron-electron interaction potential

Mesoscopic structure under consideration consists of a quantum wire coupled to two bulky (2D or 3D) highly-conducting regions which serve as leads. The electron in the wire interacts with other ones both directly and via the surface charges which are induced by other electrons on the leads. The actual form of the e-e interaction potential $U(x, x')$ was obtained upon solving the Poisson's equation for electric potential generated by the charges localized inside the quantum wire with account of the highly conducting electrodes as equipotential surfaces.

The potential $U(x, x')$ decreases as $U \approx 1/|x - x'|$ when inter-electron distance is larger than the wire radius $a$. In the middle part of the quantum wire, $U(x = x') \sim L/a$, $L$ being the wire length. In the vicinity of the contacts $(x, x' \to \pm L/2)$ $U$ goes to zero

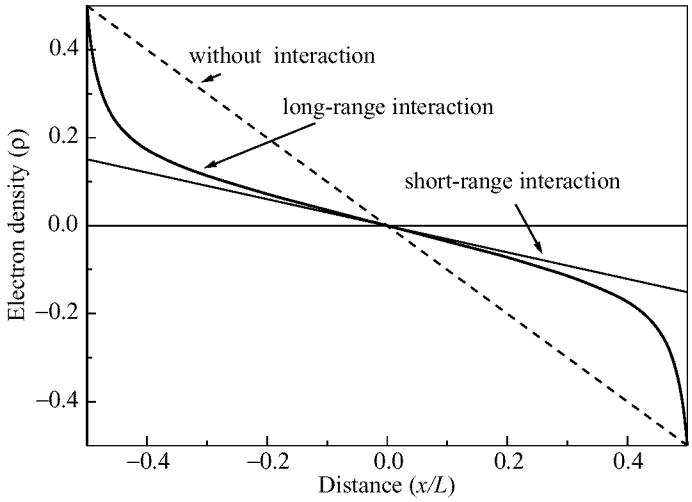


**Fig 1.** Distribution of the electron density (normalized by $2eV_a/(hv_F)$) along the quantum wire.

due to screening effect of the charges induced on the surfaces. The behavior of this kind is quite general for the interaction potential independently of the lead configuration.

## 2 Coulomb interaction effect on the charge distribution

Transport of the interacting electrons in a quantum wire structure was investigated with using the bosonization technique which is the most appropriate to describe the low-energy excitations of 1D electrons [1] and hence allows us to calculate the linear response to a voltage applied across the electrodes.

The equation of motion were obtained from the bosonized hamiltonian with direct inclusion of backscattering processes [1, 2]

$$H = \frac{1}{2\pi}\int dx\, v_F \left[(1+g_1)\pi^2\Pi^2(x,t) + (1-g_1)\,(\partial_x\Phi)^2\right]$$
$$-e\int dx\,\rho(x,t)\,\varphi_{ext}(x,t) + \frac{1}{2\pi^2}\int\int dx\,dx'\,(\partial_x\Phi)\,U(x,x')\,(\partial_{x'}\Phi) \qquad (1)$$

were $\Phi(x,t)$ is the phase field corresponding to the charge excitations, $\Pi(x,t)$ is the momentum density conjugate to $\Phi$, $g_1$ is the backscattering parameter, $\varphi_{ext}$ is external potential. $\Phi$ is related to the long wave component of the electron density $\rho$ via: $\rho = -\partial_x\Phi/\pi$.

We have developed [3] a method which allows one to solve *exactly* the equation of motion for the phase $\Phi$ in the case where the electrode surfaces are plains perpendicular to the wire. The exact solution shows that the Coulomb interaction affects significantly the charge density distribution along the wire, especially at low frequency. DC distribution of the electron density is shown in Fig. 1.

If the e-e interaction is absent, the charge density is distributed linearly with the distance (the dashed line in Fig. 1). The long-range interaction forces the charges to neutralize each other in the middle part of the wire. The LL approach with short-range interaction gives a linear distribution of the density versus the distance, which never can

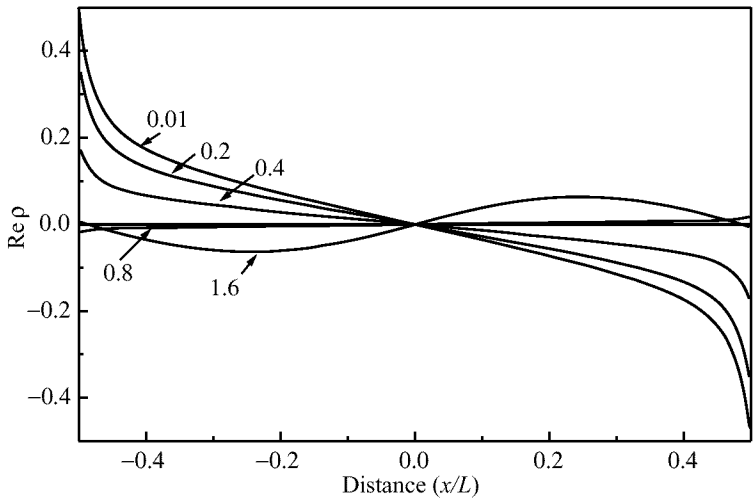


**Fig 2.** Electron density distribution along the wire for a variety of frequency. The curves are labeled by numbers those are the normalized frequency $\omega L/(2\pi v_F)$.

be fitted to the true result. Near to the contacts the actual value of $|\rho|$ is significantly larger and exponentially decreases with the distance from the contacts.

DC conductance turns out to be equal to the universal step $e^2/h$ independently of the e-e interaction. However we have found that the conductance is determined by the electron density at the contacts with leads where this density is changed sharply. The proximity effect of the electron liquid inside the wire and the electrode should give rise to a change of boundary density. This can be a possible reason of nonuniversal conductance quantization observed in Ref. [4].

When the frequency is increased, charge waves appear (Fig. 2) which propagate along the wire. In contrast with the LL model with short-range interaction, the charge wave velocity we have found, is noticably dependent on the frequency. This dependence is different from those obtained by Schulz [2] for infinite quantum wire. At low frequency the velocity renormalized by the Coulomb interaction is essentially larger than $v_F$. With increasing the frequency above a characteristic value, $\omega > [4\pi\lambda e^2 v_F/(\epsilon\hbar L^2)]^{1/2}$ ($\lambda$ being a parameter determined by the interaction potential) the long-range interaction effect decays and $v \to v_F$.

## 3 Impedance of interacting quantum wire structure

AC conductance is characterized by an oscillating behaviour of the real part of the impedance, Re$Z$, versus the frequency Fig. 3. The oscillations are caused by the charge wave resonances along the wire lenght [5]. Under the resonance condition the standing wave appears inside the wire. The time-dependent evolution of the electron density consists in flowing the electrons inside the wire from one part to another without passing through the contacts. As a consequence, the electric current component in-phase with the applied voltage is absent and the real part of both admittance and impedance goes to a low value restricted by a possible dissipation. The resonance frequency spectrum shows that the charge wave velocity decreases with the frequency.

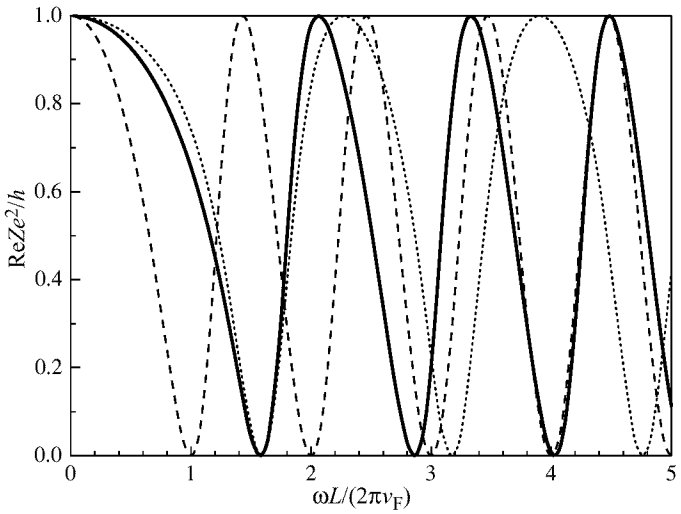


**Fig 3.** Real part of the impedance versus the normalized frequency for true long-range interaction (—), LL approach with $g = 0.63$ (– – –) and non-interacting electrons (· · ·).

## 4 Nonlinear conductance due to charging of the quantum wire

When the applied voltage is compared with the Fermi energy, the conductance becomes essentially nonlinear due to the charging of the wire. The charge in the wire is a sum of the positive background charge and the charge of the electrons incoming from the left and right leads. Applied voltage suppresses the electron flow incoming from the anode lead which results in the positive charge becomes prevaling. The electric potential of the stored charge affects the electron flow injected from the cathode lead and incoming electron density. Nonlinear electron transport is investigated by the self-consistent solution of the Schrödinger equation with an effective potential and the Poisson equation.

The present investigation is supported by INTAS (Grant No. 96-0721), Russian Fund for Basic Research (Grant No. 96-02-18276) and Russian Program "Physics of Solid-State Nanostructures" (Grant No. 97-1054).

## References

[1] J. Voit, *Rep. Progr. Phys.* **58** 977 (1995).
[2] H.J. Schulz, *Phys. Rev. Lett.* **B 71** 1864 (1993).
[3] V.A. Sablikov, B.S. Shchamkhalova, *JETP Lett.* **67** No 3 (1998).
[4] A. Yacoby, *et al.*, *Phys. Rev. Lett.* **77** 4612 (1966);
*Solid State Commun.* **101** 77 (1997).
[5] V.A. Sablikov, S.V. Polyakov, *Phys. Low-Dimens. Struct.* (to be published).

Ioffe Institute
6th Int. Symp. "Nanostructures: Physics and Technology"
St Petersburg, Russia, June 22–26, 1998.



# Fabrication of metallic nanostructures by local oxidation with a scanning probe microscope

R. J. M. Vullers, M. Ahlskog and *C. Van Haesendonck*
Laboratorium voor Vaste-Stoffysica en Magnetisme, Katholieke Universiteit Leuven
Celestijnenlaan 200 D, B-3001 Leuven (Belgium)

**Abstract.** Surfaces can be oxidized with the tip of a scanning probe microscope when applying a voltage between surface and tip. The oxidation process is voltage and humidity dependent, and can be explained in terms of anodic oxidation. The local oxidation allows the nanoscale patterning of doped silicon wafers as well as of metal films. In the case of silicon, the thin oxide layer can serve as an effective mask in a wet etching step. Sufficiently thin metal films (e.g., Ti or Al) can be completely oxidized down to the substrate, enabling the direct writing of nanostructures.

## 1 Introduction

The scanning probe microscope (SPM) has emerged as a powerful tool for modifying various surfaces at the nanometer scale [1]. While atomic manipulation is the ultimate goal, such a manipulation technique does not allow to fabricate stable structures under ambient conditions. On the other hand, the SPM offers a valuable alternative to the classical high-energy electron beam lithography. The low-energy beam, which is produced by the tip of a scanning tunneling microscope (STM), allows to locally expose thin resist layers and obtain linewidths as small as 20 nm.

The local oxidation of surfaces with an SPM was demonstrated for the first time by Dagata et al. [2]. These authors were able to transform a passivated silicon surface into a thin silicon oxide layer when applying a sufficiently large voltage between the tip of an STM and the Si surface. It was shown that the oxidation of the Si can also be achieved with the metallized tip of an atomic force microscope (AFM) [3]. The written oxide lines, which can be as narrow as 10 nm [4], can afterwards be inspected with the AFM, without inducing any further oxidation. The local oxidation of Si surfaces has been used to prepare a submicrometer side-gated MOSFET transistor [5]. SPM induced oxidation is also possible for various metal films which, when sufficiently thin, can be completely transformed into an oxide down to the substrate [6]. The local oxidation of Ti films has enabled the fabrication of a single electron transistor (SET) with lateral tunneling barriers [7]. Single-atom point contacts could be obtained by locally oxidizing an Al strip [8].

## 2 The local oxidation technique

### *2.1 Theoretical background*

Since the local oxidation is performed under ambient conditions, a water layer is always present on the sample surface. When the sample is biased positively with respect to the tip, the surface starts to be oxidized when exceeding a treshold voltage. The oxidation process can be described in terms of anodic oxidation, with the water acting as an

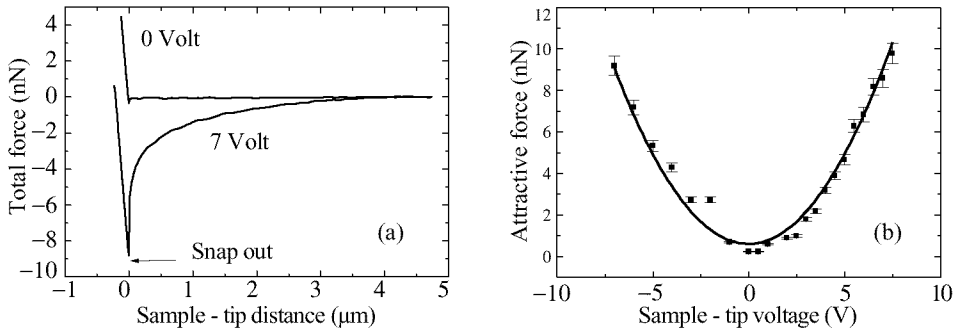


**Fig 1.** (a) Force versus distance curves for zero applied voltage and for $V = 7\,\mathrm{V}$. (b) The attractive force between tip and sample for different applied voltages.

electrolyte. Conventional electrochemical anodization requires a treshold electrical field $\sim 10^7\,\mathrm{V/cm}$ for anodization [9]. Ionic diffusion of $OH^-$ or $O^-$ occurs through the oxide layer (the exact nature of the diffusing specie is not known) towards the interface with the non-oxidized part of the sample [10]. Since a condensed water layer acts as the electrolyte, the amount of water on the surface and hence also the humidity play an essential role. It has been found for both Si [11] and Ti [12], that an increase in humidity increases the size of the written oxide lines. Stiévenard et al. [13] have suggested that the local oxidation is consistent with the Cabrera-Mott theory [14] of electrical field enhanced oxidation. Other experiments do, however, find deviations from the Cabrera-Mott model for the oxide growth [15].

### 2.2 *Influence of the tip geometry*

The actual shape of the tip is important, since it determines the electrical field distribution. On the other hand, prolonged use of the same tip results in a degradation of the tip shape due to wear. For an AFM the wear is a result of the attractive electrostatic force which appears between the tip and sample when applying a voltage. The force $F_{el}$ depends on the tip-sample distance $z$, the tip-sample capacitance $C$, and the applied voltage $V$:

$$F_{el} = \frac{dC}{dz} V^2 \quad . \tag{1}$$

The presence of a water layer will cause an additional attractive capillary force $F_{cap}$, resulting in a total attractive force

$$F_{att} = F_{cap} + \frac{dC}{dz} V^2 \quad . \tag{2}$$

When operating an AFM in the contact mode, the attractive forces will not cause an extra deflection of the cantilever. The only possible way to measure the extra forces is an analysis of the force-distance curves: Starting in contact, the tip is retracted and at the same time the cantilever deflection is measured. At first, the repulsive force will decrease, decreasing the bending of the cantilever. Due to the attractive force, the tip will remain in contact, even when the repulsive force has become zero. The cantilever will start to bend the other way, pulling at the tip. As soon as the pulling force equals

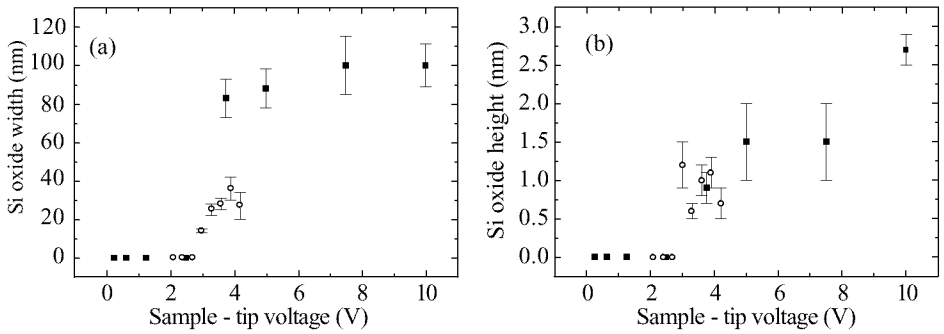


**Fig 2.** Width (a) and thickness (b) of Si oxide lines which have been written with an AFM at different applied voltages. The open and closed symbols refer to the results obtained with two different AFM tips.

the attractive forces, the tip will suddenly loose contact (snap out). Increasing the applied voltage, increases the attractive force. A typical result, which has been obtained in Leuven for a Ti film, is shown in Fig. 1(a). The attractive force is obtained from the difference between the snap out force and the force acting at long distances, i.e., $F = 0$. At zero voltage, the small deflection is entirely due to $F_{cap}$. Plotting the attractive force against the applied voltage, clearly reveals a $V^2$ dependence, as illustrated in Fig 1(b).

## 3 Patterning of silicon wafers

### *3.1 The local oxidation process*

For our experiments, we have used n-type, (100) oriented Si wafers with a resistivity of 10 mΩcm. Before starting the oxidation process, the silicon surface has to be cleaned and the native oxide needs to be removed. This can be done by immersing the sample in a bath of hydrofluoric acid (HF). The native oxide layer is etched away and replaced by a mono-atomic passivation layer which consists of H atoms attached to a clean Si surface layer. Next, a positive voltage is applied under ambient conditions between the Si and a Ti coated AFM tip. We have written lines with different voltages. After reducing the voltage back to zero, the written oxide lines are imaged with the same AFM tip. As shown in Fig. 2, there exists a threshold voltage (about 3 V) below which no oxide is formed. The oxide thickness is approximately 3 nm for an applied voltage of 10 V. The local oxidation can also be performed with an STM. We have written oxide lines for different values of the tunneling current which is maintained constant during the scanning process. No current dependence could be observed, consistent with an anodic oxidation process.

### *3.2 The etching process*

Due to the different etching speed of the silicon oxide when compared to the silicon, the written oxide patterns can be used as an effective mask in a wet etching process. Using TMAH (tetra-methyl ammonium hydroxide), a selectivity of 1000 can be achieved [16], allowing to easily transfer the written pattern into the silicon wafer. There also exists a difference in etching speed between the (100) and (111) directions, causing the lines to be etched under an angle of 55° for a (100) oriented surface. In order to write more complicated structures, one needs to be able to move the tip along a predefined

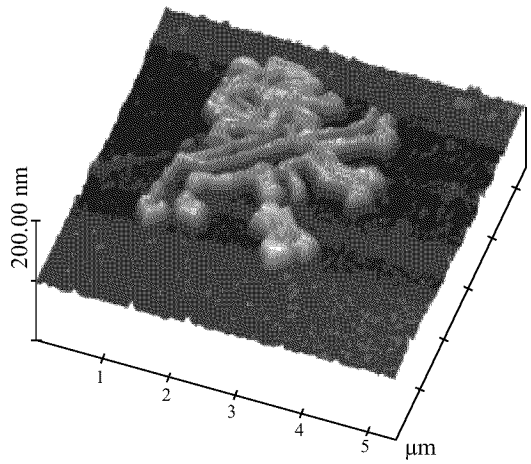


**Fig 3.** AFM picture of a mesoscopic lion obtained by local oxidation with an STM and subsequent etching of a Si wafer.

pattern (vector scan). We have made the necessary adaptions of the electronics and the software of our SPM system (Park CP) to obtain an improved control of the tip motion. The structure shown in Fig. 3 has been written with the STM and imaged with the AFM after etching.

## 4 Local oxidation of Ti films

While the silicon oxidation technique usually involves two or more steps for the fabrication of conducting mesoscopic structures, the oxidation of Ti can be used as a direct, single step patterning process. When using a thin Ti film, one can fabricate the desired pattern by oxidizing completely through the film, thus separating the conducting regions by an oxide.

### *4.1 The oxidation process*

Ti films having a thickness between 5 and 10 nm have been deposited onto oxidized Si substrates by dc magnetron sputtering. The local oxidation of these films is performed with an AFM with diamond coated tips (resistivity 2.5 mΩcm, thickness 100 nm). $TiO_x$ lines are written at different scanning speeds and for different voltages applied between the Ti film and the tip. Figure 4(a) shows the variation of the height of the oxide line when moving the AFM at different speeds. The height changes linearly with the logarithm of the writing speed [15]. Figure 4(b) shows the dependence of the height of the lines on the applied bias voltage. The treshold voltage above which we start to write oxide lines turns out to be in the vicinity of 5 V for the diamond coated tips.

### *4.2 Fabrication of narrow Ti lines*

In the inset of Fig. 5(a) we show a schematic view of our process for fabricating very narrow Ti lines. Combining electron beam lithography and lift-off techniques, we first prepare a wider Ti line (width $w_0 = 2\,\mu$m). Next, the width of the line is gradually reduced by oxidizing the outer parts of the line with the tip of our AFM. During the oxidation process the tip is scanned back and forth along horizontal lines (see arrows in

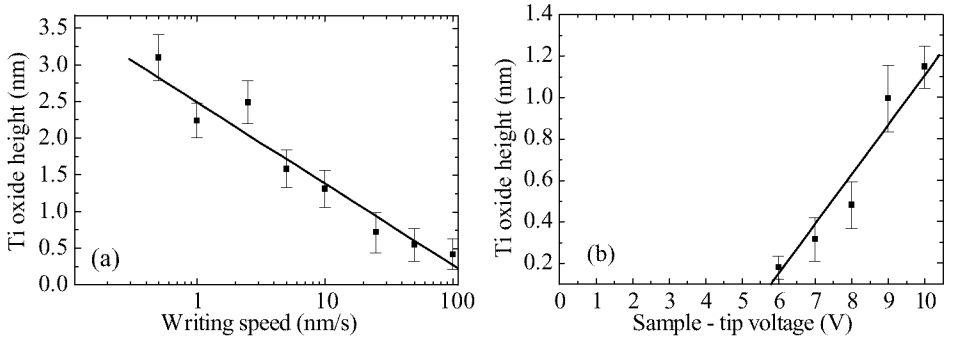


**Fig 4.** (a) Height of the written $TiO_x$ lines for different writing speeds. (b) Height of the oxide lines for different applied voltages.

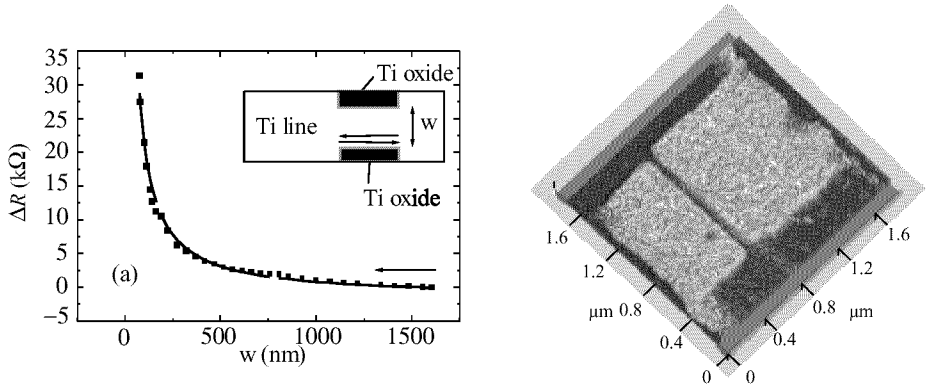


**Fig 5.** (a) The resistance change $\Delta R$ of a Ti line when reducing its width $w$ with the local oxidation technique (see inset). (b) AFM picture of the Ti line after the oxidation process.

the inset of Fig. 5(a)), reducing the metallic Ti gap to a width $w$. During the oxidation process the resistance of the remaining metallic Ti line is continuously monitored. The change in resistance $\Delta R$ is plotted against the width of the remaining gap in Fig. 5(a). Starting from the larger widths $w$, the resistance continuously increases with decreasing width. The data can be fitted using the simple relation

$$\Delta R = \rho \frac{L}{d} \left( \frac{1}{w} - \frac{1}{w_0} \right) , \tag{3}$$

with $\rho$ the resistivity of the Ti film, $L$ the length of the constriction and $d$ the thickness of the Ti film.

When the resistance reaches 30 kΩ, the oxidation is stopped by turning off the voltage and the fabricated Ti line can be imaged with the AFM. The topographical image is shown in Fig. 5(b). The brighter areas correspond to the oxide, while the darker areas correspond to the non-oxidized parts of the Ti film. The width of the remaining Ti line is 74 nm.

This work has been supported by the Fund for Scientific Research - Flanders (FWO)

as well as by the Flemish Concerted Action (GOA) and the Belgian Inter-University Attraction Poles (IUAP) research programmes.

## References

[1] For a review, see E. S. Snow et al., *Proceedings of the IEEE* **85** 601 (1997).
[2] J. A. Dagata et al., *Appl. Phys. Lett.* **56** 2001 (1990)
[3] H. C. Day and D. R. Allee, *Appl. Phys Lett.* **62** 2691 (1993).
[4] E. S. Snow et al., *Appl. Phys. Lett.* **66** 1729 (1995).
[5] P. M. Campbell et al., *Appl. Phys. Lett.* **66** 1388 (1995).
[6] For a review, see K. Matsumoto, *Proceedings of the IEEE* **85** 612 (1997).
[7] K. Matsumoto et al., *Jpn. J. Appl. Phys.* **34** 1387 (1995).
[8] E. S. Snow et al., *Appl. Phys. Lett.* **69** 269 (1996).
[9] S. K. Ghandi, *VLSI Fabrication Principles* (Wiley, New York, 1983)
[10] A. E. Gordon et al., *J. Vac. Sci. Technol. B* **13** 2805 (1995).
[11] H. Sugimura et al., *Appl. Phys. Lett.* **65** 1569 (1994).
[12] H. Sugimura et al., *Appl. Phys. Lett.* **63** 1288 (1993).
[13] D. Stiévenard et al., *Appl. Phys. Lett.* **70** 3272 (1997).
[14] N. Cabrera and N. F. Mott, *Rep. Prog. Phys.* **12** 163 (1948).
[15] Ph. Avouris et al., *Appl. Phys. Lett.* **71** 285 (1997).
[16] O. Tabata et al., *Sensors and Actuators* **34** 51 (1992).

Ioffe Institute
6th Int. Symp. "Nanostructures: Physics and Technology"
St Petersburg, Russia, June 22–26, 1998.



# Steps towards the realization of novel prototype functional devices using scanning probe microscopy

*M. Schwartzkopff*† and P. Radojkovic†
E. Hartmann‡, T. Junno‡ and L. Samuelson‡
† Physics Department E16, Technical University of Munich,
D–85747 Garching, Germany e-mail: misch@physik.tu-muenchen.de
‡ Solid States Physics/Nanometer Structure Consortium, Lund University,
Box 118, S–22100 Lund, Sweden

## 1 Introduction

Moore's principle predicts that beyond the year 2010, the typical structure dimensions of electronic memory devices will fall below 70 nm. Apart from the necessity to develop suitable lithographic techniques for mass production of sub–100–nm features, the sole reduction of the structure dimensions (top–down approach), while maintaining the present–day device architecture, will result in physical obstacles, making the invention of novel designs for future devices indispensable. It what follows, we report on novel concepts for the fabrication of a single-electron transistor (SET) and a quantum–interference transistor (QUIT), respectively.

## 2 Novel concepts for functional devices

### *2.1 Single-electron transistor*

An approach will be to use metallic nanoparticles with sizes below 30 nm as individual building blocks for the synthesis of novel functional devices by the controlled arrangement of the nanoparticles in a step–by–step fashion (bottom–up strategy). Deposited on suitable substrates, nanoparticles can be imaged, characterized, and manipulated using scanning probe microscopes (SPM) [1]. Fig. 1 shows an example for the atomic force microscope (AFM) assisted synthesis of a chain-like structure (Fig. 1b) of 20–nm–sized colloidal Au particles previously randomly deposited on a natively oxidized Si substrate (Fig. 1a); both images cover a range of 560 nm × 560 nm. Nanoparticles of less than 10 nm in diameter have successfully been used in studying single–electron phenomena, revealing pronounced steps in the scanning tunneling microscope (STM) recorded I–V characteristics at room temperature[2]. Moreover, by analyzing I–V curves taken on a pair arrangement of Ag nanoparticles deposited on a Si(111):H surface, an interaction of the two neighboring particles has been observed, most likely as a result of a mutual capacitive and/or resistive coupling[3].

Based on these experimental findings, nanoparticles are employed as individual building blocks to design devices having outstanding electrical properties which in turn can be tailored according to specific desires. Doing this, first the nanoparticles are randomly deposited on Si substrates covered with a several 100–nm–thick $SiO_2$ layer. On top of the $SiO_2$, electrodes are patterned by electron–beam lithography, followed by a metallization process and lift–off techniques. As a particularity, these electrodes are electrically interrupted by a gap of only a few 10 nm in width, thus forming source and

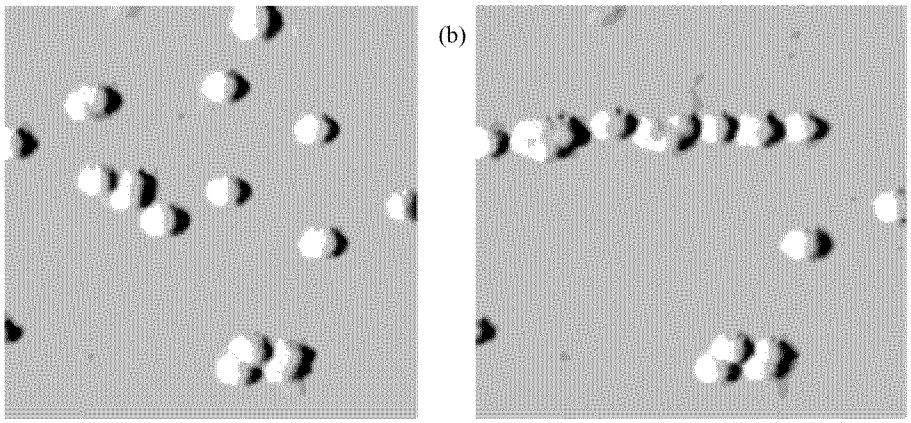


**Fig 1.** 20-nm-sized Au particles on a $SiO_2$ substrate, (a) initially randomly distributed and (b) after alining them with an AFM.

drain contacts. With the AFM, suitable nanoparticles can be selected and controllably be arranged within this gap region, so that the nanoparticles may electrically bridge source and drain. By using a three–electrode configuration (source, drain, and gate), where the gate couples capacitively to the particle arrangement, the pathway for electrons can be opened and closed, respectively, depending on the voltage applied to the gate electrode. More importantly, the electrical properties of this device can subsequently be modified by easily rearranging preselected nanoparticles with respect to their neighbors. The synthesized configuration represents a tunable prototype SET.

Referring to specialized applications, metallic lines in the 10–nm–range can directly be deposited in any desired pattern by locally decomposing an organometallic precursor in the electron beam provided by the tip of a STM operated in an ultra-high vacuum environment [4]. Following the decomposition of the precursor molecules, the metallic component is predominantly deposited onto the substrate surface and the remaining organic fragments are pumped off. While scanning the tip over the sample, 20–nm–wide conducting lines can be fabricated with lengths in the mm range (Fig. 2).

### *2.2 Quantum-interference transistor (QUIT)*

Arranging the nanoparticles within the gap region of the three–electrode system in a ring structure results in the formation of the classical Aharonov–Bohm configuration. The resultant diameter of the assembled circle actually depends on the size of the nanoparticles used, but can be as small as a few 10 nm — overall dimensions which are not available with conventional lithographic techniques. Contacting this ring structure to source and drain properly allows electrons to wend their way along two possible pathways. If the total length of both pathways is shorter than the mean-free path or coherence length in the respect material, the wave nature of moving electrons are expected to give rise to interference phenomena. In particular, the electron wave properties might be affected in one branch, e.g., by applying an appropriate voltage to the gate electrode, thus providing an opportunity to switch between destructive and constructive interference.

An alternative device structure might be to use an AlGaAs/GaAs heterostructure, at

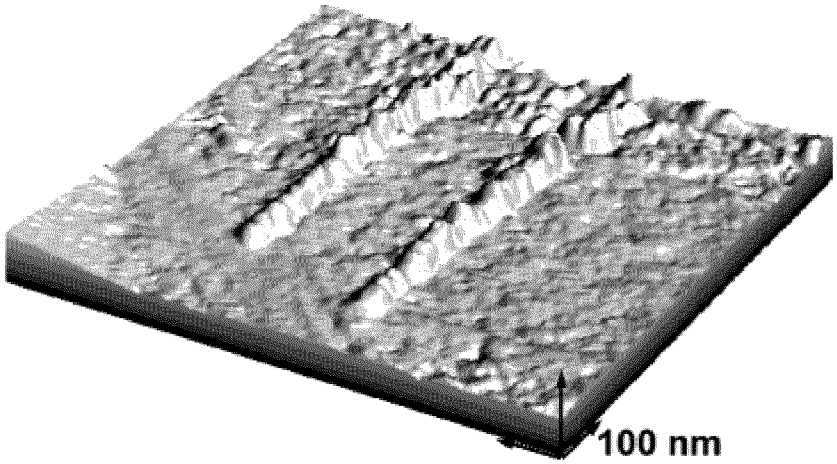


**Fig 2.** Two tungsten lines written onto a Si(111):H surface with the help of the field–induced decomposition of $W(CO)_6$ under the tip of a STM. The lines show a width of 20 nm and are some 800 nm in length.

which the AlGaAs capping layer is as thin as 30 – 40 nm in order to have the buried two–dimensional electron gas as close as possible to the surface. With the help of electrodes deposited on top and connected to a voltage source, the electron gas can be pre–confined to form a one–dimensional wire. If the AlGaAs material can locally be decomposed or even evaporated, this will result in the formation of a potential barrier in the one–dimensional electron channel. Being smaller than the width of this channel, the electrons are allowed to wend their way around this potential barrier, possibly also resulting in the development of interference phenomena. Indeed, it has recently been demonstrated that by using a laser grating method, structures of 300 nm can be fabricated owing to a laser–induced local decomposition of III–V semiconductors [5]. Detailed analyses show that the photon energy is mainly deposited in near–surface regions. Preliminary experiments using a STM revealed that by applying single-voltage pulses, 100–nm–wide pits can be formed in GaAs. Upon optimizing this process, the size of these features may significantly be reduced, thus making the 10–nm–range accessible.

## 3 Concluding remarks

Of course, it is usually a tough route to demonstrate the functionality of laboratory–built devices, but, hopefully, nanoparticles in conjunction with the unique capabilities of SPM provide a promising potential to pave the way for fabricating devices in terms of a bottom–up technology. Notwithstanding the feasibility of SPM in forming nanometer–scale structures, it should be kept in mind that the coherence length of electrons at room temperature is extremely small and typically falls below 10 nm, so that the operation of devices whose function is based on coherent transport is supposed to be limited to the very low–temperature regime.

## References

[1] T. Junno, K. Deppert, L. Montelius, and L. Samuelson, *Appl. Phys. Lett.* **66** 3627 (1995);
D. M. Schaefer, R. Reifenberger, A. Patil, and R. P. Anders, *Appl. Phys. Lett.* **66** 1012 (1995);
C. Baur, B. C. Gazen, B. Koel, T. R. Ramachandran, A. A. G. Requicha, and L. Zini, *J. Vac. Sci. Technol. B* **15** 1577 (1997);
T. Junno, S.-B. Carlsson, H. Xu, L. Montelius, and L. Samuelson, *Appl. Phys. Lett.* **72** in press;
P. Radojkovic, T. Gabriel, M. Schwartzkopff, and E. Hartmann, *Proc. Int. Symp. Nanostructures: Physics and Technology*, June 23-27, 1997, St. Petersburg, Rusia;
P. Radojkovic, M. Schwartzkopff, T. Gabriel, and E. Hartmann, *Solid State Electronics*, in press.

[2] P. Radojkovic, M. Schwartzkopff, M. Enachescu, E. Stefanov, E. Hartmann, and F. Koch, *J. Vac. Sci. Technol. B* **14** 1229 (1996).

[3] E. Hartmann, P. Marquardt, J. Ditterich, P. Radojkovic, and H. Steinberger, *Appl. Surf. Sci.* **107** 197 (1996).

[4] M. A. McCord, D. P. Kern, and T. H. P. Chang, *J. Vac. Sci. Technol. B* **6** 1877 (1988);
E. Hartmann, P. Radojkovic, M. Schwartzkopff, M. Enachescu, and P. Marquardt, *Appl. Surf. Sci.* **107** 212 (1996).

[5] M. K. Kelly, C. E. Nebel, M. Stutzmann, and G. Böhm, *Appl. Phys. Lett.* **68** 1984 (1996).

Ioffe Institute
6th Int. Symp. "Nanostructures: Physics and Technology"
St Petersburg, Russia, June 22–26, 1998.



# Charge structures interaction in low temperature STM surface investigations

N. S. Maslova†, V. I. Panov†, *S. V. Savinov*†, A. Depuydt‡ and C. Van Haesendonck‡

† Chair of Quantum Radio Physics, Moscow State University, 119899 Moscow, Russia

‡ Laboratorium voor Vaste-Stoffysica en Magnetisme, Katholieke Universiteit Leuven, B-3001 Leuven, Belgium

**Abstract.** In this work we present the results of low-temperature STM investigation of $A_{III}B_V$ semiconductors surface in situ cleaved along (110) plane. On topographic STM images we have found surface charge structures. The possibility of their observation depends on the STM tip apex charge state. We have observed peaks in local tunneling conductivity spectra. Energy position of these peaks as well as the energy position of band gap edges changes with distance from the defect. Experimental data points to the existence of interacting induced charges localized both on STM tip apex and defects on the surface or in nearest subsurface layers.

With accumulation of experimental data the correspondence of experimental tunneling conductivity spectra and unperturbed sample electron density of states become of great importance [1]. This problem is especially actual with temperature decreasing when tunneling and relaxation rates can be comparable [2]. As it was shown in [3] non equilibrium electron distribution can occur. Such distribution leads to the appearence of tunneling bias voltage dependent localized charges. In present work we show the importance of localized charges mutual influence by means of STM/STS investigation of clean GaAs monocrystals (110) surface.

All STM measurements were carried out using home build low temperature STM with in situ sample cleavage mechanism [4] at temperature 4.2 K. Heavily doped ($n \simeq 5 \times 10^{17}\,\mathrm{cm}^{-3}$) with tellurium semiconductor GaAs crystals have been investigated in our experiments. Electrical ohmic contacts were deposited by thermodiffusion method on specially cut samples. Samples were cleaved along (110) plane after cooling down to 4.2 K in pure He atmosphere. This procedure provided clean surface for at least 10 days. Because of relatively low samples conductivity STM measurements were carried out with tunneling current values in 10 pA range. Spectroscopic data was obtained by means of Current Imaging Tunneling Spectroscopy (CITS). Tunneling conductivity curves averaging over surface area gives high signal to noise ratio for numerical evaluation of differential conductivity spectra.

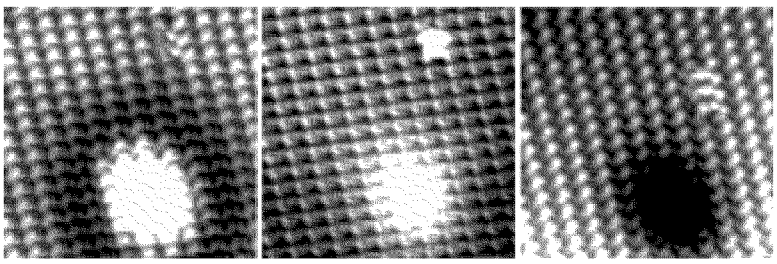

**Fig 1.** Topographic STM images of tellurium atom on (110) GaAs surface at temperature 4.2 K. Area 5.8×5.8 nm, tunneling current 20 pA. Tunneling voltage: (a) −1.5 V; (b) +1 V; (c) +0.5 V.

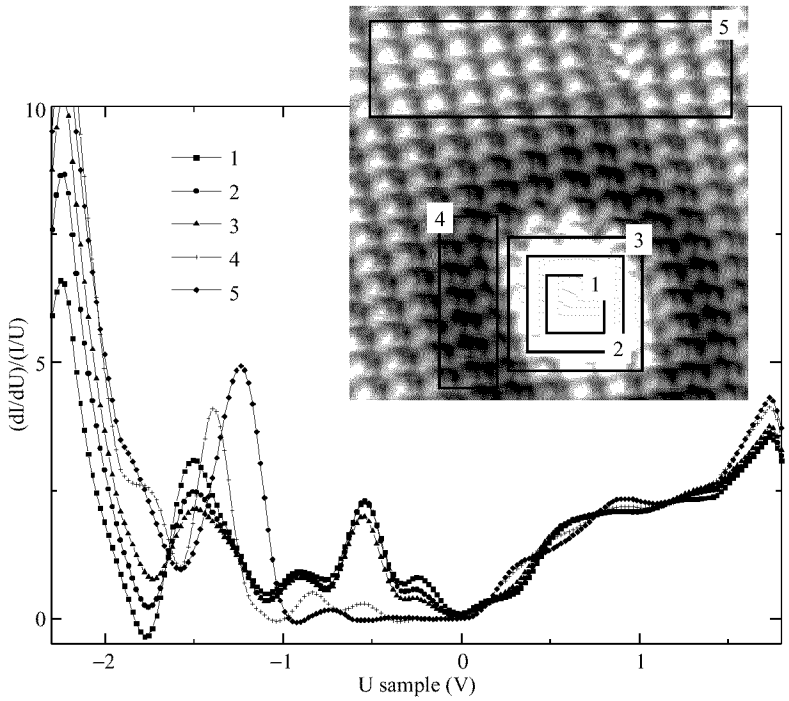


**Fig 2.** Tunneling conductivity spectra near tellurium atom on (110) GaAs surface at temperature 4.2 K. Insert depicts the image of surface area 5.8×5.8 nm in size where spectroscopic data was acquired. Each curve is the result of averaging over surface area which is marked by numbers.

For clear understanding of experimental results the direct comparison of surface defects topographic STM images at different values of tunneling bias voltage with local spectroscopy data is of great interest. Topograms of GaAs surface near the defects are depicted in Fig. 1. According to the common view [5] such type of defect is doping atom residing on the surface. Note some specific features of these images. STM image of doping atom is about 2 nm in diameter. The contrast of dopant image changes with variation of tunneling bias voltage from $+1$ V to $+0.5$ V. At negative sample bias the dark ring appears around impurity atom.

We suppose that topographic images behaviour is determined by charge effects which is confirmed by the shape of normalized density of states curves presented in Fig. 2. Each curve is the result of averaging over surface area which is marked by numbers on the insert. Let us mention the main features of tunneling conductivity curves. First, the measured band gap edges position near the defect differs from its flat surface region value. Second, the set of peaks around the defect exists in voltage range from $-1$ V to 0 V, which is absent above flat surface. Third, there is tunneling conductivity peak in the bias range $-1.5$ V to $-1$ V. The position and height of this peak depend on a distance from the defect.

It is obvious that charge interaction strongly depends on the distance between charges. Fig. 3. depicts topograms and spectroscopic data measured near impurity atom in the second subsurface layer. Contrary to STM images of surface impurity subsurface atom image does not change its contrast. At the same time the ring structure

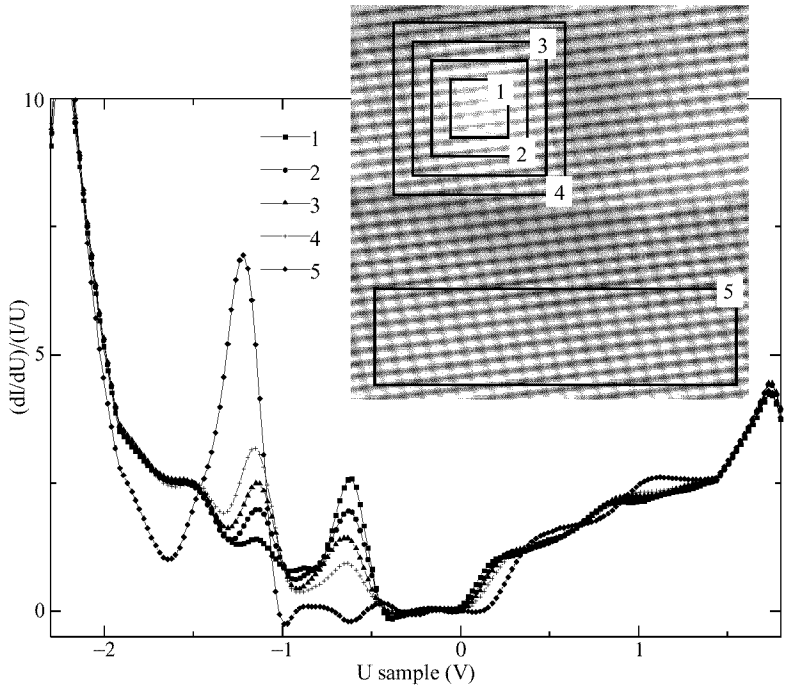


**Fig 3.** Tunneling conductivity spectra near tellurium atom in second subsurface layer at temperature 4.2 K. Insert depicts the image of surface area 7.3×7.3 nm in size where spectroscopic data was acquired. Each curve is the result of averaging over surface area which is marked by numbers. Tunneling current 20 pA, tunneling voltage −1.5 V.

still exists.

Tunneling conductivity behaviour also differs in the case of subsurface defect. There are peaks near the defect as it was before, but the energy position of the peaks does not change with the distance from the defect. The amplitude of one peak (around −1.2 V) increases while the amplitude of another one (around −0.7 V) decreases with increasing of the distance from the defect. The first one become dominant above flat surface.

We consider that tunneling conductivity peaks in band gap can be connected with Coulomb interaction of doping atoms states and induced charges, localized on STM tip apex. As it was shown in [6] on site Coulomb repulsion of localized electrons of Hubbard type is very important. Such interaction can considerably change the energy values even for deep impurity levels. As a result strong dependence of level energy on tunneling bias voltage appears.

Experimentally measured tunneling conductivity peak position does not coincide with the bulk value of unperturbed doping impurity energy levels. Experimentally obtained tunneling conductivity is not determined by simple convolution of sample and tip densities of states, especially if finite relaxation rate of nonequilibrium electrons is taken into account.

Another remarkable example of charge effects existence is Friedel oscillations observation near isolated charged defect. If the distance between neighbouring defects

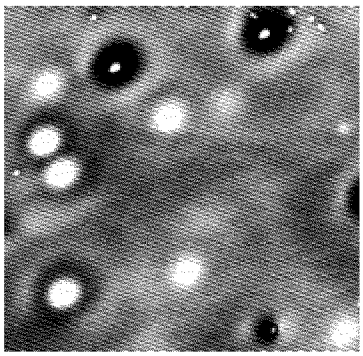

**Fig 4.** Topographic STM images of (110) GaAs surface area at temperature 4.2 K. Area 41×41 nm, tunneling current 40 pA. Tunneling voltage −1.5 V. Image gray scale corresponds to 0.05 nm.

is comparable with screening length (about 10 nm in case of GaAs) superposition of Friedel oscillations from different defects can appear. So nontrivial charge structures can be formed on the sample surface (Fig. 4). For GaAs tip-sample separation (about 0.5 nm) does not exceed the radius of enhanced charge area around the defect (more than 2 nm). So, the induced charge on STM tip apex plays the same role as the defect charge. Thus the charge states on the tip modifies experimentally observed distribution of electron density and corresponding STM image of Friedel oscillations. Apparently this is a reason why STM images on Fig. 4 and Fig. 1 are different. On the last one only one the most intensive ring is visible.

In conclusion, experimental STM/STS data are strongly influenced by induced charge interaction which considerably modifies initial unperturbed sample density of states.

The work in Moscow has been supported by the Russian Ministry of Research (Surface atomic Structures, grant 95-1.22; Nanostructures, grant 97-1086) and the Russian Foundation of Basic Research (RFBR, grants 96-0219640a and 96-15-96420). The work at the KULeuven has been supported by the Fund for Scientific Research — Flanders (FWO) as well as by the Flemish Concerted Action (GOA) and the Belgian Inter-University Attraction Poles (IUAP) research programs. The collaboration between Moscow and Leuven has been funded by the European Commission (INTAS, project 94-3562).

## References

[1] E. L. Wolf, *Principles of electron tunneling spectroscopy* (Oxford Universitary Press, Oxford, 1985).
[2] O. Agam, N. S. Wingreen, B.L. Altshuler, *Phys. Rev. Lett.* **78** 1956 (1997).
[3] N. S. Maslova, V. I. Panov, S. V. Savinov, S. I. Vasilev, A. Depuydt, C. Van Haesendonck, *JETP Lett.* **67** 2 131 (1998).
[4] S. I. Oreshkin, V. I. Panov, S. V. Savinov, S. I. Vasilev, A. Depuydt, C. Van Haesendonck, *Pribory i technica experim.* **4** 145 (1997).
[5] J. F. Zheng, X. Liu, N. Neuman, E. R. Weber, D. F. Ogletree, and M. Salmeron, *Phys. Rev. Lett.* **72** 10 1490 (1994).
[6] P. I. Arseev, N. S. Maslova, V. I. Panov, S. V. Savinov, Role of charge effects in tunneling investigations of semiconductors, *Semiconductors-97*, December 1-5, Moscow, 1997.

Ioffe Institute
6th Int. Symp. "Nanostructures: Physics and Technology"
St Petersburg, Russia, June 22–26, 1998.



# Atomic resolution observation of GaAs doped with Sn by scanning tunneling microscopy

*S. Yu. Shapoval*, V. L. Gurtovoi, U. Hakansson†, L. Samuelson† and L. Montelius†
Institute of Microelectronics Technology, Russian Academy of Sciences, 142432 Chernogolovka, Russia
† Department of Solid State Physics, Lund University, Box 118, S-221 00 Lund, Sweden

**Abstract.** Substitutional donor $Sn_{Ga}$ atoms in the near surface region below the GaAs (110) cleaved surface were observed by ultrahigh vacuum STM. Surface Sn atoms were observed as localized features, whereas subsurface Sn atoms have delocalized nature with the mean width of 2.5 nm. For an atom, elementary act of surface diffusion was observed and surface diffusion coefficient at room temperature was evaluated.

Development of nanostructure technology for semiconductor devices requires to control distribution of dopants with nm-resolution. A lot of efforts have been done in investigation of electrically active dopants in GaAs by cross-sectional scanning tunneling microscopy [1–5]. Although p-type dopants in GaAs were intensively studied, especially, Be in epitaxial layers [1], Be delta-doped layers [2], Be in modulation-doped structures [3], and Zn in bulk material [1, 4], among n-type shallow impurities only results for Si in GaAs were published [5].

In this paper, we present the first atomic resolution observation of individual Sn atoms (donor impurity) in GaAs.

Tin(Sn)-doped ($1 \times 10^{18}$ $cm^{-3}$) $n^+$ GaAs substrates grown by liquid encapsulated Czochralski technique were used as samples for STM imaging. For experiments we used a JEOL4200 UHV STM. The samples were cleaved in situ in an ultrahigh vacuum STM chamber at a pressure of $6 \times 10^{-10}$ Torr. Obtained this way, atomically flat GaAs (110) surface has low densities of defects, which do not pin the Fermi level at the vacuum-semiconductor interface [6]. Electrochemically etched and backpolished [7] tungsten tips were used. Before loading W tips were treated by hydrogen electron cyclotron resonance plasma at a pressure 3.5 mTorr for 30 min to clean and passivate the tungsten surface [7]. All STM images were taken in the constant current mode with tunneling current 0.1 nA at a sample bias $-3$ V (filled-state image). The barrier potential was determined for the regions of imaging by measuring current-tip displacement (I-s) characteristics, as well as current–voltage (I–V) characteristics were measured to assure the tip and sample surface cleanliness.

Fig. 1 shows a large-scale STM image on the (110) GaAs surface, where atomic corrugation in direction perpendicular to $[1\bar{1}0]$ is clearly seen, moreover, random white features 1.5–4.5 nm in size are also observed. These delocalized features are very similar to those observed in [5] for Si doped GaAs and attributed to subsurface Si in various subsurface layers. Different subsurface Sn features at the same bias can have different apparent height and width, which were measured by profiling across the features. Mean

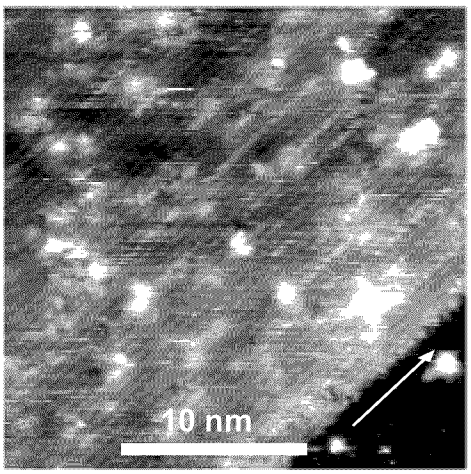


**Fig 1.** Large-scale image of a cleaved GaAs (110) doped with Sn. Random white (delocalized) features correspond to subsurface Sn donors ($I = 0.1$ nA, $V = -3$ V). Arrow shows $[1\bar{1}0]$ direction.

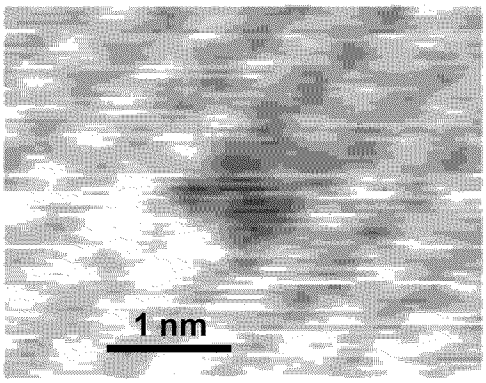


**Fig 2.** Filled state image of a Sn (localized) atom on the top layer of cleaved GaAs (110) doped with Sn ($I = 0.1$ nA, $V = -3$ V).

value of the height for the Sn from the first subsurface atomic layer is equal to 0.23 nm with standard error 0.016 nm, but the width was varied within the range of 1.5–4.5 nm.

At the same time it is possible to observe localized objects on cleaved GaAs (110) surface (Fig. 2). For the Si-doped GaAs (110) surface, calculations indicate [8], that the extra electron of the Si substitutional at a Ga site on the surface is localized around the Si atom, creating a surface $Si_{Ga}$ defect, which was observed as localized feature by STM imaging [5]. We believe that localized features in Fig. 2 corresponds to Sn atom located on the top layer of the surface similar to observation for Si doping in [5].

During our experiments all Sn subsurface atoms were stable, but we observed some additional moveable elements. Figures 3 and 4 illustrate a jump of an atom from, marked by lower arrow place in the figures to that, marked by upper arrow. Both images were

made from the same sample area (as a confirmation of this statement, it should be noted two black features as markers on the top and left-bottom parts of the figures). Besides, one could see new element formation. Instead of white feature (lower arrow, Fig. 3), black feature appears at the same place after 7 min exposure in vacuum at room temperature (Fig. 4). During 7 min of this experiment we made 4 images (first three images were analogous to Fig. 3, showing stable experimental conditions and minor influence of the tip scanning on the feature jump).

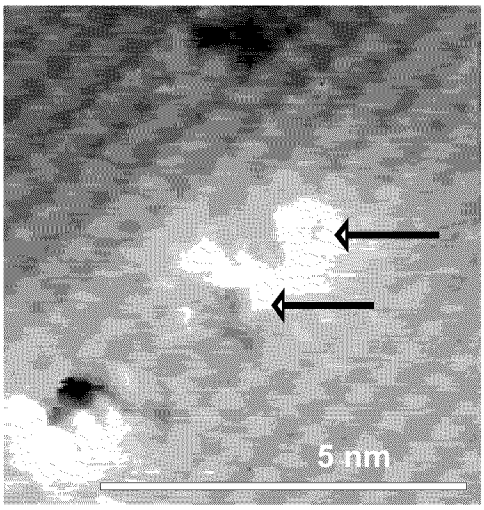


**Fig 3.** STM image of the GaAs cleaved surface with a movable feature (the starting and the ending places of a jump are indicated by arrows).

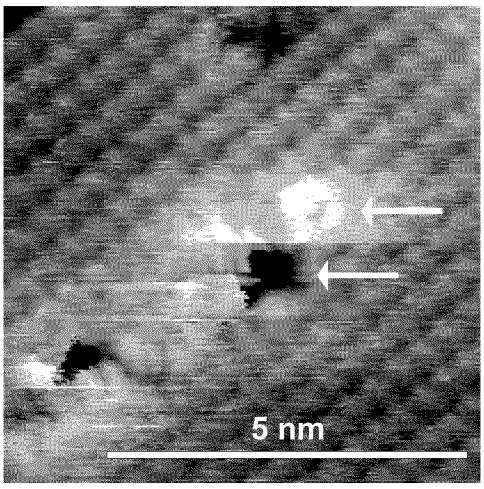


**Fig 4.** STM image of the area shown in Fig. 3 after 7 min exposure in vacuum at room temperature. The jump of an atom and a new element (black feature) formation are clearly seen.

From the distance between the features (1 nm) and the time period (7 min) we can calculate the "diffusion coefficient" $D = 2 \times 10^{-17}$ cm$^2$/s, which reflects the elementary act of the surface diffusion at room temperature. We do not know data for surface diffusion of dopants for GaAs (110) at room temperature, therefore, we will try to evaluate the surface diffusion coefficient using data for Si as a dopant. If one extrapolates the data for bulk diffusion of Si in GaAs [9] from high temperatures to 300 K, one can have an evaluation of bulk diffusion coefficient $10^{-21}$ cm$^2$/s. Surface diffusion coefficient is 3-4 orders of magnitude higher in comparison with bulk one at the same temperature [10] and have analogous temperature dependence (a decade decrease per 100°C). As a result, surface diffusion coefficient of Si for GaAs (110) should be $10^{-17}$–$10^{-18}$ cm$^2$/s, which is in rather good agreement with the above calculations. Thus, we can conclude that elementary acts of surface diffusion of dopant atoms could be observed at room temperature for reasonable time period.

This work was supported by a KVA grant of the Royal Swedish Academy of Sciences.

## References

[1] M. B. Johnson, O. Albrektsen, R. M. Feenstra, and H. W. M. Salemink, *Appl. Phys. Lett.* **63** 2923 (1993).
[2] M. B. Johnson, P. M. Koenraad, W. C. van der Vleuten, H. W. M. Salemink, and J. H. Wolter, *Phys. Rev. Lett.* **75** 1606 (1995).
[3] J. F. Zheng, M. B. Salmeron, and E. R. Weber, *Appl. Phys. Lett.* **64** 1836 (1993).
[4] J. F. Zheng, M. B. Salmeron, and E. R. Weber, *Appl. Phys. Lett.* **64** 1836 (1993).
[5] J. F. Zheng, X. Liu, N. Newman, E. R. Weber , D. F. Ogletree, and M. Salmeron, *Phys. Rev. Lett.* **72** 1490 (1994).
[6] J. van Laar, A. Huijser, and T. L. vaan Rooy, *J. Vac. Sci. Technol.* **14** 894 (1977).
[7] V. Dremov, V. Makarenko, S. Shapoval, and O. Trofimov, *Nanobiology* **3** 83 (1994).
[8] J. Wang, T. A. Arias, J. D. Joannopoulos, G. W. Turner, and O. L. Alerhand, *Phys. Rev. B* **47** 10326 (1993).
[9] E. F. Schubert, *J. Vac. Sci. Technol. A* **8** 2980 (1990).
[10] C. E. C. Wood, *J. Appl. Phys.* **71** 1760 (1992).

Ioffe Institute
6th Int. Symp. "Nanostructures: Physics and Technology"
St Petersburg, Russia, June 22–26, 1998.



# Ab initio study on spin polarization of III–V compound tips

*Makoto Sawamura*†‡, Tomohide Maruyama§ and Koichi Mukasa†‡
† CREST/JST Spin Investigation Team
‡ Nanoelectronics, Faculty of Engineering, Hokkaido University
Kita 13 Nishi 8, Sapporo 060, JAPAN
§ Hokkaido Tokai University

Recently, spin electronic states have been found to play an important role under a scanning tunneling microscope (STM) environment [1]. Spin-polarized tunneling has been reported to be observed [2, 3, 4]. Circularly polarized laser beamed on a zinc-blend crystal such as GaAs excites electrons to spin-polarized states. This mechanism has been applied to a Spin-Polarized (SP) STM. Spin-polarized electrons excited in an STM tip tunnel from the tip to the sample surface and are transferred to the unoccupied electronic states of the sample surface with allowed spin states according to the selection rule. Detecting such a tunneling process by STM, we are able to observe surface spin electronic states. On the other hand, in the nanostructure of a surface or in a molecule, spin electronic states may reveal magnetic properties [5, 6, 7]. Extremely high spin states may indicate ferromagnetism [6].

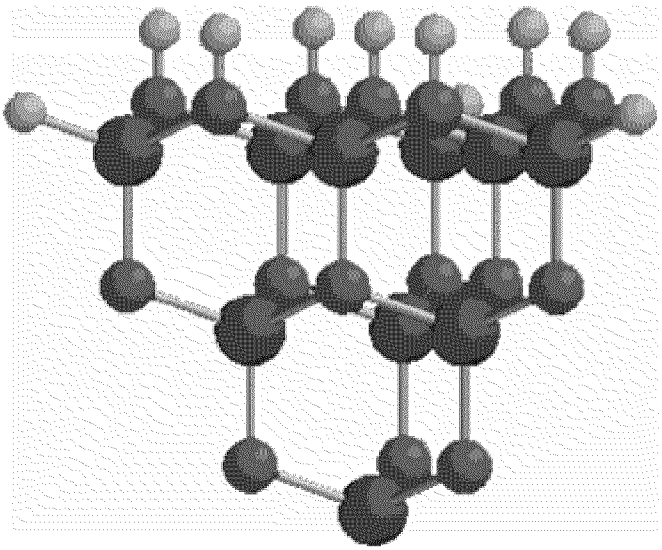

**Fig 1.** A cluster model for a GaN tip with a Ga atom at the apex in the crystallographic axis (111).

For these systems, the low spin state do not necessarily give the lowest energy. We may be able to design and create nanostructures which have such high spin. In the nanostructure of an STM tip, can electrons be spontaneously spin-polarized due to its geometry? In this study, we will show spin electronics states of GaN tips first and discuss spin polarizability in the nanostructural III–V compound tips. We constructed cluster

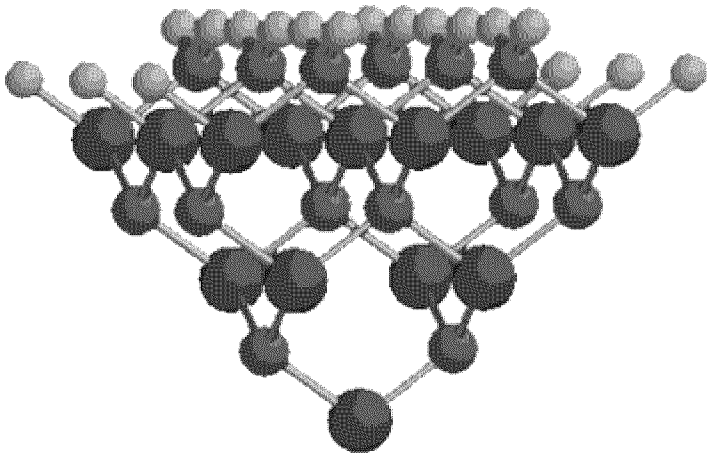

**Fig 2.** A cluster model for a GaN tip with a Ga atom at the apex in the crystallographic axis (100).

models for STM tips to investigate spin electronic structures of tips comprised of III–V compound materials, using molecular orbital first principles calculations (see Figs. 1 and 2). We used for the models the bulk atomic distances of the corresponding crystalline tips in the zinc-blend structure and terminated the dangling bonds with hydrogen atoms to reproduce the spin electronic states of the crystalline tips. We employed Unrestricted–Hartree–Fock calculations with relativistic effective core potentials. At the apexes of the tips with the axes parallel to the crystallographic axes (111) and (100), electron spins are polarized at the lowest energies. Especially, in case of a GaN tip with a Ga atom at the apex, nearly 10% of the electrons in the valence band are spin-polarized. We performed the above computations for the rest of III–V and some of II–VI comound material tips. It suggests that spin polarizability grows as the difference of electronegativities of the elements of a compound increases and can be enhanced by creating a highly symmetric nanostructure of the tip due to Jahn–Teller effect.

## References

[1] M. Sawamura, M. Tsukada and M. Aono, *Jpn. J. Appl. Phys.* Vol. **32** 3257 (1993).
[2] R. Wiesendanger, *Scanning Probe Microscopy and Spectroscopy* (Cambridge University Press, 1994).
[3] K. Sueoka et al., *Jpn. J. Appl. Phys.* **32** 2989 (1993).
[4] S. F. Alvarado et al., *Phys. Rev. Lett.* **68** 1387 (1992).
[5] S. Watanabe et al., *Jpn. J. Appl. Phys.* **36** L929 (1997).
[6] A. Sugawara et al., *J. Appl. Phys.* **82** 5662 (1997).
[7] S. Blügel, *Phys. Rev. Lett.* **68** 851 (1992).

Ioffe Institute
6th Int. Symp. "Nanostructures: Physics and Technology"
St Petersburg, Russia, June 22–26, 1998.



# Spatially resolved low-temperature scanning tunneling spectroscopy on AuFe spin-glass films

*A. Depuydt*†, G. Neuttiens†, S. V. Savinov‡, N. S. Maslova‡, V. I. Panov‡ and C. Van Haesendonck†

† Laboratorium voor Vaste-Stoffysica en Magnetisme, Katholieke Universiteit Leuven, B-3001 Leuven, Belgium

‡ Chair of Quantum Radio Physics, Moscow State University, 119899 Moscow, Russia

Recently, finite-size effects in the electrical transport properties of dilute magnetic alloys have attracted a lot of attention [1]. For very dilute Kondo alloys (concentration $c \sim 100$ ppm) the spins of the conduction electrons tend to screen the spin of the magnetic impurities, inducing a non-magnetic state below the Kondo temperature $T_K$. Intuitively, one expects that the Kondo scattering of the conduction electrons is strongly affected as soon as the sample size becomes of the order of the Kondo screening cloud. For a typical Kondo alloy such as AuFe with $T_K \approx 1$ K, the size of the Kondo screening cloud should be a few micrometer, implying that finite-size effects can be conveniently studied in thin AuFe films which have been patterned using electron beam lithography. Some experiments have indeed revealed a pronounced depression of the logarithmic increase of the resistivity at low temperatures when decreasing the sample thickness or width below 1 $\mu$m. Another experiment, involving our laboratory in Leuven, failed to observe any size effect down to 40 nm. Experiments on nanometer size point contacts indicated a strong increase of the Kondo temperature when reducing the contact size below 10 nm [2]. Theoretical calculations predict that the size effects may be closely related to the anisotropy of the local magnetic moments which is induced by the sample boundaries in the presence of spin-orbit scattering [3]. Theory also indicates that the amplitude of the size effects is affected by disorder [4] as well as by surface roughness [5].

Size effects have also been investigated in more concentrated ($c \sim 1$ at.%) spin-glass alloys [6, 7], where at lower temperatures the logarithmic increase of the resistivity caused by the Kondo effect becomes dominated by a resistivity decrease due to the spin-glass freezing process. Size effects, which can be strongly affected by uncontrolled changes in the disorder [7], appear for sample sizes below 100 nm. These effects may be related to variations in the RKKY interaction strength as well as to a transition towards a lower dimensionality for the freezing process.

In this contribution, we will demonstrate the possibility to study size effects in thin films of AuFe spin-glass alloys by investigating the differential conductance near the Fermi level with low-temperature scanning tunneling spectroscopy (STS). As confirmed by point contact experiments, the voltage dependence of the differential conductance can be directly linked to the temperature dependence of the resistivity [8]. The STS measurements provide the unique possibility to probe possible spatial variations of the size effects. Moreover, combining the STS measurements with topographic scanning tunneling microscopy (STM) images of the surface may allow to check the influence of the local surface roughness on the spin scattering processes.

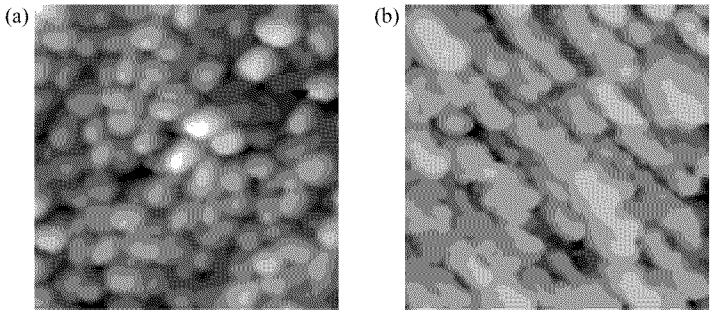


**Fig 1.** (a) STM image obtained at 300 K of a pure Au film with a thickness of 30 nm. The scanned area is 148 nm × 148 nm and the greyscale corresponds to height variations of 16 nm. The tunnel current has been fixed at 200 pA, and the sample bias at 200 mV. (b) STM image obtained at 300 K of a AuFe film with a thickness of 23 nm and an Fe concentration of 2.65 at.%. The scanned area is 144 nm × 144 nm and the greyscale corresponds to height variations of 17 nm. The tunnel current is fixed at 500 pA, and the sample bias at 50 mV.

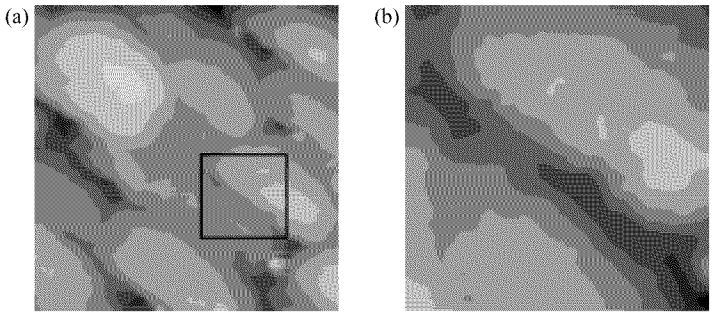


**Fig 2.** (a) STM image of the AuFe film measured at 5 K. The scanned area is 82 nm × 82 nm and the greyscale corresponds to height variations of 10 nm. The size of the square is 20 nm × 20 nm. The tunnel current is fixed at 10 pA, and the sample bias at 10 mV. (b) STM image of the region inside the black square marked in Fig. 2a.

Our experimental results, which are discussed in this contribution, have been obtained for a thin AuFe film with a thickness of 23 nm and an Fe concentration of 2.65 at.%. The film is produced by co-evaporation onto an oxidized silicon substrate. Topographic STM images of the AuFe thin film obtained at room temperature clearly reflect the polycrystalline film structure with a grain size of the order of the film thickness. The grains composing the film obviously have a different shape and size distribution when compared to the structure of a pure Au film with a comparable thickness of 30 nm and deposited onto an oxidized silicon substrate (see Fig. 1a and Fig. 1b). On the other hand, the root mean square roughness of both films turns out to be the same (2.4 nm). Additional STM experiments for different Fe concentrations will be needed to obtain a better understanding of the influence of Fe impurities on the film morphology.

We have also performed measurements of the AuFe film surface at 5 K with a low-temperature tunneling microscope. The details of our home-built microscope have been described elsewhere [9]. Fig. 2 shows STM topographical images at two different magnifications of the AuFe film surface. We have measured in detail the $I(V)$ char-

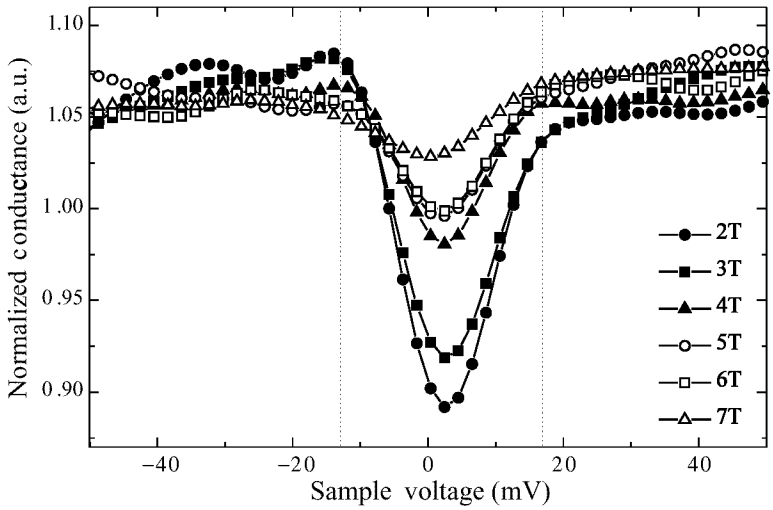


**Fig 3.** Normalized conductance $(dI/dV)/(I/V)$ curves for the AuFe thin film measured at different magnetic fields. The curves have been obtained by numerical differentiation of the $I(V)$ curves and have been averaged over $25 \times 25$ points located within a square area of 20 nm $\times$ 20 nm (see Fig. 2b).

acteristics at 5 K for the area corresponding to the image in Fig. 2b. Fig. 3 shows the normalized conductance curves, $dI/dV/(I/V)$, which have been obtained by numerical differentiation of the $I(V)$ curves. The curves in Fig. 3 have been averaged over $25 \times 25$ different points located inside the square of 20 nm $\times$ 20 nm. Fig. 3 also demonstrates the influence of a perpendicular magnetic field. The dip near the Fermi level is gradually destroyed when increasing the magnetic field.

Point contact spectroscopy has confirmed that the temperature dependence of the resistivity, $\rho$(T), is very similar to the voltage dependence of the normalized differential resistance $dV/dI(V/I)$, i.e., the inverse of the normalized differential conductance plotted in Fig. 3, provided the thermal energy is replaced with the voltage across the STM junction [2]. The dip appearing in Fig. 3 below 10 mV reflects the resonant Kondo scattering near the Fermi level. An additional sharp spin-glass maximum, which is expected to appear near V $\equiv$ 0, is absent, probably due to the limited voltage resolution of our STS measurements. The destruction of the Kondo dip in Fig. 3 by a magnetic field is consistent with the destruction of the Kondo effect by a magnetic field as soon as $\mu_B B > k_B T_K$, with $\mu_B$ the Bohr magneton. For sufficiently high magnetic fields, the Zeeman splitting of the electron energy levels inhibits the spin-flip scattering processes.

The results in Fig. 3 also reveal an asymmetry in the differential conductance about zero field. When applying a sufficiently large magnetic field, the asymmetry vanishes. A similar asymmetry has recently been observed in point contacts [10] as well as in mesoscopic spin-glass alloys [11]. This asymmetry can be linked to the anomalous thermopower in dilute magnetic alloys [12].

Figure 4 shows normalized conductance curves, $(dI/dV)/(I/V)$, for 3 different positions on the surface of the AuFe film at magnetic fields of 2 T and 5 T, respectively. Again, the curves have been obtained by numerical differentiation and have been averaged over 25 $\times$ 25 points within a square of 20 nm $\times$ 20 nm. Although the Kondo

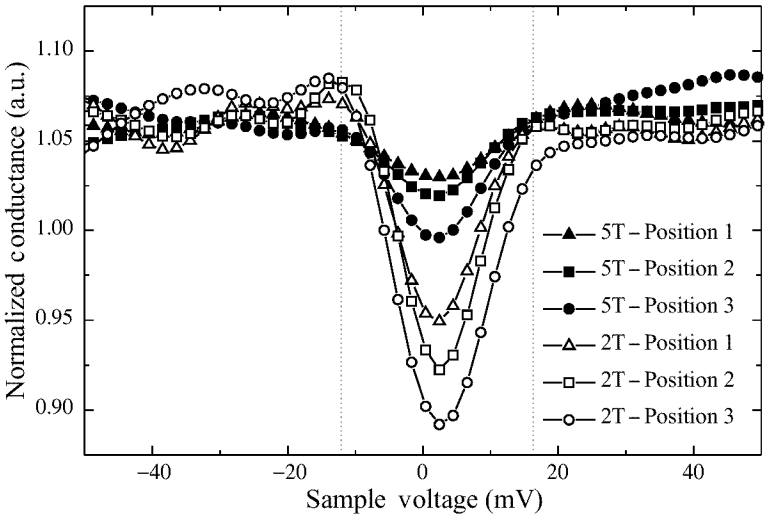


**Fig 4.** Normalized conductance $(dI/dV)/(I/V)$ curves for 3 different positions on the AuFe film at magnetic fields of 2 T and 5 T, respectively. The curves have been obtained by numerical differentiation of the $I(V)$ curves and have been averaged over 25 × 25 points located within a square of 20 nm × 20 nm.

dip is consistently destroyed by a magnetic field, the amplitude of the dip apparently depends on the position. More detailed experiments are needed to establish a closer link between the amplitude of the Kondo dip and the local film morphology (local film thickness) On the other hand, systematic measurements as a function of the AuFe film thickness may allow to clearly identify intrinsic size effects.

The work at the K. U. Leuven has been supported by the Fund for Scientific Research–Flanders (FWO) as well as by the Flemish Concerted Action (GOA) and the Belgian Inter-University Attraction Poles (IUAP) research programs. The collaboration between Moscow and Leuven has been funded by the European Commission (INTAS, project 94-3562). The work in Moscow has been supported by the Russian Ministry of Research (Surface Atomic Structures, grant 95-1.22; Nanostructures, grant 1-032) and the Russian Foundation of Basic Research (RFBR, grants 96-0219640a and 96-15-96420).

## References

[1] For a review, see M. A. Blachly and N. Giordano, *Phys. Rev. B* **51** 12537 (1995).
[2] I. K. Yanson et al., *Phys. Rev. Lett.* **74** 302 (1995).
[3] O. Újsághy, A. Zawadowski, and B. L. Gyorffy, *Phys. Rev. Lett.* **76** 2378 (1996).
[4] I. Martin, Y. Wan, and P. Phillips, *Phys. Rev. Lett.* **78** 114 (1997).
[5] V.M. Fomin et al., to appear in *Solid State Commun.*
[6] K. R. Lane et al., *Phys. Rev. B* **51** 945 (1995).
[7] G. Neuttiens et al., *Europhys. Lett.* **34** 617 (1996).
[8] Yu. Naidyouk et al., *Sov. J. Low Temp. Phys.* **8** 362 (1982).
[9] S. I. Oreshkin et al., *Pribory i technica experim.* **4** 17 (1997).
[10] N. van der Post et al., *Phys. Rev. B* **53** 15106 (1996).
[11] J. Eom et al., *Phys. Rev. Lett.* **77** 2276 (1996).
[12] G. Neuttiens et al., submitted to *Europhys. Lett.*

Ioffe Institute
6th Int. Symp. "Nanostructures: Physics and Technology"
St Petersburg, Russia, June 22–26, 1998.



# Atomic force microscopy of fullerene-indopane monolayers

*V. A. Fedirko*†, M. D. Eremtchenko†, V. R. Novak‡ and S. L. Vorob'eva‡
† Moscow State University of Technology "Stankin", 3a Vadkovski per., Moscow, 101472, Russia
‡ Zelenograd Research Institute of Physical Problems, 103460, Moscow, Russia

## Introduction

The atomic force microscopy (AFM) is a power tool for various surface objects imaging and characterisation in nanometer scale [1] including surface heterogeneity imaging [2]. The resolution up to several nanometers in the scanned plane can be realised with a sharp enough probing tip while the relief height resolution may be as high as several Angstroms. AFM also enables to make manipulations of nanometer scale with the surface objects. In [3] we reported on the results of the tunnelling electron microscopy study of $C_{60}$ fullerene monolayer structure formed by Schaefer horizontal lifting from the fullerene-surfactant mixture. In this paper we report on the results of AFM investigations of $C_{60}$ fullerene-indopane monolayers.

## Experimental

The fullerene-indopane layers

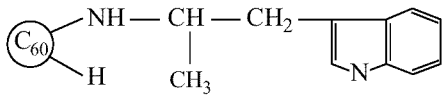


were deposited on a highly oriented pyrolytic graphite (HOPG) wafer by Schaefer horizontal lifting [4] from a water without any surfactant. For the comparison the samples were prepared by the horizontal lifting from the pure fullerene layer on the water surface. Silicon cantilevers with about 10 nm tip radius for AFM measurements were used. The tapping mode of operation was exploited. To measure the height of a layer we applied contact AFM mode and used the tip as a micromanipulator for deleting the adsorbed fullerene molecules from the part of the scanned area. Then we again scanned that fragment of the layer using the tapping mode of operation.

## Results

Figure 1 represents the relief of a sample with deposited fullerene-indopane monolayer. It shows that the continuous layer is formed. The phase contrast signal is almost constant over the same fragment which confirms the homogeneity of the scanned area. The fragment with the deleted strip of the layer is shown in Fig. 2. The width of the strip is about 80 nm. That enables to estimate the mean thickness of the layer as about 2 nm which corresponds to several fullerene-indopane monolayers. The thickness of the layer is not quite uniform, the scale of the observed knobs is about 10–20 nm in plane and of 0.5–2.0 nm in height.

Figures 3 and 4 show the AFM tapping mode images of a HOPG wafer surface after lifting from the pure fullerene layer on a water surface.

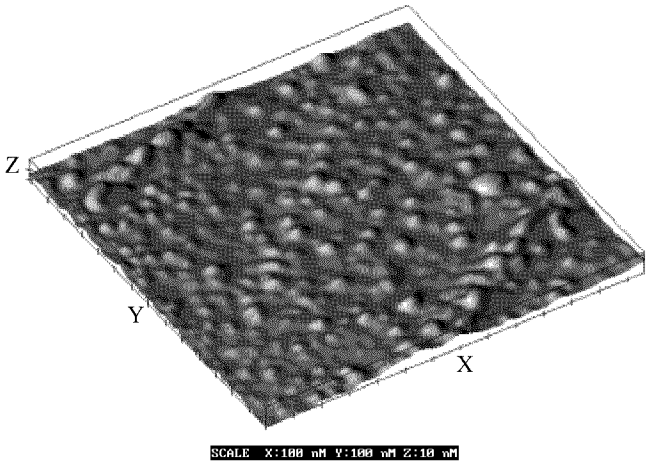


**Fig 1.** AFM relief image of fullerene-indopane monolayer on HOPG.

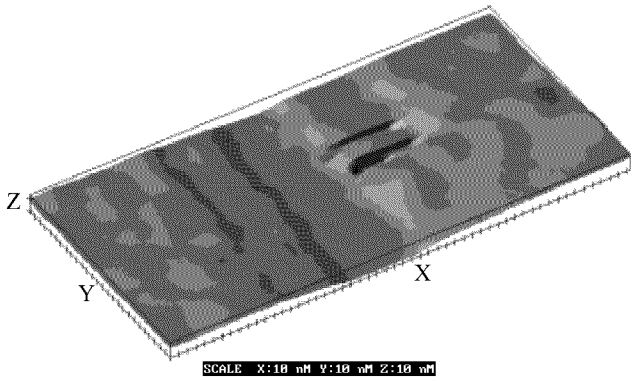


**Fig 2.** AFM relief image of fullerene-indopane monolayer on HOPG with the deleted strip of the film.

One can see fullerene clusters with the size of about 100–200 nm in plane and of 20–30 nm height both in the surface relief image of Fig. 3 and the phase contrast picture of Fig. 4. The phase contrast image indicates that the interaction between the tip and the surface atoms over clusters differs from that over the free area and thus confirm that they are of different substance.

## Conclusion

We have shown that the AFM enables imaging and characterization of fullerene monolayered surface structure. Micromanipulation in nanometer scale in the AFM contact mode is realised. The tapping mode of AFM operation and phase contrast technique proves very effective for layered surface structures study. The AFM investigation reveals a continuous fullerene-indopane film with a thickness of several molecular diameters.

The work was partially supported by Russian Research Program “Atomic Surface Structures”, project 97-3.22.

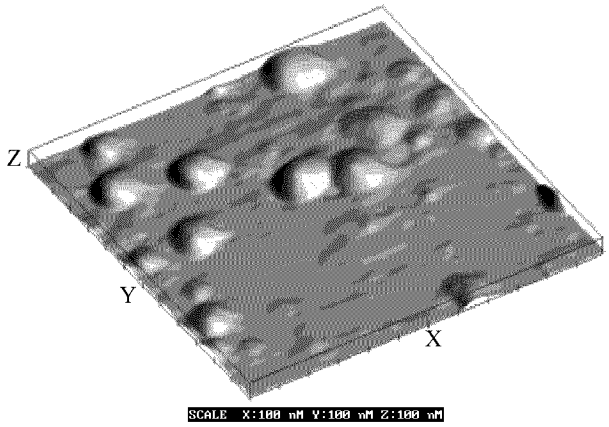


**Fig 3.** AFM relief image of $C_{60}$ clusters on HOPG.

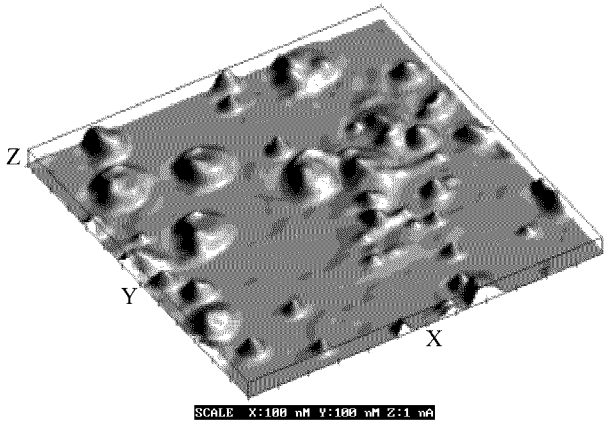


**Fig 4.** Phase contrast image of the same area.

## References

[1] S. M. Cohen, M. T. Bray, and M. L. Lightbody, eds., *Atomic force microscopy/scanning tunnelling microscopy*. U.S. Army Natick Research, Development, and Engineering Center, MA (1994).
[2] Q. Zhong, D. Innis, K. Kjoller, V. B. Elings, *Surf. Sci. Lett.* **290** L688 (1993).
[3] V. A. Fedirko, V. A. Bykov, M. D. Eremtchenko, *Fresenius J. Anal. Chem.* **355** 707 (1996).
[4] I. Langmuir and V. Schaefer, *J. Amer. Soc.* **60** 135 (1938).

Ioffe Institute
6th Int. Symp. "Nanostructures: Physics and Technology"
St Petersburg, Russia, June 22–26, 1998.



# In situ STM/STS investigation of light induced naphthacenequinone molecules conformation transformations

V. I. Panov†, S. I. Vasil'ev†, *A. I. Oreshkin*†, N. I. Koroteev‡ and S. A. Magnitskii‡

† Chair of Quantum Radiophysics, Moscow State University, 119899 Moscow, Russia
‡ International Laser Center, Moscow State University, 119899 Moscow, Russia

**Abstract.** Light induced conformational transformations of the of naphthacenequinone (NQ) molecules ordered in LB films are observed by means of scanning tunneling microscopy (STM). The distinct peak in local density of electronic states is detected which is characteric for the 2-dimential character of conductivity. Additional subband of electronic states has been found for NQ molecules in form A and not found in form B. The constant height STM images of individual molecules in the form A demonstrate an additional fine structure that indicates the conformational transition of molecules from A to B form. This transition is connected with the transfer of the phenoxy group from one oxygen to another and probably leads to shutdown some of tunneling channels.

## 1 Introduction

Photochromic molecules attract considerable and permanent interest due to their capability for reversible changing of their absorption and fluorescent spectra under irradiation at different wavelengths. In view of the development of new generation of ultra-high density optical data storage based on the use of photochromic molecules it is important to reveal fundamental mechanisms that lead to modification photohromic molecules characteristics (espesially organized in Langmuir-Blodgett (LB) films) under explosure to light. Properties of the photochromic molecules embedded either into polymeric matrices or other media (liquid crystals, solutions etc) essentially depend on their environment. Langmuir-Blodgett technique permits to produce photochromic molecular structures packed with ultra high density on the surface of a substrate. LB films are typical two-dimensional (single layer films) or three-dimensional (multilayer films) ordered assemblies. Evidently, one expect that photochromic molecules incorporated in highly ordered LB films should exhibit the behavior that is not typical for free molecules or solutions. However, very little is known about physics aspects of photochromic reactions in LB films.

For particular molecules photo isomeric changes can be observed by means of precise methods based on scanning probe microscopy (such as scanning tunnel microscopy/spectroscopy—STM/STS, scanning force microscopy—SFM etc.). These methods in principal allow one to study electronic properties [1,2] and topology of particular molecules and their variations, caused by external optical irradiation, on a substrate surface with atomic resolution.

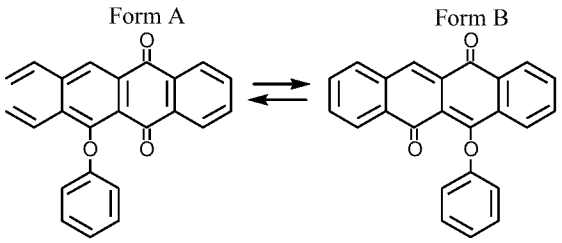


**Fig 1.** Schematic structure of two conformational forms (A and B) of 6-phenoxi–5, 12–naphthacenequinone molecules which occur during photocoloration ($A \rightarrow B$) and photobleaching ($B \rightarrow A$) reactions.

## 2 Experimental

To study the changes of electronic properties of NQ molecules and their possible conformational modifications during photochemical reactions we used STM and STS techniques. Molecules were deposited on a HOPG substrate using Langmuir-Sheffer technique to form different numbers of ordered molecular layers. Expected modification of naphthacenequinone molecular structure under transformation from para-form (form A) to ana-form (form B) is shown in Fig. 1. Variations of molecular properties in multilayer thin films caused by light irradiation may change the initial density distribution of electronic states, what be detected in STM and STS experiments.

In our experiments the photochemical reaction was initiated by light passed through interference filter with transmission maximum at 400 nm for the direct reaction ($A \rightarrow B$) and at 480 nm for the back reaction ($B \rightarrow A$). We used the incandescent lamp as a light source. After the interference filter radiation traveled through the wave-guide and than entered the tunnel gap of scanning tunneling microscope. Such a scheme has allowed to follow the changes of electronic properties of NQ molecules in processes of forward and reverse phototransitions by means of STM and STS methods.

LB film was transfered on the HOPG substrate under pressure of 5 mN/m. Average transfer coefficient $\langle k \rangle$ was equal to 0.84. We have found that LB films of naphthacenequinone molecules (1–40 monolayers) are capable to form the stable ordered structures on a surface of HOPG. The value of area occupied by each molecule is in the order of 2–2.3 $nm^2$ and is in a good agreement with the value of 2.7 $nm^2$ obtained from $\pi - S$ isotherm at the deposition pressure. Distance between molecular rows is in the range 0.58–0.6 nm and that between molecules in the row is 0.38–0.4 nm. Measurements of local density of electronic states of LB films have revealed a peak close to zero of bias voltage. In the approximation of a strong coupling it corresponds to the 2D character of differential conductivity of LB film and points to the existence of long-range interaction between molecules [3].

Another set of experiments have dealt with the investigation of LB film conductivity behavior during photoreactions. Substantial variation in the local density of electronic states for forward photoreaction has been observed for three-layer LB film. It is found that the form of the differential conductivity curve is significantly modified during photoisomerization. Upper graph depicted at Fig. 2 shows strong asymmetry of the curve for form A. There exist an additional contribution to at $Ut < 0$ in relation to form B,

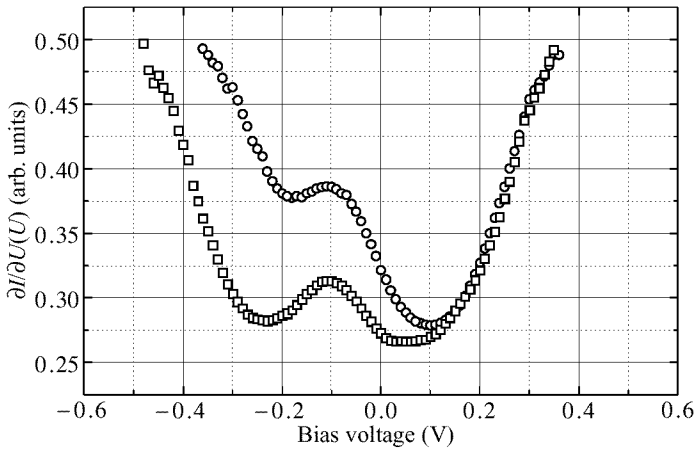


**Fig 2.** Dependence of differential conductivity of LB film on tunneling voltage (3 monolayers) before and after direct photoreaction. ○–A-form ; □–B-form.

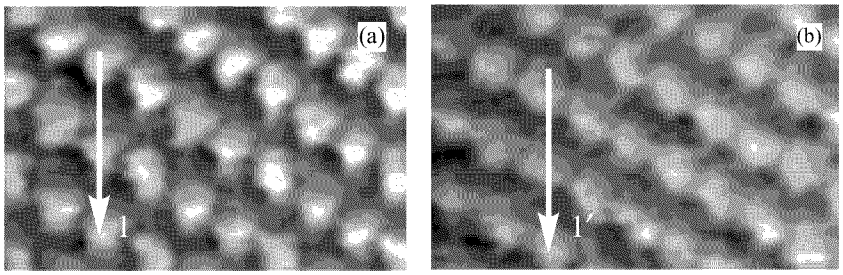


**Fig 3.** STM current images of the same portion of 3-layer naphthacenequinone LB films. a) form A, $It(x, y)$: 3.4 nm×2.2 nm×0.14 nA, b) form B, $It(x, y)$: 3.4 nm×2.2 nm×0.08 nA.

while the dependencies of LB film conductivity of A and B forms at $Ut > 0$ are rather similar. Such additive to the tunnel state density points to the origination of additional subband in the range of non filled electronic states of these LB films.

We have also studied the STM current images of individual molecules in NQ LB films. STM constant height images of 3-layer LB film corresponding to forms A and B of naphthacenequinone are presented in Fig. 3. Images (a) and (b) represent the selected site of the surface before and after direct photoreaction. Both pictures are registered under the same initial parameters: $Ut = -150$ mV; $It = 0.4$ nA. In these experiments we have found the spatial distinctions in STM current images of every molecule in LB layer for form A and B. These distinctions are clearly seen from Fig. 4 where current image sections of A and B forms of NQ molecules are depicted. The sections were get along the similar directions 1 and 1′ (see Fig. 4) for the same molecules. As seen from Fig. 4, STM constant height image of 6-phenoxi-5,12-naphthacenequinone molecules in form A has $\sim$ $0.1nA$ amplitude, while the current amplitude for molecules in form B is $\sim$ 0.04 nA. Besides, the STM current image of molecules in form A possess an additional fine structure ( see peak shifted to the edge of the molecular image). This

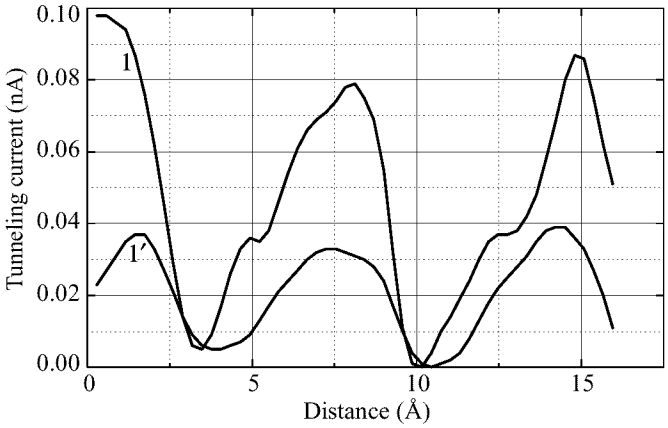


**Fig 4.** STM current image cross-sections according to arrows in Fig. 3. Curves 1, 1′ correspond to directions 1, 1′ at Fig. 3.

peculiarity is connected either with topological conformational transition of molecule or with the occurrence of additional tunneling channel after molecular conformation. To our opinion, the observed transition is due to oxygen bonding transfer that leads to occurrence of additional tunneling channel and, in ordered molecular system of LB film, to occurrence of additional subband.

## 3 Conclusion

We have demonstrated the direct observation of differential conductivity changes of NQ LB films under photochemical reaction by STM/STS methods. Unusual behavior of the differential conductivity of the molecular film probably corresponds to additional monotonous density of vacant states of the sample as a result of photoreaction and can be referred to conformational modification of naphthacenequinone molecules. The distinction in the STM constant height images of individual NQ molecules in different forms has been found that demonstrates the conformation transition during photoisomerization.

This work was financially supported by Memory Devices Inc. of the Constellation Group GmbH (Austria), partiaraly by the Russian Ministry of Research (Nanostructures, grant 97-1086, Surface atomic Structures, grant 95-1.22) and the Russian Foundation of Basic Research (RFBR, grants 96-0219640a and 96-03-32867).

## References

[1] Supriyo Datta, Weidong Tian, Seunghum Hong, R. Reifenberger, Jason I. Henderson, Clifford P. Kubiak, *Phys. Rev. Lett.* **79** 2530–2533 (1997).
[2] U. During, O. Zuger, B. Michel, L. Haussling, H. Ringsdorf, *Phis. Rev. B* **48** 1711 (1993).
[3] N.S. Maslova, Yu.N. Moiseev, S.V. Savinov, R.G. Yusupov, *JETP Letters* **58** 524–528 (1993).

Ioffe Institute
6th Int. Symp. "Nanostructures: Physics and Technology"
St Petersburg, Russia, June 22–26, 1998.



# Asymmetry of the Hall conductance fluctuations in a random magnetic field

*Yu. V. Nastaushev*†, G. M. Gusev†, A. A. Bykov†, D. I. Lubyshev†, D. K. Maude‡, J. C. Portal‡, U. Gennser§ and P. Basmaj¶

† Institute of Semiconductor Physics, Russian Academy of Sciences, Siberian Brunch, Novosibirsk, Russia

‡ Grenoble High Magnetic Field Laboratory, MPI-FKF and CNRS-LCMI, F-38042, Grenoble, France

§ Paul Scherrer Institute, CH-5232 Villigen-PSI, Switzerland

¶ Instituto de Fisica de Sao Carlos, 13560-970, Universidade de Sao Paulo, SP, Brazil

Transport in a two-dimensional electron gas (2 DEG) experiencing a random magnetic field has lately attracted intensive attention, due in large part to its relevance to the properties of the half-filled Landau level. One of the interesting features of the system is the absence of any time-reversal symmetry, which would, for example, preclude weak localization. The delocalization problem in a random magnetic field system has been studied in [1–4].

In this paper we report on measured fluctuations of the asymmetric part of the Hall conductance in small samples ($2 \times 2$ $\mu$m$\times\mu$m) with a dimpled 2 DEG. This type of structures provides an experimental alternative for studying a spatially varying magnetic field, since only the magnetic field perpendicular to the surface will affect the electrons confined in the topologically dimpled heterojunction [6]. Previously, we have reported on universal conductance fluctuations in such structures [5]. It is found, that all interference effects can be considered as interference between random walk trajectories through a random, sign alternating magnetic field. The correlation properties of UCF in a random field are governed by the second order corrections to the flux through the closed loops. Here we find, by interchanging of current and voltage leads, that fluctuations Hall resistance violates the Onsager relation, $R_{xy}(B) \neq R_{yx}(-B)$, and thus the fluctuations of the antisymmetric part of the extracted Hall conductance are not equal to the fluctuations of the Hall conductance found when inversing the magnetic field. We also find that the amplitude of the antisymmetric part of the extracted Hall conductance is of the order of $e^2/h$, as predicted for a random magnetic field.

Samples were fabricated employing overgrowth of GaAs and $Al_{0.3}Ga_{0.7}As$ materials by molecular beam epitaxy on prepatterned (100) GaAs substrates. Details of sample preparation and description of devices were reported in [6]. Samples with periodicity of dimples $d = 1\mu$m and $0.3\mu$m have been studied. The mobility of the 2 DEG is 30–70 m$^2$/Vs, and the density $5.5\times10^{11}$ cm$^{-2}$. The phase coherence length $L_f$ at $T = 50$ mK is 1-2 $\mu$m, which is comparable with the sample size (1.5–2 $\mu$m). Samples have a cross shape (see insert to Fig. 1) and four-terminal measurements of the magnetoresistance were carried out at temperatures $T = 50$ mK.

When placed in a magnetic field parallel to substrate, the electrons in the heterojunction move in sign alternating effective magnetic field [6]. In this case the total magnetic flux through the area of the steps of the dimpled surface is close to zero. Since the interference effects and universal conductance fluctuations are caused by the enclosed

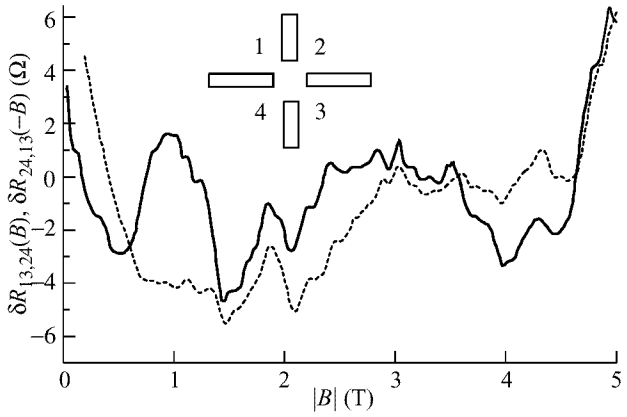


**Fig 1.**

flux through the electron trajectories, no influence of the sign alternating magnetic field on the UCF is therefore expected. However, because the electron motion imposed by the impurity disorder, a "random" number of flux is enclosed by the electron loops, in spite of the periodical nature of the dimple lattice that causes the spatial variation of the magnetic field. In [5] we considered the random walk model and obtained second order corrections to the total flux enclosed by all electron trajectories involved in the interference. This gives the correlation magnetic field in a parallel external field $B_c = 2hcb/eL_f$, where $b$ is the height of the dimples 0.1 $\mu$m, which agrees well the experimental observations.

The Hall resistance together with $B$-linear background reveals aperiodical reproducible fluctuations. Fig. 1 shows these fluctuations in detail, after subtraction of the linear part $R_{xyl}$. The Hall resistance was measured while interchanging the current and voltage leads. It is clearly seen that Hall resistance fluctuations does not obey the symmetry law. The cross correlation for the two traces $R_{1324}(B)$ and $R_{2413}(-B)$ is 60%, and correlation for traces ander the same conditions (reproducibility) is 95%.

The demonstration of an antisymmetric Hall-component fluctuation may have further implications for the possibility of extended states in a 2 DEG experiencing a random magnetic field.

This work was supported by grants RFFI No. 97-02-18402 and No. 96-02-19262.

## References

[1] S. C. Zhang and D. Arovas, *Phys. Rev. Lett.* **72**, 1886 (1994).
[2] A. G. Aronov, A. D. Mirlin, and P. Wolfe, *Phys. Rev. B* **49**, 16609 (1994).
[3] D. N. Sheng and Z. Y. Weng, *Phys. Rev. Lett.* **75**, 2388 (1995).
[4] Y. B. Kim, A. Furusaki, and K. K. Lee, *Phys. Rev. B* **52**, 16646 (1995).
[5] G. M. Gusev, X. Kleber, U. Gennser, D. K. Maude, J. C. Portal, D. I. Lubyshev, P. Basmaji, M. P. A. da Silva, J. C. Rossi, and Yu. V. Nastaushev, *Phys. Rev. B* **53**, 13641 (1996).
[6] G. M. Gusev, U. Gennser, X. Kleber, D. K. Maude, J. C. Portal, D. I. Lubyshev, P. Basmaji, M. de P. A. Silva, J. C. Rossi, and Yu. V. Nastaushev, *Surface Science* **361/362**, 855 (1996).

Ioffe Institute
6th Int. Symp. "Nanostructures: Physics and Technology"
St Petersburg, Russia, June 22–26, 1998.



# Anomalous magnetoresistance in multy-level 2D systems

*N. S. Averkiev*, L. E. Golub and G. E. Pikus
Ioffe Physico-Technical Institute, 194021 St. Petersburg, Russia

A weak localization is a quantum interference of waves propagating through the closed trajectory in the opposite directions. This interference may be destroyed by different wave phase breaking processes: magnetic field, inelastic processes, spin relaxation etc. These mechanisms give additive contributions in the total interference breaking rate.

An additional channel of interference breaking appears in quantum wells (QWs) with a few subbands of size quantization: intersubband transitions. The peculiarity of this mechanism is that its role is not restricted to the formal change of the total interference breaking time. This relates with the fact that only the states with both the same energy and momentum give the contribution to the weak localization. Since the states at the Fermi level in different subbands have different momenta there are no interference between them.

One can show that the role of the intersubband transitions leads to the averaging of the parameters which defines the weak localization. The way of the averaging depends on the relation between the interlevel transition time and the times of phase breaking due to other processes. In intensively investigated QWs with a few filled subbands of size quantization this relation can change in wide range. In this report the weak localization theory for $n$- and $p$-type QWs in which carriers occupy a few size-quantized levels is proposed.

We have shown that the anomalous contribution to the magnetoconductivity in classically weak magnetic fields $H$ in 2D multy-level systems is described by the following expression:

$$\sigma(H) - \sigma(0) = \frac{e^2}{4\pi^2\hbar} \sum_{n=1}^{N} \left[ 2 f_2\left(\frac{H}{H_1^{(n)}}\right) + f_2\left(\frac{H}{H_2^{(n)}}\right) - f_2\left(\frac{H}{H_3^{(n)}}\right) \right] , \qquad (1)$$

where $N$ coincides with the number of filled size-quantized subbands in QW and $f_2$ is the standard function:

$$f_2(x) = \ln x + \psi(1/2 + 1/x) ,$$

where $\psi(y)$ is the digamma function. The first and second terms in (1) are the contributions of the states with unit total momentum and projections $\pm 1$ and 0 respectively and the third term is the contribution of the states with zero total momentum. $H_{1,2,3}^{(n)}$ are characteristic magnetic fields which defined by times of inelastic scattering, spin relaxation and interlevel transitions.

The analysis shows that if the intersubband transition time is more than the times of phase breaking due to elastic and inelastic processes then each level of size quantization gives independent contribution to the anomalous magnetoresistance and $n$ in the expression (1) coincides with the numbers of size-quantized levels. In the case of intensive intersubband transitions the conributions from the different subbands average and the characteristic magnetic fields are defined by effective times of spin and phase

relaxation. For instnance, we have calculated the values of the characteristic magnetic fields in the most actual case of two size-quantized subbands filling.

The other peculiarity of the intersubband elastic transitions is that they accompanied by a large (the same order as the inverse QW' size) change of the quasimomentum. Therefore their intensity depends on the sort of the scattered potential: if it is short-range then the intersubband transition time may be comparable with the momentum relaxation time. In *p*-type QWs, where the spin relaxation time in the subband decreases with its filling, the intensive intersubband transitions lead to the destroying of the interference of the states with unit total momentum even in the subbands with small number of carriers. Experimentally it must manifest in that, according to (1), the magnetoconductivity is negative. In *n*-type QWs the intensive intersubband transitions effect only on the value of the diffusion coefficient and the magnetoconductivity may be positive.

This work is partially supported by RFFI (projects 96-02-16959Ю and 96-15-96955), the government program "Physics of Solid State Nanostructures" and Volkswagen Foundation.

Ioffe Institute
6th Int. Symp. "Nanostructures: Physics and Technology"
St Petersburg, Russia, June 22–26, 1998.



# Conductance quantization in quasi-2D electron systems with strong fluctuation potential

B. A. Aronzon†, D. A. Bakaushin‡, *A. S. Vedeneev*‡, E. Z. Meilikhov†, and V. V. Ryl'kov†‡

† Russian Research Center "Kurchatov Institute", 123182 Moscow, Russia
‡ Institute of Radioengineering & Electronics RAS, 141120 Fryazino, Moscow reg., Russia

We have experimentally shown that some FET-like percolating 2D electron systems (with the length comparable with the percolation correlation length and the width exceeding the latter) based on semiconductor-insulator interfaces ($Si/SiO_2$, GaAs/AlGaAs, *n*-GaAs/*i*-GaAs etc.) with strong electrostatic fluctuation potential (FP) [1] reveal the conductance quantization and drastic decrease in electron localisation degree (in minima of the chaotic potential relief) at elevated temperatures (77–300 K) [2-4]. Estimation of the correlation length has proved that investigated structures of about one micrometer gate length are the real mesoscopic ones.

We have interpreted these effects in terms of the electron transport through some paths corresponding to the percolation level lowered in comparison with the infinite cluster. The resistance of this path is controlled by a single saddle constriction of the chaotic potential relief. When the electron transport through the constriction is ballistic, the structure conductance becomes to be of quantum quasi-1D character.

To construct the physical model of the conductance quantization we have performed a number of computer experiments. Distribution and correlation functions of FP induced in 2D-electron plane by the chaotic ensemble of built-in charges were calculated. As the saddle constrictions determine both the percolation level and the conductance quantization, saddle energy distribution function, negative and positive curvatures' value order, and energy dependence of their averaged ratio were calculated as well. Energy distributions of the percolation levels for mesoscopic structures were also simulated by means of considering the percolation networks of finite sizes.

As a result, we concluded that the physical model considered could qualitatively explain the experiments and predict unusual behaviour of the similar mesoscopic systems caused by the possible strong dependence of the percolation path configuration on electric and magnetic fields.

## References

[1] V. A. Gergel' and R. A. Suris, *Sov. Phys. JETP*, **57**, 415 (1983).
[2] B. A. Aronzon, D. A. Bakaushin, N. K. Chumakov, E. Z. Meilikhov, V. V. Ryl'kov, and A. S. Vedeneev, *Proc. Int. Symp. Nanostructures: Physics and Technology*, St.Petersburg, 1997, p. 11.
[3] B. A. Aronzon, D. A. Bakaushin, A. S. Vedeneev, E. Z. Meilikhov, V. V. Ryl'kov *Sov. Physics. Semiconductors*, **31**, 1460 (1997).
[4] B. A. Aronzon, E. Z. Meilikhov, D. A. Bakaushin, A. S. Vedeneev, and V. V. Ryl'kov *JETP Lett.*, **66**, 668 (1997).

Ioffe Institute
6th Int. Symp. "Nanostructures: Physics and Technology"
St Petersburg, Russia, June 22–26, 1998.



# Interfaces correlation effect in 2D GaAs/AlAs heterostructures

*M. V. Belousov*†, A. Yu. Chernyshov†, I. E. Kozin†,
H. M. Gibbs‡ and G. Khitrova‡
† Institute of Physics, St. Petersburg State University,
St. Petersburg, Russia 198904
‡ Optical Sciences Center, University of Arizona, Tucson, Arizona 85721

**Abstract.** A single 4.5-nm GaAs quantum well (QW) is grown into GaAs/AlAs superlattices (SL). For a sample with 120-s growth interruptions (GI) at the GaAs surfaces we have exciton linewidth the same as for best quality GaAs/AlAs thin QW with long time GI at bottom and top interfaces. For the sample with 120-s and 20-s GI at the GaAs and AlAs surfaces, respectively, the smallest linewidth (1.4 meV) occurs when the AlAs thickness is exactly an integer number of monolayers (ML). Then each AlAs surface almost reproduces the large-island GaAs surface just below it (interface correlation effect), providing a better AlAs surface on which the QW is grown.

The low-temperature exciton linewidth of GaAs/AlAs QW's is generally believed to be dominated by well-thickness fluctuations [1, 2, 6, 3]. The best QW grown with GI have macrorough interfaces with large lateral size and 1 ML height islands (holes). At the typical growth conditions, an inhomogeneous linewidth is dominated by bottom interface of the QW (AlAs surface). It has a smaller scale of macroroughness than top interface of GaAs QW because a surface diffusion length of Al much shorter than Ga. In this paper we show that due to shorter Al diffusion length it is possible for the surface of a thin AlAs layer is to reproduce the GaAs surface on which it was grown. Such interface correlations make the bottom interface of QW almost as the top one and decrease exciton linewidth.

Molecular beam epitaxy was used to grow the samples on (001) oriented substrates with miscut angle $< 0.1°$. The samples were grown without substrate rotation resulting in large lateral gradients of the GaAs and AlAs layer thicknesses. Two samples NMSL15 and NMSL17 have the same structure and contain two single GaAs QW's. A control QW1 nominally of 25 ML GaAs with 35 ML AlAs barriers was grown without any GI. The second QW2 nominally of 16 ML GaAs was grown in the middle of a 80-period SL (8 ML GaAs, 6 ML AlAs). Both samples had 120-s GI's at GaAs surfaces of the SL and QW2. The sample NMSL15 had 20-s GI's also at AlAs surfaces of the SL and QW2.

The differential reflection $(dR/dE)/R$ and photoluminescence (PL) excitonic spectra were taken at $T = 10$ K. GaAs layer thicknesses in QW2 ($G_{QW2}$) could be kept constant by scanning along a contour of constant QW1 exciton energy. Then the $A_{SL}$ variation was defined by the SL period variation which is measured from the folded acoustic phonon Raman shifts, with an accuracy $\pm 0.05$ ML.

In the NMSL17 sample grown without GI after AlAs (Fig. 1(a)), there are three sharp excitonic resonances in the reflection spectra (solid lines) with energy splittings approximately same as calculated for QW2 width differing by 1 ML (monolayer splitting). The linewidth (2 meV) to monolayer splitting ($\approx 14$ meV) ratio is $\approx 0.15$, the

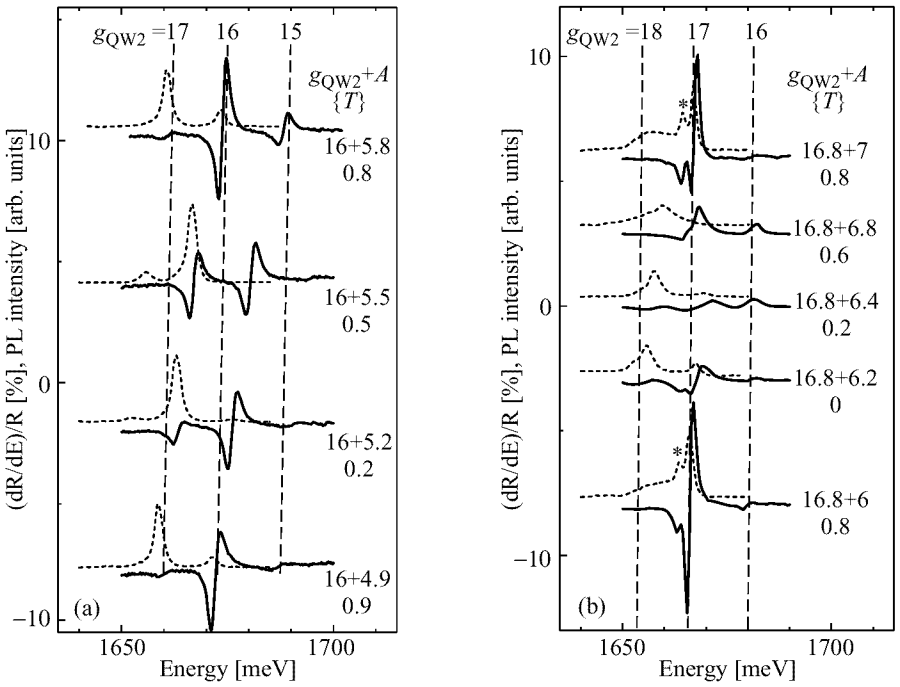


**Fig 1.** The differential reflection $(dR/dE)/R$ (solid lines) and the PL (dotted lines) exciton spectra of QW2 for the NMSL17 (a) and NMSL15 (b) as a function of AlAs layers thickness of SL ($A_{SL}$) at the constant thickness of QW2 ($G_{QW2}$).

same as for the best quality GaAs/AlAs QW's, grown with long GI's after GaAs and AlAs [2]. Hence, the lateral scale of macroroughness for both of the QW2 interfaces (top and bottom) is much larger than the exciton diameter ($\approx 20$ nm). It is very important to note that the excitonic energies and intensities are changed continuously with AlAs thickness and repeat when $A$ changes by 1 ML (but the linewidths and multiplet weighted average are almost unchanged). Hence, the local thicknesses of QW2 in the NMSL17 is noninteger in general (but its difference is integer) and increasing when $A_{SL}$ decrease. Measurements along other directions of the sample show that the relative intensities are periodically dependent upon $G_{QW2} + A_{SL}$ (this is the distance between top QW2 surface and GaAs surface just bellow QW2) with the period 1 ML.

The behavior of the NMSL15 sample grown with GI after AlAs, Fig. 1(b), is strikingly different. The excitonic resonance amplitude and width now depend strongly on the AlAs thickness. For noninteger $A_{SL}$ the peaks are shifted to higher energies and broadened to 4–5 meV. Hence, at noninteger $A_{SL}$ GI strongly decreases the lateral scale of macroroughness of the AlAs surfaces. When $A_{SL}$ is an integer, the lines are quite narrow, 1.4 meV, with the record value of a linewidth to monolayer splitting ratio ($\approx 0.1$). Hence, for integer $A_{SL}$ GI brought the improving of bottom interface of QW (evidently because its microroughness decreased after GI). But even for integer $A_{SL}$ the AlAs surface is not perfect after GI. The satellite peak just below the main peak for integer $A_{SL}$ in Fig. 1(b) shows that array of a uniform small holes is presented on a large AlAs

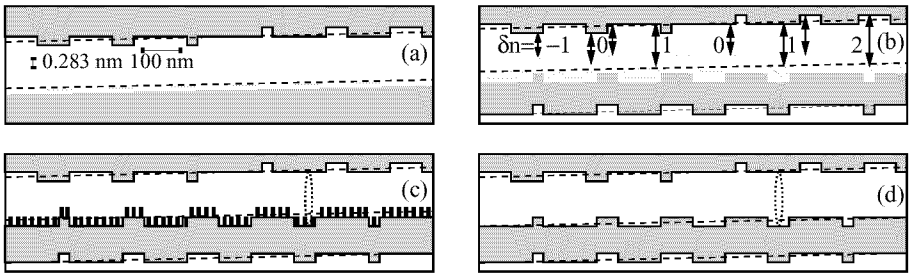


**Fig 2.** Schematic illustration of the interfaces in GaAs/AlAs heterostructures. Gray, light gray and white colors specifies AlAs, GaAlAs and GaAs respectively. The interfaces tilt angle is $0.01^\circ$.

planes (this holes are $\approx 7$ nm in size and occupy $\approx 10\%$ of the area by our estimates).

For discussion about the exciton confinement effect we have two different scales: exciton diameter ($D_{ex} \approx 20$ nm) in the QW plane and monolayer height (1 ML = 0.283 nm) across this one. The key structural parameter is the surface diffusion length $L_{D,Ga}$ (or $L_{D,Al}$). Without GI diffusion length is much shorter than $D_{ex}$ so surface is microrough and its local height $z$ coincidences with its average height $Z$ (the bottom interface on Fig. 2(a). After long time GI $L_{D,Ga} \gg D_{ex}$ and macroroughness takes place on the GaAs surface (the top interface on Fig. 2(a). Thus, the local height of the i-th surface can take one of the two values: $z_i = [Z_i]$ or $z_i = [Z_i] + 1$) with probabilities $1 - \{Z_i\}$ and $\{Z_i\}$ respectively, where rectangular and figure brackets denote integer and fractional parts of the average height of surface $Z_i$ in ML. The value $\{Z_i\}$ determinate the filling factor of the i-th surface. For $\{Z_i\} = 0$ the surface is completed and clean. Islands are formed on the surface for $0 < \{Z_i\} < 0.5$, and holes for $0.5 < \{Z_i\} < 1$. A lateral size of islands (holes) depends on diffusion length and filling factor.

Now it is very important to notice that for a real (001) substrate an average interface height $Z_i$ shifts up in the growth direction by a lot of atomic layers within the light beam spot. Even for a $0.01^\circ$ error in locating the (001) plane result in $\approx 30$ ML shift up in the average height of surface across the light spot diameter $\approx 50$ mkm. Therefore all values for the local filling factor of the i-th surface can be assumed equally probable. So, to calculate the allowed local QW thicknesses and the areas they occupy, one must average over $0 < \{Z_i\} < 1$ and to take into account that the local filling factor of two uncorrelated macrorough surfaces are related by $\{Z_{i+1}\} = \{Z_i + T\}$, where $T$ is the average distance between them. Result is dependent on interfaces correlation.

Four interface models with GI after GaAs surfaces are shown in Fig. 2. There is no GI after AlAs and no correlation with the previous interface in Fig. 2(a); therefore the slope of the microrough AlAs surface is that of the average GaAs surface. The macroroughness on the GaAs interface as shown on Fig. 2(a) give two QWs sets where the thicknesses change saw-like from $G_{QW} + 1$ to $G_{QW}$ and from $G_{QW}$ to $G_{QW} - 1$. This model without interface correlation predicts a continuous thickness distribution that does not agree with the discrete reflection spectra of Fig. 1(a).

In the Fig. 2(b) the microrough surface of the thin AlAs layer correlates with the previous GaAs surface. One can see that the QW local thicknesses ($g_{QW}$) are discrete but noninteger ($g_{QW} = [T] + \delta n - A_{SL}$) where $T = G_{QW} + A_{SL}$. For noninteger $T$ the model gives four values $g_{QW}$ ($\delta n = -1, 0, 1, 2$). For integer $T$ there is only three $g_{QW}$

($\delta n = -1, 0, 1$). Areas and hence excitonic oscillator strength for regions with different $g_{QW}$ depend on the fractional part of $T$. Thus, the interface correlation effect explains the basic tendencies in the exciton spectra of NMSL17 (Fig. 1(a)), namely number of component (4 in sum at PL and $(dR/dE)/R$ spectra for $\{T\} = 0.2 \div 0.5$), oscillator strength dependencies on the $G_{QW} + A_{SL}$ and continuous energy shift up for increasing $A_{SL}$.

A GI on the AlAs surface could destroy the correlation with the previous GaAs one if $L_{D,Al}$ is of the same order as $L_{D,Ga}$. If so, the QW local thicknesses depend only on QW average thickness ($g_{QW} = [G_{QW}] + \delta n$) but do not depend on AlAs thickness. Since this is not the case NMSL15 we conclude that $L_{D,Al} \ll L_{D,Ga}$, so there must be two lateral scales of fluctuations on the AlAs surface (Fig. 2(c) in general: the larger one repeats the large islands on the GaAs surface, the smaller consists of macrorough islands (holes) when $A_{SL}$ is noninteger (then excess of Al must go somewhere but $L_{D,Al}$ is too small). For integer $A_{SL}$, large flat regions on the AlAs surfaces are complete, and each AlAs surface repeats the GaAs surface below (Fig. 2(d)). Interface correlation with exactly the right amount of Al narrows the exciton line width at the points with integer AlAs thickness on sample NMSL15.

Support from NSF DMR, DARPA/ARO, INTAS and RFFI is gratefully acknowledged.

## References

[1] D. Gammon and B. V. Shanabrook and D. S. Katzer, *Appl. Phys. Lett.* **57** 2710 (1990).
[2] D. Gammon and B. V. Shanabrook and D. S. Katzer, *Phys. Rev. Lett.* **67** 1547 (1991).
[3] D. Gammon and E. S. Snow and B. V. Shanabrook and D. S. Katzer and D. Park, *Phys. Rev. Lett.* **76** 3005 (1996).
[4] D. Gammon and E. S. Snow and B. V. Shanabrook and D. S. Katzer and D. Park, *Science* **273** 87 (1996).
[5] M. Hübner and J. Kuhl and T. Stroucken and A. Knorr and S. W. Koch and R. Hey and K. Ploog, *Phys. Rev. Lett.* **76** 4199 (1996).
[6] F. Kopf and E. F. Shubert and T. D. Harris and S. Becker, *Appl. Phys. Lett.* **58** 631 (1991).

Ioffe Institute
6th Int. Symp. "Nanostructures: Physics and Technology"
St Petersburg, Russia, June 22–26, 1998.



# Impurity potential broadening of the Landau level as measured by an acoustoelectronic method

I. L. Drichko, A. M. Diakonov, V. D. Kagan and *I. Yu. Smirnov*
Ioffe Physico-Technical Institute, St.Petersburg, Russia

**Abstract.** In the quantum Hall regime the conductivity $\sigma_{xx}$, measured in a direct current experiment is equal to 0, whereas the alternative current conductivity $\sigma_{xx}^{ac}$ has a finite value. It has been shown [1], that from the study of this *a.c.* conductivity one could obtain valuable characteristics of 2DEG and estimate the role of random fluctuation potential. As it has been demonstrated earlier, one of the best methods for the study of $\sigma_{xx}^{ac}$ in semiconducting heterostructures is that of acoustoelectronic interaction of surface acoustic waves with 2DEG in a structure.

The SAW attenuation by the 2DEG was originally observed in [2]. If a sample is placed on the surface of a lithium niobate plate in such a way that the distance $a$ between the 2DEG channel and the surface of $LiNbO_3$ is less than the SAW length, the 2-dimensional electrons find themselfs in an alternative electric field of SAW, which captures them and drags in the direction of propagation. The energy of the alternative electric field is absorbed, SAW is attenuated and its velocity grows because of of the additional piezoelectric stiffening of the propagation medium. The absorption coefficient of a SAW can be theoretically presented in the way [3]:

$$\Gamma = 8.68\frac{K^2}{2}kA\frac{(4\pi\sigma_{xx}/\epsilon_s v)t(k)}{1+[(4\pi\sigma_{xx}/\epsilon_s v)t(k)]^2}, \frac{\text{dB}}{\text{cm}} \qquad (1)$$
$$A = 8b(k)(\epsilon_1+\epsilon_0)\epsilon_0^2\epsilon_s\exp(-2ka),$$

where $K^2$ is the electromechanical coupling coefficient of piezoelectric substrate, $k$ and $v$ are the SAW wavevector and the velocity respectively, $a$ is the vacuum gap width between the lithium niobate platelet and the sample, $\sigma_{xx}$ is the dissipative conductivity of 2DEG, $\epsilon_1$, $\epsilon_0$ and $\epsilon_s$ are the dielectric constants of lithium niobate, vacuum and semiconductor respectively. $b$ and $t$ are complex functions of $a$, $k$, $\epsilon_0$, $\epsilon_s$ and $\epsilon_1$. When $(4\pi\sigma_{xx}/\epsilon_s v)t(k) = 1$, $\Gamma$ achieves it's maximum $\Gamma_m$: $\Gamma_m = 8.68Ak(K^2/2)(1/2)$.

In our experiments we measure the absorption of SAW in a GaAs/AlGaAs heterostructure (mobility $\mu = 1.28\cdot 10^5$ cm/Vs, carrier density $n = 6.7\cdot 10^{11}$ cm$^{-2}$).

The measurements were carried out in a temperature range 1.5–4.2K, magnetic field up to 7 T, acoustic frequency 30–150 MHz. Two kinds of measurements were performed: for the first kind the acoustic power maintained low enough to provide the linearity of results, for the second kind a nonlinear behavior was studied intensively, at 1.5 K the dependence of 2DEG conductivity on acoustic power level (RF-generator output power $P$) was measured. In addition measurements of $\rho_{xx}$ and $\rho_{xy}$ were performed at magnetic fields up to 6 T and in a temperature range 0.65–4.2 K on a sample with similar parameters.

Fig. 1 illustrates the experimental dependences $\Gamma$ on $B$. The linear behavior $\Gamma(T)$, as well as the $\Gamma(P)$ at $B < 3$ T has been studied in [4, 5]. In the present work

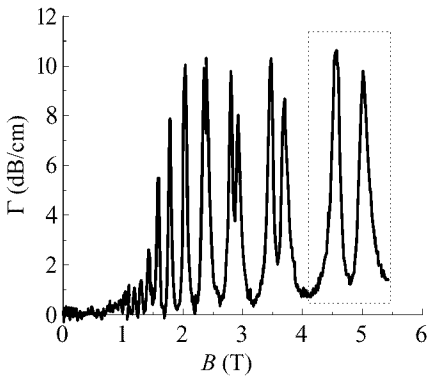


**Fig. 1.** The experimental dependences of Γ on $B$ at $T = 1.5$ K, SAW frequency $f = 30$ MHz.

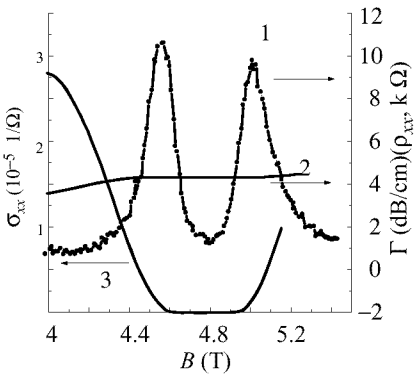


**Fig. 2.** The experimental dependences of $\Gamma(T)$ (1), $\rho_{xy}$ (2) and $\sigma_{xx}$ (3) on magnetic field at $T = 1.5$ K.

the experimental data for the magnetic fields corresponding to the middle of the Hall plateaus (quantum Hall regime) will be analyzed. It should be noticed that the analysis of the conductivity effects, performed in the present work, could be impossible in the framework of the conventional direct-current methods, because in the used magnetic field range DC conductivity is zero: the region of the Hall plateau. Meanwhile the absorption coefficient Γ behavior is characterized by dramatic peculiarities.

Fig. 2 (zoom-out of the part of Fig.1) illustrates the experimental dependences of Γ, $\sigma_{xx}$ and $\rho_{xy}$ on $B$, in the magnetic field region 4–5.5 T. Because $\sigma_{xx}$ in this $B$ region is very small, from (1) it follows that $\Gamma \propto \sigma$ therefore we can operate with Γ instead.

Fig. 3 illustrates the $\Gamma(T)$ dependences ($f = 30$ MHz) at magnetic fields corresponding to the attenuation minima (or the middle of the Hall plateau): 4.8, 3.6, and 2.9 T, which are deduced from the curves of the Fig. 1 type measured at different $T$ and $f$. Similar curves were obtained for $f = 150$ MHz also. As one can see from the figure, as $T$ grows, in a certain temperature range Γ does not depend on a temperature, but at higher temperature begins to grow exponentially; the stronger $B$, the higher $T$ at which the growth starts.

Such a dependence of Γ on $T$ could be explained, if one supposed that at these levels of a magnetic field the attenuation adds up from both the SAW attenuation ($\Gamma_2$) by the 2DEG thermally activated to the upper Landau level, and that ($\Gamma_h$) due to the hopping conductivity $\sigma_h$ of electrons, localized on the impurities in the 3-dimensional layers or hopping conductivity of 2D electrons on the localized states near the Fermi level. Both hopping mechanisms have a weak dependence on temperature [6, 7]. If $\Gamma \propto \sigma$, $\Gamma = \Gamma_2 + \Gamma_h$.

As the temperature grows, more and more 2-dimensional electrons appears at the upper Landau level, due to their activation from the bound states at the Fermi level. This leads to the growth of the weight of $\Gamma_2$ in the total absorption, and therefore the $T$ dependence of Γ becomes one of activation type.

The above speculations allowed us to obtain the value of SAW attenuation by merely subtracting $\Gamma_h$ from the experimentally measured Γ. $\Gamma_h$ is equal to the Γ in the temperature range where Γ is temperature-independent at the magnetic fields 4.8 and 3.6 T ($\Gamma_2 \ll \Gamma_h$). At $B = 2.9$ T, when there is no temperature flattening, $\Gamma_h$ was obtained,

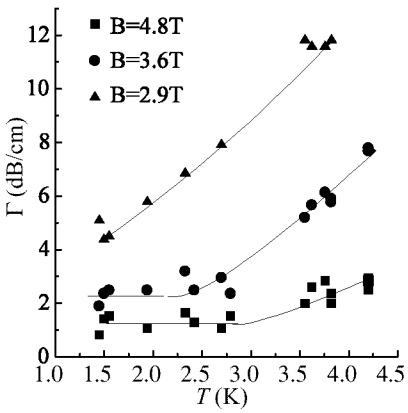


**Fig. 3.** The dependences of Γ on temperature at $f = 30$ MHz in the magnetic fields corresponding to the attenuation minima.

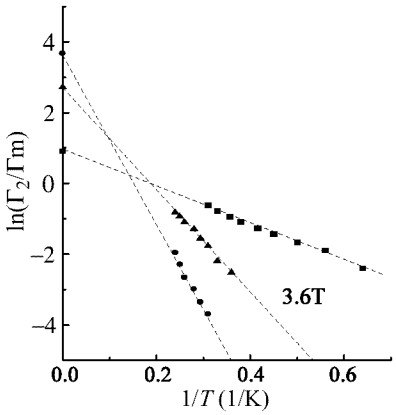


**Fig. 4.** The values of $ln\Gamma_2/\Gamma_m$ vs. $1/T$ in magnetic fields: 1—4.8, 2—3.6, 3—2.9 T at $f = 30$ MHz.

using the assumption that $\Gamma_h \propto 1/B^2$, which holds for 4.8 and 3.6 T, and has been observed in the case of 3-dimensional conductivity [6]. The values of $\Gamma_2$ obtained as a result of the subtraction were plotted as $\ln\Gamma_2/\Gamma_m$ ($\Gamma_2$ is devided by $\Gamma_m$ in order to decrease the experimental error) versus $1/T$ (Fig. 4). When done for different magnetic fields and SAW frequencies such plots indeed confirm our earlier assumption and lead to the conclusion that SAW attenuation by the 2DEG in the upper Landau level is $\Gamma_2 \propto \sigma_2 \propto n \propto \exp(-\Delta E(B)/kT)$, where $\Delta E(B)$ is the energy gap between the Fermi level and the percolation level in the Landau band, widened by the random fluctuation potential. The dependence of $\Delta E$ on magnetic field, deduced from $\Gamma_2(1/T)$ for different SAW frequencies is presented in Fig. 5. Supposing $\Delta E = \hbar\omega_c/2 - A/2$, from the ordinate cut-off point of (crossing point) the $\Delta E(B) = 0$ curve for $B = 2.1$ T one could obtain $A$, the Landau band width, which appeared to be $A = 3.4$ meV. The slope of the $\Delta(B)$ line in Fig. 5 appeared to be 0.72 1/T, which by 10 percent differs from the $e/m^*c = 0.8$ 1/T, if $m^* = 0.07m_0$ for GaAs ($m_0$ — free electron mass). Hence, $\Gamma_2(T)$ behavior is governed by the activation of 2-D electrons from the bound states at the Fermi level to the upper Landau band, widened due to the fluctuation potential.

The dependence of Γ on the RF-generator output power $P$ at the same magnetic field is shown in Fig. 6. As it can be seen from the figure, Γ increases with the increase of $P$. Keeping in mind that in the temperature range emploied, and at given magnetic fields the $\Gamma_2$ is determined by the activation of electrons to the upper Landau level from the Fermi level, Frenkel-Pool effect consisting in the activation energy decrease in electric field $E$ of a SAW [8] could be considered as a model.

$$\Gamma_2 \propto \sigma_2 \propto n(T,E) = n_0 \exp(2e^{3/2}E^{1/2}\epsilon_s^{-1/2}/kT), \tag{2}$$

where $n_0$ -carrier density in the upper Landau level at a linear approach at 1.5 K. An electric field $E$, in which 2D-electrons are when SAW propagates in a piezoelectric, is [5]:

$$|E|^2 = K^2\frac{32\pi}{\nu}(\epsilon_1+\epsilon_0)b_1(k)\frac{k\exp(-2ka)}{1+[(4\pi\sigma_{xx}/\epsilon_s v)t]^2}W, \tag{3}$$

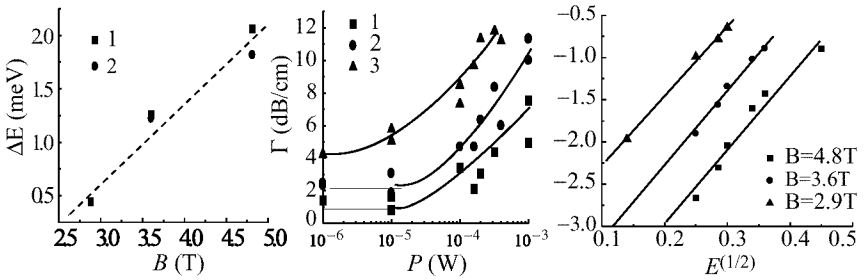


**Fig. 5.** The dependences of $\Delta E$ on magnetic field for different SAW frequencies: 1—30 MHz, 2—150 Mhz.

**Fig. 6.** The values of $\Gamma$ ($f = 30$ MHz) vs. RF output power $P$ in the magnetic fields corresponding to the $\Gamma$ minima: 1—4.8 T, 2—3.6 T, 3—2.9 T.

**Fig. 7.** The dependences of $ln\Gamma_2/\Gamma_m$ on $E^{1/2}$ for different $B$: 1—4.8 T, 2—3.6 T, 3—2.9 T at 30 MHz.

where $W$ -the input SAW power in the sample per sound track width, $b_1 = 2b \cdot t$. Expression (2) has been obtained for a d.c. electric field, but it can be shown that it holds when $E$ is the electric field of a SAW.

$Ln\Gamma_2$ plotted against $E^{1/2}$, where $\Gamma_2 = \Gamma - \Gamma_h$, and $E$ is the electric field of SAW (Fig. 7) confirms our model. Indeed, this dependence could be presented by a straight line, with the slope $2e^{3/2}/\epsilon_s^{1/2}kT = 9(E^{-1/2}cgs)$. From (2) this slope comes equal to 26.

The discrepancy between the theoretical and experimental slopes could be due to several origins: lack of the precision in the determination of RF-power at the input of the sample, the assumption of the independence of $\Gamma_h$ on $E$, and the neglect of the electron heating effects in the upper Landau level, when the input RF power is increased.

The work was supported by the RFFI 98-02-18280-a and Minnauki No. 97-1043 grants.

## References

[1] I. L. Drichko, A. M. Diakonov, A. M. Kreshchuk, T. A. Polyanskaya, I. G. Savel'ev, I. Yu. Smirnov, A. V. Suslov, *FTP* **31** 4, 451–458 (1997).
[2] A. Wixforth, J. Scriba, M. Wassermeier, J. P. Kotthaus, G. Weinmann and W. Schlapp, *Phys. Rev. B* **40** 7874 (1989).
[3] V. D. Kagan, *FTP* **31** 470 (1997).
[4] I. L. Drichko, I. Yu. Smirnov, *FTP* **31** 9, 1092–1094 (1997).
[5] I. L. Drichko, A. M. Diakonov, A. M. Kreshchuk, T. A. Polyanskaya, I. G. Savel'ev, I. Yu. Smirnov, A. V. Suslov, *FTP* **31** 11, 1357-1366 (1997).
[6] Yu. M. Gal'perin, I. L. Drichko, L. B. Litvak-Gorskaya, *FTT* **28** 3374 (1986).
[7] A. L. Efros. *Zh. Eks. Theor. Fiz.* **89** 1834 (1985).
[8] L. S. Stil'bans, *Physika Poluprovodnikov*, Sovietskoe Radio, Moskva 1967.

Ioffe Institute
6th Int. Symp. "Nanostructures: Physics and Technology"
St Petersburg, Russia, June 22–26, 1998.



# Weak localization and intersubbands transitions in $\delta$-doped GaAs

*G. M. Minkov*, S. A. Negashev, O. E. Rut and A. V. Germanenko
Institute of Physics and Applied Mathematics, Ural State University
Ekaterinburg 620083, Russia

The magnetoresistance in weak localization regime was thoroughly investigated both for the classical and quantum two-dimensional (2D) electron systems. One or several 2D subbands may be occupied in the latter case. The role of multy-subband electron structure was usually considered for heterostructures and for structures with surface quantum well. In this cases the interband relaxation time ($\tau_{inter}$) is less than the time of the phase relaxation of the electron wave function ($\tau_\varphi$) and the existence of the several occupied 2D subbands leads to replacing the diffusion coefficient (D) and $\tau_\varphi$ in the expression for magnetoresistance by their effective values only.

There are some reasons that 2D electrons in $\delta$-doping layers are the special case for weak-localization effects: (i) almost without exception more than one 2D subbands are occupied; (ii) the confined potential is symmetric therefore the electron wave functions have the fixed parity; (iii) the width of the impurity distribution is significantly less than characteristic width of the wave functions therefore the potential of the scattering centers is symmetric. These peculiarities have to lead to the fact that the transitions between the subbands with different parities are forbidden, so that the electrons in the odd and the even subbands have to give the independent contribution to the interference effects. As a result the prefactor in the expression for magnetoresistance have to be close to $2G_0$ ($G_0 = e^2/2\pi^2 h$ is the prefactor for the structures with one 2D subband).

In this report the results of the experimental investigations of the magnetoresistance of $\delta$-doped (Si) GaAs layers with the electron concentration $(0.8-6) \cdot 10^{12}$ cm$^{-2}$ in the temperature range 1.5–20 K are presented. There is shown that in the more perfect structures with electron concentration $(2-3.5) \cdot 10^{12}$ cm$^{-2}$ and Hall mobility $(1-3) \cdot 10^3$ cm$^2$/V $\cdot$ sec the prefactors are equal to $(1.4-1.6)G_0$.

The causes of the fact that the prefactor is close or less than the value of $G_0$ in the most part of the structures investigated earlier are discussed. This may be the result of the large distribution width of Si or macroscopic inhomogeneity of the $\delta$-doped layers.

The work is supported by the RFBR (Grant No. 97-02-16168) and by the Russian Program "Physics of Solid State Nanostructures" (Grant No. 97-1091).

Ioffe Institute
6th Int. Symp. "Nanostructures: Physics and Technology"
St Petersburg, Russia, June 22–26, 1998.



# Density of states of tunnel-coupled 2D electron layers in strong magnetic fields

*O. E. Raichev*
Institute of Semiconductor Physics, NAS Ukraine, Pr. Nauki 45, Kiev, Ukraine

**Abstract.** The density of states for a pair of disordered tunnel-coupled 2D electron layers in the quantum Hall regime is calculated. The interplay between the scattering-induced broadening of the Landau levels and tunnel-induced hybridization of the electron states is demonstrated. The conditions for the tunneling gap, when a single Landau level splits in two levels, are expressed through the parameters of the system. It is shown that even a symmetrical double-layer system in a strong magnetic field acquires a substantial dipole moment due to interlayer asymmetry of the disorder.

## Introduction

Electronic properties of double-layer two-dimensional (2D) electron systems formed in double quantum wells [1] (DQW's) or in wide wells [2] have attracted much attention in past years. In particular, it is found that the tunnel coupling of electron states in these systems is important for interpretation of the quantum Hall effect data [2-4], since it opens the tunneling gap separating the symmetric and antisymmetric (with respect to the layer index) states. Despite the intensive studies, the influence of the tunnel coupling on the properties of double-layer systems is not fully disclosed. Theoretical studies of the equilibrium properties and in-plane transport coefficients of the DQW's with a pronounced tunnel coupling have been done for the case of weak magnetic fields only.

In this paper we study the density of states of the electron gas in tunnel-coupled DQW's in a strong magnetic field taking into account the Landau level broadening due to elastic scattering of the electrons. Apart from the density of states, we calculate another important function, the interlayer distribution density, which describes the difference between the concentrations in the wells (in the same way as the density of states describes the total concentration). Both these functions can be used for determination of all the equilibrium quantities (for example, specific heat, magnetic susceptibility and capacitance) characterizing the double-layer system.

## 1 Basic outline of the calculations

The calculations described below are done by two methods. The first is the self-consistent Born approximation (SCBA), see [5]. The SCBA gives a reasonable description of the density of states of 2D systems for any kind of elastic disorder, but it is not an exact method. For this reason, we also apply an exact method, based upon the path integral formalism, in the "adiabatic" approximation, when a characteristic length of the inhomogeneities exceeds the magnetic length.

Consider a double-layer system in the magnetic field $H$ applied perpendicular to the layers. In the basis of left $(l-)$ and right $(r-)$ layer orbitals, the Hamiltonian of the system is

$$\frac{1}{2m}\left(-i\hbar\frac{\partial}{\partial \mathbf{x}}+\frac{e}{c}\mathbf{A}\right)^2+\varepsilon_s+\hat{h}+\hat{V}(\mathbf{x}), \tag{1}$$

where $\mathbf{A}=[\mathbf{H}\times\mathbf{x}]/2$ is the vector-potential of the magnetic field, $\varepsilon_s$ is the Zeeman energy ($s$ is the spin index), $\hat{h}$ is the potential energy matrix of the system, and $\hat{V}(\mathbf{x})$ is the matrix of the disorder potential (we consider the elastic disorder, which, besides, has no influence on the electron spin). The potential energy matrix is given as $\hat{h}=(\Delta/2)\hat{\sigma}_z+T\hat{\sigma}_x$, where $\hat{\sigma}_i$ are the Pauli matrices, $\Delta$ is the splitting energy in the absence of tunnel coupling, and $T$ is the tunneling matrix element determining the minimum splitting energy between the symmetric and antisymmetric states. The matrix of the disorder potential is $\hat{V}(\mathbf{x})=\hat{P}_l V_l(\mathbf{x})+\hat{P}_r V_r(\mathbf{x})$, where $\hat{P}_l=(1+\hat{\sigma}_z)/2$ and $\hat{P}_r=(1-\hat{\sigma}_z)/2$ are the projection matrices. The density of electron states $N(\varepsilon)$ and the interlayer distribution density $N_z(\varepsilon)$ are expressed through the retarded matrix Green function $\hat{G}^R_\varepsilon(\mathbf{x},\mathbf{x}',s)$ of the Hamiltonian (1):

$$\begin{pmatrix} N(\varepsilon)\\ N_z(\varepsilon)\end{pmatrix}=-\frac{1}{\pi}\sum_s Im\ Tr\begin{pmatrix}1\\ \hat{\sigma}_z\end{pmatrix}\left\langle \hat{G}^R_\varepsilon(\mathbf{x},\mathbf{x},s)\right\rangle, \tag{2}$$

where $Tr$ means the matrix trace, and the statistical averaging $\langle\ldots\rangle$ is carried over all possible configurations of the random potentials $V_l(\mathbf{x})$ and $V_r(\mathbf{x})$.

**A**. Within the SCBA, the averaged Green function of the Hamiltonian (1) is

$$\hat{G}_\varepsilon(n,s)=\left[\varepsilon-\varepsilon_n-\varepsilon_s-\hat{h}-\hat{\Sigma}_\varepsilon(n,s)\right]^{-1}. \tag{3}$$

We use the Landau level representation, $n$ is the Landau level number, $\varepsilon_n=\hbar\omega_c(n+1/2)$, $\omega_c$ is the cyclotron frequency, and $\hat{\Sigma}_\varepsilon(n,s)$ is the self-energy matrix. The last is given by the following equation

$$\hat{\Sigma}_\varepsilon(n,s)=\sum_{n',j,j'}\Phi_{jj'}(n,n')\hat{P}_j\hat{G}_\varepsilon(n',s)\hat{P}_{j'}, \tag{4}$$

where $j=l,r$ is the layer index. The scattering probabilities $\Phi_{jj'}(n,n')$ are expressed through the Fourier transforms of the random potential correlators $W_{jj'}(|\mathbf{x}-\mathbf{x}'|)=\langle V_j(\mathbf{x})V_{j'}(\mathbf{x}')\rangle$.

After a substitution of the Green function (3) into Eq.(4), we obtain a set of equations needed for determination of the self-energy. We assume the case of very strong magnetic fields, when the cyclotron energy is large in comparison with all other energies. This allows us to consider each Landau level separately ($n'=n$ in Eq.(4)). In this approximation, Eqs.(3) and (4) give a set of nonlinear algebraic equations, which are to be solved numerically, giving, thereafter, $N(\varepsilon)$ and $N_z(\varepsilon)$.

**B**. The path-integral representation [6] of the retarded Green function is

$$\hat{G}^R_\varepsilon(\mathbf{x},\mathbf{x}',s)=-\frac{i}{\hbar N}\int_0^\infty dt\exp\left(\frac{i}{\hbar}(\varepsilon-\hat{h})t\right)\int_{\mathbf{x}=\mathbf{x}_0}^{\mathbf{x}'=\mathbf{x}_t}\mathcal{D}[\mathbf{x}_\tau]$$
$$\times\exp\left\{\frac{i}{\hbar}\int_0^t d\tau[L_s(\mathbf{x}_\tau,\dot{\mathbf{x}}_\tau)-\hat{V}(\mathbf{x}_\tau)]\right\}, \tag{5}$$

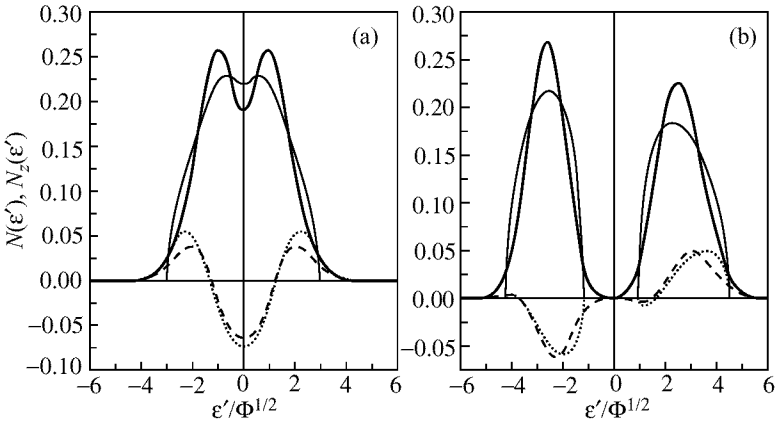


**Fig 1.** (a) Density of states $N(\varepsilon')$ (solid) and interlayer distribution density $N_z(\varepsilon')$ (dash) in units of $1/\pi a_H^2\sqrt{\Phi}$ at $\mu = 0.6$, $\gamma = 0.3$, $\Delta = 0$, and $T = \sqrt{\Phi}$. (b) The same for $\Delta = \sqrt{\Phi}$ and $T = 2.5\sqrt{\Phi}$. The SCBA results are shown by thin lines.

where $N$ is the normalization factor, and $L_s(\mathbf{x}, \dot{\mathbf{x}}) = m\dot{\mathbf{x}}^2/2 + e\mathbf{H}[\mathbf{x}\times\dot{\mathbf{x}}]/2c - \varepsilon_s$ is the free-particle Lagrangian. The direct statistical averaging of the matrix exponential expression in Eq.(5) is impossible, in contrast to scalar exponentials [6]. For this reason, some rigid approximations are done from the very beginning. We assume that the characteristic length of the inhomogeneities considerably exceeds the electronic wavelength which, in a strong magnetic field, is equal to the magnetic length $a_H$. Then, we can replace $\hat{V}(\mathbf{x}_\tau)$ by $\hat{V}$, and the path integral gives

$$N(\varepsilon') = \frac{1}{2\pi a_H^2}\left\langle \delta(\varepsilon' - V_0 - V_T) + \delta(\varepsilon' - V_0 + V_T)\right\rangle, \tag{6}$$

$$N_z(\varepsilon') = \frac{1}{2\pi a_H^2}\left\langle \frac{\Delta/2 + V_z}{V_T}[\delta(\varepsilon' - V_0 - V_T) - \delta(\varepsilon' - V_0 + V_T)]\right\rangle, \tag{7}$$

where $\varepsilon' = \varepsilon - \varepsilon_n - \varepsilon_s$ is the energy counted from the center of each spin-split Landau level, $V_0 = (V_l + V_r)/2$, $V_z = (V_l - V_r)/2$, and $V_T = \sqrt{T^2 + (V_z + \Delta/2)^2}$. The averaging in Eqs.(6) and (7) is to be done with use of a two-dimensional Gaussian distribution function [6], which is expressed through the correlators $W_{jj'}(0)$.

## 2 Results and discussion

Below we introduce the values $\Phi = [\Phi_{ll}(n,n) + \Phi_{rr}(n,n)]/2$, $\mu = [\Phi_{ll}(n,n) - \Phi_{rr}(n,n)]/[\Phi_{ll}(n,n) + \Phi_{rr}(n,n)]$ and $\gamma = \Phi_{lr}(n,n)/\Phi$. The first characterizes averaged (over the layer index) scattering within $n$-th Landau level, while the second and the third characterize the asymmetry and interlayer correlation of the disorder potential, respectively. In the case of smooth disorder, the scattering probabilities $\Phi_{jj'}(n,n')$ are given as $\Phi_{jj'}(n,n') = \delta_{nn'}W_{jj'}(0)$, and one can express $\Phi$, $\mu$ and $\gamma$ directly through $W_{ll}(0)$, $W_{rr}(0)$ and $W_{lr}(0)$. This allows to make a comparison between the results of the SCBA and path-integral method.

Fig.1 (a) shows energy dependence of $N(\varepsilon')$ and $N_z(\varepsilon')$ calculated by both methods in symmetrical conditions, $\Delta = 0$. At a finite tunnel coupling, the Landau level formed by two coupled states (the "coupled Landau level") begins to split. As the coupling

increases (larger $T$), a complete splitting occurs and the tunneling gap opens up, see Fig.1 (b). The opening of the gap leads to an additional quantized Hall plateau when the Fermi level stays in the gap. In the SCBA, the density of states has sharp edges, and one can write a strict condition for the tunneling gap. At $\Delta = 0$ the gap exists when

$$T^2 > \Phi(1+\gamma-\lambda)^2/(1-\lambda), \quad \lambda = |\mu|\sqrt{(1-\sqrt{1-\mu^2})/(1+\sqrt{1-\mu^2})}. \qquad (8)$$

At $\Delta \neq 0$, a similar analytical expression can be found for symmetrical disorder ($\mu = 0$): $T^2 > [\Phi - (\Delta/4)^2](1+\gamma)^2$. Of course, these expressions should be applied in a qualitative sense only, because the edges of the density of states cannot be as sharp as the SCBA predicts. However, they give a correct information about the influence of the disorder parameters on the tunnel splitting of the Landau levels (this is justified by the path-integral calculations). In particular, Eq.(8) shows that the interlayer correlation ($\gamma$) suppresses the gap, while the interlayer asymmetry of the disorder potential ($\mu$) favors the gap.

The interlayer distribution density $N_z(\varepsilon')$ at $\Delta = 0$ is a symmetric function with respect to the center of the coupled Landau level. It is not equal to zero because of the disorder asymmetry which means that the double-layer electron has a dipole moment even at $\Delta = 0$. At $\Delta \neq 0$, $N_z(\varepsilon')$ exists both for $\mu = 0$ and $\mu \neq 0$. Nevertheless, the dipole moment, which is proportional to the energy integral of $N_z(\varepsilon')$, goes to zero when the coupled Landau level is fully occupied.

In conclusion, we have calculated the density of states and interlayer distribution density for a pair of tunnel-coupled 2D layers in a strong magnetic field. The Landau level broadening is described with use of the self-consistent Born approximation and the path-integral approach for smooth Gaussian disorder. A possible interlayer asymmetry of the disorder potential is taken into account. The conditions for the tunneling gap are expressed through the parameters of the system.

## References


[1] J. P. Eisenstein, *Superlattices and Microstructures* **12**, 107 (1992); N. K. Patel *et. al.*, *Semicond. Sci. Technol.* **11**, 703 (1996).
[2] Y. W. Suen *et. al.*, *Phys. Rev. Lett.* **68**, 1379 (1992).
[3] S. Q. Murphy *et. al.*, *Phys. Rev. Lett.* **72**, 728 (1994).
[4] T. S. Lay *et. al.*, *Phys. Rev. B* **50** 17725 (1994).
[5] T. Ando *et. al. Rev. Mod. Phys.* **54**, 437 (1982).
[6] V. L. Bonch-Bruevich *et. al.*, *Electron Theory of Disordered Semiconductors* (Nauka, Moscow, 1981).

Ioffe Institute
6th Int. Symp. "Nanostructures: Physics and Technology"
St Petersburg, Russia, June 22–26, 1998.



# Ultrahigh-sensitive far-infrared detection based on quantum Hall devices

*S. Komiyama*†, H. Hirai†, O. Astafiev‡ Y. Kawano†, T. Sawada†
and T. Sakamoto§

† Department of Basic Science, The University of Tokyo, Komaba
‡Japan Science and Technology Corportation (JST)
§ NEC Basic Research Laboratory, Tsukuba

**Abstract.** Extremely high sensitive detection of far-infrared waves associated with cyclotron resonance in two-dimensional electron gas systems is described based on two sets of experiments. One set of experiments studies a bolometer effect of the integer quantum Hall effects. Another set of experiments is based on the bolometer effect of Coulomb blockade oscillations in a quantum dot. In addition, prediction is made on the single photon detection when a quantum dot is excited via cyclotron resonance.

## 1 Introduction

High-mobility two dimensional electron gas (2DEG) systems strongly absorb far-infrared (FIR) waves upon cyclotron resonance (CR) in high magnetic fields [1]. Combining the CR with some physical parameter of the system that is influenced by the CR, one can construct a magnetically-tunable high-sensitive FIR detector based on a 2DEG system. In this report we discuss three different mechanisms. In Sec. 2, long Hall bars in the regime of integer quantum Hall effects (IQHE) are shown to serve as an extremely sensitive detector. Section 3 describes even more sensitive detection based on a quantum dot, where a 2DEG absorbs the FIR waves while the quantum dot weakly coupled through tunneling to the 2DEG senses a change in the effective electron temperature of the 2DEG. In Sec.4, we argue that the single photon detection of the FIR waves may be possible when the dot is excited by CR. Relevant experimental results of transport measurements, which we believe to infer the realizability of the mechanism, will be described.

## 2 Quantum Hall-bars

FIR-photoresponse in 2DEG Hall bars is known to take place via three different mechanisms at present: a bulk effect [2, 3] and two types of edge effects [3, 4]. We focus our attention on the bulk effect below.

One of the remarkable characteristics of 2DEG systems in high magnetic fields is the vanishing of the longitudinal resistance in the IQHE. When a 2DEG system in the IQHE regime is illuminated with FIR waves of the photon energy equal to the Landau level energy spacing, electrons and holes are excited via CR to cause finite longitudinal resistance $\Delta R_{xx}$. We note that the induced resistivity, $\Delta\rho_{xx}$, is determined by the power density of incident waves. Therefore, the photo-induced voltage detected in a given conductor under a given intensity of illumination is proportional to the aspect ratio

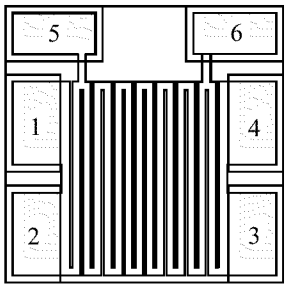


**Fig. 1.** Illustration of a long Hall bar.

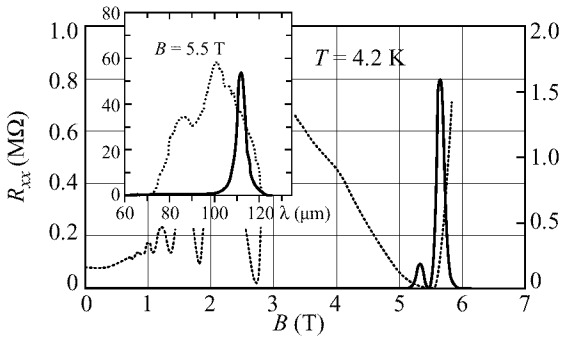


**Fig. 2.** Shubunikov de-Haas oscillations (the dotted line) and the FIR photoresponse (the solid line). The inset shows a spectral response (the solid line) studied by scanning wavelength of the tunable Ge-laser: The dotted line indicates the dependence of the laser power on the wavelength.

$L/W$ of the conductor used; viz., $\Delta V_{xx} = \Delta R_{xx} I = (L/W)\Delta\rho_{xx} I$, where $I$ is the current and $L$ and $W$ are the length and the width of the conductor.

In dissipative conductors with $R_{xx} \neq 0$, large aspect ratio does not lead to better detector-performance because the noise power density, $Sv = 4k_B T(R_H + R_{xx}) + 2eR_{xx}^2 I$, increases as well with increasing $L/W$, where $R_H$ is the Hall resistance. In the IQHE regime, where $R_{xx} = 0$ and $R_H$ takes on a fixed quantized value $h/\nu e^2$, photosignal grows without the cost of noise. Hence, long Hall bars serve as an extremely high sensitive FIR detector.

FIR photoresponse has been studied in long Hall bars fabricated on high-mobility GaAs/AlGaAs single heterostructure crystals with 4.2 K-electron mobilities, $\mu_H$, ranging from 7 to 100 $m^2$/Vs. To achieve extremely large aspect ratio ($L/W = 300 \sim 50,000$), the Hall bars are formed zigzag in a square of $4 \times 4\,mm^2$ as shown in Fig. 1.

Sharp and strong photoresponse occurs at cyclotron resonance [3]. The inset of Fig. 2 shows an example taken on a Hall bar with $L/W = 300$ ($L = 60$ mm, $W = 200\,\mu$m and $\mu_H = 80\,m^2/Vs$) placed in a magnetic field close to the $\nu = 2$ IQHE state. The sample is illuminated by the light from a tunable p-type Germanium laser [5] after sufficient attenuation. The spectral purity of the incident radiation $\Delta\lambda$ is about $2\,\mu$m, and the wavelength is continuously varied over the range $\lambda = 76 \sim 125\,\mu$m.

By using tunable cyclotron-emission from n-InSb hot-electron devices as the source of radiation, it is confirmed that observable photoresponse occurs only in the vicinity of IQHE states ($\nu = 2, 4$, and 6 with $B = 2 \sim 7$ T). An example is demonstrated in Fig. 2 with a solid line, where magnetic-field dependence of the photoresponse under the broad-band illumination (with a spectral line width of $\Delta\nu = 17\,cm^{-1}$ centered at $\nu = 70\,cm^{-1}$) is displayed. Here the sample is a Hall bar with $L/W = 3340$ ($L = 167$ mm, $W = 50\,\mu$m) fabricated on the same wafer as that of the device for the inset. The current is $3\,\mu$A.

The photoresponse does not form a single peak at the center of the IQHE state but takes two maxima at magnetic-field positions slightly off the center as noted in Fig. 2, and more clearly shown by the solid line in Fig. 3(a).

This is linked to the fact that (i) the energy of excited electrons and holes is redis-

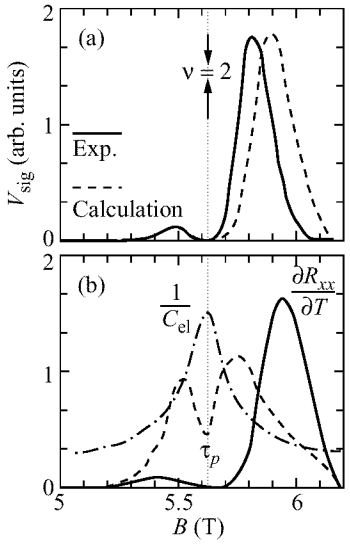


**Fig. 3.** (a) Magnetic field dependence of the photoresponse (the solid line) compared with a theoretical values (the broken line). (b) The inverse of the 2DEG heat capacity (the dash-dot line), the temperature derivative of $R_{xx}$ (the solid line) and the time constant of the photoresponse (the dots with a broken line).

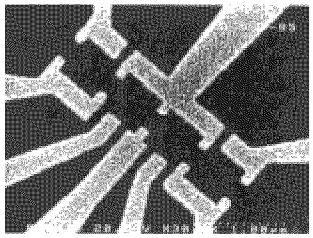

**Fig. 4.** SEM image of quantum dots studied in the experiments.

tributed to raise the effective electron temperature $\Delta T_e$ and (ii) the photoresponse arises primarily from multi-trapping process of heated electrons (holes) between localized and delocalized states. The time constant of the photoresponse is accordingly large, reaching an order of ms.

The photosignal is, most simply, expressed as

$$\Delta R_{xx} = (\partial R_{xx}/\partial T)\Delta T_e \quad \text{with} \quad \Delta T_e = P\tau_E/C_{el}, \tag{1}$$

where $P$ is the rate of energy gain due to CR, $\tau_E$ is the energy relaxation time of excited electrons and holes, and $C_{el}$ is the specific heat of the 2DEG. Magnetic-field-dependencies of the relevant quantities are shown together in Fig. 3(b). The temperature derivative of the longitudinal resistance, $\partial R_{xx}/dT$, and the time constant of the photoresponse, $\tau_P$, have been experimentally determined. The specific heat, $C_{el}$, has been theoretically evaluated by assuming a Gaussian-type density of states after Ref. [6]. The broken line in Fig. 3(b) indicates the theoretically expected values, $(\partial R_{xx}/dT)\tau_P/C_{el}$, obtained by multiplying these quantities, which reproduce fairly well the experimental line shape of the photoresponse.

Among the samples studied, the highest responsivity reaches a value of $10^6 \sim 10^7$ V/W in a Hall bar with $L/W = 50,000$ ($W = 4\,\mu$m, $L = 200$ mm and $\mu_H = 80\,\text{m}^2/\text{Vs}$) at $B = 5.6$ T ($\nu = 2$ and $\lambda = 130\,\mu$m). The noise equivalent power is roughly estimated to be as low as $1 \times 10^{-13}\,\text{W}/\sqrt{\text{Hz}}$ (in a 100 Hz-range) at 4.2 K.

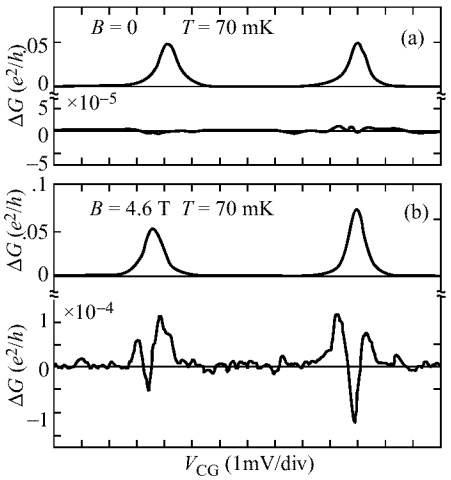


**Fig. 5.** Coulomb blockade oscillations and the modulated signal at (a) $B = 0$ and (b) $B = 4.6$ T.

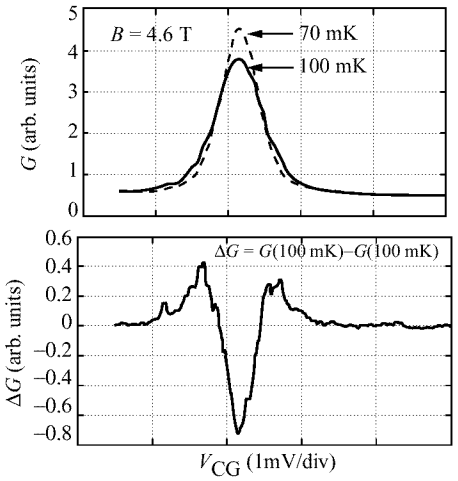


**Fig. 6.** A Coulomb blockade peak at two different temperatures (the upper) and the difference between the two (the lower).

## 3 Quantum dots: bolometer effect

When a quantum dot fabricated by lateral confinement of the 2DEG on a Hall bar is weakly coupled through tunneling barriers to the outside 2DEG, the conductance through the dot exhibits Coulomb-blockade oscillations as the number N of the electrons confined within the dot varies due to the voltage on a nearby gate electrode. Since the conductance peak value of the oscillations strongly depends on temperature, the effect of heating the surrounding 2DEG by CR is sensed by the dot in an extremely sensitive way.

Experiments are made by forming one quantum dot on the sample shown in Fig. 4 and applying the voltage of $V_{SD} = 15\,\mu$V to the quantum dot at $T = 70$ mK in the range of magnetic field $0 \leq B \leq 8$ T. Each dot in Fig. 4 is fabricated with a lithographic size of $0.6 \times 0.6\,\mu\text{m}^2$ on a $100\,\mu$m-long and $25\,\mu$m-wide GaAs/AlGaAs Hall bar with $\mu_H = 100\,\text{m}^2/\text{Vs}$ and $n_s = 3 \times 10^{15}/\text{m}^2$. A FIR emitter are installed in the mixing chamber of a dilution refrigerator together with the quantum-dot sample. The FIR emitter, placed at a distance of 25 mm from the sample, is a standard 2DEG Hall bar with a length and a width of $500\,\mu$m and $100\,\mu$m, respectively, which is fabricated on a high-mobility GaAs/AlGaAs heterostructure crystal similar to that used for the quantum-dot sample. It has been confirmed by an additional experiment that very weak but narrow-band FIR waves ($\lambda/\Delta\lambda = 50$) centered at the cyclotron resonance frequency are radiated due to cyclotron emission when a current ($100\,\mu$A) is passed through the Hall bar. The mixing chamber is placed in a superconducting solenoid, where the relative position of the quantum-dot sample to the solenoid is adjusted so that the CR energy of the quantum-dot sample is equal to the energy of the photons from the emitter. The FIR waves are guided through a $2\,\text{mm}\phi$ metal light pipe to the quantum-dot sample. The FIR power reaching the area of the quantum-dot sample ($100\,\mu\text{m} \times 25\,\mu\text{m}$) is extremely weak, roughly estimated to be of the order of 1 fW. The FIR waves are modulated by the current through the Hall-bar emitter at 20 Hz,

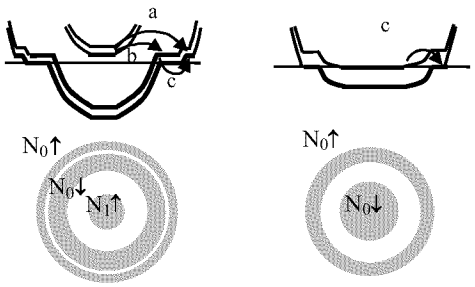


**Fig 7.** Illustrations of the Landau level energy profile in a three-level situation (the left) and in a two-level situation (the right).

and the photosignal is measured with a Lock-in amplifier.

Figure 5(a) illustrates Coulomb-blockade oscillations of conductance $G$ along with the modulated conductance $\Delta G$ in the absence of magnetic field. The amplitude of the current through the emitter is adjusted so that the Joule heating is the same as that in magnetic fields. No appreciable signal is seen in $\Delta G$, assuring that the black-body radiation from the emitter is small, and does not affect the $G$ of the dot.

Upon application of B, definite photoresponse appears as shown in Fig. 5(b) for $B = 4.6$ T. Similar photoresponse is observed in a $B$-range of 4.5 T–5.4 T, where $\nu = 2.8-2.3$ in the 2DEG outside the dot. The line shape of the photoresponse versus the control gate voltage $V_{CG}$ resembles that of the conductance change as the temperature of the quantum-dot sample is elevated, as shown in Figs. 6. The observed amplitude of the photoresponse suggests that $\Delta Te \sim 0.5$ mK, which is reasonably expected from the incident radiation power and the heat capacity of the 2DEG.

The noise equivalent power in this experiment is roughly estimated to be as low as $1 \times 10^{-15}\,\mathrm{W}/\sqrt{\mathrm{Hz}}$.

## 4 Quantum dots: single-photon detection?

One-electron states of a relatively large quantum dot (with a few hundred electrons), such as shown in Fig. 4, can be conveniently classified by the Landau level index $i\uparrow$ or $i\downarrow$ in strong magnetic fields. The left column of Fig. 7 illustrates a three-level configuration, in which the lowest three Landau levels are occupied in the dot with $N_{0\uparrow}$, $N_{0\downarrow}$, and $N_{1\uparrow}$ electrons.

Coulomb blockade peaks in strong $B$ are affected not only by the total number of electrons N but also by the electron numbers in the respective levels [7], as described below. As $B$ increases, electrons are transferred from higher levels to lower levels within the dot until the two-level configuration is eventually reached as shown in the right column of Fig. 7 [8, 9]. This transition proceeds as the three processes $a$ ($1\uparrow \rightarrow 0\uparrow$), $b$ ($1\uparrow \rightarrow 0\downarrow$) and $c$ ($0\downarrow \rightarrow 0\uparrow$) take place sequentially (with order unspecified). Each event of $a$, $b$, or $c$ is associated with a polarization within the dot, and causes the electro-chemical potential of the outer-most ring ($0\uparrow -$states) to increase discontinuously. Accordingly, each event of $a$, $b$ and $c$ caused a saw-tooth like structure in the conductance $G$ as the magnetic field is scanned; as was first demonstrated by van der Vaart et al. in the two-level case [7]. The inset of Fig. 8 illustrates an example taken on one quantum dot on the sample shown in Fig. 4, where the dot is in a conducting state

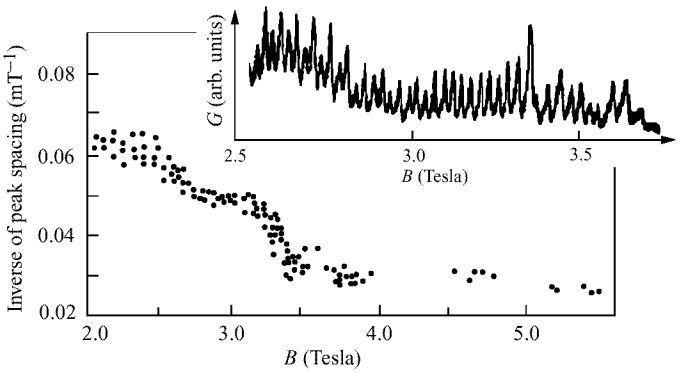


**Fig. 8.** Saw-tooth structures appearing in the conductance as $B$ is scanned (the inset). Variation of the inverse of averaged spacing of the saw-tooth peaks with $B$.

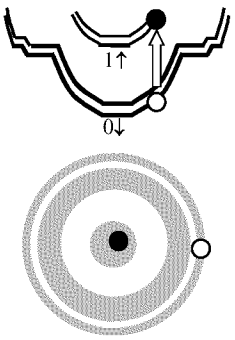


**Fig. 9.** Cyclotron resonance in a dot (the upper panel), resulting in a polarization between the inner core and the outer ring (the lower panel).

with a fixed voltage on the control gate.

The average spacing between the saw-tooth like peaks significantly increases as $B$ increases. Figure 8 summarizes results of similar measurements, made with several different voltages applied on the control gate. Let $r_a$, $r_b$ and $r_c$ be the rates at which the processes $a$, $b$, and $c$ take place per unit increase of $B$. Figure 8 is interpreted as representing the total rate, $r = r_a + r_b + r_c$. The total rate $r$ decreases by about a factor of 2 as $B$ increases to 3.4 T, above which $r$ is substantially unchanged and takes a value of 0.03 /mT. Because the area, $S_{0\uparrow}$, surrounded by the outermost ring ($0\uparrow -$states) is expected to be substantially unaffected by $B$, the sum of $r_a$ and $r_c$ is a constant determined by the dot size; viz., $r_a + r_c = S_{0\uparrow}/(h/e)$. The rate of event $b$, $r_b$, will decrease from $r_b = S_{0\downarrow}/(h/e) = S_{0\uparrow}/(h/e)$ to zero as the three-level configuration changes to the two-level configuration. Thus, Fig. 8 is interpreted as indicating the three-to-two-level transition in the interval of $B = 2.4\,\mathrm{T} \sim 3.4\,\mathrm{T}$. The diameter of the dot ($S_{0\uparrow}$) is evaluated to be $0.4\,\mu$m from the saturated value of $r = 0.03/\mathrm{mT}$.

Keeping the above in mind, suppose that one photon is absorbed via CR within the dot. An electron is excited in the 1 $\uparrow$-level leaving a hole in the 0 $\uparrow$-level in the three-level configuration as illustrated in the upper panel of Fig. 9. The electron and the hole will spatially depart from each other in the confining potential, release excess energies to the lattice, and eventually induce a polarization between the inner core and the outermost ring as symbolically indicated in the lower panel of Fig. 9. This is an effect equivalent to that caused by process $a$. This, in turn, will lead to a conductance change that can be detected in the experiments, as is expected from the data of Figs. 8.

The detection would be spoiled unless the lifetime of the induced polarization is longer than the time constant of the measurement. The lifetime may be determined by the tunneling probability of electrons between the inner core and the outer ring(s). Experiments on high-mobility 2DEG Hall bars [10] make us to speculate that the lifetime here be long, reaching the order of ms, if the dot size is not too small. The assumption of the long lifetime of the excited state of the dot is supported further by additional experiments.

When the control gate voltage is scanned at a fixed $B$, switching occasionally takes

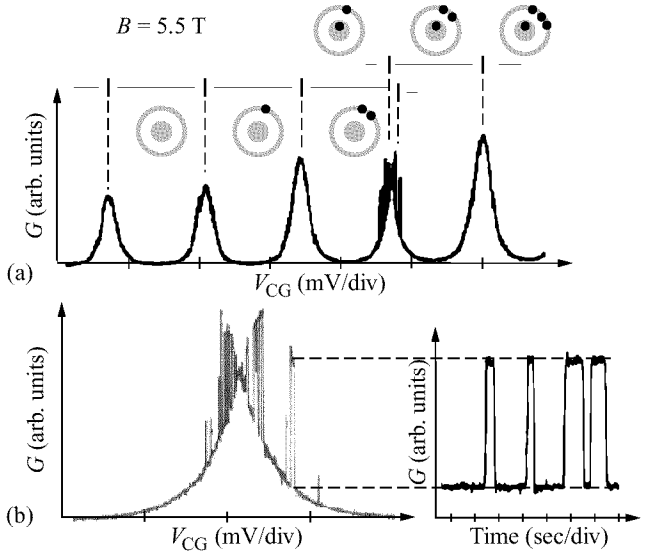


**Fig 10.** (a) Switching due to tunneling of a single electron between the inner core and the outer ring within the dot (the second peak from the right). (b) Magnified representation of the switching (the left) and its time dependence (the right).

place between two conductance peaks that correspond to different internal configurations [7]. Figure 10(a) displays an example taken on the same dot as that used for Fig. 8 in the two-level case. Figures 10(b) elucidates the switching between the conductance peak associated with $[N_{0\uparrow}(+1), N_{0\downarrow} + 1]$ and that associated with $[N_{0\uparrow} + 1(+1), N_{0\downarrow}]$, and shows that the switching time reaches the order of second, in agreement to the earlier report [7].

## 5 Discussion and conclusion

In the IQHE Hall-bar detector, the 2DEG works as an efficient absorber as well as a sensitive thermometer. In the quantum-dot detector, the 2DEG serves as an absorber while the quantum dot works as a thermometer. The performance of both types of detectors has not yet been optimized, but is among a highest level of existing detectors available in the range of FIR waves [11]. One additional merit of the IQHE Hall-bar detector is the sharp narrow-band response [3] tunable by magnetic field. Yet another merit may be the wide range of tunability. The spectral response has been studied in a magnetic field range down to 0.4 T ($\lambda = 2$ mm) [12]. The single photon detection predicted in this report may become probable when appropriate antennas structures are applied to efficiently couple a quantum dot to incident FIR waves.

*Acknowledgements*

This work has been supported by Core Research for Evolutional Science and Technology (CREST) of Japan Science and Technology Corporation (JST).

## References

[1] see for example, F. Thiele et al. *Solid State Commun.* **62** 841 (1987).

[2] Yu. B. Vasiév et al. *JETP Lett.* **56** 377 (1992).
[3] K. Hirakawa et al. *Proc. 23rd Int. Conf. Phys. of Semicond.* (Berlin, 1996, World Scientific, p. 2543).
[4] E. Diessel et al. *Appl. Phys. Lett.* **58** 2231 (1991).
[5] S. Komiyama et al. *Jpn. J. Appl. Phys.* **32** 4987 (1993).
[6] E. Gornik et al. *Phys. Rev. Lett.* **54** 1820 (1985).
[7] N. C. van Vaart et al. *Phys. Rev. B* **55** 9746 (1997).
[8] J. P. Bird et al. *Phys. Rev. B* **49** 11488 (1994).
[9] The total number of electrons N decreases as well with increasing B, giving rise to magneto-Coulomb oscillations [8]. However, the rate of decrease is far smaller and is ignored here.
[10] S. Komiyama and H. Nii *Physica B* **184** 7 (1993).
[11] see for example, G. Chanin and J. P. Torre, *"Infrared and Millimeter Waves"*, Chapter 5 of Vol. 10, Ed. by K. J. Button, 1983, Academic Press.
[12] V. I. Gavrilenko et al. *in this issue.*

Ioffe Institute
6th Int. Symp. "Nanostructures: Physics and Technology"
St Petersburg, Russia, June 22–26, 1998.



# Far-infrared spontaneous intraband emission from laser structures with quantum dots and quantum wells

*L. E. Vorobjev*†, D. A. Firsov†, V. A. Shalygin†, V. N. Tulupenko§
Yu. M. Shernyakov‡, A. Yu. Egorov‡, A. E. Zhukov‡, A. R. Kovsh‡,
P. S. Kop'ev‡, I. V. Kochnev‡, N. N. Ledentsov‡, M. V. Maximov‡,
V. M. Ustinov‡ and Zh. I. Alferov‡

† St. Petersburg State Technical University, St. Petersburg 195251, Russia
§ Donbass State Engineering Academy, Kramatorsk 343913, Ukraine
‡ Ioffe Institute, St. Petersburg 194021, Russia

**Abstract.** Spontaneous far-infrared radiation ($\lambda \simeq 10 \ldots 20$ $\mu$m) from laser structures with vertical coupled InGaAs/AlGaAs quantum dots (QD) connected with intrasubband hole and electron transitions between levels of size quantization in QD as well as with transitions from continuum to QD levels was found. Far-infrared radiation is observed only under simultaneous generation of short wavelength interband radiation ($\lambda \simeq 0.94$ $\mu$m) and has a current threshold just as short wavelength radiation. Spontaneous far-infrared radiation is observed also from laser InGaAs/GaAs structures with quantum wells (QW). Intensity of this radiation is about of order less then intensity of radiation from structures with quantum dots and has no current threshold.

## Introduction

Intersubband optical transitions of carriers in QW have been investigated in detail, the infrared detectors, modulators and lasers have been developed (see, for example [1, 2]). A study of interlevel carrier transitions in quantum dots opens the new prospects in designing the active devices for far infrared (FIR) region ($\lambda > 10$ $\mu$m). A light absorption due to electron transitions from bound states into continuum as well as due to hole transition between levels in QD have been investigated recently [3].

In this work the spontaneous FIR emission as a result of electron transitions from continuum to QD levels as well as of interlevel transitions in QD was detected. This radiation is conditioned by synchronous generation of radiation, which is caused by electron transitions between ground levels of electrons and holes ($h\nu \simeq \varepsilon_g$). The latter provides a depletion of these levels at high current injection of electron-hole pairs in QD heterolaser. The fact, that such a spontaneous radiation have been observed, may be considered as the first step of development of the FIR laser based on interlevel carrier transitions in QD.

## 1 The samples and technique of experiments

The laser structures with vertical-coupled QD described in [4] were used. The active region of such a laser consists of the $Al_{0.5}Ga_{0.5}As$ layers with self-organized $In_{0.5}Ga_{0.5}As$ quantum dots, the number of layers is 10. Stimulated radiation corresponds to near infrared (NIR) region with wavelength about 0.94 $\mu$m at 300 K. The silicon photodiode was used for registration of this radiation. The measurements were carried out with current pulse having duration about 200 ns.

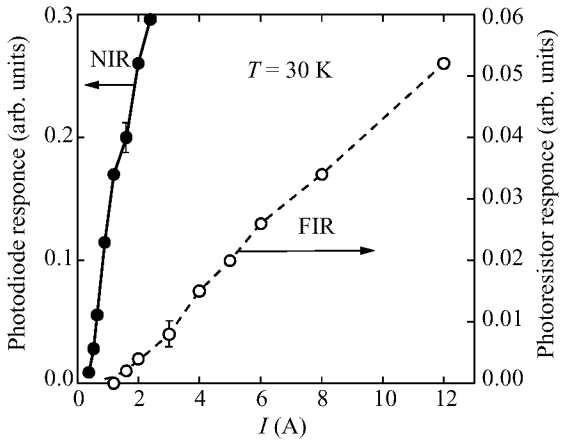


**Fig 1.** Intensity of NIR and FIR radiation from QD structure.

To find FIR radiation from these structures the Ge⟨Cu⟩ and Si⟨B⟩ photodetectors having the sensibility in spectral region $\lambda = 5 \ldots 29$ $\mu$m at $T \simeq 30$ K were used. The Ge and InSb filters placed before photodetectors cut off NIR ($\lambda = 0.94$ $\mu$m) radiation, the spectral data in the long-wave range were determined by means of set of $BaF_2$, NaCl and KBr filters. The NIR and FIR radiations were investigated simultaneously.

Also spontaneous FIR emission from laser $In_{0.2}Ga_{0.8}As/GaAs$ quantum well structures have been investigated.

## 2 Results and discussion

Fig.1 represents the typical optical-current dependencies of both stimulated NIR and spontaneous FIR emission from QD laser structures. Spectral range of FIR radiation ($10 \ldots 20$ $\mu$m) was established with the help of filters. It should be noted that dependence of intensity of spontaneous FIR radiation on laser current has a threshold closed to the threshold current of generation of stimulated NIR emission. The latter is of 0.33 A at the low temperatures that is one half of the same at the room temperature. So, FIR radiation may be registered only at the same time with generation of NIR one.

The same investigations have also been carried out in $In_{0.2}Ga_{0.8}As/GaAs$ QW laser structures with threshold current of generation of NIR radiation about 0.25 A. Spontaneous FIR emission was found out in these structures too. In this case intensity of radiation was about tenth path of that in QD structures and had no threshold dependency on an electric current.

Our qualitative explanations of phenomena observed are as follows. First let us discuss the conditions under which spontaneous FIR emission from QD laser structures is possible. It may be assumed that quantum level structure in QD used is like to that described in [5] with characteristic linear sizes of the base of pyramid being about 10...12 nm. Such the structures have only one electron level $|000\rangle$ ( in our structures two electron levels can exist), and four hole levels: $|000\rangle$, $|100\rangle$, $|001\rangle$ and $|110\rangle$. Under electron (hole) injection into AlGaAs layer an electron (hole) capture is executed by

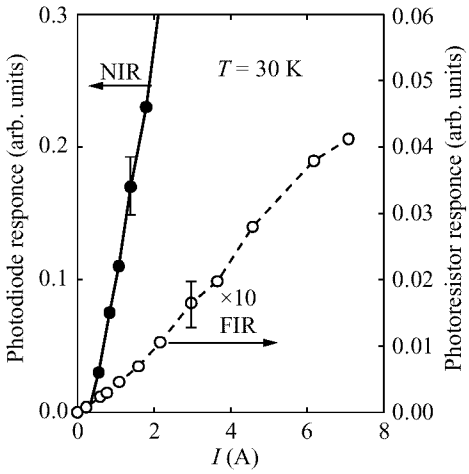


**Fig 2.** Intensity of NIR and FIR radiation from QW structure.

the states in the wetting layer for some picosecond [6, 7] with its following transitions to the electron (hole) QD level. The hole inter-level transitions are also possible. In accordance with [6] a transition time between excited and ground levels is about 40 ps.

At threshold current $I_{th}$ the ground electron (hole) states in QD are filled and optical transition from excited QD levels to ground ones are impossible.

At pumping current above $I_{th}$ the stimulated NIR emission origins, the corresponding interband transitions deplete the ground electron and hole states in QD and spontaneous FIR emission is started. The intensity of this radiation is proportional to the number of carriers in excited states $N_{ex}$ and probability the lowest levels to be desolated. $N_{ex}$ is linear current function and desolation probability increases with intensity of stimulated NIR radiation.

A current increase involves into generation more and more QD with different sizes. Owing to above mentioned reasons the FIR radiation intensity may increase faster in compare with linear law. It is confirmed with experimental results at $I > I_{th}$: $J^{\nu}_{FIR} \propto I^2$ (see Fig. 1). A further increase of current leads to linearization of the dependence. It is, probably, connected with hole (electron) ejection from excited states by intense stimulated radiation and increasing effect of Auger processes [8].

We observed also spontaneous FIR radiation from $In_{0.2}Ga_{0.8}As/GaAs$ QW structures. The carrier number in excited states (i.e. in upper subbands) is proportional to a current through a structure. Ground subbands have always unoccupied states, the holes (or electrons) pass into them. That is why the intensity of FIR radiation is proportional to a current: $J^{\nu}_{FIR} \propto I$ and has no threshold (see Fig. 2). It should be noted that carrier life time in QW excited states is of order of picosecond, it is less than one tenth of life time in QD. Owing to small life time the intensity of FIR radiation in QW was smaller than that for QD structures.

Thus, our results give a hope to receive population inversion for electrons and holes in FIR range under interband NIR generation and to create new active devices, for instance, FIR laser on the base of interlevel transitions of carriers in QD.

*Acknowledgments*

This work was supported by RFBR, Grant 96-02-17404a; INTAS-RFBR, Grant 96-615; Program "Physics of solid state nanostructures", Grant 96-1029; Russian State Program "Integration", Grant 75; NATO, Grant NATO HTECH.LG 960931; UFBR, Grant 2.4/970.

## References

[1] J. Faist, F. Capasso, D. L. Sivco et al. *Science* **264** 553 (1994).
[2] O. Gauthier-Lafaye, S. Sauvage, P. Boucaud et al. *Appl. Phys. Lett.* **70** 3197 (1997).
[3] S. Sauvage, P. Boucaud, F. H. Julien et al. *Appl. Phys. Lett.* **71** 2785 (1997).
[4] M. V. Maximov, Yu. M. Shernyakov, N. N. Ledentsov et al. *Intern. Symposium Nanostructures: Physics and Technology*, St. Petersburg, p. 202 (1997).
[5] M. Grundmann, O. Stier, D. Bimberg. *Phys. Rev. B.* **52** 11969 (1995).
[6] R. Heitz, M. Veit, N. N. Ledentsov et al., *Phys. Rev. B.* **56** 10435 (1997).
[7] N. N. Ledentsov, In: *The Physics of Semiconductors*, ed. by M. Scheffler and R. Zimmermann, World Scientific, Singapore, V. 1, p. 19 (1996).
[8] J. H. H. Sandmann, S. Grosse, G. von Plessen, J. Feldman et al. *Physica status solidi (b)* **204** 251 (1997).

Ioffe Institute
6th Int. Symp. "Nanostructures: Physics and Technology"
St Petersburg, Russia, June 22–26, 1998.



# Far infrared phenomena in p-type MQW heterostructures under lateral electric field

*V. N. Shastin*†, V. Ya. Aleshkin†, N. Bekin†, R. Zhukavin†, B. N. Zvonkov‡, O. A. Kuznetsov‡, I. G. Malkina‡, A. Muravjov†, E. Orlova†, S. Pavlov†, A. Sitdikov† and E. A. Uskova‡

† Institute for Physics of Microstructures of RAS, N. Novgorod
‡ Physical-Technical Institute of N.Novgorod State University
shastin@ipm.sci-nnov.ru

**Abstract.** Experimental investigation of the far-infrared (FIR) optical properties connected with intersubband and impurity-to-2D subband states transitions of holes in MQW $In_xGa_{1-x}As/GaAs$ and $Ge/Ge_{1-x}Si_x$ heterostructures under lateral transport was performed. The mechanism of the inversion population and the far infrared amplification on the excited states to QW state transitions under lateral heating is proposed.

## Introduction

The FIR pulsed p-Ge laser [1] intracavity electroabsorption method was developed and used for the investigation far-infrared transparency of heterostructures for the first time. The method allows to separate the hole and the lattice impacts in the FIR absorption. The measurements were made using the p-Ge laser radiation bands $50 \div 60$ cm$^{-1}$ and $80 \div 125$ cm$^{-1}$ with Faraday configuration of the magnetic fields $0.5 \div 2$ T.

The main advantage of this method is the ultrahigh sensitivity for the change of the MQW absorption coefficient. The sensitivity of relative deviation of transparency ($\Delta T/T \simeq 10^{-3}$) was determined both the pumping electric field instability and the cooling conditions. All results were interpretated in the frame of quasiclassical approach of hole heating. Energy diagrams of 2D holes (see the method [2]) and matrix elements in the case of intersubband and impurity-to-continuum states optical transitions were estimated using simplified model [3].

## 1 $In_xGa_{1-x}As/GaAs$ MQW heterostructures with $\delta$-doped barriers

$\delta$-doped p-type $In_xGa_{1-x}As/GaAs$ MQW heterostructures were grown by MOCVD technique on GaAs(001) substrates and contain 20 periods with $In_xGa_{1-x}As$ quantum wells ($0.08 \leq x \leq 0.19$), layer thickness $d = 46 \div 152$ Å, separated by GaAs 600 Å barriers. Carbon $\delta$-layers with the doping level $N_A = 10^{11} \div 3 \times 10^{12}$ cm$^{-2}$ were introduced in GaAs barrier with the distance $L$ from the quantum well edge changing from 25 to 136 Å. 20 period heterostructures were grown by MOCVD technique on GaAs(001) substrates with $In_xGa_{1-x}As$ quantum wells ($0.08 \leq x \leq 0.19$), layer thickness $d = 46 \div 152$ Å, separated by GaAs 600 Å barriers. Carbon $\delta$-layers with the doping level $N_A = 10^{11} \div 3 \times 10^{12}$ cm$^{-2}$ were introduced in GaAs closed to QW barrier interface on the distance $L$ changed from 25 to 136 Å (see Table 1.).

**Table 1.** $In_xGa_{1-x}As/GaAs:C$ MQW heterostructures.

| No. # | spacer $L$ (Å) | qw $d$ (Å) | x | $N_A$ ($cm^{-2}$) |
|---|---|---|---|---|
| 1797 | 53 | 79 | 0.19 | $3.4\times10^{11}$ |
| 1799 | 47 | 71 | 0.2 | $5.7\times10^{10}$ |
| 1801 | 50 | 49 | 0.18 | $2\times10^{11}$ |
| 1850 | 48 | 48 | 0.1 | $1.8\times10^{11}$ |
| 1884 | — | 0 | — | $2.6\times10^{11}$ |
| 1942 | 51 | 50 | 0.086 | $2.2\times10^{11}$ |
| 1943 | 90 | 46 | 0.107 | $2.2\times10^{11}$ |
| 1944 | 136 | 46 | 0.11 | $2.65\times10^{11}$ |
| 1945 | 25 | 50 | 0.107 | $2.5\times10^{11}$ |
| 1946 | 48 | 152 | 0.137 | $3.1\times10^{11}$ |
| 1947 | 51 | 52 | 0.11 | $3.1\times10^{11}$ |
| 2018 | 50 | 50 | 0.1 | $1.5\times10^{12}$ |
| 2019 | 50 | 50 | 0.1 | $2\times10^{12}$ |
| 2022 | 50 | 50 | 0.1 | $7.1\times10^{11}$ |

### *1.1 Far-infrared hole amplification in heterostructures with shallow quantum wells*

The resonant increase of the FIR transparency under the electric field was observed for heterostructures #1947, #1943 with narrow QW $\Delta \geq \hbar\omega$, where $\Delta$ is the gap between nearest subband and $\hbar\omega$ is FIR radiation quantum, while $E_{h,h1} \simeq E_{g.s.}$ and 50 Å $\leq L \leq$ 90 Å.

It can be explained by the amplification on the acceptor excited state to QW state transitions. The inversion population responsible for the gain is formed on the excited states due to real space transfer under the QW hole heating in strong electric fields $600 \leq E \leq 1400$ V/cm.

The mobilities of holes in the barrier ($\mu_B = 300$ $cm^2$/V s) and quantum well ($\mu_W =$ 3000 $cm^2$/V sec) regions [3] determine the difference of the effective temperatures in the quantum well $T_W \geq 400$ K and the barrier $T_B \simeq 100$ K for $E \simeq 10^3$ V/cm and $\nu_{ac} \simeq 3 \times 10^9$ $s^{-1}$. The population on the excited states is controlled by barrier temperature, if their coupling with QW states is weak. As a result the overpopulation of the excited state is reached ($f_{ex}/f_w \simeq 2$) and the expected FIR gain is 10 $cm^{-1}$. For the electrical field $E > 1500$ V/cm the overheating of holes in the barrier leads to the depletion of the excited states and decreases the gain.

### *1.2 Far-infrared hole absorption in heterostructures with shallow quantum wells*

Three mechanisms can be responsible for the FIR absorption in heterostructures. The first is due to the acceptor states to the QW states optical transitions. It has place despite of the spatial separation because of the overlap of working state wavefunctions. The estimation of the absorption cross-section for $gr.st. \rightarrow QWst.$ optical transitions yields $\sigma_{g.s.} \simeq 2 \times 10^{-16}$ $cm^{-2}$ (effective barrier thickness $L^* \simeq 25 \div 30$ Å).

The increase of FIR transparency was observed for the heterostructures with "shallow" QW when the lowest QW subband is above the ground state ($E_{g.s.} \simeq 26$ meV )

of the acceptor $E_{h,h1} \leq E_{g.s.}$ and $L \leq 100$ Å.

Acceptor ground state to QW state transitions determine the dependence $I(E)$ on samples #1850, #1942, #1945, #2019, #2022, where typical threshold increase of the transparency is explained by acceptor breakdown.

### *1.3 Far-infrared intersubband hole absorption in heterostructures with deep quantum wells*

The second type of FIR absorption is on the QW intersubband optical transitions, that dominates when $\Delta \simeq \hbar\omega$. At this case the electromodulation is determined by the QW holes dispersion $\mathrm{E}(k_{\|})$.

For "deep" QW ($E_{h,h1} > E_{g.s.}$) transparency was decreased under the electric field. Intersubband transitions dominate in sample #1946, where sign of the modulation corresponds to calculated subbands dispersion.

### *1.4 Far-infrared lattice absorption in QW and GaAs δ-doped barriers*

The last FIR absorption observed is caused by the lattice absorption. The decrease of FIR transparency was observed for the heterostructures with "shallow" QW with remote $L \geq 100$ Åcarbon $\delta$-layers (sample #1944) and also in test $\delta$-layers structure without $In_xGa_{1-x}As$ QW layers (#1884).

The same effect on $I(E)$ decrease was observed for the heterostructures with "deep narrow" QW (sample #1801), where $\Delta \geq \hbar\omega$. Multiphonon lattice absorption is relatively weak $\alpha < 3 \times 10^{-3}$ cm$^{-1}$, nevertheless the method allows to register it.

## 2 The selectively doped p-type Ge/$Ge_{1-x}Si_x$:B MQW heterostructures

The selectively doped p-type Ge/$Ge_{1-x}Si_x$:B MQW heterostructures were grown by MOCVD technique on pure Ge(111) substrates and contain $N$ periods $D$ ($N = 36-300$) with Ge quantum wells, separated by $Ge_{1-x}Si_x$ barriers (Table 2.).

### *2.1 Far-infrared intersubband hole absorption in the heterostructure film*

The modulation of FIR transparency was observed for the heterostructures with $\Delta \simeq \hbar\omega$ condition.

It has been shown that far-infrared characteristics of Ge/$Ge_{1-x}Si_x$:B heterostructures with QW width $d \approx 100$ Å for $0.07 \leq x \leq 0.1$ are determined by the optical transitions between 2D hole subbands $E_{hh1} \rightarrow E_{hh2}$ and for one with QW width $d \approx 170$ Å— by the transitions $E_{hh1} \rightarrow E_{hh3}$.

Electrical field applied along the MQW layer causes the far-infrared absorption due to redistribution of holes on nonparabolic 2D subbands. The electromodulation effect is far-infrared radiation frequency dependent that can be explained by hole energy diagram calculated [2].

### *2.2 Far-infrared absorption in Ge substrate*

To differ the FIR optical absorption in heterostructure film and in the substrate (pure Ge with residue impurity concentration not more than $10^{13}$ cm$^{-3}$) the test experiments were performed with the sample #432$a_8$. After the growing the MQW film was etched from the substrate and both the sign and the magnitude of modulation had changed. Small effect of FIR transparency decreasing on such Ge substrate under the applied

**Table 2.** $Ge/Ge_{1-x}Si_x$:B MQW heterostructures.

| No. # | period $D$ (Å) | qw $d$ (Å) | $N$ | $x$ | $N_A$ ($cm^{-2}$) |
|---|---|---|---|---|---|
| $125a_{18}$ | 370 | 175 | 36 | 0.08 | $2.\times10^{11}$ |
| $360b_3$ | 350 | $<102$ | 92 | 0.06 | $2.\times10^{11}$ |
| $363a_3$ | 335 | $<105$ | 300 | 0.06 | $1.2\times10^{12}$ |
| $381a_{12}$ | 245 | 115 | 54 | 0.12 | $5.\times10^{11}$ |
| $381b_5$ | 270 | 110 | 54 | 0.12 | $5.\times10^{11}$ |
| $431a_1$ | 375 | 130 | 36 | 0.052 | $2.\times10^{11}$ |
| $432a_8$ | 335 | 135 | 36 | 0.06 | $5.\times10^{11}$ |
| $444a_1$ | 240 | 107 | 120 | 0.07 | $1.\times10^{11}$ |
| $444a_2$ | 270 | 110 | 120 | 0.067 | $<10^{11}$ |

electric fields was registered. That was above the breakdown of Cu impurity centers ($\geq$ 600 V/cm) and caused by the lattice absorption.

*Acknowledgments*

Authors thank A. A. Andronov, A. V. Antonov, V. I. Gavrilenko, M. D. Moldavskaja, Yu. A. Romanov and V. L. Vax for the informational and technical support of the experiments.

The research described is supported by Grant 95-0615 from INTAS-RFBR and Grant 96-02-19275 from Russian Foundation for Basic Research (RFBR).

## References

[1] Special Issue "FIR semiconductor lasers" of *Opt. Quant. Electronics*, (Ed. E. Gornik and A. A. Andronov), **23**(2) (1991).
[2] V. Ya. Aleshkin and N. A. Bekin, *Semiconductors* **31**(2) 132 (1997).
[3] V. N. Shastin, R. Kh. Zhukavin, A. V. Muravjov, E. E. Orlova, S. G. Pavlov, B. N. Zvonkov, *Physica Status Solidi (b)*, **204** 174 (1997).

Ioffe Institute
6th Int. Symp. "Nanostructures: Physics and Technology"
St Petersburg, Russia, June 22–26, 1998.



# FIR emission and absorption due to indirect optical transitions of hot electrons in GaAs/AlGaAs QW

E. B. Bondarenko†, L. E. Vorobjev†, S. N. Danilov†, D. V. Donetsky†, V. L. Zerova†, Yu. V. Kochegarov†, *D. A. Firsov*†, V. A. Shalygin†, G. G. Zegrya‡ and E. Towe§

† St. Petersburg State Technical University, St.Petersburg 195251
‡ Ioffe Physico-Technical Institute, St. Petersburg 194021
§ University of Virginia, Thornton Hall, Charlottesville, VA22903-2442, USA

**Abstract.** Far-infrared ($\lambda = 70 \ldots 300\,\mu$m) spontaneous emission and modulation of absorption under heating 2D-electrons in strong electric field applied along GaAs/AlGaAs quantum layers are observed and investigated. Emission and absorption of light are connected with indirect transitions of hot electrons in ground subband of quantum well. Hot electron temperature is determined from comparing experimental emission spectra and theoretical ones taking into account optical phonon, impurity and interface roughness scattering as well as electron-electron scattering.

## Introduction

Intraband electron and hole transitions are intensively studied during last years. Partly, it is connected with development of fast photodetectors and modulators of infrared (IR) range. The creation of quantum cascade [1] and fountain [2] lasers gave impetus to this line of physics of low-dimensional systems. The main part of the works on the optical intraband phenomena is devoted to absorption and emission of radiation due to direct transitions of electrons between subbands. For example, emission of FIR connected with intersubband direct transitions of electrons and holes is studied in [3, 4, 5]. However light emission and absorption caused by intrasubband transitions of hot carriers has not yet investigated. In the meantime these phenomena accompany emission and absorption due to direct optical transition and can serve as a source of information about carrier properties.

The aim of the present paper was to find and experimentally and theoretically investigate spontaneous FIR emission and modulation of FIR absorption under electron heating from GaAs/AlGaAs multiple quantum well structures.

## 1 Calculation of emission spectra

We consider simple rectangular selectively doped in the barrier quantum wells with one or more (for example, two) levels $\varepsilon_1$ and $\varepsilon_2$ of size quantization. If the distance between levels $\Delta\varepsilon = \varepsilon_2 - \varepsilon_1$ is rather great then the absorption and emission of far-infrared light ($h\nu \ll \Delta\varepsilon$) with polarization $\mathbf{e}_\omega \perp OZ$ ($OZ$ is structure growth direction) can occur only due to indirect transitions of electrons within ground subband $\varepsilon_1(k_\parallel)$. The momentum conservation is provided due to processes of electron scattering. One can distinguish optical phonon, impurity, interface roughness as well as e-e scattering. It should be noted that the light polarized along the structure ($\mathbf{e}_\omega \parallel OZ$) can be absorbed

only using virtual states in the second subband $\varepsilon_2(k_{||})$ but calculations shows that the contribution of such transitions to the absorption is relatively small and we will not take them into account.

We calculated spectral density of emitted photons as

$$\frac{\mathrm{d}N}{\mathrm{d}\omega} = \rho_\omega W^{em} = \rho_\omega \sum_{\mathbf{k}'} \sum_{\mathbf{k}} w(\mathbf{k}, \mathbf{k}') f_{\mathbf{k}} (1 - f_{\mathbf{k}'}), \tag{1}$$

where wave vectors $\mathbf{k}$ and $\mathbf{k}'$ describe initial and final states of electron during light absorption, $\rho_\omega = 2n^3\omega^2/\pi c^3$ is photon density of states, $n$ is refraction index, $c$ is velocity of light, $w(\mathbf{k}, \mathbf{k}')$ is probability of quantum emission due to indirect transitions. Its value is determined in the second order of perturbation theory:

$$w(\mathbf{k}, \mathbf{k}') = \frac{2\pi}{\hbar} \left| \sum_i \frac{H^\omega H^s}{\varepsilon_0 - \varepsilon_i} \right|^2 \delta(\varepsilon_f - \varepsilon_0). \tag{2}$$

Here $\varepsilon_0$, $\varepsilon_i$ and $\varepsilon_f$ are the energies of initial, intermediate and final states of system, $H^\omega$ is matrix element of energy of interaction between electron and light, $H^s$ is matrix element of energy of interaction between electron and scattering center. We took into account electron interaction with optical phonons, impurities, interface roughness and e-e interaction. We used simplified method of calculating interface roughness scattering from [6]. The parameter of calculation was the concentration of scattering islands on GaAs/AlGaAs interface. It is shown that e-e interaction could result in absorption and emission of long wavelength light only if nonparabolicity of energy spectrum is took into account. Analytical expression of transition probabilities are obtained for non-degenerated and strongly degenerated electrons. Calculating spectral density accordingly (1) we used Fermi distribution function with electron temperature $T_e$.

## 2 The samples and experimental technique

We studied GaAs/$Al_{0.22}Ga_{0.78}As$ multiple quantum well structure consisted from 150 layers of QW of width 6 nm divided by doped 14 nm wide barriers. Spacer was 4 nm wide. The electron mobility at $T = 77$ K was 3300 $cm^2/(Vs)$. The surface electron concentration $n_s = 3 \cdot 10^{11}\ cm^{-2}$. The duration of pulses of longitudinal electric field was 200 ns. Experiment temperature was 4.2 K. Long wavelength radiation ($\lambda = 70 \ldots 300\mu m$) registered with Ge$\langle Ga \rangle$ photodetector. Radiation spectra were measured with the help of tuned InSb filter by magnetic field (see details in [7]). Far-infrared laser on hot holes in germanium was used to study modulation of light absorption coefficient in longitudinal electric field due to electron heating.

## 3 Results of experiment and calculations

The spontaneous emission spectra at different values of longitudinal electric field are presented in Fig. 1. Electron heating occurs with increase of electric field. It leads to increase of curve slopes. Results of calculations are presented in Fig. 2. The calculation of emission spectra took into account self-absorption processes. The consideration of spectral dependency of absorption coefficient introduces significant corrections to spectral density of radiation calculated from (1) (see inset in the Fig. 2). It should be

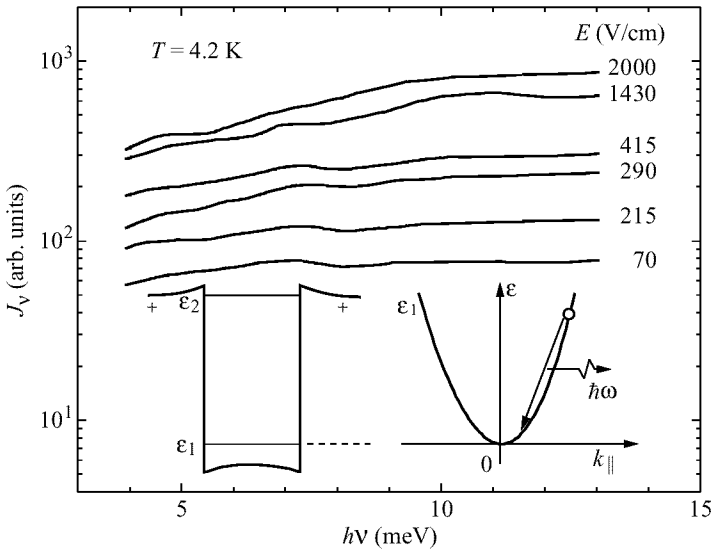


**Fig 1.** Experimental emission spectra.

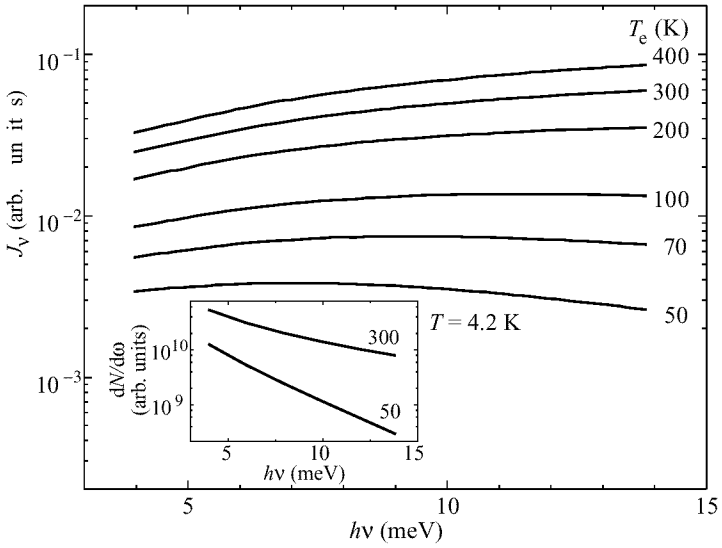


**Fig 2.** Calculated emission spectra. Spectra without considering self-absorption are presented in the insert.

noted that in different parts of spectra and at different values of electron temperature the relation between diverse scattering mechanisms is varied. So, at great electric field $E > 100$ V/cm the electron transitions with scattering on phonons and impurities contribute significantly to the spontaneous emission. Contribution of interface roughness and e-e scattering is substantially weaker.

A correlation between experimental and calculated emission spectra allowed us to obtain the electron temperature as a function of electric field. The electron temperature reaches 400 K at $E = 2$ kV/cm. Our results are agreed with data of [8] where similar radiation from single heterojunction at moderate electric field was investigated as well as with theoretical calculations of dependence $T_e(E)$.

The electric field dependencies of the change of absorption coefficient for s- and p-polarizations of submillimeter radiation are also studied. Comparison of experimental and calculated data for light absorption at different electron temperatures is carried out.

*Acknowledgments*

This work was supported in part by RFBR, grant 96-02-17404a; INTAS-RFBR, grant 615i96; Program "Physics of solid state nanostructures", project 96-1029 and State Program "Integration", project 75.

## References

[1] J. Faist, F. Capasso, D. L. Sivco et al. *Science* **264** 553 (1994).
[2] O. Gauthier-Lafaye, S. Sauvage, P. Boucaud et al. *Appl. Phys. Lett.* **70** 3197 (1997).
[3] E. Gornick, R. Schawarz, D. C. Tsui et al. *Solid State Commun.* **38** 541 (1981).
[4] L. E. Vorobjev, D. V. Donetsky, L. E. Golub. *JETP Lett.* **63** 977 (1996).
[5] V. Ya. Aleshkin, A. A. Andronov et al. *Physica Status Sol.* (b) **204** 173 (1997); **204** 563 (1997).
[6] H. Sakaki, T. Noda, K. Hirakawa et. al. *Appl. Phys. Lett.* **51** 1934 (1987).
[7] L. E. Vorobjev, D. V. Donetsky, A. Kastalsky. *Semiconductors* **29** 924 (1995).
[8] K. Hirakawa, M. Grayson, D. C. Tsui et al. *Phys. Rev.* **B 47** 16651 (1993).

Ioffe Institute
6th Int. Symp. "Nanostructures: Physics and Technology"
St Petersburg, Russia, June 22–26, 1998.



# Far infrared emission and possibility of population inversion of hot holes in MQW InGaAs/GaAs heterostructures under real space transfer

V. Ya. Aleshkin†, A. A. Andronov†, A. V. Antonov†, N. A. Bekin†, *V. I. Gavrilenko*†, I. G. Malkina‡, D. G. Revin†, E. A. Uskova‡, B. N. Zvonkov‡, W. Knap¶, C. Skierbiszewski¶, J. Lusakowski¶ and S. Komiyama§

† Institute for Physics of Microstructures of Russian Academy of Sciences, GSP-105, Nizhny Novgorod, 603600, Russia

‡ Physical-Technical Institute of Nizhny Novgorod State University, Russia

¶ GES, Universite Montpellier 2-CNRS UMR5650, place E. Bataillon, 34095 Montpellier France

§ Department of Basic Sciences, Graduate School of Arts and Sciences, University of Tokyo, Komaba, Meguro-ku, Tokyo 153, Japan

**Abstract.** Far IR emission and current-voltage characteristics of hot holes in strained MQW $In_xGa_{1-x}As/GaAs$ heterostructures at lateral charge transport are investigated. Highly nonequilibrium phenomena observed are shown to results from the real space transfer. The simple experimental criterion for the population inversion between barrier and quantum well states is put forward. The population inversion is shown to realize in "shallow" (with respect to the optical phonon energy) $In_xGa_{1-x}As$ quantum wells.

## Introduction

Recently there has been considerable interest to the hot holes in strained multi-quantum-well (MQW) $In_xGa_{1-x}As/GaAs$ heterostructures excited at lateral charge transport [1-6]. The interest is stimulated by the possibility to realize the hot carrier population inversion and the amplification of the far infrared (FIR) radiation under the real space transfer (RST) conditions. In the present paper the simple experimental criterion for the population inversion between barrier and quantum well states based on the figures obtained from the observed FIR emission and transport characteristics of hot holes is put forward.

## 1 Experimental

$In_xGa_{1-x}As/GaAs$ MQW heterostructures with $\delta$-layers of carbon at 50 Å apart from the boundaries of each InGaAs QW were grown by MOCVD on GaAs(001) substrates [1]. Pulsed electric field up to 2.5 kV/cm was applied to the structure via strip electric contacts deposited on the sample surface at $3 \div 4$ mm apart. Current-voltage (I–V) characteristics were investigated in wide temperature range $4.2 \div 300$ K. Hot hole FIR emission at $T = 4.2$ K was detected by photoresistor Ge:Ga ($\hbar\omega = 10 \div 25$ meV). Narrow band n-GaAs photodetector ($\hbar\omega = 4.2$ meV) was used for the investigation of the cyclotron emission of the hot carriers in high magnetic fields (normal to the plane of the heterostructure) up to 14 T.

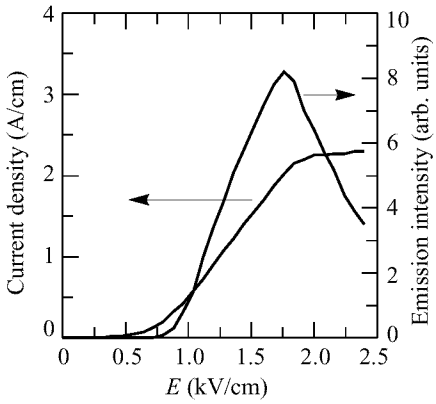


**Fig. 1.** Emission-voltage and current-voltage characteristics of the sample #2154 ($x = 0.11$, $d_{QW} = 47$ Å, $p_s = 2\times10^{11}$ cm$^{-2}$, $n_{QW} = 50$) at $T = 4.2$ K. Detector — Ge:Ga.

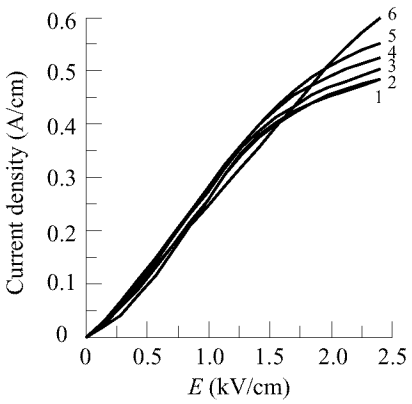


**Fig. 2.** Current-voltage characteristics of the sample #1947 ($x = 0.11$, $d_{QW} = 52$ Å, $p_s = 2\times10^{11}$ cm$^{-2}$, $n_{QW} = 20$) $T$, K: 1—4,2, 2—40, 3—60, 4—80, 5—100, 6—140.

## 2 Results and discussion

Current-voltage and emission-voltage characteristics of the sample #2154 with "shallow" (with respect to the optical phonon energy $\hbar\omega_0 = 37$ meV) QWs are given in Fig. 1. In this sample the calculated [1] position of the only hole subband hh1 in QW is 28 meV lower with respect to the edge of the valence band in the barrier. This figure is very closed to the binding energy of carbon acceptor in GaAs of 26 meV. Therefore at $T = 4.2$ K the holes may be frozen out at the impurities since the binding energy increases in the vicinity of QW. The steep rise of the current and the emission at $E > 0.3$ kV/cm results from the impact ionization of the impurities and the hole transfer from $\delta$-layers into InGaAs QWs. At further increase of the electric field the saturation of current was observed at $E = 1.8 \div 2.5$ kV/cm resulted from hot hole escape from QWs to the barrier layers (i.e. RST) where the carrier mobility drop drastically due to the increase of the effective mass and to the strong ionized impurity scattering in $\delta$-doped barriers. At the same fields the emission intensity reaches its maximum and then monotonously decreases with the electric field (Fig. 1). The cogent argument on the important role of RST in high electric fields is the behavior of I–V characteristics at higher temperatures. Fig. 2 shows I–V plots for the sample #1947 (similar to #2154) in between 4.2–140 K (cf. [3]). The saturation current increases with the rise of the temperature thus proving that the saturation is connected with the RST rather than with the optical phonon scattering as stated in [7].

The "shallow" QWs seems to be most suitable for the realization of the population inversion between barrier and well states [5, 6]. The key point of the inversion mechanism is the high effective carrier temperature in QWs ($T_w$) and the low one in the barriers ($T_b$). This results from the large difference in the carrier mobilities in the QWs and in the barriers. The theoretical criterion for the inversion [5, 6] can be expressed in the simplest form for rather reasonable case when not only the well but also barrier states are of 2D nature (that for example can take place if the barrier holes are confined

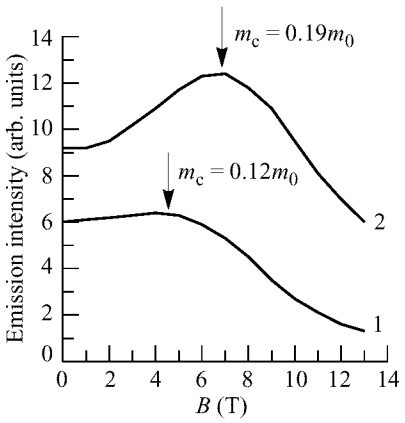


**Fig 3.** CR emission spectra for the sample #1842 ($x = 0, 22$, $d_{QW} = 81$ Å, $p_s = 2\times10^{11}$ cm$^{-2}$, $n_{QW} = 20$).

in the selfconsistent Coulomb potential at the $\delta$-layers). In this case the occupation number ratio is given by the simple relation [6]

$$p = \frac{n_b}{n_w} = \frac{T_w}{T_b} \exp\left(-\frac{\Delta}{T_w}\right). \tag{1}$$

For $T_w \approx \Delta$ and $T_w \gg T_b$ this formula gives the population inversion ($p > 1$). Direct information on the hot hole temperature in QWs was obtained from the measurements of CR emission (Fig. 3). In this experiment $\hbar\omega = 4.2$ meV is too small for the inter-subband or barrier-well transitions; so the observed radiation results from the cyclotron resonance (CR) emission in QWs with the maximum corresponding to the resonant magnetic field $H = \omega c m_c/e$ ($m_c$ is the cyclotron hole mass). As one can see from Fig. 3 the maximum on curve 1 at $E = 110$ V/cm corresponds to the effective cyclotron mass of $0.12m_0$ while at $E = 840$ V/cm the maximum is shifted to $0.19m_0$. According to the calculated energy-momentum law (that is highly nonparabolic) this increase of the cyclotron mass corresponds to the hole heating up to 30 meV, i.e. $T_w > 300$ K. On the other hand from Fig. 2 one can estimate the "barrier" hole temperatute in the sample with "shallow" QWs as low as $T_b \leq 50$ K since up to this figure the saturation current is insensitive to the increase of the lattice temperature. Moreover from these curves it is possible to estimate the ratio of the hole concentrations in "barrier wells" and in the QWs $N_b/N_w$. It is quite natural to assume from the data in Fig. 2 the hole mobility in the QWs to be independent on electric field and that in the "barrier wells" to be equal to zero. Under this assumption one should continue the linear parts of I-V curves at $T = 40 \div 100$ K as the straight line with the same slope up to $E = 2.5$ kV/cm (if the hole number in QWs would be constant). Then it is possible to estimate $N_b/N_w$ as the ratio of lengths of the vertical segments (i.e. at $E = $ const.) between the above straight line and certain I-V curve and between the I-V curve and the absciss axis. This procedure gives $N_b/N_w \approx 0.5$ for $T = 4.2 \div 40$ K at $E = 2.5$ kV/cm. On this base one

can reformulate the relation (1) in more simple and "transparent" manner:

$$p = \frac{n_b}{n_w} = \frac{N_b}{N_w}\frac{T_w}{T_b}\frac{m_w}{m_b}. \quad (2)$$

Substituting in (2) the experimentally obtained figures $N_b/N_w \approx 0.5$, $T_w \approx 300$ K, $T_b \approx 50$ K, $m_w \approx 0.19m_0$ and the well known hole effective mass in GaAs $m_b \approx 0.5m_0$ one readily gets $p \approx 1.1$. Since in the expression (2) the hole concentration in the barriers was surely underestimated by neglecting their mobility it is possible to assert the realization of the population inversion ($p > 1$) in the real MQW heterostructure.

*Acknowledgements*

This research made possible in part by Grants # 97-02-16311 from RFBR, # 094-842 from INTAS, #97-2-14 from INCAS, NATO LG HTECH.LG 960931 and from Russian Scientific Programs "Physics of Solid State Nanostructures" (# 96-1023), "Physics of Microwaves" (# 3.17), "Fundamental Spectroscopy" (# 7.8), "Leading Scientific Schools" (# 96-15-96719) and "Intergation" (# 540).

## References

[1] V. Ya. Aleshkin *et al.*, *JETP Lett.* **64** 520 (1996).
[2] D. G. Revin *et al.*, *Phys. Stat. sol.(b)* **204** 184 (1997).
[3] V. Ya. Aleshkin *et al.*, *ibid.* **204** 178 (1997).
[4] V. N. Shastin *et al.*, *ibid.* **204** 174 (1997).
[5] V. Ya. Aleshkin *et al.*, *ibid.* **204** 563 (1997).
[6] V. Aleshkin *et al.*, *Proc. 1997 International Semiconductor Device Reseach Symposium*, December 10–13, 1997 Charlottesville, USA, p. 263.
[7] M. Reddy, R. Grey, P. A. Claxton, J. Woodhead, *Semicond. Sci. Technol.* **5** 628 (1990).

Ioffe Institute
6th Int. Symp. "Nanostructures: Physics and Technology"
St Petersburg, Russia, June 22–26, 1998.



# IR lasing scheme on X-Γ transitions under real space transfer in n-type GaAs-AlAs-like MQW heterostructures

V. Ya. Aleshkin and *A. A. Andronov*
Institute for Physics of Microstructures, RAS, 603600 N. Novgorod,
GSP-105, Russia, E-mail:andron@ipm.sci-nnov.ru

**Abstract.** New mechanism for IR laser action on transition between X-valley states in AlAs and Γ valley states in GaAs under Γ-X intervalley transfer in GaAs and X valley GaAs-AlAs real space transfer is proposed. Ratio of occupation numbers in X-valleys to the numbers in Γ could be higher than 100 while amplification coefficient could be as high as 100 $cm^{-1}$. In $Ga_xAl_{1-x}As$-$Ga_yAl_{1-y}As$ MQW system, $x < 0.4$, $y > 0.4$ by changing composition the laser tunability from 3 $\mu$m to 100 $\mu$m could be achieved.

## Introduction

There is a need to find out a scheme which can provide lasing in simple MQW systems which could fill band from far to mid IR regions. Recently our group came across [1, 2] seems a universal population inversion mechanism based on RST in MQWs and lower heating (providing lower electronic temperature) of the higher laying states which could serve this goal. In particular it was pointed out [2] that the mechanism should work under mixture of intervalley and RST in n-type GaAs-AlAs-like MQWs. And the present report gives thorough discussion of the latter possibility.

## 1 X–Γ valley population inversion

In GaAs-AlAs MQW system the conduction band structure is such (Fig. 1a) that GaAs layers are wells for Γ-valley electrons while AlAs layers are wells for X-valley electrons. If GaAs thickness is not so low then the Γ-valley level in GaAs is lower than X-valley lowest level. Under high enough electric field Γ-valley electrons reach energy higher than X-valleys in GaAs and perform Γ-X intervalley transfer (IVT). Then moving spatially in X-valleys electrons perform RST to AlAs layers, "fall down" to lowest X-valley level in AlAs due to optical and intervalley phonon scatterings and are accumulated at the level due to low rate of X–Γ transfer through GaAs-AlAs interface (Fig. 1b). The rate is low due to low density of states (effective mass) and to low overlapping of X and Γ valley wave functions and weak direct X–Γ coupling at the interface (cf. e.g. [3, 4]) All these result in reduction of X–Γ intervalley scattering element to $\delta \leq 10^{-2}$ as compared with the element inside GaAs. Also electrons "leak" from GaAs to AlAs due to weak Γ-X scattering through GaAs-AlAs interface. It is this accumulation of electrons at the bottom of X-valleys in AlAs which produces X–Γ valley population inversion.

To give crude estimate of degree of the inversion i.e. ratio of occupation numbers at the bottoms of lowest levels in X and Γ valleys — $n_X$ and $n_\Gamma$ — let as consider equation

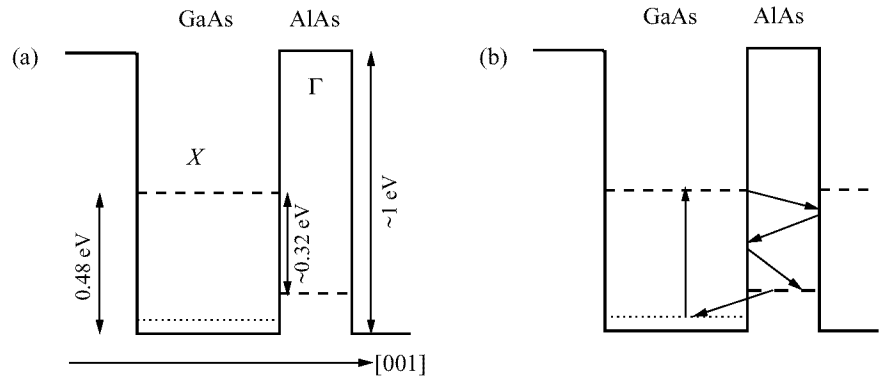


**Fig 1.** Band diagram of one period of GaAs/AlAs MQWs (a) and scheme of inversion formation process (b).

for total number of electrons in Γ valley of GaAs $N_\Gamma$. We suppose that electrons in AlAs occupy lowest level only and they have Boltzman distribution with electronic temperature $T_X$ while Γ electrons on all levels have common electronic temperature $T_\Gamma$. We will not consider here contribution of L-valley electrons: AlAs is barrier for L-valleys and in AlAs they are higher in energy than lowest X-valley level; so L-valleys only "suck up" electrons from Γ valley of GaAs increasing degree of the inversion estimated below. The equation for number of electrons in Γ valley may be written approximately as:

$$\frac{dN_\Gamma}{dt} = -\left[\nu_{\Gamma-X}^{GaAs}\exp\left(-\frac{\Delta_{\Gamma-X}^{GaAs}}{T_\Gamma}\right) + \nu_{\Gamma-X}^{I}\exp\left(-\frac{\Delta_{\Gamma-X}^{I}}{T_\Gamma}\right)\right]N_\Gamma + \nu_{X-\Gamma}^{I}N_X$$

Here $\nu_{\Gamma-X}^{GaAs}$ is effective Γ-X IVT scattering rate in GaAs, $\nu_{\Gamma-X}^{I}$ is Γ-X scattering rate through GaAs-AlAs interface, $N_X$ is total electron number at the lowest level in AlAs and $\nu_{X-\Gamma}^{I}$ is return rate from AlAs to GaAs through interface, $\Delta_{X-\Gamma}^{GaAs}$ is valley separation in GaAs and $\Delta_{X-\Gamma}^{I}$ is the separation across GaAs-AlAs interface. Ratios of the rates may be approximately written as:

$$\frac{\nu_{\Gamma-X}^{I}}{\nu_{\Gamma-X}^{GaAs}} \approx \delta\beta, \qquad \frac{\nu_{X-\Gamma}^{I}}{\nu_{\Gamma-X}^{GaAs}} \approx \delta\gamma(m_\Gamma/m_X)$$

Here $m_\Gamma$, $m_X$ are effective electron masses, $\delta \approx 10^{-2}$ is the mentioned above reduction factor, $\beta$ is factor of about unity which is determined by 3d–2d difference between scattering to X-valley continuum in GaAs and 2d Γ-X scattering through interface and by number of X-valleys involved while $\gamma$ (also about 2-4 for the case discussed below) is factor determined in a similar manner. Because for Boltzman distribution occupation numbers $n_\alpha = (\pi\hbar^2/m_\alpha T_\alpha)N_\alpha$, $\alpha = X, \Gamma$ for the steady state from the equation (1)–(2) one have:

$$\frac{n_X}{n_\Gamma} \approx \frac{(T_\Gamma/T_X)[\exp(-\Delta_{\Gamma-X}^{GaAs}/T_\Gamma) + \delta\beta\exp(-\Delta_{\Gamma-X}^{I}/T_\Gamma)]}{\delta\gamma}$$

It is well known that in GaAs at electric field of about the Gunn effect threshold ($E \approx 2$–$3$ kV/cm) the drastic rise in electron temperature appears and the temperature

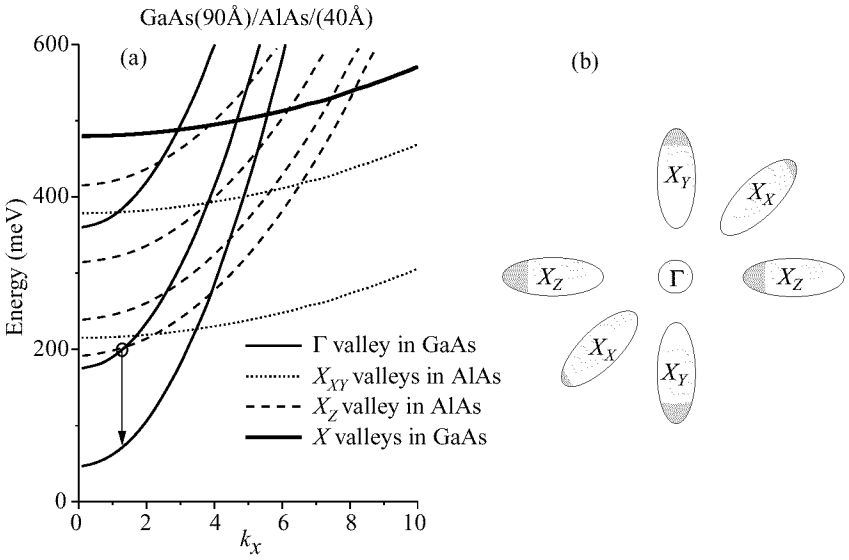


**Fig 2.** Γ−X valleys in Brilluoin zone of GaAs with *XZ* valleys situated along growth direction (b) and electronic subbands for an example structure.

quickly (at $E \approx 5$–$6$ kV/cm) rise to of about 1/3–1/2 of $\Delta_{X-\Gamma}$ — 100–200 meV. At the same time electronic temperature in X-valleys of AlAs stay low — of about half of energy of an intervalley phonon (15–20 meV) due to strong intervalley scattering. This temperature can be decreased even more if one introduce selectively doping of AlAs. Due to small factor $\delta \leq 10^{-2}$ and high ratio $T_\Gamma/T_X$ population inversion ($n_X/n_\Gamma > 1$) is easy achieved here. So we conclude: *In the* GaAs-AlAs MQW *system proposed* X–Γ-*valley population inversion should arise at electric field of about the Gunn effect threshold* $E \approx$ kV/cm *and at higher field can be colossal* — $n_X/n_\Gamma \geq 100$.

It should be also noted that in the field where high population inversion takes place almost all electrons are in X-valleys so that one could expect that there will be no static negative differential conductivity at this field and one can avoid problems related to domain formation.

## 2 Amplification coefficient

Optical transitions between X and Γ valleys become allowed due to X–Γ-valley coupling at GaAs-AlAs interface for X-valleys — along growth direction ($X_z$ valleys Fig. 2a) — and at resonant conditions when in Γ-valley there is (second) level which has energy close to that of first level in $X_z$-valleys of AlAs. Also the $X_z$-valley lowest level should be the lowest in AlAs for the electron accumulation to take place just at these level. Such situation can be achieved at low AlAs layer thickness to provide higher quantizing energy level for the side $X_x$ and $X_y$ valleys. Energy levels in a structure which satisfy all of the mention conditions are given in Fig. 2b.

To estimate amplification coefficient we suppose that all electrons are in $X_Z$-valleys of AlAs. Amplification coefficient $\mu$ for electromagnetic wave propagating along the

layers of the MQW structure can be written as:

$$\mu = 4\pi\sigma/\sqrt{\epsilon_0}c, \qquad \sigma = \frac{e^2 N_0 \hbar}{m_X T_X} f$$

Here $\epsilon_0$ is dielectric permeability and $\sigma$ is the bulk conductivity, $N_0$ is bulk electron concentration ($N_0 = N_X/d$, $d = d_{GaAs} + d_{AlAs}$ and $f$ is oscillator strength). For 2 to 1 transitions inside GaAs well $f \approx 1$; for resonant X–Γ transition (marked by circle and arrow in Fig. 2b) $f \approx 1/4$ because under resonant coupling independently of the coupling strength wave function are equally divided between two resonantly coupled wells. With $f = 1/4$, $N_X = 5\times10^{11}$ cm$^{-2}$ and $T_X = 20$ meV we get: $\mu = 5\times10^2$ cm$^{-1}$ what is quite a value!

## Conclusion

To summarize: we put forward new population inversion and lasing scheme in MQW systems based on X–Γ minima optical transitions from AlAs-like layers to GaAs-like layers under mixture of IVT and RST and present crude estimate of the inversion degree and amplification coefficient for GaAs-AlAs structure which show extremely promising figures for lasing at $\lambda \approx 8\,\mu$m. It should be emphasizes that in the alloy MQW structures $Ga_{1-x}Al_xAs$-$Ga_{1-y}Al_yAs$ with $x < 0.4$, $y > 0.4$ (at $x$ or $y$ equal to 0.4 X–Γ separation is zero in the bulk) there exist broad opportunity for change of the lasing wavelength (both to shorter and to longer wavelength) and also for reduction of electric field needed for lasing. In particular for both x and y close to 0.4 FIR lasing at wavelength longer than say $\lambda \approx 100\,\mu$m could be achieved.

*Acknowledgment*

The authors are indebted to Yu. V. Dubrovskii for providing data concerning X–Γ coupling. The research described in this publication was made possible by Grants 1-064/3, 1-074/4 from Russian Scientific Programs "Physics of Solid State Nanostructures", 3.17 from Russian Scientific Programs "Physics of Microwaves", 96-02-19275 and 97-02-16926 from Russian Basic Research Foundation and Grant 94-842 from INTAS.

## References

[1] V. Aleshkin, A. Andronov, A. Antonov, N. Bekin, V. Gavrilenko, D. Revin, E. Linkova, I. Malkina, E. Uskova, B. Zvonkov *Pis'ma Zh. Eksp. Teor. Fiz.* **64** 478 (1996).

[2] V. Ya. Aleshkin, A. A. Andronov et al, Proceedings of 1997 Intern. Semic. Device research symp., Dec. 10–13, 1997, Charlottesville, USA, Engineering Academic Outreach, Univ. of Virginia, p. 263 1997.

[3] H. C. Liu *Appl. Phys. Lett.* **51** 1019 (1987).

[4] J. J. Finley, R. J. Teissier, M. S. Skolniclk and J. W. Cockburn, R. Grey, G. Hilland M. A. Pate *Phys. Rev. B* **45** R5251 (1996).

Ioffe Institute
6th Int. Symp. "Nanostructures: Physics and Technology"
St Petersburg, Russia, June 22–26, 1998.



# Investigation of hot hole distribution and real space transfer by interband absorption in p-type InGaAs/GaAs MQW heterostructures

V. Ya. Aleshkin†, A. A. Andronov†, A. V. Antonov†, D. M. Gaponova†, V. I. Gavrilenko†, *D. G. Revin*†, B. N. Zvonkov‡, I. G. Malkina‡ and E. A. Uskova‡

† Institute for Physics of Microstructures, RAS, 603600 N. Novgorod, GSP-105, Russia, E-mail: revin@ipm.sci-nnov.ru

‡ Physical-Technical Institute of N. Novgorod State University

**Abstract.** Lateral electric field (up to 2 kV/cm) effects on transmittance in selectively doped p-type MQW $In_xGa_{1-x}As/GaAs$ heterostructures with delta-doped barriers have been studied. The peculiarities of the transmittance spectra associated with hole transitions from the acceptors to the quantum wells and with the hole escape from the quantum wells into the GaAs barriers have been observed. The hole effective temperature in the quantum wells and the population of impurity states in high electric fields were obtained.

In recent papers [1-3] the far IR emission and absorption as well as photoluminescence (PL) from 2D hot holes in MQW $In_xGa_{1-x}As/GaAs$ heterostructures at lateral transport has been investigated experimentally. The remarkable high nonequilibrium phenomena in the high electric fields were revealed under real space transfer (RST) [4] and the new mechanism of the intraband population inversion and far IR lasing was put forward [5,6]. The paper presents the first study of lateral electric field effects on the optical transmittance of p-type InGaAs/GaAs heterostructures under RST. Investigations of optical transmittance allowed us to study directly the energy hole distribution in the quantum wells and hole population on the acceptors under heating by high lateral electric field.

$In_xGa_{1-x}As/GaAs$ heterostructures ($0.07 < x < 0.2$, $d_{InGaAs} = 4.5$ to 10 nm, $d_{GaAs} = 60$ nm, $n_{QW} = 20$) were grown by MOCVD technique at atmospheric pressure on semi-insulating GaAs (001) substrates. Two delta-layers of Zn were introduced at 5 nm from both sides of each $In_xGa_{1-x}As$ quantum well in GaAs barrier layers. Typical values of 2D hole concentration were of $p_s = (0.6 \text{ to } 1.7) \times 10^{11}$ cm$^{-2}$. The lateral pulsed electric field ($E$) up to 2 kV/cm 5 to 10 $\mu$s in duration was applied to the structure via strip electric contacts deposited on the sample surface at the distance 3 to 4 mm. In addition to the transmittance the PL for the samples at $E = 0$ was also investigated. PL was excited by cw $Ar^+$ laser, dispersed by monochromator and detected by cooled photomultiplier. In transmittance experiments the light from halogen lamp was dispersed by monochromator and guided to the sample by optical fibre and detected by Ge-diode placed behind the sample. The measurements were carried out at 4.2 K. In all experiments boxcar integrator was used for data acquisition. In transmittance experiments the measured signal was proportional to the difference between the intensities of light passed through the sample without and under applied electric field.

In Fig. 1 the schematic energy band diagrams and the main optical transitions for two types of investigated heterostructures ($a$ and $b$) are shown. In the heterostructures with deep quantum wells ($x \approx 0.18$ to 0.2, $d_{InGaAs} \approx 8$ to 10 nm) the energy of the

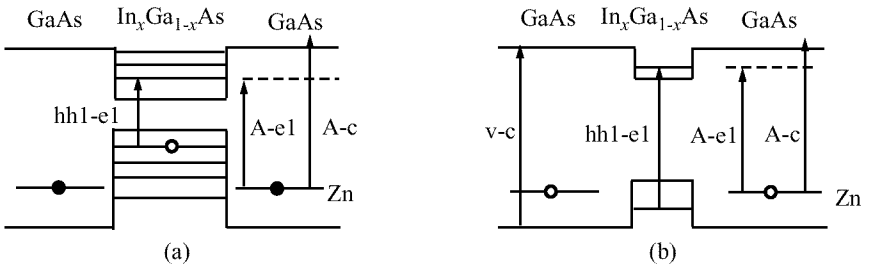


**Fig 1.** Energy zone diagrams for heterostructures with deep (a) and shallow (b) quantum wells. Possible optical transitions are shown by the arrows: hh1-e1—first heavy hole level—first electron level, A-c—acceptor—conduction band of GaAs, A-e1—acceptor-first electron level, v-c—valence band-conduction band of GaAs.

first heavy hole level (hh1) in the quantum wells with respect to the valence band edge in GaAs exceeds that of the ground state of the ionization energy of the acceptors (31 meV for Zn) and at zero electric field the acceptors are completely ionized and all holes turn to be in the quantum wells. In the heterostructures with narrow and shallow quantum wells ($x \approx 0.07$ to 0.1, $d_{\mathrm{InGaAs}} \approx 4.5$ to 5.5 nm) the energy of the first heavy hole level in the quantum well is less than the acceptor in the barrier and at zero electric field the holes are frozen at the impurities. Current-voltage characteristics in these heterostructures exhibit sharp current increase at electric field of the order of 0.3 to 0.6 kV/cm due to impact ionization of the acceptors [1].

In heterostructures with deep quantum wells at zero electric field the hole concentration in the quantum wells is high and therefore the edge of the fundamental absorption is shifted to the shortwavelength region due to Burstein-Moss effect. Hole heating results in the change of the hole distribution and hence in the tailing of the fundamental absorption edge. This leads to both the increase of the sample transmittance at the energies ($\hbar\omega$) higher than Fermi energy and the decrease of the energies lower than Fermi energy (Fig. 2a). PL spectrum at $E = 0$ is also given in Fig. 2 for comparison. The widths of low energy "negative" peaks in the transmittance modulation spectra as well as of PL one are determined by the fluctuation of the quantum wells parameters and existing of the state density tails in band gap. The widths of high energy peaks in the transmittance modulation spectra specify the effective temperature of hot holes in the quantum wells ($T_w$) that reaches approximately 300 K in intermediate electric fields and does not change at the further increase of the electric field due to high optical phonon scattering. It is clearly seen from Fig. 2a that at $E > 1.2$ kV/cm the saturation of low energy "negative" peak takes place. This saturation seems to result from the depopulation of hole states in the quantum wells i.e. the hole occupation numbers tend to zero. In Fig. 2a one can see that in the moderate electric fields 0.3 to 0.6 kV/cm the integral intensity of the "negative" peak is approximately the same as the "positive" one. This relation corresponds to the conservation of the hole number in the quantum wells. However at higher electric fields up to 1.2 kV/cm the intensity of "negative" peak increases while that of the "positive" one saturates that evidently indicates the escape of hot holes to barrier layers, i.e. RST.

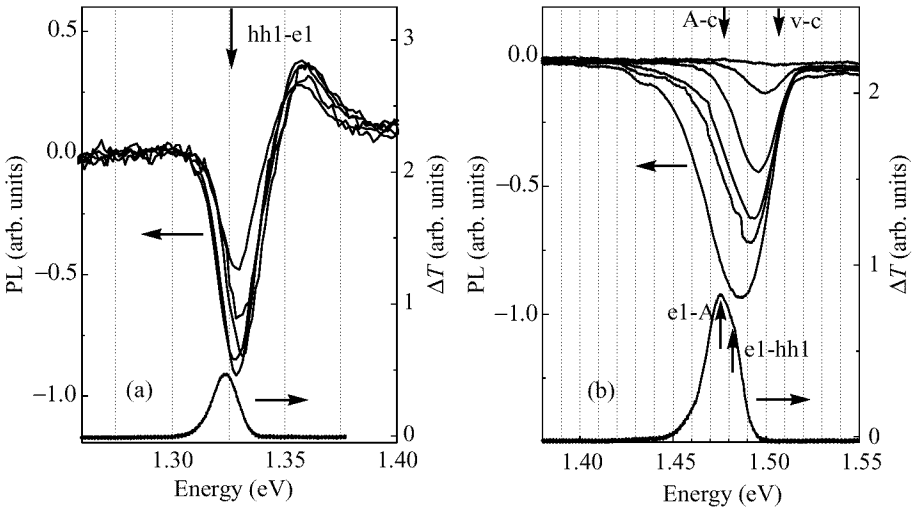


**Fig 2.** PL (at $E = 0$) and transmittance modulation spectra for 10 nm $In_{0.2}Ga_{0.8}As/GaAs$ (a) and for 5.5 nm $In_{0.08}Ga_{0.92}As/GaAs$ (b) quantum wells for lateral electric field (kV/cm): 1—0.38, 2—0.63, 3—0.95, 4—1.26, 5—1.58, 6—1.9.

In heterostructures with shallow quantum wells the transmittance modulation was not observed up to electric fields corresponding to the acceptor breakdown ($E \approx 0.3$ kV/cm). The breakdown results in the hole transfer from acceptors to the quantum wells. Ionization of acceptors leads to the increase of impurity-conduction band absorption and hence to the transmittance modulation in the frequency region in between A-c and v-c transitions (Fig. 2b). The amplitude of the negative modulation rises with the electric field thus testifying the increase of the number of the ionized acceptors. In some samples the saturation of transmittance modulation was observed that seems to result from the ionization of the most part of the impurities. In contrast to the deep quantum wells in the shallow ones no positive transmittance modulation connected with the carrier redistribution in the quantum wells was observed (cf. Fig. 2a and Fig. 2b). This result from the fact that the dominant mechanism of the modulation in the shallow quantum wells is the ionization of the acceptors. The other optical transitions seems to be responsible only for the changes in the form of spectral line and in particular in the observed low-energy shift of the modulation maximum (Fig. 2b).

Thus the transmittance measurements in high lateral electric fields are shown to be a sensitive tool to probe hot carrier distributions in deep quantum wells. The obtained high value of the hole effective temperature $T_w = 300$ K is the necessary condition for the realisation of the population inversion between barrier and quantum well states [6]. The results obtained from the transmittance modulation in the shallow quantum wells give the additional information on the population of impurity states in high electric fields that is significant for the "design" of the RST laser structure.

The work was supported in part by Grants No. 97-02-16311, 98-02-16625 from Russian Foundation for Basic Research, No. 97-1069 from Russian Scientific Program "Physics of Solid State Nanostructures" and the State Science and Technology Program "Physics of

Quantum and Wave Processes" (subprogram "Fundamental Spectroscopy", Project 7.8).

## References

[1] Aleshkin V. Ya, Andronov A. A., Antonov A. V., Bekin N. A., Gavrilenko V. I., Revin D. G., Zvonkov B. N., Lin'kova E. R., Malkina I. G. and Uskova E. A. *JETP Lett.* **64** 520 (1996).
[2] Shastin V. N., Pavlov S. G., Muravjov A. V., Orlova E. E., Zhukavin R. Kh. and Zvonkov B. N. *Physica Status Solidi (b)* **204** 174 (1997).
[3] Revin D. G., Aleshkin V. Ya., Andronov A. A., Gaponova D. M., Gavrilenko V. I., Malkina I. G., Uskova E. A. and Zvonkov B. N. *Physica Status Solidi (b)* **204** 184 (1997).
[4] Gribnikov Z. S., Hess K. and Kosinovsky G. A. *J. Appl. Phys.* **77** 1337 (1995).
[5] Aleshkin V. Ya, Andronov A. A., Antonov A. V., Bekin N. A., Gavrilenko V. I., Muravjev A. V., Pavlov S. G., Revin D. G., Shastin V. N., Malkina I. G., Uskova E. A. and Zvonkov B. N. *Physica Status Solidi (b)* **204** 563 (1997).
[6] Aleshkin V., Andronov A., Antonov A., Bekin N., Gavrilenko V., Muravjev A., Pavlov S., Revin D., Shastin V., Linkova E., Malkina I., Uskova E. and Zvonkov B. Proceedings of *International Semiconductor Device Research Symposium*, Charlottesville USA, 1997, p. 263.

Ioffe Institute
6th Int. Symp. "Nanostructures: Physics and Technology"
St Petersburg, Russia, June 22–26, 1998.



# A 35–177 $\mu$m tunable intersubband emitter for the far-infrared

*P. Harrison*, K. Donovan and R. W. Kelsall
Institute of Microwaves and Photonics,
School of Electronic and Electrical Engineering,
University of Leeds, LS2 9JT, United Kingdom
e-mail:p.harrison@elec-eng.leeds.ac.uk

**Abstract.** Under the influence of a perpendicular electric field the mini-bands of a superlattice break up and form localised electron states within each quantum well. The energy separation between adjacent well states is proportional to the field and the system has become known as a 'Stark Ladder'. This work investigates the potential of superlattices within the Stark Ladder regime as tunable intersubband emitters for the far-infrared region of the spectrum.

## 1 Introduction

The recent rapid development of unipolar semiconductor (or quantum cascade) lasers, based on intersubband transitions in quantum well structures, has been impressive, with recent reports of high power devices operating at room temperature [1]. The majority of this work has centred around emission in the mid-infrared (4–12 $\mu$m) region of the spectrum, and more recently attention has turned towards field tunable devices [2] which promise much in the way of application.

Another area of increased interest and potential exploitation of unipolar semiconductor emitters/lasers is the far-infrared (300–30 $\mu$m) or terahertz ($1–10\times10^{12}$ Hz) region of the spectrum [3]. Indeed tunable terahertz emission has been demonstrated [4]. This theoretical work explores a new design for a far-infared emitter based on intersubband transitions between the conduction band states of adjacent wells of a Stark Ladder. The main benefit of this two-level system is the extent of its tuning range, with the particular design advanced here having a subband separation tunable by an electric field from 5 to 37 meV. This tunability offers the potential for light emission from 33 to 248 $\mu$m.

## 2 Theoretical methods

The envelope function/effective mass approximations were assumed, hence the one-dimensional Schrödinger equation can be written as

$$\left(-\frac{\hbar^2}{2}\frac{\partial}{\partial z}\frac{1}{m}\frac{\partial}{\partial z}+V(z)-eF(z-z_0)\right)\psi=E_n\psi \tag{1}$$

where $V(z)$ represents the conduction band profile and $F$ is the electric field strength, note the origin $z_0$ of the field has been chosen as the centre of the quantum well structure. This was solved with a numerical shooting technique.

After some optimization, the basic design settled upon was a superlattice of 50 Å $Ga_{0.8}Al_{0.2}As$ barriers and 50 Å GaAs wells, hence the period $L = 100$ Å. One of the

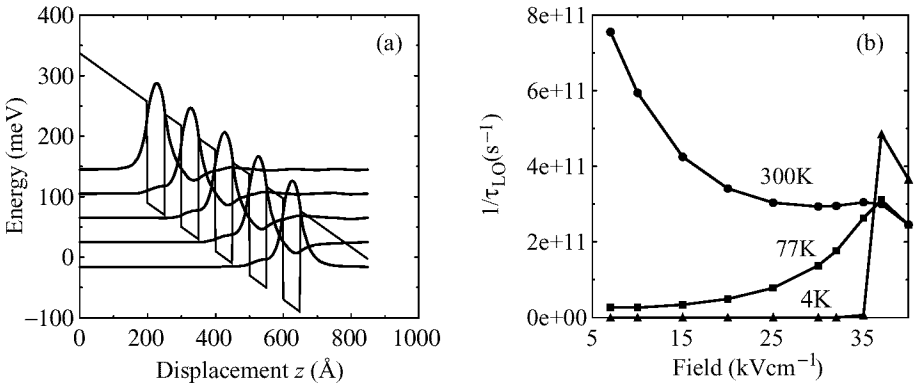


**Fig 1.** (a) Schematic representation of wave functions, energy levels and confining potentials in the Stark Ladder regime, (b) Electron-LO phonon scattering rates from well $m$ to $m+1$ as a function of electric field.

criteria being low field miniband breakup in order that the subband separations quickly satisfied the Stark Ladder demand

$$E_{n+1} - E_n = eFL \tag{2}$$

i.e. an emission frequency proportional to the field. An additional criteria being a reasonable overlap of the wave functions centred in adjacent wells to ensure relatively short spontaneous emission lifetimes. The basic design operation is similar to quantum cascade lasers—electrons scatter down the 'ladder' of localised states. As shown below the majority of energy transitions are non-radiative, but some produce the desired photons. The equal spacing of the energy levels leads to monochromatic emission, the frequency of which is proportional to the applied electric field.

It was shown that a 5 well structure was of sufficient extent to exhibit the energy level structure of the infinite superlattice, hence this system was adopted in these theoretical calculations. Fig. 1(a) illustrates the Stark Ladder regime of the superlattice. At this point the electric field is of sufficient magnitude to localize the electron wave functions to 1 or 2 wells. Calculations showed that indeed the Stark Ladder criteria of Eq. 2 was applicable for fields of 5 kVcm$^{-1}$ and upwards, hence the desired emission properties of tunability and linewidth are fulfilled. The feasibility now centres around the expected power output of the device.

With this aim, the electron-electron [5] and electron-phonon (using bulk acoustic and longitudinal optic (LO) modes [6]) scattering rates were calculated, assuming independently thermalized subbands each of carrier density $10^{10}$ cm$^{-2}$. The radiative transition rate was calculated using the approach of Smet [7]. The results confirmed that scattering rates from level $|n+1\rangle \rightarrow |n\rangle$ were equal for $n = 2$, 3 and 4: it can be seen from Fig. 1(a) that the lowest energy state $|1\rangle$ does experience an 'end' effect. Thus the rates are applicable to a hypothetical infinite structure and are discussed below.

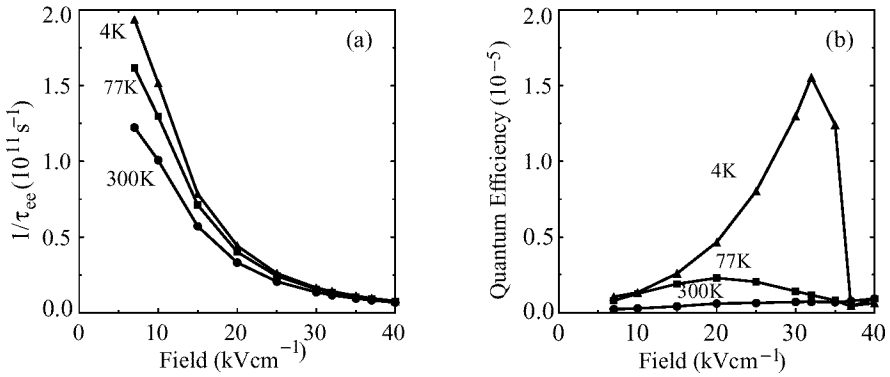


**Fig 2.** (a) Electron-electron scattering rates from well $n$ to $n+1$ as a function of electric field, (b) internal quantum efficiency.

## 3 Results and discussion

As mentioned above, there are three scattering mechanisms which, *a priori*, are expected to be relevant. However the calculations show that electron-acoustic phonon scattering is weak in this system, of the order of perhaps 5% of the electron-LO phonon rate, and can therefore be ignored. The important mechanisms of electron-LO phonon and electron-electron scattering are displayed in Figs. 1(b) and 2(a). It can be seen that typically the electron-LO phonon scattering rate is a factor of 4 larger than the electron-electron rate.

With $L$ in Å and $F$ in kVcm$^{-1}$ then the subband separation is simply given by $E_{n+1} - E_n = F$ meV which allows for easy interpretation of the electric field into an emission energy. The LO phonon energy in GaAs is 36 meV, hence the rapid 'switch on' of this scattering mechanism as the subband separation reaches this value (at $F$=36 kVcm$^{-1}$), is illustrated by the data at 4 K. The higher temperature curves of Fig. 1(b) are in contrast to this and display scattering even though the subband separation is below the LO phonon energy. This is due to emission from the high energy thermal tail of the upper subband Fermi-Dirac distribution. Whilst this thermal effect is important, an explanation of the exact field dependencies of the scattering rates requires an appreciation of the fact that the overlap of the initial and final wave functions decreases with an increasing field and the increasing subband separation leads to a increasing change in momentum between the states, both factors lead to a reduction in rate.

In contrast the temperature dependency of the electron-electron scattering rate is much weaker and derives from the thermal broadening of the distributions and the thermal dependency of the screening factor. Again the scattering rates decrease due to an increasing subband separation which requires a larger change in carrier momentum.

The effect of both these non-radiative transitions on the internal quantum efficiency, defined as the ratio of the radiative to the total non-radiative scattering rate, is displayed in Fig. 2(b). As might be expected the quantum efficiency is highest at low temperatures, due mainly to the suppression of LO phonon emission. Most importantly, at 4 K it peaks at subband separations just below the LO phonon energy at 34 meV=37 $\mu$m.

The quantum efficiency at this point is $\sim 2 \times 10^{-5}$. Although this appears quite low it needs to be considered in context. For every $N$ electrons in well $m$ say, only $\frac{1}{50,000}^{\text{th}}$ emit a photon in the process of scattering to well $m+1$. However if there are a 100 repeats in the superlattice then the number of photons emitted is $\frac{1}{500}^{\text{th}}$ of the number of electrons passing through the system. Fig. 2(b) shows that the expected performance is better at short wavelengths, down to the minimum of 35 $\mu$m ($= 35$ kVcm$^{-1}$). At longer wavelengths the expected number of photons generated decreases, the maximum wavelength is at $F = 7$ kVcm$^{-1} = 177\,\mu$m by which the quantum efficiency has fallen by a factor of 10 from its peak value.

The peak in quantum efficiency at 77 K is a factor of 8 less than that at 4 K and occurs for a subband separation of 20 meV $= 62\ \mu$m. Further increases in temperature give rise to further decreases in efficiency.

## 4 Conclusion

Intersubband transitions between the equal spaced steps of a Stark Ladder offer potential for tunable far-infrared emission. The particular design advanced here, to illustrate the principle, offers potential for emission tunable from 35 to 177 $\mu$m with a peak in efficiency at the shorter wavelengths.

## References

[1] J. Faist, F. Capasso, C. Sirtori, D. L. Sivco, J. N. Baillargeon, *J. Crystal Crowth* **175** 22 (1997).
[2] G. Scamarcio, F. Capasso, J. Faist, C. Sirtori, D. L. Sivco, A. L. Hutchinson, and A. Y. Cho, *Appl. Phys. Lett.* **70** 1796 (1997).
[3] *'New Directions in Terahertz Technology'* ed. J. M. Chamberlain and R. E. Miles, (Kluwer, Dordrecht, 1997)
[4] B. Xu., Q. Hu, and M. R. Melloch, *Appl. Phys. Lett.* **71** 440 (1997).
[5] P. Harrison and R. W. Kelsall, *Solid State Electronics* **42**(5) April/May (1998).
[6] P. Harrison and R. W. Kelsall, *J. Appl. Phys.* **81** 7135 (1997).
[7] Smet, J. H., Fonstad, C. G., and Qing Hu, *J. Appl. Phys.* **79** 9305 (1996).

Ioffe Institute
6th Int. Symp. "Nanostructures: Physics and Technology"
St Petersburg, Russia, June 22–26, 1998.



# Low-dimensional electron semiconductor structures as tunable far-infrared amplifiers and generators

*S. A. Mikhailov*† and N. A. Savostianova‡
† Max-Planck Institut für Physik komplexer Systeme, Dresden, Germany
‡ Moscow State Academy of Instrument Making and Informatics, Moscow, Russia

**Abstract.** A general analytic theory of voltage tunable solid-state far-infrared (FIR) amplifiers, generators and emitters, based on a current-driven instability of two-dimensional (2D) plasmons in a grating-coupled 2D electron system (ES) is presented.

## 1 Introduction

An idea of using the radiative decay of grating-coupled 2D plasmons in semiconductor heterostructures in order to create tunable solid-state FIR sourses was being discussed in the literature since 1980. In experimental papers, see e.g. Refs. [1, 2, 3, 4], one uses a semiconductor structure (e.g., GaAs/AlGaAs) with a 2DES at the heterointerface, and a metal grating coupler on top of the sample (Fig. 1, where the incident electromagnetic wave is absent). A strong dc current is passed through the 2DES, and 2D plasmons are excited in the system due to a current driven plasma instability [5]. The grating couples 2D plasmons to an external electromagnetic field, and their energy is converted to FIR radiation with a frequency depending on the dc current. In spite of the strong appeal of this idea and essential improvements of physical parameters of GaAs/AlGaAs samples in recent years, the intensity of the emitted radiation remains to be too weak [4] for device applications.

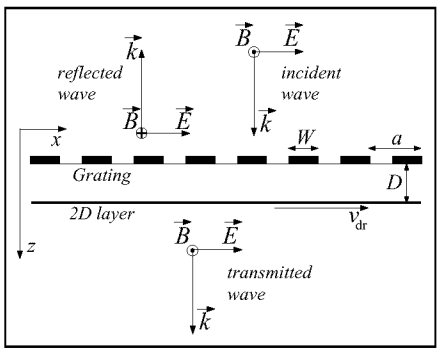


**Fig 1.** The geometry of the structure.

We present a general electrodynamic theory of a grating-coupled 2DES, both with and without the flowing dc current $j_0$. We formulate particular recommendations on how to design amplifiers (generators) with desirable characteristics, and show that voltage tunable solid-state FIR amplifiers, generators and emitters can be created in

low-dimensional electron semiconductor heterostructures with experimentally achievable parameters.

## 2 Formulation of the problem and analytic results

We consider a propagation of electromagnetic waves through the structure shown in Fig. 1 and calculate the transmission $T(\omega, v_{\rm dr})$, reflection $R(\omega, v_{\rm dr})$, absorption $A(\omega, v_{\rm dr})$ and emission $E(\omega, v_{\rm dr})$ coefficients of the structure as functions of the light frequency $\omega$, drift velocity of 2D electrons $v_{\rm dr}$, and other physical and geometrical parameters of the structure (densities, mobilities and effective masses of electrons in the 2DES and in the grating, period of the grating $a$, width of the grating strips $W$, distance between the 2DES and the grating $D$). The period $a$ and the distance $D$ (typically $\simeq 1$ $\mu$m or smaller) are assumed to be smaller than the wavelength of light $\lambda$ (typically $> 100$ $\mu$m). The calculated transmission $t(\omega)$ and reflection $r(\omega)$ amplitudes have the form

$$t(\omega) = r(\omega) + 1 = \frac{1}{\epsilon_{2D}(\mathbf{0},\omega)}\left(1 - \frac{2\pi f\langle\sigma_{1D}(\omega)\rangle}{c\sqrt{\epsilon_b(\omega)}\zeta(\omega)}\right). \tag{1}$$

The transmission, reflection and absorption coefficients are determined as $T(\omega) = |t(\omega)|^2$, *etc.* In Eq. (1), $f = W/a$, $c$ is the velocity of light, $\epsilon_b(\omega)$ is the dielectric permittivity of the surrounding medium (assumed to be uniform in all the space),

$$\zeta(\omega) = \epsilon_{2D}(\mathbf{0},\omega)\left(1 + \frac{2\pi i f\langle\sigma_{1D}(\omega)\rangle}{\omega\epsilon_b(\omega)}\sum_{\mathbf{G}}\kappa_G\alpha(\mathbf{G})W(\mathbf{G},\omega)\right) \tag{2}$$

is a response function of the structure, the sum is taken over all reciprocal lattice vectors $\mathbf{G} = (2\pi m/a, 0)$, $m$ is integer,

$$W(\mathbf{G},\omega) = 1 - \left(1 - \frac{1}{\epsilon_{2D}(\mathbf{G},\omega)}\right)e^{-2\kappa_G D}, \tag{3}$$

$$\epsilon_{2D}(\mathbf{G},\omega) = 1 + \frac{2\pi i\kappa_G}{\omega\epsilon_b(\omega)}\sigma_{2D}(\mathbf{G},\omega) \tag{4}$$

and $\sigma_{2D}(\mathbf{G},\omega)$ are the frequency and wave-vector dependent "dielectric permittivity" and the conductivity of the 2DES, $\kappa_G = \sqrt{G^2 - \omega^2\epsilon_b(\omega)/c^2}$, $\sigma_{1D}(\omega) \equiv \sigma_{1D}(x,\omega)$ is a (local) conductivity of electrons in the grating [treated as an infinitely thin 2D layer with an electron density $n_1(x)$ at $|x - ma| < W/2$ and a vanishing density at $|x - ma| > W/2$], the angular brackets mean the average over the area of a grating strip, $\langle\ldots\rangle = \int(\ldots)dx/W$, and the form-factor $\alpha(\mathbf{G})$ in Eq. (2) is determined by Fourier components of the normalized equilibrium electron density $\vartheta(x) = n_1(x)/\langle n_1(x)\rangle$ in the grating strips, $\alpha(\mathbf{G}) = |\langle\vartheta(x)e^{i\mathbf{G}\cdot\mathbf{r}}\rangle|^2$.

In Eqs. (1) – (4) electrodynamic effects are taken into account within the classical electrodynamics, nonlocal, quantum-mechanical, and scattering effects in the 2DES, as well as the influence of the flowing current $j_0$ enter the theory via an appropriate model for the conductivity $\sigma_{2D}(\mathbf{G},\omega)$, the conductivity $\sigma_{1D}(\omega)$ includes the dependence on the density and the scattering rate (or mobility) of electrons in the grating, a possible frequency dispersion of the surrounding medium is taken into account in function $\epsilon_b(\omega)$.

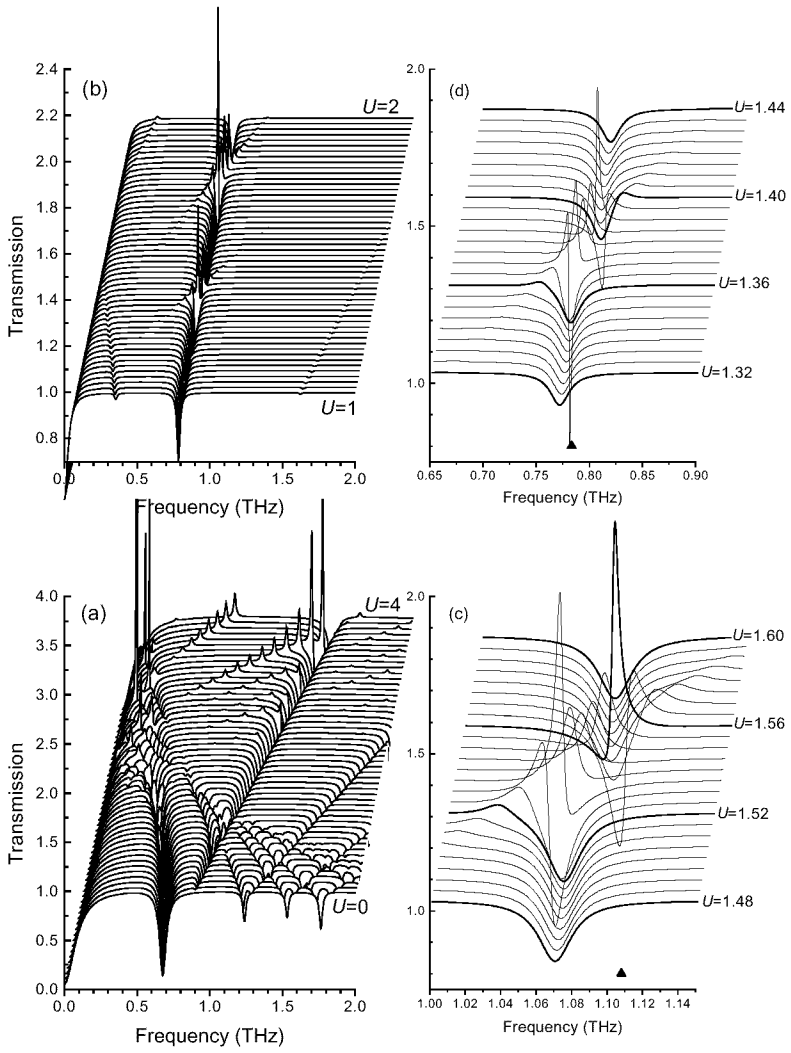


**Fig 2.** The calculated transmission coefficient $T(\omega, v_{\rm dr})$ of several structures.

## 3 Discussion

Figure 2 demonstrates the calculated transmission coefficient of the grating coupled 2DES versus the frequency of light and the dimensionless drift velocity of 2D electrons $U = v_{\rm dr}/v_{F2}$, at different values of device parameters ($v_{F2}$ is the Fermi velocity). Figure 2a shows $T(\omega, v_{\rm dr})$ in a large range of drift velocities $0 \leq U \leq 4$ at parameters taken from Ref. [4] (*metal* grating, $n_2 = 5.4 \times 10^{11}$ cm$^{-2}$, $\mu_2 = 4 \times 10^5$ cm$^2$/Vs, $a = 2$ $\mu$m, $W = 1.2$ $\mu$m, and $D = 62$ nm). One sees a rich excitation spectrum of 2D plasmon modes, but a pronounced amplification of light $[T(\omega, v_{\rm dr}) > 1]$ is achieved only at $U \simeq 3$ which is far beyond realistic experimental possibilities (the estimated maximum drift velocity of 2D electrons in Ref. [4] corresponds to $U \simeq 0.1$).

Using our results we find effective ways to reduce the threshold velocity of amplification down to experimentally achievable values. Fig. 2b demonstrates $T(\omega, v_{dr})$ in a range $1 \leq U \leq 2$ at $n_1 = n_2 = 6 \times 10^{10}$ cm$^{-2}$, $\mu_1 = \mu_2 = 2 \times 10^5$ cm$^2$/Vs, $a = 0.175$ $\mu$m, $W = 0.1$ $\mu$m, and $D = 20$ nm. Physical parameters in this example are taken from Ref. [6], where the drift velocity corresponding to $U \sim 1.8$ has been *experimentally* achieved, geometrical parameters are taken in view of possibilities of modern semiconductor technology (see, e.g., Ref. [7]). Fig. 2b clearly demonstrates that an amplification of FIR radiation is possible at experimentally achievable parameters of modern semiconductor heterostructures. Fig. 2d shows the same $T(\omega, v_{dr})$ dependence on an enlarged scale, Fig. 2c is drawn at a different value of the electron density in the grating strips ($n_1 = 1.2 \times 10^{11}$ cm$^{-2}$).

The key point which allows us to accomplish the desired aim is the use of a *quantum-wire* grating instead of commonly employed metal ones. The resonant interaction of plasma modes in the 2DES and in the grating leads to a considerable increase of the grating coupler efficiency, and finally to a reduction of the threshold velocity and an enhancement of amplification. Together with other methods [8] (including a specific choice of geometrical parameters of the structure) this allows us to reduce the threshold parameters of the amplifier down to experimentally achievable values. The operating frequency of amplifiers can be varied by the dc electric current flowing in the 2DES and/or by changing the electron density $n_1$ in the quantum wire grating (compare Figs. 2c and 2d).

## 4 Conclusion

Voltage tunable solid-state FIR amplifiers, generators and emitters can be realized in low-dimensional electron semiconductor heterostructures with experimentally achievable parameters.

## References

[1] D. C. Tsui, E. Gornik, R. A. Logan, *Solid State Commun.* **35** 875 (1980).
[2] R. A. Höpfel, E. Vass, E. Gornik, *Phys. Rev. Lett.* **49** 1667 (1982).
[3] N. Okisu, Y. Sambe, T. Kobayashi, *Appl. Phys. Lett.* **48** 776 (1986).
[4] K. Hirakawa, K. Yamanaka, M. Grayson, D. C. Tsui, *Appl. Phys. Lett.* **67** 2326 (1995).
[5] M. V. Krasheninnikov, A. V. Chaplik, *Zh. Eksp. Teor. Fiz.* **79** 555 (1980) [Sov. Phys. JETP **52** 279 (1980)].
[6] C. Wirner, C. Kiener, W. Boxleitner, M. Witzany, E. Gornik, P. Vogl, G. Böhm, G. Weimann, *Phys. Rev. Lett.* **70** 2609 (1993).
[7] D. Weiss, M. L. Roukes, A. Menschig, P. Grambow, K. von Klitzing, and G. Weimann, *Phys. Rev. Lett.* **66** 2790 (1991).
[8] S. A. Mikhailov, *submitted to Phys. Rev. B.*

Ioffe Institute
6th Int. Symp. "Nanostructures: Physics and Technology"
St Petersburg, Russia, June 22–26, 1998.



# Electron tunneling through triple barrier structure with intersubband population inversion

E. E. Vdovin, *Yu. V. Dubrovskii*, J. P. Dag†, J. W. Cockburn†, M. S. Scolnick† and I. A. Larkin†
Institute of microelectronics technology RAS
142432, Chernogolovka, Russia
† Department of Physics, University of Sheffield,
Sheffield S3 7RH, UK

Intersubband population inversion in a GaAs/AlGaAs triple barrier structure was demonstrated recently by photoluminescence spectroscopy [1]. The maximum population ratio $n_2/n_1 \approx 5$ between $n = 1$ (E1) and $n = 2$ (E2) electron subbands of the wider quantum well (QW1) was obtained when the structure was biased so that E1 was in resonance with the $n = 1$ (E1*) level of the narrower quantum well (QW2) (see insert in Fig. 1). At this bias electrons from emitter tunnel into the E2 level. E1 electrons may escape rapidly by resonant tunneling via E1*, whilst the E2 escape time from QW1 is significantly longer, since E2 electrons must tunnel non-resonantly through a relatively wide region comprising the intermediate and collector barriers and QW2. Such structures therefore provide the short E1 lifetime necessary to achieve E2-E1 population inversion, whilst maintaining a high density of E2 electrons available for E2-E1 transition.

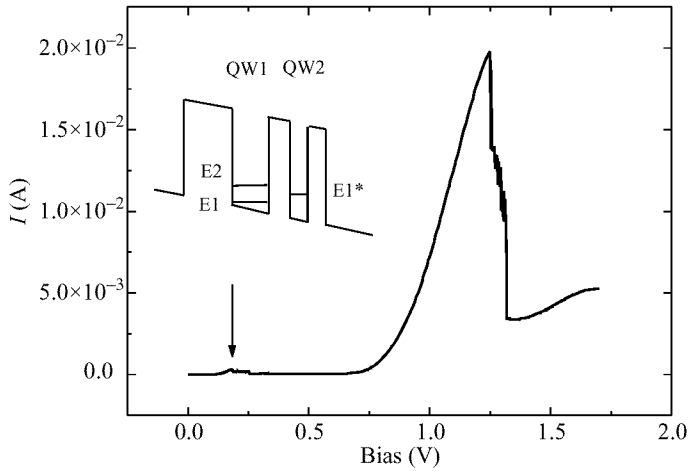


**Fig 1.** IV characteristics of the structure. Arrow shows the position of the resonant tunneling through E1 state. Insert demonstrates band diagram of the sturcture.

In this work we report the results of careful measurements of tunneling current on the same structures in a wide temperature range and magnetic field parallel to the QW which as expected should destroy resonance between E1 and E1* levels [2] at particular voltage bias. We found the features in IV characteristics which we interpreted as appearance of additional current channel linked with E1-E1* resonance.

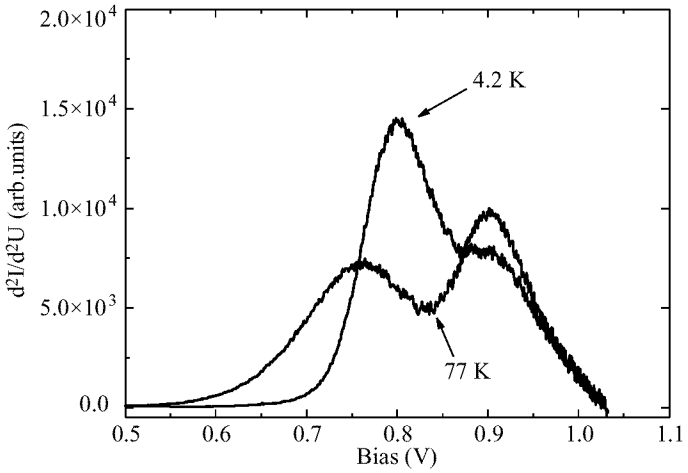


**Fig 2.** Second derivative of the current voltage characteristic at the region of population inversion at different temperatures: 4.2 K and 77 K.

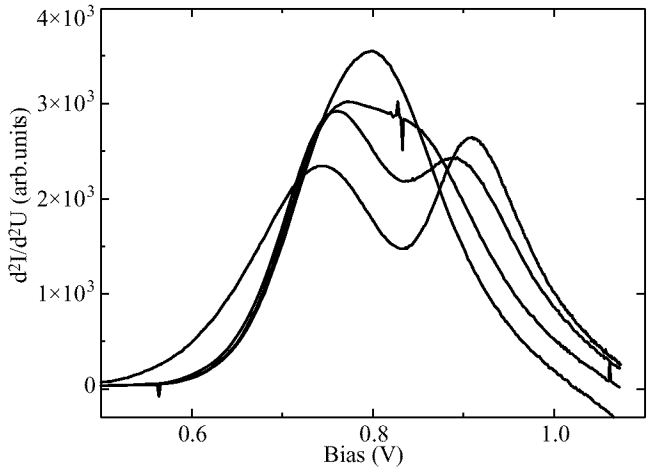


**Fig 3.** Second derivative of the current voltage characteristic at different in plane magnetic fields: 0 T, 1 T, 2 T, 4 T. Temperature $T = 60$ K.

The measured IV curves at 4.2 K is shown in Fig. 1. The inversion population was observed at voltage range (0.6–1.0) V with maximum located at 0.8 V [1]. Fig. 2 shows the second derivative of the current voltage characteristics. Two peaks appear at the same voltage range, which are more pronounced at 77 K, and are smeared out at 4.2 K. In control sample with wider second QW where E1-E1* resonance should appear at higher biases only one peak have been observed. As one peak is related to the main resonance tunneling through E2 state, we attribute the second peak to the appearance of the new additional current channel due to the E1-E1* resonance. These two peaks are more pronounced at 77 K, may be due to the higher efficiency of electron relaxation

from E2 to E1 level with phonon emission or absorption.

To prove proposed explanation the magnetic field was applied parallel to the QW plane at 60 K. It can be seen from Fig. 3 that magnetic field suppress two peaks picture because it change wave vector of the tunneling electrons on the way between two quantum wells due to the Lorentz force and as the result moves E1-E1* resonance to higher voltage and broaden it [3].

Thus we have found features in tunneling current which are related to the resonance between ground quantum well states in triple barrier structures when the current mainly determined by electron tunneling from emitter to the first excited state in the first quantum well.

This work was supported by the National program Physics of the Solid State Nanostructures (grant 97-1057), INTAS-RFBR (grant 95-849), RFBR (grant 98-02-17462), and CRDF (grant RC1-220). E.E.V. acknowledges the Royal Sociaty for financial support.

**References**

[1] Y. B. Li, J. W. Cockburn, J. P. Duck et al., *Phys. Rev. B* (1997) to be published.
[2] G. Reuscher, M. Keim, F. Fischer et al., *Phys.Rev.* **B53** 16414 (1996).
[3] L. Eaves, R. K. Hayden, D. K. Maude et al., in *High Magnetic Fields in Semiconductor Physics III*, edited by G. Landwehr, Springer Series in Solid State Sciences Vol. 101 (Springer, Berlin, 1992).

Ioffe Institute
6th Int. Symp. "Nanostructures: Physics and Technology"
St Petersburg, Russia, June 22–26, 1998.



# Control of the quantum dot energy by a photon: Observation of two-exciton and three-exciton states in quantum dots

*Yasuaki Masumoto*†‡ and Michio Ikezawa†
† Institute of Physics, University of Tsukuba, Tsukuba 305-8571, Japan
‡ Single Quantum Dot Project, ERATO, JST, Tsukuba Research Consortium, Tsukuba 300-2635, Japan

**Abstract.** Antibonding two-exciton and three-exciton states were observed in CuCl quantum dots. This observation demonstrates the controllability of the quantum dot energy by a photon.

A semiconductor quantum dot is so small that its energy is changed as a result of the absorption of a photon. Let us consider three cases. The first case is the case where any excitons are not in a quantum dot. The second case is the case where an exciton is in it. The third case is the case where a biexciton is in it. When a photon creates an exciton or an additional exciton in a dot, an exciton, two excitons and three excitons will be in the dots depending on three cases. In a bulk crystal, two excitons and three excitons can be located apart without any interaction. Then the photon energies to create an exciton and additional exciton(s) are the same. However, in a quantum dot, excitons are forced to interact with each other because of the short distance between them. If the photon energy which creates an exciton or an additional exciton in a dot depends on three cases considerably, the energy of the quantum dot is controllable by a photon.

One of two-exciton states is known as the biexciton ground state in bulk crystals. It is also observed in quantum dots and the size dependence is studied [1]. The biexciton ground state is considered as a bonding state of two-exciton states. However, an additional two-exciton state, in other words, the biexciton excited state in quantum dots has been predicted by the theory [2]. This state, an antibonding state of two excitons, is not present in the bulk crystal, while it is expected to be present uniquely in quantum dots. It is expected to depend on the size of the dots strongly. The purpose of this paper is to demonstrate the antibonding two-exciton and three-exciton states in the quantum dots [3, 4].

For the observation of two-exciton and three-exciton states, we used a model quantum dot in the weak confinement regime, a CuCl quantum dot embedded in a NaCl crystal. The picosecond-pump-and-femtosecond-probe spectroscopy was used for the investigation. The laser system we used was a 1 kHz, 300 fs Ti:sapphire regenerative amplifier system. The second harmonics of the output was spectrally narrowed passing through a spectral filter stage made of a grating and was used as the pump pulses. The spectral width was 1.7 meV which was suitable for the size-selective excitation of quantum dots, but the temporal width was elongated to 1.2 ps. The probe light was a white continuum in the femtosecond range. The time-resolved absorption spectra were measured by means of a 25 cm monochromator and a liquid nitrogen cooled charge-coupled device.

The $Z_3$ exciton and $Z_{1,2}$ exciton absorption structures observed in the upper part of Fig. 1 are shifted to the higher energy side compared to those of the bulk crystal due

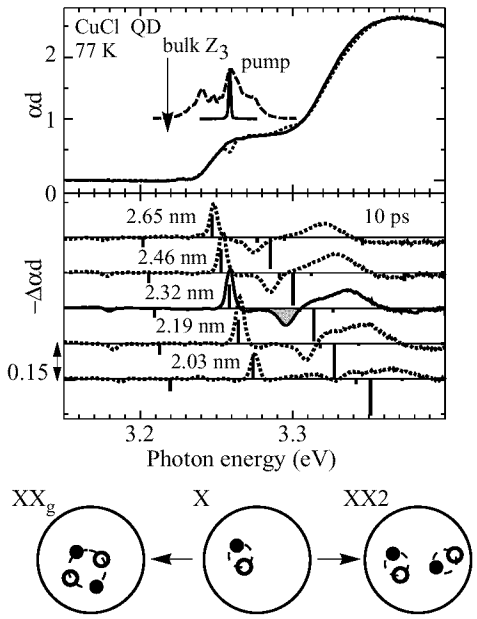


**Fig 1.** Upper figure: The solid line shows absorption spectrum of CuCl quantum dots embedded in a NaCl crystal at 77 K, while a dashed line represents that at 10 ps after photoexcitation. Lower figure: The solid line shows differential absorption spectrum corresponding to the upper figure, while dashed lines are those for different excitation photon energies. The radii of quantum dots which were excited are 2.65 nm, 2.46 nm, 2.32 nm, 2.19 nm and 2.03 nm from top to bottom, respectively. Thick solid bars are theoretical results normalized at the spectral hole. In the inset, filtered and unfiltered pump spectra are shown by a solid line and a dashed line, respectively. Two excitation processes of the two-exciton states are illustrated.

to the quantum confinement effect. The $Z_3$ exciton energy of bulk CuCl is shown by a downward arrow. According to the well-known relation between the quantum confined exciton energy and the quantum dot radius [5], the pump pulse energy size-selectively excite the quantum dots of the corresponding radius. The differential absorption spectrum in the lower part of Fig. 1 consists of a spectral hole at the pump photon energy and two induced absorption structures at both sides (3.180 eV, 3.296 eV) of the spectral hole.

Differential absorption spectra for four different pump photon energies are also shown at the lower part of Fig. 1. Two induced absorption bands shift with the change of the excitation photon energy. The theoretical induced absorption spectrum from the exciton ground state is shown by thick solid bars in Fig. 1 [4]. The energy shifts of strong bands show good correspondence with experiments. Furthermore, the relative strengths of the induced absorption lines and the spectral hole are reproduced quite well by the theory. The strong peak above the pump energy can be assigned to the induced absorption transition to antibonding two-exciton ($XX2$) state [2].

The energies of the spectral hole and the induced absorption bands are plotted in Fig. 2 as a function of the excitation photon energy. The solid circles show spectral

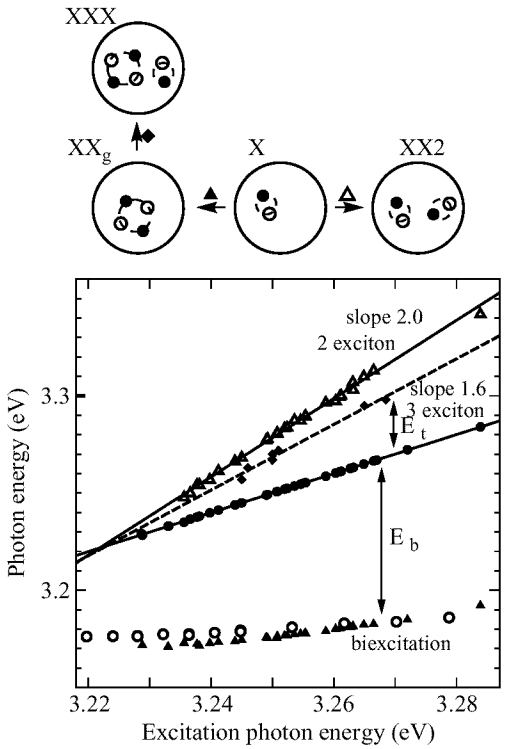


**Fig 2.** Excitation energy dependence of the structures appearing in the differential absorption spectrum. The solid circles represent spectral hole energies, and they are on a line of slope 1.0. Open (solid) triangles show the energy of the induced absorption located at the higher (lower) energy side of the spectral hole. Open circles indicate the energy of the induced absorption measured by nanosecond pump-and-probe method in Ref. [1]. Solid diamonds correspond to additional induced absorption under high-density excitation. $E_b$ denotes the biexciton binding energy defined by $2E_X - E_{XX}$ and $E_t$ shows $E_{XXX} - E_{XX} - E_X$. Then the binding energy of three-exciton state defined by $3E_X - E_{XXX}$ is given by $E_b - E_t$. The excitation processes of two-exciton states and three-exciton state are illustrated at the top part.

hole energies, and they are on a line of slope 1.0, since their energy coincides with the excitation photon energy. Open (solid) triangles exhibit the energies of the induced absorption located at the higher (lower) energy side. Open circles show the energies of induced absorption measured previously by nanosecond pump-and-probe method [1] which was identified as the transition from the exciton (X) to the biexciton ground state (XXg).

The solid line through the open triangles has a slope of 2.0. Antibonding of two excitons naturally explains the slope [4]. This line crosses the line of slope 1.0 near the $Z_3$ exciton energy of bulk CuCl. Furthermore, the spectral hole and the induced absorption on the higher energy side exhibit almost the same temporal evolution with a decay time constant of 480 ps. This fact is reasonable, because the induced absorption on the higher energy side arises from the transition from excitons pre-excited in the

quantum dots.

The three-exciton state (XXX) was found as an additional induced absorption band by two independent methods employing high-density excitation and two-color excitation. Then the biexciton luminescence became observable. In the two-color pump-and-probe method, the energy of the second pump pulse was tuned to the induced absorption caused by the first pump pulse. This combination produces two-exciton state effectively only in quantum dots of particular size and enables us to observe the induced absorption to three-exciton states. Excitation energy dependence of this induced absorption is shown in Fig. 2 by solid diamonds. The fitted line has a slope of 1.7 and this line also crosses the other two lines near the bulk $Z_3$ exciton energy. An anti-bonding combination of a biexciton and an exciton explains the slope of 1.7 [4]. The decay time of the additional induced absorption corresponds to the biexciton luminescence lifetime of 70 ps. This shows that the additional induced absorption can be assigned to transition from the biexciton ground state to a three-exciton state.

In conclusion, we found two-exciton and thre-exciton states in quantum dots in the weak confinement regime by using time-resolved size-selective pump and probe technique. These experiments open a new direction of research of many-exciton states in confined systems and demonstrate the controllability of the quantum dot energy by a photon.

The authors acknowledge Dr. S. V. Nair and Dr. T. Takagahara for the theoretical support throughout this work.

## References

[1] Y. Masumoto, S. Okamoto, and S. Katayanagi. *Phys. Rev.* B **50** 18658 (1994).
[2] S. V. Nair and T. Takagahara. *Phys. Rev.* B **53** R10516 (1996); *Phys. Rev.* B **55** 5153 (1997).
[3] M. Ikezawa and Y. Masumoto. *Jap. J. Appl. Phys.* **36** 4191 (1997).
[4] M. Ikezawa, Y. Masumoto, T. Takagahara and S.V. Nair. *Phys. Rev. Lett.* **79** 3522 (1997).
[5] T. Itoh, Y. Iwabuchi, and M. Kataoka. *Phys. Status Solidi* B **145** 567 (1988).

Ioffe Institute
6th Int. Symp. "Nanostructures: Physics and Technology"
St Petersburg, Russia, June 22–26, 1998.



# Vertical coupling of quantum islands in the CdSe/ZnSe submonolayer superlattices

*I. L. Krestnikov*, P. S. Kop'ev, Zh. I. Alferov, M. Straßburg†, N. N. Ledentsov†, A. Hoffmann†, D. Bimberg† and C. M. Sotomayor Torres‡
Ioffe Physico-Technical Institute RAS, St. Petersburg, Russia
† Institut für Festkörperphysik, Technische Universität Berlin, Hardenbergstr.36, 10623 Berlin, Germany
‡ Lehrstuhl für Materialwissentschaften in der Elektrotechnik, Bergische Unisersität GH Wuppertal, Fuhlrottstrasse 10, 42097 Wuppertal, Germany

The usual laser structures are made in an agreement with the double heterostructure geometry [1]. In this case a waveguiding effect occurs due to larger refractive index in the central layer. To get an efficient waveguiding of the lightwave in this layer the difference between refractive indices of waveguiding region and cladding layers materials should be quite large and the thickness of the waveguiding region should be comparable with the wavelength of light. This means that these materials must be lattice matched and, generally, must have large bandgap difference, as it usually occurs that only large bandgap difference provides large difference between refractive index values. For thick active layers one is, thus, limited by the condition of lattice matching. This condition is valid for all compositions in the AlGaAs-GaAs case and for some fixed compositions for other III–V ternary systems. In many cases, however, this lattice matched heterocouple does not exist (e.g. diamond, Si, etc.) or, if exists, does not provide sufficient conductivity (ZnMgSSe:N [2], GaN:Mg [3]). At the same time one can offer principally new way to realize waveguiding by using a resonant refractive index enhancement due to exciton absorption in ultrathin insertions of narrow gap material in a wide gap matrix [4]. There is no necessity in lattice matching in this case as ultrathin insertions can be elastically strained and dislocation free. To provide sufficient thickness comparable to the lightwave in crystal one can stack these insertions.

The interaction between excitons and light causes sharp adsorption line. From the Kramers-Kronig equation which relate real and imaginary parts of the dielectric constant one can thus obtain the exciton-induced modulation of the refractive index. In the case of carrier injection when the gain arises at the lower energy side of the adsorption peak, the enhancement of the refractive index is more pronounced due to increased derivative of the gain-absorption curve [5]. In this case the refractive index enhancement appears in the spectral region shifted to the lower energy side as compared to the absorption maximum. Thus, for this wavelength, optical confinement is the most efficient and, e.g. in case of absorbing substrate, minor optical losses can be realized [6]. Thus, there is an energy window with small optical losses for the light propagated in the structure plane.

In the quantum well (QW) excitons exhibit free motion in the QW plane. In this case we should think about the exciton in-plane k-vector. Excitons with finite k-vector, as it was directly shown by Gross [7], cannot recombine radiatevly. At high temperatures and carriers densities, which are typical for lasing conditions exactly, the excitons with finite k-vector dominate. So it is necessary to get an additional particle for exciton scattering to accommodate its k-vector (for example LO-phonon). This many-body

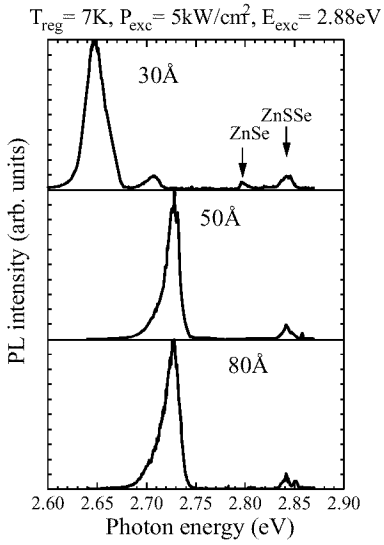


**Fig. 1.** PL of samples with different thickness of ZnSe spacer.

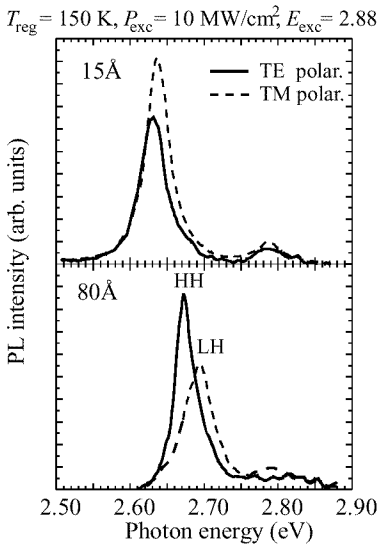


**Fig. 2.** Linear polarization dependence of edge emission for structures with 1.5 nm and 8 nm spacers.

scattering mechanism decreases material gain and shifts the gain maximum to the lower energy away from the excitonic waveguiding spectral window. To avoid this shift we proposed to use arrays of quantum dots (QDs) where excitons are effectively localized by QDs and the k-selection rules are broken [4]. Thus, to apply the concept of exciton induced waveguiding, described above, the sizes of quantum dots in all 3 dimensions should be comparable to the exciton radii. To fabricate these objects we proposed to use submonolayer (subML) CdSe depositions. SubML depositions result in dense arrays of uniform two-dimensional nanoscale islands [8]. In this paper, we discuss optical properties of subML CdSe/ZnSe superlattices (SL) with different spacers.

The structures extensively studied in this work were grown on n+ GaAs(100) substrates using a molecular beam epitaxy (MBE) [9]. All structures consist of 360 nm ZnSSe buffer and 60 nm ZnSSe cap layer lattice matched to the GaAs substrate. Between these layers there is a CdSe/ZnSe subML SL. CdSe insertion average thickness was estimated as 0.7 ML for all the structures. The ZnSe barriers have different thickness: 1.5 nm, 3 nm, 5 nm and 8 nm. The total thickness of SL is 60 nm for structures with 3 nm, 5 nm and 8 nm barriers and 30 nm for structures with 1.5 nm barriers. Consequently, the numbers of SL periods were different (20, 20, 12 and 8 consequently for 1.5 nm, 3 nm, 5 nm and 8 nm barriers).

Figure 1 shows PL spectra for structures with different spacers. The first remarkable result is that with decreasing in spacer thickness the PL drastically changes: a new peak at lower energy becomes dominant. This behavior can be explained by formation of vertically coupled QDs important for thin spacers, similar to shown for 3D InAs-GaAs QDs [10]. In this case the wavefunction of carriers in the neighbor islands are overlapped and the transition energy is lower. In this case the wavefunction of carriers in the neighbor islands are overlapped and the transition energy is lower. In the 8 nm and 5 nm cases there are only noncoupled QD emission, while the 3 nm

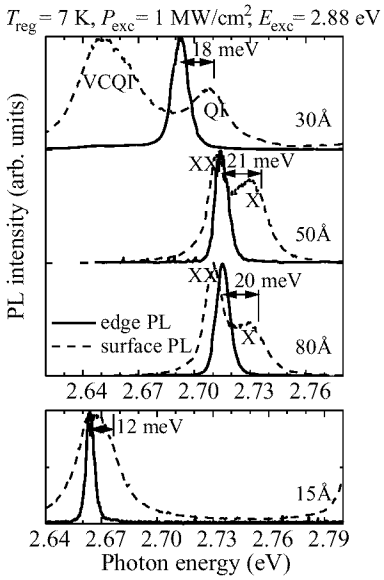


**Fig. 3.** Edge and surface PL of structures with different spacer thickness.

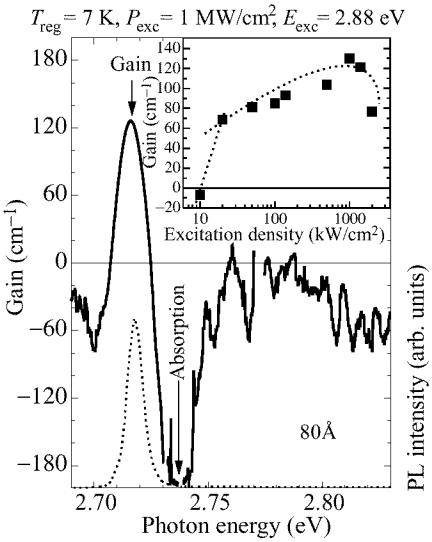


**Fig. 4.** Spectra of the gain (straight line) and stimulated emission (dotted line) of 8 nm spacer structure. Insert shows the excitation level dependence of the maximum gain value.

case shows emission from the both uncoupled and coupled states. Further decrease in spacer thickness resulted in increased intensity of coupled QDs and in full suppression of uncoupled QD luminescence.

The next possibility to prove the assumption about vertical correlation of QDs is to study polarized edge PL. As the height of the islands is only 1 or 2 MLs and lateral size is about 5 nm the symmetry of the hole wavefunction, which governs the polarization of edge emission is similar to the QW symmetry. In this case the light corresponding to HH exciton transition should be TE polarized and the light corresponding to LH exciton should have TM polarization. This behavior we can see for the 8 nm spacer structure (see Fig. 2). The lower energy TE polarized peak is corresponding to the HH exciton-induced ground state and the next — to the LH exciton-induced excited state. As opposite to this behavior for the 1.5 nm-spacer structure the situation is different. We have depolarized or weakly TM polarized emission. This tells us that the wavefunction symmetry is changed due to the vertical coupling of islands and the heavy hole wavefunction is more extended along the growth axis now.

Figure 3 shows PL from the surface at high excitation densities as well as the stimulated emission spectra measured in the edge geometry. You can see that the stimulated emission originates from uncoupled QDs except of the 1.5 nm-spacer case. In the 8 nm and 5 nm cases there are biexcitonic lines having a lower energy than the stimulated emission. This means that we have an excitonic nature of the stimulated emission. It is also confirmed by the energy positions of the stimulated emission and gain, which do not change with increasing in pump density. Thus many-carrier effects are not relevant in this case. In Fig. 3 the energy shift between the exciton ground state and the stimulated emission is also presented. For all the structures this shift is quite

smaller than the LO-phonon energy so there is a zero-phonon gain mechanism in the exciton waveguiding region.

In the Fig. 4 one can see the gain spectra well above the threshold obtained by variable stripe-length method. It is very important that even at densities two order of magnitude above the threshold there is still a region with strong excitonic absorption providing consequently an efficient exciton induced waveguiding. Without this waveguiding the positive gain can be hardly observed as internal optical losses in this structures with extremely thin buffer layers should be huge (more than 1000 $cm^{-1}$).

In the insertion to Fig. 4 the maximum value of gain versus excitation density is presented. One can see very fast onset of the gain near the threshold and then slow increasing which ends with gain saturation at very high excitation densities. This effect can be explained by the following: as stimulated emission can occur only in the narrow energy range due to exciton induced waveguiding not each QD can contribute to the gain. The number of QDs having proper transition energy is finite and after filling these QDs gain saturates. Further filling converts excitons to biexcitons and the gain in the exciton region decreases. At very high excitation levels when all the QDs are filled there is no excitonic absorption and, consequently, exciton induced waveguiding and this results in the vanishing of the gain.

In conclusions, in this paper we showed that decrease in the spacer layer thickness between subML sheets results in vertical correlation between QDs. Due to changing of the hole wavefunction symmetry edge PL of coupled QDs is weakly TM polarized while the emission of uncoupled dots is strongly TE polarized similar to QW case. Main absorption peak is not saturated when the gain peak develops at moderate excitation level while at very high excitation level saturation and suppression of the excitonic gain due to conversion of excitons to biexcitons and suppression of exciton induced waveguiding is observed.

The authors are grateful to Dr. S. V. Ivanov and S. V. Sorokin for the samples growth. This work was supported by the Russian Foundation of Basic Research (Grant No. 97-02-18138), by the INTAS 94-481 and by the Volkswagen Foundation. N. N. Ledentsov is grateful to the Alexander von Humboldt Foundation.

## References

[1] Zh. I. Alferov and R. F. Kazarinov, Double Heterostructure Laser, Authors Certificate No. 27448, Application No. 950840 with a priority from March 30, 1963.
[2] H. Okuyama, Y. Kishita, T. Miyajuma, A. Ishibashi, K. Akimoto, *Appl. Phys. Lett.* **64** 904–906 (1994).
[3] B. Monemar, *Proc. the Second Int. Conf. on Nitride Semiconductors*, Tokushima (Japan), October 27-31, 1997.
[4] N. N. Ledentsov, et al., *Appl. Phys. Lett.* **69** 1343 (1996).
[5] I. L. Krestnikov, S. V. Ivanov, P. S. Kop'ev, N. N. Ledentsov, M. V. Maximov, A. V. Sakharov, S. V. Sorokin, C. M. Sotomayor Torres, D. Bimberg, Zh. I. Alferov, *J. Electron. Materials* **27** 72–75 (1998).
[6] I. L. Krestnikov, et al. *Phys. Stat. Sol.(b)* (to be published).
[7] E. Gross, S. Permogorov and A. Razbirin, *J. Phys. Chem. Solids* **27** 1647 (1966).
[8] M. Strassburg, et al. *Appl. Phys. Lett.* **72** 942–944 (1998).
[9] S. V. Ivanov, S. V. Sorokin, P. S. Kop'ev, J. R. Kim, H. D. Jung, H. S. Park, *J. Crystal Growth* **159** 1–4 (1996).
[10] A. F. Tsatsul'nikov, et al. *Semiconductors* **30** 953–958 (1996).

Ioffe Institute
6th Int. Symp. "Nanostructures: Physics and Technology"
St Petersburg, Russia, June 22–26, 1998.



# Absorption coefficient of InGaAs V-shaped quantum wires integrated in optical waveguides by MBE growth

*F. Filipowitz*†, C. Gourgon†, D. Martin†, Y. Magnenat†, P. Giaccari†, F. Bobard‡ and F. K. Reinhart†

† Institute of Micro- and Optoelectronics
‡ Center of Electron Microscopy
Federal Institute of Technology, CH-1015 Lausanne, Switzerland

**Abstract.** Optical waveguides with InGaAs quantum wires grown by MBE integrated in the middle of their core are investigated. Photocurrents induced by guided TE and TM modes propagating parallel or perpendicular to the quantum wires have been measured and reflect the anisotropy of the optical matrix element. Spectra of the transmitted intensity of these guided modes have been measured, and the attenuation coefficient of the guided modes due to band edge optical absorption in the quantum wire is established. The attenuation coefficient and the evaluation of the overlap integral between the active material and the optical intensity permits to evaluate, for the first time, the absorption coefficient of these quantum wires.

## 1 Introduction

Due to the Van Hove singularity in the density of states, quantum wires (QWR) are thought to be good candidates for future modulators [1]. The fabrication steps to obtain high quality V-shaped GaAs QWR embedded in AlAs/GaAs superlattices on a GaAs substrate by molecular beam epitaxy (MBE) are reproducibly controlled [2]. The next step toward possible application, the integration of InGaAs QWR [3] in optical waveguides is achieved [4]. The evaluation of the attenuation coefficient [5] of guided mode propagating in optical waveguides that contains QWR is a direct evaluation of the potential possibilities of such modulators. Four different waveguides were grown to realize this evaluation, two contain InGaAs QWR of different sizes, one contains an InGaAs quantum well (QW) and one contains the barriers of the QW without any InGaAs deposition.

## 2 Sample fabrication and TEM observation

The fabrication of waveguides that contains QWR consists of three process sequences: (i) MBE growth of the lower waveguide cladding and half of the waveguide core, (ii) patterning of the core by deep UV holographic lithography and wet chemical etching, (iii) MBE growth of the lower barrier, QWR, higher barrier, second part of the core and the upper cladding.

If the lowest energy interband optical transition of the integrated QWR has a higher energy then the band gap of the materials that constitute the waveguide, the variations of transmitted intensities and induced photocurrents of guided modes due to the QWR are drowned in the variations due to the waveguide materials. The QWR must therefore have the lowest band gap among all the materials that constitute the waveguide. We

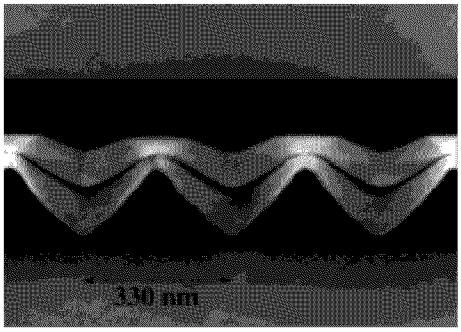


**Fig. 1.** TEM micrograph sample A.

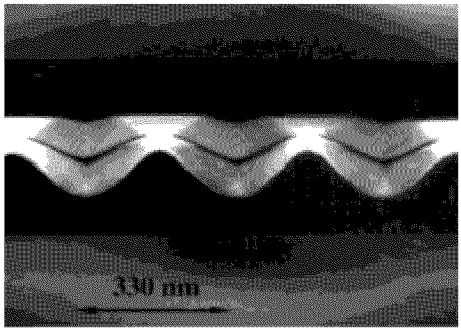


**Fig. 2.** TEM micrograph sample B.

first tried to integrate the widely studied [6–9] GaAs QWR in AlGaAs waveguides. The high dislocations density due to MBE regrowth over a non planar AlGaAs surface forced us to find another solution. Despite the lattice mismatch between $In_{0.16}Ga_{0.84}As$ and GaAs, fabrication of InGaAs QWR [3] with the same photoluminescence signals as the GaAs QWR is now reproducibly achieved. Furthermore the bandfilling effects observed at low excitation density on GaAs QWR [6] are also observed [4] with InGaAs QWR.

Figures 1 and 2 show transmission electron microscopy (TEM) micrographs of samples A and B, respectively. $In_{0.16}Ga_{0.84}As$ QWR are surrounded by a 20 periods superlattice $(AlAs)_4/(GaAs)_8$ one each side. They are in the approximative center of a GaAs waveguide core (black color on the micrograph). The 0.4 $\mu$m thick GaAs core is surrounded by 2 $\mu$m $Al_{0.15}Ga_{0.85}As$ claddings, partly visible on the micrograph. The growth was realized on a n-type GaAs substrate. The QWR, core, superlattice and 0.4 $\mu$m of the upper and lower claddings adjacent to the core are nominally undoped. The rest of the lower (upper) cladding is nominally n-doped (p-doped) with $5 \times 10^{17}$ Si (Be) impurities. The QWR integrated in sample A (B) were fabricated by the deposition of a 45 Å(34 Å) $In_{0.16}Ga_{0.84}As$ QW over a non planar GaAs core. The QWR are embedded in a $(AlAs)_4/(GaAs)_8$ superlattice for two reasons: (i) to remove them from the regrowth interface to avoid defects and impurities in the QWR and (ii) to provide higher barriers to improve the confinement of electrons and especially holes in the QWR. Samples C and D were grown to compare results obtained on sample A and B with more conventional structures. A 60 Å thick $In_{0.16}Ga_{0.84}As$ QW, surrounded by a 20 periods superlattice $(AlAs)_4/(GaAs)_8$ one each side, was deposited in the middle of the 0.4 $\mu$m GaAs core of sample C. The rest of the structures and the nominal doping profile are identical to samples A and B. Sample D is similar to sample C, except that no InGaAs was deposited. Samples C and D were grown with a single growth sequence, as no non planar structuration was necessary. The optical waveguides were designed to support only the fundamental transverse electric (TE) and transverse magnetic (TM) guided mode at a wavelength of 0.9 $\mu$m.

Ohmic contacts were deposited on both side of the diode. Capacitance–voltage (C–V) measurements realized on samples A–D indicate that the growth interruption did not modify the electrical behavior of these pin diodes.

Electrons can move freely along the [011] crystallographic direction. The growth direction, [100], is the strong confinement direction, electrons are less confined along

[01$\bar{1}$], usually called the lateral confinement direction. Comparing Fig. 1 and Fig. 2, the bigger size of the QWR of sample A is easily observed. Differences in the profile of the lower part of the GaAs core are explained in [4]. The absence of dislocations indicates the good efficiency of the desorption prior to the regrowth.

## 3 Photocurrent spectra

The probability that a photon induces an electronic transition between valence and conduction band is, in the dipole approximation, proportional to the square of the optical dipole matrix element, $|\langle f|\mathbf{e}\cdot\mathbf{p}|i\rangle|^2$ where f(i) is the conduction (valence) band state, $\mathbf{p}$ the momentum operator and $\mathbf{e}$ a unitary vector in the direction of the optical electrical field. Standard polarized photoluminescence (PL) and photoluminescence excitation made on QWR are possible for $\mathbf{e}$ aligned along two orthogonal directions only. The advantage of the integration of QWR in planar waveguide is the possibility to realize measurements with $\mathbf{e}$ aligned along three orthogonal directions. We have measured photocurrents induced by guided TM or TE modes excited by light propagating along the [011] or [01$\bar{1}$] direction using edge coupling. The light was generated by a tungsten filament and passes through a monochromator. The optical power at the monochromator exit slot is approximately 1 nW for a bandwidth of 1 nm. Results of measurements made on sample A are shown in Fig. 3 for TM modes and in Fig. 4 for TE modes. Significative photocurrents are obtained at forward bias in the range of 0.2 to 1 volt. The intensity of the photocurrent strongly depends on the applied bias, not the profile of the spectra. Due to the fact that different diodes of samples A and B were used, it will be difficult to compare photocurrent spectra on a absolute scale. The direction of the optical electrical field of TM modes is nearly parallel to the [100] direction independently of the propagation direction. The direction of the optical electrical field of a TE mode depends on the propagation direction of the mode. It is aligned along [011] ([01$\bar{1}$]) if the TE mode propagates along [01$\bar{1}$] ([011]). The photocurrent generated by the guided light is proportional to the number of absorbed photons per unit time for low light level. In this case the photocurrent is also proportional to the square of the optical matrix element of the QWR. The qualitatively different features of the photocurrents spectra are presented in Fig. 3 and Fig. 4 and reflect the anisotropy of the optical matrix element of QWR.

At the same photon energy that the photocurrent peak induced by TM modes, qualitatively different photocurrent spectra are induced by TE modes that propagate along [011] or [01$\bar{1}$]. These qualitatively different photocurrent spectra are well explained by the expected anisotropy of the optical matrix element of QWR [10].

The photocurrent spectra of sample B (not shown here) have the same features as those shown on Fig. 3 and Fig. 4. They are only shifted in energy. Sample D showed no significative photocurrent in the 900–1000 nm range.

This is the first time that the anisotropy of the optical matrix element of transitions induced by an electrical optical field aligned along [100] is observed with our technique.

## 4 Transmission spectra

Spectra of the transmitted intensity of guided modes are under investigations. At the same photon energy, the decrease of the transmitted intensity corresponds to the increase of the photocurrent intensity and to the lowest energy photoluminescence peak of the

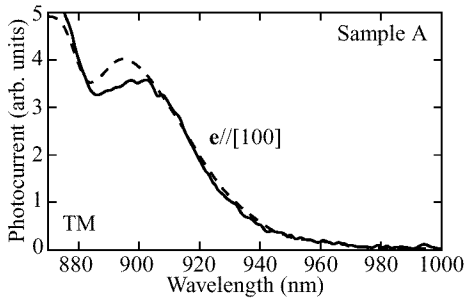


**Fig. 3.** Photocurrent induced by TM modes propagating either along [011] (dotted line) or along [01$\bar{1}$] (solid line). The direction of the optical electrical field, **e**, is indicated.

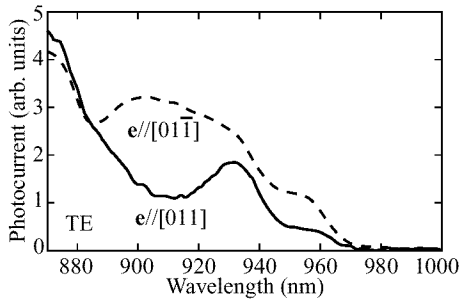


**Fig. 4.** Photocurrent induced by TE modes propagating either along [011] (dotted line) or along [01$\bar{1}$] (solid line). The direction of the optical electrical field, **e**, is indicated.

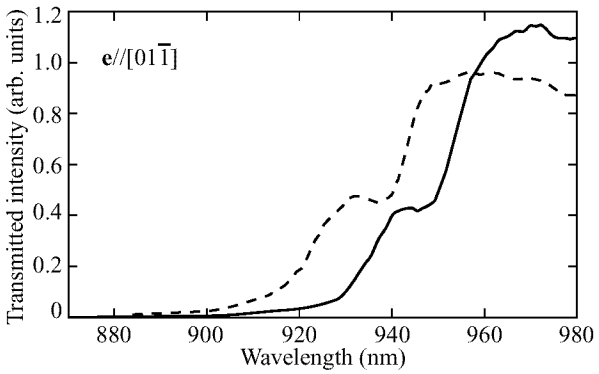


**Fig 5.** Transmitted intensity of TE modes propagating along [011] in sample A (solid line) or sample B (dotted line).

QWR. This observation establishes that the attenuation of the guided mode is due to band edge optical absorption in the QWR. An estimation of the absorption coefficient of QWR, $\alpha_{QWR}$, can be deduced from the experimental determination of the attenuation coefficient, $\alpha_{att}$, of the guided mode and the evaluation of the overlap integral between the active material and the optical intensity, $\Gamma$, using the relation $\alpha_{att} \cong \Gamma\alpha_{QWR}$.

Spectra of the transmitted intensity of guided modes are realized with a continuous wave operation Ti-Sapphire Laser with a linewidth of about 40 GHz. The optical power at the Ti-Sapphire exit was approximately 1 mW. Figure 5 shows spectra of guided TE modes propagating along [011] in samples A and B. In the case of sample A, the decrease between 950–960 nm and 930–940 nm corresponds to photocurrent peaks, shown in Fig. 4, around 955 nm and 932 nm, respectively. Furthermore the lowest energy photocurrent peak correspond to the lowest energy peak observed in PL measurements. The same correspondence between decrease of the transmitted intensity, photocurrent increase and PL peaks can be made with sample B. The energy shift between the two spectra shown in Fig. 5 is due to the difference of the QWR size. The attenuation coefficient associated with the fundamental transition observed by the

TE mode propagating along [011] in sample A (B) is estimated to be $\alpha_{att} \approx 6\,cm^{-1}$ ($\alpha_{att} \approx 5.5\,cm^{-1}$). A rough estimation of the overlap factor gives $\Gamma \cong 0.24\%$ (0.18%), thus the absorption coefficient of QWR is in the range of: $\alpha_{QWR} \cong 2.5{-}3 \times 10^3\,cm^{-1}$. This low value has to be confirmed by further experiments.

The low absorption coefficient of QWR is in agreement with the lower attenuation coefficient observed for guided modes propagating in sample A or B as compared to the guided modes propagating in sample C.

## 5 Conclusion

The absorption coefficient of QWR has been experimentally evaluated for the first time by direct measurement of transmission changes at the band edge. The low value of this absorption coefficient is in contradiction with simple theoretical expectations [1]. Photocurrent spectra show the expected anisotropy of the optical matrix element of QWR [10].

## References

[1] D.A.B. Miller, D.S. Chemla and S. Schmitt-Rink, *Appl. Phys. Lett.* **52** 2154 (1988).
[2] U. Marti, M. Proctor, D. Martin, F. Morier-Genoud, B. Senior and F.K. Reinhart, *Microelectr. Eng.* **13** 391 (1991).
[3] P.H. Jouneau, F. Bobard, U. Marti, J. Robadey, F. Filipowitz, D. Martin, F. Morier-Genoud, P.C. Silva, Y. Magnenat and F.K. Reinhart, *Inst. Phys. Conf. Ser.* **146** 371 (1995).
[4] C. Gourgon, F. Filipowitz, J. Robadey, D. Martin, Y. Magnenat, P.C. Silva, F. Bobard and F.K. Reinhart, this conference, (1998).
[5] R.G. Hunsperger, *Integrated Optics: Theory and Technology*, Springer Series in Optical Sciences, 3rd ed. (1991).
[6] R. Rinaldi, M. Ferrara, R. Cingolani, U. Marti, D. Martin, F. Morier-Genoud, P. Ruterana and F.K. Reinhart, *Phys. Rev. B* **50** 11795 (1994).
[7] R. Rinaldi, P.V. Giugno, R. Cingolani, F. Rossi, E. Molinari, U. Marti and F.K. Reinhart, *Phys. Rev. B* **53** 13710 (1996).
[8] R. Rinaldi, R. Cingolani, M. Lepore, M. Ferrara, I.M. Catalano, R. Cingolani, F. Rossi, L. Rota, E. Molinari, P. Lugli, U. Marti, D. Martin, F. Morier-Genoud, P. Ruterana and F.K. Reinhart, *Phys. Rev. Lett.* **73** 2899 (1994).
[9] F. Rossi and E. Molinari, *Phys. Rev. Lett.* **76** 3642 (1996).
[10] F. Filipowitz and F.K. Reinhart, *Helv. Phys. Acta* **70** (1997).

Ioffe Institute
6th Int. Symp. "Nanostructures: Physics and Technology"
St Petersburg, Russia, June 22–26, 1998.



# Optical reflection spectra of open ZnCdSe/ZnSe nanowires

*S. O. Kognovitsky*, V. V. Travnikov, S. A. Gurevich, S. I. Nesterov, V. I. Skopina, M. Rabe† and F. Henneberger†
Ioffe Physico-Technical Institute, St.Petersburg, Russia
† Humboldt University, Berlin, Germany

Most of the nanostructures fabricated by lithography and subsequent chemical etching have in their active zones surfaces directly open to air. Large difference between the dielectric constants of semiconductor and vacuum on vertical side walls in such structures lead to spatial redistribution of the electric components of the electromagnetic field in the vicinity of the structures. In open (unovergrown) quantum well wire (QWW) structures in particular such redistribution result in strong linear optical anisotropy [1]. This linear anisotropy is much stronger than one due to QWW effect itself and it can be observed for wires the width of which in nanoregion is much larger than necessary for quantum wire effect. Further we will use for such structures the term nanowires. Strong linear polarization along wire axes was observed in open QWW luminescence and Raman spectra in [2, 3]. The presented paper is devoted to investigation of the linear anisotropy of the optical reflection spectra in open nanowires (ONW) ZnCdSe/ZnSe.

Open ZnCdSe/ZnSe nanowires were fabricated using interference lithography with subsequent Reactive Ion Etching [4] from undoped structures contained 5 nm thick $Zn_{1-x}Cd_xSe$ single quantum well ($x = 16\%$) sandwiched between 20 nm cap and 25 nm buffer ZnSe layers and grown on GaAs (100) substrate. The period of wire-array structure was equal to $L = 250$ nm. The wires had almost rectangle cross section with width $a = 70$ nm and height $b = 60$ nm.

The investigation of the reflection spectra was carried out for one of the obtained samples with ONW at $T = 77$ K. The measurements were made at normal incident angle of the collimated (0.5°) white light beam with linear polarization parallel or perpendicular to the wire direction. Different laser lines with close excitation density values ($\sim 10\,W/cm^2$) were used for the investigation of the influence of additional photoexcitation on the reflection spectra.

The reflection spectra for the light polarized parallel ($R_\perp(\lambda)$) and perpendicular ($R_\parallel(\lambda)$) to the wire direction are presented in the Fig. 1, which shows the essential difference in the "background" (without exciton peculiarities) reflection values $R_\perp(\lambda)$ and $R_\parallel(\lambda)$. The relation $R_\perp/R_\parallel$ ranges up to 2.5 in the wavelength range 450–500 nm. An increase of the reflection coefficients in high energy region is evidently connected with broad interference minima in spectral region 440–470 nm.

The additional pumping of photocarriers by laser line 441.6 nm lead to increasing of $R_\perp$ values on $\sim 15\%$ in the all measured wavelength range but it does not change the $R_\parallel$ spectrum. Additional photoexcitation ($\lambda_{ex} = 488-632.8$ nm) inside forbidden band gap of the ZnCdSe/ZnSe structure doesn't influence on the reflection spectra.

In the initial quantum well structures additional photocarriers do not have essential influence on the reflection coefficient in wide spectral range exclusive of exciton resonance region. This points to the fact that the $R_\perp$ change is an effect typical for the ONW structures only.

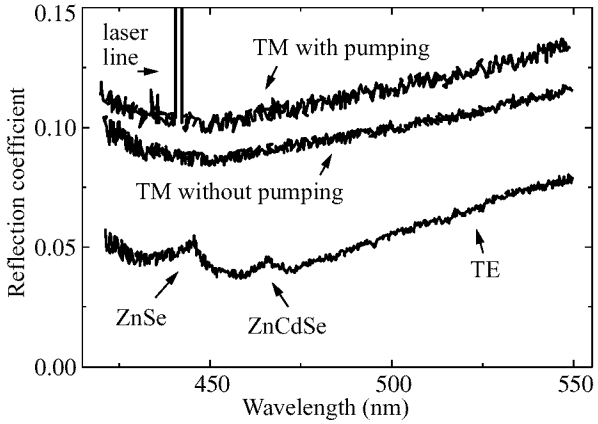


**Fig 1.**

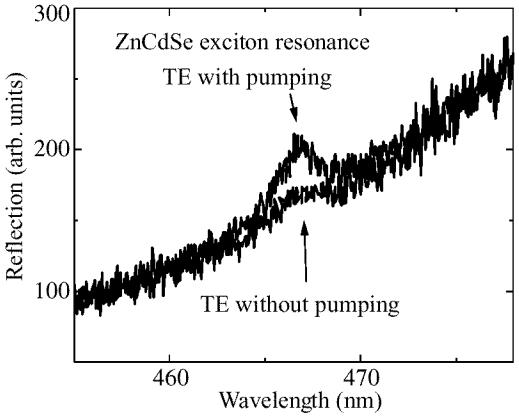


**Fig 2.**

ZnSe barrier and ZnCdSe layer exciton resonances appear only in the reflection spectra for parallel polarization $R_{\|}(\lambda)$. The $R_{\perp}(\lambda)$ spectrum doesn't have any resonance peculiarities. Amplitude of these peculiarities was sensitive to the additional pumping with photon energy more then the ZnSe forbidden gap energy. It is seen from Fig. 2 in which one of the spectra was obtained under simultaneous pumping by the laser line $\lambda_{ex} = 441.6$ nm (luminescence intensity gave neglected small contribution in registered signals). The same changes took place for ZnSe barrier exciton resonance.

The exciton resonance behaviour can be explained taking into account the anisotropy of spatial distribution of the electric component of the electromagnetic field in the vicinity of open nanowires. Local electric fields inside the ONW corresponding to parallel polarization of the external electromagnetic wave (TE-wave) must be essentially larger than corresponding values for perpendicular polarization (TM-wave) [5]. In a dipole approximation the probabilities of optical transition matrix elements are proportional to the scalar product of the local electric field and the interband dipole momentum. As a

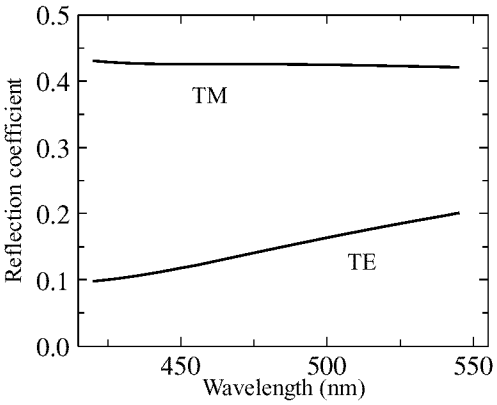


**Fig 3.**

result due to great difference of the local electric fields the optical transition probabilities for parallel polarization must be larger than the ones for perpendicular polarization. It is the reason of strong linear polarization along wire direction which was observed in luminescence and Raman spectra of open QWW [3]. The manifestation of exciton resonances only in $R_{\|}(\lambda)$ spectra is also connected with the same reason evidently and it shows that the exciton resonance oscillator strength for parallel polarization is much larger than the one for perpendicular polarization.

The influence of additional photocarriers on the exciton resonant amplitudes in the reflection spectra is the result of exciton damping decrease due to the decrease of band bending near nanowires surfaces. Such decrease usually takes place as a result of carrier trapping by charged surface states.

Behaviour of the "background" reflection spectra over the wide spectral range can interpreted in the frame of model, which have been suggested for calculation of short-period grating reflection spectra in [7]. In this case grating corresponding to the surface open ZnSe wire-array structure is considered as an anisotropic uniaxial film on GaAs substrate surface. The film is characterized by two effective refractive indexes $n_0$ and $n_e$ for the ordinary (TE) and unordinary (TM) waves correspondingly:

$$n_0^2 = a n_{\mathrm{ZnSe}}^2/L + (L-a) n_{\mathrm{air}}^2/L,$$

$$1/n_e^2 = a/\left(L n_{\mathrm{ZnSe}}^2\right) + (L-a)/\left(L n_{\mathrm{air}}^2\right).$$

The effective refractive indexes for the film were determined with the use of our real structure parameters including the real and the imaginary parts of ZnSe and GaAs material. At the calculation of the reflection spectra we took into account the reflection from two parallel surfaces (air/film, film/substrate) [8]. The calculated spectra shown in Fig. 3 can qualitatively explain such found feature of the "background" reflection spectra as the essential excess of $R_{\perp}$ over $R_{\|}$. Further theoretical analysis of the reflection spectra is in progress.

Additional photocarries usually lead to the neutralization of the charged states on the wire surface. As a result the built-in transverse electric field distribution are changed essentially. We suggest this changing to be a reason of the pumping influence on the

reflection spectrum $R_{\perp}$ only. It is necessary farther research for the full identification mechanism of this effect.

To conclude, we have found the essential linear polarization anisotropy in the reflection spectra of open nanowires over a wide spectral range. Two mechanisms is responsible for the anisotropy. The first one displayed in exciton resonance region is due to the distribution anisotropy of the electric component of the electromagnetic field in the vicinity of open nanowires. The second one connected with the "background" reflection spectra over the whole spectral range is a consequence of grating effects.

This work was supported by Russian Foundation for Basic Research (Grant No. 96-02-00131) and by NATO International Research Programs (NANO.LG 950382).

## References

[1] N. A. Gippius, S. G. Tikhodeev, A. Forchel, V. D. Kulakovskii, *Superlattices and Microstructures* **16**(2) 165 (1994).
[2] P. Ils, Ch. Greus, A. Forchel, V. D. Kulakovskii, N. A. Gippius, S. G. Tikhodeev, *Phys. Rev. B* **51**(7) 4272 (1995).
[3] J. Rubio, Z. H. van Der Meulen, N. Mestres, J. M. Calleja, K. H. Wang, P. Ils, A. Forchel, N. A. Gippius, S. G. Tikhodeev, *Sol. St. Electronics* **40** 707 (1996).
[4] S. A. Gurevitch, A. V. Kolobov, M. M. Ljubin, S. I. Nesterov, M. M. Kulagina, F. N. Timofeev, *Zh. Tech. Fiz.* **18** 85 (1992).
[5] U. Bockelmann, *Europhys. Lett.* **16**(6) 601 (1991).
[6] N. A. Gippius, S. G. Tikhodeev, L. V. Keldysh, *Superlattices and Microstructures* **15**(4) 479 (1994).
[7] P. Yeh, *Optics Communications* **26**(3) 289 (1978).
[8] E. L. Ivchenko, G. E. Pikus, *Superlattices and other Heterostructures. Symmetry and Optical Phenomena*, Springer Series in Solid-State Sciences 110, 1997.

Ioffe Institute
6th Int. Symp. "Nanostructures: Physics and Technology"
St Petersburg, Russia, June 22–26, 1998.



# Giant optical nonlinearity of heterostructures with InP self-assembled quantum dots

*V. Davydov*†‡, I. Ignat'ev†§, H.-W. Ren†, S. Sugou†¶, and Y. Masumoto†*
† Single Quantum Dot Project, ERATO, JST, Tsukuba Research Consortium, Ibaraki 300-26, Japan
‡ On leave from S. I. Vavilov State Optical Institute, St. Petersburg, Russia
§ On leave from Saint-Petersburg State University, St. Petersburg, Russia
¶ Opto-Electronics Research Laboratories, NEC Corporation, Tsukuba, Ibaraki 305, Japan
* Institute of Physics, University of Tsukuba, Ibaraki 305, Japan

**Abstract.** Quantum dots (QD) are an attractive object for study due to their expectable nonlinear properties. We studied nonlinear reflection of heterostructures with self-assembled InP QDs by use of specially designed pump-probe technique of high sensitivity. We discovered that built-in electric field present in our structures considerably enhances the effect of the QD excitation and allow us to study it at rather low level of the excitation power.

## Introduction

Among the other semiconductor nanostructures quantum dots (QDs) attract considerable interest because of their delta-like density of states. This peculiarity leads to the high nonlinearity both in optical and electrical properties of the dots. A number of the interesting manifestations of the optical nonlinearity is really found by few groups [1–3]. The investigations in this field are of particular interest because they promise wide range of applications in the fields of optics, opto-electronics and electronics.

## 1 Experimental

This work is devoted to study nonlinear reflection of the heterostructures with the InP self-assembled QDs. The structures were grown by gas source molecular beam epitaxy (GS MBE) on $n^+$ GaAs substrates. They contain one layer of InP QDs between $Ga_{0.5}In_{0.5}P$ barrier layers grown on a GaAs buffer layer. We studied a few structures with the different thicknesses of the barrier layers and the QD sizes.

Pump-probe experiments were performed by means of the setup which is schematically drawn in Fig. 1. This setup includes a femtosecond Ti:sapphire laser "Tsunami" (power source "Millenia", frequency 82 MHz, pulse duration 0.1–1 ps) which is tunable from about 700 to 850 nm. Amplitude modulation of the pump and probe beams at different frequencies, optical phase shift between them and lock-in detection of the signal modulated at the differential frequency let us to avoid noises from the scattered light and achieve high sensitivity of detection of nonlinear reflection whose detection limit is about $10^{-7}$ times of the linear reflection.

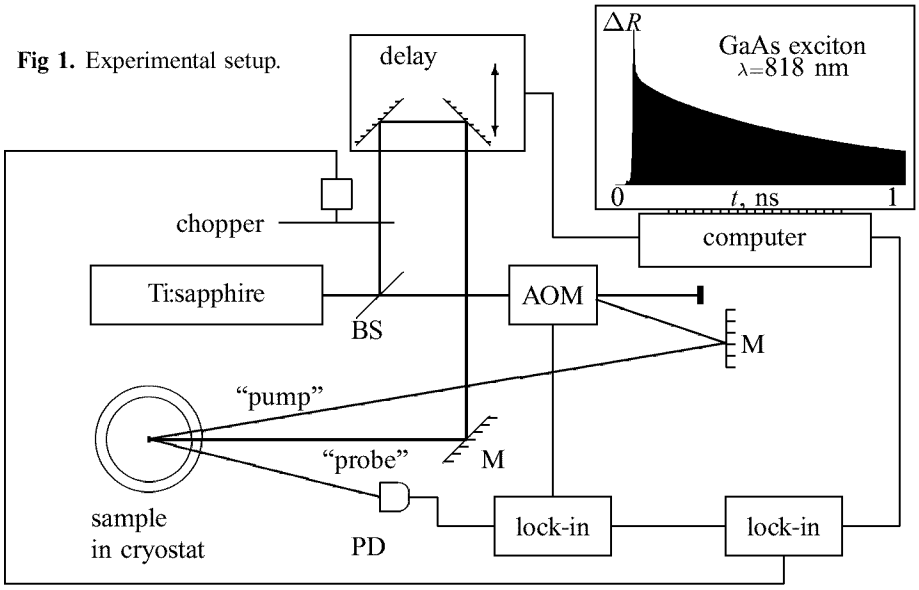


**Fig 1.** Experimental setup.

## 2 Results and discussion

In Fig. 2 the typical time dependences of a pump-probe signal are presented. This signal exhibits short risetime (equal to the time resolution of our setup) and exponential decay with a few characteristic times.

In the spectral region of the InP QD photoluminescence (PL), 710–760 nm for a sample QDO1505 where the PL intensity is at the level of 0.1 times of the peak intensity, main decay time is about 0.8 ns. This decay is presumably due to the energy relaxation in the QDs. Also there is a long component of the signal with characteristic time much longer than 12 ns that is a time separation between successive light pulses in our setup. It is seen as a constant pedestal and caused probably by the space separation due to the diffusion of the photogenerated carriers in the GaAs layer produced by pump pulses. Under the stronger excitation a fast decay time component of about 30 ps is also observed. Most probably, it is due to energy relaxation of hot carriers in the GaAs buffer layer. In the wavelength region beyond the QD PL band, a contribution of the main decay component decreases rapidly and is hardly seen up to the GaAs bulk exciton spectral region.

Pump-probe signal as is seen in Fig. 2 has an interesting spectral dependence which looks like intense oscillations with almost constant period of 6.5 nm. We studied this phenomenon in details in [4] and found that this behaviour is due to build-in electric field which is present in our structures. It leads to Franz-Keldysh oscillations (FKO) in the reflection spectrum. A study of the spectral behaviour of FKO and their dependence on pump power together with an analysis of time evolution of the signal provides us strong evidence that we really detect a change of reflection due to optical excitation of QDs in spite of the low optical density of QDs. We found that the built-in electric field

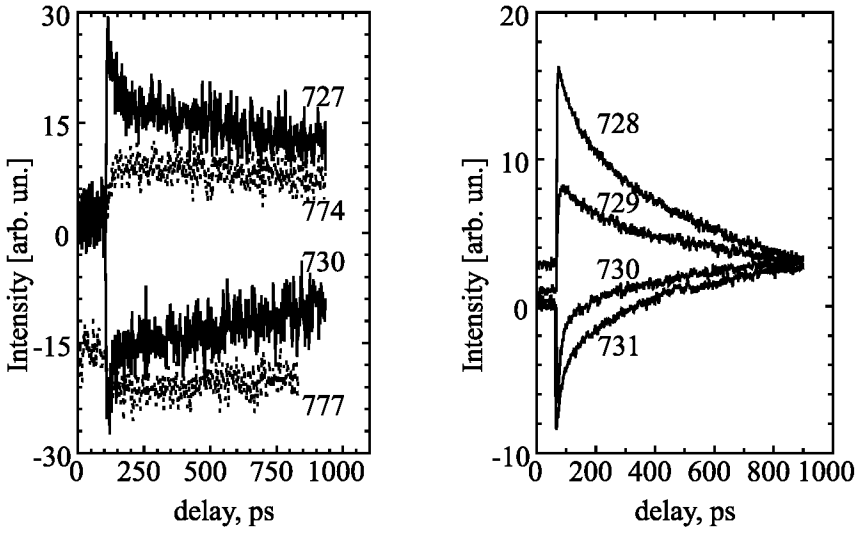


**Fig 2.** Pump-probe signal for the sample QDO1505 at the different spectral points (marked by wavelength in a units of nm) under the pump power density of $P = 0.1$ W/cm$^2$ (left panel) and 100 W/cm$^2$ (right panel).

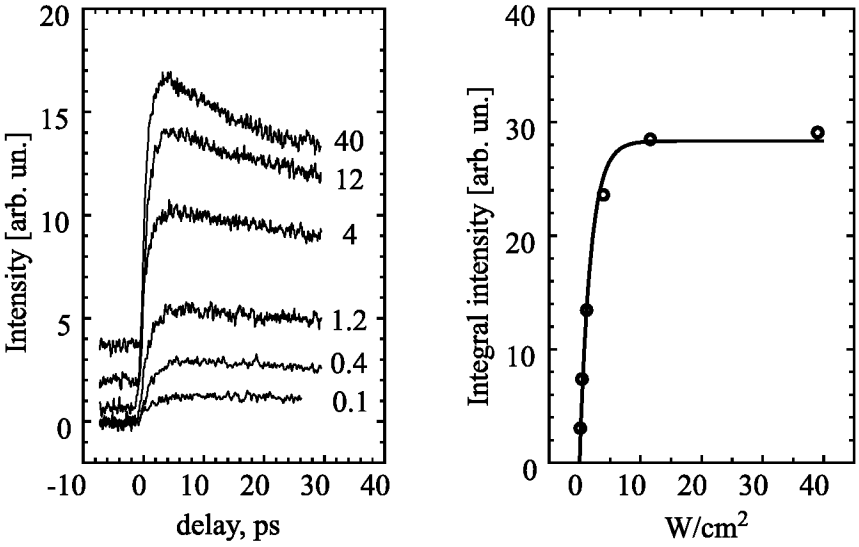


**Fig 3.** Left panel: pump-probe signal under different pump power densities (in a unit W/cm$^2$); right panel: power dependence of the integrated signal (circles) and its fitted line by (1) with $I_0 = 28$ and $P_0 = 1.8$ W/cm$^2$.

can drastically enhance the effect of the QD excitation and allows us to study it at very low excitation levels.

A dependence of the pump-probe signal on the pump power is most important for the study of the optical nonlinearity. It is shown in Fig.3 for the spectral point of 727 nm. One can clearly see that these dependences exhibit saturation which can be fitted by the simple equation

$$I = I_0 \left(1 - e^{-\frac{P}{P_0}}\right). \quad (1)$$

Saturation power $P_0$ is only about 1.8 W/cm$^2$. Inverse of the areal density of QDs estimated by means of atomic force microscopy is $0.1 \times 0.1$ $\mu$m$^2$. This means that 1.8 W/cm$^2$ corresponds to only 9 photons per dot per pulse. The saturation power has the same order of magnitude for all studied heterostructures in the spectral points inside the region of QD absorption. We do not observe any quick saturation of signal in the spectral region beyond the QD PL band.

## 3 Conclusion

The heterostructures with InP self assembled QDs are studied by the pump-probe method. We found that the build-in electric field which is present in the studied structures allows us to detect a changes of reflection due to optical excitation of QDs under extremely low pump power. In the spectral region of QD absorption, a pump-probe signal exhibits a quick saturation. Saturation power is only about 2 W/cm$^2$ or 10 photons per dot per pulse. This fact evidently shows the giant nonlinearity of the QDs.

*Acknowledgements*

We acknowledge Dr. E. Tokunaga for his efforts on tuning the software and for the creative discussions.

## References

[1] P. Castrillo, D. Hessman, M.-E. Pistol, S. Anand, N. Carlsson, W. Seifert, and L. Samuelson *Appl. Phys. Lett.* **67** 1905 (1995).
[2] S. Farfad, R. Leon, D. Leonard, J. L. Merz, and P. M. Petroff *Phys. Rev. B* **52** 5752 (1995).
[3] M. Grundmann, N. N. Ledentsov, O. Stier, J. Bohrer, D. Bimberg, V. M. Ustinov, P. S. Kop'ev, and Zh. I. Alferov *Phys. Rev. B* **53** R10509 (1996).
[4] V. Davydov, I. Ignat'ev, H.-W. Ren, S. Sugou, and Y. Masumoto *In this volume.*

Ioffe Institute
6th Int. Symp. "Nanostructures: Physics and Technology"
St Petersburg, Russia, June 22–26, 1998.



# Photoluminescence of 1.8 ML InAs quantum dots grown by SMEE on GaAs(100) misoriented surface

R. B. Juferev†, A. B. Novikov†, *B. V. Novikov*†, S. Yu. Verbin†,
Dinh Son Thach†, G. Gobsch‡, R. Goldhahn‡, N. Stein‡, A. Golombek‡,
G. E. Cirlin§, V. G. Dubrovskii§ and V. N. Petrov§

† Institute of Physics, St. Petersburg State University, 198904 St.Petersburg, Russia
‡ Institut für Physik, Technische Universität, 98684 Ilmenau, Germany
§ Institute for Analytical Instrumentation of Russian Academy of Sciences,
Rizhsky 26, 198103 St. Petersburg, Russia

**Abstract.** Photoluminescence (PL) study results of InAs/GaAs quantum dot (QD) arrays obtained by submonolayer migration enhanced epitaxy on GaAs(100) substrates misoriented towards [001] direction at InAs thickness fixed to 1.8 monolayers are reported. It is shown that PL peaks from QDs are shifted towards shorter wavelengths and their full width at half maxima decreases from 95 meV to 33 meV as misorientation angle raises from 0 to 7 degrees, corresponding to the decrease of mean lateral size of QDs and of the dispersion of their size distribution. The temperature dependence of PL spectra at 4.2–300 K may indicate to two maxima in the QDs size distribution.

## Introduction

One of the most promising ways to fabricate nanostructures is the direct quantum dots (QDs) formation due to self-organization effects during molecular beam epitaxial (MBE) growth in mismatched heteroepitaxial systems. Spontaneous formation of the arrays of three dimensional (3D) islands was observed in various semiconductor systems, in particular InAs/GaAs [1]. The properties of InAs/GaAs QDs was studied by various methods. However, the main attention was paid to the study of nanoobjects obtained by conventional MBE on singular GaAs(100) surfaces. Recent scanning tunneling microscopy (STM) study shows that the use of submonolayer migration enhanced epitaxy (SMEE) technique for QDs fabrication and/or the growth on vicinal substrates lead to the formation of QDs with lower deviation from mean size [2]. The aim of this work is the study of the photoluminescence and its temperature dependence of InAs/GaAs QD arrays obtained by SMEE on the GaAs(100) misoriented substrates.

## 1 Experiment

The structures consist of the InAs layer containing QDs confined from both sides with wide-gap GaAs and $Al_{0.25}Ga_{0.75}As$/GaAs superlattices (5 pairs, 2nm/2nm each) [3]. Singular and misoriented towards [001] and [010] direction by 3°–7° GaAs(100) semi-insulating substrates are used. For better homogeneity of temperature distribution of substrate heater and molecular fluxes on the surface, the samples are indium mounted side-by-side on the same substrate holder. For SMEE growth [2], the shutters of In and As are switched on alternatively. In our experiments, 0.5 ML portion of In deposited during each pulse is followed by exposing the surface under $As_4$ flux. The growth

conditions are maintained the same for all samples: In flux intensity is $6 \times 10^{13}$ $cm^{-2}s^{-1}$, $As_4$/In fluxes ratio is about 10, substrate temperature for InAs deposition is 470°C. The surface morphology is controlled in situ by reflection high energy electron diffraction (RHEED). Samples are grown with mean InAs thickness of 1.8 ML (just after the decomposition of pseudomorphic layer into the array of QDs) and of 3 ML, when a well-resolved spotty RHEED pattern is clearly observed.

## 2 Results and discussion

The band with the intensity maximum near 1.3 eV is observed in typical PL spectra of examined samples excited by $Ar^+$ laser at 4.2 K. This band corresponds to the exciton emission from QDs which is in agreement with the results obtained in [4]. In addition to this broad band emission peak, the lines with maxima at 1.514, 1.507 and 1.491 eV are observed near GaAs absorption band-edge. We assume these lines to be associated with the emission of GaAs free and bound excitons and acceptor state of carbon [5] from the residual atmosphere in the growth chamber, respectively. These results are confirmed by our study of PL excitation spectra and PL intensity maximum dependence on InAs layer thickness [6] and are in agreement with the results of STM study of similar structures [7] and also of the structures grown by MBE mode [4].

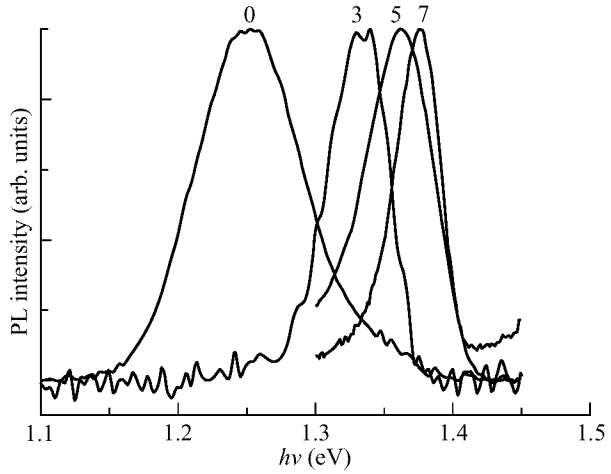


**Fig 1.** The dependence of QDs emission spectra at $T = 4.2$ K on the substrate misorientation angle towards [001] direction. The mean thickness of InAs is fixed to 1.8 ML.

Monotonous shift of intensity maximum from 1.25 eV to 1.37 eV is observed as misorientation angle towards [001] direction increases from 0° (singular substrate) to 7°. The emission band full width at half maxima (FWHM) decreases from 95 meV to 33 meV. To the best of our knowledge, the latter value is close to the record results reported on InAs/GaAs QD arrays. Strong decrease of FWHM with the rise of the misorientation angle could be attributed to the size distribution narrowing at increasing vicinity angle, while the mean lateral size of QDs decreases. Similar behavior was observed in STM studies of InAs/GaAs QDs grown by SMEE [7] methods on vicinal surfaces.

The dependence of QDs emission spectra on the substrate misorientation angle

towards [010] direction is qualitatively same but with the greater width of QD emission band. The exciton emission band of QDs is observed near 1.35 eV in PL spectrum of the sample with the surface misoriented to 5° towards [010] direction obtained at 4.2 K. This band ($QD_1$) have the weak longwave "tail". PL spectrum doesn't almost depend on the temperature up to 80 K except the moderate broadening of $QD_1$ band. At this temperature the raise of cw $Ar^+$ excitation intensity from 10 to 200 mW leads to superlinear dependence of $QD_1$ band intensity, to narrowing of the band from 80 to 65 meV and shortwave shift of its maximum 10 meV. We assume this effect to filling of QD levels and to the superluminescence.

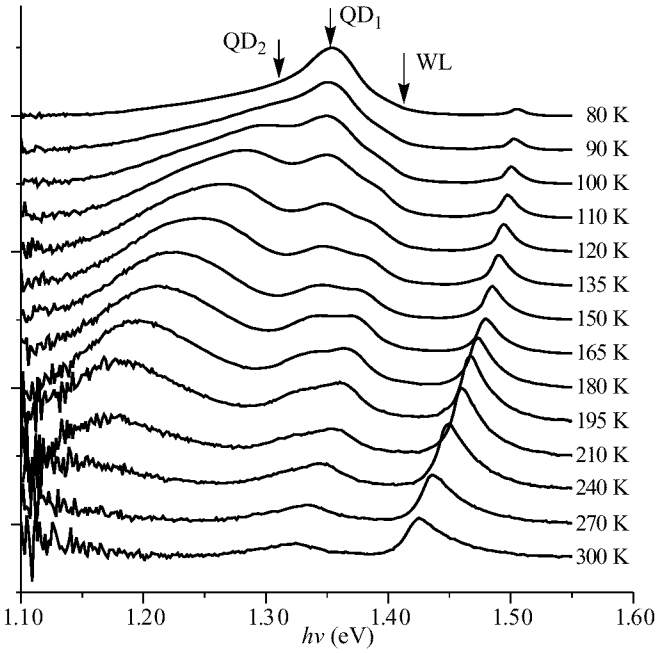


**Fig 2.** Temperature dependence of PL spectra at $T = 80-300$ K.

The relative intensity of $QD_1$ band longwave "tail" is increased at $T > 100$ K and then the latter transforms to the maximum ($QD_2$) in the PL spectrum. Besides that the once more band (WL) appears at the wavelengths shorter than the $QD_1$ one. The WL band was assumed to the emission of InAs wetting layer.

The PL complex curve has been decomposed to three gaussian contours in the whole temperature range 80–300 K. The $QD_2$ band is much more broader than $QD_1$ one and the temperature shift of $QD_2$ maximum is nearly by five times higher ($1 \times 10^{-3}$ eV/K) than temperature shifts of $QD_1$ and WL maxima. The latter shifts are near $2 \times 10^{-4}$ eV/K and are close to temperature shift of GaAs bandgap.

STM study shows that the main part of QDs ($QD_1$) has the much more narrow size distribution than the small fraction of QDs with larger size and of QD complexes ($QD_2$) [8]. We assume both QD emission band to exciton recombination in corresponding fractions of QDs with different mean size so. In result the distribution of confinement energy and its mean value is lower for $QD_1$ than for $QD_2$ and $QD_2$ energy levels form the longwave "tail" of states.

The temperature increase leads to the delocalization of carriers from $QD_1$ during their lifetime and their diffusion through wetting layer to deeper energy levels of $QD_2$. Then the temperature shift of $QD_2$ emission maximum may be also explained by carrier delocalization from shallow levels of $QD_2$ "tail" of states.

## 3 Conclusions and aknowledgments

To conclude, we have studied PL spectra of InAs QDs grown by SMEE method on the GaAs(100) substrates misoriented towards [001] direction by inclination angles up to 7°. It is shown that PL peaks become narrower and are shifted towards shorter wavelengths with the rise of misorientation angle at fixed amount of InAs deposited. This corresponds to the decrease of mean lateral size of QDs and of the dispersion of their size distribution. The existence of two maxima in the QDs size distribution obtained from temperature dependence of PL spectra is confirmed by results of STM study.

Authors thank Dr. A. O. Golubok for helpful discussion. This work was partially supported by Russian Foundation "Integration of Fundamental Science and High School–1997-2000" (grant No. 326.75).

## References

[1] Goldstein L. et al. *Appl. Phys. Lett.* **47** 1099 (1985).
[2] Tsyrlin G. E., Golubok A. O., Tipissev S. Ya. and Ledentsov N. N. *Semiconductors* **29** 884 (1995).
[3] Ledentsov N. N., Maximov M. V., Tsyrlin G. E., Petrov V. N. and Guryanov G. M. *Semiconductors* **29** 627 (1995).
[4] Patane A. et al. *Proc. 22th Int. Conf. on Phys. Semicond.*, Berlin, Germany, World Scientific **2** 1305 (1996).
[5] Abramov A. P., Abramova I. N., Verbin S. Yu., Gerlovin I.Ya., Grigor'ev S. R., Ignat'ev I. V., Karimov O. Z., Novikov A. B., Novikov B. V. *Semiconductors* **27** 647 (1993).
[6] Dubrovskii V. G., Petrov V. N., Cirlin G. E., Juferev R. B., Novikov A. B., Novikov B. V., Verbin S. Yu., Gobsch G., Goldhahn R., Stein N., Golombek A. *phys. stat. sol. (a)* to be published (1998).
[7] Cirlin G. E., Petrov V. N., Golubok A. O., Tipissev S. Ya., Dubrovskii V. G., Guryanov G. M., Ledentsov N. N., Bimberg D. *Surf. Sci.* **377-379** 895 (1997).
[8] Cirlin G. E., Petrov V. N., Dubrovskii V. G. et al. *Semiconductors* **31** 768 (1997).

Ioffe Institute
6th Int. Symp. "Nanostructures: Physics and Technology"
St Petersburg, Russia, June 22–26, 1998.



# Magnetic field effects on carriers capture to quantum dots

*G. V. Astakhov*, V. P. Kochereshko, V. P. Evtikhiev, V. E. Tokranov and I. V. Kudryashov
Ioffe Physico-Technical Institute RAS, St. Petersburg, Russia

An effect of carrier redistribution between different size quantum dots (QD) in a self-ordered InAs/GaAs QD structures has been studied by magneto-luminescence (PL) at helium temperatures.

The InAs/GaAs QDs were grown by Stranski–Krastanow method on (100) GaAs substrates. A small misorientation angle of substrate by 1–4 degree to [010] was used in order to increase the QDs density with high homogeneity and to reduce a QDs coalescence which leads to the exciton nonradiative recombination [1, 2].

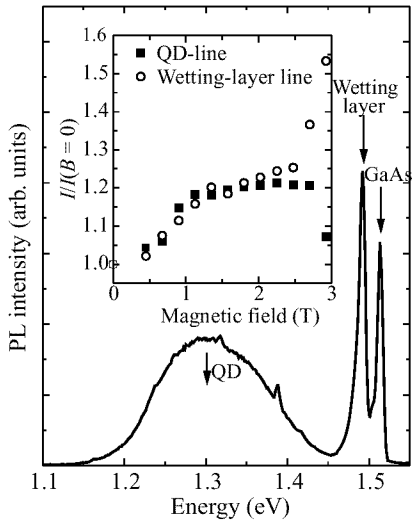


**Fig 1.** PL Spectrum from the sample with misorientation angle of substrate 4 degree at zero magnetic field. The temperature is 1.6 K. Inset: Integral intensity of QD-line (solid square) and wetting-layer line (open circle) in the magnetic field normalized on integral intensity at zero magnetic field.

The studied PL spectra (excited by HeNe laser) consists of three lines (Fig. 1). The high energy line at 1.513 eV coincides with an exciton recombination in the bulk GaAs barriers. The line at 1.494 eV (wetting-layer line) is due to an exciton recombination in InAs wetting layer. And the broad emission line at 1.3 eV (QD-line) is attributed to an exciton recombination in QDs. We studied a magnetic field effects on the PL spectra in Faraday configuration.

A remarkable modification of the integral intensity for wetting-layer and for QD-lines have been observed in magnetic fields (see inset for Fig. 1). The intensity of the QD-line increases with the magnetic field increase up to 1 T, then goes to saturate and decreases.

The intensity of the wetting-layer line increases with the magnetic field in all range of the magnetic field variations. Such dependence of the PL intensity can be attributed to a magnetic field effects on photocarrieres capture to QDs [3]. A weak magnetic field (less than 1 T) suppresses the carrier transport to nonradiative centres only. It leads to an increase of the PL integral intensity. A strong magnetic field leads to the carrier localisation and suppresses the PL intensity from QDs with consequent increase of wetting-layer luminescence. An existence of "plateau" in these dependencies (in the magnetic fields from 1 T to 2.5 T) proves the high homogeneity of QDs.

These magnetic field dependencies of QWs PL intensity allow us to estimate the QD density which was found to be of $10^8$ to $10^{10}$ per square cm for different samples and the density of nonradiative centres.

This work was supported by RFBR grant No. 98-02-18267 and Program "Nanostructures" of Russian Ministry of Science.

## References

[1] V. P. Evtikhiev, A. K. Kryganovskii, A. B. Komissarov et al. *Proc. 23 Int. Conf. Compound Semiconductors, St.Petersburg, 1996*, Inst. Phys. Conf. Ser. No. 155, Chapter 3, p. 351-354 (1996) Eds. M. Shur, R. Suris.

[2] J.-Y. Marzin, J.-M. Gerard, A. Izrael et al. *Phys. Rev. Lett.* **73** 716 (1994).

[3] G. V. Astakhov, A. A. Kiselev, V. P. Kochereshko, M. M. Moiseeva, A. V. Platonov. *Semicond. Sci. Technol* in press (1998).

Ioffe Institute
6th Int. Symp. "Nanostructures: Physics and Technology"
St Petersburg, Russia, June 22–26, 1998.



# Experimental resonant two-photon study of the lowest confined exciton fine structure in CuCl quantum dots

*A. V. Baranov*†§, S. Yamauchi†, Y. Masumoto† and A. V. Fedorov§
† Institute of Physics, University of Tsukuba, Tsukuba, Ibaraki 305, Japan
§ Vavilov State Optical Institute, St. Petersburg, 199034, Russia

**Abstract.** Fine structure of low-energy confined exciton in CuCl spherical nanocrystals has been studied by a resonant size-selective two-photon-excited luminescence (TPL) spectroscopy with high spectral resolution. A band of resonance luminescence (RL) arising due to annihilation of the lowest-energy exciton and its LO-phonon replica were observed to be doublets. Analysis has shown that the components of the doublets connect with the pair of exciton states which have been attributed to low-energy confined states (1S) of two transversal excitons ($T_1$ and $T_2$) split by the size-dependent spin-orbit interaction. The physical reason of the splitting is similar to removing of Kramers degeneration of electron states in the bulk crystals of $T_d$ symmetry.

Fine structure of optical spectra near band edge absorption and luminescence of quantum dots (QD's) is of great interest since it gives ones information about low-energy confined electrons (excitons), confined phonons, and interactions between them as well as symmetries of the quasi-particle states and selection rules of optical and phonon-assistant transitions. Fine spectral structure caused by a short-range and long-range exchange interactions ("dark" and "bright" electron-hole pair states [1], and "longitudinal" and "transversal" confined excitons states [2], respectively) have been observed as well as induced by exciton-phonon interactions (exciton-acoustic-phonon [3] and polaron [4] states).

An additional fine structure induced by spin-orbit interaction in crystals of $T_d$ symmetry has not been considered for QD's systems so far. In such crystals [5], conduction and valence bands have fine structure near the Brillouin zone center due to spin-orbit interaction removing the Kramers degeneracy of electron states with nonzero wave vector. Obviously that the splitting of electron states results in a splitting of the transversal exciton on two states $T_1$ and $T_2$. A value of the $T_1$–$T_2$ splitting is proportional to $|\mathbf{k}|^3$ for excitons involving hole from the spin-orbit-split valence band ($\mathbf{k}$ is the electron (hole) wave-vector). Although theory of this effect for QD's is yet to be developed, from general point of view it is reasonable to suppose that the $T_1$–$T_2$ splitting for QD's should be proportional to $R^{-3}$, where $R$ is the QD radius. It follows from effective mass approximation where size-dependences of physical parameters of spherical QD's can be obtained by a replacing of wave-vector modulus of quasi-particles with quantity proportional to $1/R$.

We report the high-resolution size-selective TPL spectroscopy of CuCl spherical nanocrystals where $T_1$–$T_2$ splitting seems to contribute importantly to the fine spectral structure. The resonant TPL spectroscopy of quantum dot systems presents with the important advantages to investigate a fine structure of low-energy quasi-particle states since an incident light does not practically mask features with small Stokes shifts in secondary radiation spectra at two-photon excitation [2].

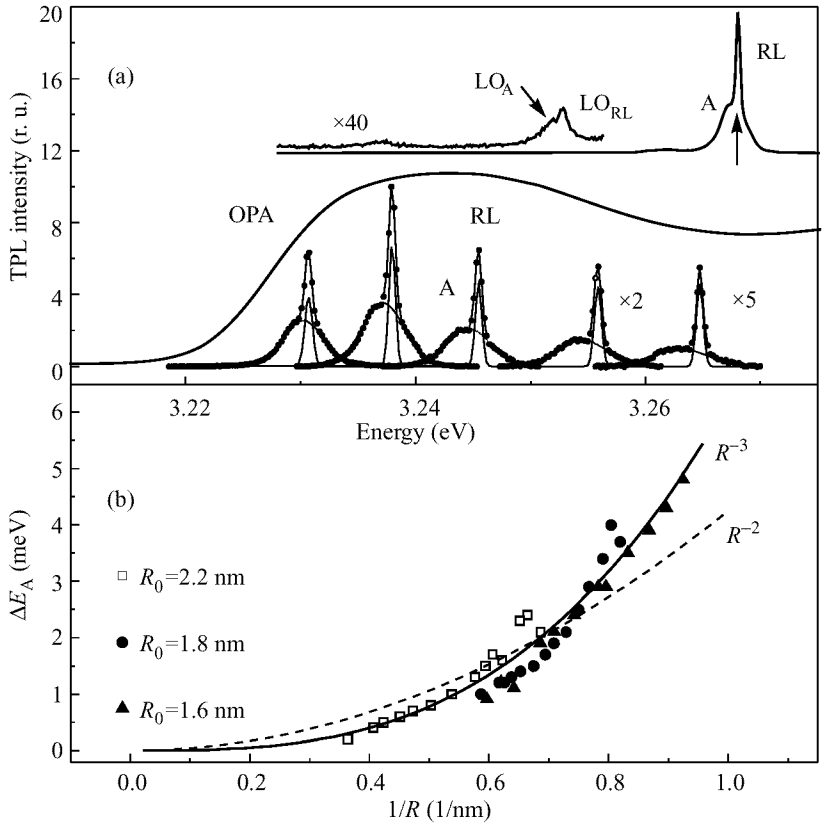


**Fig 1.**

CuCl QD's embedded in a glass matrix have been studied at 2 K. Dot's radii were in range from 2.5 to 1.2 nm. TPL was excited by a wavelength tunable Ti:sapphire laser pumped by a 3 kHz Q-switch YAG:$Nd^{+3}$ laser. The emitted light was analyzed with spectral resolution of 0.5 meV ($\sim 4$ $cm^{-1}$). For temporal analysis TPL was excited by a 2 ps Ti:sapphire laser pulse radiation; a time resolution of 150–200 ps was adopted.

Inset in Fig. 1(a) shows an example of size-selective TPL spectrum resonantly excited within inhomogeneously broadened one-photon absorption (OPA) band of $Z_3$ exciton for the specimen with a QD's mean radius, $R_0$ of 2.2 nm. The fine doublet structure with energy about twice energy of the incident photons, $2E_i$ (shown by an arrow) is clearly seen in detail in Fig. 1(a) where the doublets are shown for different $2E_i$. So, a narrow RL band of energy equal to $E_{RL} = 2E_i \equiv E_{1S}$, where $E_{1S}$ is the energy of the lowest-energy confined exciton state, have been found having a broad satellite (A-band) with Stokes shift increasing up to $\sim 4.8$ meV with increase of $2E_i$, or decrease of the nanocrystal size. The TPL spectra of specimens with $R_0 = 1.8$ and 1.6 nm show the same RL–A doublets. Analogous doublet structure consisting from narrow ($LO_{RL}$) and broad ($LO_A$) bands can be seen in the region of LO-phonon replicas of the RL and A bands (inset in Fig. 1(a)) with Stokes shifts of 25.8 meV, respectively.

Main experimental results are summarized as follows:

1. Spectral width of the RL band was found to be limited by the laser line one of

0.6 meV and much smaller than the A-band width of 3.5–4.5 meV. Ratio of spectral widths of the $LO_A$ and $LO_{RL}$ bands is about 4–5;

2. Stokes shift of the A-band ($\Delta E_A = E_{RL} - E_A$) increases from 0.4–0.5 meV to 4.8 meV with decrease of the nanocrystal radius: $\Delta E_A$ as a function of $1/R$ is presented in Fig. 1(b). It is seen that $\Delta E_A(R)$ demonstrates clear deviation from $R^{-1}$ dependence and allows approximation by rather $R^{-3}$ function than $R^{-2}$ one.

3. The RL excitation spectrum (ES) shows a resonant enhancement in the energy region corresponding to a direct two-photon generation of the 1S confined $Z_3$ exciton and reflects a size distribution of the nanocrystals [2]. Maximum of ES of the A-band coincides with that of the RL band. It means [2] that A-band arises due to direct two-photon excitation either the 1S exciton state or some exciton state with energy slightly more than 1S exciton energy. Due to broad size distribution we can not distinguish these cases by comparison of the ES positions. Integral intensity of the A-band is about four times more than that of RL at maximum of the corresponding ES.

4. Time decay measurements of TPL excited at ES maximum and measured in the regions of $2E_i$ and $2E_i - E_{LO}$, where $E_{LO}$ is the LO phonon energy, showed that decay times of the RL and A bands, and their LO-phonon replicas have the same value of about 0.6 ns. It shows that the lines considered more likely start from the same confined exciton state.

5. The RL and A bands have the same degree of linear polarization; it gives additional evidence that both the RL and A bands arises due to radiative annihilation of the same exciton state.

RL behaviors give evidence that it is resonance luminescence starting from the relatively long-living lowest energy confined exciton state. Then, the $LO_{RL}$ band results from the LO-phonon-assistant radiative annihilation of the same state.

The A-band and its LO-phonon replica ($LO_A$) in turn can arise due to a fine structure of low-energy confined exciton states. Indeed, our experimental data give evidence that the RL–A and $LO_{RL}$–$LO_A$ doublets are most likely caused by a fine structure of lowest energy 1S exciton states, namely, the $1S_{T1}$ and $1S_{T2}$ states of two transversal excitons ($T_1$ and $T_2$) split by the size-depended spin-orbit interaction. Then, the RL band and its LO-phonon replica come from two-photon excitation of the lowest energy $1S_{T1}$ exciton and its phononless and phonon-assistant radiative annihilation. At the same incident photon energy the A band and its LO-phonon replica arise from nanocrystals of larger size due to two-photon generation of the excitons in the $1S_{T2}$ state with energy of 0.4–4.8 meV more than the $1S_{T1}$ state, subsequent nonradiative transition to the $1S_{T1}$ state, and its phononless and phonon-assistant radiative annihilation.

Note that short-range exchange interaction can not be responsible for the doublets because a singlet-triplet exciton splitting for the nanocrystals has to be equal or more than that for the bulk CuCl (2.6 meV). The same reason allows ones to exclude from considerations the "longitudinal" exciton state because corresponding L–T splitting has much more values [2] than those observed for the RL–A doublet.

The essentially higher spectral width of the A-band than that of the RL band is easily understandable in framework of our scheme where the $1S_{T2}$ state is supposed to be homogeneously broadened in large part due to fast nonradiative transitions to the $1S_{T1}$ state. In such a situation, the $1S_{T2}$ excitons are simultaneously generated in nanocrystals of more broad range of sizes than the $1S_{T1}$ excitons. For each of the nanocrystals from this ensemble the narrow TPL line due to annihilation of the $1S_{T1}$ exciton created by

transitions from $1S_{T2}$ state contributes to the A-band. Since the annihilation energy is size-dependent, the A-band is envelope contour of the TPL bands with homogeneous widths equal to the RL line width. Simultaneous excitation of relatively large number of nanocrystals results also in relatively large integral intensity of the A-band. Note, the same reasons explain the difference between the $LO_A$ and $LO_{RL}$ band widths and intensities. Evidently that the decay times of the PL, A, $LO_A$, and $LO_{RL}$ bands thus considered should be approximately the same as well as their polarization properties that satisfies to our findings.

The assignment of the A-band to both the exciton-acoustic-phonon state and acoustic-phonon-assistant luminescence looks also rather unlikely because of clear distinction of $\Delta E_A(R)$ from expected $R^{-1}$ dependence. The reasons why the signal of the acoustic-phonon-assistant processes is rather weak in TPL spectra of our samples are not quite clear to us. Probably the A band contains a small contribution of the acoustic phonon signal undistinguished due to strong overlapping of two bands of different origin.

As far the observed $\Delta E_A$ size dependence, it is expected for our model of the $T_1$–$T_2$ splitting of $Z_3$ confined exciton in the CuCl quantum dots. Really, the experimental size-dependence of $\Delta E_A(R)$ [Fig. 1(b)] can be well fitted by the $R^{-3}$ function.

Two of us (A.V.B. and A.V.F.) are grateful to the RBRF, Grants Nos. 96-02-16235a, 96-02-16242a for financial support during this work.

## References

[1] M. A. Chamarro, C. Gordon, P. Lavallard, and A. I. Ekimov, *Jpn. J. Appl. Phys. Suppl.* **34-1** 12 (1995).
[2] A. V. Baranov, Y. Masumoto, K. Inoue, A. V. Fedorov, and A. A. Onushchenko, *Phys. Rev. B* **55** 15675 (1997).
[3] S. Okamoto and Y. Masumoto, *J. Lumin.* **64** 253 (1995).
[4] T. Itoh, M. Nishijima, A. I. Ekimov, C. Gourdon, Al. L. Efros, and M. Rosen, *Phys. Rev. Lett.* **74** 1645 (1995).
[5] E. O. Kane, *J. Phys. Chem. Solids* **1** 249 (1957).

Ioffe Institute
6th Int. Symp. "Nanostructures: Physics and Technology"
St Petersburg, Russia, June 22–26, 1998.



# Electron transport in a lattice of dopped many-electrons quantum dots: a gapless Hubbard insulator

*E. M. Baskin* and M. V. Entin
Institute of Semiconductor Physics, Russian Academy of Sciences, Siberian Branch,
Prosp. Lavrentyeva, 13, Novosibirsk, 630090, RUSSIA,
E-mail:Entin@isp.nsc.ru

**Abstract.** Electron states and hopping conductivity of a periodic lateral lattice of large quantum dots are studied taking into account the Coulomb effects. The intradot electron-electron repulsion produces the Hubbard gap which exceeds the single-electron levels spacing. The fluctuations of the number of impurities per a dot causes the redistribution of electrons and softens the Hubbard gap. The energy of interdot exitation varies from zero to the dot charging energy $U_C$. The variable range hopping with the typical hopping energy determined by $U_C$ was demonstrated to be a predominant mechanism of low temperature transport.

## Introduction

A periodic quantum dot lattice has brought a new goal for the solid state study, provided the artificial solid with controlled parameters such as the number of electrons per a cell, strength of electron-electron interaction, strength of interatomic tunnelling etc. Moreover, the scale of typical parameters has changed. The importance of electron-electron interaction gives rise to the Coulomb blockade, which is rather classical than quantum phenomenon.

This work was stimulated by some new experimental results on metal-non-metal transition at the crossover from antidots to quantum dots [1, 2]. The purpose of the present work is the theoretical study of electron states and hopping electron transport in a lattice of tunnel-coupled large quantum dots. We shall demonstrate that the intradot Coulomb interation leads to the appearance of Hubbard gap in the electron spectrum of the system. The fluctuations of the number of electrons per a dot smooths the gap up, producing the gapless Hubbard insulator. It will be shown that the activation energy of hopping conductivity is determined by the dot charging energy. The absence of hard gap tends to the variable range hopping in the low temperature case.

The typical sizes of modern dots lays between 100 and 500 nm. For usual electron density of $10^{11-12}$ cm$^{-2}$ this gives 50–200 electrons per a dot. The other important parameter is the Coulomb energy per electron. It has the value of capacitive charging of a dot, $U_C = e^2/2C$, where $C$ is the effective capacity of the order of the dot size. The typical value of $U_C$ has the order of 1 meV. The large number of electrons determines a gaseous picture of electron distribution inside a dot. The typical Fermi energy referred to the dot bottom is 10 meV. The distance between energy levels is $\delta = E_F/n \sim 10^{-1}$ meV, where $n$ is the mean number of electrons per a dot. The 2D screening length has the order of Bohr radius, $\sim$ 8.3 nm, which is sufficiently less than the dot size. Hence the dot has a plain bottom, strongly differs from the lattice of dots with parabolic confinement potential, considered by [3]. The other parameter, tunnelling factor $t$, is very easily controlled, varying from the maximal value $E_F/\sqrt{n}$ for barrierless dots to the exponentially small value.

Hence we shall deal with such hierarchy of parameters as

$$n \gg 1, \qquad E_F \gg U_C \gg \delta, \qquad t \ll U_C. \tag{1}$$

This combination of parameters is unusual. The large interaction makes inapplicable the single-electron models, like Anderson-Mott one, while the large number of electrons per a dot makes inapplicable the usual "single electron per single site" Hubbard model. The small ratio of interaction energy to the Fermi energy means near ideality of electron gas inside a dot, while large $U_C/\delta$ parameter determines the strong involvement of interaction into the energy levels distribution. The presence of tunnelling permits electron to propagate along the lattice of dots, while the small value of $t$ determines that in the first approximation it does not affect on the electron states of a single dot.

Another complications is the large number of electron levels in a dot. It leads to the statistical picture of levels distribution, like Wigner-Dyson one. From the other hand, the levels of different dots are independently distributed, so this distribution does not affect to the electron jumps between dots.

The situation, when the Coulomb interaction in a dot is determinative for electron states and transport is typical for Coulomb blockade. The last deals with the tunnelling between Fermi lakes via single or few dots. In this case the finite Hubbard gap for transport appears. The difference of our problem from the mentioned one is caused by multiplication of quantum dots into the lattice.

**Electron states**

Let us consider electron states in a dot, neglecting tunnelling between dots. In the gateless system the number of electrons in a dot is determined by the number of the impurities in it. If this number is the same for all dots, say $N$, the system should be the Hubbard insulator with $N$-th filled Hubbard band. Really, $N$ fluctuates. The fluctuation of this quantity has the order of statistical fluctuations $\sqrt{N}$. In the first approximation the large dot is electrically neutral and the number of electrons coincides with the number of impurities.

In the second approximation, we should take into account the fluctuations of the Fermi energy caused by the fluctuations of electron density. The value of these fluctuations is $\Delta = E_F/\sqrt{N}$. In equilibrium, the fluctuations of Fermi level are smoothed by the redistribution of electrons among dots and corresponding shifts of dot bottoms. This mechanism works if the number of electrons is large enough and $\Delta$ exceeds $U_C$. If $\Delta$ is less than $U_C$, the redistribution has no profit, giving loss in energy. If $\Delta \gg U_C$ (the case is typical), redistribution occurs. The number of redistributed electrons $\delta n_j$ in a dot $j$ is determined by the potential, necessary to equalize the local fluctuations of Fermi energy $\Delta_j = E_F(N_j - N)/N$. As a rule, the equation $e^2\delta n_j/2C = \Delta_j$ gives the fractional $\delta n_j$.

The discreeteness of $\delta n_j$ tends to impossibility to equalize the remainder of order of potential, produced by a single electron per a dot. The residual local distances between the filled states and the Fermi level $U_j$ are uniformly distributed within the range $(0, U_C)$.

In other words, the last occupied state can not be below the Fermi level more than $e^2/2C$, else the next level will be filled. The same is true for the first empty level: if it exceeds the Fermi energy more than $e^2/2C$, there should be another empty one, below the first on the distance $e^2/2C$. The first empty level in each dot is separated from the last filled by the distance $U_C$.

The activation energy for a jump between the fixed dots varies from 0 to $2U_C$. Hence the global energy gap vanishes, while local one is finite. We call this system *a gapless Hubbard insulator*.

The single-electron density of states for additional electron (hole) neglecting tunnelling linearly vanishes with the distance to the Fermi energy:

$$\rho(E) = \frac{S}{d^2}\frac{m}{\pi\hbar^2 e^2}2C|E-\mu|, \quad \text{if} \quad |E-\mu| < e^2/2C \tag{2}$$

and

$$\rho(E) = \frac{S}{d^2}\frac{m}{\pi\hbar^2}, \quad \text{if} \quad |E-\mu| > e^2/2C \tag{3}$$

where $S$ is the quantum dot arrea, $d$ is the lattice period. This behaviour, originating from *intrasite* e-e interaction, is similar to 2D Coulomb gap [4], caused by *intersite* interaction. Notice that their meanings are different.

The quantum dot lattice is an art-made system of Fermi lakes. Previously disordered system of Fermi lakes was discussed in the theory of strongly dopped and strongly compensated semiconductors [4]. In this situation the Hubbard gap is not much essential because it has the same order as the mean level spacing.

**Electron transport**

Below we shall neglect $t$ in consideration of energy spectrum and take it into account to consider transport in the lattice. The conductivity of the system is determined by electron hoppings between dots. The problem may be separated on two parts, finding a tunnel exponent and hopping optimization. We studied the probability of tunneling by means of single electron Hamiltonian of Anderson model

$$H = \sum_{i,\alpha}\epsilon_i \hat{a}_i^\dagger \hat{a}_i + \sum_{i,j}\{t\hat{a}_i^\dagger \hat{a}_{j,\beta} + H.c.\} \tag{4}$$

Here $\epsilon_i = -U_i$ for filled $\epsilon_i = U_C - U_i$ for empty states. At high temperature the transitions between the nearest neighbors take place. At low temperatures the long range hopping is preferable due to minimization of activation energy. These hoppings can be performed by means of virtual transitions through the intermediate dots, accompanied by the emission (absorption) of phonons at the start or in the finish.

Optimization of hopping probability together with the construction of percolation network of limited strong hopping gives the conductivity:

$$\sigma \sim \exp\left[-(T_0/T)^{1/3}\right], \tag{5}$$

where $T_0 = 4\beta U_C \log^2(U_C/t)$, $\beta \sim 13.8$. The hopping length is

$$l_0 = d\left[\left(\frac{U_C}{T\log\frac{U_C}{t}}\right)^{1/3}\right]. \tag{6}$$

The square brackets denote the integer part.

The formula (6) is valid for low temperature region $T \ll U_C/(2\log U_C/t)$. For high temperatures an electron prefers to jump onto the nearest neighbore.

Hence the effective conductivity is

$$\sigma \sim (t/2U_C)^2 \quad \exp\left(-\frac{\sqrt{2}U_C}{3T}\right). \tag{7}$$

## Discussion

We would like to compare the difference of transport in a quantum dot lattice and in impurity band. An impurity usually can confine a limited number of electrons. The Hubbard gap is usually too weak or too strong, so that the energy of $A^+, A^0$ and $A^-$ states have very different scales. In the case of impurity system in semiconductors the upper Hubbard $A^-$ state is known as an origin of so called "$\epsilon_2$" conductivity. The energy of this state is very low, compared to the ground state of hydrogen-like impurities. In non-compensated donor system there are no long range Coulomb forces and the states of additional electrons ($A^-$-states) and holes ($A^+$-states) on impurities are separated by a hard gap.

The principle feature of the quantum dot considered is a large number of electrons in a dot. As a result, the Hubbard energy is small, compared to not ionization bariers only, but to intradot Fermi energy. The electron gas *inside* quantum dot has a weak, perturbative interaction. But the Coulomb energy is rather strong if one consider transport between dots, for $U_C \gg t$.

An ideal quantum dot system should exhibit many Hubbard bands. The slow change of chemical potential leads to subsequent filling of subsequent Hubbard bands. So properties of the system should periodically alternate from metal to insulator. We expect this picture at least if tunnelling is strong enough and is not affected by phase-destroying thermal fluctuations.

The fluctuations of impurity numbers are much more important. If the fluctuations of local Fermi energy, caused by them, exceed the tunnelling amplitude, they result in the appearance of a gapless Hubbard insulator. When considering the gapless Hubbard insulator we neglect the influence of tunnelling on electron states, focusing on the case of hopping conductivity. We belive that the tunnelling may substantially change the properties of a gapless Hubbard insulator converting it to a "bad" metal.

The system considered is not exotic and is characterized by parameters, which are usual for lateral superlattices based on semiconductor heterostructures. It means the possibility of experimental realization of the predicted gapless Hubbard insulator.

*Acknowledgments*

We thank B. L. Altshuler for usefull discussions. The work was partially supported by Russian Foundation for Basic Researches (97-02-18397) and Folkswagen-Stiftung (Gr.I/71162). The full text of report is submitted to Europhys. Lett.

## References

[1] G. Lutjering, D. Weiss. R. Tank, K. v. Klitzing, A. Hulsmann, T. Jakobus and K. Kohler, *Workbook and Programme EP2DS XI*, Nottingham, 1995, p. 435.
[2] G. H. Gusev, X. Kleber, U. Gennser, et al. 12th International Conf. "High magnetic fields in the Physics of semiconducors", Wurzburg, Germany, 1996., Editors: G. Landwehr, W. Ossau, v. 1, p. 391.
[3] C. A. Stafford and S. Das Sarma, *Phys. Rev. Let.* **72** 3590 (1994).
[4] B. I. Shklovskii and A. L. Efros, *Electronic Properties of Doped Semiconductors*, Springer-Verlag, New-York, 1984.

Ioffe Institute
6th Int. Symp. "Nanostructures: Physics and Technology"
St Petersburg, Russia, June 22–26, 1998.



# Observation of internal electric charge in InP self-assembled quantum dots

V. Davydov†‡, *I. Ignat'ev*†¶, H.-W. Ren†, S. Sugou†§ and Y. Masumoto†*
† Single Quantum Dot Project, ERATO, JST, Tsukuba Research Consortium, Ibaraki 300-26, Japan
‡ On leave from S. I. Vavilov State Optical Institute, St.Petersburg, Russia
¶ On leave from St.Petersburg State University, St.Petersburg, Russia
§ Opto-Electronics Research Laboratories, NEC Corporation, Tsukuba, Ibaraki 305, Japan
* Institute of Physics, University of Tsukuba, Ibaraki 305, Japan

**Abstract.** Heterostructures with InP self-assembled quantum dots were studied. Strong Franz-Keldysh oscillations were found in their nonlinear reflection spectra. These oscillations manifest the presence of built-in electric field. The field originates from electric charge gathered by dots during the growth process.

## Introduction

Self assembled quantum dots (SAD) are recently a subject of the extensive study [1–5]. It is attractive to make an ensemble of quantum dots (QDs) in the single growth process. This is considered to prevent QDs surface from strong contamination. Nevertheless the structure and properties of the interface between SAD and barrier layers are still in question. Due to the small size of the dots, a fraction of surface atoms to volume atoms is relatively large. The lattice mismatch between materials of QDs and barrier layers gives rise to stresses and strains around the QDs.

In this work we studied InP self assembled QDs grown by gas source molecular beam epitaxy (GS MBE) technology. We used pump-probe method for the study of a nonlinear part of reflection and its dependence on a laser wavelength. It is found that the QD layer posesses a large amount of presumably negative electric charge. We suppose that this charge is caught by the acceptors located at the interfaces between InP QD layer and InGaP barrier layers.

## 1 Experimental

The heterostructures were grown on $n^+$ GaAs (100) substrates. Their simplified structure is shown in the inset of Fig. 1. The thickness of the barrier layers is 1000 Å for a sample QDP1779 and 1500 Å for a sample QDO1505 which were studied most thoroughly. An example of PL spectrum is shown in Fig. 1.

The experiments were carried out on the setup which includes a femtosecond Ti:sapphire laser "Tsunami" (power source "Millenia", frequency 82 MHz, pulse duration 0.1–1 ps) which is tunable from about 0.7 to 0.85 $\mu$m. Amplitude modulation of the pump and probe beams at different frequencies, optical phase shift between them and lock-in detection of the signal at the differential frequency let us to avoid noises from

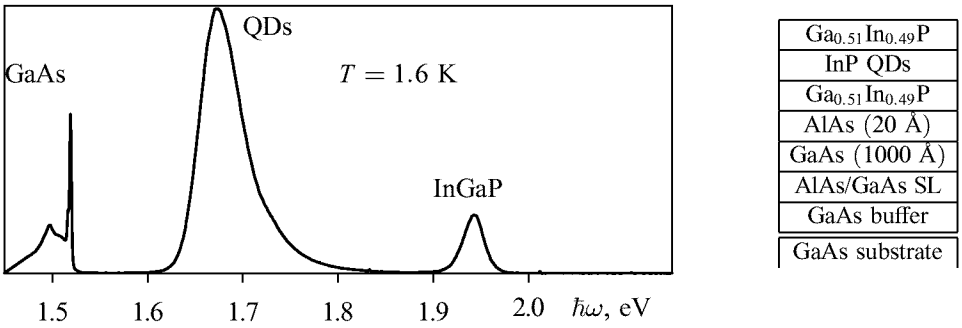


**Fig 1.** PL spectrum of sample QDO1505. "QDs", "InGaP", and "GaAs" mark accordingly PL of QDs and barrier and buffer layers excitons. Inset: structure of the studied samples.

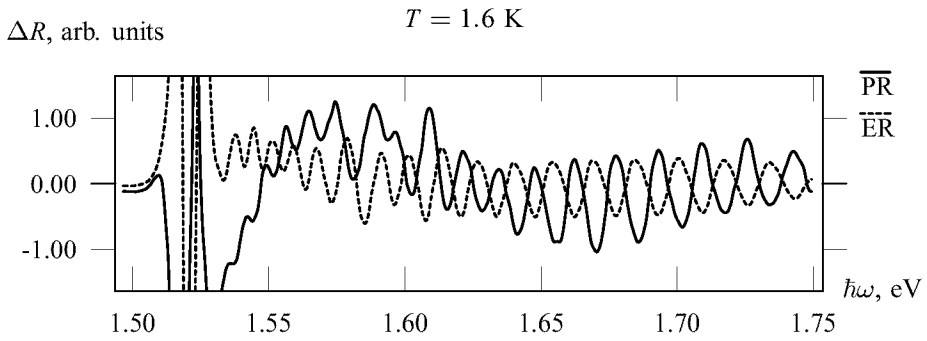


**Fig 2.** Pump-probe (PR) and electroreflection (ER) spectra of sample QDP1779.

the scattered light and achieve excellent sensitivity of detection of nonlinear reflection whose detection limit is about $10^{-7}$ times of the linear reflectance.

## 2 Results and discussion

Time dependence of the pump-probe signal is out of the scope of this paper. We discuss only a spectral dependence of the signal presented in Fig. 2. This dependence looks like an intense oscillations with almost constant period of $\approx 6.5$ nm. We have confirmed by the additional experiments that these oscillations are not caused by the light interference. All these experiments led us to the conclusion that we observe the Franz-Keldysh oscillations (FKO). To verify this supposition the sample QDP1779 was supplied with electric contacts and electroreflectance spectrum was recorded with the field modulation frequency 100 kHz. It is also presented in Fig. 2. One can see exactly the same period of oscillations.

FKO are the evidence of the built-in electric field in heteroctructures containing InP QDs. We investigated photoreflectance spectra of structures without QDs (with 6000 Å of InGaP barrier layer, with GaAs quantum well between GaInP barrier layers) and also structures with InAs QDs between GaAs barrier layers. Spectra of all these structures lack any regular oscillations. Therefore existense of the built-in electric field is caused by presence of InP SADs in the structure.

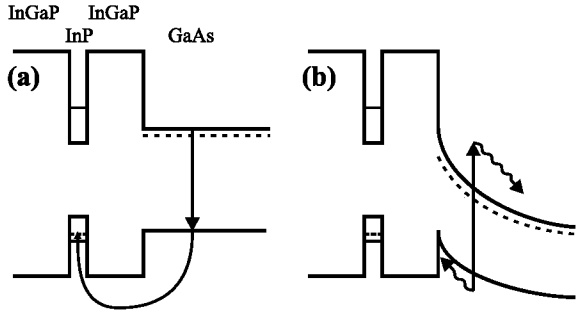


**Fig 3.** Charge transfer during structure growth (a) and photoreflection (b).

### *2.1 Model*

We offer the following model of the energy structure and the physical processes which give rise to this electric field. The interface between QDs and barrier layers contains a large number of intrinsic defects which act as effective carrier traps. We suppose that these traps are mostly acceptors. GaAs buffer layers of the investigated structures contain donors whose density is about few times of $10^{15}$ cm$^{-3}$. During the growth process, a high temperature ($\approx$ 500 °C) gives to the electrons provided by donors enough energy to jump over the barrier between the buffer layer and QDs. As a result a surplus negative charge goes into the QDs layer and opposite charge into the buffer layer. This forms a double electric layer with electric field inside. Due to the small donor concentration in the GaAs buffer, the carrier depletion occurs over considerable thickness of this layer and the electric field partially penetrates into it. The model described is schematically drawn in Fig. 3.

This model is capable of explaining main features of the signal. In the spectral region in question the photorefractive signal is caused mainly by nonlinear reflection from the GaAs buffer layer. Pump pulses produce free carriers in this layer. Their motion changes the electric field and therefore the refractive index at the given wavelength. Essentially we observe changes in the FKO phase.

In order to determine the value of built-in electric field we made semiquantitative analysis of the FKO. We utilized an approximated formula of Aspens [5]

$$E(m) - E_g = \hbar\theta \left[\frac{3}{4}(m\pi - \varphi)\right]^{2/3}, \tag{1}$$

where electrooptical energy is given by

$$\hbar\theta = \left(\frac{e^2\hbar^2F^2}{2\mu}\right)^{1/3}. \tag{2}$$

Here $E(m)$ is the energy position of the $m$-th maximum, $E_g = 1.52$ eV — GaAs bandgap, $\varphi$ — fitting parameter, and $\mu$ — reduced mass. We have gotten considerable deviation of the fitting curves $E(m)$ from the experimental curves for all studied samples which let us only approximately estimate magnitude of the field to be about 30 kV/cm. We suppose that this discrepancy is caused by the inhomogenity of the electric field in the GaAs buffer layer. Possible reason of this inhomogenity is distributed charge of the ionized donors in GaAs.

Obtained magnitude of the electric field allows us to estimate the surface charge density by the plane capacitor formula $\sigma = \varepsilon\varepsilon_0 F$. For the structures studied, it yields a charge of about 20 $e$ per QD. Such a large amount of charge changes the physical properties of InP QDs and should be taken into account in their investigations.

It should be mentioned that the electric charge of the InP QD layer was observed by S. Anand *et. al.* by DLTS technique [6]. However they studied samples with Si-doped GaInP barrier layers. In their structures electric charge of QDs is caused by the electron transfer to the potential well from the barrier layers. This charging is not related to existence of GaInP/InP interface defects.

## 3 Conclusion

This research shows that in the heterostructures with InP QDs the interface between QDs and InGaP barrier layers contains a number of defects which behave like acceptors. During the growth process at high temperature they capture electrons from other layers of the structure. This gives rise to the intrinsic electric field. The field caused strong FKO which are observed in photo- and electroreflection spectra. We discovered that in the investigated structures there is negative charge of about 20 electrons per QD. This charge essentially affects the physical properties of the QDs and should be taken into consideration in their studies.

## 4 Acknowledgements

We acknowledge Dr. E. Tokunaga for his interest in this work and efforts in software tuning. We also thank Dr. S. Nair for fruitful discussions.

## References

[1] N. Carlsson, W. Seifert, A. Peterson, P. Castrillo, M.-E. Pistol, and L. Samuelson. *Appl. Phys. Lett.* **65** 3093 (1994).
[2] A. Kurtenbach, K. Eberl, and T. Shitara. *Appl. Phys. Lett.* **66** 361 (1995).
[3] S. Raymond, S. Fafard, P. J. Poole, A. Wojs, P. Hawrylak, C. Could, A. Sachrajda, S. Charbonneau, D. Leonard, R. Leon, P. M. Petroff, J. L. Merz *Superlatt. Microstruct.* **21** 541 (1997).
[4] M. Grundmann, R. Heitz, N. Ledentsov, O. Stier, D. Bimberg, V. M. Ustinov, P. S. Kop'ev, Zh. I. Alferov, S. S. Ruvimov, P. Werner, U. Gosele, J. Heydenreich. *Superlatt. Microstruct.* **19** 81 (1996).
[5] H. Shen, and M. Dutta *J. Appl. Phys.* **78** 2151 (1995).
[6] S. Anand, N. Carlsson, M. -E. Pistol, L. Samuelson, and W. Seifert. *Appl. Phys. Lett.* **67** 3016 (1995).

Ioffe Institute
6th Int. Symp. "Nanostructures: Physics and Technology"
St Petersburg, Russia, June 22–26, 1998.



# Electron effective $g$ factor in small quantum systems

E. L. Ivchenko†, *A. A. Kiselev*† and U. Rössler‡
† Ioffe Physico-Technical Institute, RAS, 194021 St. Petersburg, Russia
‡ Institut für Theoretische Physik, Universität Regensburg,
D-93040 Regensburg, Germany

**Abstract.** The Zeeman effect for 1D and 0D electron states has been considered theoretically. We have established the relation between the point symmetry of a low-dimensional system and properties of the $g$ factor tensor $g_{\alpha\beta}$, from which, in particular, it turns out that the $g$ factor in a cylindrical wire is isotropic ($g_{xx} = g_{yy} = g_{zz}$). The actual calculation of $g_{\alpha\beta}$ is performed for the ground states in rectangular quantum wire, cylindrical wire and spherical quantum dot structures.

## Introduction

In zinc-blende semiconductors, the electron $g$ factor values change with a chemical composition in a wide range ($g \approx 2$ in wide-gap semiconductors, $-0.44$ in GaAs and approximately $-50$ in the narrow-gap InSb). This behavior, i.e. dependence of $g$ on the fundamental energy gap, $E_g$, and the spin-orbit splitting, $\Delta$, of the upper valence band, is in a good agreement with the well-known Roth equation derived in the second order of the **kp** perturbation theory. In [1] this approach was generalized to include heterostructures with quantum wells (QWs) and superlattices and the $g$ factor was calculated as a function of layer widths. A large anisotropy of the Zeeman effect for conduction electrons was predicted, which was later confirmed experimentally in the structures grown from cubic semiconductors $A_3B_5$ and $A_2B_6$ (see [2] and references therein). First measurements of $g$ factors for quantum dots have been reported more recently [3]. In the present work the theory of Zeeman effect for electrons in quasi-one- and quasi-zero-dimensional systems, namely quantum wires (QWRs) and quantum dots (QDs) is developed. The dependencies on the linear sizes are calculated for the $g$ factor tensor in cylinder and rectangular QWRs as well as in a spherical QD.

## 1 The first- and second-order $g$ factor formulae

As mentioned above, the expression for the $g$ factor in bulk semiconductors comes from the second-order **kp** perturbation theory. In this case a value of $g$ is obtained as a sum over all intermediate states. In particular, for the electron in a simple band $l$ of the bulk semiconductor of cubic symmetry with the extremum in the center of the Brillouin zone we have (magnetic field $\mathbf{B} \parallel z$)

$$g = g_0 + \sum_n \frac{|\langle l|p_+|n\rangle|^2 - |\langle l|p_-|n\rangle|^2}{E_l^0 - E_n^0}, \tag{1}$$

where $g_0 \approx 2$ is free electron Lande's factor, $\hat{p}_\pm = \hat{p}_x \pm i\hat{p}_y$, $\langle n|\hat{p}_\alpha|m\rangle$ ($\alpha = x, y, z$) is the matrix element of the momentum operator taken between states $n$ and $m$, $E_n^0$ is the state electron energy. Here and in what follows we will use the atomic units with

the electronic charge $e = 1$, Plank's constant $\hbar = 1$ and the free-electron mass $m_0 = 1$. Though principally applicable to any types of semiconductor heterostructures, this approach involves calculation of intermediate states and, therefore, is very cumbersome and practically ineffective for one- and zero-dimensional systems. In this work we propose an approach which is much more suitable for $g$ factor calculations in QWRs and QDs.

To begin with, we would like to mention, that the same result for $g$ factor can be produced in the first order by the correction

$$\delta H = \frac{1}{c}\mathbf{A}\hat{\mathbf{V}}$$

to the electron Hamiltonian linear in the magnetic field, where $\mathbf{A}$ is the vector-potential which in a homogeneous magnetic field depends linearly on the radius-vector $\mathbf{r}$, and the velocity operator $\hat{\mathbf{V}} = \partial H(\mathbf{k})/\partial\mathbf{k}$. In order to show an equivalence of both approaches, one needs (1) to write the matrix element of the operator $\mathbf{A}\hat{\mathbf{V}}$ as a product of $\mathbf{A}$ and $\hat{\mathbf{V}}$ matrix elements summed over intermediate states, and (2) to use a relation between the matrix elements of coordinate and velocity operators. Thus, we confirm that expressions for the $g$ factor, produced in the second order of the **kp** perturbation theory and in the first order by the correction $\delta H$ are equivalent. For the extended states matrix elements of $\delta H$ usually can not be directly evaluated, so as the second-order expression for the $g$ factor should be used instead.

If the wave function is localized in one of the directions $\zeta$ due to spatial confinement, the calculation of the $g$ factor in the magnetic field $\mathbf{B} \perp \zeta$ can be performed in the first order of the perturbation theory in the correction to the electron Hamiltonian. In particular, in the structure with a quantum dot, where the envelope wave function is localized in all three directions, the first-order perturbation theory can be applied and the tensor $g_{\alpha\beta}$ of $g$ factors for the ground state of the spatial quantization $e1$ is defined by the expression

$$\frac{1}{2}\mu_B\sigma_{\alpha,ss'}(g_{\alpha\beta} - g_0)B_\beta = \langle e1, s|\delta H|e1, s'\rangle. \tag{2}$$

Here $\mu_B$ is the Bohr magneton, $\sigma_\alpha$ ($\alpha = x, y, z$) are the Pauli matrices, and the spin indices $s, s' = \pm 1/2$. Equation (2) is applicable as well for the electron state at the bottom of the subband $e1$ in a quantum wire, if (1) the vector potential gauge is chosen so as it depends only on the coordinates perpendicular to the wire axis and (2) the diamagnetic contribution is subtracted from the right-hand side of Eq. (2) [2]

$$\frac{1}{c}\langle e1, s|\hat{v}_z|e1, s'\rangle\langle A_z(\mathbf{r})\rangle.$$

## 2 Kane model calculation

For the analysis of an electron $g$ factor we use the Kane model. It takes into consideration **kp** mixing of states in the conduction band $\Gamma_6$ and in the valence bands $\Gamma_8$, $\Gamma_7$ exactly, but neglects influence of the remote bands. The Schrödinger equation with the **kp** Hamiltonian $H(\hat{\mathbf{k}})$ (matrix $8 \times 8$) can be written in terms of spinors $u$ (conduction band, two components) and $\mathbf{v}$ (valence band, six components) [4]. It is possible to

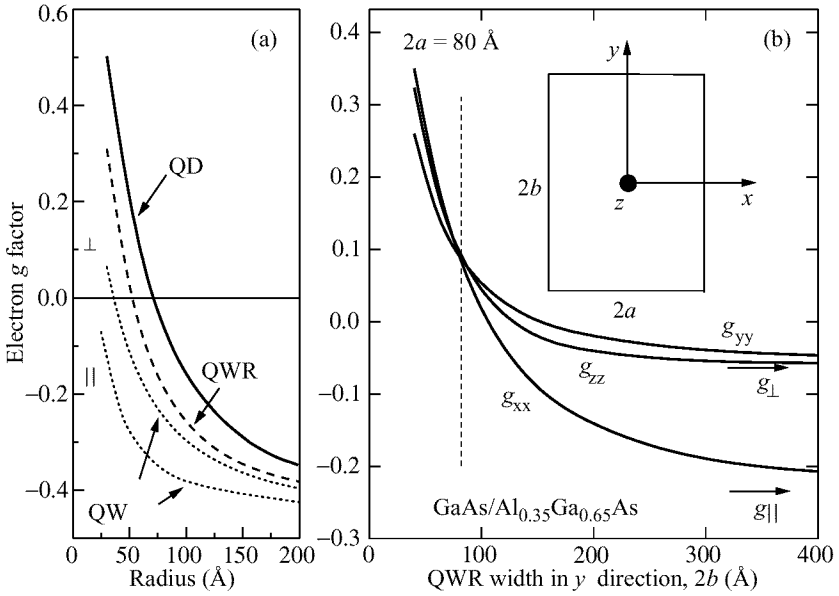


**Fig 1.** (a) Dependence of the electron $g$ factor on the structure linear sizes. Values for the spherical QD and cylindrical QWR of radius $R$ are presented by solid and dashed lines respectively. For comparison the longitudinal and transverse components of the electron $g$ factor tensor ($g_{\|}^{\mathrm{QW}} < g_{\perp}^{\mathrm{QW}}$) are shown for the single QW of width $2R$ (dotted line). (b) The $b$-dependence of the electron $g$ factor $g_{\alpha\beta}$ at the bottom of the first subband in $GaAs/Al_{0.35}Ga_{0.65}As$ QWR with a cross-section $2a \times 2b$ (see inset). Dashed line marks a case of $a = b$. Arrows show longitudinal ($g_{\|}$) and transverse ($g_{\perp}$) $g$ factor components in a 80 Å-wide QW.

reduce this system to a second-order differential equation

$$-\frac{P^2}{3}\left(\frac{2}{E_g+E}+\frac{1}{E_g+E+\Delta}\right)\nabla^2 u = E\,u\,, \tag{3}$$

for the spinor $u$, and the vector spinor $\mathbf{v}$ can be expressed via the gradient $\nabla u$ by the equation

$$P\mathbf{v} = \frac{P^2}{3}\left[\left(\frac{2}{E_g+E}+\frac{1}{E_g+E+\Delta}\right)\nabla u + \frac{i\Delta}{(E_g+E)(E_g+E+\Delta)}(\sigma\times\nabla u)\right]. \tag{4}$$

Here $E$ is the electron energy counted from the conduction band bottom $\Gamma_6$, and boundary conditions are the continuity of the spinor $u(\mathbf{r})$ and of the component of the vector $P\mathbf{v}(\mathbf{r})$ parallel to the interface normal, $P = i\langle S|\hat{p}_z|Z\rangle$.

In the Kane model the velocity operator $\hat{\mathbf{V}}$ is an $8 \times 8$ matrix with $\mathbf{k}$-independent components. Using an explicit form of this matrix, we conclude the section with the main formula for the $g$ factor calculation

$$\langle e1, s|\delta H|e1, s'\rangle = i\frac{e}{c\hbar}\int P\,\left[\left(\mathbf{A}\mathbf{v}_s^{+}\right)u_{s'} - u_s^{+}\left(\mathbf{A}\mathbf{v}_{s'}\right)\right]d\mathbf{r}\,. \tag{5}$$

## 3 Results and discussion

In Fig. 1a the electron $g$ factor in a spherical QD ($g^{QD}$) and in a cylindrical QWR ($g^{QWR}$) are presented as a function of the radius $R$. For comparison in the same graph we show longitudinal ($g_{\|}^{QW}$, $\mathbf{B} \| z$) and transverse ($g_{\perp}^{QW}$, $\mathbf{B} \perp z$) $g$ factor components for a QW of the width $2R$. The model calculation is performed for the heterosystem $GaAs/Al_{0.35}Ga_{0.65}As$. The following parameter values are used in the calculation: $E_g = 1.52$ eV, $\Delta = 0.34$ eV, $2p_{cv}^2/m_0 = 28.9$ eV for bulk GaAs ($p_{cv} = i\langle S|\hat{p}_z|Z\rangle$), and $E_g = 1.94$ eV, $\Delta = 0.32$ eV, $2p_{cv}^2/m_0 = 26.7$ eV for the barrier material, band offsets at the interface are $\Delta E_v{:}\Delta E_c = 2{:}3$. In order to take into account the contribution of remote bands we added a constant $\Delta g = -0.12$ to the $g$ factor values obtained in the Kane model. Thus, with increasing the structure size the electron $g$ factor reaches a bulk value of $-0.44$ in GaAs. With a decreasing the linear sizes the $g$ factor increases tending for $R \to 0$ to the barrier material value 0.57. Since with the reduction in the system dimensionality the role of spatial confinement increases, the following relations are fulfilled: $g_{\|,\perp}^{QW} < g^{QWR} < g^{QD}$.

Fig. 1b presents the tensor $g_{\alpha\beta}$ for an electron in the ground state in a rectangular QWR of the cross-section $2a \times 2b$ as a function of the length $b$. The other size ($2a = 80$ Å) is kept constant. For the square cross-section ($a = b$), the components $g_{xx}$ and $g_{yy}$ coincide the same, and the anisotropy $g_{zz} - g_{xx}$ is very small in agreement with the general symmetry considerations. With increasing $b$ we asimptotically approach the QW limit resulting in $g_{xx} \to g_{\|}$ and $g_{xx}, g_{yy} \to g_{\perp}$, where $g_{\|}$ and $g_{\perp}$ are the longitudinal and transverse components of the $g$ factor in a QW.

Thus, by using the Kane model we have developed a theory of the electron $g$ factor in semiconductor QWRs and QDs, and performed model calculations for the spherical dot, rectangular and cylindrical wires.

*Acknowledgements*

This work was financially supported by the Volkswagen Foundation and the Russian Foundation of Fundamental Research.

## References

[1] E. L. Ivchenko and A. A. Kiselev, *Sov. Phys. Semicond.* **26**, 866 (1992).
[2] E. L. Ivchenko, A. A. Kiselev and M. Willander, *Solid State Commun.* **102**, 375 (1997).
[3] A. A. Sirenko, T. Ruf, A. Kurtenbach and K. Eberl, *Proc. ICPS-23* (Berlin 1996), World Scientific, 1996, p. 1385.
[4] R. A. Suris, *Sov. Phys. Semicond.* **20**, 1258 (1986).
[5] A. A. Kiselev and U. Rössler, *Phys. Rev. B* **50**, 14283 (1994).

Ioffe Institute
6th Int. Symp. "Nanostructures: Physics and Technology"
St Petersburg, Russia, June 22–26, 1998.



# The effect of 1.06 $\mu$m illumination on the photoluminescence of InAs/GaAs quantum dots

*D. A. Mazurenko*†‡, A. V. Scherbakov†, A. V. Akimov†, D. L. Fedorov‡, A. J. Kent§ and M. Henini§

† Ioffe Physico-Technical Institute, St. Petersburg 194021, Russia
‡ Baltic State Technical University, St. Petersburg 198005, Russia
§ Physics Department, Nottingham University, Nottingham NG7 2RD, UK

Optical experiments with self-organised InAs/GaAs quantum dots (QD) show high quantum efficiency of photoluminescence (PL) which is important for laser applications [1]. However the channels of nonradiative carrier recombination which competes with PL in QDs are not understood yet. In the present contribution we study the effect of enhancement of PL quantum efficiency of InAs/GaAs QDs induced by subband 1.06 $\mu$m illumination.

Experiments were carried out on four samples (A, B, C, D) with InAs QDs grown by MBE on (311B) (samples A and C) or (100) (samples B and D) surface of semiinsulating GaAs substrate. Samples A and B consisted 10 layers of InAs QDs, C and D were samples with one QD layer. PL was excited by Ar-laser ($\lambda = 514$ nm) with power density $P_{\mathrm{Ar}} = 1{-}10\,\mathrm{W/cm^2}$ which is well below the saturation limit for ground electron and hole QD states in our samples. Experiments were carried out at $T = 77$ K. The PL spectral line was centred around 1.2 eV and had the spectral width of 40–80 meV depending on the sample. The PL spectrum was measured when the sample was excited by additional 1.06 $\mu$m illumination from cw or Q-switched YAG:Nd laser (power densities, $P_{\mathrm{YAG}}$, up to 500 W/cm$^2$).

Figure 1 shows the photoluminescence spectra of sample A with (curves (a) and (b)) and without (curve (c)) additional 1.06 $\mu$m illumination of YAG:Nd laser. It is seen that PL intensity increases in the presence of 1.06 $\mu$m (1.17 eV) excitation which shows the enhancement of quantum efficiency of PL induced by subband illumination. In sample A the maximum relative increase (60%) was observed. The relative increase of the PL induced by 1.06 $\mu$m illumination is sublinear with the intensity of YAG laser and the enhancement effect reaches saturation for high power density, $P_{\mathrm{YAG}}$.

The most interesting experimental result is that the relative increase of quantum efficiency depends on the wavelength of detected PL and the effect is stronger on the low-energy side of PL spectral line (see Fig. 1). This makes us to conclude that the effect of the quantum efficiency enhancement is governed by the processes directly connected with the properties of InAs QDs or InAs/GaAs interface but not with the GaAs buffer layer where carriers are initially created. Different wavelength of PL corresponds to QDs with different size. The wavelength of PL increases with the increase of the QD size. Apparently experimental results show that the relative increase of the quantum efficiency increases with the size of QD.

We explain the effect of the increase of QD quantum efficiency in terms of photoionisation of carrier traps which are playing a role of centres of nonradiative carrier recombination. Carriers created by interband (Ar-laser) excitation in GaAs are captured

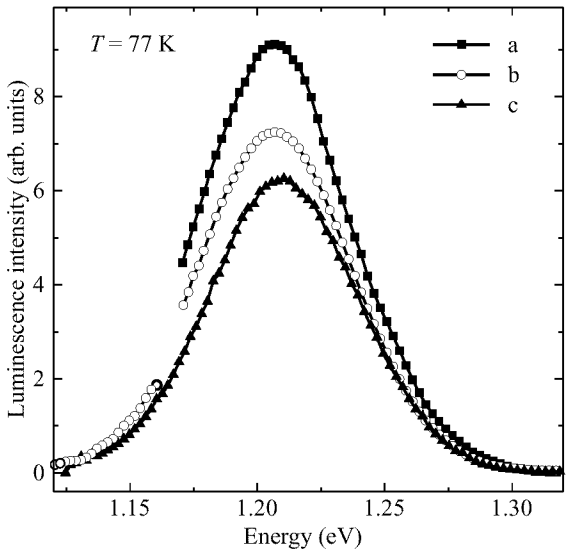


**Fig 1.** PL spectra of InAs/GaAs QDs measured at $P_{Ar} = 2.5\,W/cm^2$ and different power densities, $P_{YAG}$, of additional 1.06 $\mu$m illumination ($W/cm^2$): (a)—240; (b)—90; (c)—without 1.06 $\mu$m excitation.

to InAs QDs where they may recombine radiatively or captured by traps located at the InAs/GaAs interface. The competition between radiation and trap capture processes determines the quantum efficiency of PL. If the lifetime of carriers at the traps is long enough, then the subband 1.06 $\mu$m illumination will induce ionisation of carriers from the traps, thus giving additional chance for the carrier to participate in the radiative QD recombination resulting in PL. The value of relative increase of quantum efficiency depends on the ratio of the photoionisation rate and the lifetime of the carriers captured to traps. Thus the effect should be stronger for carriers which have a longer lifetime on the traps. The results of the experiments lead us to the assumption that carrier lifetime on the traps increases with the increase of QD size which may be due to the weaker overlap of electrons and holes participating in the nonradiative trap recombination in bigger QDs. This is reasonable if the nonradiative recombination occurs between the one carrier (e.g. electron) captured on the trap at the InAs/GaAs interface and another carrier (hole) located in the InAs QD.

The authors acknowledge the support of the work by the Russian Foundation for Basic Research (No. 96-02-16952a) and by Russian Ministry of Science program "Physics of Nanostructures" (No. 97-1037).

## References

[1] Ledentsov N.N., Grundmann M., Kirstaedter N., Schmidt O., Heitz R., Bohrer J., Bimberg D., Ustinov V.M., Shchukin V.A., Egorov A.Yu., Zhukov A.E., Zaitsev S., Kop'ev P.S., Alferov Zh.I., Ruvimov S.S., Kosogov A.O., Werner P., Gosele U., Heydenreich J. *Solid-State Electronics* **40** 785 (1996).

Ioffe Institute
6th Int. Symp. "Nanostructures: Physics and Technology"
St Petersburg, Russia, June 22–26, 1998.



# Transport in single atomic junctions: strong correlation and Coulomb blockade

*F. Yamaguchi*†, D. H. Huang‡ and Y. Yamamoto†§
† ERATO Quantum Fluctuation Project
E. L. Ginzton Laboratory, Stanford University Stanford, CA 94305
‡ ERATO Quantum Fluctuation Project
NTT Musashino R&D Center, Musashino-shi, Tokyo 180, Japan
§ NTT Basic Research Laboratories
3-1 Morinosato-Wakamiya, Atsugishi, Kanagawa 243, Japan

**Abstract.** We report here the first observation of the strong correlation and Coulomb blockade effects in a single-atomic junction (single tungsten-atom STM tip). In contrast to previous work [1, 2], the use of an atomic-scale central island makes the change in the electrostatic potential due to the variation of the number of electrons in the island greater than 1eV and thus the electron correlation effect is made more controllable and stable even at room temperature.

## 1 Experimental setup

The experiment was performed using an ultra-high vacuum (UHV) STM (JSTM–4500XT) with an operating pressure of $2 \times 10^{-8}$ Pa at 77 K and 300 K. The STM tip was made from a single crystal tungsten wire with (111) orientation. An STM tip with a pyramidal structure well protruded about 2 nm on the tip apex with a single tungsten atom at the end of the apex, which is followed by the three and six tungsten atoms in the second and third layers, respectively, was prepared by the field evaporation plus field emission technique [3]. In contrast to the previous method [4], this new technique allows us to in situ fabricate a single-atom tip inside the STM chamber. Direct observation of the tip apex by field ion microscope (FIM) confirmed that there is a single tungsten atom at the end the tip apex. Such a single atom STM tip is stable and robust for high field ($\leq$ 1 V/Å) operation, so a silicon atom and hydrogen atom can be extracted and redeposited routinely and repeatedly on a Si(100)2×1 surface [4].

## 2 Experimental results

The current-voltage characteristics between the single tungsten-atom STM tip and Au(111) or Si(100)2×1 surface. The normalized differential conductances $(\mathrm{d}I/\mathrm{d}V)/(I/V)$ vs. the applied voltage featured five to six periodic oscillation peaks in both (sample) positive and negative bias voltages, which is the unique characteristics of a Coulomb staircase in a double barrier tunnel junction. The voltage separation of adjacent oscillation peaks was $\sim$ 1.1 eV. This oscillation period was independent of tip-sample separation, temperature and substrate material.

The negative differential conductance ($\mathrm{d}I/\mathrm{d}V < 0$) was observed between the oscillation peaks. This feature existed for both Si(100)2×1 and Au(111) surfaces but is more pronounced for the Au(111) surface at 77 K.

If we apply a strong field ($>$ 2 V/Å) on the tip apex, the single tungsten atom at the end of the tip apex eventually evaporates. Such a truncated configuration without

an apex atom was also observed by FIM. Such a truncated tip did not feature any oscillatory behavior in the normalized differential conductance.

## 3 Theoretical model

A tight-binding (TB) calculation for the electronic states of a single-atom tip, taking into account field-induced energy shift of each constituent atom, shows the presence of two narrow peaks in the local density of states in the apex atom: one is below the Fermi level and the other is above it. This means that there are localized states into the apex atom which are electrically decoupled from the underlying layers by an effective tunnel barrier. The present numerical result is consistent with the previous measurements of the field emission spectrum from a single tungsten-atom tip [4].

The localized electronic state in the apex atom is thus regarded as the central island which capacitively couples to the two electrodes, the rest of the tungsten tip and the sample surface. We estimated the charging energy for the highest occupied energy level (5d) of a tungsten atom by the ab initio calculation and compared with the experimental value determined from the linearly increasing third-to-sixth photoionization energies [5]. The charging energy of the localized state in the pyramidal structure is $U \sim 1.1$ eV, which is compared with the charging energy of $\sim 12$ eV for an isolated tungsten atom.

In our experiment, the tunnel current is governed by the slower apex atom-sample tunneling event. As a positive bias voltages is applied, the Fermi level of the sample moves downward relative to the energy levels of the localized state which are split equally by $U$ due to the charging effect [6]. When the sample Fermi level goes across each one of the resonances, the sample starts extracting an electron from the localized state and new channels for tunnel current open up one by one, which results in the observed periodic oscillation peaks in the positive sample voltage. If a negative sample voltage is applied, the Fermi level of the sample moves upward to cross each one of the resonance energy levels of the localized states and the sample stars supplying the localized state with an additional electron, which results in the observed periodic oscillation peaks in the negative sample voltage.

The observed negative differential conductance between the oscillation peaks is attributed to the coherent multiple tunneling effect between the localized state in the apex atom and the sample. This was confirmed by the theoretical analysis for the Anderson model of a single atom point contact.

## 4 Conclusion

The result reported here is the first proof of the existence of Coulomb blockade oscillation and negative differential conductance in a single atomic junction. Various mesoscopic devices based on the Coulomb blockade effect and active devices based on the negative differential conductance should be realized on an atomic scale.

## References

[1] H. van Kempen, P. J. Mvan Bentum and R. T. MH Smokers *Physica Scripta* **T42** 153 (1992).
[2] C. Schonenberger, H. van Houten and C. W. J Beenakker *Physica* **B 189** 218 (1993).
[3] D. H. Huang et al., *Jpn. J. Appl. Phys.* (to be published).
[4] Vu T. Binh and S. T Purcell *Appl. Surf. Sci.* **111** 157 (1997).
[5] J. Emesley *The Elements* (Clarendon Press, Oxford) p 201, 1989.
[6] F. Yamaguchi, D. H. Huang and Y. Yamamoto *Jpn. J. Appl. Phys.* **36** 3799 (1997).

Ioffe Institute
6th Int. Symp. "Nanostructures: Physics and Technology"
St Petersburg, Russia, June 22–26, 1998.



# SPM based real-time controlled assembly of predefined nanostructures for fabrication of lateral quantum devices

*Lars Montelius*, Sven-Bertil Carlsson, Tobias Junno, Martin Magnusson, Knut Deppert, Hongqi Xu and Lars Samuelson
Division of Solid State Physics & The Nanometer Structure Consortium, Lund University, P.O. Box 118, S-221 00 Lund, Sweden
e-mail: lars.montelius@ftf.lth.se

The dimensions of electronic devices have been reduced approximately a factor of two every three years for the last 20 years, effectively meaning an increase of capacity with a factor of four. This trend, known as Moore's law, is predicted to hold for the next decade as well, although small deviations are foreseen. This means that around year 2010 the linewidths of the components produced in large scale will be below Å 100 nm. This presents a great challenge not only to the technology community for fabricating these devices, but also to the electronic design people since the electronic properties of nm-scale devices will be governed by quantum mechanics.

Presently, there is a rapid growing interest in quantum devices based on single-electron-tunneling (SET)-effects. Such SET-devices are possible candidates for single electron memories that might allow room temperature operation. Coulomb blockade effects have been observed at low temperatures in numerous tunnel barrier structures for both metals and semiconductors. The first observation of Coulomb charging effects at room temperature was obtained by creating a vertical double barrier structure using the tip of a scanning tunneling microscope and a small metal particle. However, from a practical point of view it is obvious that scanning tunneling microscopes cannot form the basis for any electronics applications where single or complex combinations of SET devices will be used.

Lately the focus of possible room temperature SET-devices have instead been shifted towards fabrication of lateral tunnel structures. For instance, Chen *et al* deposited AuPd nanocrystals in-between Au electrodes defined by e-beam lithography, and they reported clear Coulomb blockade effects at 77 K. However, the fabrication method is very hard to control and reproduce, which limits it's practical use for making devices. Other techniques that might have a larger potential for device fabrication involves some kind of self-aligning/assembly process(es) of conducting particles between metal electrodes, as reported by Klein *et al.* They managed to make a link of several colloidal Au clusters between e-beam defined electrodes. The electrodes were chemically modified in order to achieve good adhesion of the colloidal particles. However, large fluctuations in the obtained I–V spectra due to environmental changes during the measurement makes also this method not optimal.

We have during the last 2–3 years developed a new way to build extremely small scale and accurate structures for contacting of nano-objects. The principle is based on the use of the atomic force microscope (AFM) for very accurate movement of pre-fabricated nano-objects, such as lift-off defined metal discs, aerosol fabricated nano-particles and colloidal gold particles. The assembly procedure consists of moving se-

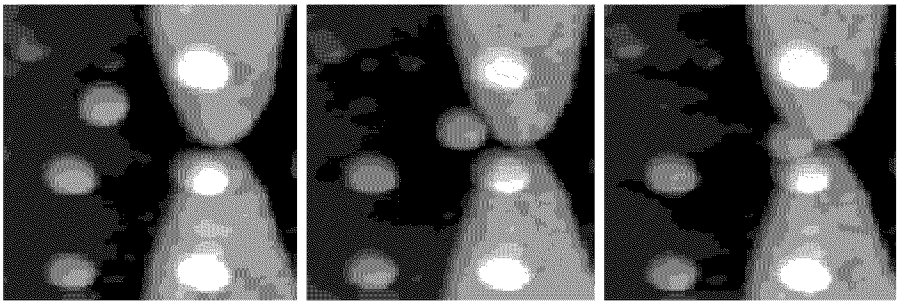

**Fig 1.** Three AFM images (740 nm × 740 nm) recorded during the manipulation of an Au disc into a gap between two Au electrode.

lected nanometer sized objects into a small gap between two metal electrodes (see Fig. 1).

The metal electrodes are defined by e-beam lithography using a conventional lift-off technique. The imaging and manipulation is done in ambient air condition using an ultra-sharp non-contact AFM tip. For imaging we used an oscillation frequency of around 170 kHz and lock-in detection of the amplitude change. The sample holder stage has been modified making electrical in-situ monitoring during the assembly procedure possible. The commercial relatively sharp AFM tips have been further processed by EBD (E-beam deposition), resulting in a carbon rich ultra sharp tip. Sometimes, the EBD tips have been further sharpened by putting the tips in an oxygen plasma, thereby thinning and sharpening resulting in a typical tip radius in the range of 10–20 nm.

The method for imaging and manipulation can be described as follows: make an image in non-contact mode, select the particle to be moved, position the tip slightly away from the particle, open the feed-back loop, advance the tip into contact with the particle, push the particle by the tip induced lateral forces to the desired position, withdraw the tip, establish feedback and acquire a new image displaying the outcome of the particle translation. One of the major advantages with our method is the possibility

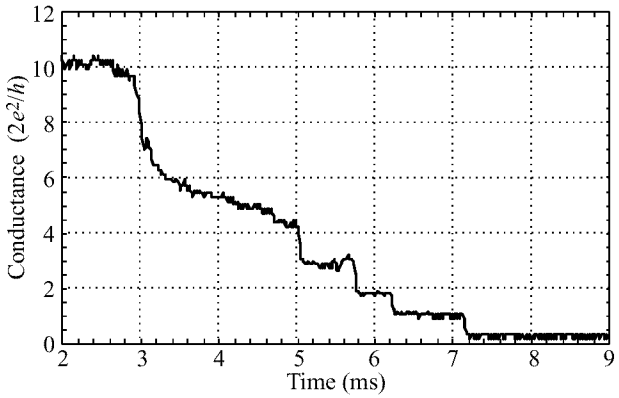


**Fig 2.** Dynamic behavior of the conductance as an Au nanodisc is being pushed out of contact with the electrodes. The applied bias voltage was 2 mV and the temperature 300 K.

to electrically monitor the assembly procedure by having a potential applied between the electrodes.

The techniques of pre-fabricating nm-scale building blocks and AFM-manipulation with simultaneous electrical measurements have for instance allowed us to build single-electron and quantum transport devices with control on the Ångström level. As examples of these results we show in Fig. 2 the experiment in which quantized point contacts (QPCs) are formed with control of the nano-wires in the range of some few Ångströms manifested in the conductivity plateaus in the units of $2e^2/h$.

Furthermore, by pushing the particles just small steps, nominally 1 Å, it is possible to stabilize the current at a certain conductance plateau level for timescales up to several 10's of minutes. In this condition, the current is stable and decoupled from environmental fluctuations since the mass of the particle is so tiny that gravitational forces are not in affect. This method of assembling structures using predefined nanosized object is to be seen as a versatile tool for nano-scale contacting and investigation of both inorganic and organic nano-objects, e.g. a particle covered with an organic "skin".

*Acknowledgment*

This work has been performed within the "Nanometer Structure Consortium" in Lund, and we gratefully acknowledge support from the Swedish National Board of Technical and Industrial Development, the Swedish Natural Science Research Council, the Swedish Technical Research Council, The Foundation of Strategic Research and the Crafoord Foundation.

## References

The material presented above is based upon the following references:

T. A. Fulton and G. J. Dolan, *Phys. Rev. Lett.* **59** 109 (1987).

U. Meirav, M. A. Kastner, and S. J. Wind, *Phys. Rev. Lett.* **65** 771 (1990).

Hongqi Xu, *Phys. Rev. B* **48** 8878 (1993).

K. Nakazato, R. J. Blaike, and H. Ahmed, *J. Appl. Phys.* **75** 5123 (1994).

W. Chen, H. Ahmed and K. Nakazato, *Appl. Phys. Lett.* **66** 3383 (1995).

T. Junno, K. Deppert, L. Montelius and L. Samuelson, *Appl. Phys. Lett.* **66** 3627 (1995).

K. Deppert and L. Samuelson, *Appl. Phys. Lett.* **68** 1409 (1996).

D. L. Klein, P. L. McEuen, J. E. Bowen Katari, R. Roth and A. P. Alivisatos, *Appl. Phys. Lett.* **68** 2574 (1996).

K. Deppert, et al., *J. Crystal Growth* **169** 13 (1996).

L. Montelius, T. Junno, S.-B. Carlsson and L. Samuelson, *Microel. Engin.* **35** 281 (1997).

T. Junno, S.-B. Carlsson, H. Xu, L. Montelius and L. Samuelson, *APL* **72** 548 (1998).

S.-B. Carlsson, K. Deppert, T. Junno, M. H. Magnusson, L. Montelius and L. Samuelson, *Semicond. Sci. Technol.* in press (1998).

Ioffe Institute SEPD.04
6th Int. Symp. "Nanostructures: Physics and Technology"
St Petersburg, Russia, June 22–26, 1998.

# Quantum Mott transition in mesoscopic semiconductors

*S. V. Vyshenski*†, U. Zeitler‡ and R. J. Haug‡
† Institute of Nuclear Physics, Moscow State University, Russia
‡ Institut für Festkörperphysik, Universität Hannover, Germany

**Abstract.** Considering a double-barrier structure formed by a silicon quantum dot covered by natural oxide, we derive simple conditions for the conductance of the dot to become a step-like function of the number of doping atoms inside the dot, with negligible dependence on the actual position of the dopants. The found conditions are feasible in experimentally available structures.

The fabrication of Si nanostructures became possible through very recently developed new technologies [1, 2]. One unique preparation technology for individual silicon quantum dots (SQD) has been reported in [2]. They are spherical Si particles with diameters $d$ in the range 5–12 nm covered by a 1–2 nm-thick natural $SiO_2$ film. Metallic current terminals made from degenerately doped Si are defined lithographically to touch each individual dot from above and from below.

To ensure metallic electrodes the donor concentration $n$ should be $n \geq n_{\mathrm{Mott}}$, where $n_{\mathrm{Mott}} = 7.3 \times 10^{17}$ cm$^{-3}$. The critical concentration $n_{\mathrm{Mott}}$ is defined by the *Mott criterion* [3], introducing the transition to a metallic type of conductivity in a semiconductor at:

$$a_{\mathrm{B}} \times (n_{\mathrm{Mott}})^{1/3} = 0.27 \qquad (1)$$

where $a_{\mathrm{B}}$ nm is the Bohr radius of an electron bound to a donor inside the Si crystal, in the case of phosphorus-donors $a_{\mathrm{B}} = 3$ nm [3].

As for the doping of the dot, the situation concerning a Mott transition in that small dots is much less trivial than the one described by Eq. (1). Let us consider dots with diameters $d = 10$ nm formed from n-doped Si with $n = n_{\mathrm{Mott}}$ as an illustrative example. Then each dot contains in average one donor. Note that we will consider degenerately $n^+$-doped electrodes with $n \gg n_{\mathrm{Mott}}$ which ensures metallic conduction up to the borders of the dot.

Real fabrication technology [2] provides a wafer with hundreds of SQDs on it with current leads towards each individual SQD. Dots in average have the same value of mean dopant concentration $n$, which is determined by the parent material of bulk silicon the dots are formed from. However, on the level of each individual SQD we will always have exactly *integer* number of doping atoms. If, as in the example above, the average number of dopants $\overline{N_{\mathrm{tot}}} = 1$ the actual number of donors in the dot can have values $N_{\mathrm{tot}} = 0, 1, 2, 3, \ldots$, with values larger than these very unlikely.

Our objective is to illustrate, that SQDs from the same wafer fall into several distinct sets of approximately the same conductance. The typical value of conductance for each set is nearly completely determined by the number $N$ of donors present in a certain part of a SQD so that $N$ labels each set of SQDs.

Summarizing the above, we need for a quantization of the conduction through a dot with $N$ donors the following conditions:

- Size $d$ of the dot comparable with Bohr radius: $2 < d/a_B < 5$.
- Average doping $n$ of the dot $n \leq d^{-3}$, leading to a mean number of dopants $\overline{N_{tot}} \leq 1$, so that $N_{tot} = 0, 1, 2$ are the most probable configurations of an individual SQD.
- Doping of the electrodes $n_{el} \gg n_{Mott}$, so that current leads are perfectly metallic.
- Dot covered by an oxide layer thick enough to suppress ballistic transport through the dot.

In fact all these condition can be simultaneously satisfied for SQD fabricated with the method mentioned above [2].

## 1 Model system

We use a simple model of a cubic SQD with $d > 2a_B$ (we will use $d = 10$ nm for estimates), covered with an oxide layer with thickness $\delta = 2$ nm, and contacted with current terminals from below and from above. The $x$-axis is oriented from top to bottom along the current flow.

A tunneling current is injected into the dot via the oxide barrier from the top (source at $x = 0$) and leaves the dot at the bottom (drain at $x = d$). Due to the presence of the oxide barriers this current is non-ballistic and non-thermal. We assume that the high potential barriers associated with the oxide layers are not much affected by the voltage and the tunneling charges. We concentrate on what happens between these effective source and drain.

In the case when the dot can be regarded as an insulating system it is reasonable to assume that the applied voltage equally drops over the potential barriers and the dots. For simplicity we neglect the difference of the dielectric constants of the oxide barriers and the dot. In this approximation we can introduce an effective voltage $V_{eff} = V(d-2\delta)/d = 0.6V$ describing the part of the total transport voltage $V$ applied between effective source and drain which drops across the dot itself.

In this rude approximation we neglect the effect of spatial quantization upon values on the ionization energy, the conductivity gap and material parameters of silicon.

## 2 Dot without donors

At $V_{eff} = 0$ the Fermi level inside the dot is situated in the middle of the gap, i.e. $E_g/2$ bellow the conduction band edge ($E_g = 1.14$ eV at 300 K).

As $V_{eff}$ grows, the bottom of the (still empty) conduction band bends down accordingly. When the conduction band in the dot close to the drain aligns with the Fermi level of the emitter we expect a drastic increase in the tunneling current. This threshold $V_{th}$ voltage for $V_{eff}$ is given by $V_{th} = E_g/(2e)$, regardless of the number $N_{tot}$ of dopants in the dot (as long as the dot is not yet metallic, of course). In the following we therefore limit our studies to voltages

$$|V_{eff}| \leq V_{th} = E_g/(2e) = 0.57 \text{ V}. \tag{2}$$

In this voltage range we have a $d$-thick barrier (formed by the dot) with always finite hight between effective source and drain. The intrinsic concentration of electrons and holes at 300 K is $1.4 \times 10^{10}$ cm$^{-3}$. Even at this high temperature the probability to have at least one intrinsic electron in a dot with size $d = 10$ nm is only $1.4 \times 10^{-8}$. So we

would expect virtually no current in this mode. This is confirmed by direct electrical tests [2] of SQD with the required properties.

## 3 Single-donor channel

Let us now consider one single single donor in the dot located at $x$ with ionization energy $E_d = 0.045$ eV (for P as a donor).

The evident channel for current flow is single-electron tunneling from the source to the empty impurity, and then from populated impurity to the drain. This channel opens as soon as $V_{\text{eff}}$ reaches a threshold $V_1$ leading to a step-like increase in the total conductance of the dot. If the impurity is located near the drain, i.e. $d - a_B < x < d$ then $V_1$ is given by

$$V_1 = E_g/(2e) - E_d = 0.525 \text{ V}. \tag{3}$$

In contrast, for a impurity located at distances $\Delta x > 2dE_d/E_g$ (that is far) from the drain, no additional current channel via a single impurity can be opened at voltages low enough voltages defined in (2) where virtually no background current is present. In the present case this value $\Delta x = 0.8$ nm, which returns us to the above criterion: only impurities located in the immediate vicinity (defined within the accuracy $a_B$) of the drain contribute to the single-impurity channel.

The probability to populate an impurity from the source, and then to depopulate it towards the drain is directly related to the overlap of the atom-like impurity wave-functions with the corresponding contacts leading to a conductance $G_1$ of this current channel

$$G_1 \propto \exp\left(-\frac{x}{a_B}\right)\exp\left(-\frac{d-x}{a_B}\right) = \exp\left(-\frac{d}{a_B}\right). \tag{4}$$

This shows that in first approximation the conductance of this channel does not depend on $x$. As shown above, a single-impurity channel already only selects impurities located within a very narrow range of $x$ close to the drain, Eq. (4) gives an additional argument for the independence of this channel conductance $G_1$ on the actual location of the impurity inside this thin layer near the drain.

## 4 Two-, three-, multi-donor channel

The above consideration shows, that due to the bend of the bottom of conduction band following the transport voltage, there is no chance to notice current flowing through a sequential chain of impurities, connecting source and drain. The contribution of such a chain will be totally masked by the current flowing directly via the conduction band. The only way for multiple impurities to manifest themselves in quantized conductance is to form multiple *parallel* singe-impurity channels situated close enough to the drain as considered above.

Therefore, if $N > 1$ impurities fall into the thin layer near the drain, we will see a switching-on of an $N$-fold channel with conductance

$$G_N = NG_1 \tag{5}$$

at the same threshold voltage $V_{\text{eff}} = V_1 = 0.525$ V as for a single-donor channels.

## Discussion

All the above considerations are only valid as long as the dot itself can be regarded as an insulating system. As the number of donors in a SQD grows, the dot becomes a metallic particle, and the conduction band edge in the dot aligns with the Fermi level of the electrodes. In a very simple estimate we define this transition to a metal when the total volume of $N$ donors with an individual volume of $4\pi/3 \times a_B^3$ exceeds the volume of the dot. This is an exaggerated version of the Mott criterion (1) which holds not only in bulk, but in a small structure, too. For the analyzed example from above this gives $N_{tot} = 8$ as a limiting value. The practically interesting set $0, 1, 2, 3, \ldots$ for both $N_{tot}$ and $N$ considered above is still far bellow this limit.

Quite a number of other mechanisms of electron transport might take place in this system, the main one being resonant tunneling. Surprisingly, even taking into account such other mechanisms [4] does not change much the main idea of the present paper.

*Acknowledgments*

Useful discussions with M. Kupriyanov and S. Oda are gratefully acknowledged. This work was supported in part by the Russian Foundation for Basic Research and by the Russian Program for Future Nanonelectronic Devices.

## References

[1] L. J. Guo, E. Leobandung, L. Zhuang, and S. Y. Chou, *Journal Vac. Sci. Technol. B* **15**(6) 2840 (1997).

[2] A. Dutta, M. Kimura, Y. Honda, M. Otobe, A. Itoh, and S. Oda, *Jpn. J. Appl. Phys.* **35** 4038 (1997).
S. Vyshenski, A. Ohata, Y. Kinugasa, Y. Hayafune, H. Hara, S.-P. Lee, K. Nishiguchi, A. Dutta, S. Oda, Active Probing of Single-Electron Effects in a Silicon Quantum Dot. *4-th Int. Symp. On Quantum Effect Electronics*, p. 45-50, Tokyo (1997).

[3] B. I. Shklovskii, A. L. Efros, *Electronic Properties of Doped Semiconductors*, Berlin: Springer-Verlag, 1984.

[4] I. A. Devyatov, M. Yu. Kupriyanov, *JETP* **77**(5) 874 (1993).

Ioffe Institute
6th Int. Symp. "Nanostructures: Physics and Technology"
St Petersburg, Russia, June 22–26, 1998.



# Proposal for neutral donors in quantum wells to act as charge storage centres for room temperature single electron memories

*P. Harrison*
Institute of Microwaves and Photonics, School of Electronic and Electrical Engineering, University of Leeds, LS2 9JT, United Kingdom
e-mail:p.harrison@elec-eng.leeds.ac.uk

**Abstract.** This work discusses a range of semiconductor materials, and demonstrates that in a II–VI compound semiconductor, the neutral donor binding energy can be enhanced with the addition of a quantum well confining potential, to a value greater than $kT$ at room temperature and simultaneously greater than the longitundinal optic phonon energy. Thus room temperature occupation is a possibility. The application of this nanoscale localisation centre as a single electron memory is discussed.

## 1 Introduction

This work is motivated by the question: *'What is the smallest centre of localisation that can be used to store a single bit of information?'* One possibility is a single impurity atom within a host semiconductor. For example, an unoccupied (ionised) donor atom could represent a '0' and an occupied (neutral) donor could represent a '1'. The fundamental physics that would have to be satisfied to make such a system interesting would be to have control over the occupational state of the donor at room temperature. This relies on two points: *'Can the electron bound to the donor be resistant to ionisation and how can one read/write the information within a device?'* In the sections below I will show theoretically that shallow hydrogenic donors can be engineered to resist ionisation by phonons at room temperature and thus exhibit long storage lifetimes. Then the work will move on to consider incorporation into contemporary single electron device geometries and possible optical read/write techniques using far-infrared lasers currently under development.

**Table 1.** LO phonon energies in selected bulk compound semiconductors (LTO mode for Si)

| Material | Phonon energy (meV) | Material | Phonon energy (meV) |
|---|---|---|---|
| Si | 62 | InAs | 30 |
| AlAs | 50 | ZnS | 43 |
| GaP | 50 | ZnSe | 31 |
| InP | 43 | ZnTe | 26 |
| GaAs | 36 | CdTe | 21 |

Simplistically one might think that the first point can be satisfied by choosing a donor and host material with a binding energy $E_b$ larger than $kT$ at room temperature (25 meV). In fact the criteria is more stringent than this in that the binding energy must be large enough to resist ionisation by common large energy (usually longitundinal optic (LO)) phonons. Table 1 gives examples of phonon energies in a selection of group IV,

III–V and II–VI. It is clear that the LO phonon energy $E_{\mathrm{LO}}$ is generally smaller in II–VI materials and in fact satisfying the criteria of $E_b > kT$ in CdTe will also satisfy $E_b > E_{\mathrm{LO}}$. The neutral donor binding energy in bulk CdTe is less than $E_{\mathrm{LO}}$, however it can easily be enhanced by placing the donors in a quantum well [1]. Furthermore very high quality CdTe-$Cd_{1-x}Mn_xTe$ quantum well structures can be grown, with photoluminescence linewidths less than 1 meV [2].

## 2 Theoretical methods

The centres of localisation (or storage) of electrons are proposed to be donor atoms in quantum wells. As stated above the quantum well potential is to be utilized in order to increase the binding energy of the neutral donor with the aim of storing the charge at room temperature and resisting ionisation by phonons. Therefore an accurate evaluation of the neutral donor binding energy within a quantum well needs to be made. The original variational approach of Hagston *et al.* [1] is employed. The trial wave function is chosen as

$$\Psi = \chi(z)\exp\left(-\frac{r''}{\lambda}\right), \qquad r'' = \sqrt{x^2 + y^2 + \zeta^2(z - r_d)^2} \tag{1}$$

where the envelope $\chi(z)$ is determined by forming the time independent Schrödinger equation integrating over the in-plane $(x - y)$ co-ordinates and solving the resulting differential equation using a numerical shooting technique [1].

Recently Roberts *et al.* [3] have shown that the lowest energy solutions, and therefore the most accurate, are indeed obtained by allowing $\zeta$ to vary the symmetry of the trial wave function $\Psi$. However good approximations are also obtained by setting $\zeta = 1$, i.e. a spherically symmetric relative motion term, with differences less than 0.1 meV. This approximation will be made in this work in the interests of reducing the, otherwise, considerable computational effort.

The envelope function approximation on which these theoretical methods are based, depends crucially on the quality of the parameterization of the material parameters, in particular the band offset, the electron effective mass, and the dielectric constant. The first, the band offset, has been deduced through carefully comparison with theory and experiment to be around 30% [2]. Hence the conduction band offset as a function of the manganese concentration in the barrier is $0.7 \times 1587x$ meV. Note that as the effective mass is related to the band structure, which itself is a function of the carrier momentum $\mathbf{k}$, then the effective mass is also a function of $\mathbf{k}$. In its simplest form this manifests itself as 'non-parabolicity' often referred to in calculations of one-dimensional systems, see Long *et al.* [4] and references therein. However in a two-dimensional system such as this, the $\mathbf{k}$-space sampling of the bound electron arises from the real-space circular orbit. Harrison *et al.* [5] calculated the electron effective mass for the same material system as this but for an electron bound to a heavy-hole in an exciton. This effective mass of $0.11m_0$ is employed in this similar system. In addition the work of Harrison *et al.* also deduced the relevant dielectric constant $\epsilon \approx 9$, which is between the static (10.6) and high frequency (7.4) values, by careful comparison of detailed theoretical calculations with experimental measurements. It should be noted that the main conclusions of this work are not dependent upon the specific values chosen for these material parameters.

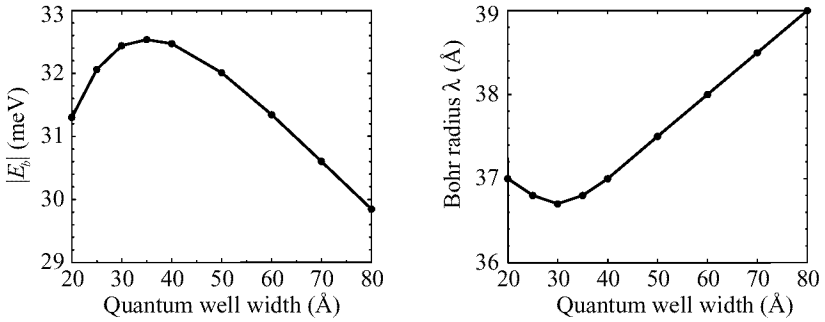


**Fig 1.** (a) Neutral donor binding energy and (b) Bohr radius, for donors at the centre of a well, as a function of well width.

## 3 Results and discussion

### *3.1 Maximising the neutral donor binding energy*

For any given material system the neutral donor binding energy within a quantum well is a function of three variables, the donor position, the quantum well width and the quantum barrier height. Earlier work [1, 3] has already established that the neutral donor binding energy is a maximum when the donor is located at the centre of the well. Hence only the second and third degrees of freedom need be explored in order to maximise the binding energy. Figure 1(a) displays the magnitude of the binding energy as a function of well width, it is clear that it displays a peak of 32.5 meV at a well width of 35 Å. This value is larger than $kT$ at room temperature, though more importantly it is considerably larger than the bulk LO phonon energy of 21 meV, hence it will be resistant to ionisation by phonon scattering. Assuming a simple Bohr atomic model would imply that the first excited state of the donor is $1/4$ of the ground state binding energy, i.e. around 8 meV, further implying that the energy for excitation is $32.5-8 \approx 24$ meV. Which means that LO phonons could not excite the occupied donor at all, which is a very important point as an excited donor could be ionised by a second phonon. Fig. 1(b) displays the corresponding Bohr radii $\lambda$. It gives an indication of the size of the donor 'quantum dot'. The maxima in binding energy corresponds closely with the minima in this localisation radius, which would determine the packing density.

Additional calculations have shown that the binding energy can be enhanced further by up to 2 meV with increasing manganese content in the barriers. Though it is acknowledged that the material quality tends to decrease for higher alloy concentrations.

### *3.2 Incorporation of single donor 'dot' into a device*

There are several ways in which the donor 'quantum dot' could be incorporated into existing single electron devices. For example, it could be used to replace the quantum dot 'floating gate' used in single electron MOS memory, recently demonstrated at room temperature [6]. In this device charge stored on a floating gate, which is varied by a control gate, affects the threshold voltage of a transistor, thus allowing the information to be read. Similiarly a 'donor dot' whose occupancy is controlled by a side gate could be utilized as a source for the 'Coloumb blockade' of single electron transport from a source to a drain.

Perhaps more long term, the donors could be the building block of an optical read/write memory system. Information could be written on a fully occupied $\delta$-layer by selective ionisation with a laser tuned to the donor binding energy, with the ionised carriers swept away by a static electric field. The information is then represented by the occupancy state of single (or perhaps groups of) donors. It could be read by a lower energy laser tuned to the excitation from the ground state to the first excited state. Light falling on a region of ionised donors would be transmitted, regions of occupied donors would be temporarily excited and disperse the radiation. Research into the required terahertz lasers is underway.

## 4 Conclusion

In summary it has been demonstrated that the neutral donor binding energy can be enhanced with a quantum well to a level where ionisation can be resisted at room temperature. The possible application as a room temperature single electron memory has been discussed.

## References

[1] W. E. Hagston, P. Harrison and T. Stirner, *Phys. Rev. B* **49** 8242 (1994).
[2] S. R. Jackson, J. E. Nicholls, W. E. Hagston, P. Harrison, T. Stirner, J. H. C. Hogg, B. Lunn, and D. E. Ashenford, *Phys. Rev. B* **50** 5392 (1994).
[3] R. G. Roberts, P. Harrison, and W. E. Hagston, *Superlatt. Microstruct.* **23** 289 (1998).
[4] Fei Long, W. E. Hagston, and P. Harrison, *The Proceedings of the 23rd International Conference on the Physics of Semiconductors* 1819 (World Scientific, Singapore, 1996).
[5] P. Harrison, Fei Long and W. E. Hagston, *Superlatt. Microstruct.* **19** 123 (1996).
[6] L. Guo, E. Leobandung, and S. Y. Chou, *Science* **275** 649 (1997).

Ioffe Institute
6th Int. Symp. "Nanostructures: Physics and Technology"
St Petersburg, Russia, June 22–26, 1998.



# Hybrid superconductor-semiconductor transistors

*D. V. Goncharov*, I. A. Devyatov and M. Yu. Kupriyanov
Institute of Nuclear Physics Moscow State University,
119899, GSP, Moscow, Vorob'evy Gory, Russia

## Introduction

The combination of superconductors with semiconductor heterostructures represents a new field of investigation in terms of new physics as well as prospects for new superconductive transistors [1-3]. Studies of the proximity effect at semiconductor/superconductor ($S/Sm$) interfaces have demonstrated success in proximity induced superconductivity. Decay length $\xi_n \approx 120$ nm and supercurrent at the electrodes spacing as large as $0.8\ \mu$m has been observed in the InAs layers [4, 5].

So far the heterostructures had limited utilization in these investigations [6, 7]. The role of heterostructures, however, could be extremely high for several reasons:

($i$) the well-advance technology permits fabrication of the high-quality barriers with controllable thickness shape and height;

($ii$) the precise control of layer doping and thickness allows fabrication of any design multilayer structure for studying the physical processes in the junction;

($iii$) the available technology provides the possibilities to fabricate the ohmic contacts to the edges of the 2D-gas layers with the interfaces having controllable transparency [8, 9].

On the other hand, the heterostructures introduce new physical features to the physical properties of the structures (geometrical resonances, resonant tunneling, quantum noise, mesoscopic effects, etc.). This opens a new field of investigation of superconducting current transfer through the structures and offers unique opportunities for development of the novel three-terminal devices.

The results obtained now, however do not look promising. The level of gate (input) voltages necessary for the switching the devices from superconducting to the highly resistive state $V_g \approx (1 \div 3)$ V several orders of magnitude lager compare to the output (or controlled) voltage $V_{out} \approx (1 \div 3)$ mV of the realized now three terminal devices [2–7]. To make these transistors operable, one must find a way to strongly increase the device transconductance and reduce $V_g/V_{out}$ ratio.

The goal of this paper is to estimate theoretically the possibility of the enhancement employing the idea of geometrical resonances in the specially designed novel three-terminal Josephson devices.

## The base

Practically in all realization of the three terminal Josephson devices the variable thickness bridge geometry has been used. The superconducting banks were deposited on the top of the semiconducting interlayer forming the "opening resonator junctions" [4–7]. The only possible way of the reduction the $V_g/V_{out}$ ratio in these devices is the decreasing the density of the carriers $n$ in semiconductor interlayer. Unfortunately, this immediately results in suppression of the decay length $\xi_n \propto n^{1/2}$ in semiconductor as well as the

transparency of the interfaces and provides serious difficulties in fabrication of the junctions. It seemed that the decision could be found by using 2D-gas as the interlayer material [3-5]. High mobility of the carriers permits to reduce the electron density $n$ on several order of magnitude (from $10^{19}$ to $10^{12}$ cm$^{-3}$) on retention of the reasonable values of the decay length $\xi_n \approx 100$ nm. But even in this case, however, the gate voltage does not change considerably being on the level of several volts.

The analysis of the mode of operation of the three-terminal semiconducting field effect transistors [10-12] has shown that there are two kinds of the 2D-gas devices. The first of them based on the depletion of the 2D-gas in the conductive channel by the gate voltage and really needs $V_g \approx (1 \div 3)$ V for the operation. In the second types (lateral 2D-gas devices [11, 12]) the advantage of the quantization the energy levels of the carriers in the potential wells forming in 2D-gas by applying a constant voltages $V_1$ and $V_2$ on a split gate has been used. In this case it has been shown that it is enough to vary the difference $V_1 - V_2$ in the scale 10 mV to rearrange the energy levels in the potential well and, hence, to control the $V_{out}$.

On the other hand it was experimentally confirmed [1] that it is possible to fabricate clean *SSmS* Josephson junctions which properties control by the geometrical resonances. Its physics does not differ from the one of the lateral 2D devices. Two naturally formed small transparent $S/Sm$ boundaries at the edges of 2D-gas formed the Fabri-Perot resonator for the carriers. So the variation the electrode spacing on a few percent results in several orders of magnitude changing of the absolute values both critical current and normal junction resistance.

The combination of these experimental facts provides the possibility of the reliable reduction of the $V_g/V_{out}$ ratio in field effect devices to a reasonable level.

**Novel field effect Josephson device**

The proposed structure consists of two superconducting banks separated by the semiconductor heterostructure with the 2D-gas layer. The interfaces between the banks and the edges of the 2D-gas form the Fabri-Perot resonator. To control the current across device it is enough slightly change by the gate voltage the de Brogue wavelength $\lambda_{DB}$ of the carriers and breaking down the resonance condition $d = n\lambda_{DB}$. Here $d$ is the electrode spacing.

To simplify the mathematical problems of analyzing the resonances in the structure we will assume that the rigid boundary conditions take place at the $S/Sm$ boundaries and that the geometrical sizes of the gate electrode is large enough so that applied to 2D-gas gate electric field is space uniform and the dependence of Fermi momentum of 2D-gas electrons $p_n$ on the gate voltage has the simplest form:

$$p_n = \sqrt{2m(E_F - eV_g)}, \tag{1}$$

where $E_F$ is 2D-gas Fermi energy. We will also assume that the condition of clean limit is fulfilled in the 2D-gas interlayer and that the transparency of the $S/Sm$ interfaces depends both on the difference of Fermi velocities of the metals and on the transparency of $\delta$-functional barriers with the strengths $W_1$ and $W_2$ located on left and right interfaces correspondingly.

Under the conditions formulated above starting from Gor'kov equations and making use of the approach developed in [1] one can arrived at the following expressions for

the supercurrent $I_s$ and normal resistance $R_n$ of the junction

$$I_s R_0 = \frac{2\pi T}{e}\sum_{\omega}\left\langle \frac{x\Delta^2 \sin\varphi}{M(\varphi,d,x)}\right\rangle, \quad R_0 = \frac{Se^2 p_n^2}{2\pi^2\hbar}, \quad \langle\ldots\rangle = \int_0^1 (\ldots)xdx \tag{2}$$

$$\begin{aligned} M(\varphi,d,x) = {} & E^2\left(\frac{1+w^2}{\gamma x}\right)\left[\sinh^2 b + \sin^2(a)\right] \\ & + \frac{2}{\gamma x}\left[\omega E(1+w^2)\sinh(2b) + w(1+w)E^2\sin(2a)\right] \\ & + 2\cos\varphi + E^2\cos(2a) + (2\omega^2+E^2)\cosh(2b) \\ & + (wE)^2\left[\cosh(2b) + 3\cos(2a)\right], \end{aligned}$$

$$E = \sqrt{\omega^2+\Delta^2}, \quad b = \frac{d}{2\xi_n x}\frac{\omega}{\pi T}, \quad a = \frac{2\pi dx}{\lambda_n}, \quad \xi_n = \frac{\hbar v_n}{2\pi T},$$

$$w = \frac{2mW_1}{p_s} = \frac{2mW_2}{p_s}, \quad \gamma = \frac{v_n}{v_s}.$$

$$R_n^{-1} = 2R_0^{-1}\left\langle \frac{8\gamma^2 x^3}{F_0 - F_1\cos(2a) - F_2\sin(2a)}\right\rangle, \tag{3}$$

$$F_0 = 16w_1^2w_2^2 + 4(w_1^2+w_2^2)\left[(\gamma x)^2+1\right] + (\gamma x)^4 + 6(\gamma x)^2 + 1,$$

$$F_1 = 16w_1^2w_2^2 - 8(w_1w_2)\left[(\gamma x)^2+1\right] - 4(w_1+w_2)^2\left[(\gamma x)^2-1\right] + \left[(\gamma x)^2-1\right]^2,$$

$$F_2 = 4\gamma x(w_1+w_2)\left[(\gamma x)^2 - 1 - 4w_1w_2\right], \quad w_{1,2} = \frac{2mW_{1,2}}{p_s}$$

Here $\omega = \pi T(2n+1)$ are Matsubara frequencies, $\Delta$ and $\varphi$ are modulus and phase difference of the order parameters of the superconducting electrodes, $v_{s,n}$ and $p_{s,n}$ are Fermi velocities and Fermi momentums of superconductor and 2D-gas correspondingly, $S$ is cross-section of the junction.

Taking into account that in practically interesting interval of the gate voltage $V_g \ll E_F/e$

$$\frac{dp_n}{dV_g} = -e\sqrt{\frac{m}{2(E_F - eV_g)}} \approx -\frac{e}{v_n}$$

we have found that the voltage gain of the device equals to

$$G = \frac{d(I_c R_n)}{dV_g} = -\frac{e}{v_n}\left[R_n\frac{dI_c}{dp_n} + I_c\frac{dR_n}{dp_n}\right], \tag{4}$$

where $I_c$ and $R_n$ determined by equations (2)–(3). Estimate from (2)–(3) by numerical calculation the optimal values of the derivatives in (4) for typical values of the parameters $v_n \approx 3\times10^5 m/c$, $\gamma \approx 0.2$, $S \approx 10^{-14}m^2$, $p_n/v_n \approx 10^{-2}m_e$ and $T/T_c = 0.25$ we arrived at $G \approx 0.4$.

This value is three order of magnitude larger compare to achieved up to now in traditional Josephson field effect transistors, but still less than unity. Thus we can

conclude that the proposed structure can be effectively used in turnable SQUIDs or other devices for adjustment the optimal working points, but not as an amplifier or logic circuits where it is necessary to have the gain larger than one.

This work was supported by Russian Scientific Program Physics of Solid State Nanostractures and Russian Fond for Fundamental Research.

**References**

[1] A. L. Gudkov, M. Yu. Kupriyanov, K. K. Likharev, *Zh. Eksp. Teor. Fiz.* **94** 319-332 (1988).
[2] A. W. Kleinsasser and W. J. Gallagher, *Modern Superconductor Devices*, 1990, Academic Press, Boston.
[3] H. Takayanagi T. Akazaki, J. Nitta, *Phys. Rev. B*, **51** 1374 (1995).
[4] T. Kawakami and M. Takayanagi, *Appl. Phys. Lett.* **46** 92 (1985).
[5] C. Nguen, J. Werking, H. Kroeger and E. L. Hu, *Appl. Phys. Lett.* **57** 87 (1990).
[6] A. W. Kleinsasser, T. N. Jackson, D. McInruff, F. Rammo, and J. M. Woddall, *Appl. Phys. Lett.* **55** 1909 (1989).
[7] A. Kastalsky, L. H. Greene, J. B. Barner and R. Bhat, *Phys. Rev. Lett.* **64** 958 (1990).
[8] D. Uhlisch, M. Yu. Kupriyanov, A. A. Golubov, J. Appenzeller, Th. Klocke, K. Neurohr, A. V. Ustinov, A. I. Braginski, In Abstracts of Invited Lectures and Contributed Papers of International Symposium "Nanostructures: Physics and Technology", St.Peterburg, Russia, 24-28 June 1996, p. 7.
[9] D. Uhlisch, M. Yu. Kupriyanov, A. A. Golubov, Th. Klocke, K. Neurohr, A. V. Ustinov, A. I. Braginski, *Physica B* **225** 197-201 (1996).
[10] H. Matsuoka, T. Ichiguchi, T. Yoshimura and E. Takeda, *IEEE Electron Device Letters* **13** N1 (1992).
[11] J. H. Randall, A. C. Seabaugh and J. H. Luscombe, *J. Vac. Sci. Technol. B* **10** N6 (1992).
[12] K. Ismail, D. A. Antoniadis and H. I. Smith, *Appl. Phys. Lett.* **55** N6 (1989).

Ioffe Institute
6th Int. Symp. "Nanostructures: Physics and Technology"
St Petersburg, Russia, June 22–26, 1998.



# Structural and tunnel characteristics of Langmuir films based on molecular cluster nanostructures

E. S. Soldatov†, S. P. Gubin‡, V. V. Khanin†, G. B. Khomutov†,
A. Yu. Obidenov†, *A. S. Trifonov*† and S. A. Yakovenko†
† Faculty of Physics, Moscow State University, 119899 Moscow, Russia
‡ Institute of General and Inorganic Chemistry, 119899 Moscow, Russia

## 1 Introducion

In development of nanoscale electronic devices, such as nanoelectronic digital circuits, the single electron tunneling effects and quantum size effects in isolated conducting nanoparticles are of principal importance. Each of these effects can be detected when charging energy and/or electronic level separation exceed the thermal energy $k_BT$. The manifestation of both effects correlates as a rule with decrease in nanoparticle size. Relevant effects were observed at room temperature in the tunneling current-voltage characteristics in a number of molecular and nanoparticle systems [1]–[8]. The principal point in these studies is the complete characterization of formed structures because random variations of the nanoparticle size and/or shape can lead to unpredictable and nonreproducible changes in the parameters of tunnel system.

Scanning tunneling microscopy (STM) allows to visualize the molecular nanostructures and to study redox processes in single molecules. The molecular structure of samples for investigations of single nanoparticles by this technique has to be monolayer on the conducting substrate.

We have proposed the approach based on the use of mixed monolayer Langmuir–Blodgett (LB) films consisted of inert amphiphyle molecular matrix and guest cluster molecules to create the reproducible stable planar nanostructures with various systems of electron tunnel junctions.

In present work the various supramolecular nanostructures based on the multicomponent LB films of stearic acid (SA) and a number of incorporated clusters have been studied by means of STM technique at room temperature. All clusters were chemically synthesized and hence had atomically equal structure and reproducible properties. Mixed monolayers on the water surface have been studied. The effects related to single electron tunneling and energy quantization of electrons were observed in formed molecular structures.

## 2 Experimental

The cluster molecules used: carboran ($C_2B_{10}H_{12}$); metallorganic cluster molecules of the close types: $Pt_4(CO)_5[P(C_2H_5)_3]_4$ — cluster I, $Pt_5(CO)_6[P(C_2H_5)_3]_4$ — cluster II, $Pt_5(CO)_7[P(C_6H_5)_3]_4$ — cluster III. Metallorganic clusters have metal nucleus surrounded by organic coating [10]. It provides the stability of cluster structure and tunnel barrier with fixed parameters.

The STM topographic measurements of the monolayer films deposited on a HOPG surface were performed using a Nanoscope-I with homemade control unit scanning tunneling microscope. The cluster molecules were studied spectroscopically by recording

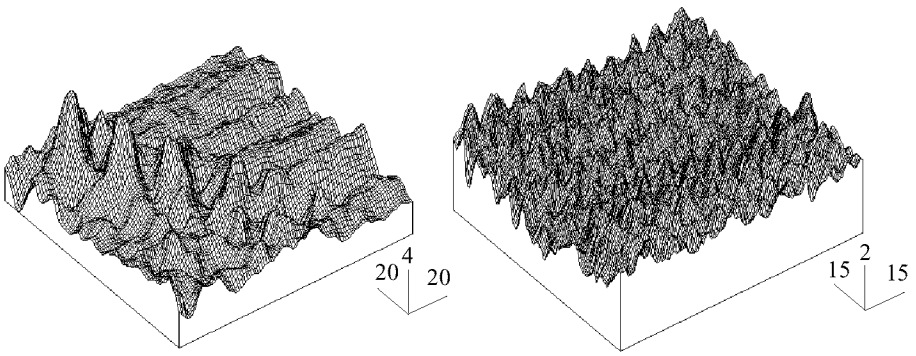


**Fig 1.** STM topographic images of mixed monolayers of molecular metallorganic clusters (a) $Pt_4(CO)_5[P(C_2H_5)_3]_4$, (b) $Pt_5(CO)_6[P(C_2H_5)_3]_4$) with stearic acid deposited by Shaefers method onto the surface of graphite substrate. $T = 300$ K.

tunneling current-bias voltage ($I$–$V$) curves in double tunnel junction geometry, where cluster is coupled via two tunnel junctions to two macroscopic electrodes (HOPG substrate and the tip of a STM). The measurement procedure consisted of the obtaining of topographic image and then positioning the tip above an isolated cluster molecule for the tunneling spectroscopy measurements.

## 3 Results and discussion

Mixed monolayers consisting of SA and clusters I, II and III reveal complex behavior not typical for mixed monolayers with immiscible components, where monolayer properties are weighted mean of the individual values [11, 12, 13].

Fig. 1 shows topographic STM images of different mixed SA/melallorganic cluster monolayers with characteristic observed structures: a chain of cluster I molecules (Fig. 1a), high ordered two-dimensional array of clusters II (Fig. 1b). The single cluster molecule and groups of clusters were also observed. Images of mixed carboran/SA monolayer (molar ratio 1:20) were similar to shown on Fig. 1b. The STM image of cluster molecules corresponded qualitatively to the size of molecule known from the structural data [10].

Spectroscopic results, namely the $I$–$V$ and $dI/dV$ characteristics are shown in Fig. 2. The curves with steps of variable widths and heights (the typical one is shown in Fig. 2 (a, b)) were observed only on the organo-metallic clusters, whereas identical smooth $I$–$V$ curves without noticeable particular features (Fig. 2(c)) were obtained everywhere else except over the cluster molecules. The $I$–$V$ curve shown in Fig. 2(c) is characteristic for single tunnel junction STM tip-substrate and its super linear course is usual for tunnel junctions [14]. All $I$–$V$ curves obtained on different points of carborane/SA monolayer surface (including clusters) were practically identical to one presented in Fig. 2(c), resembled those for single tunnel junction and pointed out the close direct electronic contact of carborane molecules with the graphite substrate. The same effects are known for fullerene molecules deposited onto metallic substrates [8]. The conductivity ($dI/dV$) curve (corresponding to the $I$–$V$ curve (a) in Fig. 2) is presented in Fig. 2(b), and apparently reveals the complex molecular level structure of ionized cluster states in processes of DTJ tunneling. This $I$–$V$ curve is determined by the tunnel junctions parameters, the energy separation of highest occupied molecular orbital

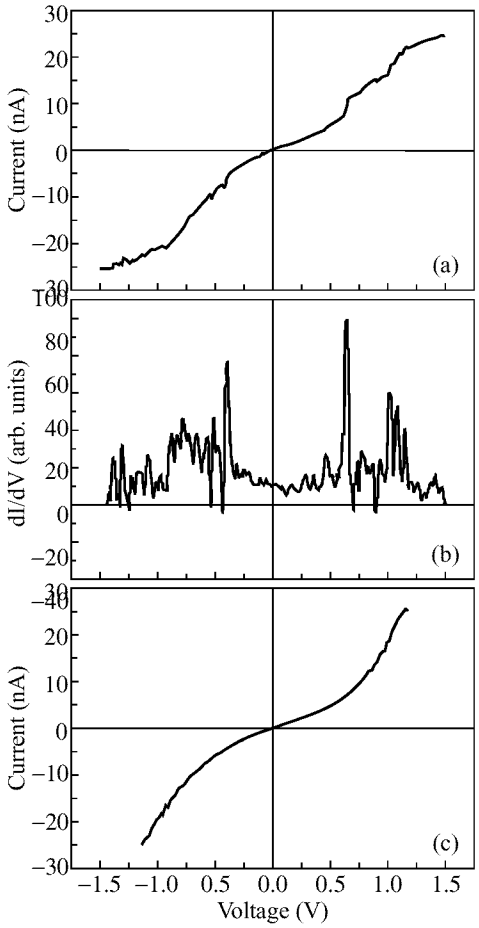


**Fig 2.** STM tunneling current–voltage ($I$–$V$) characteristics of mixed monolayer of cluster molecules $Pt_4(CO)_5[P(C_2H_5)_3]_4$ with stearic acid in ratio 1:80 recorded in double tunnel junction system STM tip-monolayer-graphite substrate at 300 K: (a) characteristic $I$–$V$ curve recorded on the cluster; (b) tunneling spectroscopic $dI/dV$ curve corresponding to curve (a); (c) typical $I$–$V$ curve recorded on the monolayer surface without metallorganic clusters.

(HOMO) and the lowest unoccupied molecular orbital (LUMO) and its combination with Coulomb single-electron charging effects during tunneling. The $I$–$V$ picture can be complicated also by molecular orbital anisotropy when tunneling current is correspondingly dependent on the tip position over the molecule and on the molecular space orientation with respect to the substrate surface. To describe quantitatively the course of DTJ $I$–$V$ curve, it is necessary to solve corresponding quantum-mechanical problem taking into account foregoing circumstances.

The curves with steps (the typical one is shown in Fig. 2(a,b)) may be interpreted as a result of single-electron tunneling in DTJ system. The size of the cluster is about 1 nm and the capacitance of the tunnel junctions can be estimated as 0.5 aF ($5 \cdot 10^{-19}$ F) [3]. This value gives the value of Coulomb blockade about 0.5 V which is close to the experimental value (Fig. 2(a)). From the Fig. 2(b) one can see that the steps on the

branches of *I–V* curve are close to periodic with the period of about 350 mV. This value is consistent with the results of the work [14] in which the period of steps on *I–V* curve of molecular SET transistor on the base of twice larger cluster was approximately twice smaller. These facts give evidence that steps on the *I–V* curves may be due to the single electron tunneling effects.

## 4 Conclusions

The approach based on the use of mixed LB films consisted of inert molecular matrix and cluster molecules is effective for formation of reproducible, stable, ordered planar nanostructures with different systems of electron tunnel junctions. The effects of single electron tunneling and/or discrete electronic levels spectrum can be observed and studied in such structures at room temperature.

*Acknowledgments*

This work was supported in part by Russian Foundation for Fundamental Researches (Grants 96-03-33766a, 97-03-32199a), the Russian Program on the Prospective Technologies for Nanoelectronics (Gr. No. 233/78/1-3) and the Russian Program on the Physics of Nanostructures (Gr. No. 96-1031).

## References

[1] H. Nejoh, *Nature*, **353** 640 (1991).
[2] C. Schonenberger, H. van Houten, H. C. Donkersloot, *Europhys. Lett.* **20** 249 (1992).
[3] A. A. Zubilov, S. P. Gubin, A. N. Korotkov, A. G. Nikolaev E. S. Soldatov, V. V. Khanin, G. B. Khomutov, S. A. Yakovenko, *Tech. Phys. Lett.* **20** 195 (1994).
[4] M. Dorogi, J. Gomes, R. Osifchin, R. P. Andres, R. Reifenberger, *Phys. Rev. B* **52** 9071 (1995).
[5] C. M. Fischer, M. Burghard, S. Roth, K. V. Klitzing, *Europhys. Lett.* **28** 129 (1994).
[6] V. Erokhin, P. Facci, S. Carrara, C. Nicolini, *Thin Solid Films* **284-285** 891 (1996).
[7] S. A. Iakovenko, A. S. Trifonov, E. S. Soldatov, V. V. Khanin, S. P. Gubin and G. B. Khomutov, *Thin Solid Films* **284-285** 873 (1996).
[8] D. Porath, O. Millo, *J. Appl. Phys.* **81** 2241 (1997).
[9] E. S. Soldatov, V. V. Khanin, A. S. Trifonov, D. E. Presnov, S. A. Yakovenko, S. P. Gubin, V. V. Kolesov and G. B. Khomutov, *JETP Lett.* **64** 556 (1996).
[10] N. K. Eremenko, E. G. Mednikov, S. S. Kurasov, *Adv. in Chem.* (Rus.) LIV 671 (1985).
[11] G. B. Khomutov, S. A. Yakovenko, E. S. Soldatov, V. V. Khanin, M. D. Nedelcheva, T. V. Yurova, *Membr. and Cell Biol.* **10** 665 (1997).
[12] G. G. Roberts (ed.), *Langmuir-Blodgett Films*, N.Y., London: Plenum Press, 1990, p. 26–27.
[13] J. M. Solletti, M. Botreau, F. Sommer, Tran Minh Duc, M. R. Celio, *J. Vac. Sci. Technol. B* **14** 1492 (1996).
[14] J. G. Simmons, *J. Appl. Phys.* **44** 237 (1983).

Ioffe Institute
6th Int. Symp. "Nanostructures: Physics and Technology"
St Petersburg, Russia, June 22–26, 1998.



# InAs nanoscale islands on Si surface: a new type of quantum dots

*G. E. Cirlin*†, V. G. Dubrovskii†, V. N. Petrov†, N. K. Polyakov†, N. P. Korneeva†, V. N. Demidov†, A. O. Golubok†, S. A. Masalov†, D. V. Kurochkin†, O. M. Gorbenko†, N. I. Komyak†, N. N. Ledentsov‡, Zh. I. Alferov‡ and D. Bimberg§

† Institute for Analytical Instrumentation RAS, St. Petersburg, Russia
‡ Ioffe Physico-Technical Institute RAS, St. Petersburg, Russia
§ Institut für Festköperphysik, Technische Universität Berlin, Germany

**Abstract.** We study epitaxial growth of InAs onSi(100) surface using molecular beam epitaxy. We found that at moderate arsenic fluxes and substarte tempeartures (470 °C) the growth proceeds in Stranski–Krastanow growth mode with formation of mesoscopic dislocated clusters on top of the two-dimensional periodically-corrugated InAs wetting layer. At lower temperatures (250 °C) a dense array of self-organized nanoscale InAs quantum dots with good size and shape uniformity is formed.

## Introduction

Silicon is a key material in modern semicondiuctor technology. Such advantages of silicon as: high heat conductivity, high stiffness, availability of stable oxide and developed technology of cheep large-area dislocation free substrates make this material advantageous for numerous applications in microelectronics. As opposite, the indirect bandgap nature of Si makes it hardly available for applications in optoelectronics, as the probability of radiative recombination of nonequilibrium is very low. With the example of III–V materials, however, it is well known; that the luminescence efficiency of indirect gap material can be dramatically improved by placing of thin layers (quantum well) of narrow gap direct gap materials inside the indirect gap matrix (e.g. GaAs layers in AlAs). Nonequilibrium carriers are trapped in direct gap regions and the luminescence efficiency can be very high, even the relative total thickness of the narrow gap material is small. However, the quantum well (QW) needs to be thick enough not to let the size quantization effect to increase the bandgap of the direct gap insertion above the bandgap of the indirect gap matrix. As the lattice constants for narrow gap III–V compounds and Si differ significantly, formation of thick-enough narrow gap III–V layers without creation of dislocations is not possible. On the other hand, again, from III–V heteroepitaxial growth experience, it is well known that the effect of spontaneous formation of nanoscale strained islands in lattice mismatched epitaxy can be applied for fabrication of coherent quantum dots (QDs) with small bandgap energies and, simultaneously, high luminescence efficiencies. We proposed to use the similar approach for fabrication of coherent narrow gap III–V quantum dots to realize high luminescence efficiency in silicon to develop a principally new approach for integration of opto- and microelectronic devices using the same silicon host material [1]. The possibility of fabrication of III–V quantum dots on silicon surface using this approach; however, is not evident.

The heteroepitaxial InAs-Si system is characterised by a very high lattice mismatch (approximately 10 percents). Here we show that under specific growth conditions InAs QDs, satisfying the necessary size requirements (essentially 3D with lateral size above 12 nm) can be fabricated on Si (100) surface.

## 1 Experimental

The growth experiments were carried out using EP1203 MBE machine (Russia) on exactly oriented Si(100) substrates, either semi-insulaing or having n-type conductivity. The Si(100) surface preparation is performed in a way similar to described in [2]. The substrates were mounted on a Mo substrate holder using an indium melt. Thermal desorption of the silicon native oxide layer was performed at substrate temperature of 820 °C in 15 min. After this procedure a well resolved $(2 \times 1)$ surface reconstruction typical for cleaved Si(100) surface has been observed. After this the substrate temperature was smoothly decreased to the desired experimental value and the InAs deposition was initiated in a conventional MBE mode. The InAs deposition rate was 0.1 monolayers per second. After the deposition of the desired average thickness of the InAs on Si surface, the sample was immediately quenched to the room temperature and removed from the growth chamber. Pieces for STM studies were then covered with silicon vacuum oil immediately after exposure to atmosphere.

For *in situ* control of the surface morphology before and during growth, calibration of the growth rate and the III–V flux ratio, reflection high energy electron diffraction (RHEED) system composed of high sensitivity video camera, video tape recorder and PC computer interconnected via specially-designed interface has been used [3]. Surface morphology was also studied *ex situ* in different scanning probe microscopy setups. For scanning tunnelling microscopy (STM), we used the samples covered with oil to prevent the surface oxide layer formation affecting reliability of STM measurements. The atomic force microscopy (AFM) measurements have been carried out in ambient pressure using uncovered samples.

## 2 Results and discussion

In case of the InAs-Si(100) deposition at moderate arsenic fluxe $(1 \cdot 10^{-6}$ torr) and substrate temperature of 470 °C, the RHEED pattern remained streaky up to deposition of 60 MLs of InAs. A transition from $(2 \times 1)$ to $(3 \times 1)$ surface reconstruction has been observed. STM images of the surface of the sample grown in these conditions are presented in Fig. 1 and Fig. 2 (n-type substrate). One can see that mesoscopic InAs clusters having a 400 nm lateral size (Fig. 1) are clearly revealed in the image. In between of the clusters one can resolve weak corrugation of the reamaining InAs wetting layer with a characteristic period of about 25 nm (see Fig. 2). AFM measurements of the sample grown in similar conditions, but on semiinsulating substrate revealed similar morphology. The results for this temperature range can be interpreted as follows, after formation of InAs coherent wetting layer on Si (100) surface, as detected by the change in the surface reconstruction, most of the InAs deposited concentrates in well-separated mesoscopic dislocated clusters. As the most of the surface remains flat, the RHEED measurements denmonstarte 2D diffraction pattern.

Very different growth scenario occurs when the substrate temperature is reduced to 250 °C. In this case RHEED pattern was converted from streaky to spotty after 5.5

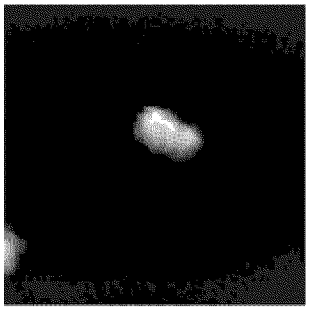

**Fig. 1.** STM image of the InAs huge clusters on the Si surface (60 ML of InAs, substrate temperature 470 °C). Scan area is 2000 nm × 2000 nm. Sides of the image are parallel to [011] and [0$\bar{1}$1] directions.

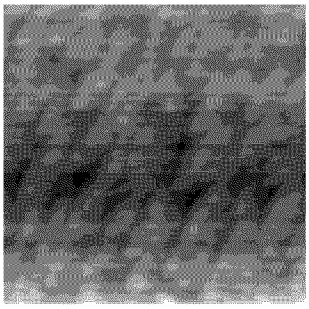

**Fig. 2.** STM image of the InAs corrugated surface in between the huge islands (60 ML of InAs, substrate temperature 470 °C). Scan area is 400 nm × 400 nm. Sides of the image are parallel to [011] and [0$\bar{1}$1] directions.

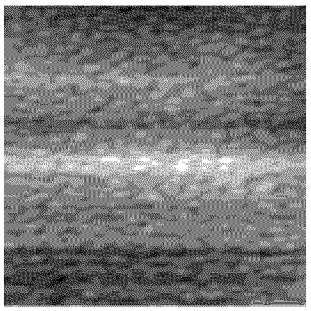

**Fig. 3.** STM image of the InAs nanoislands on Si surface (6 ML of InAs, substrate temperature 250 °C). Scan area is 400 nm × 400 nm. Sides of the image are parallel to [011] and [0$\bar{1}$1] directions.

monolayers (MLs) of InAs ware deposited. This transition indicates formation of three-dimensional islands. No further InAs deposition was performed in this case. STM image of the surface arrangement formed at 250 °C is shown in Fig. 3. On can conclude that InAs forms a remarkably dense array of uniform nanoscale islands (quantum dots) with good size and shape uniformity. For higher magnifications a well resolved crystalline shape of anysotropic QDs can be revealed. Cross-sectional analysis of the image gives the lateral size of the QD about 12 nm in one directions and 20 nm in the other, while the height of the QD is about 4 nm. The surface density of QDs is $5 \cdot 10^{11}$ cm$^{-2}$.

Considerable difference between surface morphology at 470 °C and 250 °C can be explained by a change in surface energetics with change in substrate temperature, as reported also for InAs growth on GasAs, but for change in arsenic flux. At low temperatures the total surface energy of the island is smaller than that of the underlying wetting layer due to the strain-induced renormalization of the surface energy [4]. At high temperatures, the total surface energy of the island is higher than that of the underlying wetting layer making island making ripening process energetically favourable. We note that at similar growth conditions no ripening is revealed for InAs islands formed on InAs wetting layer on GaAs(100) surface. Thus a higher diffusion coefficient for In

adatoms at higher substrate temperature does not necessarily leads to formation of mesoscopic clusters, and the energy benefit for ripening must be present as pointed in [4]. The Ostwald ripening process is kinetically controlled finally resulting in formation of large dislocated islands. Resulting surface topography thus contains mesoscopic islands and a corrugated wetting layer between them. Such a behaviour is typical for many heterosystems undergoing the Ostwald ripening and has been theoretically described in [5]. At lower temperatures an equilibrium array of islands is formed similar to the InAs-GaAs(100) growth [6], however in a much wider temperature range. Change from one mechanism to another may be related to a change in surface reconstruction either of the wetting layer or of the facets of the islands.

The characteristic time for formation of InAs nanoislands when crytical thickness (5.5 MLs) is of the order of 1 s for growth rate of 0.1 ML/s. Such a sharp 2D–3D transition has been previously observed in several semiconductor heteroepitaxial systems, in particular InAs/GaAs [6], Ge/Si [7] and theoretically considered using microscopic kinetic approach in [8].

To conclude, we proposed and denmonstrated a possibility to form InAs quantum dots of requested for optoelectronic applications size on Si surface using molecular beam epitaxy. Self organized formation of dense arrays of nanoislands uniform in size and in shape is demonstrated. The next step will be to cover InAs QDs with silicon and investigate their optical properties.

*Acknowledgements*

Authors wish to thank Dr. A. S. Berdnikov for the help in preparing the manuscript. This work was partially supported by INTAS Grant No. 96-0242 and Scientific Program "Physics of solid state nanostructures".

## References

[1] N. N. Ledentsov, in: *Proc. 23th Int. Conf. Phys. Semiconductors* Berlin, 1996, Ed. by M. Scheffler and R. Zimmermann (World Scientific, Singapoure, 1996), v. 1, p. 19.
[2] A. Ishisaka, Y. Shiraki, *J. Electrochem. Soc.* **133** 666 (1986).
[3] G. E. Cirlin, N. P. Korneeva, D. N. Demidov, N. K. Polyakov, V. N. Petrov, N. N. Ledentsov. *Semiconductors* **31** 1057 (1997).
[4] V. A. Shchukin, N. N. Ledentsov, M. Grundmann, P. S. Kop'ev, D. Bimberg. *Phys. Rev. Lett.* **75** 2968 (1995).
[5] S. A. Kukushkin, A. V. Osipov. *Prog. Surf. Sci.* **51** 1 (1996).
[6] G. E. Cirlin, G. M. Guryanov, A. O. Golubok, S. Ya. Tipissev, N. N. Ledentsov, P. S. Kop'ev, M. Grundmann, D. Bimberg. *Appl. Phys. Lett.* **67** 97 (1995).
[7] J. Zhu, K. Brunner, G. Abstreiter. *Appl. Phys. Lett.* **72** 424 (1998).
[8] V. G. Dubrovskii, G. E. Cirlin, D. A. Bauman, V. V. Kozachek, V. V. Mareev. *Tech. Phys. Lett.* (submitted).

Ioffe Institute
6th Int. Symp. "Nanostructures: Physics and Technology"
St Petersburg, Russia, June 22–26, 1998.



# Vertical correlations and anti-correlations in multi-layered arrays of 2D quantum islands

*V. A. Shchukin*†, V. G. Malyshkin†, N. N. Ledentsov† and D. Bimberg‡
† Ioffe Physico-Technical Institute, St. Petersburg 194021, Russia
‡ Technische Universität Berlin, D-10623, Germany

Recent breakthroughs in quantum wire- and quantum dot fabrication rely considerably on effects of spontaneous formation of ordered nanostructures [1,2]. Multi-sheet arrays of 3D or 2D islands are distinct from other types of nanostructures since the formation of such an array is governed by *both equilibrium ordering and kinetic-controlled ordering*. If the deposition of the first sheet of islands of material 2 on a material 1 is followed by a growth interruption, islands of an equilibrium periodic structure are formed [3,4]. If the islands are regrown by material 1, and material 2 is again deposited, a new growth mode occurs. For typical growth temperatures and growth rates, the structure of the buried islands of the first sheet does not change during the deposition of the second sheet. The second sheet of islands grows *in the strain field created by the buried islands of the first sheet.* And the structure of the second sheet reaches the equilibrium *under the constraint of the fixed structure of the buried islands of the first sheet.*

A remarkable feature of multi-sheet arrays of *3D islands* is that the buried islands in successive sheets are spatially correlated. At the surface, new islands were observed to be formed directly above buried islands [5–7]. The existing theory explaining well the correlation accounts the strain created by buried islands and shows that energetically preferred sites for nucleation of islands of the second sheet occur above buried islands [6,7]. In [6,7], buried islands were approximated as elastic point defects, and the crystal was treated as elastically isotropic medium.

In seeming contradiction to the above results, very recent experiments on multi-sheet arrays of 2D islands of CdSe in ZnSe matrix [8] unambiguously and surprisingly revealed vertical *anti-correlation* between islands in successive sheets. Surface islands are formed above the spacings in the sheet of buried islands.

Here we examine the energetics of multi-sheet arrays of 2D islands and seek the equilibrium configuration of the array of surface islands, under the constraint of a fixed array of buried islands. The two key inputs of our treatment which make it different from those of [6, 7], are as follows. *i)* We consider 2D islands of 1–2 monolayers height where the separation between successive sheets is comparable or even less than the lateral size of the islands, and we take into account their exact shape. *ii)* We take into account the elastic anisotropy of cubic crystals in question.

Since a single-sheet array of 2D islands can exist both as a 1D array of stripes and as a 2D array of compact islands (disks) [9], we address both possibilities. To extract essential physics, it suffices to examine a double-sheet array comprised of one sheet of buried islands and one sheet of surface islands. The total energy of the double-sheet array equals,

$$E_{\text{total}} = E_{\text{surf}} + E_{\text{boundaries}} + \Delta E^{(SS)}_{\text{elastic}} + E^{(SB)}_{\text{elastic}} . \qquad (1)$$

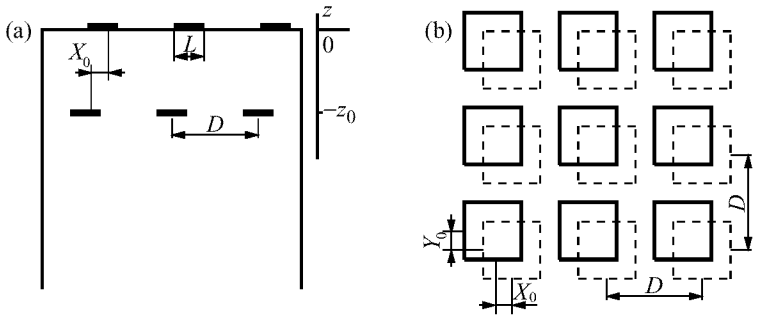


**Fig 1.** Geometry of double-sheet arrays of 2D islands. (a) Each sheet of islands forms a 1D array of stripes. The cross-section is shown. (b) Each sheet of islands forms a 2D array of square-shaped islands. The plan view is plotted. Buried islands are depicted by dashed lines, and solid lines are used for surface islands.

Here $E_{\text{surf}}$ is the sum of the surface energies of surface islands and of uncovered parts of material 1, $E_{\text{boundaries}}$ is the energy of island boundaries, $\Delta E^{(SS)}_{\text{elastic}}$ is the elastic relaxation energy of surface $(S)$ islands due to the discontinuity of the intrinsic surface stress tensor on island boundaries [3,9], $E^{(SB)}_{\text{elastic}}$ is the elastic energy of the interaction of surface islands $(S)$ and of buried islands $(B)$. We focus on the typical experimental situation of *an equal amount of the deposited material in each deposition cycle*. Then each sheet of islands alone tends to form the *same periodic structure* which corresponds to the minimum of the sum of the first three terms of Eq.(1). If the interaction between the two sheets is neglected, the surface array of islands *as a whole* can be subject to an arbitrary shift in the $xy$-plane. The strain due to buried islands has the same periodicity as the array of surface islands. Therefore the fourth term in Eq.(1) does not change the periodicity of the surface structure, and just defines its *relative position with respect to the array of buried islands* (Fig. 1). Since the interaction energy $E^{(SB)}_{\text{elastic}}$ is the only term in Eq.(1) which depends on the relative shift of the two arrays we focus only on this energy term as a function of the shift $X_0$ for 1D array of stripes (Fig. 1a) and of the shift $(X_0, Y_0)$ for 2D array of compact islands (Fig. 1b).

To evaluate the strain due to buried islands, we refer to the strain due to point defects [10]. A point defect located at $\tilde{\mathbf{r}}$ is represented by the superposition of three mutually perpendicular double forces (by an elastic dipole), and the effective body force density is $f_i(\mathbf{r}) = a_{ij}\nabla_j\delta(\mathbf{r} - \tilde{\mathbf{r}})$. A monolayer-thick inclusion in the plane $z = \tilde{z}$ with macroscopic lateral dimensions is a 2D array of point defects. It can be described by a 2D shape function $\Theta^B(\mathbf{r}_{\|})$ which equals 1 inside the inclusion, and 0 otherwise. The body force density associated with a 2D inclusion can be obtained by adding contributions of single point defects,

$$f_i(\mathbf{r}) = \frac{1}{A_0}\int d^2\tilde{\mathbf{r}}_{\|}a_{ij}\nabla_j\left[\delta(\mathbf{r}_{\|} - \tilde{\mathbf{r}}_{\|})\delta(z - \tilde{z})\right]\Theta^B(\tilde{\mathbf{r}}_{\|})\,, \tag{2}$$

where $A_0$ is unit cell area in the $xy$ plane. Equation (2) is derived under the assumption of no mutual influence between the point defects comprising the inclusion. Generally speaking, the tensor $a_{ij}$ characterizing the double force density is different for a single point defect and for a monolayer-thick inclusion. A substitutional impurity atom in

a zinc blend crystal of III–V or II–VI semiconductor has $T_d$ site symmetry, and the corresponding tensor $a_{ij}$ has the cubic symmetry. On the other hand, if the inclusion of equal substitutional impurity atoms is oriented in the (001) plane of the zinc blend crystal, has monolayer thickness and infinite lateral dimensions, *each atom of the inclusion has $D_{2d}$ symmetry*. Therefore, the tensor $a_{ij}$ characterizing a monolayer-thick buried island has a *uniaxial symmetry*.

The elastic properties of the surface islands are described by the difference of two-dimensional intrinsic surface stress tensors $(\Delta\tau_{\alpha\beta})$ of the two materials. The energy of the elastic interaction between a periodic array of buried islands and a similar periodic array of surface islands is obtained in the form of the sum over the reciprocal lattice vectors [11]

$$E_{\text{elastic}}^{(SB)} = \frac{h^B}{2A_0}\sum_{\mathbf{k}_\parallel}\left|\widetilde{\Theta}(\mathbf{k}_\parallel)\right|^2 \exp\left(i\mathbf{k}_\parallel\mathbf{R}_0\right)(\Delta\tau_{\alpha\beta})a_{lm}\nabla'_m \left[\nabla_\alpha\widetilde{G_{\beta l}}(\mathbf{k}_\parallel;z,z') + \nabla_\beta\widetilde{G_{\alpha l}}(\mathbf{k}_\parallel;z,z')\right]\Big|_{\substack{z=0\\ z'=-z_0}}, \tag{3}$$

where $\mathbf{R}_0$ is the relative sheet of the two arrays, $h^B$ is the thickness of the buried islands, $\nabla_x \equiv ik_x$, $\nabla'_x \equiv -ik_x$, $\nabla_y \equiv ik_y$, $\nabla'_y \equiv -ik_y$, $\alpha, \beta$=1,2, $l, m$=1,2,3. We treat the crystal as elastically anisotropic cubic medium and use the static Green's tensor $\widetilde{G_{il}}(\mathbf{k}_\parallel;z,z')$ from [12]. The dependence of $E_{\text{elastic}}^{(SB)}$ on the separation between the two sheets is determined by the behavior of $\widetilde{G_{il}}(\mathbf{k}_\parallel;z,z')$ as a function of $z_0$. $\widetilde{G_{il}}(\mathbf{k}_\parallel;z,z')$ is a linear combination of three exponentials, $\exp(-\alpha_s k z_0)$, where three attenuation coefficients $\alpha_s$ are functions of the direction $\mathbf{k}_\parallel$ in the surface plane [12]. The key point is that, in a cubic crystal with a negative parameter of elastic anisotropy, $\Delta = (c_{11} - c_{12} - 2c_{44})/c_{44} < 0$, which is the fact for all III–V and II–VI cubic semiconductors, two of the three $\alpha_s$ are complex conjugate. Complex attenuation coefficients $\alpha$ imply that *the static analogues of Rayleigh waves exhibit not purely an exponential decay, but an oscillatory one*. This phenomenon is known for surface acoustic waves which are *generalized Rayleigh waves* in elastically anisotropic crystals [13]. Complex attenuation coefficients lead to the conclusion that the elastic interaction between successive sheets of islands exhibits an oscillatory decay with the separation between sheets.

The interaction energy (3) has been evaluated for double-sheet arrays of stripes and for double-sheet arrays of square islands. For the separation between the two sheets, $z_0 \leq 0.5D_0$ where $D_0$ is the lateral period, the difference between the value of $E_{\text{elastic}}^{(SB)}$ for the most favorable relative arrangement, and the one for the most unfavorable arrangement, is of the order of 0.1 meV/Å$^2$. This is the same order of magnitude as a typical energy of a single sheet of surface islands [9]. *This comparison confirms that the elastic interaction between the two sheets of islands can indeed result in vertical correlation or anti-correlation between the two sheets.*

The phase diagram of Fig. 2b shows that the favorable relative arrangement of the two sheets of islands *alternates from vertical correlation to anti-correlation*, some intermediate arrangements being possible for small spacing $z_0$. The separation corresponding to the *transition* from correlation to anti-correlation *depends dramatically on the anisotropy parameter $P^B \equiv a_{zz}/a_{xx}$ of the double force density characterizing buried islands*. Our results are in agreement with existing experimental data on

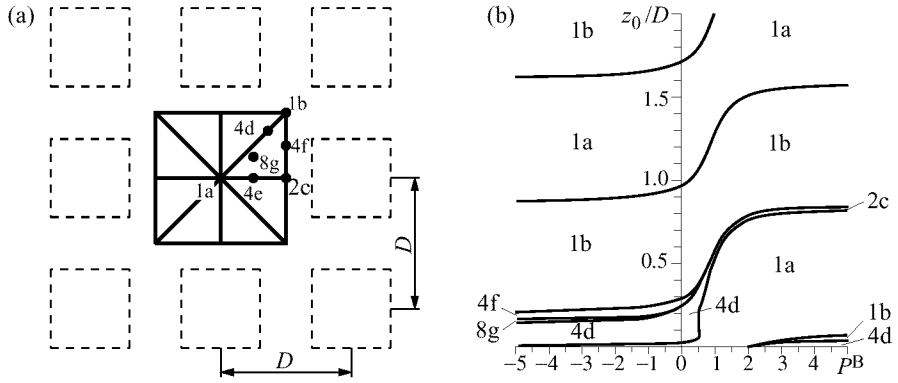


**Fig 2.** The phase diagram of a double-sheet array of square-shaped islands. (a) The relative shift $(X_0, Y_0)$ is defined by the projection of the center of a surface island onto the superlattice formed by the buried islands. Seven types of the symmetry are labeled according to [14]. (b) The phase diagram for the surface coverage 0.35. $P^B$ is the anisotropy of the double force density of buried islands, $z_0$ is the separation between the two sheets of islands, and $D$ is the period.

anti-correlations in multi-sheet arrays of 2D islands [8].

The work was supported, in different parts, by Russian Foundation for Basic Research, Grant No. 98-02-18304, by Russian Federal Program of Russian Ministry of Science and Technology "Physics of Solid State Nanostructures", Project 97-2014, and by the Joint Grant of Russian Foundation for Basic Research (96-02-00168G) and Deutsche Forschungsgemeinschaft (Sfb 296).

## References

[1] D. Bimberg, I.P. Ipatova, P.S. Kop'ev, N.N. Ledentsov, V.G. Malyshkin, and V.A. Shchukin, *Physics-Uspekhi* **40** 529 (1997).
[2] N.N. Ledentsov, V.M. Ustinov, V.A. Shchukin, P.S. Kop'ev, Zh.I. Alferov, and D. Bimberg, *Semiconductors* **32** (1998), in press.
[3] V.I. Marchenko, *JETP. Lett.* **33** 381 (1981).
[4] V.A. Shchukin, N.N. Ledentsov, P.S. Kop'ev, and D. Bimberg, *Phys. Rev. Lett.* **75** 2968 (1995).
[5] L. Goldstein, F. Glas, J.Y. Marzin, M.N. Charasse, and G. Le Roux, *Appl. Phys. Lett.* **47** 1099 (1985).
[6] Q. Xie, A. Madhukar, P. Chen, and N. Kobayashi, *Phys. Rev. Lett.* **75** 2542 (1995).
[7] J. Tersoff, C. Teichert, and M.G. Lagally, *Phys. Rev. Lett.* **76** 1675 (1996).
[8] M. Straßburg, *et al. Appl. Phys. Lett.* (1998), in press.
[9] Kwok-On Ng and D. Vanderbilt, *Phys. Rev. B* **52** 2177 (1995).
[10] J.D. Eshelby, In: *Solid State Physics* Vol. 3, Eds. F. Seitz and D. Turnbull (Academic Press, New York, 1956), p. 79.
[11] V.A. Shchukin, D. Bimberg, V.G. Malyshkin, and N.N. Ledentsov, *Phys. Rev. B* **57** (1998), in press.
[12] K. Portz and A.A. Maradudin, *Phys. Rev. B* **16** 3535 (1977).
[13] A.M. Kosevich, Yu.A. Kosevich, and E.S. Syrkin, *Sov. Phys. JETP* **61** 639 (1985).
[14] International Tables for Crystallography. Vol. A. Space Group Symmetry. Ed. T. Hahn. Reidel, Dordrecht, the Netherlands (1983).

Ioffe Institute
6th Int. Symp. "Nanostructures: Physics and Technology"
St Petersburg, Russia, June 22–26, 1998.



# Self-assembled formation of quantum dots during InGaAlAs quantum well growth

I. L. Krestnikov, *A. V. Sakharov*, N. N. Ledentsov, I. P. Soshnikov, Yu. G. Musikhin, A. R. Kovsh, V. M. Ustinov, I. V. Kochnev, P. S. Kop'ev, Zh. I. Alferov and D. Bimberg†
Ioffe Physico-Technical Institute RAS, St. Petersburg, Russia
† Institut für Festkörperphysik, Technische Universität Berlin, Hardenbergstrasse 36, 10623 Berlin, Germany

There exists a strong interest in direct techniques for fabrication of semiconductor structures with reduced dimensionallity: quantum wires and quantum dots (QDs). Currently the most developed technique to create QDs is related to self-organized formation of uniform three-dimensional islands at crystal surfaces in Stranski-Krastanow growth [1-4]. Alternative approach for nanostructure fabrication represents spontaneous phase separation in semiconductor alloys [see e.g. 5]. Recently, it was found that strained InGaAs layers grown by Metal-Organic Vapor Phase Epitaxy (MOVPE) in a GaAs matrix also exhibit lateral compositional modulations [6]. The luminescence properties of these structures, however, are similar to those in quantum wells, except of some peculiarities in luminescence polarization and lasing. In this paper we show, that spontaneous phase separation effects are much more pronounced in case of strained InGaAlAs layers in an AlGaAs matrix and result in formation of QDs demonstrating very large localization energies.

Structures investigated in this work were grown by molecular beam epitaxy (MBE) or MOVPE technologies on the GaAs (001) semiinsulating substrates. MOVPE structure comprised of a 1 $\mu$m-thick $Ga_{0.5}Al_{0.5}As$ buffer, an active layer and a 0.15 $\mu$m-thick $Ga_{0.5}Al_{0.5}As$ cap layers. Active layer represented single 10 nm $In_{0.12}As_{0.63}Al_{0.25}As$ layer confined by 0.3 $\mu$m-thick $Ga_{0.75}Al_{0.25}As$ layers on both sides. MBE structure comprised of a 0.05 $\mu$m $Ga_{0.35}Al_{0.65}As$ buffer, an active layer, and a 0.05 $\mu$m $Ga_{0.35}Al_{0.65}As$ cap layers. Active region was similar to the MOVPE case except the average In concentration was 10%. Both structures had 10 nm GaAs cap layers to prevent oxidation of Al containing layers. The growth temperature for the active region was in the both cases 500°C.

Low temperature photoluminescence (PL) spectra at different excitation densities of the MBE structure is presented on the Fig. 1. At low excitation density one can see three peaks in the energy range (1.1–1.55 eV) significantly shifted towards longer wavelength as expected for peak energy for uniform 10 nm-thick $In_{0.12}As_{0.63}Al_{0.25}As$ layer (see the QW transition energy marked by arrow). As the structure can be observed only for the case of InGaAlAs layers, one can conclude that these peaks are due to In-rich domains formed by phase separation effects during alloy growth. Multi peaks character of the emission spectrum can be explained by coexistence of domains having different size or composition QDs by sizes. Increase in the excitation density results in appearance of PL lines at energies corresponding to transitions in the uniform 10 nm-thick $In_{0.12}As_{0.63}Al_{0.25}As$ layer (1.76 eV) and in GaAlAs barrier (1.86 eV), respectively. At very high excitation level the PL peaks from QDs saturate due to finite density of

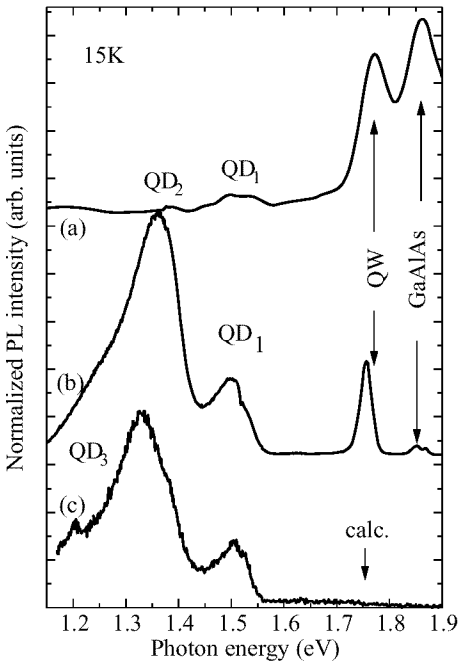


**Fig 1.** PL spectra for MBE structure measured at 17 K at different excitation level (a) 1 MW/cm$^2$, (b) 200 W/cm$^2$, (c) 50 mW/cm$^2$).

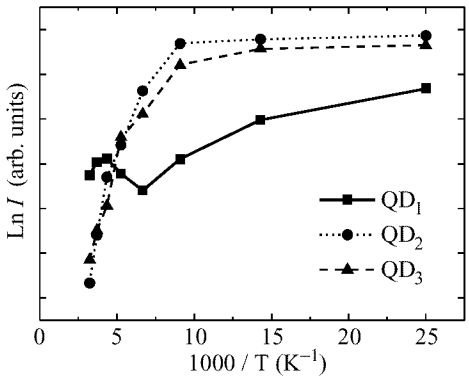


**Fig 2.** Temperature dependencies of integrated PL intensity for three different QD. Excitation density is 200 W/cm$^2$.

In-rich domains and the QW and the GaAlAs barrier luminescence become dominant. Temperature dependencies of integrated intensities of different QDs lines are presented in Fig. 2. At temperatures higher than 150 K there occurs efficient carrier redistribution between different types of the QDs. It shows significant hopping of carriers between different types of QDs at elevated temperatures.

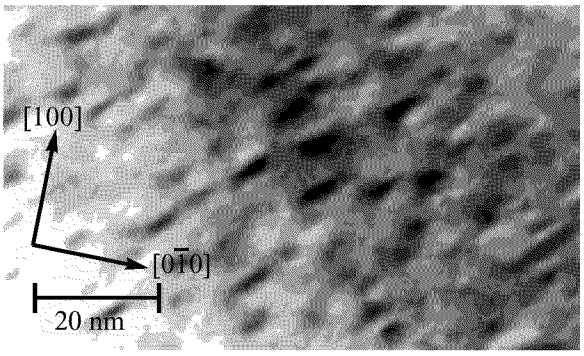


**Fig 3.** TEM image of MBE structure imaged under the strong beam condition. Note formation of elongated compositional domains.

Figure 3 shows a bright-field (200) plan-view transmission electron microscopy (TEM) image of the MBE structure. One can see QDs having characteristic lateral sizes 15 nm by 7 nm and prolonging in the [110] direction. Density of these QDs is about $2 \times 10^{11}$ cm$^2$. TEM investigations of the MOVPE structure show formation of QDs with lateral sizes less than 10 nm, the contrast modulation is weaker and the dots have symmetric shape. Density of QDs in this case is about $10^{11}$ cm$^2$. In PL spectra these dots result in appearance of a broad line placed at lower energies (1.40–1.63 eV) than the QW transition energy (1.665 eV). This agrees with smaller size and In composition as compared to MBE case.

To conclude, we demonstrate that InGaAlAs layers with very low average indium composition effectively decompose to In-rich nanoscale domains during epitaxial growth. The resulting quantum dots have significant localization energies as follows from temperature dependencies of the corresponding PL lines.

This work is supported by the Volkswagen Foundation and RFBR.

## References

[1] L. Goldstein, F. Glass, J. Y. Marzin, M. N. Charasse, G. Le. Roux. *Appl. Phys. Lett.* **47** 1099 (1985).
[2] P. M. Petroff, S. P. Den Baars, *Superlattices and Microstructures* **15** 15 (1994).
[3] M. Moison, F. Houzay, F. Barthe, L. Leprince, E. Andre, O. Vatel, *Appl. Phys. Lett.* **64** 196 (1994).
[4] N. N. Ledentsov, M. Grundmann, N. Kirstaedter, O. Schmidt, R. Heitz, J. Bohrer, D. Bimberg, V. M. Ustinov, V. A. Shchukin, P. S. Kop'ev, Zh. I. Alferov, S. S. Ruvimov, A. O. Kosogov, P. Werner, U. Richter, U. Gosele and J. Heydenreich, *Solid State Electronics* **40** 785 (1996).
[5] O. Ueda, M. Takechi, and J. Komeno, *Appl. Phys. Lett.* **54** 2313 (1989).
[6] N. N. Ledentsov, D. Bimberg, Yu. M. Shernyakov, I. V. Kochnev, M. V. Maximov, A. V. Sakharov, I. L. Krestnikov, A. Yu. Egorov, A. E. Zhukov, A. F. Tstsul'nikov, V. M. Ustinov, P. S. Kop'ev, Zh. I. Alferov, A. O. Kosogov and P. Werner, *Appl. Phys. Lett.* **70** 2888 (1997).

Ioffe Institute
6th Int. Symp. "Nanostructures: Physics and Technology"
St Petersburg, Russia, June 22–26, 1998.



# Indium segregation effects during GaAs cap-layer growth on InAs-quantum dots monitored by reflectance anisotropy spectroscopy

E. Steimetz, T. Wehnert, T. Trepk, J.-T. Zettler and *W. Richter*
Institut für Festkörperphysik, TU Berlin, Germany

**Abstract.** Performing Reflectance Anisotropy Spectroscopy (RAS) measurements during GaAs cap-layer growth on InAs quantum dots (QD) Indium segregation effects were monitored in-situ. Segregation during growth was found to be enhanced for elevated growth temperatures (775 K) and low cap-layer growth rates. A later intermixing of the islands with the GaAs cap-layer was observed during post-growth thermal annealing. For thin caps (10 nm) the RAS spectra became more and more InAs-like (2×4-like) while for 20 nm GaAs-cap-layers a smoothening of the surface but no indium related structure was found.

## Introduction

The real-time monitoring of quantum dot (QD) formation in Stranski-Krastanov growth mode by Reflectance Anisotropy Spectroscopy (RAS) in MOVPE allows the determination of the growth mode transition from 2D to 3D-growth and the later development of uncovered InAs islands [1]. The effect of surface segregation during GaAs cap-layer growth on top of the islands and later intermixing of the islands with the surrounding material are the topics of this study. Temperature dependent indium segregation effects during GaAs cap-layer growth and post-growth annealing have been monitored already for MBE growth of InGaAs-quantum wells [2], [3] and via TEM also for InAs-QDs [4]. STM studies of uncovered InGaAs islands showed that the top of the islands contains only InAs [5]. For postgrowth thermal annealing of covered InGaAs-QDs a strong blue-shift in Photoluminescence was observed, indicating an intermixing of the InGaAs layer with the surrounding GaAs [6] The suppression of indium segregation during cap-layer growth and subsequent intermixing are the remaining challenges for a routinely InAs-QD-based laser production, where elevated temperatures for the growth of the aluminium containing mirrors are necessary. We investigated the influence of different growth conditions (temperature, growth rate and total pressure) on segregation and intermixing with the GaAs cap during MOVPE growth by optical in-situ measurements. Post-growth annealing of samples with different cap-layer thickness, which showed no segregation effects during growth, allowed us to determine the minimum cap-layer thickness for a complete coverage of the islands.

## 1 Experiment

All measurements were performed in a low-pressure, horizontal MOVPE reactor. The RAS set-up [7] was attached to the MOVPE reactor via a purged, low-strain quartz window on top of the reactor. We were able to obtain spectra for photon energies ranging from 1.5 eV to 5.5 eV and to perform time-resolved measurements with a resolution better than 1 s. The shortest time for measuring one spectrum at a reasonable signal-to-noise ratio was 5 min.

## 2 In-segregation effects during cap-layer growth

In a first series of experiments the whole deposition sequence (2ML InAs/ GaAs, 5 s growth interruption and GaAs-cap-layer growth) is monitored at the As-dimer related energy of 2.6 eV. This was done for different growth temperatures. The transient measurements for 750 K and 775 K are given in Fig. 1.

Immediately after starting the InAs-deposition the reconstruction changes from c(4×4) for GaAs via (1×3) towards (2×4) for InAs and this causes a strong signal change in RAS [8]. When the growth mode transition takes place, the RAS-signal reduces, caused by a thickness reduction of the 2-dimensional InAs-wetting-layer. The islands themselves do not have any influence on the RAS-signal as long as they are small and isotropic. The overgrowth of the InAs islands with GaAs should lead to an As-rich c(4×4) reconstructed surface again, causing a reduction of the RAS-signal. For the lower growth temperature of 750 K this is really the case, but for $T = 775$ K a strong increase of the RAS signal with the onset of GaAs overgrowth was found. Since at 2.6 eV RAS is sensitive to the As-coverage of the surface [9] and the thickness of the growing In(Ga)As [10], this increase can be interpreted by a more In-rich conditions during GaAs-growth due to In-segregation.

The influence of the cap-layer thickness on the development of the surface after stopping the GaAs deposition is also shown in Fig. 1. Transients were taken for a nominal deposition of 10 nm and a 20 nm GaAs. The growth rate was determined by RAS oscillations on GaAs before. At 775 K a GaAs layer of nominally 10 nm is

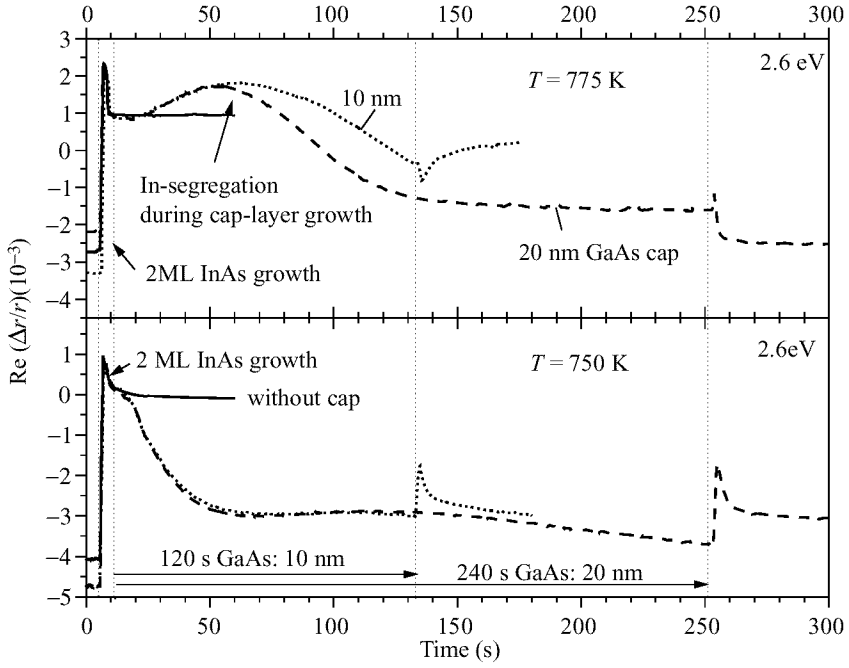


**Fig 1.** Time resolved RAS measurements during InAs-QD deposition and cap-layer growth for different growth temperatures.

obviously not sufficient to overgrow the islanded surface. After stopping the deposition the RAS transient shows an increase again, indicating that the surface still contains islanded material that is now rearranging at the surface. Ex-situ AFM measurements still showed islands at the surface for a 10 nm thick GaAs cap-layer. For the 20 nm deposition at 775 K this effect in RAS was not found, indicating that 20 nm are sufficient to cover the islands completely. In AFM a smooth surface was observed. The different slope in the RAS transients during GaAs overgrowth at 775 K might be attributed to a slightly reduced GaAs growth rate in the 10 nm experiment or might be caused by a different roughness of the initial GaAs-surface leading to a different island density. For the lower growth temperature of 750 K, no In-segregation effects during cap-layer growth were monitored. In this case even 10 nm of GaAs seem to be enough to cover the surface. But the starting RAS level for GaAs is not reached again even for 20 nm GaAs. This might be caused by a very rough surface after the whole deposition process due to the low growth temperature for GaAs. In AFM islands up to 6 nm height were found.

## 3 Post growth annealing of InAs-QDs with different cap-layers

In the second experiment InAs QDs were annealed after growth as long a changes of the surface stoichiometry, indicated by changes in the RAS signal around 2.6 eV, were found. Two monolayers InAs deposited at 750 K (no segregation during growth) were covered by GaAs at 750 K. The samples were prepared with varying cap-layer thickness (10 nm and 20 nm). In Fig. 2 the results of the annealing procedure after growth at deposition temperature are given. Fig. 2a shows the spectra before and after QD deposition with no GaAs cap-layer for reference. The InAs QD spectrum is typical

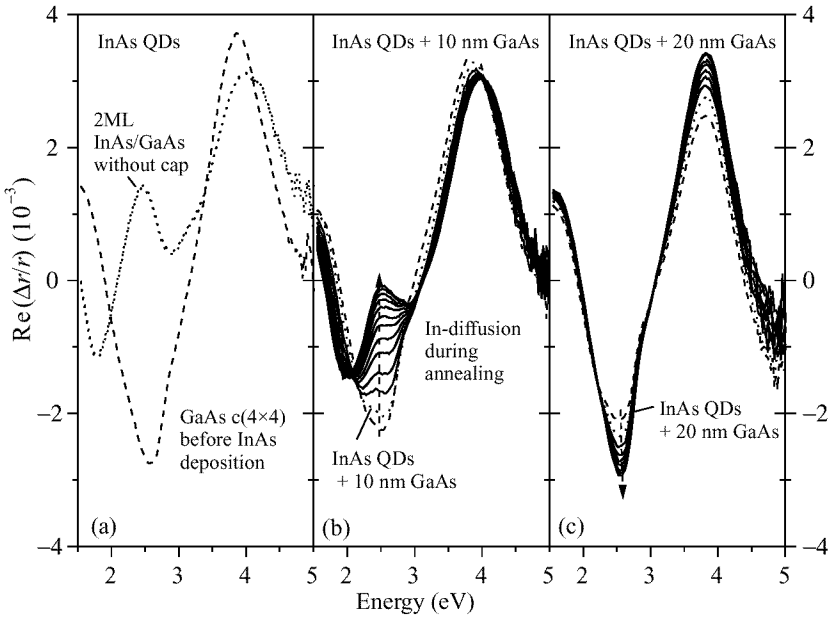


**Fig 2.** RAS spectra of uncovered, partly covered and completely covered InAs QDs and their evolution during annealing at 750 K.

for an InAs deposition slightly above the critical layer thickness. If there were clusters at the surface they would cause an additional structure in the high energy range of the RAS spectra [1]. For a QD deposition covered by 10 nm GaAs the RAS spectra after deposition show a c(4×4) reconstructed surface again, but the minimum at 2.6 eV is not as steep as it was before QD growth (see also Fig. 2a). Taking spectra every 5 minutes after the deposition a continuous change of the surface towards a more In-rich 2×4-like reconstructed surface was found. STM investigations of uncovered InGaAs islands have shown that the topmost layer of flat islands is containing only InAs [5]. We believe that the In-content in the uppermost layers is increasing during annealing due to segregation of indium atoms from the only partly covered islands to the top. For a GaAs cap of 20 nm this effect could not be observed. In contrast, here the surface seems to become smoother by annealing, indicated by a sharpening of the minimum at 2.6 eV, typical for a well ordered c(4×4) reconstruction. AFM measurements indeed showed a smooth surface.

## 4 Summary

By RAS measurements during GaAs cap-layer growth on InAs quantum dots (QD) indium segregation effects were observed in real-time. Segregation during growth was found to be enhanced for elevated growth temperatures. Post-growth annealing of samples at growth temperature resulted in an intermixing of the islands with the cap-layer material. The effect of intermixing on the surface stoichiometry is strongly dependent on the cap-layer thickness. For thin caps (10 nm) the RAS spectra became more and more InAs-like, indicating an In enrichement of the surface. For 20 nm GaAs cap-layers no indium related structure could be observed and annealing led to a smoothening of the c(4×4) GaAs surface.

## References

[1] E. Steimetz, F. Schienle, J.-T. Zettler, W. Richter, *J. Cryst. Growth* **170** 208-214 (1997).
[2] J. M. Moison, C. Guille, F. Houzay, F. Barthe, and M. Van Rompay, *Phys. Rev. B* **40** 6149-6162 (1989).
[3] M. Muraki, S. Fukatsu, Y. Shiraki, R. Ito, *Appl. Phys. Lett.* **61** 557-559 (1992).
[4] U. Woggon, W. Langbein, J. M. Hvam, A. Rosenauer, T. Remmele, D. Gerthsen, *Appl. Phys. Lett.* **71** 377-379 (1997).
[5] N. Grandjean, J. Massies, and O. Totterau, *Phys. Rev. B.* **55** R10189-R10192 (1997).
[6] F. Heinrichsdorff, M. Grundmann, O. Stier, A. Krost, and D. Bimberg, submitted to *Phys. Rev. B.*
[7] D. E. Aspnes, J. P. Harbison, A. A. Studna, and L. T. Florez, *J. Vac. Science Technol. A* **6** 1327 (1988).
[8] E. Steimetz, F. Schienle, J.-T. Zettler , W. Richter, D. I. Westwood, Z. Sobiesierski, C. Matthai, B. Junno, M. Miller and L. Samuelson: Proc. 23rd Int. Conf. Phys. Semiconductors, Vol. 2, p. 1297.
[9] K. Ploska, J. Th. Zettler, W. Richter, J. Jönsson, F. Reinhardt, J. Rumberg, M. Pristovsek, M. Zorn, D. Westwood, and R. H. Williams, *J. Cryst. Growth* **145** 44 (1994).
[10] E. Steimetz, J.-T. Zettler , W. Richter, D. I. Westwood, D. A. Woolf, Z. Sobiesierski, *J. Vac. Science Technol. B* **14** 3058–3064 (1996).

Ioffe Institute
6th Int. Symp. "Nanostructures: Physics and Technology"
St Petersburg, Russia, June 22–26, 1998.



# The bond passivation model for carbon nanoparticle growth

*V. V. Rotkin* and R. A. Suris
Ioffe Physico-Technical Institute, 194021, St. Petersburg, Polytehnicheskaya 26
e-mail: rotkin@theory.ioffe.rssi.ru

**Abstract.** The modified three parameter phenomenological model of the energetics of the carbon cluster growth is applied to the pure carbon nanocluster formation process as well as to the formation of clusters with the passivated bonds. The results in these two cases are distinct in principle. The closed spherical cluster with no dangling bonds is always energetically favourable in the original model. While the relative instability region of spheres in respect with the tubes (and moreover, with the planar graphite) opens at some critical bond softening (the analytical formulas are presented).

## 1 Three-parameter model of carbon-nanocluster energetics

The simple phenomenological three-parameter model for the calculation of the carbon nanotube formation energy has been proposed in Ref. [1, 2]. In the paper we will mainly conform to the initial model which operates with the energy of free dangling bond and will discuss what can result from the bond passivation. Let us remind some basis of the model. The specific cluster energy comparing with the infinite graphite sheet specific energy contains three additional terms (giving 3 phenomenological parameters). The possible dangling bond energy, $E_b$, multiplied by the free perimeter adds the first part of total formation energy. Typically, the closed curved cluster has the five-membered-rings (5MR) in contrast to the 6MR of the honey-comb graphite lattice. It generates the second topological parameter, $E_5$, for spheroidal cluster (more accurately, for cluster with finite Gauss curvature). Besides that, the re-hybridization of the electron orbit lying on the surface with the curvature increases the specific energy. This additional term does not deal with topology but depends on the local geometrical curvature and is proportional to some constant, $E_c$. We determined the parameters in Ref. [1, 2] as $E_b \simeq 2.36$ eV, $E_5 \simeq 17.7$ eV, $E_c \simeq 0.9$ eV$/b^2$.

These 3 parameters settle the question of relative stability of a large variety of carbon clusters of high symmetry. The parameters can be computed (involving quantum-chemical approach) or extracted from experimental data. However, it seems that just defining $E_b$, $E_5$, $E_c$ no further model versatility is possible. We will return to this question in Sec.3.

So far, we able to investigate the relative stability, for example, of the nanotube over the planar graphite sheet, or the closed spherical fullerene over other carbon nanostructures. It has been shown in [3, 4] that the planar graphite structure becomes unstable (because of the only energetical reason) to scrolling into spherical cluster of the same number of atoms at the critical cluster size ($\sim 250$ atoms). The smaller planar cluster is metastable to scrolling. The same is true for the cylindrical cluster with respect to the sphera. Let us consider it more quantitatively.

The graphite unit cell has an area $3\sqrt{3}/2$ in the dimensionless bond length units ($b^2$) and it possesses two carbon atoms. Within the model the spherical cluster energy

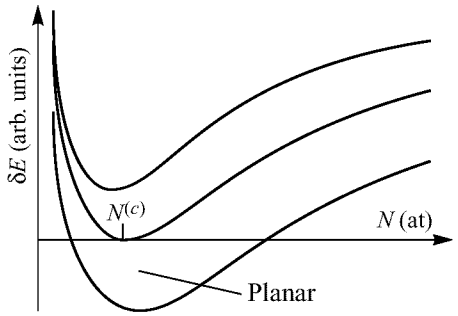


**Fig 1.** The energy difference $\delta E$ between the round graphite sheet (which has the minimal perimeter and is optimal one) and the spherical cluster – the upper curve – is always positive. The energy difference between the optimal tube and the sphere in general looks the same (compare Eq. (2) and the difference between Eq. (4) and Eq. (1)). The softening of the bond energy $E_b$ results in the lowering of these curves. At some critical softening the region of stable planar clusters opens (the region of the negative $\delta E$).

reads as [1]:

$$E_{\rm sph} = \left(E_5 + \frac{16\pi E_c}{\sqrt{3}}\right) - \frac{N_s}{N}E_c = N_s E_c \left(\frac{1}{N_{\rm lim}} - \frac{1}{N}\right) \qquad (1)$$

where we introduce the parameter $N_s = 2 \times 60\,(16\pi/3\sqrt{3})$. It arises naturally when one considers how much it costs to curve the graphite plane into the spheroidal cluster. When number of atoms exceeds the characteristic number $N_s \simeq 1160$ the correction to energy from 5MRs becomes relatively insignificant. The energy evidently stills positive till the number of atoms becomes less than $N_{\rm lim} = N_s E_c/(E_5 + 16\pi/\sqrt{3}) \simeq 24$. That means that disregarding the dangling bond energy the carbon prefers to belong to the normal graphite plane at $N < N_{\rm lim}$. Adding the dangling bond energy we change the situation drastically, the closed cluster is much more beneficial for any symmetrical shape. For example, the energy difference between the graphite sheet and the sphere of the same size $N$ is always positive:

$$E_{\rm pl} - E_{\rm sph} = 2\pi R E_b - N_s E_c \left(\frac{1}{N_{\rm lim}} - \frac{1}{N}\right) = E_c \left(12\pi E_c \sqrt{\frac{N}{N_\star}} - \frac{N_s}{N_{\rm lim}} + \frac{N_s}{N}\right). \qquad (2)$$

where $N_\star = 16\pi R_\star^2/3\sqrt{3} \sim 13$ atoms and will be discussed later. The result is shown in Fig.1 (upper curve).

## 2 Relative cluster stability: Scrolling into tube

Let compare the total energy of the sphere and the tube. Before that, we will define the "optimal tube". The optimization of the nanotube of the finite height (*i.e.* with dangling bonds on the perimeter) comes from the competition between two terms of the tube formation energy: with $E_b$, $E_c$ (evidently, one needs no 5MR for the cylindrical surface, hence no term with $E_5$ occurs).

It is favourable to decrease the radius in order to diminish the number of dangling bonds. This process costs the increasing energy of the larger curvature. So there is a minimum of energy for cluster of fixed number of atoms $N = 8\pi RH/3\sqrt{3}$. Such

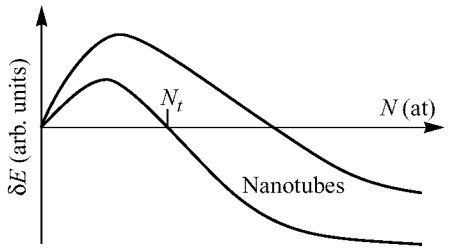


**Fig 2.** The energy difference between the optimal tube and the round piece changes sign at the number of atoms $N_t = 27/64N_\star \simeq 6$ (bottom curve). This result depends on the bond passivation because of when the variable $E_b$ increases the intersection point increases as well as $N_\star \sim E_b^{-1}$, that is shown by the upper curve.

cluster is called optimal. We will measure all lengths henceforward in the units of $b$. The height and radius of optimal tube $H$ and $R$, are co-dependent and can be uniquely written for a definite number of atoms $N$:

$$R_0 = \left(\frac{9}{16\sqrt{3}\pi}\frac{3E_c}{E_b}\right)^{\frac{1}{3}} N^{\frac{1}{3}} = R_\star \left(\frac{N}{N_\star}\right)^{\frac{1}{3}}, H_0 = 2R_\star \left(\frac{R}{R_\star}\right)^2 = 2R_\star \left(\frac{N}{N_\star}\right)^{\frac{2}{3}}. \quad (3)$$

Where we introduced a constant $R_\star = 3E_c/E_b$ having a simple meaning, it is a radius of optimal tube which area is equal to the area of sphere of the same radius (note that $H_0 = 2R_0 \equiv 2R_\star$). So the appropriate number of atoms $N_{\text{sph}} = N_{\text{opt.t.}} \equiv N_\star$. The optimal tube energy grows with $N$ moderately as:

$$E_o = 6\pi\sqrt{3}E_c \left(\frac{N}{N_\star}\right)^{\frac{1}{3}}. \quad (4)$$

Hence, comparing with the dangling bond energy of the round piece of graphite $\sim E_b\mathcal{P}$ it is beneficial to scroll it into tube (the graphite sheet of other form is unstable moreover because of the larger perimeter). The most favourable tube for such scrolling is the optimal tube. The energy difference between the optimal tube and the round piece changes sign:

$$E_o - E_{\text{pl}} = 6\sqrt{3}\pi E_c \left(\frac{N}{N_\star}\right)^{\frac{1}{3}} - 2\pi R E_b = 12\pi E_c \left(\frac{N}{N_\star}\right)^{\frac{1}{3}} \left[\left(\frac{N_t}{N}\right)^{\frac{1}{6}} - 1\right] \quad (5)$$

where the new constant $N_t = 27/64N_\star \simeq 6$ atoms is the maximal size of the beneficial plane (see also Fig.2). This consideration shows that indeed the tube has the less energy nearly always.

## 3 Could planar cluster be stable?

So far we considered the phenomenological parameters of the model as the experimentally defined constants. Could one try them as variables having the physical sense? $E_5$, $E_c$ depend mainly on the bond hybridization in the carbon network of the cluster cage. It is hard to imagine the essential change of these quantities excepting the new chemical products, such as: $B_xN_y$, $Si_x$, $C_xF_y$, $C_xH_y$ etc. We supposed to discuss it elsewhere.

In contrast, the dangling bond energy $E_b$ is suspected to deviate from the bare carbon value in the actual carbon soot formation process. This discussion turns to be extremely important when considering, for example, the usual flame products which are formed from carbonhydrates rather than the pure carbon blocks. It means that the energy of bond break/formation varies. Though it brings one additional parameter into model, the last becomes flexible and possesses new physics.

As a simple example one can evaluate the critical softening (the new parameter $\xi$) of the bond energy which results in the appearing of the planar graphite sheets stable for scrolling in the first time. It occurs when the curve given by Eq.(2) is tangent to the abscissa axis. The corresponding number of atoms is (the bottom ot the curve in the tangent point) $N^{(c)} = 3N_{\rm lim} \simeq 72$ atoms. The critical softening is given by the following formula:

$$\xi_{\rm pl-sph} = \frac{E_5 + 16\pi/\sqrt{3}}{18\pi E_c}\sqrt{\frac{N_\star}{N^{(c)}}} \simeq 0.37, \qquad (6)$$

so one need at least 2.7 times weaker bounding to have stable for scrolling graphite plane piece with a size about 70 atoms (Fig.1).

It may occur that the softening is strong enough to change the relative stability of the optimal tube over the sphere, which becomes unstable to opening into the cylinder at number of atoms $4N_{\rm lim} \simeq 96$. The critical softening in this case has no short formula, it is about 0.44.

## Summary

The three-parameter phenomenological model of the carbon nanocluster formation is reconsidered taking into account the possible varying of the dangling bond energy parameter. This leads to the significant changes in the relative stability diagram. Namely, at some critical bond softening (2-3 times comparing with the pure graphite) the region of planar graphite structure stability appears. That is the same as the instability of spherical cluster shape at some cluster size nearly about 70-100 atoms. The same region corresponds to the optimal tube which is more energetically favourable than the sphere. These results are in contrast with the conclusions made within the original model [1, 2, 3, 4]. The modified model can be applied to the growth of cluster with passivated dangling bonds, for example, for the flame product formation process.

The work was partially supported by RFBR grant No. 96-02-17926 and No. 98062 of "Fullerenes and Atomic Clusters" Programm.

## References

[1] V. V. Rotkin, R. A. Suris, *Fullerenes. Recent Advances in the Chemistry and Physics of Fullerenes and Related Materials.* Vol. II. Editors: R. S. Ruoff and K. M. Kadish. Electrochemical Society, Pennington, NJ, **PV 10-95**, p. 1263-1270, 1995.

[2] V. V. Rotkin, R. A. Suris, *Mol. Mat.*, **8**, 111-116 (1996).

[3] V. V. Rotkin, R. A. Suris, V. V. Rotkin, R. A. Suris, *Proc. of IV Int. Conf. on Advanced Materials*, S3-P3.4, Cancun, Mexico, 27 August–1 September (1995).

[4] V. V. Rotkin, R. A. Suris, unpublished.

Ioffe Institute
6th Int. Symp. "Nanostructures: Physics and Technology"
St Petersburg, Russia, June 22–26, 1998.



# InAs self-organized quantum dots grown by MOVPE in $In_{0.53}Ga_{0.47}As$ matrix

*O. V. Kovalenkov*, I. S. Tarasov, D. A. Vinokurov and V. A. Kapitonov
Ioffe Physico-Technical Institute, St. Petersburg 194021, Russia
E-mail: oleg@movpe.ioffe.rssi.ru

**Abstract.** The results of the self-assembling Stranski-Krastanow growth of InAs quantum dots embedded in $In_{0.53}Ga_{0.47}As$ by low pressure MOVPE are presented. The structures were investigated by room and liquid nitrogen photoluminescence method. The highest obtained emission wavelength of 2.1 $\mu$m at room temperature is the longest value for InAs quantum dots reported in literature until now.

## Introduction

The self-organized fabrication of the low dimensional semiconductor structures with coherent nanoscale islands (so called quantum dots) grown in Stranski-Krastanow growth mode has been a subject of intensive investigation in the last years. These structures have an unique electrophysical properties because of tree-dimensional confinement of carriers in the island volume.

One of the most extensively studied material system is the self-organized InAs islands on GaAs substrates. Semiconductor lasers based on InAs and InGaAs active region with low threshold current density (100 A/cm$^2$) and high characteristic temperature at room temperature ($T_0 = 385$ K) have been demonstrated [1, 2, 3].

However, there are a very few reports on the growth of InAs islands on InP substrates [4, 5, 6]. This material system might be a promising candidate for fabrication of low threshold QD-based lasers operating at the wavelength range of 1.5–2 $\mu$m which is important for high resolution molecular spectroscopy and atmosphere pollution monitoring.

## 1 Experimental

In this paper we present the results of self-assembling Stranski-Krastanow growth of InAs islands on InP by the low pressure metal organic vapour phase epitaxy (MOVPE). The processes were carried out in rectangular horizontal reactor operating at pressure of 100 mBar with radio frequency heating of graphite susceptor. The thrimethylgallium (TMGa), thrimethylindium (TMIn), arsine and phosphine diluted in hydrogen were used as sources of elements. The growth temperature was varied in the range of 500–600°C. Exactly oriented InP (100) substrates were used. Before the growth the substrates were degreased with the boiling organic solvents and then etched with $K_2Cr_2O_7$:HBr.

The investigated structures consist of 0.3 $\mu$m bottom cladding $In_{0.53}Ga_{0.47}As$ (hereafter referred as InGaAs) layer followed by the InAs quantum dots (QD) and 0.04 $\mu$m of

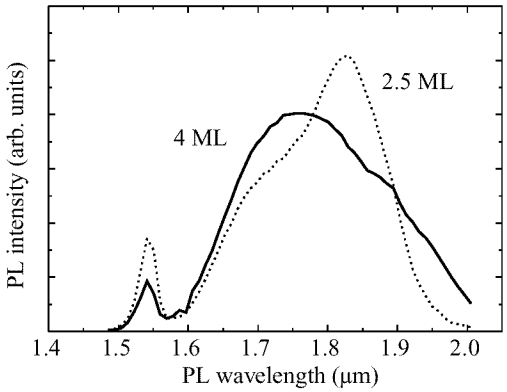


**Fig 1.** 77 K PL spectra of InAs/InGaAs QDs for two InAs deposition thicknesses.

upper InGaAs. The growth rate for barriers and QD were 8 Å/s and 2 Å/s, respectively. The nominal InAs deposition was varied between 1.5 and 4 monolayers (ML).

Inspite of the low energy gap difference between our ternary InGaAs barriers matched to InP substrate and QD we choose this material combination to avoid the parasitic V group exchange reactions of P-As on interfaces for InP/InAs system [4, 5, 6, 7] leading to formation of intermediate ternary InAsP layer [7]. The driving force behind forming a such layer comes from low binding energy of P and As. These reactions make this system sufficiently complicated and in dependence on growth conditions the various photoluminescence (PL) peak positions in the range of 0.9–1.8 $\mu$m have been obtained [4, 5, 6].

Moreover, the unintentional As/P exchange during InAs QDs growth on InP can lead to formation of ternary InAsP dots which should have a lower PL wavelength as compare to InAs ones. This can complicate of composition control in dots and, consequently, the emission wavelength in a such material combination.

## 2 Results and discussion

The room (300 K) as well as liquid nitrogen (77 K) PL measurements were performed for investigation of grown samples. As the excitation source we used the 514 nm line of argon ion laser. The excitation density was 50 W/cm$^2$.

The PL spectra of structures grown at 600°C with nominally 2.5 MLs and 4 MLs of deposited InAs are shown on Fig. 1. The growth interruption (GI) at interfaces were 5s before and after QD deposition in InAs and InP ambient, respectively. GI was introduced due to continuous growth can suppress the island formation [8, 9]. The PL peak at 1.5 $\mu$m arise from the ternary barrier. The broad high intense peaks may be attributed to emission from QDs. The splitting of peaks may testify the presence of two different size of islands.

Fig. 2 shows the 77 K PL spectra for samples containing of 4 MLs InAs nominally, grown at temperature of 600°C. Curves 1 and 2 with the same growth sequence as in the Fig. 1 show that the PL peak position does not depend on V/III ratio in gas phase at least in the range of 40 (curve 1) to 320 (curve 2). Curve 3 in Fig. 2 shows the substantial narrowing of PL peak due to introducing of long time (120 s) GI in $AsH_3$

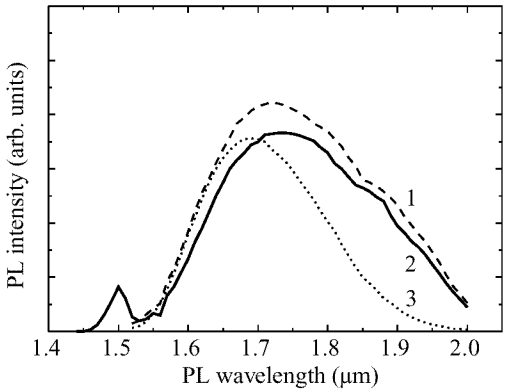


**Fig 2.** 77 K PL spectra of InAs/InGaAs QDs different growth conditions.

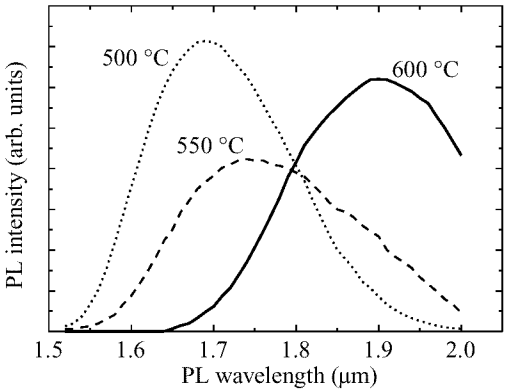


**Fig 3.** 77 K PL spectra of InAs/InGaAs QDs for different growth temperatures.

flow before QD growth. This phenomenon may be connected with reorganization of lower barrier surface what permitted to grow the more uniform in size QDs. The narrowing of PL peaks after thermal annealing of completely grown structures have been reported in literature [10].

The effect of the growth temperature on the PL spectra transformation is presented in Fig. 3 which shows the 77 K spectra of samples with 4 MLs of InAs islands nominally. After the bottom InGaAs layer has been grown at the temperature of 600°C the growth was interrupted in $AsH_3$ ambient during 120 s to decrease the temperature for QD deposition. The upper barrier was grown at the same temperature as QD region after 5 s of GI in $PH_3$ flow to QD formation. As clearly seen from Fig. 3 the lower the QD formation temperature the higher PL peak position. For lower investigated temperature of 500°C the peak is centered at 1.91 $\mu$m which corresponds 2.1 $\mu$m (0.6 eV) at room temperature. This value is the highest emission wavelength for InAs dots grown on InP substrate.

## 3 Conclusion

In summary, the self-organized InAs quantum dots embedded in InGaAs have been grown by the low pressure MOVPE. Photoluminescense measurements performed at room and liquid nitrogen temperature showed that InAs QDs grown in InGaAs matrix matched to InP substrate at appropriate growth conditions are a promising candidate for optoelectronic devices operated in spectral range of 1.9–2.1 $\mu$m. This value is the longest emission wavelength for InAs dots reported so far.

This work was partially supported by the program "Physics of solid state nanostructures" (Grant No. 96-2005).

## References

[1] Zh. I. Alferov, N. Yu. Gordeev, S. V. Zaitsev, et al., *Semiconductors* **30** 197 (1996).
[2] M. V. Maximov, N. Yu. Gordeev, S. V. Zaitsev, et al., *Semiconductors* **31** 124 (1997).
[3] M. V. Maximov, I. V. Kochnev, Yu. M. Shernyakov, et al., *Int. Phys. Conf. Ser.* N 155, ch. 7, p. 557 (1996).
[4] S. Fafard, Z. Wasilewski, J. McCaffrey, et al., *Appl. Phys. Lett.* **68** 991 (1996).
[5] A. Ponchet, A. Le Corre, H. L. Haridon, et al., *Appl. Phys. Lett.* **67** 1850 (1995).
[6] N. Carlsson, L. Samuelson, and W. Seifert, *EW MOVPE VII*, Berlin, G12 (1997).
[7] M. Mesrine, J. Massies, E. Vanelle, et al., *Appl. Phys. Lett.* **71** 3552 (1997).
[8] O. V. Kovalenkov, D. A. Vinokurov, D. A. Livshits et al. Intern. Symp. "Nanostructures: Physics and Technology", St. Petersburg, Russia, p. 141 (1996).
[9] O. V. Kovalenkov, D. A. Vinokurov, D. A. Livshits, et al., *Int. Phys. Conf. Ser.* N 155, ch. 3, p. 271 (1996).
[10] A. E. Zhukov, A. Yu. Egorov, A. P. Kovsh, et al., Int. Symp. "Nanostructures: Physics and Technology", St. Petersburg, Russia, p. 132 (1996).

Ioffe Institute
6th Int. Symp. "Nanostructures: Physics and Technology"
St Petersburg, Russia, June 22–26, 1998.



# Modelling the self-organization of boron clusters in silicon

G. G. Malinetskii, A. B. Potapov and *M. G. Stepanova*
Keldysh Institute of Applied Mathematics RAS, Moscow

**Abstract.** The paper illustrates application the theory of self-organization to practical problems in the physics on nanostructures. Starting from the principles of the theory of self-organization, the formation of dissipative structures as found experimentally in annealed highly-boron-doped silicon samples is explained. A qualitative "reaction-diffusion" model is developed which reproduces the formation of spatially ordered boron clusters distribution in the form of equidistant maxima. Perspectives of more exact quantitative models describing the extraordinary evolution of boron dopant in silicon are discussed.

## Introduction

This work gives an insight into understanding of the unusual behavior of boron dopant in silicon found experimentally beforehand [1–3]. In the experiment [1–3] the boron-doped crystalline silicon samples were additionally enriched in boron by ion implantation. The implantation led to an approximately 1000 nm-wide oversaturated region containing up to $4 \div 8 \cdot 10^{20}$ boron atoms per $cm^3$. The highly doped samples were annealed and the resulting depth distributions of the dopant were analyzed by SIMS. After annealing at 900–1075°C, complicated nonmonotonous boron distributions with several maxima and minima of the boron concentration were observed within the implanted oversaturated region. The distance between neighbouring maxima (peaks) close to 100 nm was found unchanged during the annealing and independent on the width of the implanted region. The latter, however, was crucial for the number of the peaks observed.

Thus, annealing of the boron-enriched silicon leads to a spontaneous spatial ordering of the dopant distribution. In this work a physical model is proposed to explain this unusual phenomenon.

## 1 Self-organization and formation of structures

In modern usage the spontaneous spatial ordering is known as self-organization and formation of dissipative structures [4–6]. From the theory of self-organization it follows that the transformation of homogeneous spatial component distributions into inhomogeneous ones can occur in open multicomponent systems of the Reaction-Diffusion type including interconversions of the system's components. The simplest mechanism leading to formation of spatially ordered structures such as a number of equidistant peaks can be conceived as a combination of positive and negative feedbacks (see e.g. [6]), with two principal elements being as-called short-range activation (self-maintaining of the peaks growth) and long-range inhibition (suppression of new peaks in a neighbourhood of one well developed).

In the present work we take the above fundamental results as a basis for our model of the self-organization process in hidhly doped silicon.

## 2 The model and its results

In refs. [1, 3] diffusion was suggested as the main mechanism of boron redistribution in the oversaturated samples, and the formation of the stable equidistant peaks was attributed to clusterization of the excess dopant.

In the present work, from the general principles of the theory of self-organization [4–6] it is shown that the spatial ordering of boron requires an active assistance of (at least) one further component — mobile crystalline defects. A straightforward one-dimensional model is put forward which explains spontaneous formation of the equidistant peaks in the boron depth distribution. The model includes diffusion of free boron dopant ($f$), precipitation of the excess boron into immobile clusters $p$ ($f \to p$), and dissolution of the clusters ($p \to f$) with assistance of the third component — the hypotetic mobile defects $d$. The general form of the model is

$$\begin{aligned}
\frac{\partial}{\partial t}C_f(x,t) &= \frac{\partial}{\partial x}\left(D_f\frac{\partial}{\partial x}C_f(x,t)\right) - Q_1(C_i) + Q_2(C_i)\\
\frac{\partial}{\partial t}C_p(x,t) &= Q_1(C_i) - Q_2(C_i)\\
\frac{\partial}{\partial t}C_d(x,t) &= \frac{\partial}{\partial x}\left(D_d\frac{\partial}{\partial x}C_d(x,t)\right) - \alpha_1 Q_1(C_i) + \alpha_2 Q_2(C_i) - Q_3.
\end{aligned}$$

Here $x$ is depth and $t$ is time; $C_{i=f,p,d}$ are the component's concentrations; the source terms $Q_1$ and $Q_2$ account for the transformations $f \to p$ and $p \to f$ followed by generation and annihilation of the defects, respectively; $\alpha_1$ and $\alpha_2$ are constants; and the term $Q_3$ allows for the defect sinks. Nonlinear dependencies of the sources $Q_1$ and $Q_2$ on the concentrations $C_f$, $C_p$ and $C_d$ provide an appropriate system of feedbacks to describe the spontaneous self-organization. The system of feedbacks is such that 1) the boron clusters precipitation-dissolution recycling, as a whole, generates the defects, and 2) in the presence of the defects the cluster dissolution $p \to f$ slows down. Thus, the defects eventually activate clusterization: local clouds of defects in the presence of boron clusters act like a pump drawing in the surrounding free boron and making it to precipitate into clusters. This results in a self-maintaining growth of large cluster accumulations surrounded by a "dead area" where formation of new clusters is suppressed because of a lack of the free boron. Large groups of clusters formed too close each to another fall into a competition for precipitation and containing of boron. More chances to survive has the largest and densest cluster group, as it produces more of defects which suppress dissolution.

Fig. 1a-d shows an example of numerical modelling of the boron redistribution due to the process of self-organization. It can be seen that the initial smooth depth distribution of boron displayed in Fig. 1a spontaneously splits into six peaks. One of these does not survive the competition with a stronger neighbour and disappears. Finally, a stationary pattern is formed which contains five almost equidistant peaks, as shown in Fig. 1d. In accordance with the experiment [1–3], positions of the main peaks are almost unchanged with time. The distance between the main peaks depends on the diffusion length of free boron and defects. From our model calculations a tentative estimate of the defects diffusion coefficient was obtained, $D_d = 10^{-14} \div 10^{-13}$ cm$^2$/s.

We are to emphasize that the model used in our work is one-dimensional, while the real system under consideration is three-dimensional, which should be accounted for in

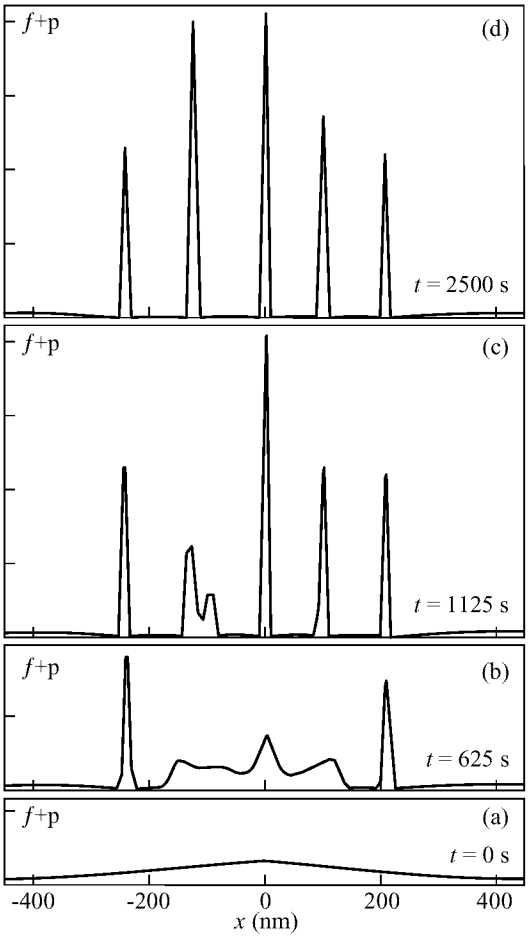


**Fig 1.** Model depth distributions of boron, $C_f + C_p$, at various stages of the self-organization. (a) an initial model distribution; (d) the final stationary distribution.

the subsequent sophisticated models. However, from the general theory [6] it can be concluded that simple approximate approaches like the present give, as a rule, a good qualitative picture of self-organization processes.

Thus, the simple qualitative "reaction-diffusion" model put forward in this work on the basis of the theory of self-organization [4–6] explains the formation of complex spatial distribution of boron in highly-doped silicon. The model predicts an important role of mobile crystalline defects which are to activate the process of self-organization. The model also allows to estimate the diffusion coefficient of the defects. We do not specify the proposed defects in this work because this requires additional experimental information. New experimental studies of the boron-implanted silicon structure are expected to provide solid grounds for more exact quantitative models of self-organization of boron clusters in silicon.

*Acknowledgments*

The authors like to thank A. M. Myasnikov for the discussion of the interesting new phenomena studied in this work.

Support from the RFBR grants 96-01-01161, 96-02-18689 and 97-01-00396 is gratefully acknowledged.

## References

[1] Myasnikov A. M., Obodnikov B. I., Seryapin V. G., Tishkovsky E. G., Fomin B. I., Cherepov E. I. *Letters to JETP* **60** 96 (1994).

[2] Myasnikov A. M., Obodnikov B. I., Seryapin V. G., Tishkovsky E. G., Fomin B. I., Cherepov E. I. *Physics and technics of semiconductors* **31** 338 (1997).

[3] Myasnikov A. M., Obodnikov B. I., Seryapin V. G., Tishkovsky E. G., Fomin B. I., Cherepov E. I. *Physics and Technics of Semiconductors* **31** 703 (1997).

[4] Haken H. *Synergetics. An introduction.*, Springer, 1977.

[5] Nikolis G., Prigogine I. *Self-Organization in nonequilibrium systems*, Wiley-Interscience, 1977.

[6] Akhromeyeva T. S., Kurdymov S. P., Malinetskii G. G., Samarskii A. A. *Chaos and dissipative structures in "reaction-diffusion" systems*, Moscow: Nauka, 1992 (in Russian).

Ioffe Institute
6th Int. Symp. "Nanostructures: Physics and Technology"
St Petersburg, Russia, June 22–26, 1998.



# Equilibrium composition-modulated structures in epitaxial films of semiconductor alloys

*V. A. Shchukin* and A. N. Starodubtsev
Ioffe Physico-Technical Institute, St. Petersburg 194021, Russia

Spontaneous formation of composition-modulated structures is a common phenomenon in III–V and II–VI semiconductor alloys [1]. There exist two distinct possibilities for the formation of such a structure. Firstly, *equilibrium domain structures* can be formed in *closed systems*. This is realized by long-time growth interruption or by post-growth annealing. Thermodynamics can be applied to describe equilibrium structures which meet the condition of the Helmholtz free energy minimum. Secondly, *non-equilibrium structures* can be formed in *open systems*. These structures are governed by growth kinetics.

Although most of observed composition-modulated structures in semiconductor alloys correspond to as-grown samples, there is a possibility for the formation of modulated structures via annealing. E. g., experiments on non-stoichiometric As-rich GaAs show the *enhancement of bulk diffusion* of As atoms under annealing and the growth of nanometer-size As clusters [2]. These data make the problem of equilibrium modulated structures in semiconductors, which can be obtained under annealing, to be a problem of both experimental and theoretical interest.

Here we study the thermodynamic stability of an alloy $A_{1-c}B_cC$ in the epitaxial film against fluctuations of alloy composition. We consider a film on the (001)-substrate of a cubic crystal and we focus on the situation where the *homogeneous alloy with the composition* $c = \bar{c}$ is *lattice-matched to the substrate*. Both the substrate and the epitaxial film are *elastically-anisotropic cubic crystals having equal elastic modulus tensors*.

The free energy of an inhomogeneous alloy is a sum of the chemical and elastic contributions, $F_{\text{inh}} = F_{\text{chem}} + E_{\text{el}}$, where $F_{\text{chem}} = \int d^3\mathbf{r} f_{\text{chem}}(c(x,y,z))$, and

$$F_{\text{el}} = \frac{1}{2}\iint\frac{dk_x dk_y}{(2\pi)^2}\int_0^h dz\int_0^h dz' \widetilde{\Delta c}^{\,*}(k_x,k_y;z)B_{\text{el}}(k_x,k_y;z,z')\widetilde{\Delta c}(k_x,k_y;z')\,. \qquad (1)$$

Here $\widetilde{\Delta c}(k_x,k_y;z)$ is the Fourier transform of the composition fluctuation $\Delta c(x,y,z) \equiv c(x,y,z) - \bar{c}$, $z = 0$ is the interface plane, $z = h$ is the planar stress-free surface, elastic properties of the crystal are described through the kernel $B_{\text{el}}(k_x,k_y;z,z')$ defined in [3], and the gradient energy ($\sim (\nabla c)^2$) [4,5] is omitted, since it is not important for alloy decomposition in the film [3]. The problem of finding the equilibrium profile of alloy composition consists of two parts. The first part is to find the criterion that the homogeneous alloy is absolutely unstable, i.e. *unstable against infinitesimal fluctuations of composition*. The second part is *to obtain the final equilibrium structure of the decomposing alloy*. The first problem was solved in [3], and the criterion of absolute instability is

$$\left(\frac{\partial^2 f_{\text{chem}}(c;T)}{\partial c^2}\right) + \lambda_0^{\min} < 0\,. \qquad (2)$$

Here $\lambda_0^{\min} = \min_{k_x,k_y} \lambda_0(k_x,k_y)$, and $\lambda_0(k_x,k_y)$ is the minimum eigenvalue of the operator $\widehat{B}_{\rm el}$ for a given $\mathbf{k} = (k_x,k_y)$. The minimum eigenvalue $\lambda_0(k_x,k_y)$ is governed by the anisotropy of the elastic modulus tensor and is attained for wave vectors along the elastically soft direction [100] or [010]. The value $\lambda_0^{\min}$is attained asymptotically as $kh \to \infty$. Fluctuations of composition corresponding to the "soft mode" are localized at the surface $z = h$ and decay away from the surface,

$$\Delta c_{\text{soft mode}}(x,y,z|\mathbf{k}) \sim \exp[-|k_x|(h-z)]\exp(ik_x x)\ ,\ |k_x|h \gg 1\ ,\ k_y = 0\,, \tag{3}$$

and similar expression is valid for the "soft mode" with $\mathbf{k} = (0,k_y)$. At high temperatures, the left hand side of Eq. (2) is positive for all compositions. The temperature $T_c$ and the composition $c_0$ where the l.h.s. of Eq. (2) vanishes for the first time correspond to the critical point of alloy instability in the epitaxial film.

The final structure of decomposing alloy was found numerically in [6], where the model regular solution approximation [7] was used for the chemical free energy of an alloy. An equilibrium structure was found, but neither the miscibility curve, nor the dependence of the period on temperature were obtained in [6].

Here, to obtain the *final equilibrium structure of the decomposing alloy* we focus on the vicinity of the critical point, i.e., on $T \approx T_c$ and $c \approx c_0$, and use the Ginzburg–Landau type of expansion of $F_{\rm inh}$. We take the composition fluctuation is *a linear combination of soft modes* of the form of Eq. (3). Since numerical calculations show composition profile to be *one-dimensional*, we focus on composition modulation in the $x$ direction. By taking into account the asymptotic behavior of the eigenvalue of $\widehat{B}_{\rm el}$ for soft modes [3], $\lambda_0(k_x,0) = \lambda_0^{\min} + B_1\exp(-2|k_x|h)$, one obtains the expansion for $\Delta F = F_{\rm inh} - F_{\rm hom}$ as follows,

$$\begin{aligned}\Delta F \int_0^h dz \int dx \Bigg\{ &\left[\frac{1}{2}\left(\frac{\partial^2 f_{\rm chem}}{\partial c^2}\right)(c(\mathbf{r})-c_0)^2 - \frac{1}{2}\alpha\tau(c(\mathbf{r})-c_0)^2 + \frac{1}{4}D(c(\mathbf{r})-c_0)^4\right] \\ &- \left[\frac{1}{2}\left(\frac{\partial^2 f_{\rm chem}}{\partial c^2}\right)(\bar{c}-c_0)^2 - \frac{1}{2}\alpha\tau(\bar{c}-c_0)^2 + \frac{1}{4}D(\bar{c}-c_0)^4\right]\Bigg\} \\ &+ \frac{1}{2}\int \frac{dk_x}{(2\pi)}\int_0^h dz\left[\lambda_0^{\min} + B_1\exp(-2|k_x|h)\right]|\widetilde{\Delta c}(k_x,0;z)|^2\,. \end{aligned} \tag{4}$$

Here $\tau = (T_c - T)/T_c \ll 1$, $\alpha = -T_c(\partial^3 f_{\rm chem}/\partial T\partial^2 c)$, $D = \frac{1}{6}(\partial^4 f_{\rm chem}/\partial c^4)$. We seek the composition profile as a periodic function $\Delta c(x,y,z) = \sqrt{2\alpha/D}\sqrt{\tau}\varphi(x,z)$. Here $\varphi$ is combination of soft modes of Eq. (3) corresponding to composition modulation in $x$-direction with the period $d_x$. By substituting $\Delta c(x,y,z)$ of the above form into the free energy of Eq. (4), one obtains

$$\Delta F = Ah\frac{6\alpha^2\tau^2}{D}\left[\frac{1}{k_x^{(0)}h}J + 2\frac{B_1\exp(-2k_x^{(0)}h)}{\alpha\tau(2k_x^{(0)}h)}|a_1|^2\right]\,, \tag{5}$$

where $A$ is the substrate area, and

$$J = k_x^{(0)2}\int_{-\frac{d_x}{2}}^{\frac{d_x}{2}} dx\int_0^h dz\left[\frac{1}{2}\left(-1+3\eta^2\right)\varphi^2(x,z) + \eta\varphi^3(x,z) + \frac{1}{4}\varphi^4(x,z)\right]\,. \tag{6}$$

Here $\eta$ is proportional to the deviation of the average alloy composition $\bar{c}$ from the critical composition $c_0$, $\eta = (\bar{c} - c_0)/\sqrt{\tau}$; $a_1$ is amplitude of the first Fourier harmonic of $\varphi$. It follows from Eq. (6) that $J$ does not depend on $k_x^{(0)}$. Minimization of $\Delta F$ from Eq. (5) with respect to $k_x^{(0)}$ shows that the second term in Eq. (5) is small compared to the first one. It allows *to split the problem into two parts*, and to obtain the *composition profile within one period of the structure* first, and to find the *period* afterwards. This is the key advantage of using Landau–Ginzburg expansion of $F_{inh}$ which enables us to proceed as compared to [6]. Similar advantage of using Landau–Ginzburg theory was emphasized in [8] for a related problem of equilibrium composition-modulated structures in *bulk samples* of quaternary alloys.

The lowering of the total free energy of the system due to fluctuations of composition, $\Delta F < 0$, means that the minimization of $J$ from Eq. (6) yields a non-trivial solution providing $J < 0$. If $|\eta| < 1/\sqrt{3}$, the quadratic coefficient in Eq. (4) is negative, i.e. the alloy is absolutely unstable. Then there obviously exists a solution which gives $J < 0$. The equation $\eta = \pm 1/\sqrt{3}$ yields *the spinodal curve* of the alloy epitaxial film near the critical temperature $T_c$. Due to cubic terms in $J$, a solution providing $J < 0$ may exist also in a certain region of $\eta$ where $|\eta| > 1/\sqrt{3}$. The value $|\eta| = \eta^*$, where the solution providing $J < 0$ ceases to exist, corresponds to *the miscibility curve*. If $|\eta| > \eta^*$, the homogeneous alloy epitaxial film is absolutely stable. If $1/\sqrt{3} < |\eta| < \eta^*$, the homogeneous alloy epitaxial film is metastable. Numerical minimization of $J$ yields the final structure of the alloy within one period. The form of the structure is close to one obtained in shcha. The modulation amplitude is maximum at the surface and decays away from the surface. Analysis of $J$ versus $\eta$ yields $\eta^* = 0.784$, i.e. it gives *the miscibility curve in the vicinity of the critical point*,

$$T_{\text{miscibility}}(\bar{c}) = T_c - \frac{T_c}{\eta^{*2}}(\bar{c} - c_0)^2 . \tag{7}$$

Then, given $J$, the criterion of the minimum with respect to $k^{(0)}h$ reads

$$\frac{\exp(2k^{(0)}h)}{(k^{(0)}h)} = \frac{B_1}{\alpha\tau(-J)}|a_1|^2 . \tag{8}$$

To calculate the period $d$, we take, as an example, $GaAs_{1-c}Sb_c$ where $T_c = 740$ K [3]. Evaluation of $d$ from Eq. (8) yields, for $T_c - T = 10$ K, $d = 1.4h$, for $T_c - T = 100$ K, $d = 2.0h$. Thus, the period is a weak logarithmic function of $(T_c - T)$ and is of the order of the film thickness $h$.

With further lowering of $T$, all modes of fluctuations contribute to the equilibrium structure. To estimate the miscibility curve at arbitrary $T$, we use the ansatz of [9], where composition is independent of $z$, $\Delta c(x, y, z) = c_1(x)$. If we construct a curve which bounds the region on $T - c$ phase diagram corresponding to alloys unstable against such a fluctuation, this curve will lie inside the exact miscibility curve. The equilibrium phase diagram of alloy epitaxial film is shown in Fig. 1.

To conclude, we have solved a *non-linear problem* for the final equilibrium structure of phase-separating alloy in an epitaxial film in the vicinity of the critical point. The *exact phase diagram* in variables "temperature – average composition" is constructed, containing the region of absolutely unstable, metastable, and stable alloys. The *period* of equilibrium structure is found. An equilibrium composition-modulated structure with a

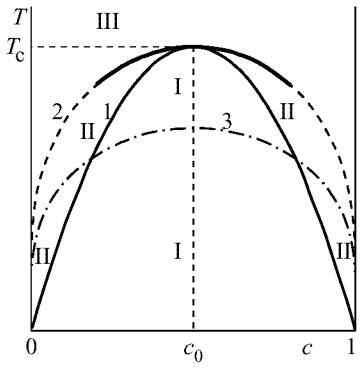


**Fig 1.** Equilibrium phase diagram of an alloy in the epitaxial film. $(c_0; T_c)$ is the critical point of alloy instability against spinodal decomposition. 1 is the spinodal curve; the solid part of the curve 2 is the calculated miscibility curve (Eq. (7)); the dashed part of the curve 2 is the schematic miscibility curve for arbitrary temperatures; 3 is the miscibility curve calculated by the ansatz of Glas [9]. (I) is the region of the absolutely unstable alloys, (II) is the region of metastable alloys, and (III) corresponds to stable alloys.

one-dimensional periodicity in the surface plane is a *spontaneously formed quantum-wire superlattice.*

The work was supported by Russian Foundation for Basic Research, Grant 98-02-18304, by Russian Federal Program of Russian Ministry of Science and Technology "Solid State Nanostructures", Project 97-2014, by Russian Federal Program of Russian Ministry of Science and Technology "Surface Atomic Structures", Grant 95-2.23, and by Russian Federal Program "Leading Research Schools", Grant No. 96.15-96.348.

## References

[1] A. Zunger and S. Mahajan. In: *Handbook on Semiconductors*, Ed. T. S. Moss. V. 3, Ed. S. Mahajan, Elsevier, p. 1399 (1994).
[2] N. A. Bert *et al. Semicond. Sci. Technol.* **12** 51 (1997).
[3] I. P. Ipatova, V. G. Malyshkin, and V. A. Shchukin. *J. Appl. Phys.* **74** 7198 (1993).
[4] J. W. Cahn. *Trans. Met. Soc.* **242** 166 (1968).
[5] A. G. Khachaturyan. *Theory of Structural Transformations in Solids* (Wiley, New York, 1983).
[6] I. P. Ipatova, V. G. Malyshkin, and V. A. Shchukin. *Phil. Mag. B* **70** 557 (1994).
[7] M. Ilegems and M. B. Panish. *J. Phys. Chem. Solids* **35** 409 (1974).
[8] I. P. Ipatova, V. G. Malyshkin, A. Yu. Maslov, and V. A. Shchukin. *Semiconductors* **27** 158 (1993).
[9] F. Glas. *J. Appl. Phys.* **62** 3201 (1987).

Ioffe Institute
6th Int. Symp. "Nanostructures: Physics and Technology"
St Petersburg, Russia, June 22–26, 1998.



# Investigation of self-organized nanoheterostructure properties in InGaAsP solid solutions

*I. S. Tarasov*, I. N. Arsent'ev, N. A. Bert, L. S. Vavilova, V. A. Kapitonov, A. V. Murashova and N. A. Pikhtin
Ioffe Physico-Technical Institute, St. Petersburg 194921, Russia
E-mail: tarasov@hpld.ioffe.rssi.ru

**Abstract.** Properties of self-organized InGaAsP nanoheterostructures grown on InP and GaAs substrates have been investigated by photoluminescence and transmission electron microscopy (TEM) methods. The dependence of epitaxial growth temperature and solution supercooling on the rate of self-organization of periodical InGaAsP nanoheterostructures has been determined. Periodical picture in the plan view and cross section of TEM image of InGaAsP epitaxal layers have been observed.

## Introduction

In our previous works it was shown experimentally that in the miscibility and spinodal decomposition region of quaternary InGaAsP solid solutions the formation of self-organized periodical nanoheterostructures takes place during the growth process [1, 2, 3]. Boundaries of miscibility and spinodal decomposition regions for liquid phase epitaxy grown InGaAsP epitaxial layers lattice matched to InP and GaAs were determined. Also initial technological conditions for unstable growth of InGaAsP epitaxial layers by liquid phase epitaxy method were obtained. In present work we continued study of InGaAsP solid solution lattice matched to InP and GaAs in the miscibility and spinodal decomposition region at technological conditions facilitating the unstable growth of epitaxial layers.

## 1 Results and discussion

According to theoretical predictions [4] a decrease of growth temperature of epitaxial layer widens the boundary of miscibility and spinodal decomposition region. In this connection we investigated the influence of growth temperature on the effect of formation of self-organized InGaAsP nanoheterostructures lattice matched to InP. Epitaxial layers grown at 650, 600 and 550 °C were investigated by photoluminescence method. It was found that temperature decrease first leading to the improvement of nanoheterostructure self-organization effect ($T = 600$ °C) then results in it decrease ($T = 550$ °C). Such discrepancy with theoretical predictions we connected with the fact that in theoretical model the temperature dependence of diffusion coefficient had not been taken into account. In order to investigate the influence of nonequilibrium condition of liquid phase on self-organization process of nanoheterostructures in epitaxial layers of InGaAsP solid solutions the temperature of solution supercooling was varied. Supercooling temperature was increased up to the value when it becomes difficult to remove solution from the substrate. Experiment was carried out at two cooling velocities of the solution —

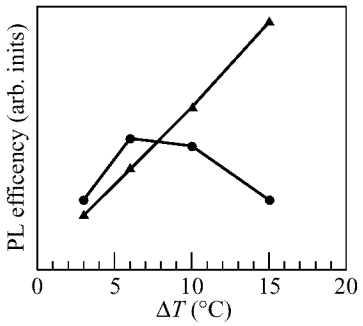


**Fig 1.** The dependence of photoluminescence line efficiency of InGaAsP/InP epitaxial layer on supercooling temperature of the solution for two cooling velocities (triangles — 0.1 °C/min, circles — 2 °C/min).

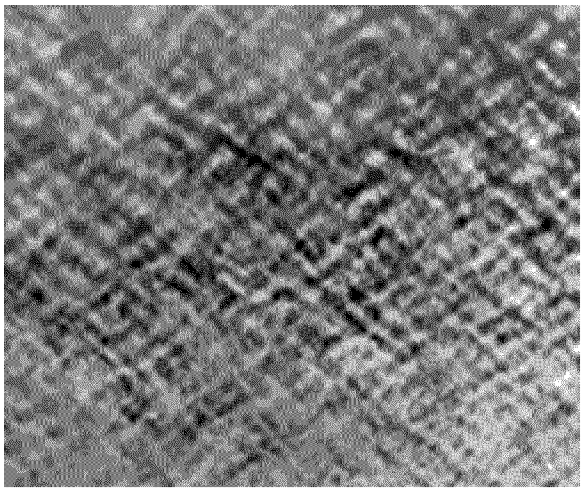

**Fig 2.** TEM image in the plan view of InGaAsP/InP epitaxial layer.

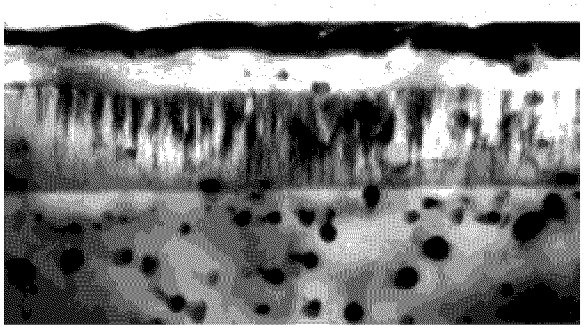

**Fig 3.** TEM image in the cross section of InGaAsP/InP epitaxial layer.

0.1°C/min and 2 °C/min. Fabricated samples were investigated by photoluminescence method. The rate of nanoheterostructure self-organization effect was evaluated by efficiency of photoluminescence lines. The dependence of efficiency of photoluminescence line which characterizes nanoheterostructure formation on supercooloing temperature of the solution is presented on Fig. 1

An increase of solution supercooling temperature results in the increase of photoluminescence line efficiency for samples grown at 0.1 °/min cooling velocity. For the samples grown at 2 °/min cooling velocity and at 10 °C supercooling temperature the decrease of photoluminescence line efficiency was observed. At 15 °C supercooling temperature it was impossible to remove the solution from the substrate. In our opinion it confirms the fact that nanoheterostructure self-organization effect increases with the increase of nonequilibrium state of solution liquid phase. Fabricated samples were also investigated in plan view and cross-section by transmission electron microscope EM-420. The most difficulties presented the preparation of samples on InP substrate for the view in cross section due to the formation of islandes during ion-beam sample processing. The original method of sample preparation allowing to minimize this effect was developed. TEM images in plan view and cross section of typical epitaxial layer samples are presented in Fig. 2 and Fig. 3, respectively. A large scales on both photographs are the same. In plan view and cross section periodically repeated regions with different solid solution composition were observed. The self-organized nanostructure dimensions were found to be 500–600 Å.

## 2 Conclusion

On the base of carried out investigations the influence of diffusion coefficient temperature dependence on nanoheterostructure self-organization effect was observed with the decrease of growth temperature. The increase of nanoheterostructure self-organization effect with the increase of supercooling solution temperature was shown. Periodical structure in plan view and cross section in TEM images of samples was observed.

## References

[1] I. S. Tarasov, L. S. Vavilova, N. I. Katsavets, et al., Intern. Symp. "Nanostructures: Physics and Technology", St. Petersburg, Russia, Abstracts, p. 362 1996.
[2] I. S. Tarasov, L. S. Vavilova, I. P. Ipatova, et al., 23 Int. Symp. on Compound Semiconductors, ISCS-23, St. Petersburg, Russia, p. 117 1996.
[3] L. S. Vavilova, A. V. Ivanova, V. A. Kapitonov, et al., *Semiconductors* **32** 131 (1998).
[4] I. P. Ipatova, V. G. Malyshkin, V. A. Shchukin, *J. Appl. Phys.* **74** 7198 (1993).

Ioffe Institute
6th Int. Symp. "Nanostructures: Physics and Technology"
St Petersburg, Russia, June 22–26, 1998.



# InGaAs quantum wires in [110] and [1$\bar{1}$0] gratings: two V-grooves directions, two behavior of the regrowth interface

*C. Gourgon*†, F. Filipowitz†, J. Robadey†, D. Martin†, Y. Magnenat†, P. C. Silva†, F. Bobard‡ and F. K. Reinhart†

† Institute of Micro- and Optoelectronics
‡ Center of Electron Microscopy
Federal Institute of Technology, CH-1015 Lausanne, Switzerland

**Abstract.** InGaAs quantum wires are obtained by holographic lithography and MBE regrowth on V-grooves. The influence of some fabrication steps on the interface is presented. The [110] and [1$\bar{1}$0] gratings are compared in terms of etching profiles and the evolution of the grating shape during the desorption and the epitaxial regrowth.

## 1 Introduction

There is great interest in reducing the physical size of semiconductor structures to take advantage of quantum effects for optical and optoelectronic applications. Semiconductor wires are expected to result in sharp gain and absorption spectra. Quantum wires grown on patterned substrates are obtained by the combination of holographic lithography and epitaxial growth [1]. Several techniques have been developed to produce nanostructures [2], but the great interest of this one is that small lateral sizes are obtained without the problem of non radiative recombinations on the sidewalls which occur with the classical e-beam lithography/etching method. Heterostructures with GaAs wires have been studied, but it is difficult to integrate these wires in a AlGaAs waveguide because of the presence of aluminium which induces growth defects at the V-groove interface. To avoid this problem, the same technique has been used for InGaAs wires in GaAs waveguides. It is more difficult to provide uniform and high density arrays of wires with low growth defects density as in the first case [3]. Two kinds of structures have been grown: InGaAs quantum wires on [110] V-grooves and InGaAs Distributed FeedBack lasers (DFB) on [1$\bar{1}$0] second order gratings. In this paper, we compare the profil and the behavior of the V-groove in the two crystallographic orientations at different fabrication steps.

## 2 Fabrication: holographic lithography and MBE growth

The first step consists in the MBE growth of the AlGaAs cladding and the half GaAs waveguide (0.3 $\mu$m) on a n-doped (100) GaAs substrate. A grating is obtained on the surface by deep UV holography with a doubled $Ar^+$ laser at $\lambda = 257$ nm [4]. It comes from the high contrast of the fringes created by the reflection of the laser on a mirror perpendicular to the sample. Its period is determined by the incidence angle of the laser beam. Its reflection on the surface is eliminated by an antireflective coating layer (70 nm thick $Si_3N_4$). The ratio between the period and the lateral width of the lines depends on the exposure time. In this way, we can influence the etching profile of the

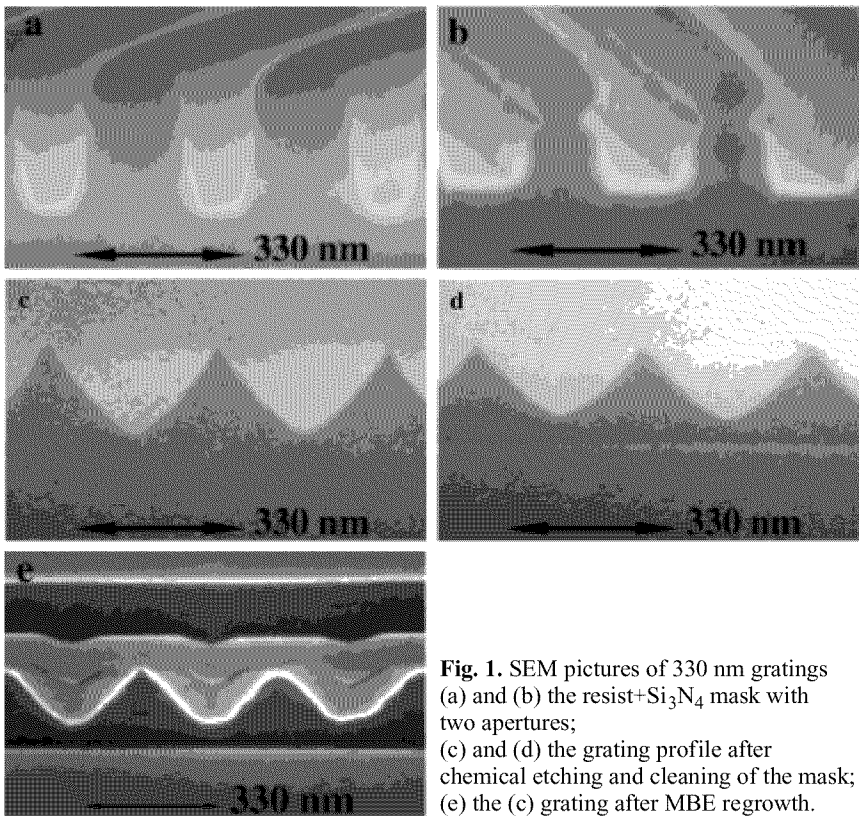


**Fig. 1.** SEM pictures of 330 nm gratings (a) and (b) the resist+$Si_3N_4$ mask with two apertures; (c) and (d) the grating profile after chemical etching and cleaning of the mask; (e) the (c) grating after MBE regrowth.

V-grooves, that are described in next section. This mask is transferred from the resist to the $Si_3N_4$ layer by reactive ion etching with a $CF_4/H_2$ plasma.

The $[1\bar{1}0]$ V-grooves are etched in commonly used $H_2SO_4/H_2O/H_2O_2$ solution. It develops {111}A facets in this direction, whereas the profile shows an important underetching in the [110] orientation. For this reason the [110] V-grooves are etched in a $CHKO_3/H_2O/H_2O_2$ solution. The grating surface is then protected by a thermic oxide grown at 230°C. Prior to the MBE regrowth, this oxide is removed by a desorption. This interface treatment and the regrown structure depend on the grating orientation.

## 3 Quantum wires on [110] V-grooves

InGaAs quantum wires have been grown on [110] gratings with periods of 330 nm. The structure consists in a AlAs/GaAs superlattice buffer, a $In_{0.16}Ga_{0.84}As$ quantum wire, an other AlAs/GaAs superlattice, the second part of the GaAs waveguide and the AlGaAs cladding layer. The complete structure has been described elsewhere [5].

SEM micrographs of Fig. 1 show the grating at different fabrication steps, for two ratio between the mask lines and the period: 60% in (a) and 40% in (b). This is obtained by different exposure times. The surfaces formed by the chemical etching are not exactly {111}B facets (As planes), but a combination of planes with higher indices $\{n11\}$ with $n > 1$, which gives this curved profile. The large mask (a) leads to a deeper V-groove (c) than in (d). The grating depths are 190 nm and 130 nm respectively. This

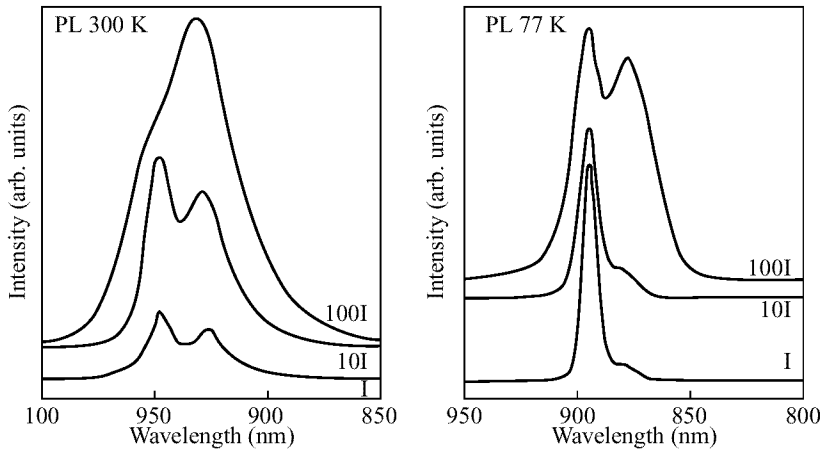


**Fig 2.** PL spectra of InGaAs wires grown on [110] grating between AlAs/GaAs superlattices at 300 K and 77 K, for three excitation densities.

difference has an influence on the quantum wire shape.

The oxide is removed by thermic desorption at 640°C under $As_4$ pressure. It reduces processing defects and impurities at the regrowth interface. The result is a rounding of the corners and a lowering of the modulation depth. This phenomenon is more important for shallow etching profiles (d). Differences of adatom diffusion lengths lead to different growth rates on the V-groove facets [6]. The low mobility of Al atoms tends to preserve the shape of the grating, whereas mass transport occurs during the growth interruption following the InGaAs layer that leads to crescent-shape wires [4]. If the same process is done on $[1\bar{1}0]$ gratings, {001} planes are formed on the bottom, and the structure is faster planarized. A SEM picture of the total structure is shown in Fig. 1(e). The layers are revealed by a selective chemical etching of a cleaved surface. The quantum wire is visible by the black line in the middle of the grating structure. On the both sides of the wire, the gray layers represent the AlAs/GaAs superlattices, and black ones the GaAs waveguide. The lower dark layer is the one where the V-grooves are defined. The second GaAs layer, on top of the gray superlattice, is completely planarized. TEM pictures are analyzed in [5]. To understand completely the regrowth characteristics, we have to take into account the evolution of the strain field in these structures.

Photoluminescence spectra of InGaAs wires embedded in AlAs/GaAs superlattices are shown in Fig. 2 for different excitation densities (I, 10I, and 100I). The ground state and the first excited level resulting from the lateral confinement are seen at 948 and 930 nm (PL at 300 K) with a splitting of 17 meV. The spectra exhibit a striking bandfilling with increasing the photogeneration rate as already reported on GaAs wires [7]. The peak associated with the first excited state is very well defined and intense as compared to the ground state, even for low excitation density. This shows the improvement in the control of each fabrication step.

## 4 Distributed feedback lasers in $[1\bar{1}0]$ V-grooves

Distributed feedback gain-coupled lasers based on InGaAs wires have been grown on [110] gratings [8]. Some efforts have been done on the surface cleaning, but the laser

characteristics are limited by the defects at the regrowth interface. A hydrogen plasma desorption has been developed [9]. It appears that this treatment has a large influence on the grating, but this effect depends on the orientation of the V-grooves. For [110] lines, we observe an important planarization of the surface.

The same process has been used in the $[1\bar{1}0]$ orientation to define second order gratings (280 nm). The chemical etching defines {111}A facets which correspond to Ga planes. In this case, the grating profile is transformed, but the V-grooves are preserved. The difference of the planes, As in [110] and Ga in $[1\bar{1}0]$ explains the behavior specific to the direction. DFB lasers have been grown on $[1\bar{1}0]$ gratings, with a $In_{0.18}Ga_{0.82}As$ quantum well. This active layer is flat, due to the faster planarization in this direction. The structure is defined so that the lateral width of the QW is equal to a 3/4 grating period. Figure 3 shows that the effect of the desorption depends on the etching profile. In (b), the sharpness of the top is more important than in (a). In Fig. 3(c) and 3(d), we see the structure after regrowth on gratings (a) and (b), respectively. The active layer (one or three QWs) is located in the middle of the GaAs waveguide. A AlAs/GaAs superlattice reduces the defects density at the interface. It appears as a gray line following the V-shape. We can compare the evolution of this superlattice for smooth or sharp etching profiles. In the two cases, the {111}A facets are stable, but the top of the grating is different. In (c), the curved top is changed in {311} planes by the desorption. During the regrowth the {111}A planes are reconstructed, as it is shown on TEM micrographs [10], but the {311} based surfaces tend to limit the density of dislocations which may appear at the apex formed by the intersection of the reconstructed {111}A planes. In Fig. 3(d), the sharp grating is not changed by the desorption, and the triangular shape on the top remains constant with the growth. The conservation of the {111}A planes tends to create stacking faults and dislocations emerging from the apex. The efficiency of the desorption depends on the grating shape that is determined by the holographic exposure time and the chemical etching homogeneity. By controlling all theses steps and by using a high quality regrowth we can fabricate reproducible InGaAs DFB laser structures. Threshold current densities as low as 250 $A/cm^2$ have been achieved at room temperature [9]. We have also grown structures with multiple quantum wells (Fig. 3(d)) to limit the sensitivity to the regrowth interface and to avoid the saturation of the QW luminescence. This should lead to a better reproducibility of the active layer quality and laser properties. A technologic process has been developed to define small stripes of 4 $\mu$m on the waveguide cladding, with a $SiCl_4/Cl_2/Ar$ plasma etching followed by a planarization of the surface and the deposition of p-contacts, to increase the current injection in the active layer and reduce the likelyhood of lateral laser modes.

## 5 Conclusion

The results show the influence of the holographic exposure and chemical etching on the desorption efficiency. We expect a better control of the V-groove profile, and the interface evolution during the desorption and the MBE regrowth, which is important for the reproducibility of the structures and their optical properties. The completely different behavior on the two grating directions [110] and $[1\bar{1}0]$ has been shown. This improvement in the fabrication steps allows to develop the integration in a waveguide of two kinds of InGaAs based structures: quantum wires in [110] V-grooves and DFB

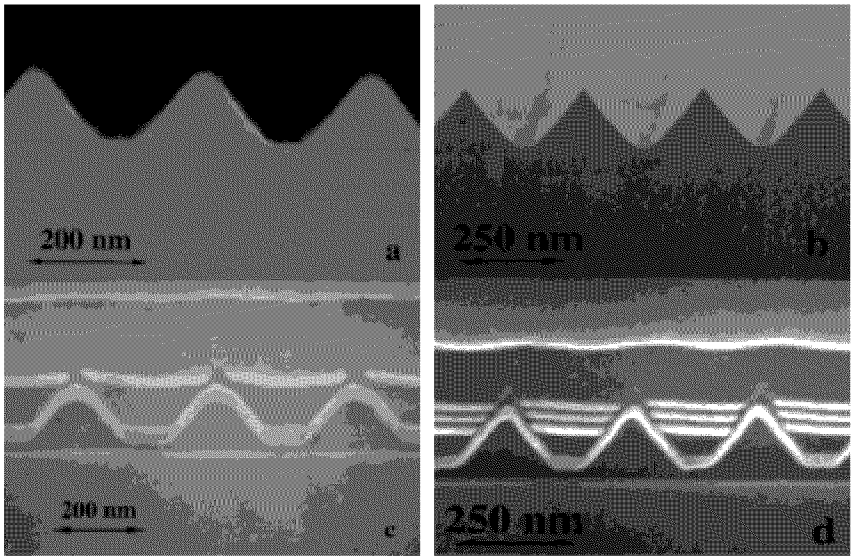


**Fig 3.** SEM pictures of 280 nm [$1\bar{1}0$] gratings; (a) and (b): Etching profiles. (c) and (d): the same gratings after MBE regrowth.

lasers in [$1\bar{1}0$] gratings. In this second case, structures with three QWs combined with a new process technology should lead to ease the problem of strong threshold current variations.

## References

[1] E. Kapon, *Optoelectronics* **8** 429 (1993).
[2] R. Cingolani and R. Rinaldi, *Rivista del Nuovo Cimento*, 16, 1993.
[3] P. H. Jouneau, F. Bobard, U. Marti, J. Robadey, F. Filipowitz, D. Martin, F. Morier-Genoud, P. C. Silva, Y. Magnenat and F. K. Reinhart, *Inst. Phys. Conf. Ser.* **146** 371 (1995).
[4] U. Marti, M. Proctor, D. Martin, F. Morier-Genoud, B. Senior and F. K. Reinhart, *Microelectronics Eng.* **13** 391 (1991).
[5] F. Filipowitz, present conference.
[6] F. S. Turco, S. Simhony, K. Kash, D. M. Hwang, T. S. Ravi, E. Kapon and M. C. Tamargo, *J. Cryst. Growth* **104** 766 (1990).
[7] R. Rinaldi, M. Ferrara, R. Cingolani, U. Marti, D. Martin, F. Morier-Genoud, P. Ruterana and F. K. Reinhart, *Phys. Rev. B* **50** 11795 (1994).
[8] J. Robadey, U. Marti, R. O. Miles, M. Glick, F. Filipowitz, M. Achtenhagen, D. Martin, F. Morier-Genoud, P. C. Silva, Y. Magnenat, P. H. Jouneau, F. Bobard and F. K. Reinhart, *IEEE Photonics Technol. Lett.* **9** (1) 5 (1997).
[9] J. Robadey, D. Martin, M. Glick, P. C. Silva, P. H. Jouneau, U. Marti and F. K. Reinhart *Electronics Lett.* **33** (4) 297 (1997).
[10] J. Robadey et al. (to be published).

Ioffe Institute
6th Int. Symp. "Nanostructures: Physics and Technology"
St Petersburg, Russia, June 22–26, 1998.



# InP based materials for long wavelength optoelectronics grown in multiwafer planetary reactors

*M. Deschler*, R. Beccard, D. Schmitz, M. Deufel, H. Protzmann and H. Jürgensen
AIXTRON AG, Kackertstr. 15–17, D-52072 Aachen, Germany
Tel.: +49 (241) 89 09-0, Fax: +49 (241) 89 09-40, E-Mail: heu@aixtron.com

Multiwafer MOVPE growth is a well established technique for the mass production of III–V compounds. Especially GaAs based materials like AlGaAs, GaInP and AlGaInP are grown in multiwafer Planetary Reactors®. These reactors allow the simultaneous growth of 7, 15, 35 or $95\times2''$ wafers. As shown in earlier publications, the Planetary Reactors® combine a very high growth efficiency with extreme uniformities in thickness and composition. However, there is also a growing demand for InP based materials to be grown in multiwafer reactors in order to increase the throughput in the production of long wavelength optoelectronics devices.

In this paper we want to present data on the growth of InP based materials ($Ga_xIn_{1-x}As_yP_{1-y}$) in a Planetary Reactor®. The reactor that has been used is an AIX 2400 system allowing the growth of $15\times2''$ wafers or $8\times3''$ wafers. As a demonstration material GaInAsP with an emisssion wavelength of approx. 1.5 $\mu$m was choosen.

The results show that the excellent uniformity that is well-known for GaAs based materials is also found for GaInAsP on InP. Without any optimization, wavelegth uniformities as low as 1 nm were obtained. Thickness uniformities of 2% were measured. Furthermore, doped samples were grown. As dopants silane and dimethylzinc were used. Sheet resistivity measurements performed on these samples reveal uniformities around 1%.

The results demonstrate that Planetary Reactors® are an efficient tool for the mass production of GaInAsP alloys lattice matched to InP. The uniformity data show that the unique Planetary double rotation principle allows the growth of homogenous GaInAsP without any tuning of flow rates or gas velocities. Since the GaInAsP composition is very sensitive towards changes of the growth temperature, a very uniform wafer temperature is indicated. This is also confirmed by the excellent doping uniformity. As a conclusion, we find that Planetary Reactors® are the ideal tool for an efficient mass production of InP based compounds.

Ioffe Institute
6th Int. Symp. "Nanostructures: Physics and Technology"
St Petersburg, Russia, June 22–26, 1998.



# Enhanced two-demensional precipitation of excess As in LT-GaAs delta-doped with Sb

*N. A. Bert*†, V. V. Chaldyshev†, A. A. Kosogov§*, A. A. Suvorova†,
V. V. Preobrazhenskii‡, M. A. Putyato‡, B. R. Semyagin‡and P. Werner§
† Ioffe Physico-Technical Institutre, St. Petersburg 194021 Russia
‡ Institute of Semiconductor Physics, Novosibirsk 630090 Russia
§ Max-Plank Institut für Mikrostrukturphysik, Halle D-06120 Germany
* On leave from Ioffe Physico-Technical Institutre, St. Petersburg 194021 Russia

**Abstract.** We have used, for the first time, isovalent delta-doping with antimony instead of indium to produce two-dimensional sheets of arsenic nano-clusters in GaAs films grown by molecular beam epitaxy (MBE) at low (200°C) temperature. The precipitation kinetics at Sb delta-layers is found to be enhanced as compared to that for In delta-doping. It provides an opportunity to improve the cluster spatial ordering. In addition, at early precipitation stages, the microstructure, morphology and orientation relationship of the clusters attached to Sb delta-layers are found to differ from those conventional for As clusters in LT-GaAs films including As clusters at the In delta-layers.

## 1 Introduction

GaAs grown by MBE at low substrate temperatures of 200–250°C (LT-GaAs) is a very attractive material for microwave and optoelectronic applications [1–3]. Being nonstoichiometric in an as-grown state, it contains an extremely high concentration ($10^{20}\,cm^{-3}$) of intrinsic point defects of which the main are excess As atoms in the forms of As antisites and As interstitials. Upon subsequent annealing, the excess As precipitates in nm-size clusters buried in GaAs matrix, and the material exhibits a high electrical resistivity, high carrier mobility and very short lifetime of nonequilibrium charge carriers. Since the As clusters play a crucial role in the electrical and optical properties of LT-GaAs, it is of importance to control the density and spatial distribution of As cluster arrays. The As cluster density has been shown to vary from layer to layer in LT-AlGaAs/GaAs [4] and LT-InGaAs/GaAs [5] heterostructures. An accumulation and depletion of As clusters can be also produced [6] by nonuniform incorporation of an impurity. When Si or In is inserted in a LT-GaAs film as delta-layers, two-dimensional As cluster sheets have been demonstrated [7-8] to appear. Before, we succeeded [9-11] in obtaining two-dimensional precipitation of As clusters in LT-GaAs films uniformly doped with Si donors, Be acceptors or undoped by means of additional delta-doping with In that is an isovalent impurity replacing Ga in group III sublattice. In this work, we use, for the firs time, delta-doping with antimony, i.e. group V element, and show an enhanced two-dimensional precipitation of excess As as compared with the case of indium delta-doping.

## 2 Experimental

The LT-GaAs films used in this work were grown by MBE at a substrate temperature of 200°C on undoped semi-insulating 2-inch GaAs(001) substrates in a dual-chamber system "Katun". The films contained 80 nm spaced Sb delta-layers which were introduced in the GaAs matrix by using the antimony beam while the arsenic beam was interrupted. The Sb deposit in each delta-layer was equivalent approximately to 1 monolayer (ML). Similar LT-GaAs films delta-doped with indium were also grown at the same growth temperature and As/Ga beam ratio. The growth procedure is described in more detail elsewhere [12]. The grown samples were cut into few parts of which one was kept as-grown and the others were annealed under As overpressure at 500, 600 or 700°C for 10, 30 or 60 min.

Optical absorption measurements in the near-infrared (0.8–1.2 mm) region (NIRA), conventional (TEM) and high-resolution (HREM) electron microscopies were applied to study the samples. Philips EM 420 and JEOL JEM 4000EX microscopes were exploited. Cross-sectional TEM specimens were prepared by a conventional $Ar^+$ ion-milling procedure as well as by cleaving technique.

## 3 Results and discussion

Cross-sectional TEM of the as-grown LT-GaAs films revealed thin layers located just at the positions expected for Sb or In delta-layers from the growth procedure. NIRA spectra recorded at room temperature showed an increased absorption, conventionally attributed to As antisites, in all the as-grown samples. The As excess was estimated from these spectra to be 0.5 at.% for both Sb delta-doped and In delta-doped LT-GaAs films. The equal contents of excess As in both kinds of the samples idicate that isovalent Sb doping does not supress the extra As incorporation during the film growth.

The microstructure of the Sb delta-layers was studied by HREM. Observations of the Sb delta-layers in the as-grown samples by lattice imaging revealed Sb to be dispersed within 4–5 ML that is similar to the case of In delta-doping [13] and results from some surface roughness of the film growing at a temperature as low as 200°C. Despite

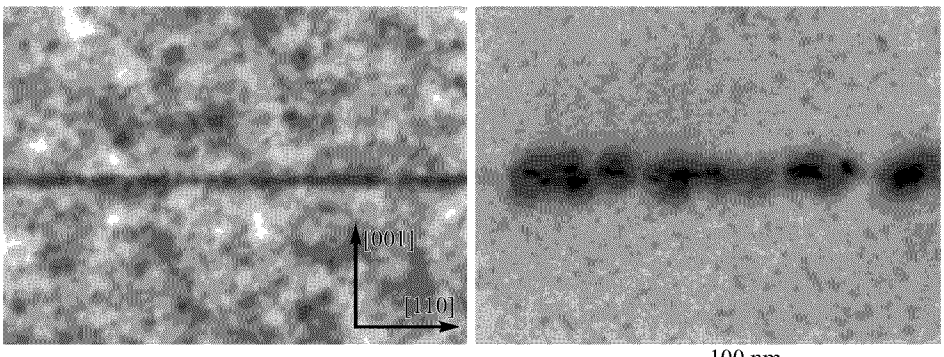


**Fig 1.** Dark-field 002 cross-sectional images of LT-GaAs films delta-doped with In (a) and Sb (b) and annealed at 500°C for 10 min. An essential difference in cluster accumulation at the In and Sb delta-layers is clearly seen.

this broadening the delta-layers accumulate clusters which are forming upon annealing, whereby the precipitation kinetics is found to differ for Sb delta-doping and In delta-doping. Fig. 1 presents TEM micrographs taken from the In or Sb delta-doped films grown and annealed under the same conditions. As can be seen, the clusters attached to the Sb delta-layers are essentially bigger and, in addition, provide stronger strain-induced contrast than those at In delta-layers. The lateral size of the clusters at the Sb delta-layers is up to 7 nm while it reaches only 3 nm for In delta-doping. In contrary, clusters dispersed in-between the delta-layers occur to be smaller in the case of Sb doping.

Annealing at higher temperatures (600, 700°C) led to an increase in size of the clusters attached to Sb delta-layers, that is illustrated by Fig. 2. The cluster size has been estimated to be 13 nm for an annealing temperature of 600°C and 19 nm for an annealing temperature of 700°C. At the same time, the estimated density of the clusters attached to the Sb delta-layers reduced from $6 \times 10^{10}\,\mathrm{cm}^{-2}$ down to $3 \times 10^{10}\,\mathrm{cm}^{-2}$. In parallel, the size of small clusters suspended in-between the Sb delta-layers increased from 2 nm up to 5 nm when elevating annealing temperature from 500 to 700°C. The cluster density in three-dimensional array in-between the Sb delta-layers reduced one order of magnitude: from $1.5 \times 10^{17}\,\mathrm{cm}^{-3}$ for an annealing temperature of 500°C down to $1.6 \times 10^{16}\,\mathrm{cm}^{-3}$ for 700°C.

The cluster microstructure and morphology for high annealing temperatures (600–700°C) have been observed to be similar to those conventional for As clusters in LT-GaAs films including clusters attached to In delta-layers. Fig. 3a shows a high-resolution image of such a cluster exhibiting moire fringes running nearly along (111) GaAs matrix planes. However, at the initial growth stages the microstructure, morphology and orientation relationship of the clusters attached to Sb delta-layers have been found to differ from conventional ones. It is demonstrated by Fig. 3b where a high-resolution image of the cluster attached to Sb delta-layer in LT-GaAs film annealed at 500°C is presented. On our opinion, two reasons may contribute to this phenomena. First, along with excess arsenic, antimony can take part at the cluster nucleation an growth. Second, the strain distribution around the Sb delta-layers can be different from that around the In delta-layers. The changed strain is indicated by a strong strain contrast at the dark-field image (Fig. 2) of the clusters at the Sb delta-layers.

## 4 Summary

So, the cluster accumulation happens more effectively in the films delta-doped with Sb as compared with those delta-doped with In. It provides an opportunity to improve the cluster spatial ordering. In addition, at early precipitation stages, the microstructure, morphology and orientation relationship of the clusters attached to Sb delta-layers are found to differ from those conventional for As clusters in LT-GaAs films including As clusters at the In delta-layers.

*Acknowledgments*

This work was supported, in its different parts, by RFBR, Ministry of Sciences and Technology of Russian Federation under the programs Fullerens & Atomic Clusters and Solid State Nanostructures as well as DFG bilateral grant No. 436 RUS 113/322/0(R,S).

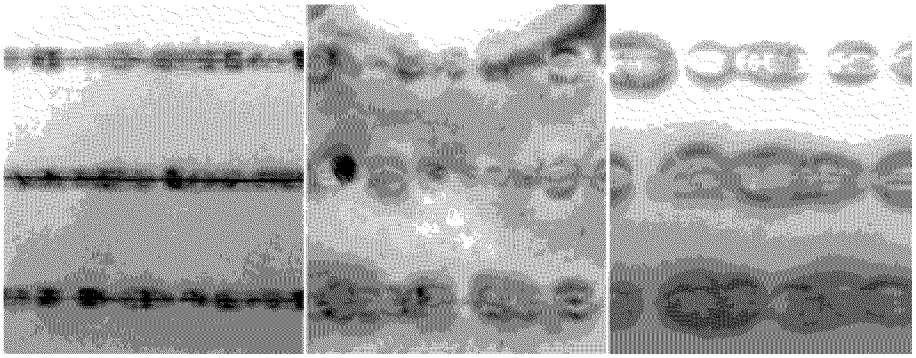


**Fig 2.** Dark-field 002 cross-sectional images showing the clusters growing at the Sb delta-layers when elevating annealing temperature from 500 (a) to 600 (b) and to 700°C (c). The annealing time is 10 min in each case.

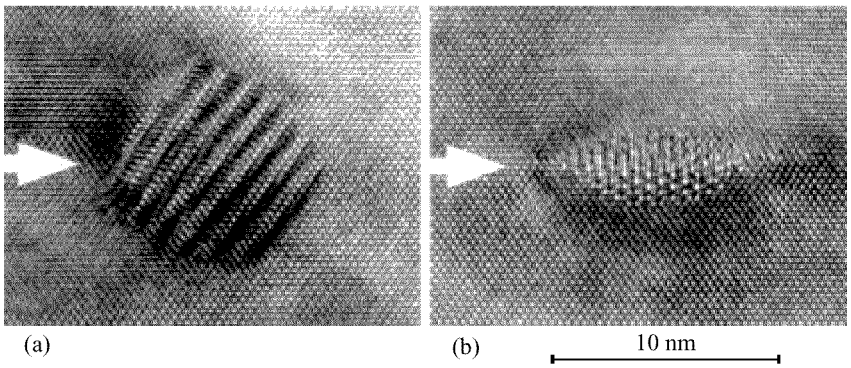


**Fig 3.** High-resolution images along [010] of the clusters attached to the Sb delta-layer in LT-GaAs films annealed for 10 min at (a) 600°C and (b) 500°C. The position of the Sb delta-layer is arrowed.

## References

[1] F. W. Smith, A. R. Calawa, C.-L. Chen, et al. *IEEE Electron Devices Lett.* **EDL-9** 77 (1988).
[2] M. R. Melloch, D. C. Miller, and B. Das. *Appl. Phys. Lett.* **54** 943 (1989).
[3] T. R. Rogers, C. Lei, B. G. Streetman, and D. G. Deepe. *J. Vac. Sci. Technol. B* **11** 926 (1992).
[4] K. Mahalingam, N. Otsuka, M. R. Melloch et al. *J. Vac. Sci. Technol. B* **10** 812 (1992).
[5] T. M. Cheng, Albert Chin, C. Y. Chang et al. *Appl. Phys. Lett.* **64** 1546 (1994).
[6] M. R. Melloch, N. Otsuka, K. Mahalingam et al. *Appl. Phys. Lett.* **61** 172 (1992).
[7] T. M. Cheng, C. Y. Chang, and J. H. Huang. *J. Appl. Phys.* **76** 5697 (1994).
[8] T. M. Cheng, C. Y. Chang, A. Chin et al. *Appl. Phys. Lett.* **64** 2517 (1994).
[9] N. A. Bert, V. V. Chaldyshev, N. N. Faleev et al. *Proc. of Intern. Symp. "Nanostructures: Physics and Technology"* p. 185, 1995.
[10] N. A. Bert, V. V. Chaldyshev, N. N. Faleev et al. *Semicond. Sci. Technol.* **12** 51 (1997).
[11] N. A. Bert, V. V. Chaldyshev et al. *Appl. Phys. Lett.* **70** 3146 (1997).
[12] N. A. Bert, V. V. Chaldyshev, Yu. G. Musikhin et al. *Semiconductors* (1998) (in press).

Ioffe Institute
6th Int. Symp. "Nanostructures: Physics and Technology"
St Petersburg, Russia, June 22–26, 1998.



# Delta-doping of GaAs by Sn

*V. A. Kulbachinskii*†, V. G. Kytin†, R. A. Lunin†, M. B. Vvedenskiy†, V. G. Mokerov‡, A. S. Bugaev‡, A. P. Senichkin‡, P. M. Koenraad#, R. T. F. van Schaijk§ and A. de Visser§

† Low Temperature Physics Department, Moscow State University, Moscow, Russia
‡ Institute of Radioengineering and Electronics, RAS, Moscow, Russia
# Physics Department,Eindhoven University of Technology, The Netherlands
§ Van der Waals-Zeeman Institute,University of Amsterdam, The Netherlands

**Abstract.** GaAs structures $\delta$-doped by Sn with various densities of Sn have been grown and investigated. The Hall effect and Shubnikov–de Haas effect have been investigated for temperatures 0.4 K $< T <$ 12 K in magnetic fields up to 38 T. The maximum density of free electrons achieved was $8.3 \times 10^{13}$ cm$^{-2}$. The resistance oscillations observed for a magnetic field parallel to the $\delta$-layer were associated with singularities in the calculated density of states.

## Introduction

Tin has been rarely used for $\delta$-doping in GaAs because of its high segregation ability [1]. On the other hand, this donor impurity is less amphotere compared with silicon, which is usually used as dopant for $\delta$-layers. The investigation of Tin $\delta$-doping in GaAs on singular substrates is important for research on Tin $\delta$-doping on vicinal substrates. These latter structures show a perspective for obtaining one-dimensional electronic channels [2, 3].

## 1 Samples

The GaAs($\delta$-Sn) structures were grown by molecular-beam epitaxy. On semi-insulating GaAs (Cr) substrate (001) a buffer layer of *i*-GaAs (240 nm) was grown. At a temperature of 450°C a tin layer was deposited in the presence of an arsenic flux. The structures were covered by a layer of *i*-GaAs (width 40 nm) and a contact layer *n*-GaAs (width 20 nm) with a concentration of silicon $1.5 \times 10^{18}$ cm$^{-3}$. The design density of tin in the $\delta$-layer smoothly varied from $N_D = 2.9 \times 10^{12}$ cm$^{-2}$ in sample No. 1 up to $N_D = 2.5 \times 10^{14}$ cm$^{-2}$ in sample No. 7.

## 2 Results

The temperature dependence of the resistance of samples No. 1 up to No. 7 is shown in Fig. 1a. The Hall effect and the magnetoresistance were measured at temperatures 0.4 K $< T <$ 12 K in magnetic fields up to 10 T and pulsed fields up to 38 T. The obtained values of the Hall concentration $n_H$ and the Hall mobility $\mu_H$ at $T = 4.2$ K are shown in Table 1. The concentration of free electrons in the tin-doped structures does not saturate as function of design doping density, as was observed in Si $\delta$-doped structures [4].

In magnetic fields $B < 0.2$ T at low temperatures a negative magnetoresistance was observed for all samples. In strong magnetic fields the Shubnikov–de Haas effect

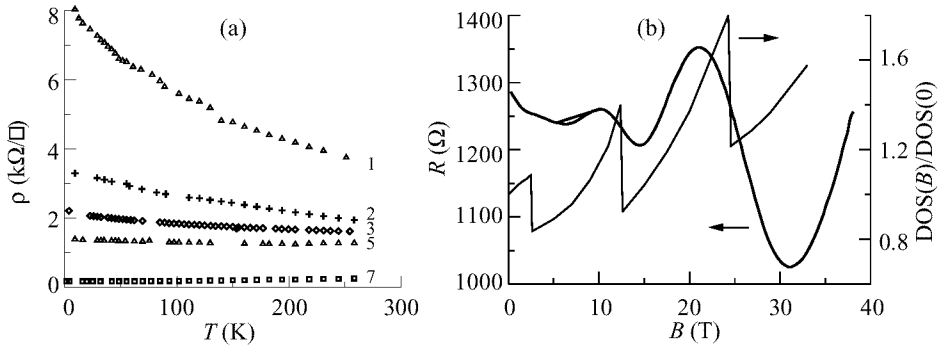


**Fig 1.** a) Temperature dependence of the sheet resistivity for different samples. b) Experimental dependence of the resistance on parallel magnetic field and the calculated DOS at the Fermi energy for sample No. 6.

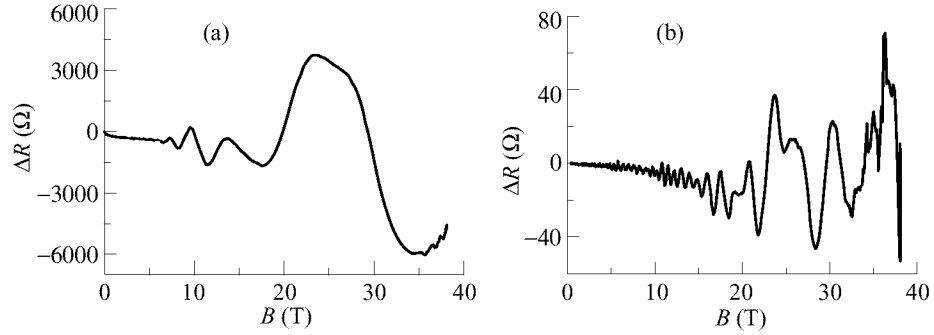


**Fig 2.** Oscillating part of the magnetoresistance for sample No. 6 (a) and No. 7 (b).

was observed at $T = 4.2$ K in the investigated structures (Fig. 2 and 3). The angular dependence of the oscillation frequency revealed, that the oscillations were caused by two-dimensional carriers. The electron concentrations of the subbands, determined from the maxima in the Fourier spectra, and the electron quantum mobilities, obtained from the width of the peaks in the Fourier spectra, are shown in Table 2.

**Table 1.** Hall density $n_H$, sum of the Shubnikov–de Haas concentrations $n_{SdH}$ in all subband and Hall mobility $\mu_H$ at temperature $T = 4.2$ K for samples No. 1–7.

| Sample No. | $n_H$ ($10^{12}$ cm$^{-2}$) | $\Sigma n_{SdH}$ ($10^{12}$ cm$^{-2}$) | $\mu_H$ (cm$^2$/Vs) |
|---|---|---|---|
| 1 | 1.74 | 2.75 | 1530 |
| 2 | 3.23 | 1.04 | 540 |
| 3 | 2.63 | 2.03 | 1080 |
| 4 | 10.4 | 6.15 | 1200 |
| 5 | 8.35 | 8.09 | 1150 |
| 6 | 14.5 | 8.73 | 1940 |
| 7 | 83.5 | 45.3 | 1170 |

**Table 2.** The electron concentration $n_{SdH}$ and the quantum mobility $\mu_q^{SdH}$ obtained from the Shubnikov–de Haas effect at $T = 4.2$ K; the self-consistently calculated concentration $N_S$; the calculated quantum mobility $\mu_q^t$ of electrons due to multi-subband scattering on ionized impurities; experimentally determined $B_{||}$ and calculated depopulation magnetic field $B'_{||}$ for samples No. 1 and No. 6.

| Sample No. | $i$ subbands No. | $n_{SdH}$ ($10^{12}$ cm$^{-2}$) | $N_S$ ($10^{12}$ cm$^{-2}$) | $\mu_q^{SdH}$ (cm$^2$/Vs) | $\mu_q^t$ (cm$^2$/Vs) | $B_{||}$ (T) | $B'_{||}$ (T) |
|---|---|---|---|---|---|---|---|
| | 0 | 1.76 | 1.75 | 1340 | 1570 | – | – |
| 1 | 1 | 0.99 | 0.99 | 1450 | 1590 | 18.6 | 22.5 |
| | 2 | – | 0.30 | – | 2940 | 4 | 8.0 |
| | 0 | 4.08 | 4.02 | 860 | 1290 | – | – |
| | 1 | 2.33 | 2.80 | 1660 | 1450 | – | 45.3 |
| 6 | 2 | 1.56 | 1.59 | 2120 | 2380 | 25.8 | 24.5 |
| | 3 | 0.76 | 0.67 | 3000 | 4460 | 12.6 | 12.5 |
| | 4 | – | 0.06 | – | 3530 | 4.4 | 3.0 |

## 3 Discussion

The band diagrams, wave functions and electron concentration in each subbands were calculated by solving self-consistently Schrödinger and Poisson equations [5]. Non parabolicity of the conduction band in the Γ point and the exchange-correlation contribution to the electrostatic potential were included. The width of the δ-layer of ionized impurities, used in the calculations as a adjustable parameter, was approximately equal to 16 nm for all samples. Such a width for a δ-layer is bigger than in Si δ-doped structures [4], but is rather small for Tin [1].

The electron quantum mobilities due to multi-subband scattering on ionized impurities [5, 6] were calculated. The screening of the Coulomb scattering potential was taken into account within the random-phase approximation [6]. The calculated mobilities are in reasonable agreement with our experimental results (see Table 2).

In sample No. 7 with the highest electron concentration the conductance band in the L point is filled by electrons at low temperatures (according to Ref. [4] this occurs at a concentration of ionized impurity greater than $N_D = 1.6 \times 10^{13}$ cm$^{-2}$). If the highest frequency in the Fourier spectrum (Fig. 3b) corresponds to the lower subband $i = 0$ in the Γ point with concentration $9.75 \times 10^{12}$ cm$^{-2}$, then, according to our calculations, two subbands should be filled in the L point with concentration $3.7 \times 10^{13}$ cm$^{-2}$ and $2.0 \times 10^{13}$ cm$^{-2}$ (the corresponding frequencies are designated by asterisks in Fig. 3b). This is the first experimental observation of such a high concentration of electrons in δ-doped GaAs structures, at which a conductance band at the L point is populated at helium temperatures.

The measurement of magnetoresistance in magnetic field parallel to the δ-layer allows one to determine accurately the number of occupied subbands [7]. For the magnetic field B directed along the y-axis and the vector potential equal to $\mathbf{A} = (Bz,0,0)$, the

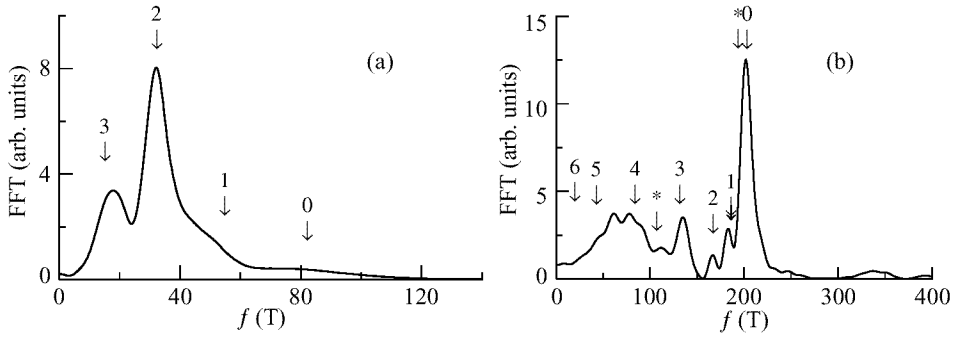


**Fig 3.** Fourier spectrum of the Shubnikov–de Haas oscillations for sample No. 6 (a) and No. 7 (b). Arrows correspond to calculated subbands in the Γ point. Asterisks correspond to calculated subbands in the L point.

Schrödinger equations reads:

$$\left[\frac{p_y^2}{2m^*} + \frac{1}{2m^*}(p_x + ezB)^2 - \frac{\hbar^2}{2m^*}\frac{\partial^2}{\partial z^2} + \Phi(z)\right]\Psi = E\Psi,$$

where the potential $\Phi(z)$ is a sum of an electrostatic potential, determined from the Poisson equation, and the exchange-correlation potential. The total density of states (DOS) at the Fermi level increases with increasing magnetic field and drops after the subband level has crossed the Fermi level (Fig. 1b).

The work was supported by the Russian Foundation for Basic Research (Grant No. 97-02-17396) and by the Dutch organizations N.W.O. and F.O.M.

## References

[1] J.J. Harris, et. al. *J. Appl. Phys. A* **33** 87 (1984).
[2] A. de Visser, et. al. *Pisma JETP* **59** 340 (1994) (*JETP Lett.* **59** 363 (1994)).
[3] V.A. Kulbachinskii, et. al. *Physica B* **229** 262 (1997).
[4] A. Zrenner, et. al. *Semicond. Sci. Technol.* **3** 1203 (1988).
[5] V.A. Kulbachinskii, et. al. *JETP* **110** 1517 (1996) (*JETP* **83**(4) 841 (1996)).
[6] G.-Q. Hai, N. Studart, F.M. Peeters. *Phys. Rev. B* **52** 8363 (1995).
[7] A.F.W. van de Stadt, et. al. *Physica B* **211** 458 (1995).

Ioffe Institute
6th Int. Symp. "Nanostructures: Physics and Technology"
St Petersburg, Russia, June 22–26, 1998.



# Optimization of MBE-grown GaAs planar doped barrier diode structures

*N. A. Maleev*‡†, A. Yu. Egorov†, M. F. Kokorev‡, A. R. Kovsh†, V. V. Volkov§, V. M. Ustinov† and A. E. Zhukov†

‡ Radioengineering and Electronics Department, State Electrotechnical University Prof. Popov 5, 197376, St. Petersburg, Russia

† Ioffe Physico-Technical Institute RAS, St. Petersburg, Russia

§ Svetlana-Electronpribor, Close Stock Company, Engels 27, 194156, St. Petersburg, Russia

The planar doped barrier (PDB) GaAs structures are used in many high-speed semiconductor devices [1] including microwave planar doped barrier diodes (PDBDs). These unipolar diodes have a multi layer semiconductor structure (Fig. 1) with ultra thin $p^{++}$ layer sandwiched between two undoped layers. That structures can be synthezed only using modern epitaxial technologies, i.e. MBE or MOCVD. The current conduction mechanism in PDBD is governed by the thermionic emission of the major carriers over the built-in potential barrier. Since the barrier is formed in the bulk of the structure, better stability and lower noise are expected comparing to the Schottky diodes having surface-barrier. The further advantage of the PDBDs is the adjustable height of the barrier. This fact allows to fabricate low-barrier microwave diodes for zero-bias detectors and low-drive mixers [2].

The key point for fabrication of reproducible PDB structures is $p^{++}$ layer charge and position control [3]. Another main factor is the low level of background doping. Therefore MBE seems to be the most suitable technology for these devices. There are two types of PDB structures: one of them is on the high-conductivity $n^+$ substrates and another one is on the semi-insulating substrates. The first type provides more simple diode technology but the second type is needed for realization of planar and coplanar diode constructions. These diode constructions are appropriated for MIC and millimeter wave devices [4].

There are some specific problems in MBE growth of PDBD stucture on SI substrate. This structure must have two relatively thick $n^+$ layers. The thick bottom layer is used to provide low series resistance. It usially has thickness of 4–5 $\mu$m. The top $n^+$ layer is used for alloy ohmic contact formation. Reduction in thickness of the top $n^+$ layer beyond 0.3 $\mu$m whould lead to practical problems in alloy ohmic contact fabrication. Usially the MBE growth is carried out at 600°C at growth rate of 1 $\mu$m/h. Consequently the long MBE process is typical for PDBD structure on the SI substrate.

In this work we present new design and technology for planar PDBDs. The main features of our approach are as follows:

1. Combination of vapor phase epitaxy with MBE. VPE is used for growth of thick bottom $n^+$ layer. The other layers were grown by MBE.
2. $n^+$ $In_{0.5}Ga_{0.5}As$/grad InGaAs/GaAs contact layer and non-alloyed Ti/Pt/Au top ohmic contact were used instead of the standard $n^+$ GaAs/AuGe/Ni/Au alloy contact. This approach provides the low contact resistance ($< 6 \times 10^{-6}$ $\Omega\,cm^2$) and high yield ($> 90\%$).

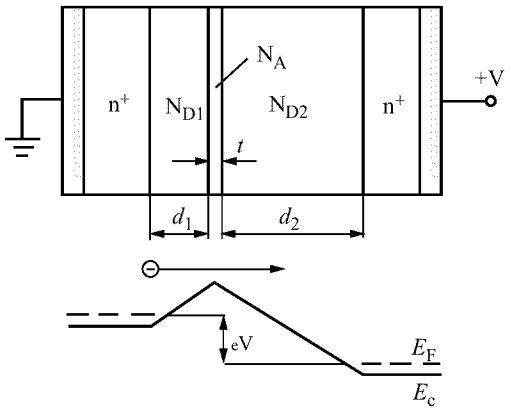


**Fig 1.** The structure and band diagram of the PDBD. ($t < 100$ Å, $N_A < 10^{18}$ cm$^{-3}$, $d_1 < 100$ Å, $d_2 < 5000$ Å).

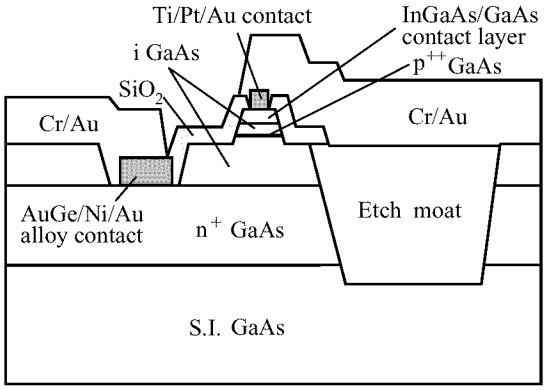


**Fig 2.** Designed PDBD structure.

3. For millimeter wave frequency applications planar diodes are required [4]. For this reason an existing process for the planar mixer GaAs Schottky diode manufacturing was adopted for the PDB structures. The designed PDBD structure is shown in Fig. 2.

Process-development wafers were grown by MBE in Ioffe Physico-Technical Institute on Si-doped $n^+$ GaAs (100) substrates. Before growing the films the substrates were thermally outgassed in the growth chamber at 610°C for 10 minutes under $As_4$ flux. The MBE growth was carried out at 600°C at growth rate of 1 $\mu$m/h under As stablized condition. Si and Be were used as $n$- and $p$-dopants, respectively.

The device construction and technology were performed in the Svetlana-Electronpribor. Device numerical modelling and characterization were made in State Electrotechnical University. Test structures were fabricated to evaluate the PDB structure parameters. They consisted of chips with 70 $\mu$m diameter etched mesas and AuGe-Ni-Au top and bottom metallizations. DC performance of some test devices are summarized in Table 1 (where $\Phi_b$ is potential barrier height, $n$ is ideality factor).

Then semiconductor structure parameters were extracted from I–V and C–V measurements using inverse modelling approach. The simple PDBD model [1] were used

**Table 1.** Test PDBDs parameters.

| | $\alpha$ | | | | | | | | |
|---|---|---|---|---|---|---|---|---|---|
| $\beta$ | Sample | $d_1$ nm | $d_2$ nm | $t$ nm | $N_A$ $cm^{-3}$ | $n_{calc}$ | $n_{exp}$ | $\Phi_{bcalc}$ mV | $\Phi_{bexp}$ mV |
| 2 | 2-640 | 200 | 100 | 10 | $4 \cdot 10^{17}$ | 1.5 | 1.52 | 368 | 577 |
| 3 | 2-680 | 150 | 30 | 10 | $10^{18}$ | 2.2 | 1.34 | 344 | 476 |

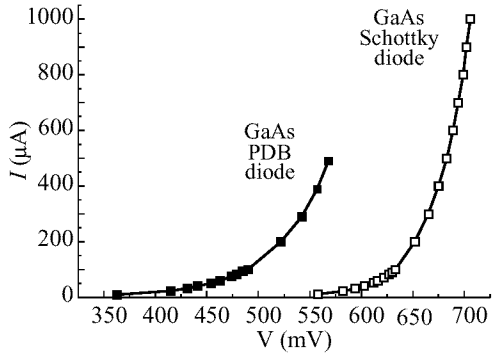


**Fig 3.** Mesured cirrent-voltage characteristics.

for this purpose in combination with numerical modelling of C–V characteristics [5].

The PDB structure and growth process parameters were optimized using obtained experimental results. The $n^+$-GaAs/SI-GaAs epitaxial structure was fabricated by VPE in JSC Elma-Malachite (Moscow, Russia). Then GaAs PDB structure with InGaAs/GaAs contact layer was grown by MBE in PTI and planar diodes were fabricated. Typical room temperature forward bias I–V characteristics for PDBD and GaAs Schottky diodes are shown in Fig. 3. Comparison is made with a standard planar microwave GaAs Schottky diode with same contact configuration. It can be seen that the PDB diode has lower barrier height.

An initial assessment has shown that the low frequency noise generation ($IF <$ 1 MHz) is significantly less for the PDB diodes then for GaAs Schottky diodes. Microwave measurements were made in a balanced mixer over the frequency range of 9–10 GHz.

## References

[1] Shur M. *GaAs devices and circuits* Plenum Press, N.Y. and London, 1987.
[2] Dale I., Conde A., Neylon S., Kearney M. J., *IEEE MTT-S Digest*, pp. 467–470 1989.
[3] Szentpali B., Tuyen V. V., *20th Workshop on Compound Semiconductor Devices and Integrated Circuits*, Vilnus, Lithuania, May 1996. pp. 60–61.
[4] Garfield D. G., Mattauch R. J., Weinreb S., *IEEE Trans. on Microwave Theory and Techn.*, **39**, No. 1, 1–5 (1991).
[5] Kokorev M. F., Egorov A. Yu., Gordina N. A., Kuzmenkov A. G., Maleev N. A., Presnov V. I., Ustinov V. M., Zhukov A. E., *Nanostructures: Physics and Technology*, Int. Symp., St.Petersburg, Russia, June 1997, pp. 259–262.

Ioffe Institute
6th Int. Symp. "Nanostructures: Physics and Technology"
St Petersburg, Russia, June 22–26, 1998.



# GaN grown on (101) neodium gallate by MBE with magnetron RF plasma source

V. V. Mamutin†, *V. A. Vekshin*†, V. N. Jmerik†, T. V. Shubina†,
A. A. Toropov†, A. V. Lebedev†, N. A. Sad'chinov†, N. F. Kartenko†,
S. V. Ivanov†, P. S. Kop'ev†, A. Wagner‡, W. Strupinski‡ and A. Jelenski‡
† Ioffe Physico-Technical Institute, 194021 St. Petersburg, Russia
‡ Inst. of Electronic Mat. Technology, Warsaw, Poland

The MBE technology is a very promising technique to grow GaN-based nanostructures for different optoelectronic applications. However, the lack of a suitable lattice-matched substrate is especially critical for the MBE technology due to the severe rate restriction on the buffer layer thickness. The sapphire, commonly used as a substrate for growing GaN related materials is characterized by a large difference (16%) in the lattice parameter with gallium nitride. New $NdGaO_3$ substrates have the much better lattice matching ($\sim$ 1%) and, hence, are promising for the nitrides epitaxial growth [1]. Another serious problem is a lack of efficient enough nitrogen exciter that limits a maximum growth rate of high-quality epilayers.

In this paper we report on the first successful attempt of MBE GaN epitaxial growth on the neodim gallate substrates. We demonstrated also the feasibility for the III-nitrides MBE growth of an original compact coaxial magnetron (CCM) plasma source with radio-frequency (RF) capacitively coupled discharge, compatible with modern MBE requirements. This source has allowed us to reach the growth rates as high as 0.1 $\sim$ 0.5 $\mu$m/h with good GaN crystalline quality. Electrical, structural and luminescence properties of GaN films have been examined.

GaN epilayers have been grown by plasma-assisted molecular beam epitaxy (MBE) on $Al_2O_3$ (0001) (as reference samples) and $NdGaO_3$ (101) substrates in a home made EP 1203 MBE setup. The 13.56 MHz RF power up to 200 W is applied to the central electrode of the CCM RF source. In addition to the RF electric field, an axial constant magnetic field tunable up to 0.8 T is produced by solenoid coils. The central electrode and the plasma chamber walls are covered with pirolytic boron nitride. This movable source mounted on a 4.5″ flange of the MBE installation provides a 40–140 mm variation of distance between the output source aperture and a substrate surface. Nitrogen background pressure in the growth chamber is slightly higher than 10–4 Torr. Turbo-molecular pump with effective pumping rate of $\sim$ 350 l/s is used.

Preliminary testing of the plasma source characteristics reported in [2] has been performed using optical emission spectra (OES) recording in the 350–790 nm wavelength range. The characteristic lines of excited $N_2$ molecules and molecular ions are dominant in the spectrum, while there is no pronounced lines of excited atomic nitrogen. In general features, this discharge is closer to that of electron cyclotron resonance source rather than to that of inductively coupled source. An increase in the discharge pressure up to 1 Torr, as well as both the rf power and the magnetic field result in a monotonous increase in intensities of all the lines, while the intensity ratio between ions and molecules changes. It allows us to vary the temperature and concentration of

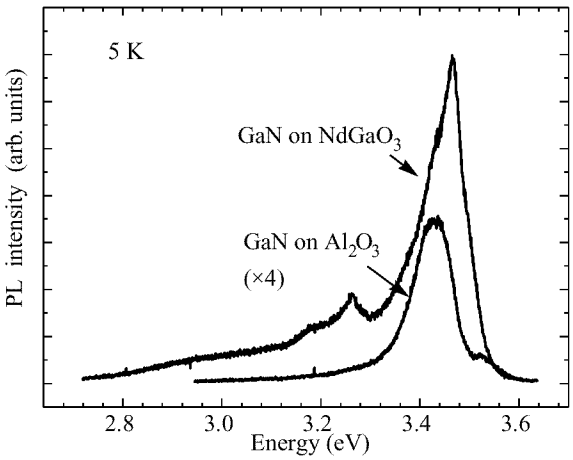


**Fig 1.**

electrons in the discharge in a wide range, and, hence, to change both qualitatively and quantitatively the output nitrogen flux.

Slight nitridization was used before growth and then low-temperature GaN buffer layers were grown at 550 °C. The GaN layers were grown at 700–750 °C. The temperature was measured by an infrared optical pyrometer. The growth rates were in 0.07–0.2 $\mu$m/h range. The substrates were not chemically etched but only rinsed in solvents and were thermally cleaned at $\sim$ 700 °C in vacuum just before the growth.

Deposited GaN films were characterized by scanning electron microscope (SEM), x-ray diffraction (XRD), photoluminescence (PL), Raman spectroscopy and capacity-voltage (C/V) measurement. Crystalline quality was determined by RHEED (reflection high energy electron diffraction) and XRD using CuK$\alpha$ radiation. PL measurements were performed from 5 K up to room temperature using a He–Cd laser as an excitation source. Surface morphology and thickness were studied by Cam Scan electron microscope. Electrical properties of the GaN epilayers were determined by C/V measurements.

RHEED demonstrated streaky pattern during growth both on $Al_2O_3$ and $NdGaO_3$ substrates. XRD established monocrystalline GaN film with the same (0001) orientation as an $Al_2O_3$ substrate and with x-ray rocking curve width of GaN (002) peak of about 1°. GaN on $NdGaO_3$ was of the same orientation and of comparable quality. The room-temperature electron concentration for GaN both on $Al_2O_3$ and on $NdGaO_3$ was $n \sim 10^{16}$ cm$^{-3}$.

The typical PL spectra are shown in Fig. 1. The low-temperature spectrum of GaN on $NdGaO_3$ (solid line) shows main peak at 3.47 eV, which is attributed to emission of a donor-bound exciton [3-5], and the lower laying peaks near 3.26 eV, which may be associated either with the donor-acceptor pair transition and it's phonon replica, or with $D^0x$ transition in cubic GaN inclusions [6]. The former explanation looks more reasonable and is also confirmed by the fast decrease of the peaks intensity with the temperature increase (see Fig. 2). The 3.475 eV line in the $n-$ type layers is a well known transition due to the recombination of the excitons bound to neutral donors

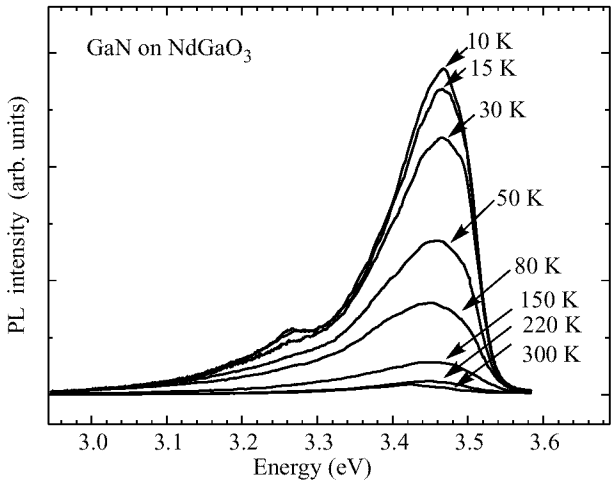


**Fig 2.**

associated with nitrogen vacancies [7]. The origin of the donors can be either native defects or residual impurities [8] and is the subject of future investigations. The spectra exhibit a negligible intensity of the yellow emission band at both room and liquid helium temperatures. The dotted curve in Fig. 1 represents a low temperature PL spectrum of a GaN grown on a $Al_2O_3$. The linewidth is slightly less than for the GaN on $NdGaO_3$, however, the latter displays about twice higher PL efficiency.

In summary, we have demonstrated a feasibility of new $NdGaO_3$ substrates for MBE growth of GaN layers. Additionally, we report a compatibility of a new type plasma-source with MBE requirements and it's capability to provide the growth rate up to 0.5 $\mu$m/h.

This work was supported in part by RFBR Grants as well as by Program of Ministry of Sciences of RF "Physics of Solid State Nanostructures".

## References

[1] Okasaki H., Arakawa A., Asahi T., Oda O. and Aiki K. *Sol. St. Electron.* **41** 263-266 (1997).
[2] V. Mamutin et al, *Technical Physics Letters* (to be published).
[3] Hellman H.S., Brandle C.D., Schneemeyer L.F. et al, *MRS Internet J. NSR.* 1996, 1, Art. 1.
[4] Strauss U., Tews H., Riechert H. et al, *MIJ NSR.* 1996, 1, Art. 44.
[5] Leroux M., Beaumont B., Grandjen N. et al, *MIJ NSR,* 1996, 1, Art.25.
[6] Ren B.G., Orten J.W., Cheng T.S., Foxon C.T. et al, *MIJ NSR* 1996, 1, Art. 22.
[7] Smith M., Chen G.D., Li J.I. et al, *Appl. Phys. Lett.* **67** 3387 (1995).
[8] Teisseyre H., Nowak G., Leszczynski M. et al, *MIJ NSR* 1996, 1, Art. 13.

Ioffe Institute
6th Int. Symp. "Nanostructures: Physics and Technology"
St Petersburg, Russia, June 22–26, 1998.



# Correlation between structural and optical properties of nanocrystal particles prepared at low temperature plasma-enhanced chemical vapor deposition

*D. Milovzorov*†‡§, T. Inokuma†, Y. Kurata† and S. Hasegawa†

† Department of Electronics, Faculty of Technology, Kanazawa University, 2-40-20 Kodatsuno, Kanazawa 920, Japan

‡ Institute of Radioengineering and Electronics, Russian Academy of Science, Mokhovaya str. 11, Moscow 103907, Russia

§ Present address: The Institute of Physical and Chemical Research (RIKEN) Wako, Saitama 351-01, Japan

In recent years a great interest has been generated in formation of semiconductor with nanocrystals, due to their unique properties resulting from quantum confinement in systems of reduced dimensions [1, 2]. For these materials there is a potential for fabricating optoelectronic devices and optical amplifiers.

Polycrystalline silicon (poly-Si) film synthesis has been deposited on quartz, glass (Corning 7059) and Si (100) substrates by low temperature plasma-enhanced chemical vapor deposition (PECVD)using $SiH_4/H_2$ and $SiF_4/SiH_4/H_2$ gas mixtures. The substrates were cleaned for 20 min, by nitrogen and hydrogen plasma respectively, just before the deposition of poly-Si films. The rf power supply was 20 W (at 13.56 MHz). The $SiH_4$ flow rate was maintained at 0.6 sccm. The hydrogen flow rate was varied from 5 to 46 sccm. Using a $SiF_4$ gas diluted with He (He: 95%, $SiF_4$: 5%) the $SiF_4$ was varied from 0 to 0.5 sccm. The total gas pressure was 0.2 or 0.3 Torr.

The structural properties of the poly-Si films were investigated by means of x-ray diffraction (SHIMADZU XD-D1) employing a diffractometer with the slit width 0.1 mm, set in the front of the detector. The XRD relative intensity was defined as the integrated area including the following corrections; the difference in film thickness for each sample was corrected using the x-ray absorption coefficient for Si, and the XRD intensity of a given texture was further normalized using corresponding x-ray intensities for Si powder. The average grain size, $\delta$, in the depth direction was estimated from the half-width value of the x-ray spectrum by means of the Scherrer formula [3].

The volume fraction of crystalline phase, $\rho$, was estimated from the intensity of Raman spectra by the procedure proposed by Tsu et al [4], that is, a Raman spectra consists of two components: crystalline Si (c-Si) phase corresponds the spectral peak near 520 $cm^{-1}$ and amorphous Si (a-Si) phase at around 480 $cm^{-1}$. The $\rho$ values were estimated from the intensity ratio of the above two components using the ratio of the integrated Raman cross section for crystalline and amorphous phases. The crystalline volume fraction for the films used was between 60% and 80%.

Photoluminescence (PL) was analysed using a Jobin Yvon RAMANOR HG 2S spectrometer coupled with a cooled photomultiplier tube (Hamamatsu Photonics K.K.). The 488 nm $Ar^+$ laser line with power ranging from 300 to 500 mW was used as the PL excitation source.

The chemical structure for the surface region on crystallites was investigated by

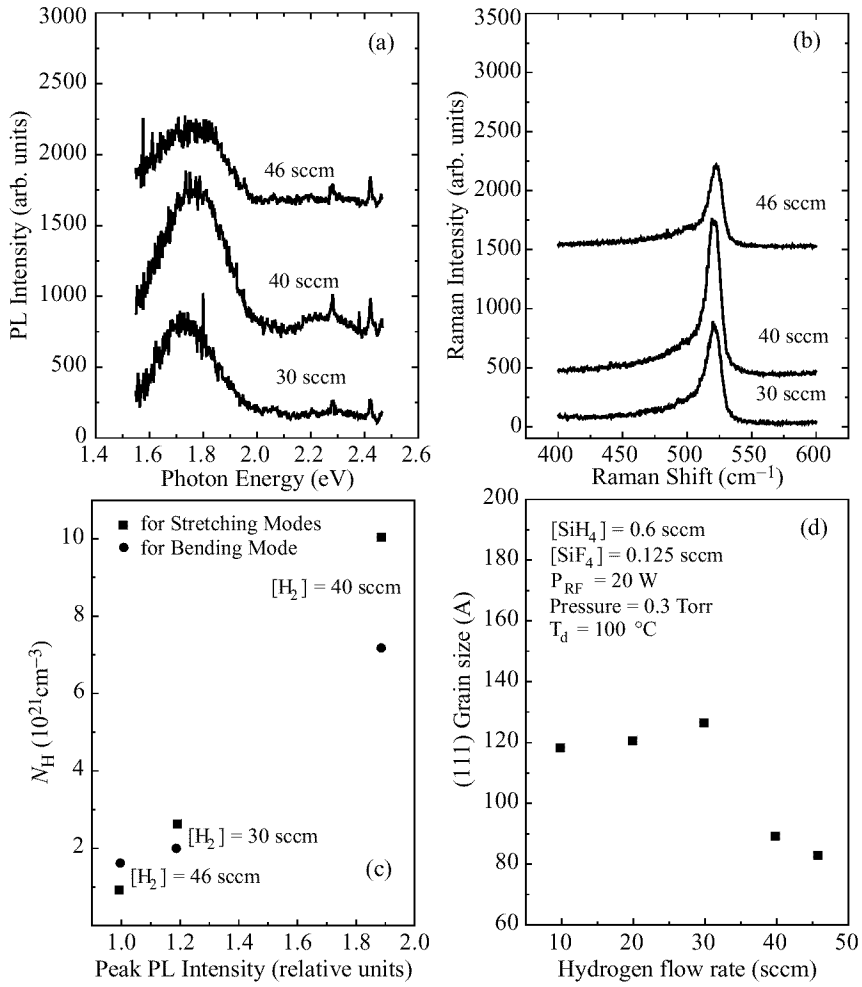


**Fig 1.**

means of Fourier-transformed infrared spectrometer (JASCO FT/IR-610). The density of given bonds can be estimated by the following way:

$$N^{v}_{\mathrm{SiM}} = A^{v}_{\mathrm{SiM}} I^{v}_{\mathrm{SiM}}, \qquad (\mathrm{M} = \mathrm{H\ or\ O})$$

where $A^{v}_{\mathrm{SiM}}$ is proportionality coefficient, $I^{v}_{\mathrm{SiM}}$ is the intensity of the SiM absorption spectrum with the given frequency $v$.

Using low temperature PECVD of $SiF_4/SiH_4/H_2$ gas mixture we produced the poly-Si films which contains hydrogenated nanocrystallites with different luminescent properties. Figure 1(a,b,c,d) illustrates the relationship between PL spectra, Raman spectra, density of bonds for hydrogen stretching and bending modes, and average grain size as function of hydrogen flow rate, respectively. The temperature of deposition was 100°C.

The PL peak energy of hydrogenated nanocrystals is sensitive to the deposition conditions. Figure 2 shows the increase of PL energy as function of average grain size under

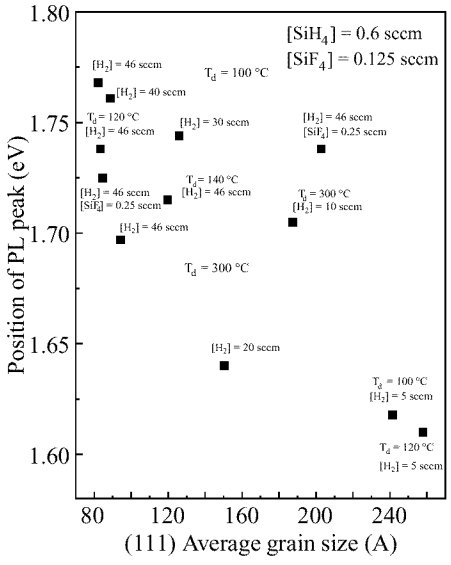


Fig. 2.

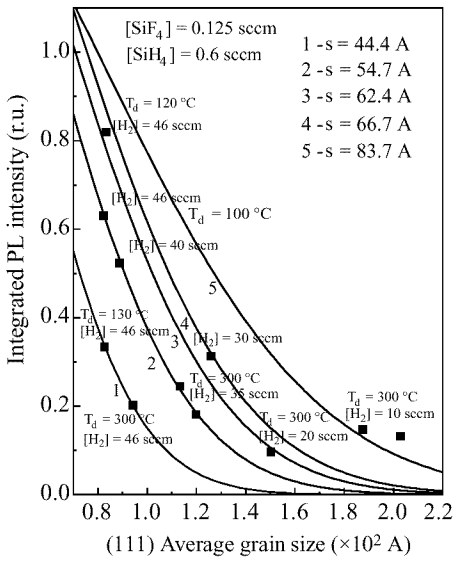


Fig. 3.

different PECVD conditions. Each point in this results illustrates the correlation between the PL peak energy and average value of grain size. PL peak energy corresponds the energy band gap of crystallites and is result of the presence the small nanoparticles in left tail of size distribution. We can see that highest points in Fig. 2 are realized with low temperature (100°C) conditions. It is connected with wider size distributions with strong long left tail which contain a great amount of nanocrystallites. The increase in the deposition temperature causes the decrease of the PL peak energy. In this case, the band gap energy of the crystalline core state is lower than the $\sim 1.65$ eV interface state [5]. The size-dependent PL characteristics in hydrogenated nanocrystals is result in presence delocalized states in the Si crystalline core. It is obvious that as the crystallite size decreases the highest occupied state energy decreases and the lowest unoccupied state energy increases. By changing preparation conditions of deposition such as deposition temperature, hydrogen or $SiF_4$ flow rates there is adjustable the size distribution of crystallites and their hydrogenation. The presence of dangling bonds would suppress the PL response. The termination of dangling bonds with hydrogen removes localized defect states from the energy range near the Fermi energy in the surface region on crystallites.

Figure 3 shows the integrated PL intensity as function of average grain size. The calculated curves for the PL intensity were obtained by assuming the state-to-state spontaneous transition probability and absorption coefficient [6]. Our PL response model involves absorption in the quantum confined Si cores, and emission due to transitions between states in terminated layers. The results of calculation according to the model are presented by solid lines in Fig. 3. In these calculated curves, the size dependence of the integrated PL intensity can be expressed in the following form: $I \sim \rho \exp(-\delta k/2)$ where $\rho$ is proportional constant, and $k = 1/\sigma^2$; $\sigma$ is standard deviation. The values of the standard deviation estimated from solid lines in Fig. 3 changed from $\sigma = 44.4$ Å

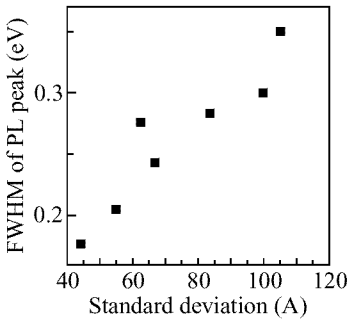


**Fig 4.**

(curve 1) to $\sigma = 83.7$ Å (curve 5). We find a tendency that the standard deviation becomes larger as the deposition temperature decreases. However, at low temperature, highly efficient PL can not be found. This may be because high integrated PL intensity of films deposited at low temperature is realized due to the great spectral width. As a consequence, for high performance of the material the use of higher deposition temperature (200–300°C) and high hydrogen dilution ratio is more preferable, because the film which has small $\sigma$ value, which has a relatively small $\sigma$ value, will result in the PL response with narrow width of energy. Figure 4 shows the correlation between the width of PL spectra and value of $\sigma$ (which is estimated from different curves in Fig. 3). As seen in Fig. 4, the width of PL spectra decreases with decreasing $\sigma$ values. Therefore, we can suppose that spectral width of PL is proportional to the standard deviation of size distribution of crystals.

In conclusion, we have synthesized poly-Si films with controlled size distribution of nanocrystals and sufficient luminescent properties. The correlation between structural and optical properties of the poly-Si films allows us to determine the optimal deposition conditions for preparation films with high PL response with narrow width of energy.

The authors are indebted to Professor T. Shimizu for the use of Raman spectrometer, and also to Mr. M. Syed for his assistance with experiments. One of the authors (D.M.) thanks the Faculty of Technology, Kanazawa University where this work has been done for assistance and hospitality.

## References

[1] Y. Kanemitsu, *Phys. Rev. B* **53** 13515 (1996).
[2] B. Delley and E.F. Steigmeier, *Phys. Rev. B* **47** 1397 (1993).
[3] B.D. Cullity, *Elements of X-ray Diffraction*, Addison-Wesley, Reading (1978), p. 102.
[4] R. Tsu et al, *Appl. Phys. Lett.* **40** 534 (1982).
[5] Y. Kanemitsu and S. Okamoto, *Mat. Res. Soc. Symp. Proc.* **452** 195 (1997).
[6] M.S. Hybertsen and M. Needels, *Phys. Rev. B* **48** 4608 (1993).

Ioffe Institute
6th Int. Symp. "Nanostructures: Physics and Technology"
St Petersburg, Russia, June 22–26, 1998.



# Surface relief influence on rheed oscillations shape during MBE growth

I. G. Neizvestny, *N. L. Shwartz* and Z. Sh. Yanovitskaya
Institute of Semiconductor Physics RAS,
Russia, Novosibirsk 90, pr. Lavrenteva, 13

Molecular beam epitaxy (MBE) is one of the basic methods for low-dimensional structures production. RHEED intensity oscillations being widely practiced as the method of growing surface control allow to determine thickness of the obtained film with an accuracy of one monolayer. However, oscillations damping with time and distortions of their shapes decrease the accuracy of thickness determination. Surface relief have a great impact on electronic properties of grown structures. But it's a cumbersome task to combine MBE technology with the direct observation of the surface during the growth process. Complicated shape of oscillations contains information not only on the number of growing monolayers but on the initial microrelief, evolution of this relief through the surface processes and the final morphology of grown layer. Relationship between RHEED oscillations shapes and microrelief of growing film is demonstrated.

Simulation of MBE growth process was carried out by Monte Carlo method in assumption of the SOS deposition on the Kossel crystal (100) surface. Simulations were performed on the lattice with $160 \times 160$ atom places for cyclic boundary conditions [1-2]. Surface step density oscillations along with a computer film demonstrating surface relief evolution during the growth process were obtained by simulation. Simulations of MBE growth processes on the vicinal surfaces with equidistant steps and echelons of steps as well as on the surfaces with initially formed two-dimensional islands at different effective surface temperatures were carried out. Surface step density oscillations of islands and steps in simulation process were compared with RHEED oscillations obtained during MBE growth of Ge on Ge(111) [3]. The lowest temperature of the surface corresponds to the three-dimensional growth mode and the highest one to step-flow mode.

Fig. 1(a) demonstrates RHEED oscillations obtained during homoepitaxy of Ge on the surface with (111) orientation at various surface temperatures and the deposition rate equal to 2.5 nm/min. Step density as a function of deposited dose is represented in Fig. 1(b). Migration length was measure of the effective surface temperature. In our model migration length is defined by the number of diffusion steps per unit time. Increasing of the surface temperature is equivalent to a rise in diffusion step numbers that is increasing diffusion length. The maximum migration length used in simulations corresponds to the pure step flow mode and the minimum one to the two-dimensional island growth mode. Three-dimensional growth mode was not considered in this work.

All results presented in Fig. 1(b) were obtained by simulation on the stepped surfaces. Maximum terrace width $L$ was 160 atomic units. Terraces could be separated by monoatomic steps, or by steps echelons of four monolayers height. Oscillations damping shapes were depended on the parameter $L/l$. Three bottom curves Fig. 1(b) correspond to echelon type initial relief. For curves 1–2 parameter $L/l \gg 1$, so there were no step flow and no decay of echelons. Increasing number of the simulated curve corresponds to the increasing of $L/l$. For the curve number 1 $L/l$ is so high that oscillations behavior

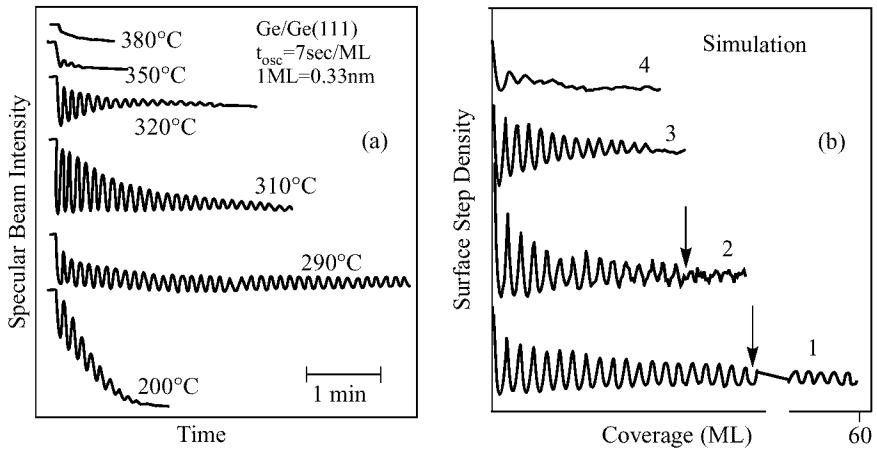


**Fig 1.**

is similar to their behavior on the flat surface. For the curve 2 echelons are practically undecayed during growth process but one could observe shift of the lower step in parallel with creation behind it of the region depleted with islands. This causes rapid damping of oscillations through forming specific structure of island with asynchronous nucleation [4]. Increasing of $L/l$ brings to echelons decay: appearance of narrow terraces free of islands with simultaneous decrease of the initial terrace width with two-dimensional growth taking place. This fact causes rise of the lower envelope of the oscillation curve through surface step density decrease (curve 3 Fig. 1(b)). Further increase of $L/l$ leads to complete decay of echelons and formation of the surface with equidistant steps. Initial relief with equidistant steps of monolayer height corresponds to curves 4 and 5. For migration length $l$ of about $L/4$ one row of islands is continuously formed before moving step during growth process. One could see only one minimum in curve 4 during first monolayer deposition. No oscillation in step density curve could be seen for $L/l > 2$. Some decrease in step density with time appreciable in curve 5 could be associated with kinetic roughness of steps.

Surface relief formed due to coexisting of two growth modes during MBE process: two-dimensional island creation and step flow was considered. The reason of oscillations damping in chosen interval of parameters is not three-dimensional growth mode but creation of islands system reproducing in time named asynchronous structure [4]. The view of linear asynchronous structure is represented in Fig. 2(a). This type of surface relief corresponds to the curve 2 Fig. 1(b) after damping of oscillations. In this structure islands arranged along the lines parallel to the steps were nucleated simultaneously, however in given monolayer islands near the top terrace were nucleated earlier than others, and near the low one — later. Thus asynchronous nucleation took place. The moment of nucleation as well as the size of the island depend on the distance between the nucleus and the step. Linear asynchronous structure reproducing its form apparently moves during deposition process. So its perimeter in the average is remained constant causing damping of oscillations.

The top view of the surface corresponding to the curve 1 is represented in Fig. 1(b).

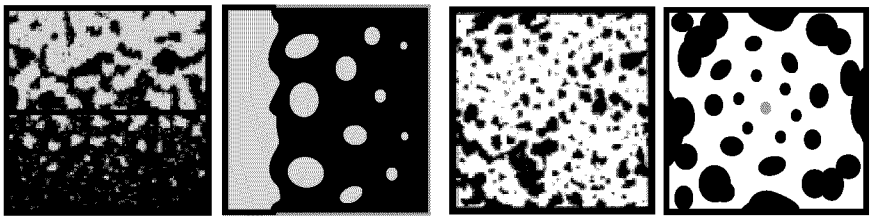


**Fig 2.**

The system of islands with increasing average radius as they move away from some center with vacancy-island could be seen in Fig. 1(b). Since islands near center with vacancy-island nucleated later than at the periphery due to the outflow of adatoms in vacancies such system of islands was named circular asynchronous structure. Circular asynchronous structure could be formed on the singular surfaces as well as on the vicinal ones with wide terraces without step flow. Oscillations damping in the initial part of the curve 1 Fig. 1(b) is accounted by the forming stage of circular asynchronous structure. Slightly damping oscillations observed late in time are characteristic of asynchronous structure of the circular form. Arrangement of such circular structures is maintained in every following monolayer.

One could often observe nonmonotonic amplitude modulations of RHEED oscillations in addition to their damping. Such type of distortions could be due to the initial relief which consists of steps of opposite directions and the coexistence of step flow and two-dimensional nucleation growth modes during growth process [5].

Simulation of MBE growth under changes of molecular beam intensity during deposition process demonstrates nonmonotonic amplitude distortions of step density oscillations mentioned above. This type of simulations was performed for explanation of available experimental RHEED oscillations obtained during Ge/Ge(111) deposition using two sources of different intensities [6]. Equivalent to variation of flux intensity in experiments is migration length variation according to the ratio $l \sim (D/I)^{(1/4)}$ [7] in simulations.

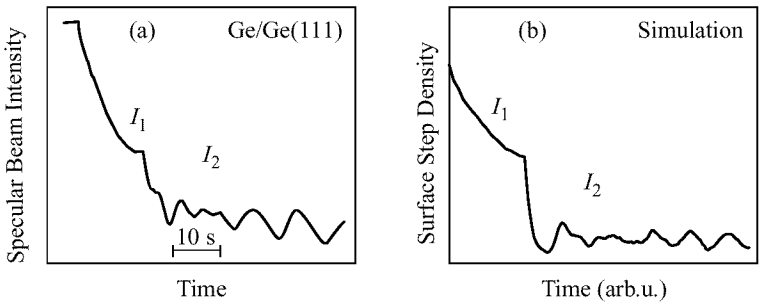


**Fig 3.**

RHEED oscillations and step density oscillations under changing flux intensity during

growth process are represented in Fig. 3. ($I_1$ — initial flux, $I_2$ — final flux, $I_1 < I_2$). For experimental and simulated curves one could observe similar oscillations shapes. After half monolayer deposition in low intensity flux large islands were formed on the terraces of simulated surface along with the creation of regions free of islands behind moving steps. Further deposition in higher flux results in simultaneous islands nucleation on the flat parts of the terraces and on the large islands grown earlier. Oscillation frequency of step density for these two systems of islands are different, that leads to the distortion of oscillations until the flux with intensity $I_2$ will determine growth process.

Thus the shape of RHEED oscillations is directly determined by the peculiarities of the surface morphology. Initial surface relief as well as its transformation during growth process influence on the oscillations shape. This allows in a number of cases just in the MBE process according to the shapes of oscillations to draw conclusions not only about the thickness of the layer but about its surface relief as well.

This work was supported by the Russian Foundation for Fundamental Research (Grant No. 96-02-19032) and the State Program 012 "Surface Atomic Structures" (Project No. 95-1.2).

## References

[1] Yanovitskaya Z.Sh., Slytskiy B.A. *Poverhnost'*, (Russian), **3** 78–86 (1991).
[2] Pchelyakov O.P., Yanovitskaya Z.Sh., Ryzhenkov I.P., Katkov I., Neizvestny I.G. *Poverchnost'* (Russian), **5** 20 (1996).
[3] Pchelyakov O.P., Markov V.A., Sokolov L.V. *Braz. J. Phys.* **24** N 1. 77–85 (1994).
[4] Yanovitskaya Z.Sh., Neizvestny I.G., Shwartz N.L., Katkov M.I., Ryzhenkov I.P. *Phys. Low-Dim. Struct.* **7/8** 47 (1996).
[5] Katkov M.I., Neizvestny I.G., Ryzhenkov I.P., Shwartz N.L., Yanovitskaya Z.Sh. *Phys. Low-Dim. Struct.* **5/6** 13 (1997).
[6] Pchelyakov O.P., Markov V.A., Sokolov L.V. *Private communication.*
[7] Ghaisas S.V,.Sarma S. *Phys. Rev. B.* **46** N 11 7308 (1992).

Ioffe Institute
6th Int. Symp. "Nanostructures: Physics and Technology"
St Petersburg, Russia, June 22–26, 1998.



# Correlation between electrical and optical properties of polymer nanostructures based on polydiacetylene

*E. G. Guk*, M. E. Levinshtein, V. A. Marikhin and L. P. Myasnikova
Ioffe Physico-Technical Institute of RAS

**Abstract.** A change in optical properties of conducting polydiacetylene THD (poly-1,1,6,6-tetraphenylhexadiinediamine) under doping has been investigated for the first time. Spectral dependencies of extinction coefficient were studied in the range 400-25000 $cm^{-1}$ either for non-doped PDA THD (with d.c. conductivity $\sigma < 10^{-9}$ S/cm) or for doped polymer at various doping levels (the ultimate value of conductivity is about $5\times10^{-3}$ S/cm). The obtained data allow to suggest that in PDA with conductivity $\sigma > 10^{-4}$ S/cm a high concentration of the charge carriers takes place. The observed sufficiently low macroscopic conductivity is attributed to the complicated hierarchy of structural units which is typical of polymeric materials. The results are compared to the corresponding data obtained for conducting polyacetylene.

## Introduction

At the previous symposium (Nanostructures: Physics and Technology-97) we reported for the first time the electrical and noise properties of doped polydiacetylene–the only class of conjugated polymers capable of solid state polymerization. The conductivity of any conductive polymer has its origin in transport of a free carrier (soliton or bipolaron) along a conjugated sequences in polymer molecules. These sequences can be considered as quasi-one-dimensional wires of 1.5–15 nm length (10–100 C=C bonds). The macroscopic conductivity of polymers depends on concentration and mobility of the carriers along the wires, as well as on the probability of the carrier "jumps" from one wire to another one inside of a separate fibril and from one fibril to another fibril. The experience in investigation of other doped polymers evidences that the only study of electrical behaviour of the doped polymer does not allow to estimate the relative contribution of the different processes to macroscopis polymer conductivity.

In the present work for the first time the optical properties of a doped conducting PDA THD are investigated both in the vicinity of the edge of the intrinsic absorption and in IR region. Studying the extinction in the vicinity of the edge of the intrinsic absorption may give the independent information on the concentration of the charge carriers as a function of the doping conditions and doping level.

The analysis of IR absorption spectra in a region up to 5000 $cm^{-1}$ and the comparison the obtained data with known spectra for conducting PA (see, for instance, [1]) also allows to get some additional information on the concentration of free carriers. Besides, these investigations enable one to follow the changes in a vibration spectra of initial polymer upon doping.

## 1 Results and discussions

In Fig. 1(a) the spectral dependencies of extinction coefficient are shown for PDA THD doped to various doping levels in a region of 5000–25000 $cm^{-1}$. Solid line 1

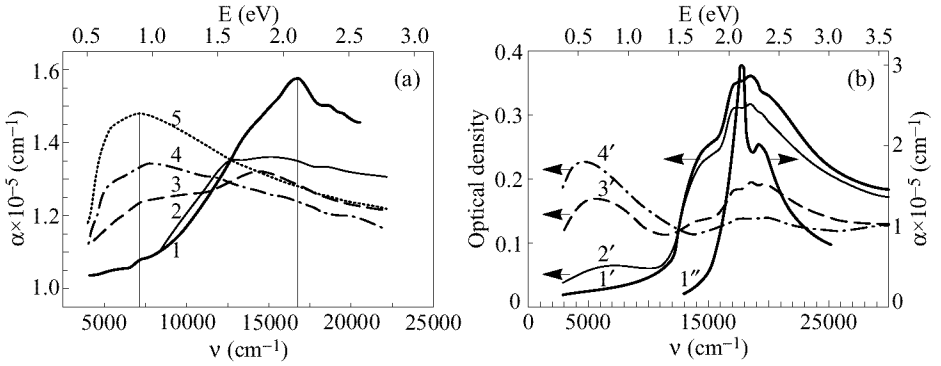


**Fig 1.** Spectral dependencies at various doping levels: (a) for doped PDA THD and (b) for doped PA. (a): 1—the undoped PDA sample ($\sigma < 10^{-9}$ S/cm), 2—$\sigma \sim 10^{-6}$ S/cm, 3—$\sigma \sim 10^{-5}$ S/cm, 4—$\sigma \sim 10^{-4}$ S/cm, 5—$\sigma \sim 10^{-3}$ S/cm. (b): 1′—the undoped PA sample, 2′—$\sigma = 20$ S/cm, 3′—$\sigma = 50$ S/cm, 4′—$\sigma = 100$ S/cm. [1], 1″— the dependence for PDA dispersed in PMMA matrix.

corresponds to a spectrum of undoped initial polymer. Quantitative value of extinction coefficient has been calculated with regard to the density of PDA THD single crystals.

It is known that the average length of a conjugated sequence in a polymer can be estimated from the value of the energy corresponding to extinction maximum: the energy corresponding to absorption maximum reduces with increasing of a conjugated length and reaches the ultimate value $\simeq 2$ eV at sufficiently large conjugated length. For polyacetylene, for instance, $E_0 \simeq 2.1$ eV has been observed [1] (Fig. 1(b)). Analising the curve 1 in Fig. 1(a) one can conclude that in the investigated PDA THD exposed to intensive mechanical disintegration an average conjugated length remains practically intact.

From Fig. 1(a) it is seen that with the increase of a doping level a longwave maximum is generated in a near IR region at $E_1 \simeq E_0/2$ , and the amplitude of this maximum grows with increasing doping. On the contrary, an amplitude of the maximum at $E = E_0$ corresponding to the maximum for undoped material monotonically decreases with increasing of doping level. A picture is qualitatively resembles a change in optical absorption spectra repeatedly observed for polyacetylene upon doping (Fig. 1(b)). The comparison of these spectra allows to draw a conclusion that the doping mechanism of polydiacetylene and polyacetylene are qualitatively analogous. One should, however, pay an attention to a very important fact: in polyacetylene, a large scatter in the values of macroscopic conductivity (over several order of magnitude) is observed at relatively low conductivity, when the absorption at $E = E_0$ remains significantly higher than that at $E = E_1$. At the same time, at high level of doping, when the absorption at $E = E_1$ exceeds that at $E = E_0$ the macroscopic conductivity is always appears to be highly enough ($\sigma \sim 10$–$100$ S/cm). The absorption at $E = E_1$ for curve 5 (Fig. 1(a)) is equal practically to the initial absorption at $E = E_0$ in undoped PDA THD and the absorption peak at $E = E_0$ is suppressed at the great extent. Nevertheless, the macroscopic conductivity in PDA appears to be lower by a factor of 4–5 orders of magnitude than that in polyacetylene. Of course, even for one and the same material (polyacetylene)

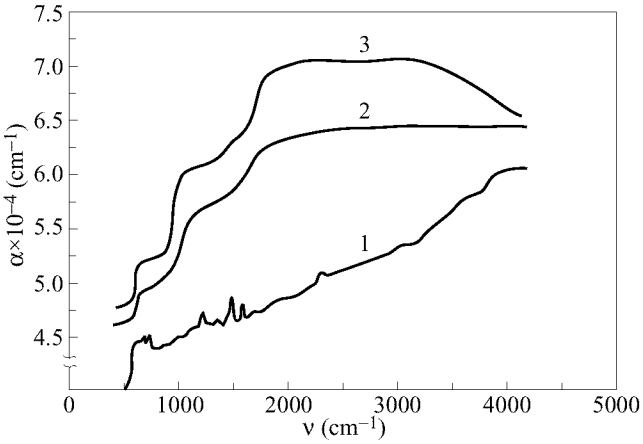


**Fig 2.** Spectral dependence of extinction coefficient of doped PDA THD for various doping levels. 1—the undoped sample, 2—$\sigma \sim 10^{-4}$ S/cm, 3—$\sigma \sim 10^{-3}$ S/cm.

the scatter in conductivity may be of several order of magnitude for the same values of $\alpha(E_1)/\alpha(E_0)$. Relative quantity of free carriers taking part in macroscopic conductivity may strongly (exponentially) vary depending on orientation of fibrils in a polymer, density of "fibrillar net", mutual disposition of polymer molecules and dopant chains. All things being equal, various portions of the carriers can be concentrated (in dependence on polymer structure) in the isolated clusters and "dead ends", or in conducting chains of an infinite cluster providing macroscopic conductivity.

The data given above show that the common concentration of the carriers in PDA THD with the reached level of conductivity is, probably, not less than that in polyacetylene with conductivity $\sigma \sim 10-100$ S/cm (which corresponds already to "metallic" conductivity. Nevertheless, the ultimately reached value of conductivity for doped PDA THD is $3\times10^{-2}$ S/cm, i.e. significantly less than that for polyacetylene.

The question arises which structural peculiarities of PDA is responsible for the large difference in conductivity. The analysis of SEM micrographs of needle-like PDA THD single crystals shows that the fibrils are perfectly aligned inside each single crystal. The order in fibril arrangement is much higher than that in "unoriented" polyacetylene. However, one should take into account two facts; first, the single crystals in a macroscopic sample have been chaotically oriented; second, it looks from our preliminary experiments that a single crystal surface comprises the potential barrier hindering exchange the free carriers between the neighbouring fibrils belonging to different single crystals.

Thus, to the transport mechanisms (which is characteristic of polyacetylene), in PDA operates an additional one-intercrystalline transport between the fibrils belonging to different single crystals. There is a hope that more perfect disposition of microcrystals and "suitable damage" of intercrystalline boundaries will allow in the future to increase significantly the conductivity of PDA THD using the same doping technique.

The spectral dependencies of extinction coefficient of PDA THD in IR region (400–4000 $cm^{-1}$) are shown in Fig. 2.

A curve 1 is the absorption of original undoped polymer. As distinct to the spectrum of undoped polyacetylene [1], a spectrum of PDA THD demonstrates relatively small number of typical maxima of low enough intensity: a lot of types of vibration transitions permitted in polyacetylene, in PDA are forbidden by the selection rules.

In the doped material (Fig. 2, the curves 2 and 3) the absorption bands typical of the original PDA THD are not observed. As distinct to polyacetylene, the doping does not lead to the appearance in a spectrum the new absorption bands.

In a spectrum of doped PDA THD the "steps" in the region $\nu \sim 625$ cm$^{-1}$, $\sim 1000$ cm$^{-1}$ and $\sim 1800$ cm$^{-1}$ are well pronounced. A sharp growth of extinction coefficient is also observed in a spectrum of undoped PDA THD with increasing $\nu$ higher than $\nu \sim 625$ cm$^{-1}$ (Fig. 2, curve 1). There are not analogous peculiarities in a spectrum of undoped material at $\nu \sim 1000$ cm$^{-1}$ and $\nu \sim 1800$ cm$^{-1}$. The nature of these peculiarities are not fully clear by now.

The increase of extinction coefficient in a longwave region is usually associated with the absorption on the free carriers. Actually, with increasing of conductivity of a polymer the absorption in a longwave region grows monotonically both for PA and PDA THD. Absorption in "classical" semiconductors differs, however, from conjugated polymers in that, the absorption $\alpha$ in conventional semiconductors (Si, Ge, GaAs a.o.) grows with increasing wave length $\lambda$ ($\alpha \sim \lambda^2$). This is caused by a fundamental reason: lower the energy of photon, lower impulse has to get a "free carrier" from the lattice (phonons) or from the impurities in order to absorb the quantum of light. An opposite situation takes place for the polymers: for the majority of bands, the absorption drops with increasing wave length. For PDA THD this tendency is more distinctly pronounced than for PA. This also confirms the assumption that the majority of carriers generating upon doping is concentrated in isolated clusters and "dead ends".

This work is supported by Russian Foundation of Basic Investigations (grant No. 96-03-32462).

## References

[1] Tanaka J. And Tanaka M. in *Handbook of conducting polymers*, ed. T. A. Scotheim, N.Y.-Basel: Marcel Dekker, 1986, v. 2.

Ioffe Institute
6th Int. Symp. "Nanostructures: Physics and Technology"
St Petersburg, Russia, June 22–26, 1998.



# Effect of localized vibrations on the Si surface concentrations of hydrogen or deuterium

I. P. Ipatova†, *O. P. Chikalova-Luzina*† and K. Hess‡
† Ioffe Physical Technical Institute, Russian Academy of Sciences
‡ § Beckman Institute,The University of Illinois

## Introduction

Hydrogen is an important technological component for silicon surface passivation during the fabrication of metal oxide semiconductor (MOS) devices. In a recent development [1] deuterium has been substituted for hydrogen in the process of passivation. This resulted in the significant decrease of hot carrier degradation. Being isotopes, deuterium and hydrogen have vitually identical electronic properties. Therefore the significant difference in adatom behavior as observed in [1] must be related to the surface lattice dynamics.

The significant difference in the isotope atoms behavior occurs not only under extreme nonequilibrium conditions but even in the equilibrium properties of isotope atoms on the surface.

This paper deals with the calculations of the concentrations of adatoms H (or D) on the surface of Si which is in thermodynamic equilibrium with hydrogen or deuterium gas.

The description of the equilibrium between the Si surface and the gas of molecules requires the knowledge of both the chemical potential of H(D) on the surface and the chemical potential of H(D) in the gas. Along with the electronic contribution, the chemical potential of the adatom has the vibration contribution which can be found from the lattice dynamics of the impurity atoms on the surface. The chemical potential of H(D) atom in the gas is known from the thermodynamics of two atomic gases. The equality of the chemical potentials of H(D) atoms on the surface and in the gas in the thermodynamic equilibrium enable us to find the surface equilibrium concentrations of the adatoms. The difference of H and D surface concentrations results from the difference of H and D surface localized vibrations. It is shown that the surface concentration of D-adatoms is by 10 to 15 times higher then the concentration of H-adatoms.

## 1 Dynamics of adatoms on the surface of Si

In order to find the surface localized vibration frequencies, we consider the general form of the equation of the motion for the semiinfinite crystal with some adatoms

$$(\bar{L} - \bar{D})\bar{u} = 0 \tag{1}$$

where $\bar{L}$ represents vibrations of the perfect crystal with the surface and $\bar{D}$ is the perturbation matrix of the adatoms, $\bar{u}$ is the column of the displacement of all the atoms.

For simplicity the nonreconstructed surface (100) of Si with the symmetry of the simple square is considered. We assume that the adatom of the mass $M^{(H)}$ is bound

in the "on–site" configuration to the surface atom of Si with the mass $M$ by the force constant $\gamma\prime$. Restricting ourself by the nearest neighbour approximation for the description of the interaction of the adatoms with the crystal, one can get for the case of the low concentration of the adatoms the following characteristic equation for finding the adatom localized vibration frequency

$$1 - \frac{\gamma'\omega^2}{\omega^2 - \omega_0^2} G(\omega^2) = 0, \tag{2}$$

where $\omega_0^2 = \gamma'/M^{(\mathrm{H})}$, $G(\omega^2)$ is the diagonal element of the Green's function matrix $\bar{G} = \bar{L}^{-1}$.

The Green's function $G(\omega^2)$ can be given in terms of the frequency distribution function of the perfect crystal $g_0(\omega^2)$ [2]

$$\mathrm{Re}G(\omega^2) = \frac{1}{M} \int_0^{\omega_L^2} \frac{g_0(\Omega^2)}{\omega^2 - \Omega^2} d\Omega^2. \tag{3}$$

Here $g_0(\omega^2)$ is normalized to the unity. The quantity $\omega_L$ is the maximum frequency of the crystal with the free surface.

Since the localized vibration frequency of the light adatom $\omega_{\mathrm{loc}}$ satisfying to Eq. (2) is significantly higher than the maximum frequency of the Si phonon spectrum, the main contribution in the integrant at $\omega = \omega_{\mathrm{loc}}$ is given by the high frequency optical vibrations. Because the optical branches have the small dispersion, the important optical part of the distribution function could be approximated by a $\delta$-function

$$g_0(\omega^2) \approx g_0^{\mathrm{opt}}(\omega^2) = \delta(\omega^2 - \omega_L^2). \tag{4}$$

From Eqs. (2)–(4) the algebraic biquadratic equation for the determination of the surface localized frequency $\omega_{\mathrm{loc}}$ is obtained:

$$1 - \frac{\omega_1^2(\omega^2 + \omega_L^2)}{(\omega^2 - \omega_0^2)\omega^2} = 0. \tag{5}$$

Using the numerical value of the force constant $\gamma\prime$ from [3] $\gamma\prime = 8.8 \times 10^4 \mathrm{din} \cdot \mathrm{cm}^{-1}$, we calculated from Eq. (5) the following localized frequencies of H (or D) stretching localized modes: $\omega_{\mathrm{loc}}^{(\mathrm{H})} = 2.34 \times 10^{14}\,\mathrm{s}^{-1}$ $\omega_{\mathrm{loc}}^{(\mathrm{D})} = 1.70 \times 10^{14}\,\mathrm{s}^{-1}$. We note that $\omega_{\mathrm{loc}}^{(\mathrm{H})} > \omega_{\mathrm{loc}}^{(\mathrm{D})}$. These frequencies differ from the experimental data $\omega_{\mathrm{str}}^{(\mathrm{H})} = 3.96 \times 10^{14}\,\mathrm{s}^{-1}$, $\omega_{\mathrm{str}}^{(\mathrm{D})} = 2.83 \times 10^{14}\,\mathrm{s}^{-1}$ [4]. The discrepancy is apparently the result of our simple approximation.

It is shown in [5] that the account of the next nearest neighbour approximation and of the noncentral forces would result in bending modes obtained along with above mentioned stretching modes. The experimental value of the double degenerate at $\Gamma$ — point bending mode of H(D) on the surface of Si is $\omega_{\mathrm{bend}}^{(\mathrm{H})} = 1.17 \times 10^{14}\,\mathrm{s}^{-1}$ [4]. Because the bending mode frequency is lower then the stretching mode frequency, stretching modes are the most important for the calculation of the partition function of the system.

## 2 Chemical potential of H(D) adatom on the surface

In our case of the low surface concentration of adatoms they constitute a two-dimensional dilute solution on the surface of Si. The vibrational part of the partition function of the solution can be given in terms of the frequency distribution function $g(\omega^2)$ of the crystal with adatoms on the surface

$$Z_{\text{cryst}} = \frac{N_{\text{surf}}!}{N_{\text{adatom}}!(N_{\text{surf}} - N_{\text{adatom}})!} \exp\left[-\int_0^{\omega_{\max}^2} d\Omega^2 g(\Omega^2) \ln\left(2\sinh\frac{\hbar\Omega}{2T}\right)\right]. \quad (6)$$

Here $N_{\text{surf}}$ is the total number of the dangling bonds on the surface and $N_{\text{adatom}}$ is the number of the adatoms. The combinatorial factor represents the possibility of interchanging within both the occupied and empty surface sites. The frequency $\omega_{\max}$ is the maximum frequency of the vibrations for the crystal with adatoms on the surface.

With high accuracy, the total frequency distribution function may be given by

$$g(\omega^2) = 3N_{\text{Si}} g_0(\omega^2) + N_{\text{adatom}} 3\delta(\omega^2 - \omega_{\text{loc}}^2). \quad (7)$$

Substituting (7) in (6) and using the equation for Helmgolz free energy $F = -T \ln Z$ and the equation for the chemical potential of the adatom $\mu_{\text{adatom}} = (\partial F/\partial N_{\text{adatom}})_{TV}$, we get the chemical potential for hydrogen adatom

$$\mu_{\text{surf}}^{(\text{H})} = T \ln n_{\text{adatom}}^{(\text{H})} + 3T \ln\left[2\sinh\frac{\hbar\omega_{\text{loc}}^{(\text{H})}}{2T}\right] + \varepsilon_{\text{H}}, \quad (8)$$

and for deuterium adatom

$$\mu_{\text{surf}}^{(\text{D})} = T \ln n_{\text{adatom}}^{(\text{D})} + 3T \ln\left[2\sinh\frac{\hbar\omega_{\text{loc}}^{(\text{D})}}{2T}\right] + \varepsilon_{\text{D}}. \quad (9)$$

Because binding energies of isotopes are equal, $\varepsilon_{\text{H}} = \varepsilon_{\text{D}}$ and the difference of chemical potentials comes from the difference of localized frequencies $\omega_{\text{loc}}^{(\text{H})} \neq \omega_{\text{loc}}^{(\text{D})}$ only.

## 3 Chemical potential of H(D)-atoms in the gas phase

The chemical potentials of H and D atoms in the gas is obtained from the conditions of the chemical equilibrium for the reaction of $H_2(D_2)$ dissociation and from the chemical potential of molecule consisting of two identical atoms [6].

$$\mu_{\text{gas}}^{(\text{H})} = \frac{1}{2}[T \ln P_{\text{H}_2} - c_p T \ln T - \zeta_{\text{H}_2} T + \varepsilon_0] \quad (10)$$

and

$$\mu_{\text{gas}}^{(\text{D})} = \frac{1}{2}[T \ln P_{\text{D}_2} - c_p T \ln T - \zeta_{\text{D}_2} T + \varepsilon_0] \quad (11)$$

Here $P_{\text{H}_2}(P_{\text{D}_2})$ is the gas pressure, $c_p$ is the specific capacity at the constant pressure, $\zeta_{\text{H}_2} = \ln[(I_{\text{H}_2}/\hbar^5)(M_{\text{H}_2}/2\pi)^{3/2}]$ and $\zeta_{\text{D}_2} = \ln[(I_{\text{D}_2}/\hbar^5)l(M_{\text{D}_2}/2\pi)^{3/2}]$ are the chemical constants of the hydrogen gas or the deuterium gas, respectively ($I_{\text{H}_2}$ and $I_{\text{D}_2}$ being the momentum of inertia of the molecules), $\varepsilon_0$ is the binding energy of the molecule in the gas.

## 4 Concentration of H(D) atoms

The substitution of chemical potentials (8) and (10) for hydrogen or (9) and (11) for deuterium in the condition of thermodynamic equilibrium $\mu_{\text{surf}}^{(\text{H})} = \mu_{\text{gas}}^{(\text{H})}$ and $\mu_{\text{surf}}^{(\text{D})} = \mu_{\text{gas}}^{(\text{D})}$, respectively, allows to find the concentration of hydrogen atoms and the concentration of deuterium atoms on the Si crystal surface in the thermodynamic equilibrium

$$n_{\text{adatom}}^{(\text{H})} = P_{\text{H}_2}^{1/2} T^{c_p/2} \left[ \frac{I_{\text{H}_2}}{\hbar^5} \left( \frac{M_{\text{H}_2}}{2\pi} \right)^{3/2} \right]^{1/2} \exp\left[ -\frac{\mu_1^{(\text{H})}}{T} \right] \exp\left[ -\frac{\frac{1}{2}\varepsilon_0 - \varepsilon_{\text{H}}}{T} \right] \quad (12)$$

$$n_{\text{adatom}}^{(\text{D})} = P_{\text{D}_2}^{1/2} T^{c_p/2} \left[ \frac{I_{\text{D}_2}}{\hbar^5} \left( \frac{M_{\text{D}_2}}{2\pi} \right)^{3/2} \right]^{1/2} \exp - \left[ \frac{\mu_1^{(\text{D})}}{T} \right] \exp\left[ \frac{\frac{1}{2}\varepsilon_0 - \varepsilon_{\text{D}}}{T} \right]. \quad (13)$$

Since the localized frequencies $\omega_{\text{loc}}^{(\text{H})}$ and $\omega_{\text{loc}}^{(\text{D})}$ satisfy the condition $T < \hbar\omega_{\text{loc}}^{(\text{H})}, \hbar\omega_{\text{loc}}^{(\text{D})}$ and $I_{\text{H}_2}/I_{\text{D}_2} = M_{\text{H}_2}/M_{\text{D}_2}$, one can get the following equation for the ratio of the concentrations

$$\frac{n_{\text{surf}}^{(\text{H})}}{n_{\text{surf}}^{(\text{D})}} = \left( \frac{M_{\text{H}_2}}{M_{\text{D}_2}} \right)^{5/4} \exp\left[ -\frac{3\hbar[\omega_{\text{loc}}^{(\text{H})} - \omega_{\text{loc}}^{(\text{D})}]}{2T} \right]. \quad (14)$$

It is seen from Eq. (14) that the concentration of deuterium exceeds significantly the concentration of hydrogen due to the difference of both the isotope masses and the localized frequencies.

Using experimental values for localized frequencies of H and D we have found that the ratio of concentrations is about 15 at the typical technological temperature $T = 700$ K.

*Acknowledgements*

One of us (K.H.) acknowledges the support of the US Office of Naval Research. Two authors (I.I.P. and O.P.Ch.-L.) are thankful for support, in different parts, by the Russian Federal Program "Surface Atomic Structures", grant 95-2.23, and by Russian Federal Program of Ministry of Science and Technologies "Solid State Nanostructures", grant 2.001.

## References

[1] J. W. Lyding, K. Hess, and I. C. Kizilyalli, *Appl.Phys. Lett.* **68** 2526 (1996); I. C. Kizilyalli, J. W. Lyding, and K. Hess, *IEEE Electron Device Lett.* **18** 81 (1997).

[2] E. W. Montroll, A. A. Maradudin, G. H. Weiss and I. P. Ipatova, *Theory of Lattice Dynamics* (Academic Press, New York and London, 1971.

[3] L. Miglio, P. Ruggerone and G. Benedek, *Physica Scripta*, **37** 768 (1988).

[4] P. Jacob, P. Dumas, and Y. J. Chabal, *Appl. Phys. Let.* **59** 867 (1991); V. A. Burrows, Y. J. Chabal, G. S. Higashi, K. Raghavachary, and S. B. Christman, *Appl. Phys. Lett.* **53** 998 (1988).

[5] W. A. Harrison, *Solid State Theory* (McGraw-Hill Book Company, New York-London-Toronto, 1970).

[6] L. D. Landau and E. M. Lifshitz, *Statistical Physics* (Addison-Wisliy Publishing Co., Inc., Reading, 1958), Chap. IX.

Ioffe Institute
6th Int. Symp. "Nanostructures: Physics and Technology"
St Petersburg, Russia, June 22–26, 1998.



# Conductivity and atomic structure of isolated multiwalled carbon nanotubes

A. Yu. Kasumov†‡, H. Bouchiat†, *B. Reulet*†, O. Stephan†, I. I. Khodos‡, Yu. B. Gorbatov‡ and C. Colliex†§

† Laboratoire de Physique des Solides, Associé au CNRS,
Bât 510, Université Paris–Sud, 91405, Orsay, France
‡ Institute of Microelectronics Technology and High Purity Materials,
Russian Academy of Sciences, Chernogolovka 142432 Moscow Region, Russia
§ Laboratoire Aim. Cotton (UPR CNRS 3321), B.t 505 Universit.
Paris–Sud,91405, Orsay, France

**Abstract.** We report associated high resolution transmission electron microscopy (HRTEM) and transport measurements on a serie of isolated multiwalled carbon nanotubes. HRTEM observations, by revealing relevant structural features of the tubes, shed some light on the variety of observed transport behaviors, from semiconducting to quasi-metallic type. Non Ohmic behavior is observed for certain samples which exhibit "bamboo like" structural defects. The resistance of the most conducting sample exhibits a pronounced maximum at 0.6 K and strong positive magnetoresistance.

We report the results of simultaneous investigations of the electric properties and structure of nanotubes in the transmission electron microscope. The technique used for isolating an individual nanotube is qualitatively different from the other studies [1, 2, 3]. It allows studying in HRTEM the structure of the nanotube. The method consists in the following: a focused laser beam "shakes off" a nanotube from the target onto a sample with a $Si_3N_4$ membrane covered with a metal film [4, 5]. A submicron width slit about 100 $\mu$m in length has previously been cut in the membrane by focused ion beam; the nanotube connects the edges of the slit (see Fig. 1) and shorts the electric circuit whose resistance was over 1 G$\Omega$ before the nanotube was "shaken off". In the following we successively discuss electron microscopy observations and transport measurements on a family of tubes indexed as $Au_N$, $Sn_N$, $Bi_N$ depending on the nature of the used metal contact.

Most investigated nanotubes cannot be described only as perfect sets of coaxial cylinders, but exhibit defects which can affect the transport mechanisms. In particular a defect so called bamboo defect in the literature [6], has been identified in many cases: the inner shells of the nanotube are interrupted and separated by fullerenic semi-spheres while the outer shells remain continuous, (see Fig. 1A). The presence of such defects is indicated in Table 1. We will see that the presence of these defects affects transport properties when there exists a possibility of conduction between the outer and inner shells.

We have tentatively separated the different temperature dependences observed depicted in Fig. 2 in 3 main types of behavior: semi-conducting, (type $I_A$, $I_B$) and quasi-metallic, (type II) which can be caracterized by the ratio $\alpha_R$ between the values of the resistance at 100 K and 293 K, it is above 1000 for $I_A$, of the order of 100 for $I_B$ and below 10 for type II tubes.

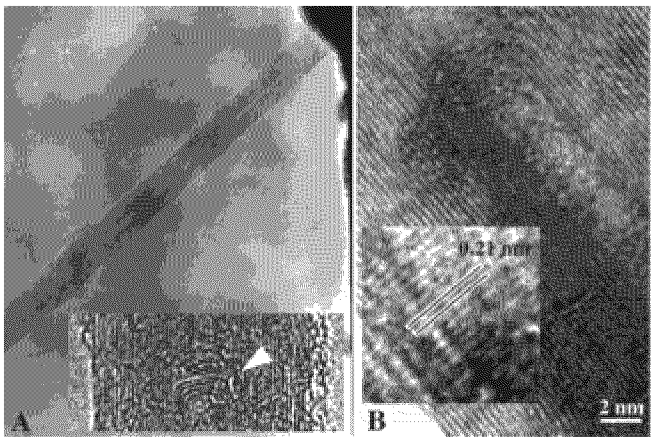


**Fig 1.** HRTEM on studied samples: A—partial view of a connected nanotube (only one metallic pad is visible). Some carbonaceous material, due to electron damage during observation, is visible on the surface of the nanotube. Inset: HRTEM of a bamboo defect. B—HRTEM picture of Sn2 tube showing evidence of ordered stacking of zig-zag type shells.

**Table 1.** Resistance and structural parameters of various nanotubes. $\Phi_{out,in}$ and $L$ are respectively the external, internal diameters and length between the 2 metallic contacts.

| Sample name | $\Phi_{out,in}$ (nm) | # of shells | L ($\mu$m) | Bamboo defects | $R$ ($\Omega$) 293 K | $\alpha_R$ | Type |
|---|---|---|---|---|---|---|---|
| Au1 | 25, 7 | 26 | 2.1 | No | $1.0\ 10^6$ | $> 10^3$ | $I_A$ |
| Sn2 | 40, 3 | 55 | 0.33 | No | $2.1\ 10^4$ | $> 10^5$ | $I_A$ |
| Sn5 | 25, 5 | 29 | 0.45 | Yes | $2.5\ 10^6$ | $> 10^3$ | $I_A$ |
| Au2 | 16, 5 | 16 | 0.36 | Yes | $6.7\ 10^5$ | 140 | $I_B$ |
| Sn10 | 7, 2 | 7 | 0.35 | Yes | $5.8\ 10^6$ | 86 | $I_B$ |
| Sn11 | 13, 7 | 9 | 0.17 | Yes | $1.8\ 10^6$ | 40 | $I_B$ |
| Bi4 | 12, 4 | 11 | 0.4 | Yes | $2.8\ 10^4$ | 1.2 | II |
| Au3 | 25, 3 | 29 | 0.17 | No | $1.9\ 10^3$ | 4 | II |
| Au4 | 26, 5 | 31 | 0.33 | No | $2.0\ 10^5$ | 6 | II |

Type $I_A$ and $I_B$ tubes exhibit a semiconducting behavior between 300 K and 200 K, with approximative exponentially activated temperature dependence of the resistance (see Fig. 2). All the gap values lie between 2000 and 3000 K, this reasonably excludes some contribution of the contact resistance to these gaps which are similar to values in amorphous carbon [7]. For each type $I_B$ tube, a saturation of the resistance around $10^8$ $\Omega$ is observed below 100 K. This saturation does not exist for type $I_A$ samples. It is striking that all these $I_B$ tubes contain one "bamboo" defect and are also characterized by their strongly non linear $I$–$V$ characteristics below 100 K [10]

Type II tubes exhibit a "quasi-metallic" behavior. Their resistances increase more slowly than exponentially at low temperature, varying approximatively like $1/T^x$ with $x = 0.5$ for Au3 and $x = 2$ for Au4 (see Fig. 2), a slower increase was observed for Bi5 [4]. We never see any increase of resistance at high temperature similar to what is observed in "bulk" samples of SWNT [8]. Note however that this type of true "metallic" behavior has only been recorded so far in "bulk" samples or ropes of SWNT and has never been reported for isolated nanotubes. On the Au3 sample we could also perform very low temperature transport measurements, shown in Fig. 3. The $R(T)$ curve

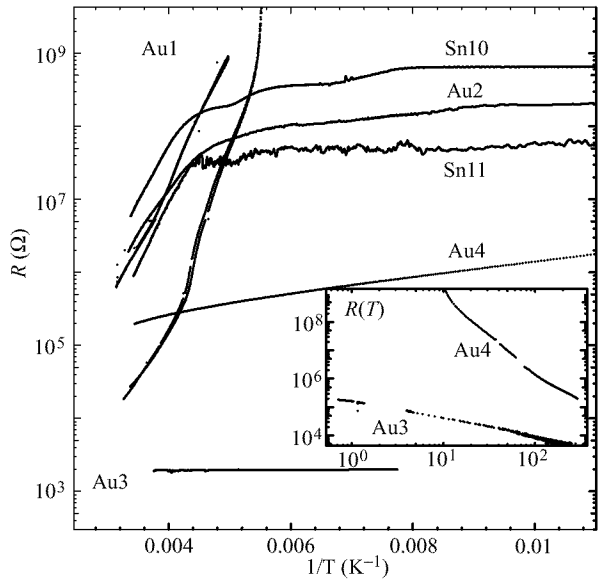


**Fig 2.** High temperature resistance of the tubes, showing evidence of semiconducting behavior for most of them. Inset: Resistance of Au4 and Au3 samples on a wider temperature range, which exhibita power law increase at low temperature.

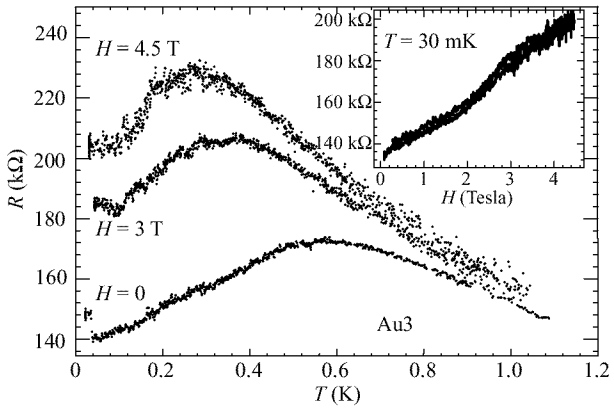


**Fig 3.** Low temperature resistance and in inset, magnetoresistance of the Au3 sample.

exhibits a broad maximum around 0.6 K. The amplitude and position of this maximum vary drastically with the magnitude of magnetic field applied perpendicularly to the tube axis. It shifts to lower temperature with increasing magnetic field and reaches higher resistance values. Accordingly, one observes a large positive magneto-resistance approximatively linear in magnetic field (with a 50% increase for an applied field of 4 T.) To our knowledge it is the first time that such remarkable features have been observed in the resistance measurements of nanotubes.

One important issue for understanding transport properties of these nanotubes is the separation between the contribution of the most external shell, which is the only one directly connected to the metallic pads, and the possible contributions of internal shells. This is determined by the ratio $\eta = R_{\text{ext}}/R_t$ between the resistance $R_{\text{ext}}$ of this external

shell and the resistance $R_t$ connecting this shell to internal shells. We expect the value of $R_t$ to drastically depend on the spatial correlation between atomic positions in adjacent graphite planes which determine the overlap between $\pi$ orbitals perpendicular to these planes. The value of $\eta$ may then fluctuate a lot between different nanotubes and also depend on temperature. We naturally expect that $\eta \ll 1$ for (metallic) type II nanotubes. The combination of HRTEM observations and transport measurements suggests that $\eta \ll 1$ also for type $I_A$ nanotubes. One convincing example is the Sn2 sample which, according to HRTEM observations, contains many zig-zag shells arranged in a nearly perfect graphitic order. According to theoretical predictions [9], depending of their diameter, we can expect that $1/3$ of these shells are metallic. However the measured temperature dependence of the resistance indicates a semiconducting behavior. These two results can be reconciled if transport takes place in the semiconducting external shell of the tube and if there is no possibility of conduction through internal metallic shells.

The situation is different for type $I_B$ samples, where Fig. 2 indicate a residual tunneling conductivity at low temperature which scales approximatively like the surface of the inner section of the tube. A possible explanation of these findings could be tunneling on a metallic inner shell of the tube, behaving as a Coulomb island, separated from the metallic pads by external shells which are insulating at low temperature but however offer the possibility of electron transfer through high but finite tunneling resistance $R_t$. HRTEM observations reveal a complex situation with the existence of "bamboo" like defects [10].

In conclusion, simultaneous HTREM and resistance measurements performed on the same characterized samples, highlight the importance of internal structural defects when compared to the helicity parameters, in the mechanism of electron conductivity. We have also shown that the outer shell determines the resistance for most insulating or conducting tubes. Specific "bamboo" type defects could be identified which are fundamental for the understanding of intermediate behavior, where internal shells contribute to electronic transport through tunnel junctions. We have finally demonstrated that measuring transport properties of nanotubes is specially interesting at very low temperatures with the existence of an anomaly in the temperature dependence, highly sensitive to the strength of magnetic field.

We acknowledge our colleagues P. Ajayan, T. Giamarchi, D. Jérôme, P. Launois, R. Moret for help and discussions. A. K. acknowledges the University of Orsay for an invited professor position. We have also benefited from support of Russian Foundations for Basic Research and Solid State Nanostructures.

## References

[1] L. Langer et al., *Phys. Rev. Lett.* **76**, 479 (1996).
[2] H. Dai et al. *Science* **272**,523 (1996).
[3] T. W. Ebessen et al., *Nature* **382**, 54 (1996).
[4] A. Yu. Kasumov, I. I. Khodos, P. M. Ajayan and C. Colliex, *Europhys. Lett.* **34**, 429 (1996).
[5] A. Yu. Kasumov et al., *Phys. Rev. Lett.* **75**, 4286 (1995).
[6] S. Iijima, P. M. Ajayan, T. Ichihashi, *Phys. Rev. Lett.* **69**,3100 (1992).
[7] J. Robertson, *Advances in Physics* **35**, 317 (1986).
[8] J. E. Fisher et al., *Phys. Rev.* **B 55**, 4921 (1997).
[9] R. Saito et al., *Appl. Phys. Lett.* **60**, 2204 (1992).
[10] A. Yu. Kasumov, H. Bouchiat, B. Reulet, O. Stephan, I. I. Khodos, Yu. B. Gorbatov and C. Colliex, to be published.

Ioffe Institute
6th Int. Symp. "Nanostructures: Physics and Technology"
St Petersburg, Russia, June 22–26, 1998.



# Structures and electronic transport in nanoelectronic devices based on carbon nanotube complexes.

*S. Melchor*†, S. Savinskii‡ and N. Khokhriakov‡
†Granada University (Spain)
‡Udmurt University (Russia)

**Abstract.** The geometrical structure of and electron transport in carbon nanotube complexes are studied. A general method to construct theoretically three-tube unions for nanotubes of different types is developed. Then study electron packet evolution in obtained structures using semiempirical tight-binding model in $\pi$-electron approximation.

## Introduction

Carbon nanotubes-tubulenes, discovered in 1991 by Iijima [1], are molecular cylindrical surfaces which are close-packed with atomic carbon hexagons and are obtained by the thermal decomposition of graphite. They can be represented geometrically as the result of gluing a strip cut from a single graphite plane. Normally nanotubes are classified by two indexes $i_1$ and $i_2$, those define nanotube chirality and radii. Depending on the indexes, a set of atomic carbon structures with a wide spectrum of conducting properties is obtained — from semiconductors with gap widths of 0–2 eV to semimetals, of which graphite is a typical representative [2].

Using this fact, many authors have thought [3] that nanodiodes could be studied theoretically and then can be manufactured. This nanodiodes can be made of two carbon nanotubes of different indexes and different electronic band structure. Now there are some calculations about the conductivity of these structures [4], and there are also works with experimental data about point defects in nanotubes, but by now there are only a few number of them.

We think that the next step could be investigating nanotransistors, and it is possible to imagine that they can be constructed by joining three tubes at the same end. Each one of this tubes may be equivalent to the different semiconductor type in a standard NPN transistor. In our situation, we can have two identical tubes (N zones) and another one with different chirality and band structure (P zone).

## 1 Geometrical structure of the three-tubed connection

We have developed a general method to construct theoretically this kind of three-tube unions in an easy way. Our structure will consist now in three tubes joined by a union (from now, the union) where we must place six heptagons, as the Euler's theorem says, but we don't know where. At least, we know that an heptagon placed inside a graphitic lattice produces a negative curvature in this surface, like in the schwarzites, and the points of the union with this kind of curvature are between the beginning of each pair of tubes. That is the reason why we can assume that the heptagons will be near this points.

Now, if we want to know if every union with 6 heptagons can lead to a global structure with three tubes, we must center our attention in the position of the heptagons near the points of negative curvature. We can always connect them by paths consisting of a certain number of carbonated rings, which can be pentagons, hexagons or heptagons. We may think that in our three-tubed structure we can connect the six heptagons by three paths (strips made of rings) glued at their ends, so each tube is held by two strips.

As an example, in a knee tube (tube that presents a curved aspect, but it is really a pair of tubes with different chirality joined one each other) the structure has one strip connecting the pentagon and the heptagon (as in this structures we have the same number of heptagons and pentagons) which leads to both tubes.

But we can make ourselves this question: How can this strip lead to two tubes? If we fix both ends of the strip, we will obtain a tube-like structure, to which we may only add hexagons to verify if a cylinder can appear. That is the same technic we already know to form a normal nanotube (we take a vector and superpose the two hexagons at the start and end of the vector) but it is more general. For example, in a strip made only of hexagons, we can superpose the two hexagons in the end of the strip in six different ways, by rotating one hexagon over another. It is clear that if we do this with only hexagons we will never obtain a tube, but a cone. But if we have heptagons or pentagons maybe it will be useful.

Now, if we are going to study the different effects produced by heptagons and pentagons in these strips, we need to arrive to this conclusion: When we add hexagons next to the strips we must obtain tubes, and that is the reason why if we follow by continuity the orientation of the added hexagons, its change must be 0.

So, if we locate an heptagon or a pentagon in the strip, we can do it in two different ways, 'up' and 'down', that means that the strip is curved upwards or downwards, respectively. We always fixed two arbitrary orientations at the end and at the beginning of the strip. For simplicity we take a specified one and we do it this way: We draw a path of hexagons, and we mark two parallel orientations at the end and the beginning of the strip. Then we substitute some of the hexagons by pentagons and heptagons in positions 'up' or 'down'.

Within these specifications, it is easy to observe that the heptagon in the position 'up' induces a turn of 0 and in the position 'down', a turn of 60°.

Directly we can do the same with pentagons in positions 'up' and 'down', which produces turns of -60 in the position 'up' and 0 in the position 'down'.

If we closed our strip the way we showed before, to obtain over and below the union two tubes, we need that the rotation induced becomes 0. It must be no a multiple of 360, because this produces a different topology structure, like a plane, or a fulleren cup. We will return to this discussion later in our work. We can now write two equations that the structure must verify to lead to two tubes. Let $h_a$, $h_{a'}$ the number of heptagons that produces a turn of 60 in the side $a$, and in $a'$, and $p_a$, $p_{a'}$ the number of pentagons that produces a turn of $-60$ in both sides.

$$60(h_a - p_a) = 0$$

$$-60(h_{a'} - p_{a'}) = 0.$$

The conclusion is obvious: we must have the same number of pentagons and heptagons. We need this only for training to afford the construction of a union to glue three tubes.

With three tubes, the tubes will be formed by two strips, so we must take account of this in our equations. We must also be careful with the connections of each pair of strips, because in everyone there is a change of the references' orientation.

When we go from one strip to another, if the references were chosen as we said, we can see that the reference turns an angle of $180 - \alpha$, where a is the angle between strips a and b in the first of the two hexagons that connect the three strips. (The same way $\beta$ and $\gamma$ are the angles between $b$ and $c$, and between $c$ and $a$. We will denote the angles in the other hexagon with $\alpha'$, $\beta'$ and $\gamma'$.) This is because the turn of the reference is the angle complementary of $\alpha$. And if the reference is turned a certain angle, we must subtract this angle to our equations.

These will remain like this:

$$60(h_a - p_a + h_{b'} - p_{b'}) - (180 - \alpha) - (180 - \alpha') = 0$$

$$60(h_b - p_b + h_{c'} - p_{c'}) - (180 - \beta) - (180 - \beta') = 0$$

$$60(h_c - p_c + h_{a'} - p_{a'}) - (180 - \gamma) - (180 - \gamma') = 0.$$

If we use the fact that, if the strips are joined by an hexagon, the sum of the three angles (of each hexagon) is 360, we can conclude this:

$$60(h_A + h_B + h_C - p_A - p_B - p_C) = 360$$

where we denoted with $h_A$,$h_B$ and $h_C$ the respective sums of $h_a$ and $h_{a'}$, $h_b$ and $h_{b'}$, $h_c$ and $h_{c'}$, that is the total number of pentagons and heptagons in the strips A, B and C. It implies an excess of six heptagons, as we previously knew, but the important fact is that we have found three equations that the union must follow to lead to three tubes.

So, we can vary the position of the heptagons and pentagons in the strips, as the length of the strip in order to obtain different structures. Now we also know the rules we must follow to obtain three tubes. We also here propose a method to denote this kind of structures, describing the strips by its indexes and marking the positions of the pentagons and heptagons in them.

## 2 Electron transport in nanotube complexes

A characteristic feature of the energy structure of the valence electrons of a single graphite plane is the existence of $\pi$-electrons, whose states can be described by a simple analytical model, at Fermi level; $\sigma$-electrons at the Fermi-level have an energy gap of the order 10 eV. When a ideal tubulene is glued from a strip cut from a graphite plane, the perturbation of the $\sigma$ and $\pi$-electrons depends on the dimensionless parameter $a/R$, where $a$ is the distance between the closest atoms in the graphite plane and $R$ is the radius of the tubulene. For the tubulenes with a large radius this perturbation is weak, and accordingly the electronic spectrum of a tubulene can be obtained from that of an isolated graphite plane; this approximation is widely employed in the literature and is termed zone folding [2]. For tubulenes with small radii, the finiteness of the perturbation, which can result hybridisation of the $\pi$- and $\sigma$-electrons, must be taken into account. However for simplicity we applied $\pi$-electron model in present investigation of electron transport in nanotubes and their complexes. The hamiltonian matrix is constructed in semiempirical tight-binding model in nearest-neighbouring approximation.

We have applied before this model to calculate electronic structure and properties of ideal graphitic nanotubes [5].

The quantum state of $\pi$-electron in infinite carbon nanotube is classified by two quantum numbers, m — magnetic quantum number and $k_z$ — the electron impulse along the nanotube axis. Electronic state energy depends on nanotube radius, chirality, numbers m and $k_z$. In the elastic scattering on the nanotube connection the scattering amplitude depends on radii and chiralities of connected tubes. It may be calculated by numerical integration of nonstationary Schrodinger equation. It is necessary to make Gauss electron wave packet with fixed m on the one of the nanotubes. The packet length along the tube depends on dispersion of the impulse $k_z$. Numerical integrating of Schrödinger equation in tight-binding approximation give us the packet evolution across the nanotube connection, so one may obtain the scattering amplitude. We use the norm-conserving numeric schemes based on Pade-approximation of the evolution operator on the each time step. This method allow us to calculate the electron transport in the complexes described before and in other more complicated structures those can be useful to construct nanodevices.

## References

[1] Iijima S. *Nature.* **354** 56 (1991).
[2] Hamada N. *Phys. Rev. Lett.* **68** 1579 (1992).
[3] Ebbesen T. *Phys. Today.* **49** 26 (1996).
[4] Chico L. *Phys. Rev. B. Condensed Matter* **54** 2600 (1996).
[5] Savinskii S. *JETP* **84** 1131 (1997).

Ioffe Institute
6th Int. Symp. "Nanostructures: Physics and Technology"
St Petersburg, Russia, June 22–26, 1998.



# Polariton spontaneous emission superradiance in III–V semiconductor doped with quantum wells or quantum dots

*M. Singh*†, V. I. Yukalov‡ and W. Lau†

† Department of Physics, University of Western Ontario, London, Canada

‡ Bogolubov Laboratory of Theoretical Physics, Dubna, Russia

The most interesting phenomena in photonic band gap materials are the formation of photon-atom bound states and suppression of spontaneous emission from the photon-atom bound state [1]. Recently, Rupasov and Singh have studied the quantum electrodynamics of a two-level atom placed within a frequency dispersive medium whose polariton spectrum contains a energy gap [2]. They found that if the atomic resonance frequency lies within the gap, then the spectrum of the system contains a polariton-atom bound state with an eigenfrequency lying within the gap. The radiation and medium polarization of the bound state are localized in the vicinity of the atom. In photonic band gap materials, the existence of the photonic band gap is due to multiple photon scattering by spatially correlated scatters, while in dispersive media such as semiconductors and dielectrics, the energy gap is caused by photon coupling to an elementary excitation (excitons, optical phonons etc.) of the media.

The aim of the present paper is to study the spontaneous emission rate of photons for III–V semiconductors doped with $N$ two-level atoms. Here the two-level atom represents a quantum well or a quantum dot. Making use of the spherical harmonic representation and the dipole resonance approximation, we derive an effective model Hamiltonian of the system, which, in the limiting case of empty space, coincides with the model Hamiltonian obtained in the liturature. To find the self-energy function of the system, we diagonalize exactly the Hamiltonian in the one-polariton sector of the entire Hilbert space. To study the spontaneous decay rate of the initially excited atomic states of the polariton-atom system, we consider the atomic resonance frequencies of the atoms lie either inside the polariton gap or the polariton continuous spectra. For $N = 2$, we found that the spontaneous decay rate and superradiant effects as follows. We consider the case in which one atom is in the excited state while the other is in the ground state with no polaritons present in the system and the atomic resonance frequencies of two atoms lie in the polariton continuous spectra. It is found that when the interatomic distance between the atoms becomes very large, the spontaneous decay rate of the excited atomic state is equal to that of the single atom case. For very small interatomic distances, it is found that the rate of spontaneous emission from the symmetric state is two times that of the single atom case. This phenomenon in quantum optics is called superradiance. For the polariton-atom system in the antisymmetric state, the spontaneous emission rate is found to be zero. This phenomenon is related to subradiance in quantum optics. Numerical calculations are performed for the spontaneous decay rate of an excited atomic state in GaSb and GaAs. Non-equilibrium and nonlinear effets have also been studied.

## References

[1] S. John, *Phys. Rev. Lett.* **58** 2486 (1987).
[2] E. Yablonovitch, et al, *Phys. Rev. Lett.* **67** 2295 (1991).
[3] V. I. Rupasov and M. Singh, *Phys, Lett. A* **222** 258 (1996).

Ioffe Institute
6th Int. Symp. "Nanostructures: Physics and Technology"
St Petersburg, Russia, June 22–26, 1998.



# Non-linear Meissner effect in mesoscopic superconductors

*P. Singha Deo*†, V. A. Schweigert‡, F. M. Peeters† and A. K. Geim§
† Department of Physics, University of Antwerp (UIA), B-2610 Antwerpen, Belgium
‡ Institute of Theoretical and Applied Mechanics, Russian Academy of Sciences, Novosibirsk 630090, Russia
§ High Field Magnet Laboratory, University of Nijmegen, 6525 ED Nijmegen, the Netherlands

**Abstract.** Magnetization measurements on superconducting bulk samples and large radius cylinders had resulted in the Phenomenological London's theory that is found to be violated in recent magnetization measurements in superconducting mesoscopic discs that exhibit a non-linear Meissner effect. In this work we show that the Ginzburg-Landau (GL) eqn. can explain this non-linear Meissner effect both in quality and quantity.

Recently Geim *et al* [1] used sub-micron Hall probes to detect the magnetization of thin (thickness down to $d \sim 0.07\,\mu$m) *single* superconducting Al discs with radius down to 0.3 $\mu$m. For such systems the coherence length ($\xi(0) \sim 0.25\,\mu$m) is comparable to the size of the disc and finite size effects are very important. With increasing disc radius the magnetization of the system first shows the behavior of a type II superconductor, then of a type I superconductor and by further increasing the disc radius multiple steps are seen in the magnetization which can be dubbed a multi-type I superconducting behavior. This behavior was explained by us [2] where we included the particular geometry of the system in the Ginzburg-Landau (GL) theory for superconductivity which is coupled to the Maxwell equations in order to take into account the bending of the magnetic field lines around the superconducting disc. The rich behavior seen experimentally is due to a competition between surface superconductivity, bulk superconductivity and the geometrical demagnetizing effects.

Another striking effect seen in these systems is the non-linear Meissner effect which we will address here. For example, for the sample of radius $R \sim 0.5\,\mu$m the magnetization for small magnetic fields increases linearly with external field, as expected for a type I superconductor, but increasing the field above about 40 Gauss (for $T = 0.4$ K) the magnetization increases less fast with external field and strong non-linear behavior is observed. This remarkable deviation from London's theory will be explained here from the GL theory using our previous numerical approach [2, 3].

We fix the radius of the disc to be 0.3 $\mu$m, coherence length to be $\xi(0) = 0.25\ \mu$m and penetration length $\lambda(0)$ to be 0.07 $\mu$m. We plot the magnetization versus applied magnetic field for 10 different thickness $d$, in Fig. 1. The values of $t = d/\xi(0)$ are shown in the figure. It can be seen that for $t = 0.1$, 0.2 and 0.3 the disc shows a second order phase transition to the normal state. Whereas for $t = 0.4$, 0.5, 0.6, 0.7, 0.8, 0.9 and 1.0 we find a first order phase transition to the normal state. The magnetization (multiplied by 0.5) as calculated from the Linearized GL (LGL) theory which is independent of the thickness of the sample is shown by dashed lines for the same $R$ and $\xi(0)$.

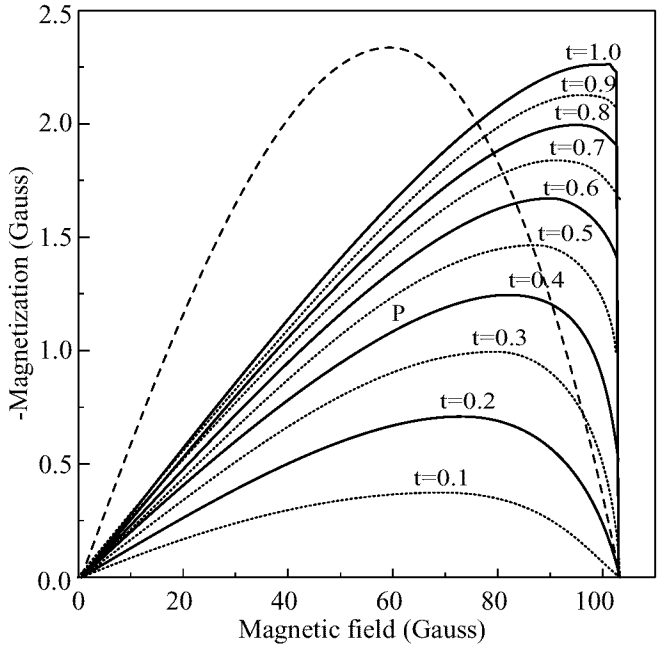


**Fig 1.** Numerically obtained magnetization versus the external magnetic field for a superconducting disc for ten values of $t = d/\xi(0)$ shown in the figure. Radius is kept fixed at $= 0.3$ $\mu$m, $\xi(0)$ at 0.25 $\mu$m and $\lambda(0)$ at 0.07 $\mu$m. The dashed curve is obtained by solving the LGL eqn.

Hence the finite thickness effect explains why a disc can sometimes show a first order and sometimes a second order phase transition to the normal state as is found in the experiment. For example, in Fig. 2, we show that a disc of $R = 0.44$ $\mu$m, $d = 0.15$ $\mu$m, $\xi(0) = 0.275$ $\mu$m and $\lambda(0) = 0.07$ $\mu$m can exhibit a magnetization (in increasing magnetic field) like that of a disc whose magnetization was measured in the experiment and whose $R$ was reported as 0.5 $\mu$m, $d$ as between 0.07 $\mu$m and 0.15 $\mu$m, $\xi(0)$ as 0.25 $\mu$m and $\lambda(0)$ as 0.07 $\mu$m. The large solid dots are the experimental data and the solid curve is our numerical calculation. The dotted curve is a tangent to the experimental data at the origin. So note that the coherence length has been changed by 10% and radius by 12% to reproduce the experimental result. These are well within the errors of their experimental determination. The magnetization has been scaled by $0.626/4\pi$. A detector size larger than the sample size can underestimate the magnitude by a factor of $4\pi$. The field distribution along a radial line starting from the center of the disc is shown in the inset for 11 values of the external applied field. The values of the applied fields is also mentioned on the curves. For the first 10 curves it can be seen that the field is minimum at the center of the disc. It increases drastically with distance from the center and becomes maximum at 0.44 $\mu$m which is precisely the radius of the disc. This means the field is strongly expelled from the center of the disc. The 11th curve (applied field=70.86 Gauss) corresponds to the critical field.

Magnetization measurement on bulk samples and large radius cylinders had shown that in the pure Meissner state, the sample behave as a perfect diamagnet which means

magnetization is proportional to the applied field with a susceptibility of -1. This experimental observation lead to a phenomenological theory well known as London's theory. It can be seen from the magnetization measurement on discs (see Fig. 2) that London's theory is not valid for discs because the magnetization is proportional to the applied field initially but above 40 Gauss this linear behavior deviates strongly (*i.e.,* it deviates from the dotted curve). The GL theory can explain this non-linear Meissner effect very well as can be seen from the solid curve in Fig. 2. Before analyzing this effect in detail first we want to point out that as the thickness is varied the critical field $H_c$ at which the transition to the normal state occurs remains the same. This can be analytically argued in a very simply way. At the critical field the amount of flux contained by the sample is given by the critical field multiplied by the area of the disc. As at the critical field the LGL theory is as good as the GL theory. Hence the flux enclosed by the sample and the upper critical field is independent of the thickness as in the LGL theory.

It can be seen from the inset in Fig. 2 that as the applied field is increased from 0 the field only penetrates near the boundary of the disc (which is due to Meissner effect) but at the critical field it suddenly distributes uniformly over all regions inside the disc. The jump in the magnetization (corresponding to first order transition) occur due to this sudden redistribution of the field. In the LGL theory the field is always uniform at all applied fields and this sudden redistribution of field leading to a jump in the magnetization is absent. So the magnetization gradually goes to zero, resulting in non-linear Meissner effect as can be seen from the dashed curve in Fig. 1. Very thin discs ($t = 0.1, 0.2, 0.3$) have a similarly uniform distribution of magnetic field (due to large enhancement of penetration length with decreasing thickness) over the whole sample as in the LGL theory, and also show a non-linear Meissner effect resulting in a second order phase transition to the normal state. As we slowly increase the thickness of the disc the field will be expelled from the disc as in a cylinder. Hence beyond a certain thickness the disc will start showing a sudden redistribution of field and a first order transition to the normal state.

Consider the magnetization curve for $t = 0.4$ in Fig. 1. Initially the magnetization increases linearly with the magnetic field. Beyond a point P shown in Fig. 1 there is a deviation from the linear behavior and the sample exhibits a non-linear Meissner effect. In discs thinner than $t = 0.4$ the magnitude of magnetization decreases, the point of deviation from linear Meissner effect and the peak value shifts to smaller fields. But since the upper critical field remain constant it does not exhibit a jump to 0 like that in LGL theory. On the other hand it can be seen that for thicker discs the non-linear Meissner effect is gradually disappearing. In the limit i.e., for cylinders the peak coincides with the critical field and and the jump occur directly from the maximum value and hence there is no non-linear Meissner effect [4]. Only in this regime London's theory is valid. Hence the non-linear Meissner effect is connected to the nature of phase transition.

From Fig. 2 (solid curve) it can also be seen that even in the linear part of the magnetization curve the susceptibility is less than 1 in magnitude and so the sample is not a perfect diamagnet This is due to the finite size of the sample. Although the magnetic field decreases inside the sample in a finite size sample it never becomes zero. One can see from Fig. 2 (inset) that a large magnetic field is present at the center of the disc and it increases as the applied field is increased.

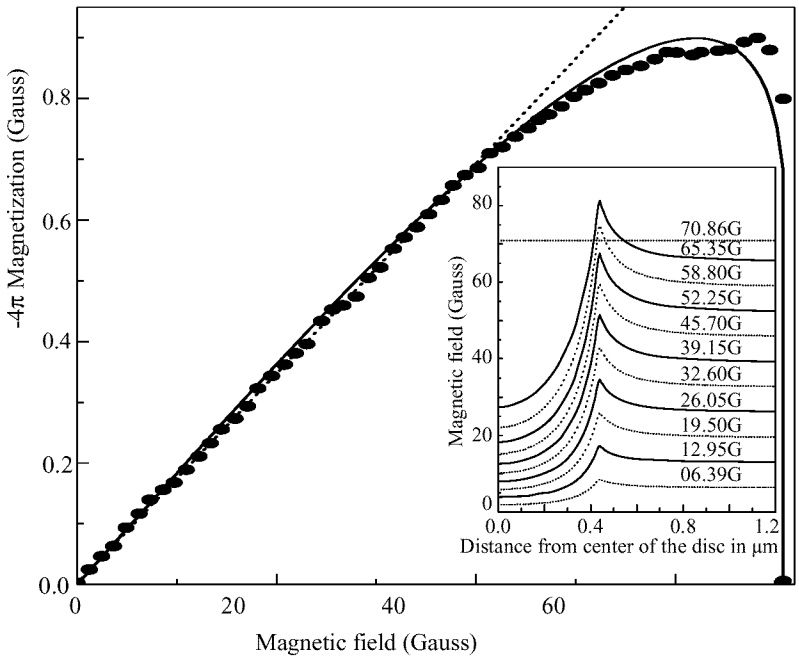


**Fig 2.** Our numerical solution (solid curve) and the experimental data (dark circles) for magnetization versus increasing magnetic field at 0.4K. The dotted curve is a tangent to the experimental data at the origin. The parameters used are given in the text. The inset shows magnitude of magnetic field along a radial line starting from the center of the sample, for 11 values of the applied field mentioned on the curves.

This work is supported by the Flemish Science Foundation (FWO-Vl) grant No. G.0232.96, the European INTAS-93-1495-ext project, and the Belgian Inter-University Attraction Poles (IUAP-VI). One of us (PSD) is supported by a postdoctoral felowship of FWO and FMP is a Research Director with FWO-Vl.

## References

[1] A. K. Geim *at al*, *Superlatt. Microstruct.* **21** (1997);
A. K. Geim *et al*, *Nature* **390** 259 (1997);
A. K. Geim *et al*, *Appl. Phys. Lett.* (in press).
[2] P. Singha Deo *et al*, *Phys. Rev. Lett.* **79** 4653 (1997).
[3] V. A. Schweigert and F. M. Peeters, (unpublished) (1998).
[4] For small radius cylinders there can be a small non-linear Meissner effect. To see non-linear Meissner effect we can take a large radius sample and enhance its penetration length by decreasing its thickness (which is the case of a thin disc) or take a thick sample and decrease its radius to the magnitude of the fixed penetration length (which is the case of a small radius cylinder).

Ioffe Institute
6th Int. Symp. "Nanostructures: Physics and Technology"
St Petersburg, Russia, June 22–26, 1998.



# Hierarchy of effective-mass equations for semiconductor nanostructures

E. E. Takhtamirov and *V. A. Volkov*
Institute of Radioengineering and Electronics of RAS,
Mokhovaya, 11, 103907 Moscow, Russia

**Abstract.** It has been developed a generalization of the Kohn–Luttinger envelope-function method that is applicable for description of the electron and hole states in many-layer (001) heterostructures, composed of related lattice-matched III–V semiconductors, with atomically abrupt heterointerfaces. It was shown that additional contributions to the standard one-band effective-mass equations may be classified with powers of the parameter $\bar{k}a_{\max} \ll 1$, where $1/\bar{k}$ is the characteristic size of the envelope function, and the length $a_{\max}$ is of the order of the lattice constant. It was formulated a hierarchy scheme for the effective-mass equations, the $n$th level of which accounts for taking into consideration all corrections up to $(\bar{k}a_{\max})^n$. Zero level of the hierarchy corresponds to the standard effective-mass equations with position-independent effective mass. On the first level of the hierarchy each heterointerface gives an additional $\delta$-function contribution to the potential energy. Only on the second level the position-dependent effective mass appears as well as corrections for the weak non-parabolicity of the spectrum and spin-orbit interface interaction. At higher levels of the hierarchy non-local contributions appear, and a one-band differential effective-mass equation does not exist.

Currently the question on applicability of the envelope-function (EF) method of Luttinger and Kohn [1] and the effective-mass (EM) equations for real nanostructures is discussed intensively [2]. There are several problems associated with the envelope-function method for heterostructures. The first one is whether the method can really be applicable when studied are the structures whose potential changes considerably on the lattice constant scale. As the matter of fact to researchers' attention the question has been overtopped with the second problem concerning the correct form of the effective kinetic energy operator (KEO) in the effective-mass method, which is just the one-band EF approximation, when EM parameters are position-dependent. To avoid this second problem some authors prefer using complicated many-band EF schemes even when the simple one-band approximation would provide them with at least qualitatively correct solution. Eliminating the KEO problem this way one still has a trouble with the first question. The main goal of the work is to derive simple EM equations for heterostructures taking into account abruptness of the heterostructure potential as well as position-dependent EM. Considered are the (001) heterostructures composed of related (band offsets are small as compared to the band gaps) lattice-matched III–V semiconductors. The presented below result is a kind of recipe, but the recipe based on a rigorous formalism of the Luttinger–Kohn EF method [2].

Generally, one-band EF equations (an equation for simple band and a set of equations for degenerate band) are obtained via a perturbation theory procedure. So there must be small parameters. When one deals with shallow states, the typical energy of which $\bar{E}$ is small as compared to the typical energy separation from other bands $\bar{E}_g$, such a small parameter is $\sqrt{\bar{E}/\bar{E}_g}$. The small parameter may be put down as $\lambda\bar{k}$; here $\bar{k}$ is

the characteristic wave number of the state in question, and $\lambda = 2\hbar\bar{P}/(m_0\bar{E}_g)$, where $\bar{P}$ is the typical interband matrix element of momentum and $m_0$ is the free electron mass. When the proper band edge EM $m$ is mainly formed with the $\mathbf{k}\cdot\mathbf{p}$ interaction, we may adopt $\lambda \sim \hbar/\sqrt{m\bar{E}_g}$. Another small parameter emerges when we face abrupt changes of the heterostructure potential. The parameter is $a\bar{k}$, where $a$ is the lattice constant. It is important that for a good deal of materials we have $a \sim \lambda$ (e.g. for GaAs $\lambda \approx 6$ Å). This is the reason why we should retain terms to the same order in these two parameters in the one-band EF equations. Now we are about to discuss the obtained EM equations. The equations are presented the way they govern electron and hole states in a (001) symmetric quantum well of width $L$ in the absence of external potentials, and $L = \mathcal{N}a/2$, where $\mathcal{N}$ is an integer.

In the usual (bulk) EM equation [1] for electrons

$$\left[\hat{T} + V(z)\right] F_c = EF_c,$$

the KEO and potential energy have standard form:

$$\hat{T}_{\text{bulk}} = \frac{\mathbf{p}^2}{2m}; \quad V_{\text{bulk}}(z) = \Delta E_c\{\Theta(-z) + \Theta(z-L)\}, \tag{1}$$

where $m$ is the bulk EM, $\Delta E_c$ is the conduction band offset, $F_c$ is the conduction band EF. The function $V_{\text{bulk}}$ describes the rectangular shape of the conduction band QW. Allowing for $\mathbf{k}\cdot\mathbf{p}$ interaction with remote bands as well as terms arisen due to abrupt change of the potential at the heterointerfaces give an opportunity to classify these contributions with powers of the parameter $\bar{k}a_{\max} \ll 1$, where $a_{\max} = \max(\lambda, a)$. We present the hierarchy scheme for the EM equations, where the $n$th level of the hierarchy accounts for taking into consideration all corrections up to $(\bar{k}a_{\max})^n$.

**Conduction band QW states near $\Gamma$ point**

0e) Zero level of the hierarchy for electrons. The effective Hamiltonian has "bulk" form (1), that is

$$\hat{T}^{(0)} = \hat{T}_{\text{bulk}}; \quad V^{(0)}(z) = V_{\text{bulk}}(z).$$

We emphasize that at this (the main!) level of the hierarchy $m(z) = const$.

1e) First level of the hierarchy. As taken into account are terms having $a\bar{k}$ smallness, KEO does not change, and in the potential energy there appear $\delta$-function corrections:

$$\hat{T}^{(1)} = \hat{T}_{\text{bulk}}; \quad V^{(1)}(z) = V_{\text{bulk}}(z) + d_1\{\delta(z) + \delta(z-L)\}.$$

The appearance of the two $\delta$-functions at the heterointerfaces is due to abrupt change of the potential and corrections arisen as we describe the real (non-abrupt) form of the heterostructure potential with the Heaviside step-functions. The parameter $d_1$ depends both on bulk properties of the structure components and the microscopic form of the transition region of the heterojunction (HJ), and generally differs for each different heterointerface.

2e) Second level of the hierarchy. If we wish to take into account corrections of the order of $(a\bar{k})^2$, $(\lambda\bar{k})^2$ and $(a\bar{k})(\lambda\bar{k})$, we should deal with the equation where the concept of the position-dependent EM appears:

$$\hat{T}^{(2)} = \frac{1}{2}m^{\alpha}(z)\,\mathbf{p}m^{\beta}(z)\,\mathbf{p}m^{\alpha}(z) + \alpha_0\mathbf{p}^4 + \beta_0\left(\mathrm{p}_x^2\mathrm{p}_y^2 + \mathrm{p}_x^2\mathrm{p}_z^2 + \mathrm{p}_y^2\mathrm{p}_z^2\right);$$

$$V^{(2)} = V^{(1)} + d_2 \left[\mathbf{p} \times \mathbf{n}\right] \cdot \sigma \left\{\delta\left(z\right) - \delta\left(z - L\right)\right\}$$

Here $m(z)$ is the position-dependent band edge EM, $\alpha_0$ and $\beta_0$ are the weak non-parabolicity parameters, $\mathbf{n}$ is the unit $Oz$-axis vector, $\sigma$ are the Pauli matrices. The parameters $\alpha$ (for $\beta$ we have $2\alpha+\beta = -1$) and $d_2$ also depend on bulk properties of the materials of the structure as well as on the microscopic structure of the heterointerface, and should be different for each different HJ (we have a symmetric structure, so the parameters are the same for both HJs). The parameter $d_2$ originates from spin-orbit interaction, which is taken into account through the perturbation theory, the typical spin-orbit interaction parameter being considered to be of the order of the band offsets (the case takes place for a good deal of heterostructures).

Now we present the reasons why one cannot achieve better accuracy for the one-band approximation in the framework of differential equations of finite order. Originally the many-band set of $\mathbf{k}\cdot\mathbf{p}$ equations is a set of $\mathbf{k}$-space integral equations, and $\mathbf{k}$-space is restricted with the first Brillouin zone. For shallow states one may use an approximate canonical transformation of the set (or another unitary perturbation scheme) and move onto the one-band EF approximation. It is important that not all $\mathbf{k}$ belonging to the first Brillouin zone may now correctly contribute to such an equation. The evidence comes from the following. For a bulk material one may use a series to present the spectrum $\epsilon(\mathbf{k})$ of the states near $\Gamma$ point. Such a series has a finite radius of convergence $K_0$, which is determined with the strength of the $\mathbf{k}\cdot\mathbf{p}$ interaction and proximity of other bands. The estimation gives $K_0 \sim 1/\lambda$. This way for the one-band EF equation $\mathbf{k}$-space is restricted with radius $K_0$ rather than the first Brillouin zone boundary. To obtain differential equations in $\mathbf{r}$-space one should go beyond the $\mathbf{k}$-space effective limits. The procedure would induce an exponentially small error if either potential or EF were smooth on the lattice constant scale. That would mean the Fourier transform of either potential or EF drops exponentially as $\mathbf{k}$ increases. But in our case we have abrupt heterostructure potential. One may see from all above that $F_c$ is not smooth, in particular its second derivative has two discontinuities with the relative jumps of the order of unit. This means that if $L$ is large enough, e.g. the conduction band EF Fourier transform $\mathcal{F}_c(\mathbf{k}) \propto 1/(k_z)^3$. So, the principal error of the one-band method is $(\bar{k}/K_0)^3 \sim (\lambda\bar{k})^3$. It is the error that does not allow one to reach better accuracy than that given with the second level equation.

### Hole QW states near $\Gamma$ point

The only difference between the EM method for conduction and valence bands lies in more complicated character of the EF equations for the latter case. This way zero hierarchy level of accuracy of the one-band EM method is plain. As for the second one, the proper equation has so many parameters, some of which depend on specific microscopic details of heterointerfaces, that in practice it would be useless, and similar equation for simple band could have probably satisfied the academic interest. So, we present the first grade. In this approximation the Hamiltonian for valence band states is a sum of the standard (bulk) $6 \times 6$ KEO matrix, and the potential energy $6 \times 6$ matrix. It is the latter that is presented below. We use the basis $\{|J, j_z\rangle\}$ of eigenfunctions of the total angular momentum $J$ and his projection $j_z$, which are linear combinations of

the $\Gamma_{15}$ valence band edge Bloch functions and spin. We adopt the following ordering:

$$\left|\frac{3}{2},\frac{3}{2}\right\rangle,\quad \left|\frac{3}{2},-\frac{3}{2}\right\rangle,\quad \left|\frac{3}{2},\frac{1}{2}\right\rangle,\quad \left|\frac{3}{2},-\frac{1}{2}\right\rangle,\quad \left|\frac{1}{2},\frac{1}{2}\right\rangle,\quad \left|\frac{1}{2},-\frac{1}{2}\right\rangle,$$

and the phase agreement is the same as in [1]. So, the potential energy matrix is

$$\mathbf{V} = \begin{pmatrix} V_{\Gamma_8}\mathbf{1} & V_0\sigma_y & -i\sqrt{2}V_0\sigma_y \\ V_0^\dagger\sigma_y & V_{\Gamma_8}\mathbf{1} & \mathbf{0} \\ i\sqrt{2}V_0^\dagger\sigma_y & \mathbf{0} & V_{\Gamma_7}\mathbf{1} \end{pmatrix}. \tag{2}$$

Here

$$V_{\Gamma_8} = E_{\Gamma_8} + \Delta U_{\Gamma_8}\{\Theta(-z) + \Theta(z-L)\} + \chi_1\{\delta(z) + \delta(z-L)\},$$
$$V_{\Gamma_7} = E_{\Gamma_7} + \Delta U_{\Gamma_7}\{\Theta(-z) + \Theta(z-L)\} + \chi_2\{\delta(z) + \delta(z-L)\},$$
$$V_0 = \chi_3\{\delta(z) - \delta(z-L)\}.$$

The notations are the following: $E_{\Gamma_8}$ and $E_{\Gamma_7}$ are the $\Gamma_8$ and $\Gamma_7$ band edge energies of the well material, $\Delta U_{\Gamma_8}$ and $\Delta U_{\Gamma_7}$ are the proper band offsets. Two parameters $\chi_1$ and $\chi_2$ have the same origin as $d_1$ for the conduction band case, and the parameter $\chi_3$ appears only as we correctly process the abrupt changes of the heterostructure potential (that means the parameter vanishes for smooth potentials). The last parameter defines in particular the strength of the zone center mixing of light and heavy holes [3].

In conclusion we presented three grades of accuracy that can be achieved in the one-band EF approximation, and this way formulated three hierarchy levels for the EM equations. There are effects that cannot be described using the zero level of the hierarchy, e.g. zone center light hole-heavy hole mixing in the valence band. There are also effects that can be dealt with only using the second-level equations of the hierarchy, e.g. spin splitting of the subbands when longitudinal electric field is applied (when the presence of the terms like the one proportional to $d_2$ is crucial), or some optical transitions.

The work was supported by RFBR (project 96-02-18811), RFBR-INTAS (95-0849), the Federal Programs "Physics of Solid State Nanostructures" (96-1019), and "Surface Atomic Structures" (95-3.1).

## References

[1] Luttinger J. M., Kohn W. *Phys. Rev.* **97** 869 (1955).
[2] Volkov V. A., Takhtamirov E. E. *Uspekhi Fiz. Nauk* **167** 1123 (1997) [*Physics-Uspekhi*, **40** No. 10 (1997)].
[3] Ivchenko E. L., Kaminski A. Yu., Rössler U. *Phys. Rev.* **B54** 5852 (1996).

Ioffe Institute
6th Int. Symp. "Nanostructures: Physics and Technology"
St Petersburg, Russia, June 22–26, 1998.



# Resonant and correlation effects in the tunnel structures with sequential 2D electron layers in a high magnetic field

*Yu. V. Dubrovskii*, E. E. Vdovin, Yu. N. Khanin, V. G. Popov,
D. K. Maude†, J-C. Portal†, T. G. Andersson‡ and S. Wang‡
Institute of microelectronics technology RAS,142432, Chernogolovka, Russia
† HMFLG-CNRS, Grenoble, France
‡ Chalmers University of Technology and Göteborg University,
Departament of Physics, Göteborg, Sweden

Experiments concerning the high magnetic field suppression of the tunnelling current between 2DEG's [1, 2] have given rise to an intensive theoretical discussion [3] and a number of different models have been already proposed to explain the experimental findings. There is a general agreement that the observed suppression is related to Coulomb correlations between 2D electrons in a high magnetic field. The current understanding of the observed phenomena is far from the clarity and is the subject of intensive studies world-wide.

In this work we report the first results on the tunnelling between two 2DEGs in a high magnetic field parallel to the current which was realised on a GaAs/AlGaAs/GaAs heterostructure with a single doped barrier at liquid helium temperatures and in magnetic field up to 23 T. In this kind of structures two-dimensional electron accumulation layers with electron concentration $N_{2D} \sim (1.6 - 3.0) \times 10^{11}\,\mathrm{cm}^{-2}$ are formed on both sides of the barrier due to the 20 nm thick barrier doping and are separated from highly n-doped contact regions by lightly n-doped spacer layers 70 nm thick. The main difference between our and earlier experiments [1, 2] is the absence of a serial resistance along the 2DEGs. This would allow one to study the tunnelling conductivity in arbitrary magnetic fields including the case of integer filling factors when the current through the 2DEG is carried by edge states.

The current-voltage $IV$ characteristic of this structure demonstrates negative differential conductance (NDC) (Fig. 1, curve "a", labelled by arrow A) at negative bias without magnetic field and some features at positive bias (arrow B on the same Figure). The capacitance does not show any dependence on voltage bias. This means that applied external voltage drops mainly across the barrier and gives us arguments to relate measured $IV$ characteristics only with tunnelling between 2DEG's.

We argue that NDC is due to the resonance between ground states of 2DEG's (0-0 transition) and nonlinear increase in current at positive bias to the resonance between ground state of one 2DEG and first excited state of another one (0-1 transition). In this picture we presume that 2DEG's have different as grown electron concentration. Fitting of negative bias part of our $IV$ data to simple theoretical expression [4] gives the difference of electron concentration in accumulation layers $\sim 1.2 \times 10^{11}\,\mathrm{cm}^{-2}$. At voltage bias only few mV we have observed SdH like oscillations with only one period corresponds to $N_{1,2D} \sim 3 \times 10^{11}\,\mathrm{cm}^{-2}$. We relate this fact to the different energy broadening $\Gamma$ in electron layers and observation of oscillations from 2DEG with lower one. Estimation of energy broadening from magnetic field when SdH like oscillations in tunnelling current appear and from above fitting to theoretical expression for $IV$

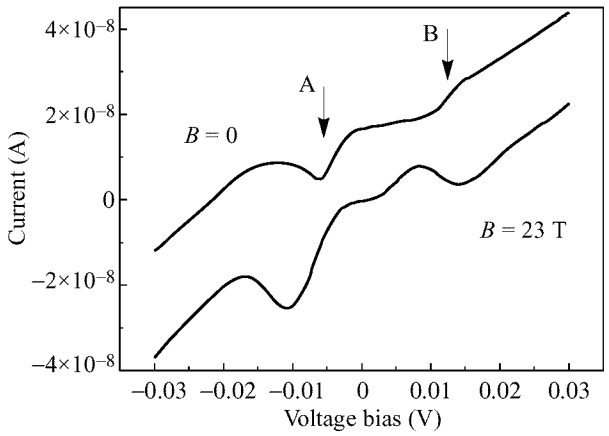


**Fig 1.** Current-voltage dependences without (a) and at magnetic field 23 T (b). Curves are shifted verticaly for clarity. Arrows indicate pecularities on *IV* curve without magnetic field (Details in the text).

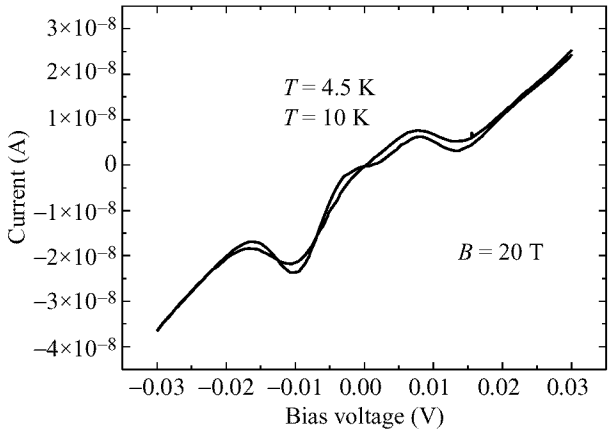


**Fig 2.** Current-voltage dependences at magnetic field 20 T for different temperatures.

characteristic around resonance gives $\Gamma_1 = 0.6$ meV and $\Gamma_2 = 2.1$ meV. It should be noted here that energy broadening in our samples is much higher than in samples used before in work [1] and higher, but of the same order, than used in work [2].

In magnetic field parallel to the current higher than 15 T ($\nu < 1$) the *IV* characteristic are drastically changed (Fig. 1, curve "b"). We note that any spin splitting have not been observed in our structures. Now NDC appears at both voltage polarities. We assign this behaviour to the magnetic field induced resonance at zero voltage . Indeed, when only one Landau level is occupied in both electron layers the Fermi level in contact regions pinned Landau levels and both 2DEG's, in spite of the different electron concentration, are brought to the tunnelling resonance. The *IV* characteristics in a magnetic field are similar to ones observed in references [1, 2] but more asymmetrical. The tunnelling current is suppressed near zero bias. It can be seen from Fig. 2 where *IV* curves are

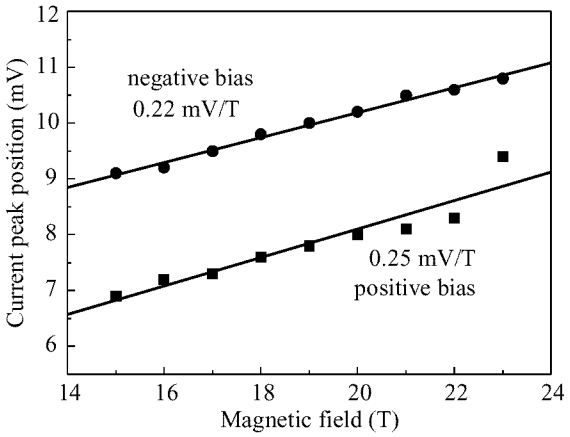


**Fig 3.** Dependences of the current peaks position as a function of magnetic field. Straigt lines are shown only as the guide for the eye.

shown for 4.2 K and 10 K. We assign this behaviour to the manifestation of the electron Coulomb correlation tunnelling gap introduced by the magnetic field [3]. Dependence of the current peaks position on magnetic field show linear dependence (Fig. 3) in agreement with previous observation [2], but in contrast to the current theories [3] predicted $B^{1/2}$ dependence.

At first sight it seems that asymmetry of $IV$ curves in high magnetic field is related to slight off-resonance of the system. Nevertheless we compare our results with $IV$ characteristic functional form which expected for tunnelling gap and was well established in previous experiments [2]. This form should be $I = I_0 \exp -\frac{\Delta}{V}$, where $\Delta$ is the gap parameter. To our surprise we determined different $\Delta_p = 3$ meV and $\Delta_n = 5$ meV for positive and negative bias correspondingly. These can not be explained by slight off-resonance conditions and give some indications that tunnelling gap is determined by Coulomb interaction only in one 2DEG. An analysis of our data show that most likely the magnitude of the tunnelling gap which is of the order of Coulomb interaction correlates with emitter electron concentration, but additional analysis is necessary to prove this assertion.

The suppression of tunnelling current by magnetic field have been observed when one of the 2DEG's is under exact $\nu = 2$ condition. An analysis of experimental data to understand the physical reason for this suppression are in progress now.

Thus we have investigated the tunnelling between 2DEG's in a high magnetic field in the structure with pure vertical transport for the first time. High magnetic field induced resonant tunnelling between 2DEG's with different electron concentration due to the pinning of the last Landau levels by Fermi level in contact regions. This gave us opportunity to investigate and compare our research of the tunnelling current suppression in a high magnetic field near zero bias with previous ones.

This work was supported by the National program "Physics of the Solid State Nanostructures" (grant 97-1057), INTAS-RFBR (grant 95- 849), RFBR (98-02-17462) and CRDF (RC1-220).

## References

[1] J. P. Eisenstein, L. N. Pfeiffer, and K. W. West, *Phys. Rev. Lett.* **69** 3804 (1992).
[2] K. M. Brown, N. Turner, J. T. Nicholls et al., *Phys. Rev.* **B50** 15465 (1994).
[3] S. He, P. M. Platzman, B. I. Halperin, *Phys. Rev. Lett.* **71** 777 (1993);
S.-R. E. Yang and A. H. MacDonald, *Phys. Rev. Lett.* **70** 4110 (1993);
F. G. Pikus and A. L. Efros, *Phys. Rev. Lett.* **73** 3014 (1994);
C. M. Varma, A. I. Larkin, E. Abrahams, *Phys. Rev.* **B49** 13999 (1994);
P. Johansson and J. M. Kinaret, *Phys. Rev.* **B50** 4671 (1994);
S. R. Renn and B. W. Roberts, *Phys. Rev.* **B50** 7626 (1994);
M. E. Raikh and T. V. Shahbazyan, *Phys. Rev.* **B51** 9682 (1995);
I. L. Aleiner, H. U. Baranger, L. I. Glazman, *Phys. Rev. Lett.* **74** 3435 (1995).
[4] N. Turner, J. T. Nicholls, E. H. Linfield et al., *Phys. Rev.* **B54** 10614 (1996).

Ioffe Institute
6th Int. Symp. "Nanostructures: Physics and Technology"
St Petersburg, Russia, June 22–26, 1998.



# Electrical and optical studies of tunneling transport phenomena in Zn(Cd)Se/Zn(Mg)SSe quantum well and superlattice structures

*A. V. Lebedev*†, S. V. Sorokin†, A. A. Toropov†, T. V. Shubina†, N. D. Il'inskaya†, O. Nekrutkina†, S. V. Ivanov† and P. S. Kop'ev†, G. R. Posina‡ and B. Monemar‡

† Ioffe Physico-Technical Institute RAS, St. Petersburg, Russia
‡ University of Linkoping, S-581 83 Linkoping, Sweden

Resonant-tunneling diodes (RTD) based on wide band-gap II–VI compounds will hardly be able to compete ever with the well known devices based on III–V semiconductors, due to the relatively large effective masses of carriers and small available band offsets. However, comprehensive understanding and proper use of the tunneling effects may result in important improvements and new concepts as regards to the optoelectronics devices like light-emitting diodes and injection lasers operating in the green and blue spectral regions. A particular shortcoming of the previously reported devices has been an enhanced carrier leakage over heterobarriers, resulting from insufficient band offsets of the available bulk materials. It has been recently suggested and experimentally shown that a short-period superlattice (SL) used in the active region of ZnCdSe/ZnSSe/ZnMgSSe separate confinement heterostructure (SCH) lasers instead of the bulk wave-guide layers can significantly improve the electronic confinement [1]. This approach has allowed one to decrease the threshold power density of the room-temperature optically-pumped lasers down to 20 kW/cm$^2$ at 490 nm. To extend this approach to injection lasers, further research is needed, aimed at optimization of carrier tunneling transport along the SL axis. Another potential application of II–VI tunneling structures concerns bipolar RTDs which are currently considered to be perspective as high-speed electroluminescence devices [2].

In this paper, we present electrical and optical studies of ZnCdSe/ZnMgSSe/ZnSSe double-barrier resonant-tunneling structures and ZnSSe/Zn(Cd)Se short-period SLs, focusing on their tunneling properties. All the structures are grown by molecular-beam epitaxy (MBE) pseudomorphically to a GaAs(001) substrate. The growth technique and conditions have been reported elsewhere [3]. The SL structures consist of a ZnSSe/ZnCdSe SL surrounded by thick layers of ZnMgSSe quaternary alloy. A wider ZnCdSe quantum well (QW) is embedded in the center of the SL. The Cd content in the ZnCdSe ternary alloy layers vary in different samples from 25% to 0% (pure ZnSe), however, for all the structures the SL parameters where chosen to balance carefully alternating compressive and tensile strains between the ZnCdSe and ZnSSe constituent layers in order to achieve the multilayer structure lattice-matched to a substrate as a whole. A double-barrier (DB) $n - i - n$ resonant tunneling structure contains a 40 Å wide ZnSe QW placed between 45 Å wide ZnMgSSe barriers. The resonant structure is surrounded by the $n$-type ZnSSe:Cl buffer and contact layers, with 50 Åwide spacers of undoped ZnSSe adjacent to the barriers.

The temperature-dependent continuous wave (cw) and time-resolved (TR) photoluminescence (PL) and PL excitation (PLE) spectra were measured to characterize the

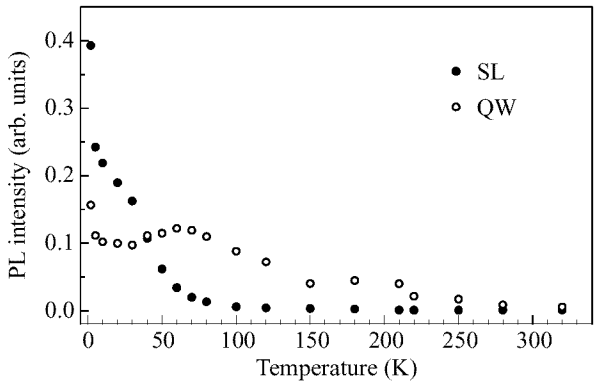


**Fig 1.**

SL transport properties. The low-temperature PL spectrum excited by the 351 nm line of an Ar ion laser demonstrates two lines comparable in intensity. Both cw PLE spectra and TR PL spectra (measured by streak camera with 15 ps time- resolution) enable one to attribute this lines to excitonic emission in the SL (the higher energy line) and in the wider QW.

Fig. 1 displays integrated intensity of the lines as a function of temperature for the sample containing a 42-period (42 Å — $ZnS_{0.15}Se_{0.85}$ / 12 Å — $Zn_{0.87}Cd_{0.13}Se$) SL with an embedded 70 Å — $Zn_{0.87}Cd_{0.13}Se$ QW. The intensity of PL associated with the SL decreases monotonously with the temperature increase and disappears completely at about 100 K. In contrast to that, the dependence for the QW PL is non-monotonous with a peak value at about 70 K. Note that this line is well visible up to room temperature. To explain the PL behavior we calculated the band line-ups and confinement energies in the SL samples. For the sample of Fig. 1 the calculated miniband widths are 72 meV, 9 meV and 104 meV for electrons, heavy holes and light holes, respectively. The lowest heavy-hole exciton is essentially localized in the SL wells due to the low heavy-hole mobility along the SL axis, which explains the dominant intensity of the SL PL at low temperatures. However, the bottom of the light-hole miniband in this structure is only 5–10 meV above the top of the heavy-hole one, providing efficient thermal occupation of the light-hole states with the temperature increase. This process is responsible for the enhanced transfer of holes along the growth direction, followed by their capture in the QW and energy relaxation down to the lowest heavy-hole QW level. This agrees well with the temperature-induced increase in the QW PL intensity. At even higher temperatures the QW PL intensity decreases again due to the enhanced contribution of non-radiative recombination channels. This interpretation is also confirmed by measuring the PL decay time as a function of temperature. The SL PL lifetime decreases drastically down to 30–50 ps at 60–80 K, indicating fast temperature-enhanced tunneling escape. This behavior is generally typical for all the SL samples studied, while the light-hole activation energies reasonably depend on the SL parameters.

Electrical measurements have been performed to proof the unipolar electron resonant tunneling transport in ZnSe/ZnMgSSe/ZnSSe DB heterostructure. Fig. 2 demonstrates a typical 300 K I–V characteristic which involves a pronounced negative-differential-resistance region up to 300 K. Under the dark condition, the excitonic contribution to this

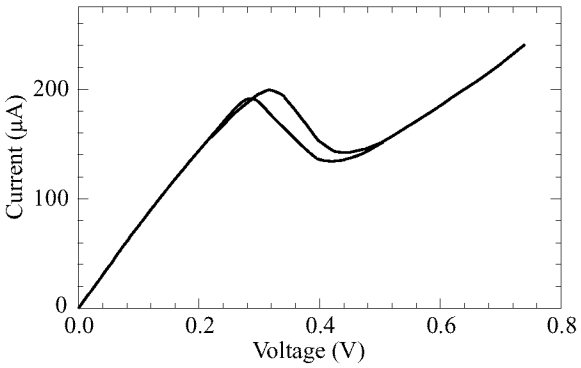


**Fig 2.**

process is expected to be negligible due to the absence of holes in this unipolar structure. Under illumination, the I–V characteristic changes both due to the light-induced space charge redistribution and the exciton-assisted resonant tunneling [4], however, more detailed experiments are required to separate the two processes.

In summary, we have presented design and studies of ZnSe-based QW tunneling structures grown by MBE, which are potentially suitable for different opto-electronic applications in green and blue spectral regions. The ZnSSe/Zn(Cd)Se SLs are found to be well applicable as highly-transparent hole emitters efficiently operating at 300 K due to the temperature-enhanced transport within the light-hole miniband. A pronounced room-temperature *N*-shaped current-voltage (I–V) characteristic has been reported for the first time for the II–VI wide-bandgap heterostructures that offers a scope for further development of high-frequency optical oscillators and bistable devices.

*Acknowledgements*

This work has been supported in part by the Russian Foundation for Basic Research and by Program of Ministry of Science of RF "Physics of solid-states nanostructures".

## References

[1] S. Sorokin, S. Ivanov, A. Toropov, T. Shubina, I. Sedova, M. Tkatchman, P. Kop'ev and Zh. Alferov, *Proceedings of Int. Symposium "Nanostructures: Physics and technology"*, St.Petersburg, p. 206, 1997.
T. V. Shubina, S. V. Ivanov, A. A. Toropov, G. N. Aliev, M. G. Tkatchman, S. V. Sorokin, N. D. Il'inskaya, P. S. Kop'ev, *J. Crystal Growth* (to be published).

[2] C. Van Hoof, J. Genoe, R. Mertens, and G. Borghs, E. Goovaerts, *Appl. Phys. Lett.* **60** (1) 77-79 (1992).

[3] S. V. Ivanov, S. V. Sorokin, P. S. Kop'ev, J. R. Kim, N. D. Jung, H. S. Park, *J. Crystal Growth*, **159** 16 (1996).
S. V. Ivanov, S. V. Sorokin, I. L. Krestnikov, N. N. Faleev, B. Ya. Ber, I. V. Sedova, P. S. Kop'ev, *J. Crystal Growth* (1998) (to be published).

[4] H. Cao, G. Klimovitch, G. Bjork, and Y. Yamamoto, *Phys. Rev. Lett.* **75** (6) 1146-1149 (1995).

Ioffe Institute
6th Int. Symp. "Nanostructures: Physics and Technology"
St Petersburg, Russia, June 22–26, 1998.



# Analytical theory of the coherent generation in the resonant-tunneling diode

*Vladimir F. Elesin*
Moscow State Engineering Physics Institute (Technical University)
115409 Moscow, Kashirskoe shosse, 31 Russia
E-mail:vef@supercon.mephi.ru

The experiments on the observation of generation in the resonant-tunneling diode (RTD) in the region of ultra-high frequencies (up to 712 GHz, E. R. Brown *et al.* 1991) has demonstrated the perspectives for using of such structures as sources of generation. However, the observed output power of these generators was too small. The physical nature of such small values of the output power as well as the ways and perspectives to increase it remain still unclear despite a considerable number of theoretical works. Unfortunately, majority of these works employ numerical approach giving no way for their analysis. Developed analytical theories are phenomenological in essence. At the same time, the coherent system requires the rigorous quantum-mechanical description.

The consequent quantum-mechanical theory of the coherent generation in the RTD is developed in the present work. Exact analytical solution of the set of equations describing the generation is obtained for the case of weak electromagnetic field. The expressions for the active and reactive components of the polarization currents are derived. It is shown that these expressions are essentially different from those obtained in earlier published works employing semi-phenomenological approaches. The analysis of results enabled one to elucidate the mechanism of generation in the RTD and to show that it is principal different from the generation mechanism in lasers. Moreover, the values of threshold pumping currents and generation frequencies were calculated. The dependence of these quantities on the structure parameters was determined also. The developed model gives one a possibility to estimate the optimal parameters of the structure as well as the perspectives of RTD-based generators.

Ioffe Institute
6th Int. Symp. "Nanostructures: Physics and Technology"
St Petersburg, Russia, June 22–26, 1998.



# Fabrication and electrical properties of the monolayer of oxidized nanometer-size metallic granules

*S. A. Gurevich*, V. M. Kuznetsov, V. M. Kozhevin, D. A. Yavsin,
D. A. Zakheim, V. V. Khorenko and I. V. Rozhansky
Ioffe Physico-Technical Institute RAS, 194021 St. Petersburg, Russia

**Abstract.** A new method for the fabrication of 10 nm metallic granules is suggested, which is based on fission of liquid drops produced by laser oblation. A monolayer of such granules was deposited on the insulating substrate and then partly oxidized in air. It is shown that the conductivity of this layer, measured in lateral geometry, occures due to electron tunneling between oxidized metallic granules having the charging energy as high as 300 meV.

## Introduction

Several techniques have been suggested [1, 2] to fabricate the structures comprising nanometer-size metallic particles separated by tunnel barriers. The conductivity of 3D [1], 2D [2], and quasi-1D [3] conductors made of such granulated materials have been studied intensively to show that single-electron charging energy of individual particle is one of the main parameter determining the transport properties even at relatively high temperature. As it follows from recent consideration [4], such materials are promising for the fabrication of single-electron devices operating at room temperature. In this work we report on new technique for fabrication of low size dispersion 10 nm Cu granules which were first embedded on the insulating substrate in one monolayer and then partly oxidized to form the inter-granular barriers of native Cu oxide. The I–Vs and temperature dependence of conductivity of such layer were studied in lateral geometry.

## 1 Fabrication of experimental samples

Used in this work the method of nanometer-size Cu granules formation is based on fission of charged liquid metallic drops initially produced by laser oblation. The schematic of the experimental setup is shown in Fig. 1. The metallic Cu target was placed on rotating mount fixed inside the vacuum chamber (grounded) which was pumped down to $10^{-5}$ Pa. The DC voltage (3 kV) was supplied to the anode placed 7 cm apart from the target. The beam from pulsed AIG $Nd^{3+}$ laser was introduced into the chamber through the side port and focused on the target surface to produce the power density about $10^9$ W/cm$^2$. Finally, the alumina substrate was fixed near the anode as shown in Fig. 1.

The laser oblation of the Cu target results in flashing out the Cu particles with the dimensions wide spread in the range from the atomic size up to few microns. The largest particles (maternal drops) are liquid, which was checked in special experiment. These particles get charged in the plasma cloud and may become to be unstable if the Coulomb repelling force is higher than the surface tension. The instability threshold is

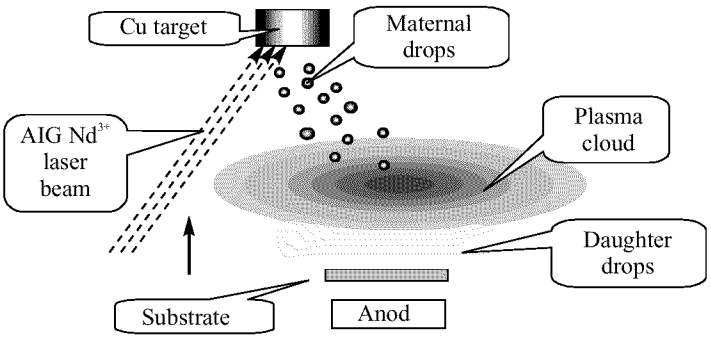


**Fig 1.** Schematic of experimental setup for Cu granules formation.

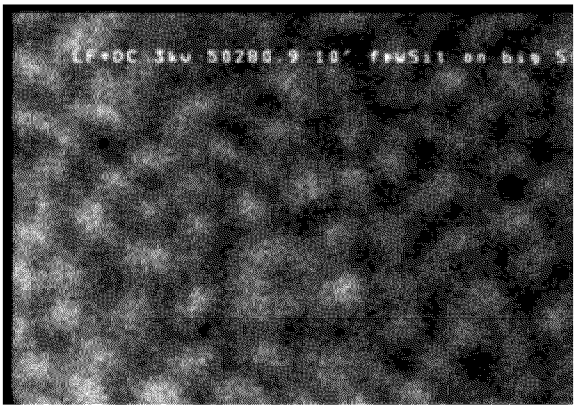

**Fig 2.** SEM image of fabricated monolayer (plan view).

given by Rayleigh condition [5]:

$$\frac{Q^2}{16\pi\alpha R^3} \geq 1, \tag{1}$$

where $\alpha$ is the surface tension, $R$ and $Q$ are the radius and the charge of maternal drop. Charged up to Rayleigh limit (1) each maternal drop ejects daughter drops which are also unstable and produce the next generation of daughter drops. This proces of drop fission stops when the drop size comes to a certain minimum value. This final size is controlled by the rate of autoelectronic charge emission from the drop surface and is determined by the material work function. As shown in Fig. 1, the daughter drops are collected at the substrate surface. In our experiments the minimum size of Cu drops was about 10 nm and one monolayer of these granules was deposited. Certain amount of small (atomic size) Cu particles also reaches the substrate.

When the structure was taken out from the vacuum chamber it was exposed in air during some time. In such a situation, the Cu granules (and the background of atomic-size particles) were naturally oxidized in the atmosphere. Thus, the structure containing Cu granules covered by native Cu oxide was formed. SEM image of the resulting structure is shown in Fig. 2 (plain view). As one can see in this figure the granules

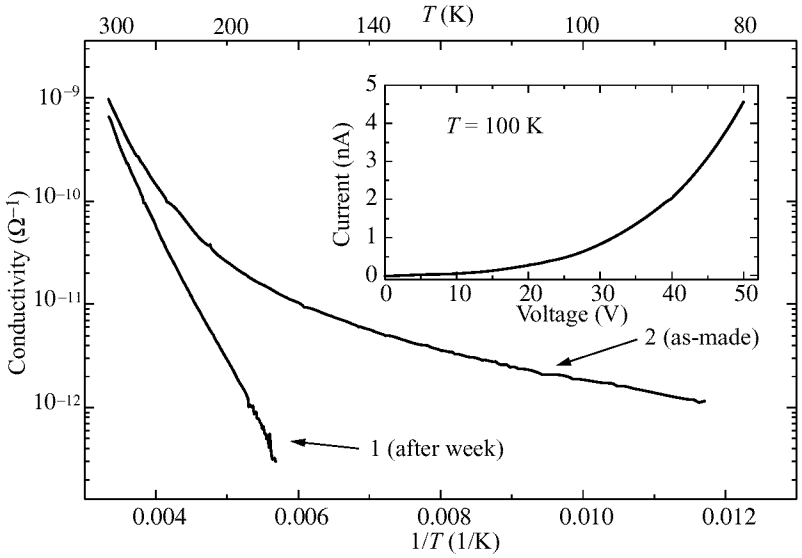


**Fig 3.** I–V curve and temperature dependences of structure conductivity.

have well defined size, about 10 nm, and they are dense packed, closely contacting the neighbors.

Taken from the chamber, the structure was deliberately etched by $Ar^+$ ions and then Cr contacts ($400 \times 400\,\mu m^2$) were deposited on the top of the layer, the gap between the contacts being $5\,\mu m$. The conductivity of the layer was measured in lateral geometry.

## 2 Experimental results and discussion

The inset in Fig. 3 shows the example of dc I–V curve measured at 100 K. At voltages below $\sim$ 10 V the characteristic is linear but at higher voltages the exponential-like behavior is observed. This voltage corresponds to intergranular voltage drop about $kT$ at 100 K and thus separates so-called low-field and high-field regimes [1]. Fig. 3 shows also the temperature dependencies of conductivity measured in low-field regime. The curve (1) was obtained after the same sample was kept in the room ambient during one week, while the curve (2) was measured just after the sample preparation. In both cases the temperature-activated conductivity is observed. The slope of curve (1) corresponds to the activation energy equal to 300 meV, which is associated with the charging energy of a metallic granule having the diameter and effective dielectric constant product $d\epsilon = 5$ nm. In well-oxidized structure such granules may exist inside the oxide shell. As one can see in Fig. 3, the conductivity of as-made layer (curve 2) has strictly different behavior: at low temperatures the conductivity is higher and the activation energy is small, about 30 meV (in the range 90–130 K). Apparently, at low temperatures the conductivity of as-made sample reveals the input of another transport mechanism. This mechanism may be electron hopping between some weakly localized states. We believe these states are associated with the background of small Cu particles, which "contaminate" as-made sample and disappear in due course of film oxidation.

## 3 Conclusion

We have fabricated 2D layer of closely packed nanometer-size metallic granules. After appropriate oxidation of this layer, pure exponential temperature dependence of low-field conductivity was observed with the activation energy as high as 300 meV which is well consistent with the charging energy of metallic granules residing inside the shell of native oxide. Such a behavior of conductivity is assumed to result from very low size dispersion in the system, which is of particular interest for further design of single-electron devises.

This work was supported in part by RFBR grant No. 98-02-18210, the Program of the Ministry of Science of RF "Physics of Solid-State Nanostructures" grants NN 97-2014, 97-1035, State Program "Micro- and Nanoelectronic Technology" grant 151/57/1.

## References

[1] B. Abeles, P. Sheng, M. D. Coutts, Y. Arie, *Adv. Physics* **24** 407 (1975).
[2] W. Chen, H. Ahmed, K. Nakazoto, *Appl. Phys. Lett.* **66**(24) 3383 (1995).
[3] E. Bar-Sadeh, Y. Goldstein, C. Zhang, H. Deng, B. Abeles, O. Millo, *Phys. Rev.* **B50** 8961 (1994).
[4] S. V. Vyshenski, *Phys. Low-Dim. Structures* **11/12** 9 (1994).
[5] W. N. English, *Phys. Rev.* **74** 179 (1948).

Ioffe Institute
6th Int. Symp. "Nanostructures: Physics and Technology"
St Petersburg, Russia, June 22–26, 1998.



# Interband magnetotunneling in RTS with type II heterojunctions

*A. Zakharova*
Institute of Physics and Technology of the Russian Academy of Sciences,
Nakhimovskii Avenue 34, Moscow 117218, Russia

In resonant tunneling structures (RTS) with type II heterojunctions such as InAs/-AlSb/GaSb RTS with a GaSb quantum well and GaSb/AlSb/InAs RTS with an InAs quantum well, the interband tunneling of electrons through the quasibound states in the valence band quantum well or holes from GaSb through the quasibound states in the conduction band quantum well occurs. These interband RTS showed sufficiently high values of peak-to-valley current ratio at room temperature [1], [2] and attracted a considerable attention of researchers. In papers [3], [4] the interband magnetotunneling in RTS made from InAs, AlSb, GaSb was investigated. In strong magnetic field normal to the interfaces, the interband tunneling current oscillations were observed conditioned by the interband tunneling through different Landau levels [3]. The magnetic field parallel to interfaces results in a considerable shift in peak voltage [4]. The interband magnetotunneling in InAs/AlSb/GaSb RTS in the magnetic field parallel to interfaces was considered theoretically in Ref. [5]. The aim of this paper is to investigate theoretically the interband magnetotunneling in structures with type II heterojunctions in magnetic field normal to interfaces. The transmission coefficients corresponding to the tunneling processes from the states of each Landau level with conservation and changing of the Landau-level index were calculated using the eight-band Kane model. We show that in the InAs/AlGaSb/GaSb RTS (see Fig. 1) the interband tunneling probability for transitions with changing the Landau-level index may be comparable with the interband tunneling probability with conservation of the Landau-level index, that can result in the additional peaks on the current-voltage (I–V) characteristics of these RTS.

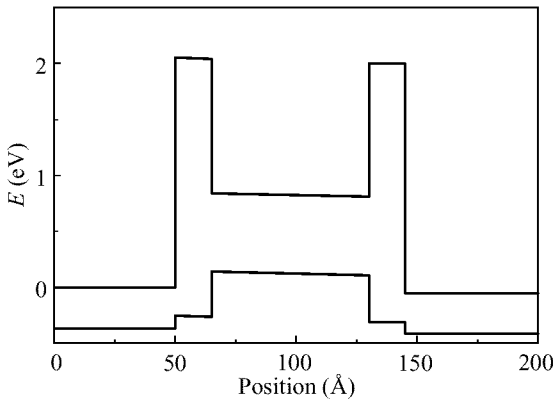


**Fig 1.** Conduction and valence band diagram of InAs/AlSb/GaSb RTS.

We use the **kp** band model, which takes into account the coupling of the conduction band with three valence subbands exactly and neglects the higher bands to investigate

the interband tunneling processes in RTS such as InAs/AlGaSb/GaSb RTS, whose conduction and valence band diagram is shown in Fig. 1. In this way we consider only the interband tunneling processes through the light hole states in the quantum well. These processes are dominant for the values of external bias, when the interband resonant tunneling processes through the light hole states can occur [6], [7]. We consider only the coherent tunneling neglecting the phonon-assisted processes, which can be essential in structures with thick barriers [8]. If the axis z is normal to interfaces, than an $8 \times 8$ Hamiltonian can be written in the following form

$$\hat{H} = \begin{pmatrix} \hat{H}_{+-} & \hat{H}_{--} \\ \hat{H}_{++} & \hat{H}_{-+} \end{pmatrix}, \tag{1}$$

where

$$\hat{H}_{\pm\mp} = \begin{pmatrix} E_C(z) & \sqrt{2}iP\hat{k}_z/\sqrt{3} & -iP\hat{k}_z/\sqrt{3} & P\hat{k}_\pm \\ -\sqrt{2}iP\hat{k}_z/\sqrt{3} & E_V(z) & 0 & 0 \\ iP\hat{k}_z/\sqrt{3} & 0 & E_V(z) - \Delta(z) & 0 \\ P\hat{k}_\mp & 0 & 0 & E_V(z) \end{pmatrix}, \tag{2}$$

and

$$\hat{H}_{\pm\pm} = \begin{pmatrix} 0 & P\hat{k}_\pm/\sqrt{3} & \sqrt{2}P\hat{k}_\pm/\sqrt{3} & 0 \\ P\hat{k}_\pm/\sqrt{3} & 0 & 0 & 0 \\ \sqrt{2}P\hat{k}_\pm/\sqrt{3} & 0 & 0 & 0 \\ 0 & 0 & 0 & 0 \end{pmatrix}. \tag{3}$$

Here $\hat{k}_\pm = \mp i(\hat{k}_x \pm i\hat{\tilde{k}}_y)/\sqrt{2}$, $\hat{k}_x = -i\partial/\partial x$, $\hat{\tilde{k}}_y = -i\partial/\partial y + |e|Bx/(\hbar c)$, $\hat{k}_z = -i\partial/\partial z$, $E_C(z)$, $E_V(z)$ are the conduction and valence band edges, $\Delta(z)$ is the split-off energy, $P = -\hbar^2 < s|\partial/\partial z|p_z > /m_0$, where $s$, $p_z$ are the basis states of the conduction and valence bands, $m_0$ is the free electron mass. We have supposed, that the magnetic field $B$ is parallel to axis $z$, so that $B_z = B$, $B_x = 0$, $B_y = 0$; and the components of vector potential are: $A_y = Bx$, $A_x = A_z = 0$. We use the same basis functions as in Ref. [9] and neglected $g$-factor of the free electron. Then the envelope functions obey the equations

$$\sum \hat{H}_{ij}\psi_j = E\psi_i, \qquad i = 1, 2, \ldots, 8. \tag{4}$$

In (4) $\psi_i$ is an envelope function, $E$ is the energy. At the heterointerfaces should be continuous the following functions

$$\psi_1, \qquad \sqrt{2}\psi_2 - \psi_3, \qquad \psi_5, \qquad \sqrt{2}\psi_6 - \psi_7 \tag{5}$$

to conserve the probability current density component normal to interfaces.

The equation system (4) in a bulk material have two solutions for a given value of energy $E$ and Landau-level index $n$ with wave vector components $k_z^\pm$ and opposite average values of spin. For the first solution $\psi_1 \neq 0$, $\psi_5 = 0$, for the second solution $\psi_5 \neq 0$, $\psi_1 = 0$ [10]. In the conduction band these two solutions correspond to the states with spin $s \approx \pm 1/2$, respectively. In the heterostructure due to the spin-orbit interaction, the mixing at the heterointerfaces of the states with opposite spin orientations

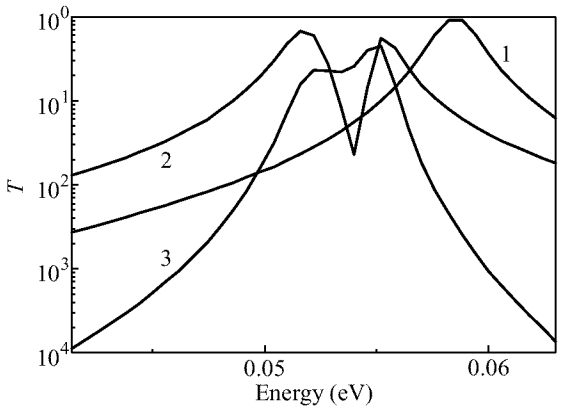


**Fig 2.** Transmission coefficients versus energy.

of Landau levels $n$ and $n+1$ occurs. So that electron from the state corresponding to Landau-level index $n$ with spin parallel to magnetic field can tunnel not only into the similar state to the right side of RTS, but also into the state corresponding to Landau-level index $n+1$ with spin opposite to magnetic field. Only the states with Landau-level index $n = 0$ and spin opposite to the magnetic field are not mixed with the other states.

To investigate the interband resonant tunneling in the presence of magnetic field, we use the transfer matrix method. The transfer matrices were calculated to obtain the transmission coefficients for the transitions from the states with different spin orientations, corresponding to each value of Landau-level index. The results of calculations for the InAs/AlGaSb/GaSb RTS under bias 0.05 V are presented in Fig. 2. The investigated structure contains two InAs contact layers doped by donors, two 25 Å AlGaAs barriers and 50 Å GaSb quantum well. The value of magnetic field is equal to 15 T. We have used the same parameters as in Ref. [9].

Curve 1 in Fig. 2 corresponds to the transitions from the electron states to the left of the double barrier structure with spin opposite to the direction of magnetic field corresponding to the value of $n = 0$ into the similar states to the right of it. Curve 2 represents the transmission coefficient versus energy for the transitions from the states in the conduction band of the left InAs layer corresponding to the Landau-level index $n = 0$ and spin parallel to the magnetic field into the similar states to the right of tunneling structure. Curve 3 represents the transmission coefficient versus energy for the transitions from the states in the conduction band of the left InAs layer corresponding to the Landau-level index $n = 0$ and spin parallel to the magnetic field into the states to the right of the double barrier structure with Landau-level index $n = 1$ and opposite direction of spin. All these resonant tunneling processes occur through the light hole quasibound states in the quantum well. Due to strong mixing of the quasibound states in the valence band quantum well corresponding to the values of $n = 0$ and $n = 1$, resonant tunneling in the case of curves 2 and 3 occurs through two states in the quantum well with different spin orientations, which correspond to the same subband of size quantization. For this reason the dependencies $T(E)$ have two peaks. This effect can result in the existence of the additional peaks on the I–V characteristics of the InAs/AlGaSb/GaSb RTS.

This work was supported by Russian Foundation of Fundamental Research under Grant No. 97-02-16438.

## References

[1] R. Soderstrom, D.H. Chow, and T.C. McGill, *Appl. Phys. Lett.* **55** 1094 (1989).
[2] L.F. Luo, R. Beresford, K.F. Longenbach, and W.I. Wang, *Appl. Phys. Lett.* **57** 1554 (1990).
[3] E.E. Mendez, H. Ohno, L. Esaki, W.I. Wang, *Phys. Rev. B* **43** 5196 (1991).
[4] R.R. Marquardt, D.A. Collins, Y.X. Liu, D.Z.-Y. Ting, and T.C. McGill, *Phys. Rev. B* **53** 13624 (1996).
[5] Y.X. Liu, R.R. Marquardt, D.Z.-Y. Ting, T.C. McGill, *Phys. Rev. B* **55** 7073 (1997).
[6] I. Lapushkin, A. Zakharova, V. Gergel, H. Goronkin, S. Tehrani, *J. Appl. Phys.* **82** 2421 (1997).
[7] A. Zakharova, *Semicond. Sci. Technol.* (to be published).
[8] A. Zakharova, *J. Phys.: Condens. Matter* **9** 4635 (1997).
[9] V. Ryzhii, and A. Zakharova, *Semicond. Sci. Technol.* **8** 377 (1993).
[10] R. Bowers, and Y. Yafet. *Phys. Rev.* **115** 1165 (1959).

Ioffe Institute
6th Int. Symp. "Nanostructures: Physics and Technology"
St Petersburg, Russia, June 22–26, 1998.



# Influence of localization on the optical nonlinearities induced by exciton-exciton interaction in semiconductor nanostructures

*Jørn M. Hvam* and Wolfgang W. Langbein
Mikroelektronik Centret, The Technical University of Denmark, Building 345 east, DK–2800 Lyngby, Denmark

**Abstract.** The signature of exciton-exciton interaction in the four-wave mixing response at the fundamental excitonic resonance is investigated as a function of the localization strength in GaAs single and multiple quantum wells. The four-wave mixing is found to be dominated by signals induced by exciton-exciton interaction. For co-polarization of the incident pulses, excitation-induced dephasing (EID) is dominating the signal generation, while for cross-linear polarized excitation, the signal is generated from bound and unbound biexciton transitions. The relative strength of the EID compared to phase-space filling shows a maximum for localization energies comparable to the homogeneous broadening. The biexciton binding energy increases for localization energies comparable to or larger than the biexciton binding, while the biexciton continuum edge shifts to energies above the exciton resonance. Simultaneously, the binding energy gets inhomogeneously broadened, and the oscillator strength of the biexciton continuum is reduced by the quantization of the excitonic states in the localization potential.

## 1 Introduction

The role of exciton-exciton interactions in the nonlinear coherent response of semiconductor nanostructures is discussed intensively in recent literature [1, 2, 3, 4]. The important role of the excitation-induced dephasing [5, 6] has been pointed out. The description of the nonlinear optical response by few-level models including bound and unbound biexciton states [4, 7, 8], as introduced by Bott *et al.* [1], has been compared with the solutions of the Semiconductor Bloch Equations beyond the Hartree-Fock approximation [9, 10, 11]. For localized systems, the theoretical description using few-level models is the only one presently feasible. In the inhomogeneously broadened case, the excitonic as well as the biexcitonic four-wave mixing (FWM) signal is a photon echo [12, 13, 14]. The biexcitonic FWM shows a fast, non-exponential decay in delay time due to the inhomogeneous broadening of the biexciton binding energy [15]. Also, the average binding energy of the biexciton is enhanced by the localization [16, 17, 18, 19].

In this paper we give an overview over the influence of exciton localization on the EID and the biexcitonic spectrum. In the absence of localization, the biexciton spectrum consists of one bound and a continuum of unbound states [11]. The onset of the continuum is at twice the exciton energy at zero center-of-mass motion ($\mathbf{K} = 0$). In FWM experiments, mainly the bound state and the onset of the continuum is active due to the exciton $\mathbf{K} = 0$ components of the respective biexciton states. The localized biexciton case can be compared to previous investigations on three-dimensionally confined quantum dot systems [20]. Here, one observes unbound (excited) biexciton states above the two-exciton energy [21, 22] additionally to the bound biexciton state [23]. In structures with statistical disorder, the random potential leads to localized zero-dimensional states

[19]. Consequently, localization should similarly lead to a quantization of the biexciton continuum.

## 2 Samples and experiment

We use a set of GaAs quantum well (QW) samples with well thicknesses between 4 nm and 25 nm, embedded in $Al_{0.3}Ga_{0.7}As$ barriers. They are grown by molecular beam epitaxy on nominally undoped (100) GaAs substrates, and are single QW (SQW) or 10–15 period multiple QW (MQW) structures. We perform polarization-dependent transient FWM in reflection or transmission geometry with spectrally resolved, time-integrated detection. The incident pulses in the directions $\mathbf{k}_1$ and $\mathbf{k}_2$ with $\tau_{12}$ temporal separation were generated by a self–mode–locked Ti:sapphire laser at 76 MHz repetition rate. The pulses are chirp compensated and spectrally shaped to a duration between 100 fs and 3 ps. The pulse spectra were adjusted to overlap the heavy-hole 1s exciton and biexciton transition, while excluding higher resonances. The FWM signal in the $2\mathbf{k}_2 - \mathbf{k}_1$ direction is selected spatially by pinholes and detected spectrally resolved by a combination of a spectrometer and an optical multichannel analyzer. The excited exciton densities are $1-5 \times 10^9/\mathrm{cm}^2$. All experiments are performed at 5 K lattice temperature.

## 3 Results and discussion

The polarization selection rules in FWM can be used to single out transitions from the ground state of the crystal $|0\rangle$ to one of the optically active exciton states X, or transitions from an X state to a biexciton state (bound XX or unbound XX$^*$). The involved selection rules are derived from a five-level optical Bloch equation model displayed in either a circular-polarized or linear-polarized exciton basis [1, 14], as indicated in Fig. 1a,b.

Using co-circular polarized $\mathbf{k}_1$ and $\mathbf{k}_2$ pulses ($\sigma^+\sigma^+$), no biexcitonic transitions can be excited (Fig. 1a). The FWM signal is ($\sigma^+$) polarized, and originates from the $|0\rangle$-X transition. The corresponding FWM spectra (Fig. 1c) show accordingly a single resonance with an inhomogeneous broadening $\Gamma_X$ that is increasing with decreasing well width.

In the nearly homogeneously broadened 25 nm SQW (homogeneous broadening $2\gamma_X = 2\hbar/T_2 \approx 140\ \mu$eV, $\Gamma_X \approx 30\ \mu$eV,), the FWM signal is a free polarization decay (FPD) for $|\tau_{12}| < \hbar/\Gamma_X$. On the other hand, in the inhomogeneously broadened 10 nm and 4 nm QWs the FWM signal is a photon echo (PE), and is suppressed for $\tau_{12} < -\hbar/\Gamma_X$ [12]. We have confirmed the PE nature of the FWM signal by time-resolved FWM, and we do not observe the change from FPD to PE with delay time for cross-linear polarization as previously reported [24, 25].

The ($\sigma^+\sigma^+\sigma^+$) signal can be in general due to excitation-induced dephasing (EID) [5, 6], Local field effects (LFE) [26], and phase-space filling (PSF). For the 25 nm sample, the signal does no show a step-like increase from negative to positive delay (Fig. 1c), indicating that PSF, that is only active for positive delay, is not dominant. EID and LFE are distinguished by the beating with the two-photon coherence (TPC) at negative delay (Fig. 2a). The beating observed for ($\rightarrow\rightarrow\rightarrow$) polarization is largely suppressed for ($\rightarrow\uparrow\rightarrow$) polarization, thus excluding the polarization-independent LFE, and leaving EID as the dominant ($\sigma^+\sigma^+\sigma^+$) and ($\rightarrow\rightarrow\rightarrow$) FWM mechanism. The weak beating for ($\rightarrow\uparrow\rightarrow$) polarization is due to a small LFE contribution.

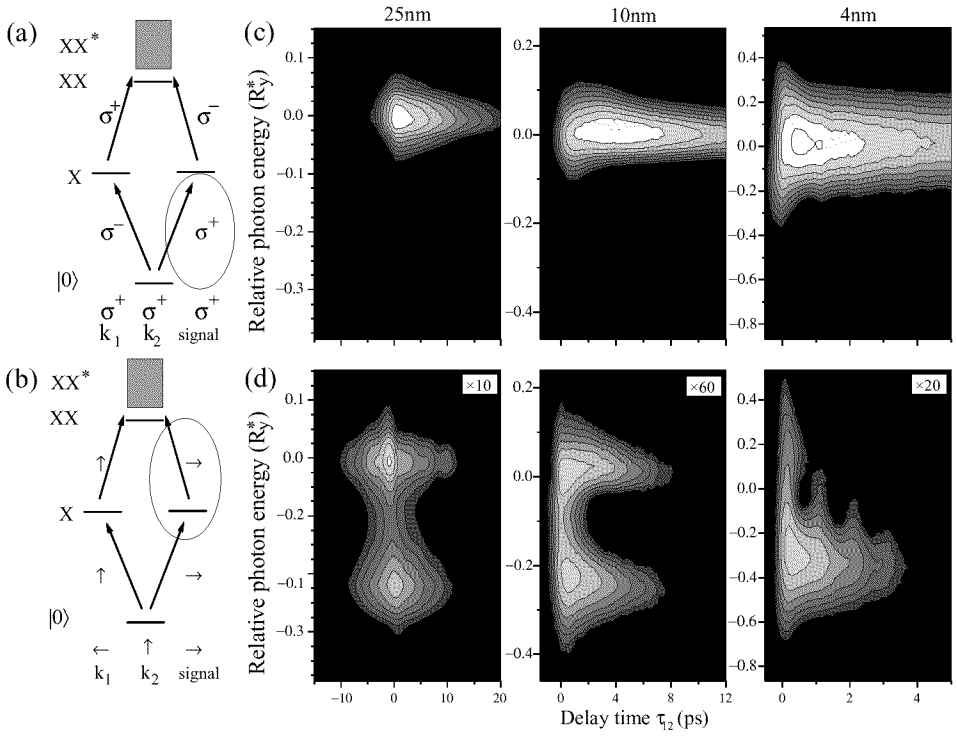


**Fig 1.** (a)-(b) Schematic representation of the considered five-level system and its optical transitions for a circular (a) or a linear (b) polarized exciton basis. The transitions emitting the FWM signal $P^{(3)}$ in $2\mathbf{k_2} - \mathbf{k_1}$ direction are encircled. (c)-(d) Spectrally resolved FWM intensity as a function of $\tau_{12}$ for co-circular ($\sigma^+\sigma^+\sigma^+$) (c) and cross-linear ($\rightarrow\uparrow\rightarrow$) (d) polarization of the excitation and detection. Data for the 25 nm and 10 nm SQWs, and the 4 nm MQW are given. The logarithmic contour scale covers 3 orders of magnitude. The intensity scalings between the two polarization configurations are given. The photon energy is offset with the respective $|0\rangle$-X transition energy $E_X$, and scaled with the exciton binding energy $R_y^*$. The excitation spectra cover the displayed photon energy range.

The EID changes character in an inhomogeneous system. If the EID is dependent only on the macroscopic density, it should vanish due to destructive interference within the inhomogeneous distribution and no PE is generated [6]. On the other hand, if the EID is dependent only on the microscopic densities, the EID generates a PE intensity with a quadratic delay-time dependence relative to the PSF signal.

The observed signal intensity ratio between ($\rightarrow\rightarrow\rightarrow$) and ($\rightarrow\uparrow\rightarrow$) polarization increases for a small inhomogeneous broadening (Fig. 2b) and always keeps larger than 10. This shows that EID is the dominant FWM mechanism also in the inhomogeneously broadened case. However, the delay-time dependence of the time-integrated ($\rightarrow\rightarrow\rightarrow$) FWM signal at the exciton transition matches closely the expected response of the PSF in the inhomogeneous case, and does not show an additional $\tau_{12}^2$ dependence, as demonstrated by the fitted curves according to the PSF mechanism [12] (Fig. 2a). The

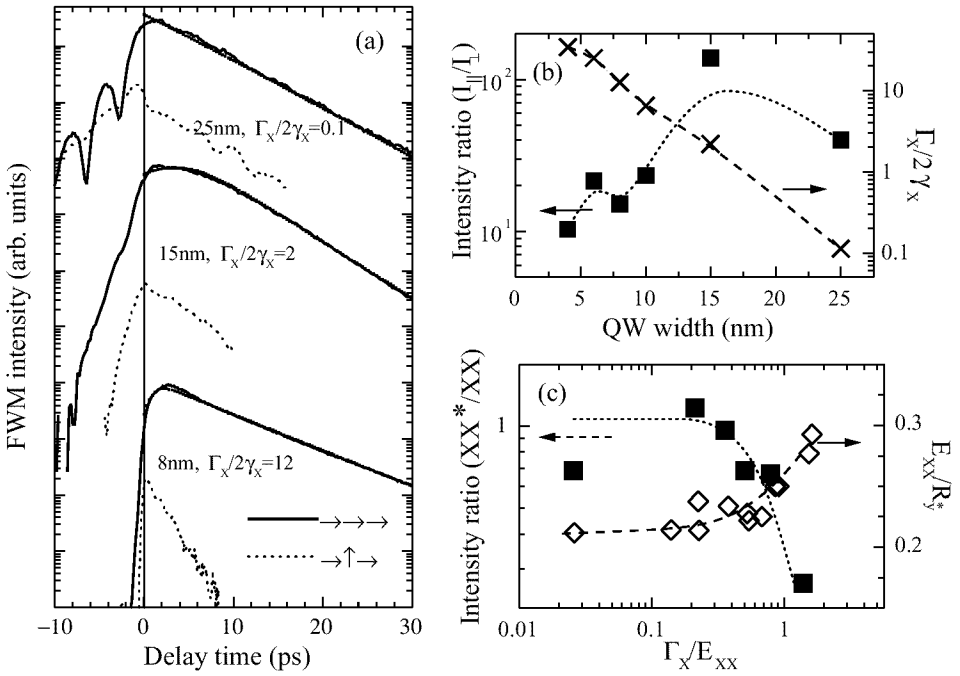


**Fig 2.** (a) Time-integrated FWM intensity at the 0⟩-X transition energy using (→→→) (solid line) and (→↑→) (dotted line) polarization for SQW widths as indicated. The data are vertically offset for each SQW width. Dots: fitted behaviour for PSF in presence of inhomogeneous broadening. The ratio between inhomogeneous $\Gamma_X$ and homogeneous $2\gamma_X$ broadenings is given. (b) Signal intensity ratio between (→→→) and (→↑→) polarization at zero delay time (squares), and inhomogeneous to homogeneous broadening ratio $\Gamma_X/2\gamma_X$ (crosses) as a function of well width. The lines are guides for the eye. (c) biexciton to exciton binding energy ratio $E_{XX}/R^*_y$ (diamonds) and ratio between the X-XX* and X-XX FWM intensity at a $\tau_{12} = h/E_{XX}$ (squares) as a function of the biexcitonic localization $\Gamma_X/E_{XX}$. The lines are guides for the eye.

EID in inhomogeneously broadened systems is thus not described simply by neither of the above pictures.

A possible description is given by an EID dephasing rate $\gamma'(\Delta E)$, which is scaling with the inverse energy separation $\Delta E^{-1}$ between two interacting subsystems within the inhomogeneous distribution. This results in an EID delay-time dependence similar to PSF. Direct measurements of $\gamma'(\Delta E)$ by FWM with an additional, spectrally narrow prepump [27, 28] are in agreement with this model. For large inhomogeneous broadening, the EID contribution decreases (Fig. 2b). This might be due to the smaller exciton density of states D(E) or a smaller wavefunction overlap. A detailed analysis of the FWM processes in dependence of the inhomogeneous broadening will be published elsewhere [29, 28].

Using cross-linear polarized $\mathbf{k}_1$ and $\mathbf{k}_2$ pulses (→↑), the FWM signal originates only from the X-XX and X-XX* transitions. It is (→) polarized, and due to PSF. We want to emphasis here that the X-XX* transition is different from the |0⟩-X transition, and

thus shows in general different oscillator strengths and dephasing times, even though it can have the same transition energy. Previously, the observed different dephasing times for co and cross-linear polarization have been explained by disorder induced coupling [30] or EID [5, 27].

The measured $(\rightarrow\uparrow\rightarrow)$ FWM signal (Fig. 1d) consists of two distinct resonances, namely the X-XX and X-XX$^*$ transition, with the relative energies $E_{\mathrm{XX}}$ and $E_{\mathrm{XX}^*}$ to the $|0\rangle$-X energy $E_{\mathrm{X}}$. The total signal intensity is reduced by one to two orders of magnitude compared to $(\sigma^+\sigma^+\sigma^+)$ polarization due to the missing EID contribution and due to the distribution of the exciton oscillator strength into two spectrally separated transitions (assuming here that the oscillator strength of the exciton is not changed significantly by the exciton-exciton interaction).

In the 25nm SQW, the signal decay for $\tau_{12} < 0$ shows the dephasing of the XX ($T_2 = 7\,\mathrm{ps}$) and XX$^*$ ($T_2 = 6\,\mathrm{ps}$) states. An exciton dephasing with $T_2 = 9\,\mathrm{ps}$ is deduced for $\tau_{12} > 0$, in agreement with the value found for $(\sigma^+\sigma^+\sigma^+)$ polarization. The biexciton continuum edge transition X-XX$^*$ coincides with the energy of the $|0\rangle$-X transition ($E_{\mathrm{XX}^*} = 0$). The respective homogeneous broadenings $2\gamma_{\mathrm{XX}^*} = 220\,\mu\mathrm{eV} > 2\gamma_{\mathrm{XX}} = 180\,\mu\mathrm{eV} > 2\gamma_{\mathrm{X}} = 140\,\mu\mathrm{eV}$ show that the biexcitonic states have a higher scattering cross-section. However, the scattering rate is not simply doubled, indicating that the spin-scattering of the excitons forming the biexciton is reduced.

In the inhomogeneous broadened case with $\Gamma_{\mathrm{X}} < E_{\mathrm{XX}}$ (as for the 10 nm SQW), the two biexciton resonances are still spectrally separated. Note that here the energy of the X-XX$^*$ transition is higher than the $|0\rangle$-X transition, i.e. $E_{\mathrm{XX}^*} > 0$, showing that these transitions are in fact different. The biexcitonic FWM signals decay significantly faster than the exciton signal for $(\sigma^+\sigma^+\sigma^+)$ polarization, which shows $T_2$ times larger than 8 ps for all investigated samples. This is due to the inhomogeneous broadenings $\Gamma_{\mathrm{XX(XX}^*)}$ of the biexcitonic energy shifts $E_{\mathrm{XX(XX}^*)}$, introduced by the disorder [15], as can be explained as follows. After the arrival of $\mathbf{k}_1$, the first-order polarization is propagating at the $|0\rangle$-X frequency $\omega_{\mathrm{X}}$. After the arrival of $\mathbf{k}_2$, the corresponding third-order polarization is propagating on the X-XX(XX$^*$) frequency $\omega_{\mathrm{XX(XX}^*)}$ until the emission of the PE. Since the frequencies of the two transitions ($\omega_{\mathrm{X}}$, $\omega_{\mathrm{XX(XX}^*)}$) are not perfectly correlated [12, 31] (i.e. there are no $\alpha > 0$, and $\beta$ for which $\hbar\omega_{\mathrm{XX(XX}^*)} = \alpha\hbar\omega_{\mathrm{X}} + \beta$ holds), the rephasing of the PE is incomplete, and the signal decay is determined by $\Gamma_{\mathrm{XX(XX}^*)}$ (assuming that the PE width is small compared to the dephasing times i.e. $\gamma_{\mathrm{X}}, \gamma_{\mathrm{XX(XX}^*)} \ll \Gamma_{\mathrm{X}}$).

The $(\rightarrow\uparrow\rightarrow)$ FWM signal again changes character for $\Gamma_{\mathrm{X}} \geq E_{\mathrm{XX}}$ (like in the 4 nm MQW). The quantum beat between the X-XX and X-XX$^*$ transition now present in delay time because the PE duration is smaller than the beat period [14, 31]. Additionally, the X-XX$^*$ signal shows a reduced strength compared to the nearly free case, and the energy shift $E_{\mathrm{XX}^*}$ of the unbound biexciton is clearly visible.

The FWM decay rate for both biexcitonic transitions is strongly increasing with increasing $\Gamma_{\mathrm{X}}$ (see Fig. 1d and 2a). This shows that $\Gamma_{\mathrm{XX(XX}^*)}$ are increasing (assuming that $\gamma_{\mathrm{XX(XX}^*)} \ll \Gamma_{\mathrm{XX(XX}^*)}$, which is reasonable since $\gamma_{\mathrm{X}} \ll \Gamma_{\mathrm{XX}}$). The energy shifts $E_{\mathrm{XX(XX}^*)}$ of the biexcitonic transitions for various QW widths can be extracted from the FWM spectra for $(\rightarrow\uparrow\rightarrow)$ polarization (see Fig. 1d). The respective $\Gamma_{\mathrm{X}}$ gives rise to the increasing spectral width of the transitions with decreasing well width. An increasing $E_{\mathrm{XX}}/R_y^*$ with increasing localization is observed (see Fig. 2c). This results from a quenching of the zero-point kinetic energy of the exciton-exciton motion in the biexciton

[16, 17]. Simultaneously, the repulsion energy $E_{XX^*}$ increases by approximately the same amount. This is due to the finite splitting between the ground and excited state of the exciton center-of-mass motion in the localization potential. The oscillator strength of the X-XX* transition is decreasing relative to the X-XX transition in the strong localization case $\Gamma_X \geq E_{XX}$. We attribute this to the lower $\mathbf{K} = 0$ component of the excited localized exciton state.

## 4 Conclusions

In conclusion, we have shown that the optically active biexcitonic spectrum in quantum wells is strongly influenced by a localization potential, which is inevitably introduced by the interfaces. With increasing degree of localization, the binding energy of the bound state increases, and the unbound biexciton state (biexcitonic continuum) is quantized to higher energies. This also creates an inhomogeneous broadening of the bound and unbound biexcitons energies relative to the corresponding exciton energy. As a result, the biexcitonic four-wave mixing signal shows a fast decay in delay time due to the incomplete rephasing of the photon echo. This explains previously observed strong polarization dependence of the FWM dynamics at the excitonic transitions as due to biexcitonic interactions.

We want to acknowledge helpful discussions with D. Birkedal and P. Borri. The authors want to thank J. Riis Jensen and C.B. Sørensen, III-V Nanolab, for growing the high-quality GaAs samples. This work was supported by the Danish Ministries of Research and Industry in the framework of CNAST.

## References

[1] K. Bott *et al.*, *Phys. Rev. B* **48** 17418 (1993).
[2] K. H. Pantke *et al.*, *Phys. Rev. B* **47** 2413 (1993).
[3] K. Ferrio and D. Steel, *Phys. Rev. B* **54** R5231 (1996).
[4] A. Paul, J. Bolger, A. Smirl, and J. Pellegrino, *J. Opt. Soc. Am. B* **13** 1016 (1996).
[5] Y. Z. Hu *et al.*, *Phys. Rev. B* **49** 14382 (1994).
[6] H. Wang *et al.*, *Phys. Rev. B* **49** R1551 (1994).
[7] E. Mayer *et al.*, *Phys. Rev. B* **51** 10909 (1995).
[8] G. Finkelstein, S. Bar-Ad, O. Carmel, and I. Bar-Joseph, *Phys. Rev. B* **47** 12964 (1993).
[9] W. Schäfer *et al.*, *Phys. Rev. B* **53** 16429 (1996).
[10] V. Axt, G. Bartels, and A. Stahl, *Phys. Rev. Lett.* **76** 2543 (1996).
[11] T. Östreich, K. Schönhammer, and L. Sham, *Phys. Rev. Lett.* **74** 4698 (1995).
[12] J. Erland *et al.*, *Phys. Rev. B* **50** 15047 (1994).
[13] T. Saiki, M. Kuwata-Gonokami, T. Matsusue, and H. Sakaki, *Phys. Rev. B* **49** 7817 (1994).
[14] T. F. Albrecht *et al.*, *Phys. Rev. B* **54** 4436 (1996).
[15] W. Langbein *et al.*, *Phys. Rev. B* **55** R7383 (1997).
[16] W. Langbein and J. M. Hvam, *Phys. stat. sol. (b)* **206** 111 (1998).
[17] W. Langbein and J. M. Hvam, unpublished.
[18] W. Langbein, P. Borri, and J. Hvam, in *RDPS 98, Trends in Optics and Photonics Series*, edited by D. Citrin (Optical Society of America, Washington D.C., 1998), Vol. 18.
[19] K. Brunner *et al.*, *Phys. Rev. Lett.* **73** 1138 (1994).
[20] Y. Z. Hu, M. Lindberg, and S. W. Koch, *Phys. Rev. B* **42** 1713 (1990).
[21] U. Woggon *et al.*, *Phys. Rev. B* **47** 3684 (1993).
[22] M. Ikezawa, Y. Masumoto, T. Takagahara, and S. V. Nair, *Phys. Rev. Lett.* **79** 3522 (1997).

[23] Y. Z. Hu *et al.*, *Phys. Rev. Lett.* **64** 1805 (1990).
[24] M. D. Webb, S. T. Cundiff, and D. G. Steel, *Phys. Rev. Lett.* **66** 934 (1991).
[25] H. Schneider and K. Ploog, *Phys. Rev. B* **49** 17050 (1994).
[26] M. Wegener, D. Chemla, S. Schmitt-Rink, and W. Schäfer, *Phys. Rev. A* **42** 5675 (1990).
[27] P. Borri *et al.*, *Phys. stat. sol. (a)* **164** 61 (1997).
[28] W. Langbein, P. Borri, and J. M. Hvam, unpublished.
[29] W. Langbein, P. Borri, and J. M. Hvam, *IQEC 1998 OSA Technical Digest Series* (Optical Society of America, Washington D.C., 1998).
[30] D. Bennhardt *et al.*, *Phys. Rev. B* **47** 13485 (1993).
[31] S. T. Cundiff, *Phys. Rev. A* **49** 3114 (1994).

Ioffe Institute
6th Int. Symp. "Nanostructures: Physics and Technology"
St Petersburg, Russia, June 22–26, 1998.



# Excitons in semiconductor quantum wires crystallized in transparent dielectric matrix

*V. Dneprovskii*†, T. Kobayashi‡, E. Mulyarov§, S. Tikhodeev§ and E. Zhukov†
† Physics Faculty, Moscow State University, 119899 Moscow
‡ Department of Physics, Tokyo University, Japan
§ Institute of General Physics, 117942 Moscow, Russia

Linear and nonlinear absorption of excitons with binding energies exceeding 100 meV has been observed at room temperature in GaAs, CdSe and InP quantum wires (QWRs) crystallized in transparent dielectric matrix (in crysotile asbestos nanotubes). The peculiarities of linear and nonlinear absorption have been explained by exciton transitions and by phase space filling of excitons in QWRs. The increase of the binding energy of excitons in QWRs arises no only due to quantum confinement but also due to dielectric enhancement of excitons [1].

As it is shown in [2]–[4] exciton transitions dominate in semiconductor QWRs — the abnormally strong concentration of oscillator strength becomes apparent at the frequencies of exciton transitions.

The existing methods of semiconductor QWRs fabrication do not allow to prepare samples with a suitable volume and density of nanostructures for optical absorption and nonlinear optical absorption measurements without application of a near field optical microscope. We have used the samples prepared by the method [5], [6] that allows to fabricate the samples with high density of QWRs. The molten semiconductor material was injected and crystallized in the hollow cylindrical channels of crysotile asbestos nanotubes. The measured diameter of this channels is 4.8 nm (for most of them) and 6 nm. The sample is a regular close packed structure of parallel crysotile asbestos transparent 30 nm diameter nanotubes filled with ultrathin crystalline GaAs, CdSe or InP wires.

The linear absorption spectra of QWRs crystallized in crysotile asbestos nanotubes are presented in Fig. 1. We attribute the absorption bands ("hills") of these spectra to exciton absorption in QWRs and the background to the absorption of the bulk semiconductor (part of the semiconductor material was crystallized between the nanotubes of crysotile asbestos). The measured energies of exciton transitions in QWRs (heavy hole–electron, light hole–electron excitons in GaAs and InP QWRs; the holes of A and B bands - electron excitons in CdSe QWRs) correspond to those calculated (arrows in Fig. 1) using a variational technique accounting for the effect of dielectric enhancement in the cylindrical QWRs. The calculated binding energies of excitons in QWRs surrounded by dielectric matrix (crysotile asbestos) exceed 100 meV.

The increase of the binding energies of excitons in QWRs crystallized in dielectric matrix compared to the bulk semiconductor, two-dimensional system and one-dimensional semiconductor surrounded by another semiconductor with nearly the same dielectric constant arises not only due to the quantum confinement but also due to the dielectric enhancement. The attraction between electron and hole becomes stronger because of the great difference in dielectric constants of semiconductor QWR and di-

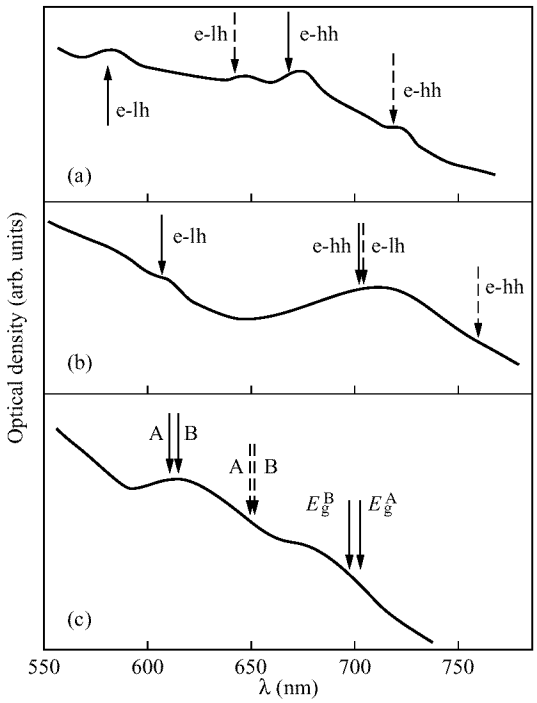


**Fig 1.** Linear absorption spectra for GaAs (a), InP (b) and CdSe (c) semiconductor quantum wires, crystallized in crysotile asbestos nanotubes. The calculated values of the energies of exciton transitions are shown by arrows for quantum wires with 4.8 nm diameter (full line) and 6 nm (dashed line).

electric matrix. The great broadening of exciton absorption bands arises probably due to the size dispersion of crystallized QWRs (inhomogeneous broadening).

Picosecond laser spectroscopy method (pump and probe technique — the measurement of differential transmission (DT) spectra using picosecond continuum as a probe beam) has been applied to investigate the physical processes leading to strong dynamic nonlinearities in semiconductor QWRs. It has allowed to exclude the background caused by the linear absorption of the bulk semiconductor and to distinguish the changes of transmission that arise in the case of high density of the excited excitons. The DT spectrum of CdSe QWRs crystallized in crysotile asbestos nanotubes is presented in Fig. 2 for different delay $\Delta t$ between the pumping and probing pulses. Two bands of nonlinear absorption are strongly pronounced in DT spectra. We attribute the high energy band and its red shift at higher excitation to the saturation of the exciton transitions in CdSe QWRs and to the renormalization of the one-dimensional energy gap [7]. The bleaching of the low energy band and its blue shift may be attributed [8] to the Mott transition in the bulk CdSe (the vanishing of excitons due to the screening or phase space occupation) and gap shrinkage together with dominating band filling (Bursstein-Moss effect).

The dominant effect responsible for the observed bleaching of the exciton absorption in the investigated semiconductor QWRs has been revealed — phase space filling.

The great binding energies of excitons in QWRs crystallized in transparent dielectric,

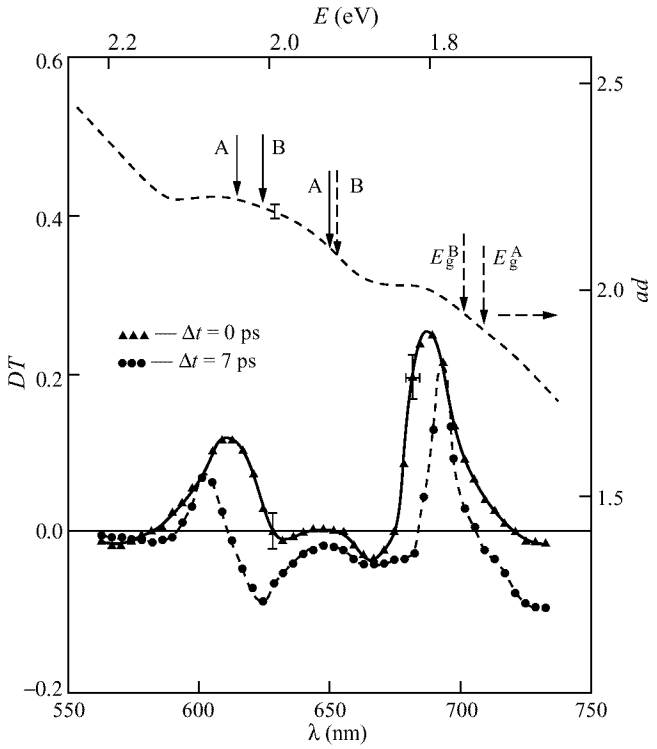


**Fig 2.** The linear and differential transmission spectra for CdSe quantum wires crystallized in crysotile asbestos nanotubes.

the possibility to change the energies of exciton transitions by changing the diameter of QWR, strong and fast exciton nonlinearity open new possibilities for the creation of "excitonic" optoelectronic devices that may operate at room temperatures.

This research was made possible in part by Grants 96-2-17339, 97-2-17600 of the Russian Foundation for Fundamental Research and Grants 97-1083, 97-1072 of the Russian Ministry of Science program "Physics of Solid Nanostructures". We thank V. Poborchii and S. Romanov for the samples of nanostructures crystallized in crysotile asbestos, N. Kisilev and D. Zaharov for the measurements with electron microscope.

## References

[1] Mulyarov E. A. and Tikhodeev S. G. *JETP* **84** 151 (1997).
[2] Ogawa T. and Takagahara T. *Phys. Rev.* **B43** 14325 (1991).
[3] Ogawa T. and Takagahara T. *Phys. Rev.* **B44** 8138 (1991).
[4] Glutch S., Chemla D.S. *Phys. Rev.* **B53** 15902 (1996).
[5] Poborchii V. V., Ivanova M. S., Salamatina I. A. *Superlat. and Microstr.* **16** 133 (1994).
[6] Dneprovskii V., Gushina N., Pavlov O., Poborchii V. V., Salamatina I. and Zhukov E. *Phys. Lett.* **A 204** 59 (1995).
[7] Benner S. and Haug H. *Europhys. Lett.* **16** 579 (1991).
[8] Egorov V. D., Hoang Xuann Nguyen, Zimmermann R., Dneprovskii V. S., Kashke M. and Khechinashvili D. S. *phys. stat. sol. (b)* **159** 403 (1990).

Ioffe Institute
6th Int. Symp. "Nanostructures: Physics and Technology"
St Petersburg, Russia, June 22–26, 1998.



# Electric field dependent dimensionality of excitonic states in single quantum well structures with asymmetric barriers

*Yu. A. Aleshchenko*, I. P. Kazakov, V. V. Kapaev, Yu. V. Kopaev and A. E. Tyurin
P. N. Lebedev Physics Institute of RAS, 117924 Moscow, Russia

**Abstract.** 2D–3D transformation of excitonic states dimensionality with an external electric field parallel to the growth axis has been observed in GaAs/$Al_xGa_{1-x}As$ single quantum well (QW) structures with asymmetric barriers. When the maximum of electronic wavefunction shifts to the lower barrier with field, the exciton binding energy starts to decrease. With further increase of field the transformation of 2D exciton to the quasi-3D exciton takes place. The latter involves a heavy hole in QW and an electron of resonant above-barrier state.

## Introduction

The dispersion law $E(k)$ for single QW structure with asymmetric barriers has been theoretically studied in our previous paper [1]. It was shown that the localized state of electron exists only within the limited region of wave-vectors $(0, k_c)$ in the layer plane. At $k = k_c$ 2D–3D transformation of electronic states dimensionality takes place and it is possible to control $k_c$ value and consequently the dimensionality of states by electric field.

In this paper the experimental confirmation of this effect is obtained by photoluminescence (PL) spectroscopy.

## 1 Samples and experimental procedure

Undoped QW of $d = 10$, 4 or 3 nm width inserted between top $Al_{0.4}Ga_{0.6}As$ and bottom $Al_{0.06}Ga_{0.94}As$ barriers of 10 and 30 nm width, respectively, were grown by MBE on semiinsulating GaAs substrates with 250 nm thick GaAs buffer layer. The QW widths were chosen so that in the former two cases ($d = 10$, 4 nm) the electron confined state in the well existed without external electric field while in the structure with 3 nm QW the electron state was no longer confined. One should expect in the latter case the 2D–3D dimensionality transformation of electronic state and corresponding exciton. The possibility to apply the electric field to the structure was provided by insertion of $n^+$GaAs:Si layer of 50 nm in thickness after the buffer layer as a bottom electrode and by doping of top GaAs layer with Si impurity. The active layers of the structure were inserted between top and bottom $n^+Al_xGa_{1-x}As$:Si spacers with $x$, thickness and doping level of 0.4, 30 nm, $6.5\times10^{17}$ $cm^{-3}$ and 0.06, 25 nm, $(3-6)\times10^{16}$ $cm^{-3}$, correspondingly. The doping levels of spacers were choosen to satisfy the flat band conditions without external electric field.

The PL spectra were excited at 80 K by 488 nm line of $Ar^+$ laser with the power density on the sample lower than 40 W/$cm^2$. The spectra were analyzed by 0.82 m double grating spectrometer and detected by photomultiplier in photon counting mode.

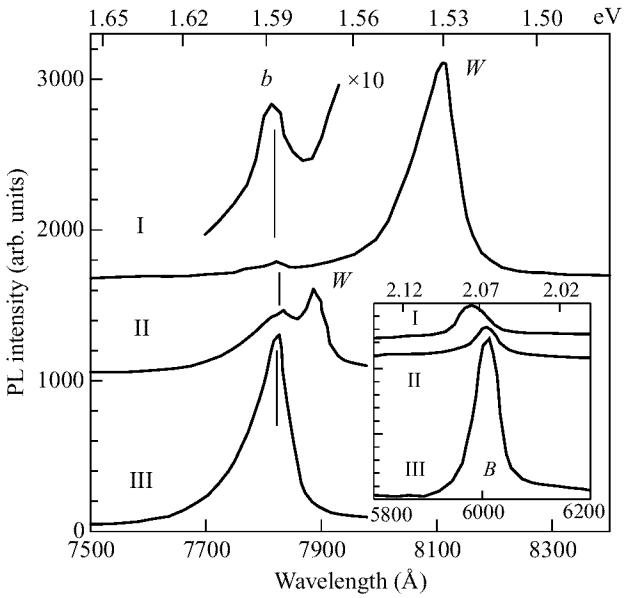


**Fig 1.** PL spectra of structures with $d = 10$ (I), 4 (II) and 3 (III) nm. The shortwavelength parts of respective spectra are shown in the inset.

## 2 Experimental results

The PL spectra of the structures with $d = 10$, 4 and 3 nm are shown in Fig. 1. The common features in the photoluminescence spectra of these structures near 1.585 and 2.07 eV are due to the contributions of lower and higher barriers respectively. Besides these features an intense peak of excitonic transition between the first space-quantized sublevels of heavy hole valence and conduction bands appears in the spectrum of the structure with 10 nm QW. Upon narrowing QW width down to 4 nm this peak loosens its intensity, broadens and shifts to the peak of lower barrier since the electron sublevel appears to be near the QW edge from the side of lower barrier. As for the structure with $d = 3$ nm the excitonic peak of QW is not detected and the corresponding 2D electron state doesn't exist.

In order to trace the excitonic state evolution with monotonous variation of lower barrier height a semitransparent top metallic electrode was evaporated on the sample with $d = 4$ nm and the contacts were prepared to it and to the $n^+$ buffer layer. As the negative voltage is applied to the top electrode the height of lower barrier decreases and the electronic state moves to the top of the barrier. The peak of corresponding 2D exciton in its turn moves to lower energies (curve $W$ in Fig. 2) with the decrease of applied voltage. According to our calculations 2D electron state must dies out in fields corresponding to the voltage of $-0.5$ V, but excitonic peak under discussion still persists in the spectra. The point is that along with the shallowing of QW for electron the well becomes deeper for hole and hole localization increases with field. The Coulomb field of such hole localizes the electron and leads to the increase of effective depth of QW for the latter by few eV. This effect however can't explain the retention of excitonic state at

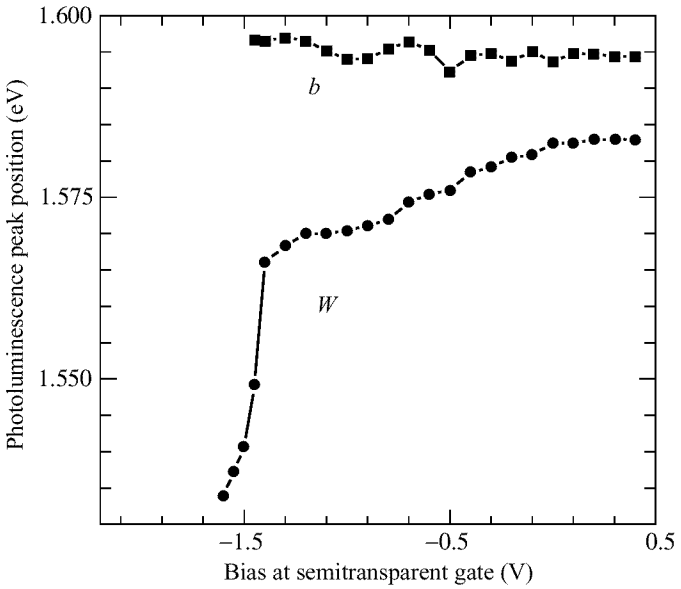


**Fig 2.** Experimental biass dependences of excitonic peak positions for lower barrier ($b$) and QW ($W$).

voltages lower than $-0.6$ V. In the voltage range of $-0.6 \div -1.4$ V the biass dependence of exciton peak energy becomes flat. This dependence steepens after $-1.4$ V which is inherent for indirect transitions. The electric field breaks QW exciton in the region of $-1.6$ V while the 3D exciton of lower barrier is ruptured earlier at the voltage of $-1.45$ V (curve $b$).

## 3 Theory

For theoretical interpretation of the experimental results the Schroedinger equation for electron and hole with their Coulomb interaction was numeriaclly solved using the variational method. To take into account the above-barrier states, the model of quasi-continuous spectrum formed by the artificial infinite barriers was used (the barriers are situated well away from the QW).

The variational function was chosen as:

$$\Psi_{\text{ex}}(z_h, z_e, \rho) = \sum_{m=1}^{\infty} a_m \Psi_m^e(z_e) \Psi^h(z_h) \exp(-\alpha\rho),$$

where $\Psi_m^e(z_e)$—the wave function of the $m$-state of electron spectrum, $\Psi^h(z_h)$—hole wave function, $\alpha$—variational paramenter. Using this function allows one to take into account the hole Coulomb effect on the electron spectrum. The calculations show that the localized states of the electron and the hole are bound in 2D-exciton with the binding energy of $\sim 8$ meV without external field. With the decrease of the voltage applied to the structure the exciton binding energy is reduced.

Approximately at $U_c = -0.6$ V the electron state localized in the well rises above lower barrier top and the exciton becomes indirect quasi-3D couple. The transitions

from the H1 hole state occure to the continuous spectrum on the electron quasi-level defined by the maximum of overlap integral between the linear combination of the electron wave functions related to the continuos spectrum and the localized heavy hole state. The behaviour of QW exciton at voltages above $U_c$ $(-0.6 \div -1.6\ \mathrm{V})$ is consistent with the existence of electron above-barrier localized states. The latter are related to the resonances in the continuos spectrum because of reflections at the heterointerface of $Al_{0.06}Ga_{0.94}As$ and the lower contact layer of $n^+GaAs$.

*Acknowledgements*

This work has been supported in part by the Russian Foundation for Basic Research and Russian Programme "Physics of Solid State Nanostructures".

## References

[1] Kapaev V. V. and Kopaev Yu. V. *JETP Lett.* **65** 202 (1997).

Ioffe Institute
6th Int. Symp. "Nanostructures: Physics and Technology"
St Petersburg, Russia, June 22–26, 1998.



# Dynamic properties of excitons in GaAs/AlAs superlattices from optically detected magnetic resonance and level anticrossing

P. G. Baranov†, *N. G. Romanov*†, A. Hofstaetter‡, B. K. Mayer‡, A. Scharmann‡, W. von Foerster‡, F. J. Ahlers§ and K. Pierz§
† Ioffe Physico-Technical Institute, RAS, 194021 St. Petersburg, Russia
‡ 1. Physics Institute, University of Giessen, Heinrich-Buff-Ring 16, D 35392 Giessen, Germany
§ Physikalische-Technische Bundesanstalt, Braunschweig, Germany

**Abstract.** Level-anticrossing measurements in linearly polarized light and ODMR recorded with different microwave chopping frequencies allowed to distinguish between excitons with different dynamic properties and to study their spectral variations in type II GaAs/AlAs superlattices.

## Introduction

Optical detection of magnetic resonance (ODMR) and exciton level-anticrossing (LAC) allowed exact determination of electron and hole $g$-factors and direct measurements of the exciton exchange splittings in both type II and type I GaAs/AlAs superlattices (SL) with sub-$\mu$eV resolution (see [1-3] and references therein). The obtained experimental dependencies can be applied for characterization of the SL period and the QW width [4]. A direct link between the order of the exciton radiative levels and the interface, normal (AlAs on GaAs) or inverted (GaAs on AlAs), was established in [5]. The lowest radiative level is [110]-polarized for excitons at the normal interface and $[1\bar{1}0]$-polarized for excitons at the inverted interface. This made possible separate investigations of the opposite interfaces in type II SL [6].

Since both ODMR and LAC signals are sensitive to the interplay of optical and microwave pumping, radiation and relaxation rates, these techniques can be applied to a study of exciton dynamics . In the present paper, we report on a LAC and ODMR study which demonstrates a variation of dynamic properties of excitons in type II SLs as a function of the emission energy and exciton localization.

## 1 Experimental results and discussion

Three SLs with the same nominal composition (1.73 Å GaAs/2.65 Å AlAs) were grown by MBE with the substrate kept at 620°C both without interruptions (sample P90) and with 30 s interruptions after AlAs layers (P91) and GaAs layers (P92). The actual composition of the samples was controlled by ODMR and Raman characterization. LAC was recorded by monitoring the [110] and $[1\bar{1}0]$ components of emission. 24 and 35 GHz ODMR spectra were obtained by monitoring microwave-induced variations of one of circularly polarized components of luminescence with chopping of microwaves at 10 Hz–100 kHz and a lock-in detection.

At anticrossing of a highly populated non-radiative level with a depopulated radiative one exciton emission with the polarization corresponding to the radiative level increases

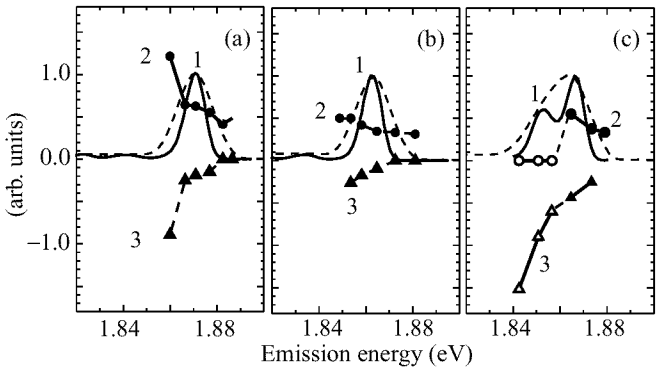


**Fig 1.** Emission spectra (curves 1), the ratio of the amplitude of "direct" LAC signals of the excitons localized at the normal interface to that for excitons localized at the inverted interface (curves 2) and the ratio of "indirect" to "direct" LAC amplitudes for excitons localized at the inverted interfaces (curves 3) in samples P90 (a), P91 (b) and P92 (c). $T = 1.6$ K.

giving rise to a positive LAC signal which we call "direct". At the same time population of the another radiative level with the opposite polarization can decrease due to relaxation, which produces a negative "indirect" LAC. Existence of such LAC signals [6] follows from the solution of rate equations derived in [7]. Fig. 1 shows emission spectra (curves 1), the ratio of the amplitudes of "direct" LAC signals for excitons localized at the normal interface to that for excitons localized at the inverted interface (curves 2) and the ratio of "direct" and "indirect" LAC signals (curves 3) for the samples P90, P91, P92. In the latter case the ratio is negative. Dotted lines are the emission spectra taken with a reduced spectral resolution which was used while detecting LAC.

Curves 2 in Fig. 1(a,b,c) show that in all samples excitons are preferentially localized at the inverted interface, the relative concentration of excitons at the normal interface increases with the decrease of the emission energy. The ratio of the normal to inverted excitons in the centre of the emission lines are 0.6 for P90 and 0.35 for P91. For low- and high-energy emission lines in P92 the ratio is about 0 and 0.5, respectively, i.e. there is no or very few excitons localized at the normal interface within the low energy emission line. Curves 3 in Fig. 1 (a,b,c) reveal changes in the interplay of the radiation and relaxation times. The effect of relaxation between the exciton levels which produces indirect LAC is more pronounced at the low-energy side of the emission lines in P90 and P91. The relaxation effects are the largest for the low-energy line of P92.

Different dynamic properties of excitons in SL grown with interruptions after GaAs layers were confirmed by ODMR. Fig. 2 shows ODMR recorded in P92 by monitoring $\sigma^+$ and $\sigma^-$ — emission components with microwave chopping frequencies $f = 200$ Hz and 100 kHz. Two ODMR lines marked as "exc." correspond to exciton electron spin-flips and are split by the exchange interaction [1-3]. The line in the center ("e") belongs to electrons in distant electron-hole pairs [1, 2]. Microwave-induced resonant transitions between a more populated non-radiative exciton level and a depopulated radiative one increase emission from the latter (see inset in Fig. 2). At low chopping frequency magnetic resonance is detected as variation of both circularly polarized components of emission since due to relaxation "indirect" ODMR signals are observed. At high

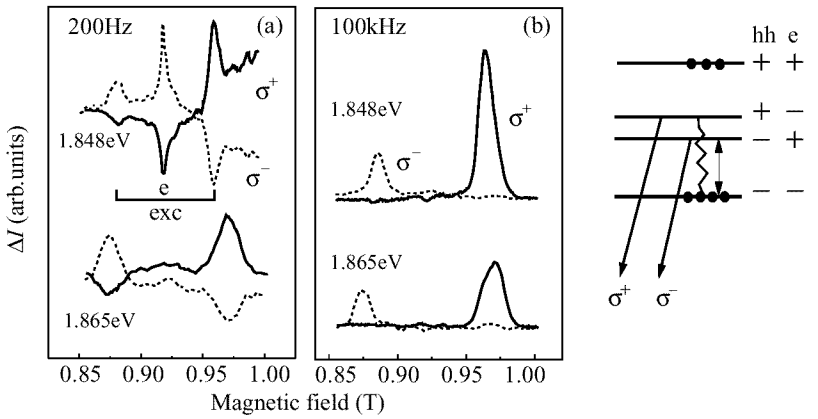


**Fig 2.** ODMR for two luminescence lines in P92 recorded with the microwave chopping frequency 200 Hz (a) and 100 kHz (b) by monitoring the intensity of two circularly polarized emission components. Inset shows the exciton energy levels and resonant transition for low-field exciton ODMR line. $\nu = 24$ GHz. B // [001].

chopping frequency ODMR is manifested in one polarization as expected in case of slow relaxation.

By choosing an appropriate microwave chopping frequency one can separate exciton and electron-hole recombination. Electron ODMR signal disappears at $f > 1{-}2$ kHz which implies longer radiative and relaxation times of such a recombination. 35 GHz ODMR of exciton holes was detected at $f = 390$ Hz and microwave power 400 mW while only "unbound" hole ODMR was seen at lower power (10 mW).

The high-field ODMR signals of excitons obtained with $f = 10$ kHz are shown in Fig. 3(a). ODMR recorded within the emission line 1.865 eV is a superposition of two signals which belong to excitons localized at the normal and inverted interfaces. For both excitons there is no "indirect" ODMR in $\sigma^-$ polarization. This means that the relaxation times are larger than the radiative times and modulation period. The low-energy emission line 1.848 eV belongs to excitons localized at the inverted interface in the region of monolayer-step GaAs islands [6]. The behavior of ODMR of these excitons is different: "indirect" ODMR disappears for $f > 30$ kHz only. This implies that for such excitons hole relaxation is much faster in agreement with the results of measurements of the "indirect" LAC signals. The reason of such a different behavior is still not completely understood and requires further studies.

Spectral dependencies of ODMR are shown in Fig. 3(b). Although the resonance fields for excitons "norm" and "inv1" coincide it is possible to resolve their emission lines since there is no ODMR in $\sigma^-$-polarization for excitons "norm".

In conclusion, LAC measurements in linearly polarized light and ODMR recorded with different microwave chopping frequencies allowed to distinguish between excitons with different dynamic properties and to study their spectral variations in type II GaAs/AlAs SL. A drastic difference in the exciton localization at normal and inverted interfaces and their dynamic behavior was found for excitons in a SL grown with interruptions after GaAs layers. Exciton and electron-hole recombination was resolved due

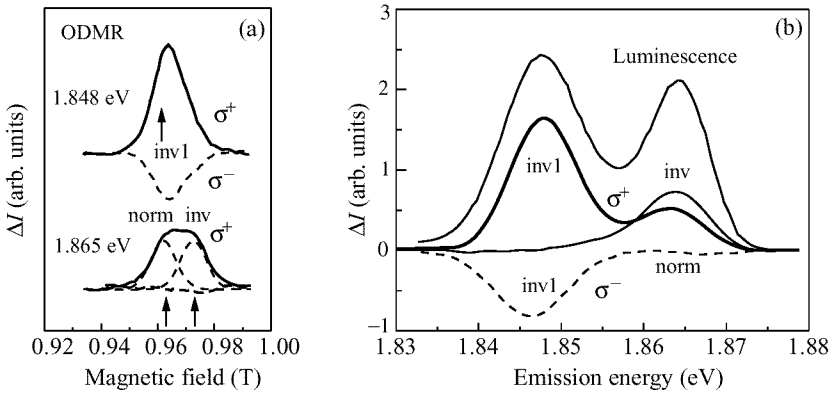


**Fig 3.** (a) ODMR recorded with chopping at 10 kHz by monitoring two circularly polarized emission components within the peaks of emission lines in P92; (b) spectral variations of the ODMR signals.

to their different characteristic times. Time-resolved ODMR measurements in which ODMR is detected with a time delay relative to the light excitation pulse seem to be very promising for an investigation of exciton dynamics and are in progress.

This work was supported in part by the Volkswagen foundation under grant No. I/70958 and the Russian Foundation for Basic Research under grant No. 96-02-16927.

## References

[1] van Kesteren H.W., Cosman E.C., van der Pool W.A.J.A., and Foxon C.T. *Phys. Rev.* **B41** 5283 (1990).

[2] Baranov P.G., Mashkov I.V., Romanov N.G., Lavallard P., and Planel R. *Solid State Commun.* **87** 649 (1993).

[3] Baranov P.G. and Romanov N.G. in: *The Physics of Semiconductors* ed. J. Lockwood (World Scientific, 1994) v. 2, p. 1400.

[4] Baranov P.G., Romanov N.G., Mashkov I.V., Khitrova G.B., Gibbs H.M. and Lunges O. *Phys. Solid State* **37** 1648 (1995)

[5] Baranov P.G., Mashkov I.V.,Romanov N.G., Gourdon C., Lavallard P. and Planel R. *JETP Letters* **60** 445(1994).

[6] Baranov P.G., Romanov N.G., Hofstaetter A., Scharmann A., Schnorr C., Ahlers F.J., and Pierz K. *JETP Letters* **64** 754 (1996).

[7] Ivchenko E.L. and Kaminski A.Yu. *Fiz. Tverd. Tela* **37**, 1418 (1995).

Ioffe Institute
6th Int. Symp. "Nanostructures: Physics and Technology"
St Petersburg, Russia, June 22–26, 1998.



# Spectroscopic and structural aspects of femtosecond dynamics of reflectivity of AlGaAs/GaAs superlattices

Yu. K. Dolgikh†, S. A. Eliseev†, Yu. P. Efimov‡, A. A. Fedorov†, I. Ya. Gerlovin†, G. G. Kozlov†, *V. V. Ovsyankin*†, V. V. Petrov‡, B. V. Stroganov† and V. S. Zapasskii†

† S. I. Vavilov State Optical Institute, 199034 St. Petersburg, Russia
‡ Institute of Physics, St. Petersburg State University, 198904 Russia

**Abstract.** In this paper, we present results of studying dynamics of nondegenerate (two-colour) photoreflection of the AlGaAs/GaAs superlattices. These results show unique potential of these methods (i) for identification of sources of inhomogeneous broadening of optically-active 2D excitons, (ii) for analysis of fine structure of excitonic states hidden in inhomogeneous broadening, and (iii) for determination of spectral distribution of probability of radiative annihilation of 2D excitons and its relation to structural disorder.

## Spectroscopy of quantum beats in 2D excitonic states

Beginning from the pioneering works [1, 2], the spectroscopy of quantum beats (SQB) has occupied a stable position in the row of other methods of the superhigh-resolution spectroscopy [3], its merits being mostly associated with its capability of revealing the structure of excited-states hidden in the inhomogeneously (Doppler- or statically) broadened bands.

For the SL, the ability of the SQB to detect hidden structure of the states can be interestingly revealed in the interference of the "bright" (B) ($J = 1$) and "dark" (D) ($J = 2$) HH-excitons. The structural defects induce an anisotropic potential of localization, which causes splitting of levels of the localized excitons [4, 5]. Thus, the spectrum of the quantum beats of a uniform ensemble of localized HH-excitons may contain up to six different frequencies. Preparation of coherent superposition of the B-and D-excitons with comparable amplitudes by direct optical excitation is impossible because of huge difference between dipole moments of the corresponding transitions. However, it can be produced by populating these states via recombination from optically excited states of the 2D (e-h)-continuum provided that this mechanism is characterized by the rates much higher than the highest frequencies of the quantum beats. The ac component of the differential reflectivity excited by this way, and the Fourier-transform (spectrum) of the quantum beats for the $SL = 30 \times (7\,\text{nm}\,Ga_{0.7}Al_{0.3}As/7\,\text{nm}\,GaAs)$ grown by the MBE technique with no growth interruption are shown on Fig. 1.

A number of conclusions of principal importance can be drawn based on qualitative analysis of these results. First of all, interest is the fact itself that the quantum beats are detected in the subsystem of the "bright" and "dark" states. This, to the best of our knowledge, is, basically, the first direct observation of the process of quantum relaxation of states, having no alternative relaxation chanals. The second conclusion is that though the structure under study was grown with no smoothing of the hetero-interfaces, it contains a rather limited number of exciton-localizing potentials, which corresponds, as

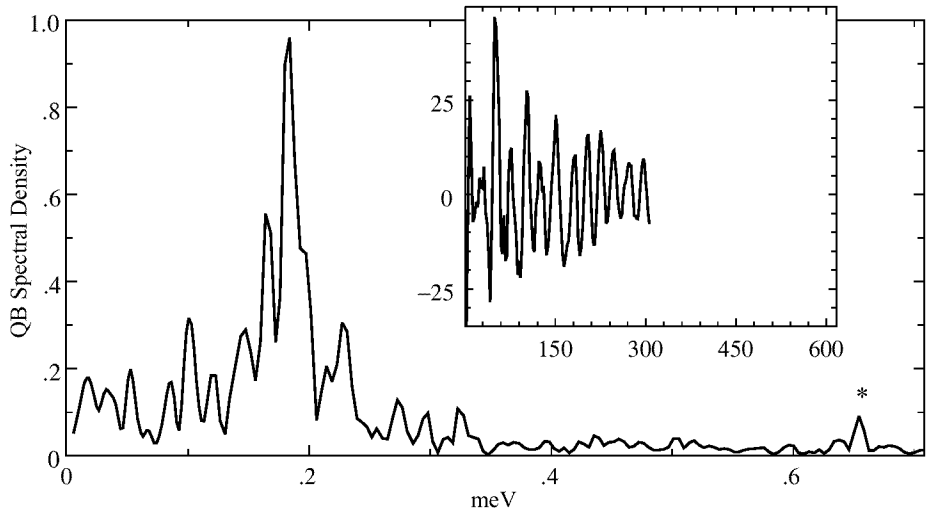


**Fig 1.** Ac component of the differential reflectivity and its Fourier-transform.

we belive, to few types of structural defects. The value of the symmetric exchange coupling $\approx 0.17$ meV. The values of the asymmetric exchange splitting strongly depend on structure of the localizing defect and lie in the range between 0.015 and 0.08 meV. The third conclusion, which we consider to be also of great importance is that in the structures of this type the irreversible dephasing of the excitons at $T < 10$ K is determined only by the energy relaxation ($\Gamma_2 = 0.5\Gamma_1$). This conclusion is based on the fact that the quantum beats of the photoreflectivity are damping in parallel with population decay of the excitonic states (see below). And, finally, one should pay attention to the fact that the first mode of SL splitting (0.65 meV) of HH-excitons is noticable in QB spectrum. It means that rate of phonon assistant transition with this energy is less than radiative relaxation rate of localized HH-excitons ($\sim 3 \cdot 10^9\,\mathrm{sec}^{-1}$).

## Distribution of the radiative transition rates and coherence radii of HH-excitons in the GaAlAs/GaAs superlattices

For ideal GaAlAs/GaAs SL-structures, the radiative relaxation rates are expected to lie in the range of $10^{11}-10^{12}\,\mathrm{sec}^{-1}$ [6, 7]. In real structures, the elastic scattering of 2D-excitons by impurities, fluctuations of composition, and nonuniformities of hetero-interfaces leads to smearing of low-frequency edge of the excitonic states density and confines their spatial coherence. In this case, the oscillator strengths of polaritons, which would concentrate, in ideal structures, in excitons with small 2D wave vectors $k_{\mathrm{ex}} \leq k_{\mathrm{phot}}$, appear to be distributed over a wider range of the lower excitonic states [8]. The function of distribution of the oscillator strengths $G(f)$ is a highly important characteristic of optical susceptibility and at the same time, as will be shown below, can characterize the quality of the SL-structure much more accurately and specifically then the HH-exciton's absorption bandwidth widely used for this purpose. The function $G(f)$ can be determined by any method which allows to measure evolution of population of optically active excitonic states generated under their resonance excitation with

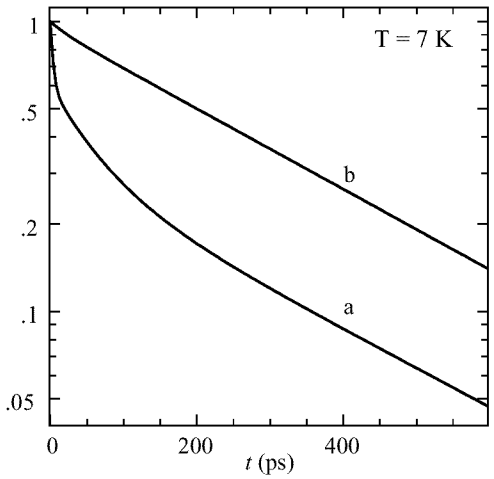


**Fig 2.**

no cascade-type population processes, which may involve rather long-lived intermediate states. In the method of nondegenerate differential photoreflection, this problem is solved by superposing the frequency of the pump fsec pulse onto the HH-exciton's absorption band maximum and by shifting the probe pulse frequency to long-wavelength side. For orthogonal polarizations of the pump and probe light pulses, the signal of the differential photoreflection is controlled by two processes with characteristic dependences on time delay between the pulses $t_D$. A part of the signal, we are interesting in, proportional to $\rho_{ex}(t)$, characterizes amplitude variation of coherent scattering of the probe beam due to the pump-induced changes of population of the excitonic states. The second process is related to non-scalar interaction controlling the coherent four-photon scattering.

Its dependence on $t_D$ virtually coincides with the correlation function squared $K_{12}(t_D)$ of the pump and probe fields. Both signals can be easily extracted from experimental curve $\delta R(t_D)$ using the functional equality: $\rho_{ex}(t) \propto \delta R(t_D) - \text{const}|K_{12}(t_D)|^2$. The dependences $\rho_{ex}(t)$ obtained by this way for two SL (the nominaly pure $SL_1$-(a) and Fe-doped $SL_2$-(b)) and its multi-exponential fits:

$$\rho(t) \propto \sum_{i=1}^{3} A_i \exp(-\Gamma_1^i t) \tag{1}$$

are shown in Fig. 2.

Where $A_1 = 0.41$, $A_2 = 0.32$, $A_3 = 0.27$ for $SL_1$ and $A_1 = 0$, $A_2 = 0.05$, $A_3 = 0.95$ for $SL_2$, $\Gamma_1^1 = 2.6 \cdot 10^{11}$, $\Gamma_1^2 = 1.7 \cdot 10^{10}$, $\Gamma_1^3 = 3 \cdot 10^9\,\text{sec}^{-1}$. We will interprete these results based on the simplest model of 2D excitons in systems with structural disorder and associate the lowest rate observed in the experiment ($\Gamma_{1\min} = 3 \cdot 10^9\,\text{sec}^{-1}$) to radiative rate of the localized excitons with coherence radius $R_{coh} \approx a_B = 12$ nm. In this model, the ratio of the rates $\Gamma_{1i}/\Gamma_{1\min}$ is determined by the ratio of areas of optical coherence of the corresponding states: $(R_{coh}/a_B)^2$. Thus the higest rate observed in experiment $\Gamma_{1\max} = 2.6 \cdot 10^{11}\,\text{sec}^{-1}$ should be associated with excitons

having $R_{coh} = 9a_B$. The weights $A_i$ evidently specify relative amount of the structure's sites which form the states with a given $\Gamma_1^i$.

Work was supported by RFBR.

## References

[1] E. B. Alexandrov, *Optika i Spectroskopiya* **17** 957 (1964).
[2] J. N. Dodd, R. D. Kaul, D. M. Warrington, *Proc. Phys. Soc.* **84** 176 (1964).
[3] S. Haroche,in "High Resolution Laser Spectroscopy", ed. K. Shimoda, Springer, Heidelberg (1976), p. 256.
[4] E. Blackwood, M. J. Snelling, R. T. Harley, S. R. Andrews, C. T. B. Foxon, *Phys. Rev. B* **50** 14246 (1994).
[5] D. Gammon, E. S. Snow, B. V. Shanabrook, D. S. Kaster, and D. Park, *Phys. Rev. Lett.* **76** 3005 (1996).
[6] V. M. Agranovich and O. A. Dubovskii, *JETP Lett.* **3** 223 (1966).
[7] L. C. Andreani,F. Tassone, and F. Bassani, *Solid State Commun.* **77** 641 (1991).
[8] A. V. Kavokin, *Phys. Rev. B* **50** 8000 (1994).

Ioffe Institute
6th Int. Symp. "Nanostructures: Physics and Technology"
St Petersburg, Russia, June 22–26, 1998.



# Exciton-polariton band structure in quantum-dot lattices

*E. L. Ivchenko*†, Y. Fu‡ and M. Willander‡
† Ioffe Physico-Technical Institute, 194021 St.Petersburg, Russia
‡ Physical Electronics and Photonics, Department of Microelectronics and Nanoscience, University of Gothenberg and Chalmers University of Technology, Fysikgränd 3, S-412 96 Göteborg, Sweden

**Abstract.** We develop a theory of exciton polaritons in three-dimensional quantum-dot lattices with the period comparable to the light wavelength. A system of the Maxwell equations and nonlocal material relation are used to derive the dispersion equation in a rather general and well-converging form. A possibility of analytical description of the dispersion is questioned and discussed. The photon band structure is calculated for a face-centered-cubic lattice with spherical dots of the radius exceeding the bulk-exciton Bohr radius. The dispersion along the $\Gamma - X$ and $\Gamma - L$ lines is characterized by a strong anticrossing between bare transverse photon and exciton branches and by remarkable overlapping band gaps. Approaching the $U$ and $W$ points the exciton-polariton branches converge and the gap becomes negligible.

Recently van Coevorden et al. [1] have calculated the optical band structure of a three-dimensional (3D) lattice of resonant two-level atoms. They have solved numerically the dispersion equation for light waves in a face-centered-cubic atomic lattice and demonstrated that, in the certain range of parameters, there exists an overlap of photonic band gaps in all directions in the frequency region near the two-level resonance. Here we consider the photonic (or more precisely, exciton-polaritonic) band structure of lattices formed by a 3D periodic array of quantum dots (QDs).

We start from the Maxwell equations

$$\Delta \mathbf{E} - grad\ div\ \mathbf{E} = -\left(\frac{\omega}{c}\right)^2 \mathbf{D}\ ,$$
$$div\ \mathbf{D} = 0 \qquad (1)$$

for the electric field **E** and the displacement vector **D**. The nonlocal material equation relating **D** and **E** is taken in the form (see [2])

$$\mathbf{D}(\mathbf{r}) = \varepsilon_b \mathbf{E}(\mathbf{r}) + 4\pi \mathbf{P}_{exc}(\mathbf{r})\ , \qquad (2)$$

$$4\pi \mathbf{P}_{exc}(\mathbf{r}) = T(\omega) \sum_{\mathbf{a}} \Phi_{\mathbf{a}}(\mathbf{r}) \int \Phi_{\mathbf{a}}(\mathbf{r}')\mathbf{E}(\mathbf{r}')d\mathbf{r}'\ . \qquad (3)$$

Here **a** are the lattice translation vectors enumerating quantum dots, $\Phi_{\mathbf{a}}(\mathbf{r}) = \Phi_0(\mathbf{r}-\mathbf{a})$ is the envelope function $\Psi_{exc}(\mathbf{r}_e, \mathbf{r}_h; \mathbf{a})$ of an exciton excited in the **a**th QD at coinciding electron and hole coordinates: $\Phi_{\mathbf{a}}(\mathbf{r}) = \Psi_{exc}(\mathbf{r}, \mathbf{r}; \mathbf{a})$. The other notations are

$$T(\omega) = 2\pi \frac{\varepsilon_b \omega_{LT} \omega_0 a_B^3}{\omega_0^2 - \omega^2}\ , \qquad (4)$$

$\omega_{LT}$ and $a_B$ are the exciton longitudinal-transverse splitting and Bohr radius in the corresponding bulk semiconductor, $\omega_0$ is the QD-exciton resonance frequency, $\varepsilon_b$ is the background dielectric constant which is assumed to coincide with the dielectric constant of the barrier material. In the following we neglect the overlap of exciton envelope functions $\Psi_{\mathbf{a}}$ and $\Psi_{\mathbf{a}'}$ with $\mathbf{a} \neq \mathbf{a}'$ so that excitons excited in different dots are assumed to be coupled only via electromagnetic field.

It follows from Eq. (2) that $div\ \mathbf{E} = -(4\pi/\varepsilon_b)\ div\ \mathbf{P}_{exc}$ which allows to rewrite the first Eq. (1) as

$$\Delta\mathbf{E} + k^2\mathbf{E} = -4\pi k_0^2 \left(1 + k^{-2} grad\ div\ \right) \mathbf{P}_{exc}\ , \tag{5}$$

where $k_0 = \omega/c$, $k = k_0 n_b = \omega n_b/c$ and $n_b = \sqrt{\varepsilon_b}$.

We seek for Bloch-like solutions of Eq. (5) satisfying the translational symmetry $\mathbf{E}_{\mathbf{K}}(\mathbf{r} + \mathbf{a}) = \exp(i\mathbf{K}\mathbf{a})\ \mathbf{E}_{\mathbf{K}}(\mathbf{r})$ where the wave vector $\mathbf{K}$ is defined within the first Brillouin zone. The exciton-polariton dispersion $\omega(\mathbf{K})$ can be shown to satisfy the equation

$$\mathrm{Det}||\delta_{\alpha\beta} - R_{\alpha\beta}(\omega, \mathbf{K})|| = 0\ , \tag{6}$$

where $\alpha, \beta = x, y, z$, $\delta_{\alpha,\beta}$ is the Kronecker symbol and, for QD lattices,

$$R_{\alpha\beta} = \frac{k_0^2 T(\omega)}{v_0} \sum_{\mathbf{b}} \frac{|I_{\mathbf{K}+\mathbf{b}}|^2 S_{\alpha\beta}(\mathbf{K}+\mathbf{b})}{|\mathbf{K}+\mathbf{b}|^2 - k^2}\ , \tag{7}$$

$$I_{\mathbf{Q}} = \int \Phi_0(\mathbf{r}) e^{i\mathbf{Q}\mathbf{r}} d\mathbf{r}\ ,\ S_{\alpha\beta} = \delta_{\alpha\beta} - \frac{Q_\alpha Q_\beta}{k^2}\ , \tag{8}$$

$\mathbf{b}$ are the reciprocal lattice vectors and $v_0$ is the volume of the lattice primitive cell.

Similarly to [1] we consider a face-centered-cubic lattice with the lattice constant $a$ and the unit-cell volume $v_0 = a^3/4$. It is convenient to introduce a dimensionless parameter $P = (\pi\sqrt{3}c/a\omega_0 n_b)^3$ and the dimensionless frequency $\Omega = \omega/\omega_0$. The calculation is performed for spherical QDs with the radius $R$ exceeding the Bohr radius $a_B$ in which case we have

$$I_{\mathbf{Q}} = \pi \left(\frac{2R}{a_B}\right)^{3/2} \frac{\sin QR}{QR[\pi^2 - (QR)^2]}\ . \tag{9}$$

Then Eq. (7) can be transformed into

$$R_{\alpha\beta}(\Omega, \mathbf{K}) = N \frac{\Omega^2}{\Omega^2 - 1} \sigma_{\alpha\beta}(\Omega, \mathbf{K})\ , \tag{10}$$

$$\sigma_{\alpha\beta}(\Omega, \mathbf{K}) = \sum_{\mathbf{b}} \frac{f(|\mathbf{K}+\mathbf{b}|R)\, S_{\alpha\beta}(\mathbf{K}+\mathbf{b})}{\Omega^2 - \Omega^2(\mathbf{K}+\mathbf{b})}\ , \tag{11}$$

$$N = \frac{64}{\pi} \frac{\omega_{LT}}{\omega_0} \left(\frac{R}{a}\right)^3\ ,\ f(x) = \left[\frac{\pi^2 \sin x}{x(\pi^2 - x^2)}\right]^2\ , \tag{12}$$

$\Omega(\mathbf{Q}) = cQ/\omega_0 n_b$. Eq. (6) is equivalent to the three separate equations $R_j(\Omega, \mathbf{K}) = 1$ where $R_j$ $(j = 1, 2, 3)$ are eigenvalues of the matrix $R_{\alpha\beta}$. For high-symmetry points of the Brillouin zone, the symmetry imposes certain relations between the $R_{\alpha\beta}$ components

**Table 1.** Dispersion equations written in terms of $R_{\alpha\beta}$ for different **K** points in the Brillouin zone.

| **K** $(2\pi/a)$ | Nonzero components of $R_{\alpha\beta}$ | Dispersion equations |
|---|---|---|
| $\Gamma$ $(0, 0, 0)$ | $R_{xx}$=$R_{yy}$=$R_{zz}$ | $R_{xx}$=1 |
| $X$ $(0, 0, 1)$ | $R_{xx}$=$R_{yy}$, $R_{zz}$ | $R_{xx}$=1, $R_{zz}$=1 |
| $L$ $(1/2, 1/2, 1/2)$ | $R_{\alpha\alpha}$=$R_{xx}$, $R_{\alpha\beta}$=$R_{xy}$($\alpha \neq \beta$) | $R_{xx} - R_{xy}$=1, $R_{xx}$+2$R_{xy}$=1 |
| $W$ $(1/2, 0, 1)$ | $R_{xx}$, $R_{yy}$=$R_{zz}$ | $R_{xx}$=1, $R_{yy}$=1 |
| $K$ $(3/4, 0, 3/4)$ | $R_{xx}$=$R_{zz}$, $R_{yy}$ , $R_{xz}$=$R_{zx}$ | $R_{xx}\pm R_{xz}$=1, $R_{yy}$=1 |
| $U$ $(1/4, 1/4, 1)$ | $R_{xx}$=$R_{yy}$, $R_{zz}$, $R_{xy}$=$R_{yx}$ | $R_{xx}\pm R_{xy}$=1, $R_{zz}$=1 |

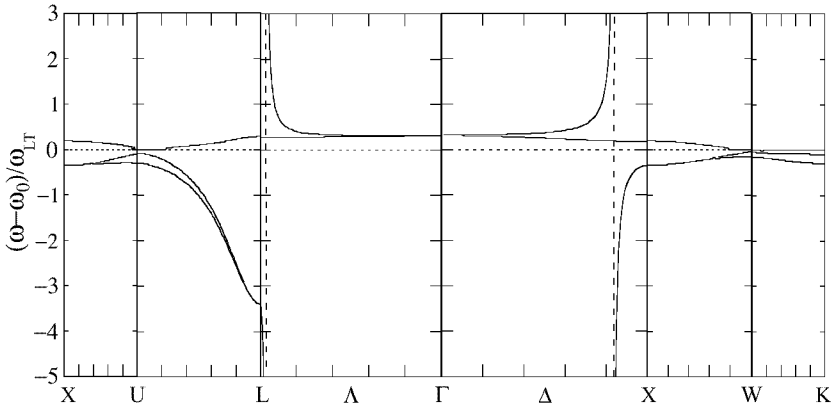


**Fig 1.** Exciton-polariton dispersion near the exciton resonance frequency $\omega_0$ in a face-centered-cubic lattice of spherical QDs characterized by the following set of parameters: $P = 1.1$, $R/a = 1/4$ and $\omega_{LT}/\omega_0 = 5\times10^{-4}$. The dashed lines show the photon dispersion in the empty lattice, i.e. for $\omega_{LT} = 0$, the dotted horizontal line indicates the value $\omega = \omega_0$.

and the eigenvalues $R_j$ can be readily expressed via these components as illustrated in Table 1 for the points $\Gamma, X, L, W, K$ and $U$.

Further simplifications follow taking into account a small value of the parameter $N$ in Eq. (10) since, in semiconductors, the ratio $\omega_{LT}/\omega_0$ typically lies between $10^{-4}$ and $10^{-3}$. Then in the frequency region given by the condition $|\Omega - 1| \ll P^{1/3} - 1$ one can readily use the approximate equation $\Omega - 1 \approx (N/2)\sigma_j(1, \mathbf{K})$ where $\sigma_j$ are eigenvalues of the $\sigma_{\alpha\beta}$ matrix.

Fig. 1 shows the photonic band structure calculated for the dots of radius $R = a/4$ and for $P = 1.1$, $\omega_{LT}/\omega_0 = 5 \times 10^{-4}$. The dispersion on the $\Lambda$ line is characterized by a giant anticrossing between the branches of bare transverse photon and exciton modes. At the $X$ point, the gap is determined by the separation between the longitudinal and lower transverse branches, it is still remarkable and exceeds $0.5\omega_{LT}$. However near the points $U$ and $W$ the excitron-polariton branches converge and the gap almost disappears. Note that the anticrossing can be described with a high accuracy by retaining in the sum over **b** in Eq. (11) the two terms due to $\mathbf{b} = 0, -(4\pi/a)(0, 0, 1)$ for the $\Delta$ points and $\mathbf{b} = 0, -(2\pi/a)(1, 1, 1)$ for the $\Lambda$ points.

The 3D QD arrays with periods comparable with the light wavelength ($P \approx 1$)

and with sizes exceeding the bulk-exciton Bohr radius could be grown artificially or by embedding semiconductor microcrystals into the pores of porous materials like the synthetic opal [3]. It should be mentioned that the developed theory takes into account a contribution of only one exciton resonance which is valid if the separation between the exciton size-quantization levels is much larger than the bulk value of the exciton longitudinal-transverse splitting, $\omega_{LT}$. In the opposite limit of extremely large bulk-exciton translational effective mass one can use the local material relation $\mathbf{D}(\mathbf{r}) = \varepsilon(\mathbf{r}, \omega)\mathbf{E}(\mathbf{r})$ as it was done by Sigalas et al. [4] for phonon-polaritons in a two-dimensional lattice consisting of semiconductor cylinders.

E. L. I. acknowledges partial support from Russian Foundation of Basic Research.

## References

[1] D. V. van Coevorden, R. Sprik, A. Tip, and A. Lagendijk, *Phys. Rev. Lett.* **77** 2412 (1996).
[2] E. L. Ivchenko and A. V. Kavokin, *Fiz. Tverd. Tela* **34** 1815 (1992) [*Sov. Phys. Solid State* **34** 968 (1992)].
[3] Yu. A. Vlasov, V. N. Astratov, O. Z. Karimov, A. A. Kaplyanskii, V. N. Bogomolov and A. V. Prokofiev, *Phys. Rev. B* **55** 13357 (1997).
[4] M. M. Sigalas, C. M. Soukoulis, C. T. Chan, and K. M. Ho, *Phys. Rev. B* **49** 11080 (1994).

Ioffe Institute
6th Int. Symp. "Nanostructures: Physics and Technology"
St Petersburg, Russia, June 22–26, 1998.



# Optical effect of electric field on indirect exciton luminescence in double quantum wells of GaAs

V. V. Krivolapchuk, *E. S. Moskalenko*, A. L. Zhmodikov,
T. S. Cheng† and C. T. Foxon†
Ioffe Physico-Technical Institute RAS, 194021, St. Petersburg, Russia
† Department of Physics, University of Nottingham,
University Park NG7 2RD, Nottingham, UK

Studies of double quantum wells (DQW) have attracted considerable interest from both theoretical and experimental point of view. This interest is caused partially by the possibility to utilize the electronic properties of DQWs in various optoelectronic devices. From the other hand the physical interest arises from the considering the DQW system as a promising candidate to study excitonic properties with respect to the single-exciton problem as well as to the exciton-exciton interaction processes. The central point of physical interest in DQW is the study of indirect exciton (IX) transition (consisting of an electron ($e$) and a hole ($h$) localized in different quantum wells (QW) of the same DQW) which possesses a much longer radiative lifetime relative to the direct exciton ($e$ and $h$ are located within the same QW). This fact allows one to create the IX gas of high density even at moderate pumping intensities and as a consequence to expect the revealing on experiment of some interesting properties related to collective excitation in the IX gas of high density, which were predicted theoretically (see [1] and references therein).

As concerns of experimental investigations, there are very few papers [2, 3] which report the revealing of collective phenomenon in the IX system, namely the reduction of the IX line width in GaAs DQW [2] and the observation of the huge broad band noise in the Hz range scale of the IX line integrated intensity in coupled QW of AlAs/GaAs induced by a magnetic field [3].

In the present report we study the IX line shape in photoluminescence (PL) spectra originating from the DQW of GaAs depending on the electric field value applied to the structure. We observe unusual IX line shape behaviour in the definite range of bath temperatures and pumping intensities and discuss our results in terms of possible revealing of the collective excitations in a dense IX gas which were predicted in [1].

## Samples and experimental details

The samples were taken from wafer NU1117 consisting of 1 mm GaAs buffer layer followed by three DQWs. The structure was grown in Nottingham University (UK) by MBE at $T = 630$ °C on 0.4 mm thick (001) GaAs substrate. The thickness of the narrow barriers of $Al_{0.33}Ga_{0.67}As$ between the QWs in DQW is 3.82 nm and that of the QWs in DQW differ by 2ML (0.57 nm) of GaAs with layer widths (QW/barrier/QW in nm) of 20.07/3.82/19.50, **10.18/3.82/9.61** and 8.20/3.82/7.63. In the present contribution we will concentrate on the results obtained on the DQW shown in bold. A constant electric field $V_{dc}$ was applied across the whole structure (Fig. 1a) between two indium contacts deposited on the substrate surface and the sample's face with DQWs. The latter contact was made with single pin hole giving the possibility to collect luminescence

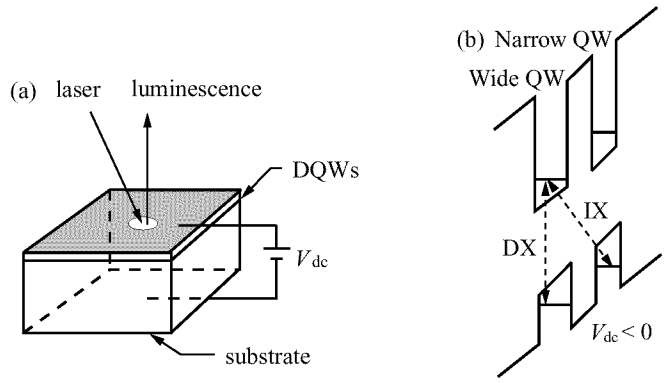


**Fig 1.** Experimental setup (a) and schematic band diagram of "indirect regime" (b).

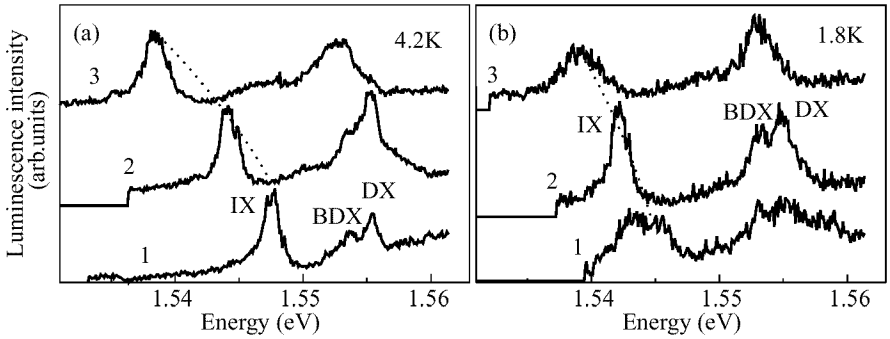


**Fig 2.** PL spectra taken at $P = 1$ mW and $\lambda = 765.2$ nm (a): $T = 4.2$ K, $V_{dc} = -0.5$ V (1), $-1$ V (2), $-1.5$ V(3) and (b): $T = 1.8$ K, $V_{dc} = -0.8$ V (1), $-1.3$ V(2), $-1.6$ V (3).

which was excited by the cw-Ti-sapphire laser ($730 < \lambda < 815$ nm, max power $P$ up to 100 mW) providing the below barrier excitation and laser beam was focused down to a spot of 0.1–0.2 mm in diameter. Bath temperature $T_b$ was varied in the range of $1.8 < T_b < 10$ K.

## Experimental results and discussion

Experiments were carried out in the "indirect regime" schematically shown in Fig. 1b which is characterized by the lowest energy position of the IX relative to the DX in PL. In the regime of moderate electric fields ($< 10^5$ V/cm) across the DQW when quadratic Stark shift is negligible, DX line position should be electric field independent while that of IX should vary essentially with $V_{dc}$. This is clearly demonstrated by the data of Fig. 2 which shows $V_{dc}$ influence on the PL spectra taken at $T_b = 4.2$ K (Fig. 2a) and $T_b = 1.8$ K (Fig. 2b). Indeed, with increasing $V_{dc}$ value DX line and line of DX bound to the impurity (labelled as BDX) have the same spectral positions while IX line considerably shifts to lower energies, reflecting the exact value of electric field $V_{DQW}$ applied across the particular DQW under investigation.

It is seen that at $T_b = 4.2$ K (Fig. 2a) IX line shifting to lower energies with increasing $V_{dc}$ (and hence $V_{DQW}$) has approximately unchanged spectral shape — its full width at half maximum (FWHM) slightly increases while at $T_b = 1.8$ K (Fig. 2b) IX behaves in a different way. Really IX line is wider at low and high $V_{dc}$ (curves 1

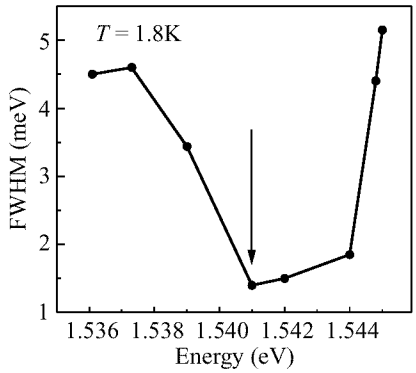


**Fig 3.** The IX FWHM value versus its spectral position (reflecting the particular value of $V_{DQW}$ taken at $P = 1$ mW and $T = 1.8$ K.

and 3 in Fig. 2b) and becomes considerably narrower at voltages in between (curve 2 in Fig. 2b). This FWHM evolution at $T_b = 1.8$ K is clearly seen from the plot shown in Fig. 3.

To understand this phenomenon let us consider how the changes in the external electric field (and hence in $V_{DQW}$) can affect the FWHM of IX PL line. First of all the width of IX line in DQW is inhomogeneous and is determined by a wide range of transition energies of IX localized on interface potential fluctuations which are caused mainly by the well (barrier) width fluctuations in the samples of very high quality. In the samples grown with growth interruption the lateral (in plane) size of QW (barrier) width fluctuations $L_{x,y}$ is much larger than exciton diameter $a_{ex}$, so PL spectrum consists of several distinctly separated lines, originating from the recombination of excitons localized in corresponding parts of QW [4]. In the same time in samples grown without interruption of growth (as corresponds to our case) the $L_{x,y}$ and $a_{ex}$ are of the same order [4] and hence typical PL spectrum consists of a single broad line.

The dramatic narrowing of the IX line observed at $T_b = 1.8$ K (Fig. 3) with increasing $V_{DQW}$ (when spectral position of IX line shifts to lower energies) we attribute to a phase transition in the exciton system from a normal regime to a collective regime or condensed state which appears in the dense gas of IX. Indeed if the exciton system makes a transition to a new collective (condensed) state, which is characterized by a long-range order, the excitonic energy levels will be determined by a potential averaged over the size much larger than the diameter of a single exciton $a_{ex}$, and hence PL line broadening due to the interface roughness will be washed out which eventually lead to the drastic line sharpening.

Our results demonstrate not only IX line narrowing (as it was reported in [2]) but also its broadening with further increase of $V_{dc}$ (Fig. 3). Electric field applied to the DQW changes the overlap of the wavefunctions of $e$ and $h$ of IX in the growth direction and hence the radiative lifetime of IX $\tau_R$ which is inversely proportional to that overlap. This makes it possible to increase $\tau_R$ essentially (by increasing $V_{dc}$) and as a result to make exciton gas thermalized to bath temperature better. So the effective tuning of $\tau_R$ allows one to escape the problem of short exciton radiative lifetimes which usually is the main reason preventing exciton condensation to a new phase. Thus we conclude that the IX line narrowing is due to electric field induced increasing of $\tau_R$. Evidently the formation of a new condensed state (revealing in our case as a line

narrowing) should be more favourable at lower temperatures which is in full agreement with our data (compare Fig. 2a and 2b). The reason why PL line broadens with further increase of $V_{dc}$ is more complicated and can be understood on the base of theoretical calculations which were performed in [1]. Authors of paper [1] considered the system of IX in DQW and predicted the possibility of a new condensed phase appearance in definite range of parameters, namely the IX concentration (or the in-plane separation of two neighbouring excitons) and the distance $D$ between $e$ and $h$ of IX in the growth direction (another words IX dipole moment $eD$ value). This theoretical analysis shows that the main part of the energy of interacting IX system is given by dipole-dipole repulsion interaction though there is the definite range of parameters where the energy of IX system is decreased (comparing to the non-interacting excitons) and hence a new condensed phase is the lowest stable energy state of the IX system. We believe that this is the case when line narrowing takes place (Fig. 3). Further increase of $V_{dc}$ inevitably leads to increasing of interparticle distance D of IX (and hence its averaged dipole moment) which leads to predominance of dipole-dipole repulsion interactions and this as a consequence breaks down the exciton condensed state. As a result IX line broadens and its FWHM acquires the same value (at high $V_{dc}$ — or low energy spectral position) as it was before condensation (at low $V_{dc}$ — or high energy spectral position) — see Fig. 3.

It is important to note that huge oscillations in IX PL intensity were detected at $V_{dc}$'s values which correspond to the sharp increase of FWHM (shown as vertical arrow in Fig. 3). These oscillations can be interpreted in terms of two phases (normal and condensed) coexistence in the IX system which should take place near the point of phase transition. It should be stressed out that the effect of IX line narrowing (at $T = 1.8$ K) is more pronounced at used pumping intensity $P$ of 1 mW which corresponds to IX concentration of $10^{10}$ cm$^{-2}$ while it is still detectable at $0.25 < P < 5$ mW. At lower (higher) pumping intensities (IX gas concentrations) the in-plane interparticle distances are too long (short) to form a condensed state (as expected from the calculations in [1]) in a full range of $V_{dc}$ values investigated.

In conclusion we observed IX line narrowing (accompanied by huge oscillations of the IX line PL intensity) at $T = 1.8$ K in DQW of GaAs. This is believed to be the evidence of new condensed state formation in a dense gas of IX. Altering the electric field strength allowed us to perform fine tuning of the IX radiative lifetime and its averaged dipole moment — the two crucial parameters which govern the condensed state appearance (at fixed IX gas concentration and bath temperature), another words the external electric field can be used as an effective tool to map out the phase diagram of a dense IX gas.

We are gratefully thankful to Prof. A. A. Kaplyanskii for permanent attention and support of this work, to Prof. Yu. E. Lozovik for fruitful discussions, to Mr. D. A. Mazurenko for help in experiments and to Russian Foundation for Basic Research No. 98-02-18296 for financial support.

## References

[1] Yu. E. Lozovik, O. L. Berman, *Sov. Phys. JETP* **111** 1879 (1997).
[2] T. Fukuzawa, E. E. Mendez, I. M. Hong, *Phys. Rev. Lett.* **64** 3066 (1990).
[3] L. V. Butov, A. Zrenner, G. Abstreiter, G. Bohm, G. Weimann, *Phys. Rev. Lett.* **73** 304 (1994).
[4] M. Tanaka, H. Sakaki, *J. Cryst. Growth* **81** 153 (1987).

Ioffe Institute
6th Int. Symp. "Nanostructures: Physics and Technology"
St Petersburg, Russia, June 22–26, 1998.



# Resonant waveguiding and lasing in structures with InAs submonolayers in an AlGaAs matrix

*A. F. Tsatsul'nikov*, N. N. Ledentsov, M. V. Maximov, B. V. Volovik, A. Yu. Egorov, A. R. Kovsh, V. M. Ustinov, A. E. Zhukov, P. S. Kop'ev, Zh. I. Alferov, I. E. Kozin†, M. V. Belousov† and D. Bimberg‡

Ioffe Physico-Technical Institute RAS, St.Petersburg, 194021, Russia
† Institute of Physics, St. Petersburg State University, Petrodvoretz, St. Petersburg, 198904, Russia
‡ Institute für Festkorperphysik, Technische Universität Berlin, Hardenbergstr. 36, D-10623 Berlin, Germany

Recently significant interest arose in semiconductor heterostructures with submonolayer (SMs) insertions of narrow gap material. Spontaneous formation of arrays of uniform two-dimensional islands has been demonstrated for II–VI and III–V materials systems [1, 2]. These structures, which can be considered as arrays of quantum dots (QDs) in view of the lateral sizes involved (about 4–5 nm) exhibit unique optical properties: increase in the exciton binding energy due to lateral confinement, high photoluminescence (PL) efficiency and large oscillator strength [3] even for ultrathin coverages. Besides, it was shown that for stacked CdSe SMLs in an ZnMgSSe matrix lasing can occur without external waveguiding as a result of the modulation of the refractive index near the exciton resonance energy [4–6].

In this work we study optical properties III–V structures with SML InAs insertions in an AlGaAs matrix. Lasing under photoexcitation is demonstarted for the structure without external optical confinement. Lasing occurs on a low energy side of the exciton resonance at low excitation densities pointing to the importance of this structures for improved optical confinement in AlGaAs injection laser operating in the visiblel range, excitonic waveguides and self-adjusted microcavities.

Investigated structures were grown by molecular-beam epitaxy on GaAs(100) substrate. First a 0.3 $\mu$m-thick GaAs buffer has been grown followed by a 0.7 $\mu$m-thick $Al_{0.32}Ga_{0.68}As$ layer. The active region comprised of 20 GaAs quantum wells of 1 nm width separated by 5 nm $Al_{0.32}Ga_{0.68}As$ spacer layers. The average Al composition of the active layer was only by 5 % lower than in surrounding matrix resulting in a strong penetration of the lightwave in the GaAs matrix if no resonant enhancement of the refractive index in the active layer is provided. InAs insertions having an average 0.5 ML thickness were inserted in the centre of these GaAs quantum wells. From both side active region was confined by thin 10 nm $Al_{0.4}Ga_{0.6}As$ layers to prevent transport of carriers towards the surface and the semiinsulating substrate. A 100 nm-thick $Al_{0.32}Ga_{0.68}As$ layer followed by a 10 nm GaAs cap layer were grown on top. Growth temperature for buffer and cladding layers was 600 °C. Active region was grown at 485 °C to prevent reevaporation and surface segragation of In.

Fig. 1 shows PL, PL excitation (PLE) and optical reflection (OR) spectra of the investigation structures. PLE and OR spectra have features at energies of 1.761 eV and 1.801 eV denoted as QD1 and QW, respectively. As revealed in resonant PL and excitation density studies, the PL peak is composed of two lines.

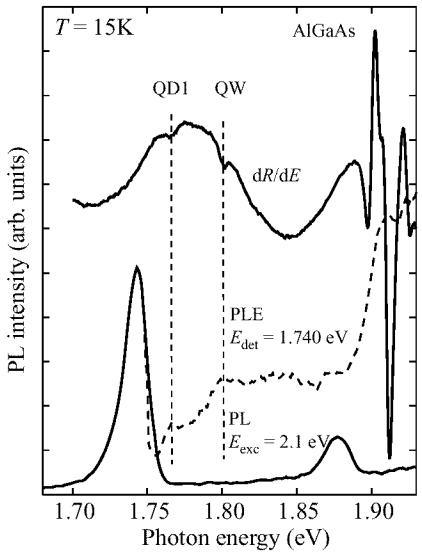


**Fig. 1.** PL, PLE and OR spectra of the investigated structure.

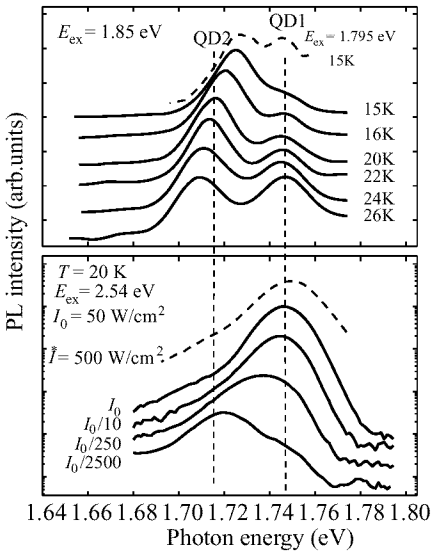


**Fig. 2.** PL spectra at different temperatures and excitation by light with photon energy 1.85 eV (a) and different excitation densities (b).

Temperature dependence of the PL spectra for exciting photon energy of 1.85 eV (a) and the excitation density dependence (b) of the PL spectra are shown in Fig. 2. Temperature variation in a range of 15–25 K results in significant changes in the PL spectrum. QD2 line intensity decreases with respect to the QD1 line and it shifts significantly toward smaller photon energies. The spectral position of the QD1 line is not changed. At low temperatures and low excitation densities QD2 line dominates in the PL spectrum (Fig. 2b). Increase in excitation density results in rapid saturation of the intensity of QD2 line and QD1 line starts to dominate.

Investigated structure represents a stack of narrow GaAs quantum wells (QWs) with microscopic localization areas induced by InAs QDs. Existence of two peaks (QD1 and QD2) in the PL spectrum at low excitation density indicates formation of two types of QDs. Relative increase in the QD1 line intensity with respect to the QD2 line one points to low density of QDs responsible for QD2 line. Significant long wavelength shift of the PL maximum with temperature increase is typical for recombination via QDs states [7]. Increase in temperature leads to evaporation of carriers from small QDs which determine the short wavelength side of the PL spectrum. This results in significant (as compared to the temperature dependence of the band gap) shift of the PL maximum toward low photon energies. Narrow temperature range in which the QD2 PL spectrum changes points to low density of such QDs. On the other hand, the temperature shift of the QD1 line is close to the temperature dependence of the AlGaAs band gap pointing to high density of related states. QD2 states can be related to islands having two-monolayer height or to vertically-coupled islands.

PL spectra are changed remarkably for excitation energy below and above 1.8 eV (Fig. 2a). Calculations of the heavy-hole exciton energy level in narrow GaAs QW and

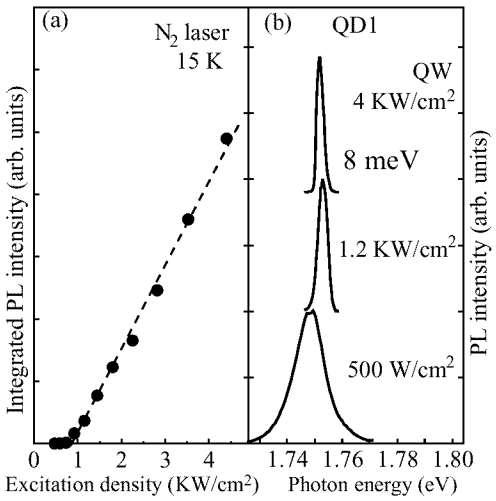


**Fig. 3.** Dependence of the integral PL intensity on pumping level (a) and PL spectra at different pumping (b).

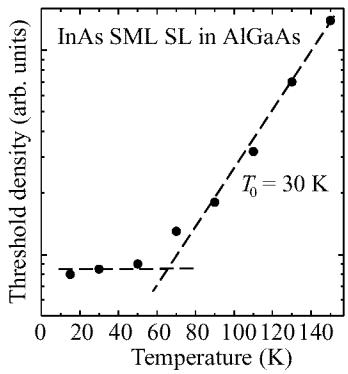


**Fig. 4.** Temperature dependence of the threshold excitation density.

the comparison of PL, PLE (e.g. step-like PLE behaviour at 1.8 eV) and OR spectra (sharp oscillation occurs at 1.8 eV) points that the states at this energy are related to the onset of the QW states.

To study lasing the 1 mm-long Fabri–Perot cavity was cleaved. The luminescence was excited from the surface using a pulsed $N_2$ laser beam focused in a stripe. Fig. 3a shows dependence of the integral PL intensity detected from the edge of the structure versus excitation density. A strong enhancement of the slope efficiency occurs at 800 W/cm$^2$ (see Fig. 3a). We attribute this behavior to lasing, which is further confirmed by the narrowing of the emission line (Fig. 3b). The lasing occurs at 1.750 eV, which is in the very vicinity of the exciton feature QD1 in the OR spectrum (1.761 eV). Thus, lasing occurs via the exciton ground state in InAs SML QDs. The threshold excitation density at 15 K is 800 W/cm$^2$. The calculated corresponding injection current density value is only about 200 A/cm$^2$. This value of threshold current is an upper estimation due to unknown surface leakage of nonequilibrium carriers for their near surface excitation using ultraviolet laser.

In Fig. 4 the temperature dependence of threshold excitation density is shown. At temperatures below 50 K the threshold excitation density is almost temperature-insensitive. This behaviour agrees with the QD nature of excitons trapped at InAs islands. Qualitatively similar dependence is observed for injection lasers with three-dimensional In(Ga)As/(Al)GaAs QDs [8]. At higher temperatures the threshold density increases exponentially with characteristic temperature of $T_0 = 30$ K. Such an increase of the threshold intensity results from thermal evaporation of carriers from InAs SML islands to the QW continuum. The maximum temperature for lasing for maximum excitation density used in our experiment was 170 K. We note that the temperature stability of the threshold density can be significantly improved by using wider gap cladding layers, narrower GaAs quantum wells, or by using a concept of vertically-coupled QDs.

To conclude, lasing without external optical confinement is demonstrated in III–V structures structures with InAs submonolayers in an AlGaAs matrix. We expect that these structures are very attractive for improvement of optical confinement in AlGaAs and InGaAsP lasers operating in visible spectral range, for creation of excitonic waveguides and vertical cavity lasers with self-adjusted cavity mode.

This work was supported by the Russian Foundation of Basic Research and Volkswagen Foundation.

## References

[1] P. D. Wang, N. N. Ledentsov, C. M. Sotomayor Torres, P. S. Kop'ev, and V. M. Ustinov, *Appl. Phys. Lett.* **64** 1526 (1994).

[2] V. Bressler-Hill, A. Lorke, S. Varma, P. M. Petroff, K. Pond, and W. H. Weinberg, *Phys. Rev. B* **50** 8479 (1994).

[3] M. V. Belousov, N. N. Ledentsov, M. V. Maximov, P. D. Wang, I. N. Yassievich, N. N. Faleev, I. A. Kozin, V. M. Ustinov, P. S. Kop'ev and C. M. Sotomayor Torres, *Phys. Rev. B* **51** 14346 (1995).

[4] N. N. Ledentsov, I. L. Krestnikov, M. V. Maximov, S. V. Ivanov, S. L. Sorokin, P. S. Kop'ev, Zh. I. Alferov, D. Bimberg and N. N. Ledentsov, C. M. Sotomayor Torres, *Appl. Phys. Lett.* **69** 1343 (1996).

[5] N. N. Ledentsov, I. L. Krestnikov, M. V. Maximov, S. V. Ivanov, S. L. Sorokin, P. S. Kop'ev, Zh. I. Alferov, D. Bimberg and N. N. Ledentsov, C. M. Sotomayor Torres, *Appl. Phys. Lett.* **70** 2766 (1997).

[6] I. L. Krestnikov, S. V. Ivanov, P. S. Kop'ev, N. N. Ledentsov, M. V. Maximov, A. V. Sakharov, S. V. Sorokin, A. Rosenauer, D. Gerthsen, C. M. Sotomayor Torres, D. Bimberg, Zh. I. Alferov, *Materials Science and Engineering B* (in press).

[7] A. F. Tsatsul'nikov, N. N. Ledentsov, M. V. Maximov, A. Yu. Egorov, A. E. Zhukov, S. S. Ruvimov, V. M. Ustinov, V. V. Komin, I. V. Kochnev, P. S. Kop'ev, Zh. I. Alferov, D. Bimberg, *Semiconductors* **30** 938 (1996).

[8] Y. Arakawa, H. Sakaki, *Appl. Phys. Lett.* **40** 939 (1982).

Ioffe Institute
6th Int. Symp. "Nanostructures: Physics and Technology"
St Petersburg, Russia, June 22–26, 1998.



# Injection laser based on composite InAlAs/InAs vertically coupled quantum dots in AlGaAs matrix

*A. R. Kovsh*, A. E. Zhukov, A. Yu. Egorov, N. V. Lukovskaya, V. M. Ustinov, Yu. M. Shernyakov, M. V. Maximov, A. F. Tsatsul'nikov, B. V. Volovik, A. V. Lunev, N. N. Ledentsov, P. S. Kop'ev, Zh. I. Alferov and D. Bimberg†
Ioffe Physico-Technical Institute,
Politekhnicheskaya 26, 194021, St.Petersburg, Russia
† Institut für Festkörperphysik, Technische Universität Berlin,
D-10623 Berlin, Germany

Three-dimensional carrier quantum confinement in the active region has been predicted to lead to remarkable improvements of characteristics of injection laser, i.e., ultralow threshold current density ($J_{th}$), high characteristic temperature [1], increased gain and differential gain [2]. Significant progress is currently achieved in fabrication and studies of lasers based on quantum dots (QD) formed by the spontaneous transformation of highly strained layer into an array of three-dimensional islands [3]. Low threshold current density at room [4] and cryogenic [5] temperatures, extremely high characteristic temperature [6], and considerably increased material gain [7] have been reported.

However, the areal density of self-organised QDs has been reported to be around $\sim 5 \times 10^{10}\,\mathrm{cm}^{-2}$ [8], it means that only a finite number of charge carries can contribute to lasing. The finite density of states in QD array leads to the saturation of the optical gain at a certain value. This effect is the most strongly pronounced in a laser containing one QD plane in active region where the superlinear increase in $J_{th}$ with output losses is observed [9]. Using vertically coupled QDs considerably reduces the gain saturation [9].

In the present work we report on the further increasing the maximum optical gain in a QD laser by directly increasing the areal density of QDs.

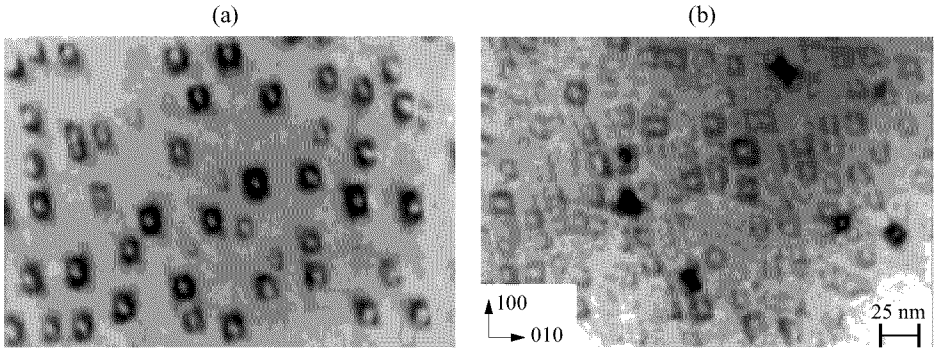


**Fig 1.** Plan-view transmission electron microscopy image of InAs (a) and InAlAs (b) QDs.

Fig. 1 shows the plan-view transmission electron microscopy images of QDs formed by the deposition of InAs (Fig. 1a) and InAlAs (Fig. 1b) layers on AlGaAs surface. The sheet concentration of InAlAs QDs is about $2 \times 10^{11}\,\mathrm{cm}^{-2}$, which is much higher

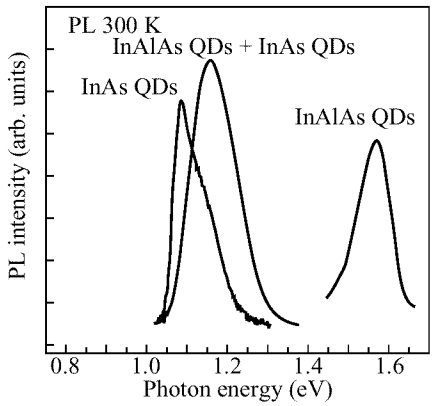


**Fig 2.** Photoluminescence spectra of structures with QDs in AlGaAs matrix.

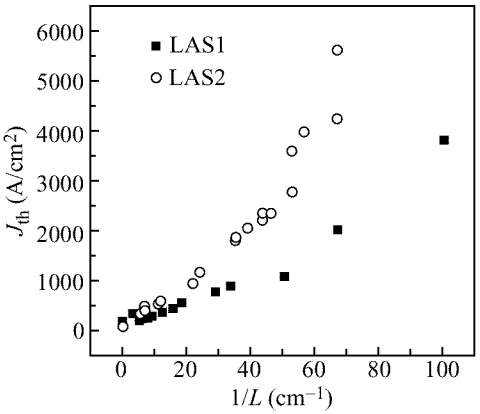


**Fig 3.** Threshold current density ($J_{th}$) vs reciprocal cavity length ($1/L$) for LAS1 and LAS2 structures.

than that of InAs QDs possibly owing to the lower migration rate of Al atoms on a growing surface. We assume that using the effect of vertical alignment of QDs [10] we can considerably increase the density of the QD array by depositing first InAlAs QDs followed by In(Ga)As QD planes. Since the bandgap of InAlAs is much larger than that of In(Ga)As, the optical transition energy in the QD array will be determined by In(Ga)As QDs, whereas the density will be set by the InAlAs QDs.

The structures studied were grown by solid-source molecular beam epitaxy (MBE) under the same growth conditions. The first structure contained one plane of InAlAs QDs in $Al_{0.15}Ga_{0.85}As$ matrix, the second contained three planes of InAs QDs separated by 50 Å $Al_{0.15}Ga_{0.85}As$ spacers, and for the last sample, QD array was formed by successive deposition of InAlAs and three InAs QD planes separated by 50 Å $Al_{0.15}Ga_{0.85}As$ spacers. Fig. 2 shows photoluminescence (PL) spectra of the structures described above. Pre-deposition of InAlAs leads to the blue-shift of the PL line as compared to the purely InAs QD sample. This fact is presumably due to the reduction

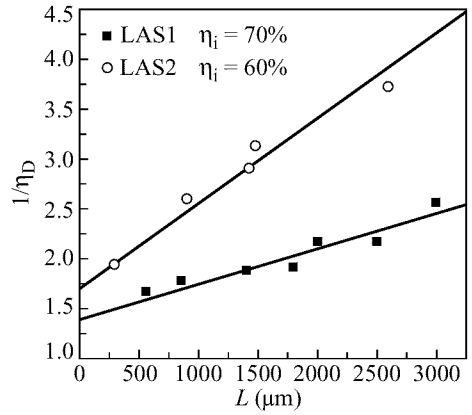


**Fig 4.** Reciprocal differential efficiency $(1/D)$ vs cavity length $(L)$ for LAS1 and LAS2 structures.

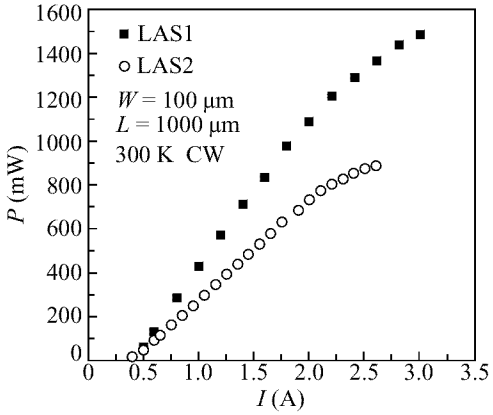


**Fig 5.** Light output power $(P)$ vs continuous wave drive current $(I)$ for LAS1 and LAS2 structures.

in sizes of QDs. Since the effective thickness of deposited InAs is the same, this should lead to the increase in QD density [11].

Fig. 3 shows Jth as a function of reciprocal cavity length (which is directly proportional to output losses) for the composite InAlAs/InAs QD laser (LAS1) and the similar structure without InAlAs QDs (LAS2) [12]. One can see that the $J_{th}$ of LAS1 is higher than the $J_{th}$ of LAS2 at infinite cavity length (four cleaved facet samples). But when the cavity length is decreased (output losses are increased) the $J_{th}$ of the latter structure increases steeper than in the case of the LAS1. For low losses the lasing is achieved at lower pumping current in laser with lower surface density of QDs and when losses are high the inverse relation is observed. This fact is in agreement with theoretical estimations given in [13].

Using the InAs QDs with higher density also leads to an increase in differential efficiency in the wide range of cavity lengths, internal quantum efficiency, and maximum output power. These effects are demonstrated in Figs. 4 and 5 where the data for LAS1 and LAS2 are given.

In conclusion, we have shown the increase in areal density of InAs self-organized vertically-coupled QDs by depositing InAlAs QD pre-layer. Injection laser with increased QD density demonstrated increased optical gain, differential efficiency and output power.

This work was supported by Russian Foundation for Fundamental Research (Grant 96-02-17824), the Program of the Ministry of Science of RF "Physics of Solid-State Nanostructures".

## References

[1] Y. Arakawa, and H. Sakaki, *Appl. Phys. Lett.* **40** 939–941 (1982).
[2] M. Asada, Y. Miyamoto, and Y. Suematsu, *J. Quantum Electron.* **QE-22** 1915–1921 (1986).
[3] P. M. Petroff and S. P. DenBaars, *Superlat. Microstruct.* **15** No. 1 15–21 (1994).
[4] V. M. Ustinov, A. Yu. Egorov, A. R. Kovsh et al, *J. Cryst. Growth* **175/176** 689–695 (1997).
[5] V. M. Ustinov, A. E. Zhukov, A. Yu. Egorov et al, *Electron. Lett.* (to be published) (1998).
[6] N. Kirstaedter, N. N. Ledentsov, M. Grundmann et al, *Electron. Lett.* **30** No. 17 1416–1417 (1994).
[7] N. Kirstaedter, O. G. Schmidt, N. N. Ledentsov et al, *Appl. Phys. Lett.* **69**(9) 1226–1228 (1996).
[8] S. S. Ruvimov, P. Werner, K. Scheerschmidt et al, *Phys. Rev. B* **51** No.20, 14766–14769 (1995).
[9] O. G. Schmidt, N. Kirstaedter, N. N. Ledentsov et al, *Electron. Lett.* **32**(14) 1302–1304 (1996).
[10] A. Yu. Egorov, A. E. Zhukov, P. S. Kop'ev et al, *Semiconductors* **30**(9) 879–883 (1996).
[11] A. Yu. Egorov, A. E. Zhukov, P. S. Kop'ev et al, *Semiconductors* **30**(8) 707–710 (1996).
[12] S. V. Zaitsev, N. Yu. Gordeev, V. I. Kopchatov et al, *Jpn. J. Appl. Phys.* **36**(6B) Part 1, 4219–4220 (1997).
[13] L. V. Asryan and R. A. Suris, *Proc. Int. Symposium "Nanostructures: Physics and Technology"* St. Petersburg, Russia, Jun 24-28, 1996, Abstracts, 354–357.

Ioffe Institute
6th Int. Symp. "Nanostructures: Physics and Technology"
St Petersburg, Russia, June 22–26, 1998.



# Effect of spatial hole burning and multi-mode generation threshold in quantum dot lasers

*L. V. Asryan* and R. A. Suris
Ioffe Physico-Technical Institute RAS, St. Petersburg, Russia,
E-mail: asryan@theory.ioffe.rssi.ru

**Abstract.** Theoretical analysis of the spatial hole burning in quantum dot (QD) lasers is given. The multi-mode generation threshold is calculated. The processes of the thermally excited escapes of carriers away from QDs are shown to control the multi-mode generation threshold. The dependences of the multi-mode generation threshold on the root mean square of relative QD size fluctuations, cavity length, surface density of QDs, and temperature are obtained.

## Introduction

In [1]–[3], theory of threshold current density of a quantum dot (QD) laser and its temperature dependence has been developed having regard to inhomogeneous line broadening caused by the dispersion in QD sizes. The optimum parameters of the laser structure minimizing the threshold current density have been calculated as the functions of the QD size dispersion, total losses, and temperature.

This article discusses the effect of spatial hole burning and multi-mode generation threshold in QD lasers. As in conventional quantum well (QW) or bulk lasers (as well as in solid state lasers) [4, 5], spatial hole burning in QD lasers is due to the non-uniformity of the stimulated recombination of carriers along the longitudinal direction in the waveguide. Due to the fact that, at and above the lasing threshold, the electric field of the emitted light is a standing wave and is a periodic function of the longitudinal coordinate, the stimulated recombination of the carriers will be more intensive in the QDs located at the antinodes of the light intensity, while it will be less intensive in the QDs located at the nodes. As a result, overfilling of the QDs located near the nodes may take place. This leads to the lasing generation of the other longitudinal modes (together with the main mode) with antinodes distinct from those of the first mode. A problem of the multi-mode generation is of first importance for the laser applications. A study of the physical processes controlling the multi-mode generation threshold is necessary to find the ways of suppressing the additional modes and to offer the proper design of single-mode operating lasers.

## 1 Processes controlling the spatial distributions of carriers

In QW or bulk lasers, diffusion in the active region will tend to smooth out the non-uniform carrier distributions and population inversion along the longitudinal direction, thus suppressing totally or partly the effect of spatial hole burning [4, 5].

In QD lasers, diffusion will play a similar yet minor role. The point is that the carriers, contributing to the stimulated emission, are those totally confined in QDs. There are also free carriers in the optical confinement layer (OCL) which contribute to the spontaneous

emission, thus increasing the threshold current density. The free-carrier densities and the confined carrier level occupancies in QDs are coupled to each other by the rate balance equations. Due to this coupling, diffusion of free carriers should equalize to some extent the level occupancies in different QDs. Hence, two processes control the spatial distribution of free and confined carriers along the longitudinal direction. These processes are: the thermally excited escapes of the carriers from QDs to the continuous spectrum states and the diffusion of free carriers along the longitudinal direction.

The slowest process of the two above controls the carrier space distribution. In this work, the thermally excited escapes from QDs, rather than the diffusion, are shown to limit smoothing-out the carrier space distribution. There is an evident analogy to spatial hole burning in bulk lasers containing impurity centers in the active region [6, 7]. Non-vanishing values of the characteristic times of thermally excited escapes are shown to control the multi-mode generation threshold in QD lasers.

The following simple reasoning is worth presenting here. The fluxes of the thermally excited escapes of the electrons and holes from QDs are proportional to $f_{\mathrm{n,p}} N_{\mathrm{S}} / \tau_{\mathrm{n,p}}^{\mathrm{g}}$, where $f_{\mathrm{n,p}}$ are the mean electron and hole level occupancies in QDs, $N_{\mathrm{S}}$ is the surface density of QDs, $\tau_{\mathrm{n,p}}^{\mathrm{g}}$ are the characteristic times of thermally excited escapes of electrons and holes from QDs being given as [1]

$$\tau_{\mathrm{n}}^{\mathrm{g}} = \frac{1}{\gamma_{\mathrm{n}} n_1} = \frac{1}{\sigma_{\mathrm{n}} v_{\mathrm{n}} n_1} \qquad \tau_{\mathrm{p}}^{\mathrm{g}} = \frac{1}{\gamma_{\mathrm{p}} p_1} = \frac{1}{\sigma_{\mathrm{p}} v_{\mathrm{p}} p_1}. \tag{1}$$

Here $\gamma_{\mathrm{n,p}} = \sigma_{\mathrm{n,p}} v_{\mathrm{n,p}}$, $\sigma_{\mathrm{n,p}}$ are the cross sections of electron and hole capture into a QD, and $v_{\mathrm{n,p}}$ are the thermal velocities of electrons and holes. In Eq. (1), $n_1 = N_{\mathrm{c}}^{\mathrm{OCL}} \exp[-(\Delta E_{\mathrm{c}} - \varepsilon_{\mathrm{n}})/T]$ and $p_1 = N_{\mathrm{v}}^{\mathrm{OCL}} \exp[-(\Delta E_{\mathrm{v}} - \varepsilon_{\mathrm{p}})/T]$ where $N_{\mathrm{c,v}}^{\mathrm{OCL}} = 2(m_{\mathrm{c,v}}^{\mathrm{OCL}} T / 2\pi\hbar^2)^{3/2}$ are the conduction and valence band effective densities of states for the OCL material, $\Delta E_{\mathrm{c}}$ and $\Delta E_{\mathrm{v}}$ are the conduction and valence band offsets at the QD–OCL heteroboundary, $\varepsilon_{\mathrm{n,p}}$ are the quantized energy levels of an electron and hole in a mean-sized QD (measured from the corresponding band edges), and the temperature $T$ being measured in terms of energy.

The free-hole diffusion flux is proportional to $2kD_{\mathrm{p}}p$, where $p = p_1 f_{\mathrm{p}}/(1 - f_{\mathrm{p}})$ is the free-hole density [1, 2], $k = (2\pi/\lambda_0)\sqrt{\epsilon}$, $\lambda_0$ is the wavelength at the maximum gain, $\epsilon$ is the dielectric constant of the OCL, and $D_{\mathrm{p}}$ is the hole diffusion constant. Since $D_{\mathrm{n}}$ is greater than $D_{\mathrm{p}}$, the free-electron diffusion is not the limiting factor.

The ratio of the hole escape flux to the diffusion one is $(1 - f_{\mathrm{p}})(N_{\mathrm{S}} \sigma_{\mathrm{p}} v_{\mathrm{p}})/(2kD_{\mathrm{p}})$. It is controlled by the cross section of hole capture into a QD and by the surface density of QDs. It is typically much less than unity. What this means is the process of thermally excited escapes is the slowest and hence the limiting one. Should this ratio be close to or greater than unity, both the processes above will control smoothing-out the spatial distribution of carriers. The multi-mode generation threshold in this case will be less than that in the case of small ratio.

## 2 Multi-mode generation threshold

An examination of the problem yields the following equation for the excess of injection (pump) current density over the threshold current density of the main (closest to the maximum of the gain spectrum) mode required for oscillating the next longitudinal

mode:

$$\delta j = j_2 - j_{\text{th}} = \frac{|\delta g|}{g^{\max}} \frac{eN_S}{\dfrac{(1-f_n)}{\gamma_n n_1} + \dfrac{(1-f_p)}{\gamma_p p_1}} = \frac{|\delta g|}{g^{\max}} \frac{eN_S}{\tau_n^g (1-f_n) + \tau_p^g (1-f_p)} \tag{2}$$

where $j_{\text{th}}$ and $j_2$ are the threshold current densities of the main and the next longitudinal modes, respectively, $g^{\max}$ is the gain spectrum maximum, and $f_{n,p}$ are the mean electron and hole level occupancies in QDs required for the lasing of the main mode. The absolute value of the difference in the gain of the main and the next modes is

$$|\delta g| = \frac{1}{2} \left| \frac{\partial^2 g}{\partial E^2} \right| (\delta E)^2 = \frac{1}{2} \left| \frac{\partial^2 g}{\partial E^2} \right| \left( \hbar \frac{c}{\sqrt{\epsilon}} \frac{\pi}{L} \right)^2 \tag{3}$$

where the derivative is taken at $E = E_0$, $E_0$ is photon energy of the main mode, $\delta E = \hbar(c/\sqrt{\epsilon})(\pi/L)$ is the separation between the photon energies of the neighbouring modes ($\Delta m = \pm 1$), and $L$ is the cavity length.

For Gaussian distribution of relative QD size fluctuations [1],

$$\frac{|\delta g|}{g^{\max}} = \frac{1}{2} \left( \frac{\hbar \dfrac{c}{\sqrt{\epsilon}} \dfrac{\pi}{L}}{(\Delta\varepsilon)_{\text{inhom}}} \right)^2 \tag{4}$$

where $(\Delta\varepsilon)_{\text{inhom}} = (q_n \varepsilon_n + q_p \varepsilon_p)\delta$ is the inhomogeneous line broadening due to fluctuations in QD parameters (e.g., sizes), $q_{n,p} = -(\partial \ln \varepsilon_{n,p} / \partial \ln a)$ and $\delta$ is the root mean square (RMS) of relative QD parameter (size) fluctuations [1].

The threshold current density of the main mode is [1]–[3]

$$j_{\text{th}} = \frac{eN_S}{\tau_{QD}} f_n f_p + ebBn_1 p_1 \frac{f_n f_p}{(1-f_n)(1-f_p)} \tag{5}$$

where $\tau_{QD}$ is the radiative lifetime in QDs, $b$ is the OCL thickness, and $B$ is the radiative constant for the OCL.

The relative excess of injection current density over the threshold current density of the main mode required for oscillating the next longitudinal mode is

$$\frac{\delta j}{j_{\text{th}}} = \frac{|\delta g|}{g^{\max}} \frac{\tau_{QD}}{\tau_n^g (1-f_n) + \tau_p^g (1-f_p)} \frac{1}{f_n f_p + \dfrac{\tau_{QD}}{N_S} bBn_1 p_1 \dfrac{f_n f_p}{(1-f_n)(1-f_p)}}. \tag{6}$$

We shall restrict our consideration to the case of charge neutrality in QDs when

$$f_n = f_p = \frac{1}{2} \left( 1 + \frac{N_S^{\min}}{N_S} \right) \tag{7}$$

where $N_S^{\min} = (4/\xi)(\sqrt{\epsilon}/\lambda_0)^2 \tau_{QD} ((\Delta\varepsilon)_{\text{inhom}}/\hbar) \beta (a/\Gamma)$ is the minimum surface density of QDs required to attain lasing at given losses $\beta$ and inhomogeneous line broadening $(\Delta\varepsilon)_{\text{inhom}}$ [1, 2], $\xi$ is a numerical constant appearing in QD size distribution function, $a$ is the mean size of QDs, and $\Gamma$ is the optical confinement factor in a QD layer (along the transverse direction in the waveguide).

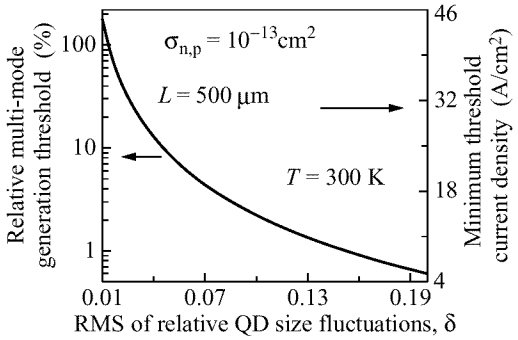


**Fig 1.** Relative multi-mode generation threshold and the minimum threshold current density of the main mode versus the RMS of relative QD size fluctuations $\delta$.

## 3 Results and discussion

Analysis of (6) shows that, for the structure optimized at a given $(\Delta\varepsilon)_{\text{inhom}}$ (for which the threshold current density of the main mode is a minimum), $\delta j/j_{\text{th}} \propto [(\Delta\varepsilon)_{\text{inhom}}]^{-2}$ for small $(\Delta\varepsilon)_{\text{inhom}}$, and $\delta j/j_{\text{th}} \propto [(\Delta\varepsilon)_{\text{inhom}}]^{-7/4}$ for large $(\Delta\varepsilon)_{\text{inhom}}$.

As is easy to see from (1) and (6), $\delta j/j_{\text{th}}$ depends strongly on the cross sections of electron and hole capture into a QD, $\sigma_{n,p}$. Calculation of $\sigma_{n,p}$ is beyond the scope of the present article. Here, to estimate the multi-mode generation threshold, we take $\sigma_{n,p} = 10^{-13}$ cm$^2$ (which is much less than the geometrical cross section of a QD). At room temperature and at $L = 500$ $\mu$m, Fig. 1 shows the relative multi-mode generation threshold (the solid curve) and the minimum threshold current density of the main mode (the dashed curve) versus the RMS of relative QD size fluctuations $\delta$. Each point on the curves corresponds to the specific structure optimized at the given $\delta$. For the structures with $\delta = 0.05$ and 0.1, $\delta j/j_{\text{th}} \approx 8\%$ and $2\%$, respectively; the minimum threshold current density values are 14 and 25 A/cm$^2$, respectively. The inclusion of violation of the charge neutrality in QDs [2] will enhance the multi-mode generation threshold.

Thus an increase in the QD size dispersion not only increases the threshold current density but decreases the multi-mode generation threshold as well.

*Acknowledgments*

The work has been supported by the RFBR, grants No. 96-02-17952 and 96.15–96.348 and the Program "Physics of Solid State Nanostructures" of Ministry of Science and Technical Policy of Russia, grant No. 97-1035.

## References

[1] Asryan L. V. and Suris R. A. *Semicond. Sci. Technol.* **11** 554 (1996).
[2] Asryan L. V. and Suris R. A. *IEEE J. Select. Topics Quantum Electron.* **3** 148 (1997).
[3] Asryan L. V. and Suris R. A. *Electronics Letters* **33** 1871 (1997).
[4] Statz H., Tang C. L. and Lavine J. M. *J. Appl. Phys.* **35** 2581 (1964).
[5] Tang C. L., Statz H., and deMars G. *J. Appl. Phys.* **34** 2289 (1963).
[6] Suris R. A. and Shtofich S. V. *Soviet Phys. Semicond.* **17** 859 (1983).
[7] Suris R. A. and Shtofich S. V. *Soviet Phys. Semicond.* **16** 851 (1982).

Ioffe Institute
6th Int. Symp. "Nanostructures: Physics and Technology"
St Petersburg, Russia, June 22–26, 1998.



# Anisotropic polarization of emitted and absorbed light in ZnSe based laser structures and thin ZnSe films

*L. Worschech*†, W. Ossau and G. Landwehr
Universität Würzburg, Am Hubland; 97074 Wurzburg, Germany
† Physikalisches Institut der Universität Würzburg Am Hubland, 97074 Wurzburg, Germany
email: worschec@physik.uni-wuerzburg.de

We report on the linearly polarized luminescence observed in ZnSe based laser structures. Different mechanisms of anisotropic polarization of the luminescence are identified. The incorporation of extended defects, an anisotropic relaxation of the residual strain and the influence of small environmental differences between local nearly equivalent sites of electronic binding potentials manifest themselves in variations of the degree of linearly polarized luminescence. An anisotropy of an efficient absorption process is investigated, which is assumed to reduce drastically the light emission efficiency of the optoelectronic device. The corresponding absorption coefficient is estimated. In order to reveal different origins of the anisotropic polarization, the luminescence of thin epitaxially grown ZnSe films is analyzed in detail. A considerable linear polarization collinear to a $[\bar{1}10]$ axis of the Y line at 2.61 eV detected in the photoluminescence spectra of thin ZnSe will be presented. The luminescence associated with point defects on lattice sites, e.g. the nitrogen acceptor, exhibits a preferential direction of the electric field vector **E** in the plane perpendicular to the axis of growth, when the layer thickness is in the order of 1 $\mu$m. A propagation of extended defects is studied by the time dependent changes of the degree of linearly polarized luminescence. The electronic structure and the symmetry of defects are analyzed by luminescence spectroscopy in high magnetic fields.

Ioffe Institute
6th Int. Symp. "Nanostructures: Physics and Technology"
St Petersburg, Russia, June 22–26, 1998.



# CdSe fractional-monolayer active region of MBE grown green (Zn,Mg,Cd)(S,Se) lasers

*S. Sorokin*, S. Ivanov, A. Toropov, T. Shubina, A. Lebedev, I. Sedova, A. Sitnikova, O. Nekrutkina and P. Kop'ev
Ioffe Physico-Technical Institute RAS, St. Petersburg, Russia

Due to the recent progress in obtaining relatively long-lived GaN-based lasers, the accent of (Mg,Zn,Cd)(S,Se) system laser applications has been shifted to a green region of visible spectrum, which is of great importance for a large-screen projection television and for the applications needed in low-power well-visible by human eye laser pointer. In this paper, a new type of active region using a fractional monolayer (FML) insertion is proposed and studied. As it has been shown previously [1], the wavelength of light emission from single CdSe fractional monolayer (ML) varies from 450 to 530 nm, depending on the nominal CdSe thickness (0.2–3 ML, respectively). Here we focus on the relatively thick insertions (2.5–3 ML) to obtain laser emission in green. At the moment there are contradictory data on the CdSe layer morphology and critical thickness depending on growth conditions. The critical thickness is estimated to be about 3 ML (RHEED oscillations). Particularly, the formation of optically active quantum dots at exceeding this value has been reported [2]. However, there is no reliable data on the intrinsic structure of thin CdSe layer close to the critical thickness as well as on possibility of its application as a laser active region.

All the structures used in this study were grown by molecular beam epitaxy (MBE) on GaAs (001) substrates with a GaAs buffer layer grown in separate III–V MBE setup. The details of MBE growth as well as composition control of quaternary and ternary (ZnMg)SSe and ZnCdSe alloys have been described elsewhere [3, 4]. Both optical and structural (XRD and TEM) characterization techniques were used.

To elucidate the structural and optical quality of FML the structure containing single 2.5 ML CdSe insertion in ZnSe matrix has been grown by migration enhanced epitaxy mode of the MBE technique [1, 5]. Plan-view TEM image of this structure is shown in Fig. 1. One can see a high density of dot-like objects with the average lateral size of 30–40 nm. They seem to be related to CdSe insertion, because such objects are not observed in the plan-view TEM image of the cap ZnSe layer. The TEM image reveals specific defects associated with the largest dot-like objects probably indicating their strain relaxation.

The data on optical characterization of such structure are rather complicated. At low excitation level (tungsten lamp) the spectra of low temperature (5 K) photoluminescence (PL) demonstrate a 40 meV wide single peak near 500 nm. According to the PL excitation spectra the line is non-homogeneous that is also confirmed by the PL time-resolved experiments. The PL spectra at higher excitation level (351 nm line of 20 mW argon laser) show additional feature: weak wide line ($\sim$ 250 meV) at $\sim$ 2.2 eV. This line is commonly attributed in literature to the defects related luminescence. However, the spectra of resonant light scattering also reveal a distinctive line at this energy.

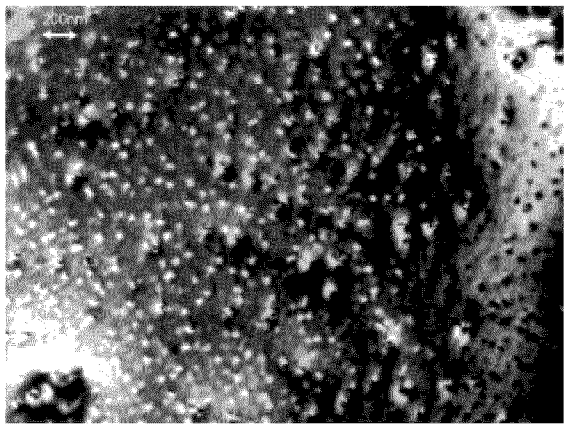

**Fig 1.** Plan-view TEM image of structure with single CdSe FML.

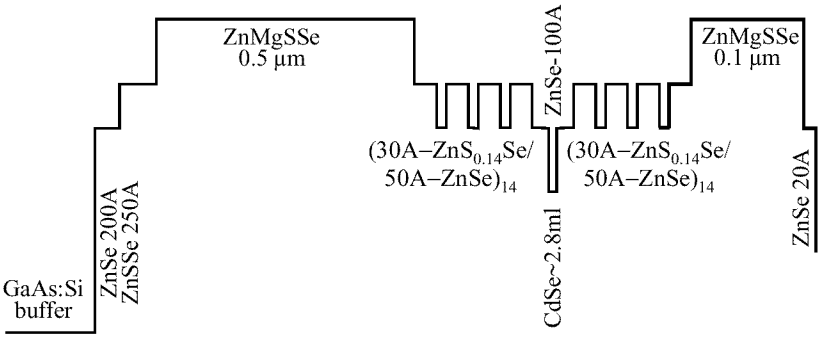


**Fig 2.** Schematic diagram of structure (**A**).

To check the feasibility of CdSe/ZnSe FML structures (near CdSe critical thickness) as an active region of laser structures the special optically pumped structure have been grown (named below as (**A**)) consisting consequently of 0.5 $\mu$m-$Zn_{0.92}Mg_{0.08}S_{0.14}Se_{0.86}$ layer, 0.1 $\mu$m-$ZnS_{0.12}Se_{0.88}$/ZnSe SPSL, 10 nm ZnSe quantum well centered with 2.8 ML CdSe insertion, 0.1 $\mu$m-$ZnS_{0.12}Se_{0.88}$/ZnSe SPSL and top 0.1 $\mu$m-ZnMgSSe layer. The schematic diagram of the structure is presented in Fig. 2. Two reference structures have been grown additionally. The first one (**B**) differs by the absence of CdSe FML (pure ZnSe QW), whereas the second (**C**) contains ordinary ZnCdSe QW of 25% cadmium content and emits in the same spectral range (500–520 nm). The general structure design has been reported elsewhere [6, 7]. The CdSe insertion provides an additional freedom in structure design, allowing one to vary lasing wavelength independently from the SPSL well and barriers composition.

The low-temperature PL and PL excitation measurements of the structure (**A**) (Fig. 3) confirm that the CdSe/ZnSe active region is very similar to the single 2.5 ML layer structure. The line is wider (80 meV) and slightly red shifted due to using of ordinary MBE growth mode at CdSe deposition [5]. The sharp ($\sim$ 7 meV) excitonic peaks from ZnSe QW are well-resolved in PL excitation spectra at the 500–516 nm registration wavelength. The peaks from ZnSSe/ZnSe SPSL are observed mainly at the registration wavelength corresponding to the emission from 10 nm wide ZnSe QW.

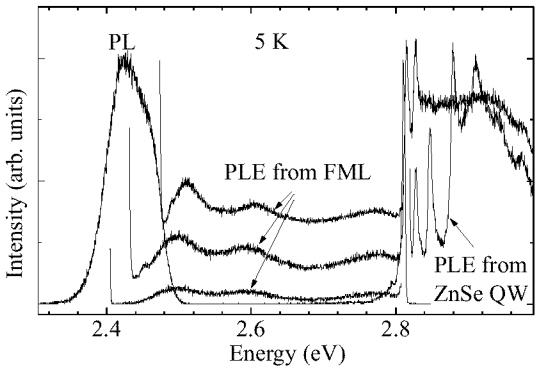


**Fig 3.** PL and PLE spectra of structure (**A**).

All structures demonstrate laser generation at room temperature. The wavelengths of laser generation of structures (**A**) and (**C**) are in the same spectral range but the threshold power density of structure (**A**) is almost 1.5 times lower than that of the structure (**C**) ((16–19) kW/cm$^2$ and (24–27) kW/cm$^2$, correspondingly). The structure (**B**) emits in blue region ($\sim$ 460 nm) with the $\sim$ 44 kW/cm$^2$ threshold power density that is practically lowest ever reported for II–VI's for this spectral range. In summary, the performed optical and structural characterization do not permit to conclude on the nature of the objects responsible for such high efficiency 300 K laser generation. The lasing arises in the spectral region where both dot-like and QW-like objects may emit light. Although more detailed studies are needed to elucidate the origin of this phenomena, the structures with CdSe FML active region are found to be extremely promising for green laser application, which respect to those with ordinary QW active region.

This work was supported in part by RFBR Grants as well as by Program of Ministry of Sciences of RF "Physics of Solid State Nanostructures".

## References

[1] S. V. Ivanov, A. A. Toropov, T. V. Shubina, S. V. Sorokin, A. V. Lebedev, I. V. Sedova, P. S. Kop'ev, G. R. Pozina, J. P. Bergman, and B. Monemar, *Journal of Applied Physics* (1998) (to be published).

[2] F. Flack, N. Samarth, V. Nikitin, P. A. Crowell, J. Shi, J. Levy, D. D. Awschalom, *Phys. Rev. B,* **54** 17312 (1996).

[3] S. V. Ivanov, S. V. Sorokin, P. S. Kop'ev, J. R. Kim, H. D. Jung, H. S. Park, *J. Crystal Growth* **159** 16 (1996).

[4] S. V. Ivanov, S. V. Sorokin, I. L. Krestnikov, N. N. Faleev, B. Ya. Ber, I. V. Sedova, and P. S. Kop'ev, *Journal Crystal Growth* (1998) (to be published).

[5] S. Ivanov, A. Toropov, S. Sorokin, T. Shubina, I. Sedova, O. Lublinskaya, G. Pozina, B. Monemar, P. S. Kop'ev, *Abstracts of the IIIrd Russian Conference on Physics of Semiconductors, Moskow* 1997, p. 345.

[6] S. Sorokin, S. Ivanov, A. Toropov, T. Shubina, I. Sedova, M. Tkatchman, P. S. Kop'ev and Zh. Alferov, *Proceedings of International Symposium on Nanostructures: Physics and Technology, St.-Petersburg* 1997, p. 206–209.

[7] T. V. Shubina, S. V. Ivanov, A. A. Toropov, G. N. Aliev, M. G. Tkatchman, S. V. Sorokin, N. D. Il'inskaya and P. S. Kop'ev, *Journal Crystal Growth* (1998) (to be published).

Ioffe Institute
6th Int. Symp. "Nanostructures: Physics and Technology"
St Petersburg, Russia, June 22–26, 1998.



# Collective spontaneous emission of femtosecond pulses in quantum-well semiconductor lasers

*A. A. Belyanin*, V. V. Kocharovsky and Vl. V. Kocharovsky
Institute of Applied Physics, Russian Academy of Science,
46 Ulyanov Street, 603600 Nizhny Novgorod, Russia

**Abstract.** A new type of accessible sources of ultrashort optical pulses based on the phenomenon of collective coherent recombination (superradiance) of electrons and holes in semiconductor heterostructures is proposed. The novel regime of an ultrafast operation of quantum-well semiconductor lasers is analyzed, in which a quasiperiodic sequence of superradiant pulses of duration up to 30 fs and peak intensity exceeding 100 MW/cm$^2$ is emitted under a continuous pumping from a low-Q cavity of length $\sim 30-100\,\mu$m.

## 1 Introduction

Superradiance (SR) in an ensemble of excited two-level atoms was predicted by Dicke in 1954 and confirmed experimentally in the seventies; see, e. g., [1, 2] for recent reviews. At a sufficiently high density $N_a$, a sample of atoms that are excited by a short pumping pulse into an incoherent state on one of the upper energy levels emits, after a certain delay time $t_d$, a powerful coherent pulse of SR. The phenomenon is due to an effective mutual phasing of the atomic dipole oscillators over the time $t < t_d$. The duration of the SR pulse, $t_p$, and the delay time are much shorter than the times of incoherent spontaneous emission and collisional relaxation in a medium. This is the distinctive feature of collective spontaneous emission, i. e. SR which makes the phenomenon so *different from standard lasing.*

However, in most solid-state lasers, including semiconductor lasers, the incoherent relaxation of polarization is much faster than the rate of stimulated radiative transitions, and cooperative effects in the oscillators' dynamics are suppressed. That is why the semiconductor lasers still do not exhibit experimentally the SR generation regime. In this report we point out that under certain conditions (basically, high photon losses from a cavity and very high pumping rate) SR becomes possible in quantum-well (QW) heterostructures, where the energy density of states is increased as compared with bulk semiconductors. We calculate the parameters of ultrashort coherent pulses obtained under *continuous pumping*, and demonstrate that the use of recombination SR can simplify essentially the technique of femtosecond pulse generation in semiconductors. Finally, the feasibility of obtaining superradiant generation from Ge/GeSi QWs is investigated.

## 2 Analysis of Maxwell–Bloch equations for semiconductor optics

The resonant interaction of most active media (including semiconductors) with coherent radiation is adequately described by Maxwell–Bloch equations [1-4]. In the semiclassical and mean-field approximations, and for slowly varying complex amplitudes of the field,

$\mathbf{E}(t)$, and polarization, $\mathbf{P_k}$, they take the following form:

$$d\mathbf{E}/dt + \mathbf{E}/T_E = (2\pi i\omega\Gamma/\mu^2)\sum_{\mathbf{k}}\mathbf{P_k}, \tag{1}$$

$$d\mathbf{P_k}/dt + (1/T_2 + i(\omega_{\mathbf{k}} - \omega))\,\mathbf{P_k} = -id^2\Delta N_{\mathbf{k}}\mathbf{E}/2\hbar, \tag{2}$$

$$d\Delta N_{\mathbf{k}}/dt + (\Delta N_{\mathbf{k}} - \Delta N_{\mathbf{k}}^p)/T_1 = \mathrm{Im}(\mathbf{E}^*\mathbf{P_k})/\hbar. \tag{3}$$

Here $\omega$ and $\mu$ are the eigenfrequency and the refraction index of a given axial mode of a cavity. We will assume for simplicity that only the fundamental transverse mode is self-consistently excited, with $\mu \simeq 3.5$ and the optical confinement factor $\Gamma < 1$. The field decay time $T_E$ in an open cavity of length $L$ takes a simple form in the case of purely radiative losses: $T_E \simeq 4\mu L/|c\log(R_1R_2)|$, where $R_{1,2}$ are the reflection factors at the cavity facets, $c$ is the velocity of light in vacuum.

Taking into account only direct radiative transitions, we introduce an inversion, $\Delta N_{\mathbf{k}}(t)$, and an amplitude of polarization, $\mathbf{P_k}(t)$, of a given "**k**-oscillator", that is, an electron and hole that have dipole moment $d$, quasimomentum $\mathbf{k}$, energies $\mathcal{E}_{e,h}$, and recombine emitting a photon of energy $\hbar\omega_{\mathbf{k}} = \mathcal{E}_e(\mathbf{k}) + \mathcal{E}_h(\mathbf{k})$. In Eq. (3) the term $\Delta N_{\mathbf{k}}^p$ is an inversion density supported by pumping (in the absence of generation). The time $T_1$ determines the incoherent relaxation rate of inversion. The time $T_2$ characterizes the incoherent relaxation of polarization for a given **k**-oscillator (an electron-hole pair). Its value is typically very small, $T_2 \sim 0.1$ ps at room temperature, and is determined by the intraband scattering processes.

The criterion of SR (or superfluorescence) is usually formulated in terms of a linear initial-value problem, i. e., as a requirement that the growth rate of small initial perturbations of field and polarization in the *initially inverted* medium should exceed the incoherent relaxation rates [1, 2]: $\omega'' > 1/T_1, 1/T_2, \Delta\omega$, where the latter quantity is an effective inhomogeneous broadening determined by a band filling of particle states. It can be shown [2, 5] that in *bulk* semiconductors the requirements $\omega'' > 1/T_2$ and $\omega'' > \Delta\omega$ are usually incompatible, and incoherent relaxation should suppress or greatly reduce cooperative effects in stimulated recombination.

To increase the rate of stimulated recombination needed for SR, one can change the density of particle states by reducing an effective dimension of an electron-hole plasma in a semiconductor sample. Previous proposals included, e. g., excitonic SR [6] and SR in a quantizing magnetic field [2, 5]. Both schemes are not very practical since they require low temperatures or strong magnetic fields exceeding 0.3 MG. The SR regime in QWs discussed in this report seems to be achievable at room temperatures and under injection pumping.

We have analyzed numerically and analytically [7] the dispersion properties and dynamics of hot cavity modes and found that the conditions necessary for SR are satisfied in heterostructures consisting of 7–10 QWs with active layer thicknesses $L_z \lesssim$ 50 Å and confinement factor $\Gamma \gtrsim 0.1$. For definiteness, the numerical estimates here and below are given for GaAs/AlGaAs QWs. The calculations were also made for other popular materials, with similar results.

## 3 Collective recombination and generation of femtosecond SR pulses

In order to obtain pulsed SR generation under a continuous pumping one must search for the range of parameters in which the regime of stationary laser generation becomes

*unstable*. Analysis of the phase space of Maxwell-Bloch equations (1)–(3) shows [7] that instability occurs when $3/T_2 \lesssim \bar{\omega}''$, $(1/T_1 + 1/T_2) \lesssim 1/T_E \lesssim \bar{\omega}''$ and the pumping rate exceeds some threshold value specified below for given structure parameters. Here the reference value of the growth rate is $\bar{\omega} \simeq 2 \times 10^{13}$ s$^{-1}$. Note an unusually high value of the required photon losses which implies a very low-Q (short) cavity. Indeed, it is the decay of the field that makes the steady state unstable against the stabilizing action of the polarization decay. An example of one-mode quasiperiodic SR generation in this range is presented in Fig. 1. We have also taken into account a slow "switching on" of a pumping by including a factor $(2/\pi)\arctan(\tau/50)$ into the pumping term $\Delta N_{\mathbf{k}}^{p}$ in Eq. (3).

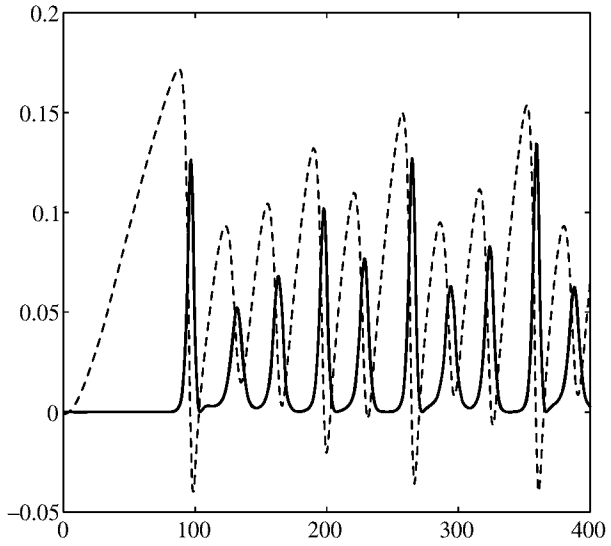


**Fig 1.** The normalized radiation density $e^2$ (solid line) and inversion $n$ summed over the particle states in the spectral bandwidth $0.7\bar{\omega}''$ (dashed line) as functions of dimensionless time $\tau = \sqrt{2}\bar{\omega}''t$ in the regime of SR pulse generation under continuous pumping. Normalized relaxation times are $\tau_1 = 30$, $\tau_2 = 5$, $\tau_E = 2.5$.

For a structure of cavity length $L = 30\,\mu$m and confinement factor $\Gamma = 0.1$, consisting of $N$ QWs with active layer thickness $L_z = 50$ Å, the coherent pulses shown in Fig. 1 have duration $t_p \simeq 50$ fs, the period between pulses $T \simeq 1$–$2$ s, peak power $\gtrsim 1$ , and peak output intensity per pulse $I = \mu^2|E|^2L/(8\pi T_E) \simeq 100N$ MW/cm$^2$. Note that to provide a short enough decay time $T_E$, the reflection factors and the cavity length should be small, $R_1R_2 \sim 0.1$ and $L \sim 30$–$100\,\mu$m.

The pumping may be either continuous or pulsed. To provide high enough injection rate of carriers, the pumping current density should be very large, $J \gtrsim 3 \times 10^3 N$ A/cm$^2$. Therefore, to prevent an excessive heating at room temperature, the pumping by short enough (submicrosecond) current pulses is desirable.

Another potential field of application for SR is a generation of coherent light pulses in the indirect band-gap semiconductors. Consider for definiteness Ge/GeSi QWs. It seems that the most promising way to reach the high level of stimulated radiative

recombination in Ge active layers is to employ *direct* radiative transitions between the Γ-valley in the conduction band and the top of the valence band ($\Gamma'_2 - \Gamma'_{25}$ transition). An absolute energy minimum of the conduction band, located in the $L_1$-point, is lower than the $\Gamma'_2$-minimum. Therefore, usually, the nonequilibrium carriers injected to the Γ-valley migrate very quickly to the *L*-minimum, with only a small fraction of them recombining radiatively. However, suppose that we are able to inject carriers to the direct minimum with the rate sufficient for the onset of collective SR recombination. In this case, since SR recombination has femtosecond timescale and proceeds faster than the intraband scattering of carriers to the *L*-minimum, nearly all carriers should contribute to the emission of femtosecond SR pulses. This may provide the unique way to obtain coherent optical emission from stimulated radiative recombination of carriers in Ge/Si structures.

This work has been supported in part by Russian Foundation for Basic Research through grant 98-02-17224 and by the EU Commission - DG III/ESPRIT Project CTIAC 21042.

## References

[1] Zheleznyakov V. V., Kocharovsky V. V. and Kocharovsky Vl. V. *Usp. Fiz. Nauk* **159** 193-260 (1989) (*Sov. Phys. Usp.* **32** 835-890 (1989)).
[2] Belyanin A. A., Kocharovsky V. V. and Kocharovsky Vl. V. *Quantum & Semiclass. Optics* **9** 1-44 (1997).
[3] Haug H. and Koch S. W. *Quantum Theory of the Optical and Electronic Properties of Semiconductors*, Singapore: World Scientific, 1994.
[4] Chow W. W., Koch S. W. and Sargent III M. *Semiconductor Laser Physics*, Berlin: Springer-Verlag, 1994.
[5] Belyanin A. A., Kocharovsky V. V. and Kocharovsky Vl. V. *Laser Physics* **2** 952-964 (1992).
[6] Misawa K., Jao H. and Kobayashi T. *J. of Lumin.* **48&49** 269-272 (1991).
[7] Belyanin A. A., Kocharovsky V. V. and Kocharovsky Vl. V. *Quant. & Semiclass. Optics* in press (1998); *Izvestiya RAN. Ser. Fiz.* **62** 372-383 (1998).

Ioffe Institute
6th Int. Symp. "Nanostructures: Physics and Technology"
St Petersburg, Russia, June 22–26, 1998.



# Radiative characteristics of InAs/InGaAs/InP quantum dot injection lasers

*V. I. Kopchatov*†, S. V. Zaitsev, N. Yu. Gordeev, A. Yu. Egorov,
A. R. Kovsh, V. M. Ustinov, A. E. Zhukov and P. S. Kop'ev
Ioffe Physico-Technical Institute RAS
Politekhnicheskaya, 26, St.-Petersburg, 194021, Russia

## Introduction

Quantum dot (QD) heterostructures have recently became the subject of the intensive research. Injection lasers with an active region based on InGaAs/AlGaAs QD have shown ultralow threshold current density ($J_{th}$) [1]. However, the emission wavelength of QDs formed on GaAs substrate is limited by the value of 1.3 $\mu$m. It has been previously shown that the QD emission range can be extended up to 2 $\mu$m by embedding the InAs QDs into an InGaAs matrix grown on InP substrate [2]. In this work we study threshold, temperature and power characteristics of InAs/InGaAs/InP injection lasers.

## 1 Experimental methods

The laser heterostructure was grown on n-type InP (100) substrate by solid-source molecular beam epitaxy (MBE). The substrate temperature was 500 °C for the deposition of all layers. Vertically coupled quantum dots (VECODs) were self-organized during the successive deposition of several sheets of QDs. An active region consisted of three InAs QD planes separated by 5-nm-thick InGaAs spacers.

Both four-cleaved facet samples and 100 $\mu$m-wide stripe geometry lasers were studied. Laser characteristics were investigated under pulse excitation (1.5 $\mu$s pulse duration, pulse interval equals to 100) in the 77–300 K temperature range. InSb photodiode was used for the optical signal registration. Using of different approaches described previously [3, 4] allows us to investigate both spontaneous and stimulated emission in the wide pumping current density range.

## 2 Results and discussion

An investigation of electroluminescence of four-cleaved facet samples shows the threshold current density as low as 11 A/cm$^2$ and the lasing wavelength 1.894 $\mu$m at 77 K. To our knowledge, this is the lowest $J_{th}$ for a QD injection laser have ever reported before. The linear dependence of the lasing wavelength vs. temperature (Fig. 1) clearly indicates the conservation of the lasing mechanism in the 77-200 K temperature interval. No lasing was observed over 200 K.

The threshold current density of stripe geometry lasers as a function of radiative output losses at 77 K is shown in Fig. 2. It is seen that there is a sharp superlinear growth of the threshold current density with increasing losses. Similar behavior of the $J_{th}$ has been observed in InAs/GaAs QD lasers before. Those heterostructures were grown by MBE as well and had a single sheet of QDs in an active region [5]. We think that the main reason for such drastic increasing of the $J_{th}$ is the gain saturation

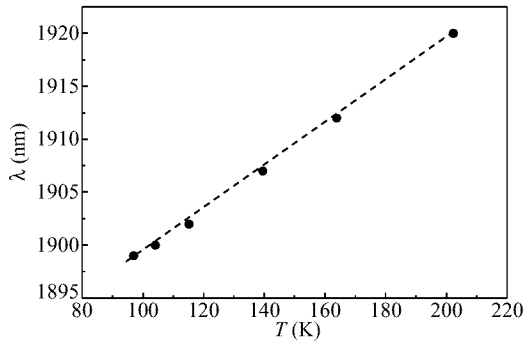


**Fig 1.** Temperature dependence of the lasing wavelength.

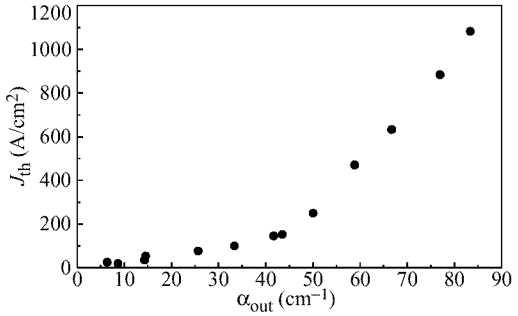


**Fig 2.** Threshold current density versus radiative output losses.

in QDs. To all appearances it is typical for QD lasers having a few sheets of QDs (no more than 3) in an active region. For example, the gain saturation was observed earlier in (In,Ga)As/GaAs injection lasers grown by MOCVD and that heterostructure had a single sheet of QDs [6].

Figure 3 shows that at 77 K only 40% of carriers take part in the stimulated emission. It is very good result for the first QD lasers in InAs/InGaAs/InP system.

The dependence of the lasing wavelength vs. threshold current density is shown in Fig. 4. There are two pronounced parts in it. These results are in good agreement with the $J_{th}$ dependence vs. radiative output losses (Fig. 2). We believe that there are two mechanisms by which the recombination is realized. The output losses interval of approximately from 50 cm$^{-1}$ to 60 cm$^{-1}$ (it corresponds to the laser cavity length range from 210 $\mu$m to 175 $\mu$m and $J_{th}$ from 250 A/cm$^2$ to 450 A/cm$^2$, respectively) is crucial with a view of the change of lasing mechanism. Electroluminescent investigation of the

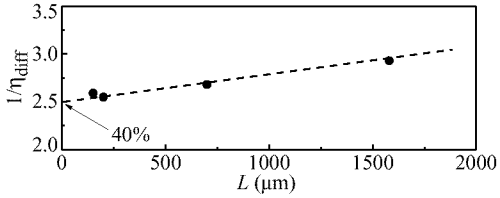


**Fig 3.** Dependence of the inverse differential quantum efficiency of stimulated emission versus laser cavity length.

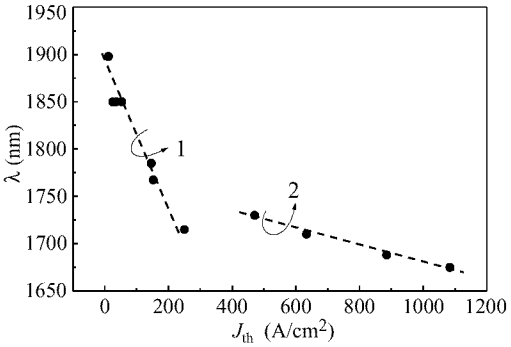


**Fig 4.** Dependence of the lasing wavelength versus threshold current density.

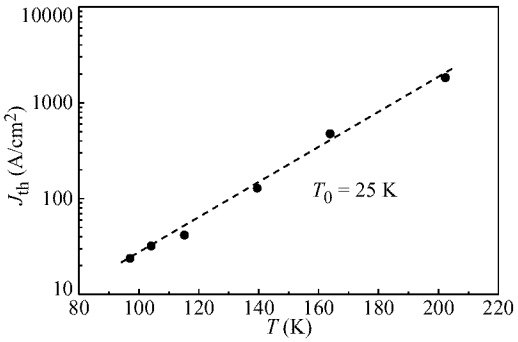


**Fig 5.** Temperature dependence of the threshold current density.

stripe geometry lasers shows that the stimulated radiative recombination goes via QD states only for the laser cavity length ($L$) more than 200 $\mu$m. Dot line of Fig. 4 marked "1" corresponds to this case. A further decrease in the $L$ leads to the gain saturation via the states of QDs. Lasing switches to higher states. It can be both excited states of QDs and states of the wetting layer. Less wavelength relates to lasing via those states. Dot line of Fig. 4 marked "2" corresponds to it.

The dependence of the threshold current density vs. temperature is shown in Fig. 5. In the temperature range of 77-200 K the $J_{th}$ varies very significantly and is described by the characteristic temperature $T_0 = 25$ K. Sudden increase of the threshold current density was also observed earlier [6] and is caused by thermal evaporation of carriers from QD states to the adjacent layer which makes it necessary to increase the injection current density required to maintain the given gain. Moreover, an increase in the temperature from 77 K to 150 K reduces the radiative spontaneous recombination rate by the factor of 3. In addition, Fig. 6 shows that the same rise of the temperature leads to the decrease of differential quantum efficiency of stimulated emission by the factor of 4. So, main reasons for the characteristic temperature's low value are the non-radiative recombination and the carrier escape from QD states.

## 3 Conclusions

The possibility of the achievement of the threshold current density as low as 11 A/cm$^2$ at 77 K in lasers based on InAs/InGaAs/InP has been shown. Lasing wavelength

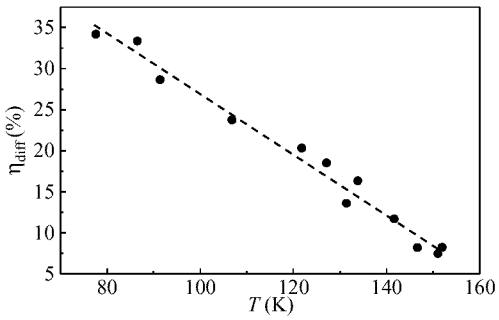


**Fig 6.** Temperature dependence of the differential quantum efficiency.

reached 1.894 $\mu$m. It was found out that there were several causes preventing lasing at the higher temperatures (more than 200 K). The non-radiative recombination and the carrier escape have been studied. The improvement of the QD laser heterostructure's crystal perfection and the increase of the number of QD's sheets in an active region embedded into a wider bandgap matrix must lead to low threshold lasing via the states of QD at room temperature.

## References

[1] V. M. Ustinov, A. Yu. Egorov, A. E. Zhukov, M. V. Maksimov, A. F. Tsatsulnikov, N. Yu. Gordeev, S. V. Zaitsev, Yu. M. Shernyakov, N. A. Bert, P. S. Kop'ev, Zh. I. Alferov, N. N. Ledentsov, J. Bohrer, D. Bimberg, A. O. Kosogov, P. Werner, and U. Gosele, *Journal of Crystal Growth* **175/176** 689 (1997).

[2] A. E. Zhukov, V. M. Ustinov, A. Yu. Egorov, A. R. Kovsh, A. F. Tsatsulnikov, M. V. Maksimov, B. V. Volovik, A. A. Suvorova, N. A. Bert, and P. S. Kop'ev, "Strained quantum islands of InAs in an (In,Ga)As/InP matrix", *Proc. Int. Symp. Nanostructures: Physics and Technology* St.Petersburg, Russia, p.341 (1997).

[3] S. V. Zaitsev, N. Yu. Gordeev, V. I. Kopchatov, A. M. Georgievski, V. M. Ustinov, A. E. Zhukov, A. Yu. Egorov, A. R. Kovsh, N. N. Ledentsov, P. S. Kop'ev, D. Bimberg, and Zh. I. Alferov, *Semiconductors* **31(9)** 1106 (1997).

[4] S. V. Zaitsev, N. Yu. Gordeev, V. I. Kopchatov, V. M. Ustinov, A. E. Zhukov, A. Yu. Egorov, N. N. Ledentsov, M. V. Maximov, P. S. Kop'ev, and Zh. I. Alferov, *Japanese Journal of Applied Physics* **36** 4219 (1997).

[5] S. V. Zaitsev, N. Yu. Gordeev, V. M. Ustinov, A. E. Zhukov, A. Yu. Egorov, M. V. Maximov, A. F. Tsatsulnikov, N. N. Ledentsov, P. S. Kop'ev, and Zh. I. Alferov, *Semiconductors* **31(5)** 539 (1997).

[6] Zh. I. Alferov, N. Yu. Gordeev, S. V. Zaitsev, P. S. Kop'ev, I. V. Kochnev, V. V. Komin, I. L. Krestnikov, N. N. Ledentsov, A. V. Lunev, M. V. Maximov, A. V. Sakharov, A. F. Tsatsul'nikov, and Yu. M. Shernyakov, *Semiconductors* **30(2)** 357 (1996).

Ioffe Institute
6th Int. Symp. "Nanostructures: Physics and Technology"
St Petersburg, Russia, June 22–26, 1998.



# Blue shift of electroluminescence in AlGaAsSb/InGaAsSb double heterostructures with asymmetric band offset confinements

*M. P. Mikhailova*, B. E. Zhurtanov, K. D. Moiseev, G. G. Zegrya, O. V. Andreychuk, T. I. Voronina and Yu. P. Yakovlev
Ioffe Physico-Technical Institute, RAS, 194021, St.Petersburg, Russia

Lately there has been intensive research in mid-infrared III–V semiconductor diode lasers emitting from 3 to 5 $\mu$m. An important application of these lasers is ecological monitoring and tunable diode laser spectroscopy. Sb-based lasers operating at up to 180–200 K in pulsed mode and 110–120 K in cw mode were realized [1, 2]. Novel type II laser structures using an intersubband transitions were demonstrated [3, 4]. Main physical processes limiting operation temperature of the longwavelength lasers are non-radiative Auger recombination, intervalence band absorption, carrier heating as well as current leakage due to poor electron and hole confinement. Attempts were made to improve electron and hole confinement by using MBE grown laser structures with high Al-content cladding layers [5]. Further progress in improving mid-infrared laser performances is connected with new physical approaches to laser structure desing optimization.

We report here the first results on creation and electroluminescence (EL) study of AlGaAsSb/InGaAsSb double heterostructures (DH) with high Al-content (64%) confined layers ($E_G = 1.474$ eV) and a narrow-gap active layer ($E_G = 0.326$ eV) grown by LPE method. Two kinds of diode laser structures were fabricated on N- and P-GaSb substrates, below we will be referring to them as structure A and structure B respectively (Fig. 1). These structures consisted of the following layers: structure A N-GaSb/N-$Al_{0.64}Ga_{0.36}AsSb$/n-$In_{0.94}Ga_{0.06}As_{0.82}Sb_{0.18}$/P-$Al_{0.64}Ga_{0.36}AsSb$/P-GaSb and structure B had inverted sequence of the layers of the same compositions of quaternary solid solutions, P-GaSb/P-$Al_{0.64}Ga_{0.36}AsSb$/p-$In_{0.94}Ga_{0.06}As_{0.82}Sb_{0.18}$/N-$Al_{0.64}Ga_{0.36}AsSb$/N-GaSb The N- and P-type layers of the AlGaAsSb solid solutions were obtained by Te and Ge doping, respectively. The narrow-gap active layer of the n-InGaAsSb was undoped and the p-InGaAsSb layer was doped by Zn to $1\times10^{17}$ cm$^{-3}$. The thickness of the confined layers was as high as 2 $\mu$m, and the active layer thickness was in the range 0.4–1.4 $\mu$m.

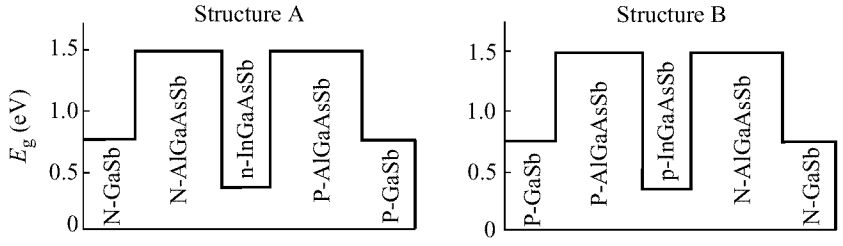


**Fig 1.** Energy band profiles of laser structures A and B.

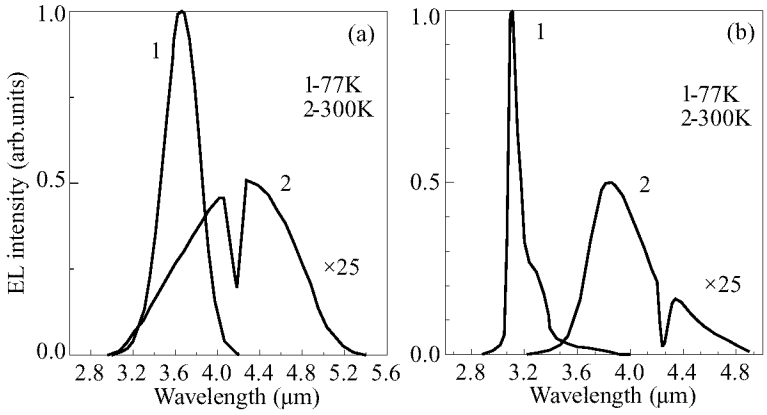


**Fig 2.** Electroluminescence spectra of the N-AlGaAsSb/n-InGaAsSb/P-AlGaAsSb (a) and P-AlGaAsSb/p-InGaAsSb/N-AlGaAsSb (b).

The main problem of the LPE growth of the InAs-rich narrow-gap solid solutions lattice-matched to GaSb and wide-gap AlGaAsSb is a big difference in the values of the thermoconductivity and thermal expansion coefficients of these materials. To solve this problem we used a special thermodynamic calculation of equilibrium phase diagrams of the quaternary solid solutions and an original growth technique. High quality lattice-matched epilayers were grown onto GaSb (100) substrate by liquid phase epitaxy using a horizontal graphite multiwell sliding boat. The temperature of epitaxy was about 600 °C. The lattice mismatch of the $Al_{0.64}GaAsSb$ epitaxial layers as low as 0.05% was obtained. The lattice mismatch of the $In_{0.94}GaAsSb$ epitaxial layers was about of 0.3% at room temperature.

Mesa-stripe laser structures with stripe widths 11–45 $\mu$m and the cavity length 300 $\mu$m were fabricated by standard photolithography. EL spectra were measured using MDR-4 grating monochromator and a lock-in amplifier. The emission signal was registered by liquid N2-cooled InSb photodetector. We studied spectra of spontaneous emission and emission intensity versus drive current at 77 and 300 K under quasi steady-state. Spectra of coherent emission in pulsed mode were studied at $T = 80–150$ K, as well as temperature dependence of the threshold current. In laser structures A spontaneous emission was obtained at $\lambda = 3.8$ $\mu$m ($h\nu = 326$ meV) at $T = 77$ K and $\lambda = 4.25$ $\mu$m ($h\nu = 291$ meV) at room temperature which corresponds to energy gap of the InGaAsSb active layer. The emission band had a Gaussian symmetric shape. Full width at half maximum (FWHM) of the emission band was 34 meV (77 K) and increased up to 90–115 meV at 300 K (Fig. 2a). The emission intensity varied linearly with drive current and decreased by a factor of 30 as temperature was raised from $T = 77$ K to 300 K. Lasing with single dominant mode at $\lambda = 3.776$ $\mu$m ($T = 80$ K) was achieved. Threshold current as low as $\sim 60$ mA and the characteristic temperature $T_0 = 26$ K in the temperature range 80–120 K were observed.

In turn, in structures B an intensive spontaneous emission and superluminescence were only obtained. Electroluminescence with very narrow asymmetric bands (FWHM = 7–10 meV at 77 K and 30 meV at 300 K) was observed (Fig. 2b).

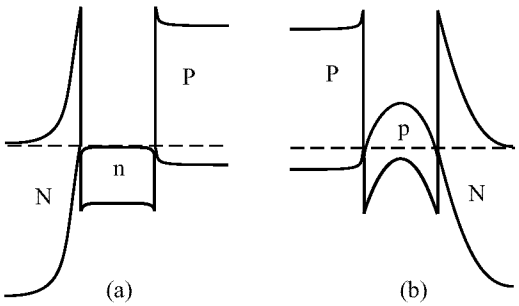


**Fig 3.** Energy band diagrams of laser structures A and B with high asymmetric band offset confinement.

A blue shift of the emission band maximum of up to 60–70 meV was found relative to the emission band maximum in structures A. EL was peaking at photon energies $h\nu = 380-402$ meV ($\lambda = 3.08-3.26$ $\mu$m). It is interesting to note that in B-structures the emission wavelength does not practically change in a wide range of drive current (50–170 mA) and them sligthly increases with further current rising.

To explain the obtained experimental results we examined the energy band diagrams of both laser structures. We found that in our case the $Al_{0.64}Ga_{0.36}AsSb/In_{0.94}Ga_{0.06}AsSb$ heterojunction was close to broken gap at $T = 300$ K with zero energy gap between the valence band of wide-gap semiconductor and the conduction band of the narrow-gap active layer. Such systems behave as semimetals with ohmic current-voltage characteristics at room temperature [6]. Band energy diagrams of the DH laser structures had strongly asymmetric band offsets: $\Delta E_C = 1.46$ eV and $\Delta E_V = 0.31$ eV (Fig. 3).

We explain the observed strong dissimilarity of EL spectra in structures A and B by their being due to different radiative recombination transitions. It was found in structures A the radiative recombination occurs in the active layer and corresponds to band-to-band recombination ($h\nu = 326$ meV at $T = 77$ K) (Fig. 3a). In these laser structures we used N- and P-AlGaAsSb cladding layers doped in excess of $8 \times 10^{17}$ cm$^{-3}$ which improved the hole and electron confinements and reduced the built-in serial resistance of the confining layers.

In turn, in structures B there were used lightly doped ($1-5 \times 10^{17}$ cm$^{-3}$) P-AlGaAsSb confined layers. We suppose that in these structures the radiative recombination transitions occur near the P-AlGaAsSb/p-InGaAsSb interface (Fig. 3b). This is supported also by electron beam induced current measurements. The observed intensive EL and blue shift of the emission band maximum relative to the emission band maximum in structures A can be satisfactorily explained by indirect (tunnel) optical transitions of localized electrons and holes from the quantum well levels across the p-p heterointerface (Fig. 4). In this case a two-dimensional electron gas can form in the quantum wells near the interface on the side of InGaAsSb solid solution due to electron resonant transfer from deep acceptor levels situated in the lightly doped wide-gap AlGaAsSb layer ($E_A = 400$ meV, a native defect $V_{Al}Sb_{Al}$) [7]) to the conduction band of the narrow-gap InGaAsSb one. Thereupon, under applied bias the tunnel radiative recombination leads to appearance of the narrow emission bands with photon energy $h\nu = 0.37-0.40$ eV which will be different from the energy band gap of the narrow-

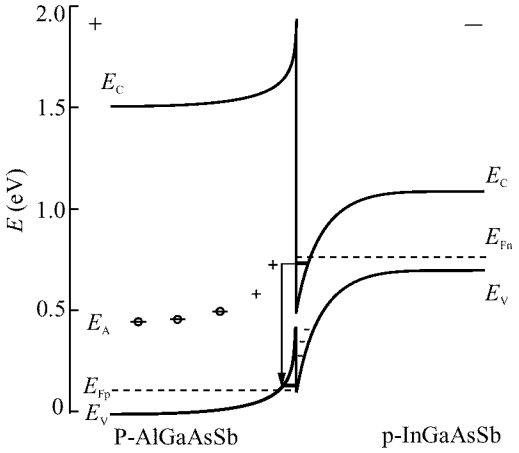


**Fig 4.** Energy band diagram of the type II P-AlGaAsSb/p-InGaAsSb heterojunction under applied bias.

gap semiconductor ($E_G = 0.326$ eV) and exceeding it. It is evident in this case the EL emission wavelength must not depend on applied bias as far as a lattice heating contribution is not substantial and we observed it really in the experiment. A similar "blue" shift was observed recently by us in DH laser structures with confined layers contenting Al of 34% in solid solution [8].

This work was supported in part by the Russian program "Solid-State nanostructures physics", project #96-1010 and Russian Basic Research Foundation, project #96-02-17841a.

## References

[1] H. K. Choi, G. W. Turner *Appl. Phys. Lett.* **67**, 332 (1995).
[2] T. N. Danilova, A. N. Imenkov, O. G. Ershov, M. V. Stepanov, V. V. Sherstnev, Yu. P. Yakovlev *Semiconductors*, **29** (7), 667 (1995).
[3] Yu. P. Yakovlev, M. P. Mikhailova, G. G. Zegrya, K. D. Moiseev, O. G. Ershov *Techn. Digest CLEO-96*, USA, Anaheim CA, 2-7 June 1996, p. 170.
[4] C. H. Lin, R. Q. Yang, D. Zhang, S. J. Murry, S. S. Pei, A. A. Allerman, S. R. Kurtz *Electr. Lett.* **33**(7), 598 (1997).
[5] H. K. Choi, G. W. Turner, Z. L. Liau *Appl. Phys. Lett.* **65**, 2251 (1994).
[6] M. P. Mikhailova, I. A. Andreev, T. I. Voronina, T. S. Lagunova, K. D. Moiseev, Yu. P. Yakovlev *Semiconductors*, **29** (4) 353 (1995).
[7] F. Fuchs, J. Schmitz, H. Obloh, J. D. Ralsto, P. Koidl *Appl. Phys. Lett.* **64** 1665 (1994).
[8] K. D. Moiseev, M. P. Mikhailova, O. V. Andreychuk, B. E. Samorukov, Yu. P. Yakovlev *Tech. Phys. Lett.* **23** (5) 364 (1997).

Ioffe Institute
6th Int. Symp. "Nanostructures: Physics and Technology"
St Petersburg, Russia, June 22–26, 1998.



# IR luminescence (1.6–1.9 $\mu$m) of compressive-strained InGaAs/InP quantum wells grown by MOVPE

*Z. N. Sokolova*, O. V. Kovalenkov, D. A. Vinokurov,
V. A. Kapitonov and I. S. Tarasov
Ioffe Physico-Technical Institute, St. Petersburg 194021, Russia
E-mail: zina@quant.ioffe.rssi.ru

**Abstract.** We report metal-organic chemical-vapor deposition-grown $In_xGa_{1-x}As/In_{0.53}Ga_{0.47}As/InP$ double heterostructures emitting at 1.65–1.85 $\mu$m at room temperature. The active region consists of a 25–100 Å thick compressivelly strained $In_xGa_{1-x}As$ quantum wells with composition $x$ in interval 0.69–0.81. Comparison with our theoretical results shows that the shape of our quantum wells grown by metal-organic vapour phase epitaxy is not rectangular.

## Introduction

Semiconductor lasers emitting in the midwavelenght infrared (MWIR) band (1.5–5 $\mu$m) have potential applications in high-resolution molecular spectroscopy, optical fiber communication, laser radar, and gas analysis with high sensitivity and speed. Particular attention was given to III–V semiconductor MWIR lasers with Sb contents [1, 2]. Contrary to receive the emission wavelength up to 2.0 $\mu$m we use InGaAs/InP heterostructures with strained active region. To the best of our knowledge, so far the detailed study of strained InGaAs quantum wells (QWs) has not provided. Usually strained InGaAsP heterostructures emitted up to 1.5 $\mu$m have been investigated [3, 4].

## 1 Growth

In this work we report double heterostructures $In_xGa_{1-x}As/InP$ ($x = 0.69–0.81$) emitted at 1.65–1.85 $\mu$m grown by metal-organic vapour phase epitaxy (MOVPE). The low pressure (100 mBar) (LP MOVPE) equipment with rectangular cross-section horizontal reactor and radio-frequency heating of graphite susceptor was used. The trimethylgallium (TMGa), trimethylindium (TMIn), arsine ($AsH_3$) and phosphine ($PH_3$) were used as sources. Growth temperature was 600°C.

The heterostructures consist of a 25–100 Å thick undoped compressivelly strained (lattice mismatch 1–2%) active region of $In_xGa_{1-x}As$ ($x = 0.69–0.81$) sandwiched by 0.2 $\mu$m thick unstrained $In_{0.53}Ga_{0.47}As$ confinement layers, lattice matched with InP substrate.

## 2 Results and discussion

Photoluminescence (PL) study of grown heterostructures has been performed at room temperature. $Ar^+$ laser with 488 nm line has been used for excitation with density of 50 W/cm$^2$.

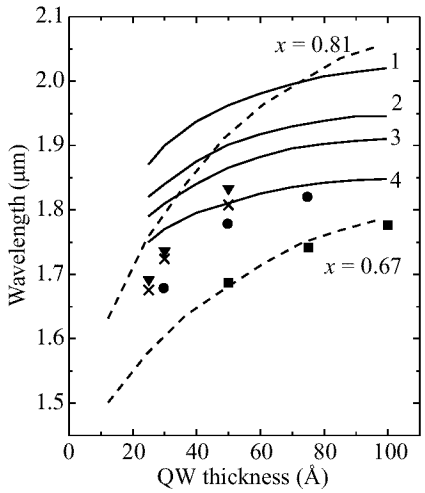


**Fig 1.** PL data of $In_xGa_{1-x}As$ QWs vs well thickness for different composition ($x$) at 300 K.

Figure 1 demonstrates the emission wavelength of $In_xGa_{1-x}As/In_{0.53}Ga_{0.47}As$ QWs as function of QW thickness at room temperature. Dots are our experimental data for QWs with different indium content in the well: (triangle): $x = 0.81$, (cross): $x = 0.76$, (circle): $x = 0.73$, (square): $x = 0.69$. The dotted curves are the experimental results for composition $x = 0.81$ and $x = 0.67$ from [5]. The solid curves (1–4) are our theoretical data for the same composition $x$: 1—0.81; 2—0.76; 3—0.73; and 4—0.69. The calculation has been made for the electron transitions to the first heavy hole level, because determined by strain energy gap between the heavy hole and light hole subbands in $In_xGa_{1-x}As$ compressivelly strained QWs fits into the interval: 64 meV ($x = 0.69$) — 115 meV ($x = 0.81$). Calculations have shown that the QWs in conduction band are very shallow in investigated heterostructures with $In_{0.53}Ga_{0.47}As$ confirement layers. Therefore the wavelength dependence of QW's thickness connected with heavy hole quantization only and the slope of the curves is not sharp in Fig. 1.

It follows from Fig. 1 that the shape of our calculated and measured curves are indentical, but theoretical results shift into the long-wavelength range. The discrepancy between theory and experiment in our opinion is attributable to the fact that the QWs interfaces are not ideal, what can be explained by In segregation from interfaces. As a result, the shape and so the width of the QWs has changed. On the other hand, the segregation can variate the average composition of the solid solution in QWs, especially for narrow wells.

Figure 2 shows our measured dependence of wavelength versus composition $x$ in $In_xGa_{1-x}As$ QWs at 300 K. As shown from figures, the wavelength of 2 $\mu$m can be obtained in strongly compressively strained (lattice mismatch 2%) QWs with width up to 100 Å.

## 3 Conclusion

We have presented $In_xGa_{1-x}As/In_{0.53}Ga_{0.47}As/InP$ heterostructures with compressive-strained QWs grown by LP MOVPE. Preliminary studies of these samples demonstrate

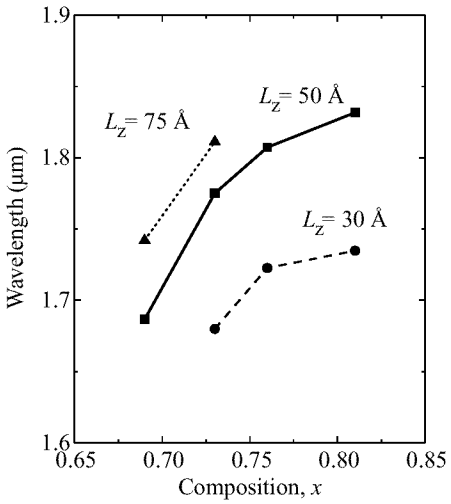


**Fig 2.** PL data of $In_xGa_{1-x}As$ QWs vs composition ($x$) for different well thickness at 300 K.

the emission wavelength in a range 1.65–1.85 $\mu$m. Comparison of our theoretical and experimental data shows that the shape of grown QWs is not rectangular because of indium segregation from QW's interfaces.

This work was supported by the Russian Foundation for Basic Research, grant No. 98-02-18266 and the program "Physics of solid state nanostructures", grant No. 96-2005.

## References

[1] J. Diaz, H. Yi, A. Rybaltowski, et al., *Appl. Phys. Lett* **70** 40 (1997).
[2] D. Z. Garbuzov, R. U. Martinelly, H. Lee, et al., *Appl. Phys. Lett* **69** 2006 (1996).
[3] P. J. A. Thijs, L. F. Tiemejer, J. J. M. Binsma, et al., *IEEE J. Quant. Electron* **QE-30** 477 (1994).
[4] D. Z. Garbuzov, L. Xu, S. R. Forrest, et al., *Electron. Lett* **32** 1717 (1996).
[5] J. Dong, A. Ubukata, K. Matsumoto, *Jpn. J. Appl. Phys.* **36** 5468 (1997).

Ioffe Institute
6th Int. Symp. "Nanostructures: Physics and Technology"
St Petersburg, Russia, June 22–26, 1998.



# DFB laser diode with variable diffraction grating period

*G. S. Sokolovskii*, A. G. Deryagin and V. I. Kuchinskii
Ioffe Physico-Technical Institute RAS, Polytechnicheskaya 26, St.Petersburg, Russia

Single-mode semiconductor DFB lasers are considered to be an optimal light sources for optical communicational and information processing systems. DFB lasers with first order corrugation demonstrate the best threshold characteristics. However, "classical" first-order DFB laser has noncontrollable corrugation phase at the laser facets and, because of this, poor single longitudinal mode operation yield.

In 1976 Haus and Shank [1] have proposed and theoretically investigated DFB laser with tapered structure. They have shown that coupling and Bragg parameter variations along the laser structure remove the threshold degeneracy of the 1-st order DFB lasers and cause light generation exactly at the Bragg frequency. It is important to notice that coupling and Bragg parameters variations can be obtained not only by the effective refractive index variation, but by the corrugation period ($\Lambda$) modulation as well.

The simplest case of the antisymmetric taper DFB is the coupling and Bragg coefficients step at the centre of the DFB structure. Such a step can be created by the insertion of the quater-wave section ($\lambda/4$) between two equal uniform DFB structures. Experimentally $\lambda/4$-shifted DFB lasers demonstrate single-mode generation only near threshold current and even for small pumping currents ($I > I_{\text{th}}$) "spatial hole burning" in the ($\lambda/4$-shift region causes spectrum degeneration from single-mode to multimode.

To obtain DFB laser with sufficiently more uniform light intensity distribution along the active region (i.e. with greatly reduced "spatial hole burning") we propose to use tapered structure caused by the variation of the refractive index modulation period along the laser structure.

Diffraction grating was created by the holographic photolitography method. Holographic photoresist exposure procedure was carried out according to the "corner" scheme (Fig. 1a). The argon laser ("Spectra-physics-2020", $\lambda_0 = 0.3511\,\mu$m) after widening and spatial filtration illuminated the sample and the mirror, fixed at the 90° as regards to each other. Interferention pattern period "$\Lambda$" was determined by the angle of the "corner" turn according to the relation:

$$\Lambda = \frac{\lambda_0}{2\sin\alpha} \tag{1}$$

where $\alpha = 0$ corresponds to the normal angle of the light incidence on the sample.

For the creation of the diffraction grating with variable period we propose to use the "corner" scheme with sufficient illumination beam divergence. Generally, some grating period variation takes place always, but usually (long distance from the "corner" to pin-hole and small distance from the sample to the centre of the "corner") it is less than 0.01 Å/cm, and the grating period is accurately given by the expression (1).

But for the significantly reduced $l$, the strongly increased coordinate dependence of the grating period is observed. The grating period dependence on the $y$ coordinate

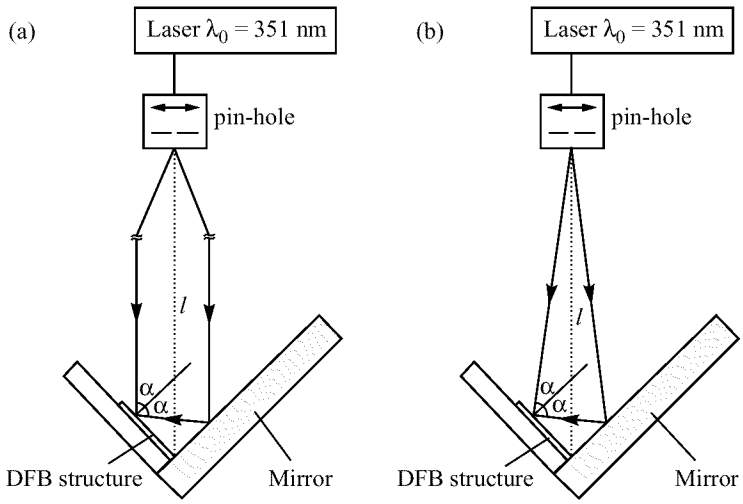


**Fig 1.** The "corner" scheme of holographic photolitography.

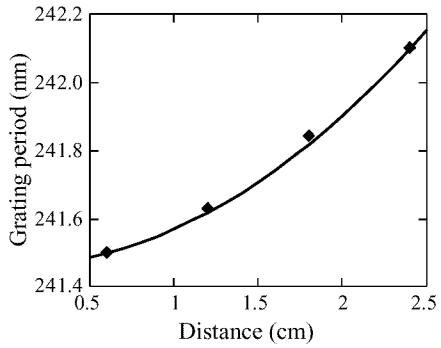


**Fig. 2.** Grating period vs distance from the centre of the "corner" for the "corner" scheme of holographic photolithography for $\lambda_0 = 351.1$ nm, $\alpha = 46.64^\circ$ and $l = 40$ cm.

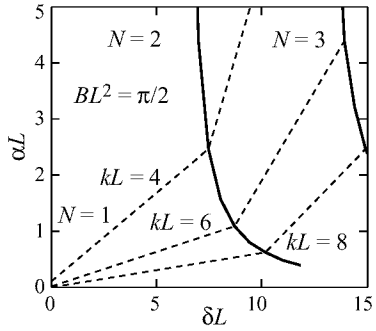


**Fig. 3.** The approximate gain coefficients vs frequency deviations with DFB coupling as a parameter for DFB structure with variable grating period.

(perpendicular to the grooves of the grating) is given by the following expression:

$$\Lambda = \lambda_0 \left( \frac{l \sin\alpha + y}{\sqrt{l^2 + 2yl\sin\alpha + y^2}} + \frac{l \sin\alpha - y}{\sqrt{l^2 - 2yl\sin\alpha + y^2}} \right)^{-1} \qquad (2)$$

where $l$ is the distance from the pin-hole to the centre of the "corner".

In the present work we have used $\times 80$ ($F = 0.5$) microobjective for the beam widening and the 15 $\mu$m pin-hole for the spatial beam filtration. We have obtained good quality diffraction gratings with 0.24 $\mu$m grating period, 0.1–0.15 $\mu$m corrugation depth and up to 0.5 Å/cm grating period variation.

According to [1] Bragg deviation for the tapered DFB structure is expressed as follows: $\delta(y) = \beta - [(\pi/\Lambda(y)]$. Unfortunately the expression (2) is too complicated for the direct substitution. It can be significantly simplified by expressing the coordinate $y$

as the sum $y = Z_0 + z$. This transition must be understood as follows. The distance from the centre of the "corner" to the considered point $y$ is the sum of the distance from the centre of the "corner" to the centre of the laser $Z_0$ and the distance from the centre of the laser to the considered point $z$: $Z_0 \gg z$; $l \gg Z_0$. Using this condition and

$$\lim_{x\to 0} \frac{1}{\sqrt{1 \pm x}} = 1 \mp \frac{x}{2} \tag{3}$$

and neglecting the small terms of the second order one can obtain:

$$\beta(z) = \frac{\pi}{\Lambda(z)} = \frac{\pi}{\Lambda_0} - Bz \tag{4}$$

where

$$\Lambda_0 = \frac{\lambda_0}{2\sin\alpha[1 - 2(Z_0^2/l^2)]} \qquad B = \frac{\pi}{\lambda_0}\frac{8Z_0\sin\alpha}{3l^2}. \tag{5}$$

We consider the medium with quasiperiodical corrugation of refractive index:

$$n(z) = n + n_1 \cos\left[2\beta(z)z\right]. \tag{6}$$

The system of differential equations for coupled waves $R$ and $S$ in this case is as follows:

$$\begin{aligned} -(\mathrm{d}R/\mathrm{d}z) + [\alpha - \mathrm{i}\delta(z)]\,R &= \mathrm{i}k(z)S \\ (\mathrm{d}S/\mathrm{d}z) + [\alpha - \mathrm{i}\delta(z)]\,S &= \mathrm{i}k^*(z)R \end{aligned} \tag{7}$$

$$\delta(z) = \beta - \beta(z) = \delta_0 + Bz, \quad k(z) = k_0 \exp(\mathrm{i}Bz^2) \tag{8}$$

where $\delta_0$ is the Bragg deviation at the "centre" of the structure — the "effective" Bragg deviation and $k_0$ is the "effective" coupling:

$$\delta_0 = \beta - \beta(0) = \frac{n\omega}{c} - \frac{\pi}{\Lambda_0}, \quad k_0 = \frac{\pi n_1}{\Lambda_0}. \tag{9}$$

It must be noted, that the "effective" coupling and Bragg deviation are the values of these parameters for the convenient DFB structure. Note, that at the frequency matched to the centre of the frequency gap of the DFB laser with diffraction grating period $\Lambda_0$, Bragg deviation becomes the antisymmetrical function of the distance. The last means that this case is particular and the frequency $\omega = \pi c/n\Lambda_0$ is the centre of symmetry of the threshold gain spectrum of the DFB laser with variable diffraction grating period.

Substituting (8) in (7) one can obtain for $R(z)$ and $S(z)$:

$$R'' - \mathrm{i}2BzR' + \left(3B^2z^2 + \mathrm{i}4Bz + \mathrm{i}B - k_0^2 - \alpha^2\right)R = 0 \tag{10}$$

$$S'' + \mathrm{i}2BzS' + \left(3B^2z^2 + \mathrm{i}4Bz - \mathrm{i}B - k_0^2 - \alpha^2\right)S = 0 \tag{11}$$

where $\alpha = \alpha + \mathrm{i}\delta$ is the gain coefficient. Estimation of the gain coefficients for different modes of DFB laser with variable diffraction grating period is the ultimate aim of this work.

The particular solutions of (10) and (11) are:

$$r(z) = \exp\left(\frac{\mathrm{i}Bz^2}{2}\right) D_\nu(\xi_r), \qquad s(z) = \exp\left(-\frac{\mathrm{i}Bz^2}{2}\right) D_{-\nu}(-\xi_s) \tag{12}$$

where $\nu = ik_0^2/4B$, $\xi_r = 2z\sqrt{iB} - \alpha/\sqrt{iB}$, $\xi_s = 2z\sqrt{-iB} + \alpha/\sqrt{-iB}$.

To obtain the gain coefficients it is possible to analyze the considered structure on the computer or to use the perturbation approach providing the physical insight into the behaviour of DFB structures with variable grating period. In the limit of low-gain and high Q the threshold gain is inversely proportional to the external Q-factor of the resonant transmission mode [1].

$$2\alpha = \frac{\omega_0}{v_g}\frac{1}{Q_{\text{ext}}} \tag{13}$$

where $\omega_0$ is the frequency of the resonant mode, $v_g$ is the group velocity, and external Q-factor is:

$$\frac{1}{Q_{\text{ext}}} = \frac{P_s}{\omega_0 W} \tag{14}$$

where $P_0$ is the output power of the resonant mode according to the first order of perturbation approach, and $W$ is the energy accumulated by the structure:

$$P_s = |R_0 + \Delta R|^2 - |S_0 + \Delta S|^2 \Big|_{z=-L/2}^{z=L/2}, W = \frac{1}{v_g}\int_{-L/2}^{L/2} |R_0|^2 - |S_0|^2 \, dz. \tag{15}$$

In our case the grating period variation is small in comparison to the step of diffraction grating. Hence, the amplitudes $R$ and $S$ variation from these amplitudes for the uniform grating is small. Thus we can put the zero-order amplitudes $R_0$ and $S_0$ equal to the solutions for the convenient DFB laser with zero loss:

$$S_0 = \pm A \sinh\left[\gamma\left(z \pm \frac{L}{2}\right)\right], \qquad R_0 = \pm\frac{\gamma A}{ik_0^*}\cosh\left[\gamma\left(z \pm \frac{L}{2}\right)\right], \qquad z \lessgtr 0 \tag{16}$$

where $\gamma = |k_0|$ is constant along the structure.

Using (6)–(9) and $|R_0| \approx |S_0|$, one can get:

$$\alpha L = \frac{|k_0|L}{\sinh(|k_0|L) - |k_0|L}\left(1 + \frac{BL^2}{|k_0|L}\right). \tag{17}$$

The resonant frequencies and thresholds for the modes of higher orders can be obtained by the same procedure. In this case $\beta = \sqrt{\delta^2 - |k_0|^2}$ and

$$\alpha L = \left(\frac{2m\pi}{|k_0|L}\right)^2, \qquad \delta L = \pm\sqrt{(2m\pi)^2 + (|k_0|L)^2}. \tag{18}$$

Gain coefficients of DFB laser with variable period of diffraction grating defined by (17)–(18) with feedback efficiency $k_0L$ as a parameter are represented in the Fig. 3.

The above calculations shows that the proposed DFB laser diode with variable period of diffraction grating has the single-frequency gain spectrum like a $\lambda/4$ laser and uniform light intensity distribution like the convenient DFB laser.

The work was done under the financial support of RFBR (grant No. 96-02-17864a).

## References

[1] H. Haus, C. Shank, "Antisymmetric taper of distributed feedback lasers", *IEEE J. Quantum Electron.* **QE-12** No. 9, 532-539 (1976).

Ioffe Institute
6th Int. Symp. "Nanostructures: Physics and Technology"
St Petersburg, Russia, June 22–26, 1998.



# Dual modulation of laser diode emission polarization

*G. S. Sokolovskii*, A. G. Deryagin and V. I. Kuchinskii
Ioffe Physico-Technical Institute RAS, St. Petersburg, Russia

Coexisting, switching and bistability of TE/TM-polarizations of radiation of laser diodes with strained active layer has been investigated in [1-4]. The phenomenological model explicating the effect of polarization switching and bistability was developed in [5, 6]. Later on the analytical expressions for polarization switching time were obtained [7]. These expressions allows one to evaluate the influence of different laser diode parameters on polarization switching time.

Laser diodes with switching or bistable polarization of radiation may be extremely useful for data transfer and processing systems, for example, for wavelength division multiplexing systems [8]. It seems to be very important to investigate the possibilities for direct modulation of laser diode emission polarization. The modulation of the state of polarization of the optical carrier can eliminate anisotropic gain saturation (polarization hole burning) in the erbium-doped fiber amplifiers, which can severely degrade the optical signal-to-noise ration in optically-amplified ultra-long lightwave systems [11]. High-speed polarization scramblers are employed in modern optical communicational systems to depolarize the optical carrier launched into the transmission fiber. Semiconductor lasers with depolarized emission are, therefore, very promising devices for optical communication systems because they can be integrated with modulators in a single compact monolithic devices.

In present work the dual modulation (by pump current and confinement factor modulation) possibility is considered to be a method for direct control of radiation polarization. In particular it can be a method to obtain the depolarized laser emission.

The main idea of dual modulation is as follows. The power-current characteristic of the laser diode with polarization switching has a region where degree of polarization and output power are the linear functions of the pump current [7]. Location of this region on power-current characteristic depends, in particular, on optical confinement factor. Thus, it seems possible to change the degree of polarization by confinement factor variation and to keep constant output power by pumping current. The modulation of the confinement factor can be carried out by applying the potential on the side contacts of the laser diode [10].

The system of the rate equations [7] taking into account the confinement factors of TE/TM modes $\Gamma_{TE/TM}$ is as follows:

$$\begin{aligned}
\frac{dN}{dt} &= \frac{I}{qV} - g_{TE}(N - N_{TE})(1 - \varepsilon_{EE}S_{TE} - \varepsilon_{EM}S_{TM})S_{TE} - g_{TM}(N - N_{TM}) \\
&\quad \times (1 - \varepsilon_{ME}S_{TE} - \varepsilon_{MM}S_{TM})S_{TM} - \frac{N}{\tau} \\
\frac{dS_{TE}}{dt} &= \Gamma_{TE}g_{TE}(N - N_{TE})(1 - \varepsilon_{EE}S_{TE} - \varepsilon_{EM}S_{TM})S_{TE} + \Gamma_{TE}\beta\frac{N}{\tau} - \frac{S_{TE}}{\tau_{TE}} \qquad (1) \\
\frac{dS_{TM}}{dt} &= \Gamma_{TM}g_{TM}(N - N_{TM})(1 - \varepsilon_{ME}S_{TE} - \varepsilon_{MM}S_{TM})S_{TM} + \Gamma_{TM}\beta\frac{N}{\tau} - \frac{S_{TM}}{\tau_{TM}}
\end{aligned}$$

where $N$ is the carrier concentration, $S_{TE/TM}$ is the density of TE/TM-polarized photons, $g_{TE/TM}$ is the linear gain for TE/TM-polarized light, $\tau_{TE/TM}$ is the lifetime of TE/TM-polarized photons, $N_{TE/TM}$ is the transparency concentration for TE/TM-polarized light, $\tau$ is the carrier lifetime, $\varepsilon_{ij}$ are the nonlinear gain coefficients, $\beta$ is the spontaneous emission coefficient, $q$ is the elementary charge and $V$ is the volume of the active medium.

Usually the system of rate equations is analyzed by the numerical methods. This approach can not describe the process dynamics in the explicit form. Authors of [7] have proposed to apply the Lyapunov method [9] to analyze the stability of solutions of the rate equations system. As a result of the analysis the eigenvalues of the rate equations system were obtained. The last represent the characteristic time for transition of the system from one steady state to another. The stability of the system (1) was analysed using the constant carrier density approximation $dN/dt = 0$. This condition allows one to perform the very convenient transformation:

$$\begin{aligned}\frac{dS_{TE}}{dt} &= \Gamma_{TE} g_{TE}\left(\frac{I}{qV} - \frac{S_{TE}}{\Gamma_{TE}\tau_{TE}} - \frac{S_{TM}}{\Gamma_{TM}\tau_{TM}} - \frac{N_{TE}}{\tau}\right) \\ &\quad \times (1 - \varepsilon_{EE} S_{TE} - \varepsilon_{EM} S_{TM})\, S_{TE} - \frac{S_{TE}}{\tau_{TE}} \\ \frac{dS_{TM}}{dt} &= \Gamma_{TM} g_{TM}\left(\frac{I}{qV} - \frac{S_{TE}}{\Gamma_{TE}\tau_{TE}} - \frac{S_{TM}}{\Gamma_{TM}\tau_{TM}} - \frac{N_{TM}}{\tau}\right) \\ &\quad \times (1 - \varepsilon_{ME} S_{TE} - \varepsilon_{MM} S_{TM})\, S_{TM} - \frac{S_{TM}}{\tau_{TM}}\end{aligned} \tag{2}$$

After linearization of the modified rate equations system we can get its eigenvalues named according to [7] stability (instability) coefficients:

$$\begin{aligned}P_{TE/TM} &= \Gamma_{TE/TM} g_{TE/TM} \tau \left(\frac{I}{qV} - \frac{s_{TM/TE}}{\Gamma_{TM/TE}\tau_{TM/TE}} - \frac{N_{TE/TM}}{\tau}\right) \\ &\quad \times \left(1 - \varepsilon_{EM/ME} s_{TM/TE}\right) - \frac{1}{\tau_{TE/TM}}\end{aligned} \tag{3}$$

where $s_{TE/TM}$ is the TE/TM-polarized photons density in the absence of the photons of another polarization:

$$\begin{aligned}s_{TE/TM} &= \frac{1}{2}\left[\frac{1}{\varepsilon_{EE/MM}} + \Gamma_{TE/TM}\tau_{TE/TM}\left(\frac{I}{qV} - \frac{N_{TE/TM}}{\tau}\right)\right] \\ &\quad - \left\{\frac{1}{4}\left[\frac{1}{\varepsilon_{EE/MM}} + \Gamma_{TE/TM}\tau_{TE/TM}\left(\frac{I}{qV} - \frac{N_{TE/TM}}{\tau}\right)\right]^2\right. \\ &\quad \left. - \frac{\Gamma_{TE/TM}\tau_{TE/TM}}{\varepsilon_{EE/MM}}\left(\frac{I}{qV} - \frac{N_{TE/TM}}{\tau} - \frac{1}{\Gamma_{TE/TM} g_{TE/TM}\tau_{TE/TM}\tau}\right)\right\}^{1/2}\end{aligned} \tag{4}$$

As was shown in [7] three combinations of stability coefficients are possible: both coefficients are positive — TE and TM modes coexist; both coefficients are negative — bistable state; and, lastly, the stability coefficients have different signs — in this case the laser diode emits the radiation for which the eigenvalue is negative.

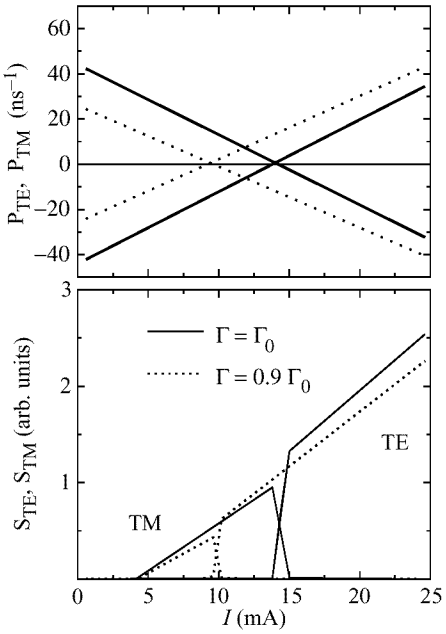


**Fig. 1.** Power-current characteristic and stability coefficients vs pumping current for different confinement factor values.

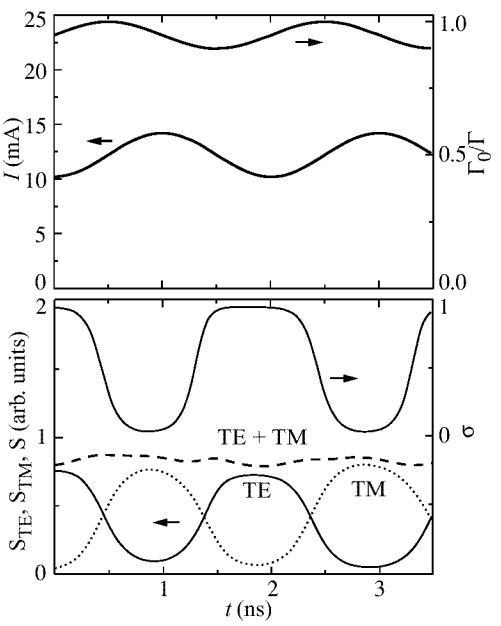


**Fig. 2.** Time dependence of TE/TM-photon densities and degree of polarization of laser diode radiation for dual modulation. Pumping current and confinement factor modulation is also represented.

Fig. 1 represents the power-current characteristics for TE and TM-polarized radiation for two values of confinement factor Γ. One can see that changing of confinement factors $\Gamma_{TE/TM}$ allows to change the position of the polarization switching point on the laser diode power-current characteristic (Fig. 1). For laser diode parameters, used in our calculations, the ten percent changing of confinement factor causes the 1.5 times change of polarization switching current. However one can tune the polarization degree of laser diode radiation by modulating of confinement factor and keep the constant output power by pumping current variation (Fig. 2). The relaxation oscillations caused by changing of the confinement factor can be eliminated by appropriate phase shift of the pump current modulation regarding to the phase of $\Gamma_{TE/TM}$ modulation [10].

In order to simplify the calculations of amplitude of $\Gamma_{TE/TM}$ modulation, one can determine the polarization switching current $I_{sw}$, i.e. the pump current value corresponding to the unpolarized laser diode radiation. The exact value of $I_{sw}$ can be calculated by putting $S_{TE} = S_{TM} = S_{sw}$, $dS_{TE}/dt = dS_{TM}/dt = 0$ in (2):

$$I_{sw} = \frac{1}{\Gamma_{TE} g_{TE} \tau_{TE} \tau (1 - \varepsilon_E S_{sw})} + \left(\frac{1}{\tau_{TE}} + \frac{1}{\tau_{TM}}\right) S_{sw} + \frac{N_{TE}}{\tau}$$

$$S_{sw} = B - \sqrt{B^2 - C}$$

$$B = \frac{1}{2}\left(\frac{1}{\varepsilon_E} + \frac{1}{\varepsilon_M} + \frac{1}{\Gamma_{TE} g_{TE} \tau_{TE} \varepsilon_E \Delta N} - \frac{1}{\Gamma_{TM} g_{TM} \tau_{TM} \varepsilon_M \Delta N}\right)$$

$$C = \frac{1}{\varepsilon_E \varepsilon_M}\left[1 + \left(\frac{1}{\Gamma_{TE} g_{TE} \tau_{TE}} - \frac{1}{\Gamma_{TM} g_{TM} \tau_{TM}}\right)\Delta N\right] \tag{5}$$

$$\varepsilon_E = \varepsilon_{EE} + \varepsilon_{EM}, \quad \varepsilon_M = \varepsilon_{MM} + \varepsilon_{ME}, \quad \Delta N = N_{TE} - N_{TM}$$

The polarization switching region caused by modulation of $\Gamma_{TE/TM}$ is limited by the values of switching current corresponding to the minimum and maximum values of $\Gamma$. It must be noted that the hysteresis on power current characteristic of the laser diode [7] can substantially decrease the width of the polarization switching region defined by (5).

In summary, we have considered the laser diode dual modulation (by pump current and confinement factor variation) possibility to be a method to control the polarization of the laser radiation. The carried out mathematical modelling of the laser diode under the dual modulation proved the possibility of direct control of laser radiation polarization keeping the output power near to be constant.

The authors would like to thank F. N. Timofeev for helpful discussions. The work was done under the financial support of RFBR (grant # 96-02-17864a).

## Appendix 1

Laser diode parameters used in calculations were as folows [7]:
$g_{TE} = 1.45\times10^{-6}\,cm^3/s$, $g_{TM} = 1.40\times10^{-6}\,cm^3/s$, $\tau_{TE} = 2.0$ ps, $\tau_{TM} = 1.61$ ps, $N_{TE} = 4.5\times10^{17}\,cm^{-3}$, $N_{TM} = 3.29\times10^{17}\,cm^{-3}$, $\tau = 3$ ns, $\varepsilon_{EM} = 2.0\times10^{-17}\,cm^3$, $\varepsilon_{EE} = 1.0\times10^{-17}\,cm^3$, $\varepsilon_{ME} = 4.5\times10^{-17}\,cm^3$, $\varepsilon_{MM} = 6.0\times10^{-17}\,cm^3$.

## References

[1] D. Akhmedov, N. P. Bezhan, N. A. Bert, S. G. Konnikov, V. I. Kuchinskii, V. A. Mishurnyi, and E. L. Portnoi, *Sov. Tech. Phys. Lett.* **6** 304 (1980).
[2] V. A. Elyukhin, V. R. Kocharyan, E. L. Portnoi, and B. S. Ryvkin, *Sov. Tech. Phys. Lett.* **6** 305 (1980).
[3] K. G. Kalandarishvili, S. Yu. Karpov, V. I. Kuchinskii, M. N. Mizerov, E. L. Portnoi, and V. B. Smirnitskii, *Sov. Tech. Phys. Lett.* **28** 959 (1983).
[4] A. G. Deryagin, D. V. Kuksenkov, V. I. Kuchinskii, E. L. Portnoi, V. B. Smirnitskii, *IEE Proc.-Optoelectron.* **142** No. 1, p. 51-54 (1995).
[5] Y. C. Chen, J. M. Liu, *Optical and Quantum Elctronics* **19** S93–S102 (1987).
[6] G. Ropas, A. Le Floch, G. Jezequel, R. Le Naour, Y. C. Chen, J. M. Liu, *IEEE J. Quant. El.* **QE-23** No.6, 1027-1031 (1987).
[7] G. S. Sokolovskii, A. G. Deryagin, V. I. Kuchinkii, *Tech. Phys. Lett.* **23** 373-376 (1997).
[8] P. M. Hill, R. Olshansky, W. K. Burns, *IEEE Phot. Tech. Lett.* **4** No.5, 500-502 (1992).
[9] A. M. Lyapunov, *The general problem of the stability in motion* [in Russian], Gostekhizdat, Moskow (1950).
[10] S. A. Gurevich, M. S. Shatalov, G. S. Simin, *Int. J. of High Speed Electronics and Systems* **8** No.3, 547-574 (1997).
[11] M. G. Taylor, *IEEE Photon. Tech. Lett.* **5** 1244-1246 (1993).

Ioffe Institute
6th Int. Symp. "Nanostructures: Physics and Technology"
St Petersburg, Russia, June 22–26, 1998.



# Near-field radio-frequency modulated reflectance in semiconductor structures

*A. O. Volkov* and O. A. Ryabushkin
Institute of Radio Engineering and Electronics, Russian Academy of Sciences, Fryazino, Moscow District, 141120, Russia, E-mail: aov228@ire216.msk.su

**Abstract.** In this paper we suggest Near-field configuration Radio-frequency Modulated light Reflectance technique (NRMR). NRMR spectra from GaAs/AlGaAs heterostructure were experimentally obtained. These spectra demonstrate a dramatic change in the reflectance. We have shown that the near-field radio-frequency perturbation are transferred along the heterostucture plane over extremely large distances which may be as large as several millimeters.

## 1 Introduction

Recently, Radio-frequency Modulated Reflectance (RMR) was proposed, as a novel optical modulation spectroscopy of semiconductor structures [1] and its great promise was shown at low temperatures with respect to traditional methods, such as photoluminescence (PL), electroreflectance and photoreflectance (PR). RMR principle is in the radio-frequency (rf) or microwave electric field effect on a light reflection from the structure. The effect of NRMR is due to influence of a local rf field formed by electrodes one of which is much smaller then rf wavelength on a heterostructure dielectric permeability. Being locally enhanced rf electric field excites the sample much stronger than in RMR case. Earlier we have observed a large lateral photo-perturbation propagation in GaAs/AlGaAs, registered by local PL and PR measurements [2]. The NRMR perturbation spreads far more than the photo-excited charges and fields do [2–4].

## 2 Experiment

We investigated GaAs/$Al_xGa_{1-x}As$ heterostructures with two dimensional electron gas grown by molecular beam epitaxy with parameters commonly used in high electron mobility transistors (Fig. 1). To provide near-field radio-frequency perturbation sample was placed between plane electrode (pel, 1 cm$\times$1 cm) and cylindrical electrode (cel, $\oslash$ 100 $\mu$m) (Fig. 2). 20 MHz rf voltage was applied. Amplitude of rf voltage was modulated at 2 kHz. Reflectance was measured by means of optical fibers F1 and F2. All experiments were carried out at the temperature $T = 77$ K, rf voltage 300 V and spectral resolution 0.7 meV.

Fig. 3 shows the scheme of the experimental set-up which we have used to investigate the NRMR effects (Fig. 3). Lamp (L) light is focused into the fiber F1. Receiving fiber F2 guides light reflected from the sample surface to the spectrometer. Photodetector (PD) registers both dc and ac signals. Then ac signal is processed bymeans of the lock-in amplifier, low-frequency generator (lf), rf high-voltage generator (rf) and time delay circuit (tD).

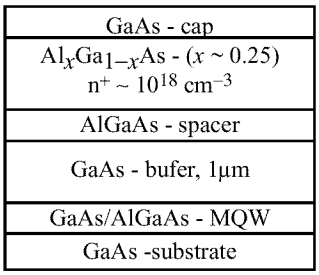


**Fig. 1.** Schematic cross section of modulation doped heterostructure.

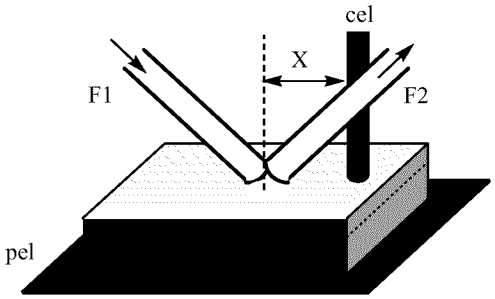


**Fig. 2.** Electrodes and optical fibers spatial arrangement.

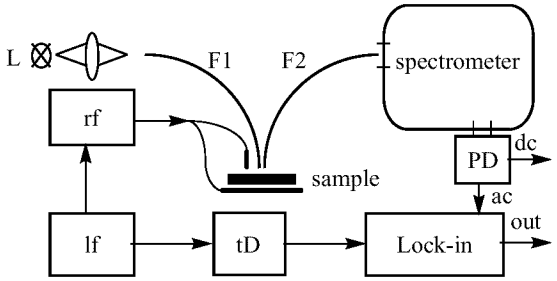


**Fig 3.** Experimental set-up.

## 3 Results and discussion

Fig. 4 shows the NRMR spectrum obtained when the probing light spot was separated from the cylinder electrode by the distance $X \sim 2$ mm. The change in the reflectivity exceeds 4% in the energy region of GaAs band gap (1.508 eV). RMR spectrum (multiplied by a factor 10 for comparison in Fig. 4) was formed at the same voltage as for NRMR but applied to capacitor plane electrodes producing homogeneous perturbation. RMR spectrum shape was described quantitatively by a model of [1] which takes into account the modulation of the internal homogeneous electric fields. But NRMR spectrum is obtained in strong non-homogeneous field. In this case NRMR spectrum shape is described qualitatively by model in [1] for interband transition near to $M_0$ critical point. The broadening of NRMR spectrum part at $E < E_g$ is explained by heating effects of two-dimensional electron gas in the external rf field.

Changing the probing light intensity from 1 mW/cm$^2$ to 100 mW/cm$^2$ did not modify the spectrum significantly. As the intensity was increased from 100 mW/cm$^2$ to 1 W/cm$^2$, respective optical response diminished and became non-linear with respect to rf amplitude. In the case of strong probing light intensity the out-of-phase component of NRMR response becomes considerable. Shown in Fig. 5 are two spectra (in one scale) obtained at the same external conditions. But the former (thin line) was obtained synchronously with the perturbation modulation signal, the latter (thick line) was obtained with 90° phase shift, which corresponds to 125 $\mu$sec time delay. It means that the heterostructure optical properties are changed with respect to rf perturbation appearance moment not only simultaneously but also with a some time delay. It validates

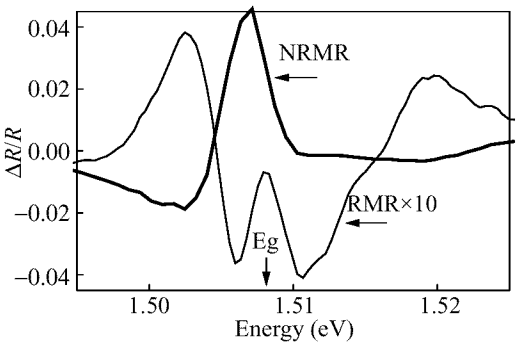


**Fig 4.** RMR and NRMR spectra, probing light intensity 1 mW/cm$^2$.

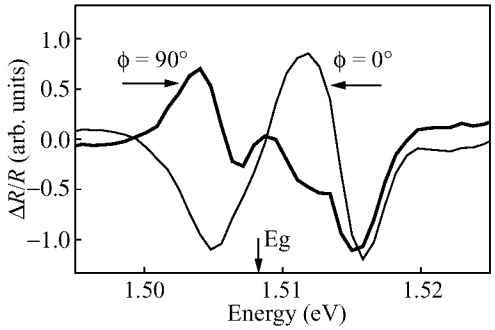


**Fig 5.** Phase dependence of NRMR spectrum with probe intensity 1 W/cm$^2$.

the multi-region GaAs buffer layer model suggested in [1]. Measuring the two NRMR spectra shifted one to another by phase of 90° permits one to investigate the charge carriers transposition in layer. Strong effect of modulated near-field on a light reflectance gives a new possibilities in the design of appropriate high-speed optical modulators, with reflected beam profile being controlled.

*Acknowledgments*

We would like to thank Sablikov V. A. for helpful discussions and encouragement in the course of this work.

This work is supported by Russian Foundation for Basic Research (grant 96-02-18476-a) and Russian Ministry of Science under the Program "Physics of solid state nanostructures" (grant 97-1054).

## References

[1] Ryabushkin O. A. and Sablikov V. A. *JETP Lett.* **67** (1998) (to be published).
[2] Ryabushkin O. A., Sablikov V. A., Volkov A. O. and Mokerov V. G. *Compound Semiconductors 1996*, Inst. Phys. Conf. Ser. No 155, 137-140 (1997).
[3] Sablikov V. A., Polyakov S. V. and Ryabushkin O. A. *Fiz. Tekh. Poluprovodn.* **31**, 393 (1997) (*Semiconductors* **31**, 329 (1997)).
[4] Ryabushkin O. A. and Sablikov V. A. *Pis'ma Zh. Tekh. Fiz.* **22**, 73 (1996) (*Tech. Phys. Lett.* **22**, 338 (1996)).

Ioffe Institute
6th Int. Symp. "Nanostructures: Physics and Technology"
St Petersburg, Russia, June 22–26, 1998.



# Admittance spectroscopy of Schottky barrier structures with self-assembled InAs/GaAs quantum dots

*P. N. Brounkov*†‡, A. A. Suvorova† A. E. Zhukov† A. Yu. Egorov† A. R. Kovsh† V. M. Ustinov† S. G. Konnikov† S. T. Stoddart‡ L. Eaves‡ and P. C. Main‡

† Ioffe Physico-Technical Institute, 194021, St. Petersburg, Russia

‡ Department of Physics, University of Nottingham, NG7 2RD Nottingham, UK

**Abstract.** Capacitance- and conductance-voltage characteristics have been measured at various frequencies and temperatures for a Schottky barrier structure containing three sheets of self-assembled InAs quantum dots in an n-GaAs matrix. By changing the temperature and the frequency of the measuring signal, it is possible to control quantum dot part of capacitance of the structure. It was shown that analysis of the admittance spectra allows us to obtain information about dynamic parameters of quantum dots.

## Introduction

In recent years there has been great interest in the properties of heterostructures containing self-assemled quantum dots (QDs) [1-8]. It has been shown that capacitance-voltage ($C(V)$) spectroscopy may be used to investigate the electronic structure of QDs [5-8]. In this paper we report an admittance spectroscopy study of a structure with a Schottky barrier on a n-type layer containing an array of vertically-coupled quantum dots (VECQDs). This technique allows us to study dynamic properties of QDs.

## 1 Experimental details

The samples are based on a type I InAs-GaAs heterostructure and were grown by MBE on a $n^+$-GaAs substrate. The array of VECQDs consists of three sheets of InAs QDs with a 50 Å thick GaAs spacer inserted between the InAs islanding layers. The QDs were formed in situ as the result of the transformation of an elastically strained InAs layer with effective thickness 1.7 ML on a lattice mismatched GaAs layer. The QDs may be used as stressors to form the next layer of QDs, provided the thickness of the spacer is less than 100 Å [3, 4]. In this case the QDs are vertically aligned (stacked) and electronically coupled in the growth direction. Therefore each stack of QDs may be considered as a one large QD (like a pillar). The VECQDs were sandwiched between a 0.5 $\mu$m-thick GaAs cap and a 1 $\mu$m-thick GaAs buffer layer. Both the cap and buffer layers were uniformly doped with Si at a level of about $2 \times 10^{16}$ cm$^{-3}$ except for 100 Å thick undoped spacers on each sides of the VECQDs layer. Schottky barriers were made by deposition of Au through a shadow mask (350 $\mu$m diameter).

The capacitance ($C$) and conductance ($G$) characteristics of the devices were measured over a frequency range of 10 kHz to 1 MHz using an HP4275A LCR meter. The amplitude of the measuring signal ($V_{\text{osc}}$) was 10 mV.

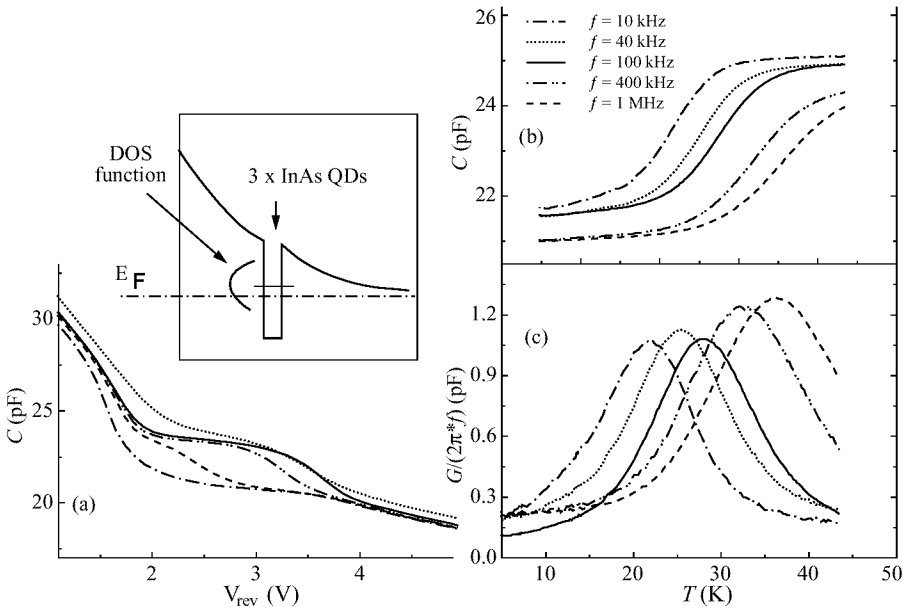


**Fig 1.** (a) $C(V)$ characteristics of QD structure at $f = 1$ MHz measured at digfferent temperatures: ·— 15 K, – – 30 K, —··— 50 K, — 77 K, ··· 200 K. The insert shows the conduction band diagram of the structure. (b) $C(T)$ and (c) $G(T)$ characteristics of QD structure at $V_{rev} = -2.75$ V.

## 2 Results and discussion

There is a step in the $C(V)$ characteristic related to the discharging of the QDs (Fig. 1a) [6-8]. According to the model presented in Refs. [6-8], the width of a plateau in the $C(V)$ characteristic depends on the steady state occupation of the electron levels in the QDs. This, in turn, is determined at a given temperature by the sheet concentration $N_{qd}$ of QDs and the Fermi–Dirac function depending on the relative positions of the electron level in the QDs ($E_{qd}$) and the bulk Fermi level ($E_F$) in the GaAs matrix (insert on Fig. 1a) [6-8]. The sheet concentration of QDs was found to be $N_{qd} = 5 \times 10^{10}$ cm$^{-2}$ from a plan-view transmission electron microscopy image. The density of electron states in the QD sheet may be approximated by a Gaussian function, which describes the spread of energies associated with the distribution of QD sizes [3]. By fitting measured $C(V)$ characteristics to the model [7, 8] we find that the density of electron states in VECQDs corresponds to a Gaussian distribution with centre at $E_{qd} = 70$ meV from the bottom of the GaAs conduction band and standard deviation of $\Delta E_{qd} = 80$ meV.

Our model describes fairly accurately the experimental $C(V)$ and $N_{CV}$(W) characteristics at temperatures higher than 70 K. However, discrepancies between the model and experimental data are observed at $T < 70$ K, when the step in the $C(V)$ characteristic is suppressed. It is due to the fact that the calculated capacitance of the QD structure is derived from the equation $C = \Delta Q/\Delta V$, based on "quasi-static" conditions, i.e., the temporal change in the charge variation $\Delta Q$ caused by the increment of the reverse bias $\Delta V$ is neglected. However, in practice, the capacitance is measured by superimposing

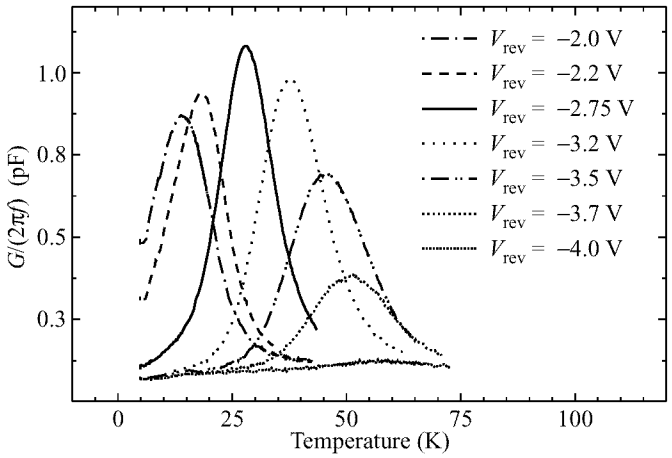


**Fig 2.** $G(T)$ characteristics of the QD structure, measured at $f = 100$ kHz for different values of the $V_{rev}$.

a small oscillation signal $V_{osc}$ at a frequency $f$ on the applied DC reverse bias $V_{rev}$. Note that $V_{osc}$ modulates the charge both at the edge of the space charge region ($dQ_{3D}$) and at the point where the Fermi level crosses the electron level in the QDs ($dQ_{qd}$).

A theoretical treatment of the C(V) characteristics of QD structures [5-7] indicates that in the region of the capacitance plateau from −2.0 V to −3.5 V (Fig. 1a) the change in the space-charge-region width $\Delta W$ due to the increment of the reverse bias $\Delta V$ becomes so small that $dQ_{qd}$ is larger than $dQ_{3D}$, i.e. $C_{qd}$ is higher than $C_{3D}$ (Fig. 1a). As the temperature is lowered from 70 K to 15 K, the quantum part of capacitance $C_{qd}$ decreases (Fig. 1a), despite the fact that the occupation of QDs tends to be saturated [6, 7]. At $T = 15$ K, $C_{qd}$ disappears entirely (Fig. 1a). Considering that escape of electrons from the QDs is a slower process than capture [3], at $T = 15$ K the thermionic emission rate of electrons ($e_n$) from the QDs is much lower than the angular measurement frequency $2\pi f$, i.e. freezing-out of electrons on QD levels takes place [8]. This freezing-out of the carriers in the QDs sheet at low temperatures is a distinctive property of zero-dimensional systems and is not observed in quantum-well structures possessing in-plane conductivity [9].

The thermionic emission rate depends exponentially both on the temperature and the energy of the QD electron levels, therefore through the change of the measurement frequency and the temperature we can control the quantum part of capacitance $C_{qd}$. In Fig. 1b,c $C(T)$ and $G(T)$ characteristics of QD structure measured at $V_{rev} = -2.75$ V are depicted. Temperature of the recovery of the $C_{qd}$ depends on the measurement frequency. Each steps in capacitance corresponds to the peak in conductance. Since the array of self-assembled QDs has a Gaussian density-of-states, we can study different part the QD energy spectra through the change of the reverse bias (insert on Fig. 1a). As the $V_{rev}$ is increased the position of the conductance peak goes to higher temperature (Fig. 2). It means the more deaper states contributes to the quantum part of capacitance $C_{qd}$. Note, that there is no signal in $G(T)$ spectrum if $V_{rev} > -4$ V, because in this case QDs are practically empty (Fig. 1a, Fig. 2).

## 3 Conclusions

We have investigated the frequency-dependent admittance spectra of an n-GaAs structure containing self-assembled InAs QDs. It was found that the $C(T)$ and $G(T)$ characteristics of the quantum part of capacitance $C_{qd}$ depend on the relation between the thermionic emission rate $e_n$ of electrons from QDs and the angular measurement frequency $2\pi f$. Analysis of the admittance spectra can give us information about dynamic parameters of the QDs.

*Acknowledgments*

This work was supported by the INTAS-RFBR program 95-IN-RU-618 and by EPSRC. P.N.B. and L.E. thank the Royal Society and EPSRC, respectively, for support.

## References

[1] L. Goldstein, F. Glas, J. Y. Marzin, M. N. Charasse, and G. Le Roux. *Appl. Phys. Lett.* **47** 1099 (1985).
[2] D. Leonard, M. Krishnamurthy, C. M. Reaves, S. P. Denbaars, and P. M. Petroff. *Appl. Phys. Lett.* **63** 3023 (1993).
[3] N. N. Ledentsov, M. Grundmann, N. Kirstaedter, O. Schmidt, R. Heitz, J. Bohrer, D. Bimberg, V. M. Ustinov, V. A. Shchukin, P. S. Kop'ev, Zh. I. Alferov, S. S. Ruvimov, A. O. Kosogov, P. Werner, U. Richter, U. Goesele and J. Heydenreich. *Solid State Electr.* **40** 785 (1996).
[4] G. S. Solomon, J. A. Trezza, A. F. Marshall, J. S. Harris,Jr. *Phys. Rev. Lett.* **76** 952 (1996).
[5] G. Medeiros-Ribeiro, D. Leonard, and P. M. Petroff. *Appl. Phys. Lett.***66** 1767 (1995).
[6] P. N. Brunkov, S. G. Konnikov, V. M. Ustinov, A. E. Zhukov, A. Yu. Egorov, V. M. Maximov, N. N. Ledentsov, P. S. Kop'ev. *Semiconductors* **30** 492 (1996).
[7] P. N. Brounkov, N. N. Faleev, Yu. G. Musikhin, A. A. Suvorova, A. F. Tsatsul'nikov, V. M. Maximov, A. E. Zhukov, A. Yu. Egorov, V. M. Ustinov, P. S. Kop'ev, S. G. Konnikov. *The Physics of Semiconductors*, Singapore: World Scientific, 1996.
[8] P. N. Brounkov, N. N. Faleev, Yu. G. Musikhin, A. A. Suvorova, A. F. Tsatsul'nikov, V. M. Maximov, A. Yu. Egorov, A. E. Zhukov, V. M. Ustinov, N. N. Ledentsov, P. S. Kop'ev, S. G. Konnikov. *Inst. Phys. Conf. Ser. 155*, Bristol: IOP, 1997.
[9] P. N. Brounkov, T. Benyattou, G. Guillot. *J. Appl. Phys.* **80** 864 (1996).

Ioffe Institute
6th Int. Symp. "Nanostructures: Physics and Technology"
St Petersburg, Russia, June 22–26, 1998.



# Micromagnetic properties and magnetization reversal of Ni nanoparticles studied by magnetic force microscopy

*A. A. Bukharaev*†, D. V. Ovchinnikov†, N. I. Nurgazizov†, E. F. Kukovitskii†, M. S. Kleiber‡ and R. Wiesendanger‡

† Kazan Physical Technical Institute Russian Academy of Sciences, Sibirsky Tract, 10/7, Kazan, 420029, Russian Federation

‡ Institute of Applied Physics,Jungiusstrasse 11, 20355, Hamburg, Germany

**Abstract.** Ni nanoparticles with sizes ranging from 40 to 400 nm formed by thermal annealing of thin film were investigated by atomic and magnetic force microscopy *in situ* in presence of applied magnetic field up to 300 Oe. By comparison of the corresponding experimental AFM and MFM images and computer simulated MFM images, the small particles with diameter below 100 nm were found to be in single domain state. The the direction of total magnetization of greater particles is defined by their shape anisotropy. The MFM image features and the magnetization reversal mechanism of such particles are explained in terms of a vortex magnetization.

## Introduction

Scanning probe microscopy permits simultaneous measurements of the topography and magnetic stray field of the sample with nanometer-scale resolution [1]. It is essential, that it is possible to study magnetization reversal of surface structures with magnetic force microscopy (MFM) *in situ* using an external magnetic field [2]. A special interest at the present time is caused by planar magnetic nanostructures, containing isolated ferromagnetic single domain nanoparticles because of their potential as ultra high density magnetic storage media (so-called quantized magnetic disks—QMD [3]).

The detection of uniformly magnetized ferromagnetic nanoparticles obtained after thermal annealing of the thin nickel film with MFM and the studying of the dependence of magnetization reversal process in such particles on their shapes and sizes in the presence of applied magnetic field are the purposes of the present work.

## Experiments and discussion

Surface topography images with nanometer-scale resolution were obtained with scanning probe microscope P4-SPM-MDT. Magnetic measurements were taken by Nanoscope III. In both microscopes a.c. mode was used. Working in lift mode with double scanning of each line with registrating at first a relief and then magnetic interaction allows to obtain simultaneously the topographical and magnetic image of the same place of a surface. The resulting magnetic image consists of dark and light sites (so-called magnetic contrast), corresponding to areas with various magnetic interaction of a magnetic tip with a surface [1].

The Si cantilevers coated by Fe were used during magnetic measurements. Previously the tip was magnetized so that its magnetization direction was perpendicular to the sample surface. During the experiments on magnetization reversal *in situ* the MFM

was placed between electromagnet poles so as external magnetic field ranged from −300 up to +300 Oe was along the surface plane.

The Ni films were prepared on fused quartz substrates with vacuum evaporation. The AFM images show that such film consists of the tightly adjoining Ni islands completely covering the substrate, with their profile heights ranging from 30 up to 70 nm. In other words, the metal islands are connected to themselves by bridges.

After annealing in atmosphere at 800°C well separated particles mainly of two types were obtained: small with diameter from 60 up to 150 nm and height up to 65 nm (Fig. 1*a*), and greater with diameter from 250 up to 400 nm and height up to 250 nm. Majority of particles with the lateral sizes less then 150 nm have the shape close to spherical, however, among the greater particles there are the axial particles with the aspect ratio 1:2 (more rarely 1:3). From measurements on boundary of film-substrate it is well visible that the particles are placed separately and do not touch each other. The AFM data shows, that during the annealing the bridges between metal islands tear because the metal islands tend to have the thermodynamically equilibrium shape, defined by forces of surface tension, at high temperature. The observable film transformation is known as a self-coalescence process [4].

Visible lateral sizes of the small particles, with radius comparable to tip radius, can be essential larger than true ones due to known tip-sample convolution effect. Therefore earlier offered numerical deconvolution technique was used for estimating of the lateral sizes of particles [5]. The corrected diameters of particles with the visible lateral sizes less than 150 nm were approximately on 30 percents less owing to convolution with such tip. The small particles with heights up to 70 nm had nearly spherical shape, as their real diameters were equal to 80–90 nm.

The known formula for magnetic interactions [1] have been used for computer simulation of the MFM images from the Ni particles. A particle was approximated by the cylinder, height and diameter of which coincide with the sizes of the particle. The cylinder was divided into 900 fragments. Each fragment was substituted by a single magnetic dipole, which was placed in a barycentre of the fragment. In single domain state when the magnetic moments of all fragments of the particle are oriented uniformly along the surface the corresponding magnetic image should have characteristic view, presented in Fig. 1*b*. The magnetic contrast (dark and light areas on the MFM image) is connected with formation of magnetic poles on the ends of single-domain ferromagnetic particle. The line which connects centers of light and dark areas on the magnetic image shows the direction of vector of summarized particle magnetization (**M**).

In case of absence of an additional external field, the MFM images with enough strong magnetic contrast which is characteristic to uniform magnetization, were observed only from rather small spherical particles, with a visible diameter less than 100 nm that is well conformed to known theoretical and experimental value of the critical size of a single domain state for Ni particles, which is equal to 60 nm [6]. The magnetization of axial ones was directed along a long axis of the particle, that is along an easy axis of magnetization.

Under rather small external magnetic field (300 Oe) all magnetic moments of Ni spherical particles line up along the field with saving a high degree of an order (Fig. 1*c*). After change of direction of the external magnetic field on 180° magnetization vector **M** of the particle also turns on 180° (Fig. 1*d*), that is characteristic of magnetic reversal

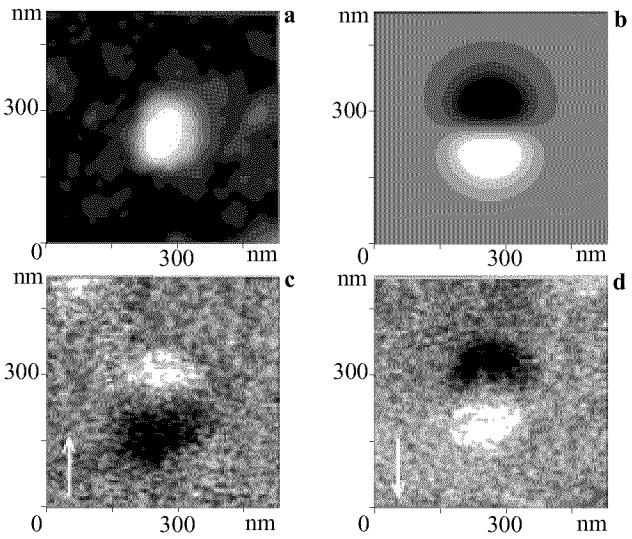


**Fig 1.** Magnetization reversal of single domain Ni particle in an external magnetic field. *a*—topographic image of the particle; *b*—computer simulation of MFM-image, corresponding to this particle. *c*, *d*—experimental MFM-image of the same particle at the presence of field 300 Oe (direction of the field is marked by the arrows).

of single domain particles [2].

The magnetic contrast from lager particles is much weaker and has more complex structure. It testifies that such particles are not single domain and are magnetized non-uniformly. The experimental magnetic images of these particles do not show domain walls. It allows to assume, that vortex distribution of magnetization is characteristic for the larger particles. The presence of magnetization turbulences in a particle should considerably reduce the magnitude of magnetic interaction of a microprobe with such particle and also reduce magnetic contrast.

The process of magnetic reversal of larger particles differs from magnetic reversal of single domain particles. The switching on of an additional external field (300 Oe) during measurements appreciably strengthens magnetic contrast, first of all for axial particles with magnetization directed along the field or under a small angle to it, what speaks about increase of a degree of uniformity of their magnetization. It is essential, that the direction of a vector of a total magnetization **M** for axial particles does not coincide with an external field and builds along a long axis of the particle, that coincides with an axis of easy magnetization of the particle connected to its shape anisotropy. The features of magnetic reversal of axial particles, apparently, are connected to their individual hysteresis properties, that is to influence of such factors as its shape anisotropy, magnetic crystalline anisotropy, remanent magnetization, external field magnitude on a degree of magnetic order of separate particle. The assumption of non-uniform magnetic reversal of large particles with formation of vortex structures is well enough coordinated with experimental researches and theoretical accounts carried out earlier by other methods [7].

Thus, in the work the first results demonstrating successful applying of atomic and

magnetic force microscopy for study of morphology, micromagnetism and magnetization reversal of Ni nanoparticles obtained by coalescence method are submitted. The isolated metal particles with the lateral sizes from 40 up to 400 nm and height from 40 up to 250 nm were fabricated on the surface of fused quartz. The particles with size less than 100 nm had the shape close to spherical. The larger flat particles were both round, and axial with aspect ratio 1:2 mainly. By comparison of the corresponding topographical and magnetic images, and also with computer simulation of the magnetic images it was found, that the particles with size less than 100 nm are single domain and easily switch in a direction of an external field, keeping a uniform magnetization. The increase of a degree of uniformity of magnetization in magnetic field is characteristic for larger axial particles, however, the direction of total magnetization of such particles is defined by an anisotropy of their shape, instead of external field. The features of the magnetic images of particles with the size more than 150 nm and mechanisms of their magnetization reversal is associated with the presence of vortex structure of magnetization in them.

The work is supported by Program "Physics of solid state nanostructures" (Grant 96-1034), by Russian Basic Research Foundation (Grant 96-02-16323) and by Russian Ministry of Sciences and Technologies (Grant 143/57/4).

## References

[1] Grutter P., Mamin H. J. and Rugar D. *Magnetic Force Microscopy (MFM): Scanning Tunneling Microscopy. II.*, Berlin: Springer Verlag, 1992.
[2] Lohndorf M., Wadas A., Lutjering G., Weiss D., Weisendanger R. *Z. Phys. B* **101** 1 (1996).
[3] Chou S. Y., Kraus P. R., Kong L. *J. Appl. Phys.* **79** 6101 (1996).
[4] Trusov L. I., Holmyansky V. A. *Island Metal Films*, Moscow: Metallurgiya, 1973.
[5] Bukharaev A. A., Berdunov N. V., Ovchinnikov D. V., Salikhov K. M. *Microelectronics.* **26** 163 (1997).
[6] Kondorsky E. I. *Izvestya of AS USSR. Physical series.* **42** 1638 (1978).
[7] Fredkin D. R., Koehler T. R. *J. Appl. Phys.* **67** 5544 (1990).

Ioffe Institute
6th Int. Symp. "Nanostructures: Physics and Technology"
St Petersburg, Russia, June 22–26, 1998.



# Space-charge spectroscopy of self-assembled quantum dots InAs in GaAs

N. V. Bazlov†, *O. F. Vyvenko*†, O. A. Trofimov†,
A. Yu. Egorov‡, A. R. Kovsh‡, V. M. Ustinov‡ and A. E. Zhukov‡
† Insitute of Physics of St. Peterburg State University,
198904 St. Petersburg, Russia
‡ Ioffe Physico-Technical Institute RAS,
194021 St. Petersburg, Russia

**Abstract.** Semiconducting structure containing the planes of self assembled InAs quantum dots (QD) in the GaAs matrix are studied by means of junction space charge spectroscopy methods. The effects associated with low temperature GaAs covering layer, with the wetting layer (WL) and with QDs itself are separated. It is found that DLTS signal in the structures with the high density of the QD exhibits not usual properties. A new model is proposed that takes into account the electron capture from the free electron "lake" arising due to a large repulsive barrier of the QD planes.

## 1 Introduction

At the present the electronic properties of semiconducting structures containing self-assembled quantum dots (QD) are studying intensively both theoretically and experimentally. A satisfactory agreement was found between the theory and experimental data obtained by means of the optical spectroscopy methods [1]. Recently, junction space charge spectroscopy, such as capacitance voltage profiling (CV) [3] and deep level transient spectroscopy (DLTS) [2, 4] was used for the measurements of semiconducting structures with QD. It was found that the shape and other properties of the DLTS peaks distinguished noticeably from the ones due to usual point-like defects as well as due to quantum well structures [5]. The peculiarities observed does not allowed to get an unambiguous information about the electron transitions between the local energy states of QD and semiconductors bands.

In this work we present the results of our investigation of InAs/GaAs QD by means of CV, DLTS, as well as admittance spectroscopy (AS) and optical DLTS (ODLTS). We propose a new explanation of the origin of the capacitance transients in the Schottky-diodes with the plane of a high QD density.

## 2 Samples

The structures studied were grown on (100) Si-doped GaAs substrates by solid-source molecular beam epitaxy (MBE) in Riber 32P apparatus using As4 species and atomic fluxes of indium and gallium. Silicon was used for n-type doping. All structures were grown under standard for MBE condition of enrichment by group V element (As). After annealing of substrate in growth chamber at 620 °C during 10 minutes the 0.2 $\mu$m layer of GaAs with high level of Si-doping was deposited. The next 0.8 $\mu$m layer

slightly doped with silicon contained 10 nm of undoped GaAs. The structures under investigation differed by amount of InAs deposited in the middle of undoped layer and contained 4, 1.7 and 1 monolayer (ML) of InAs, and the last sample contained no InAs insertion. The substrate temperature was 485 °C for the deposition of InAs and 10 nm GaAs covering layer to exclude effects of In segregation and reevaporation and 600 °C for the rest of the structure. In the case of the sample without InAs the substrate temperature also decrease to 485 °C at deposition of 10 nm GaAs. According to the data of transmission electron microscopy, 1 ML of InAs is equivalent the wetting layer (WL) thickness (i.e. no quantum dots), whereas 1.7 ML is sufficient to form quantum dots (QDs), (i.e., QDs on WL). Thus, having such set of the samples the effects associated with low temperature GaAs covering layer, WL, and, finally, with QDs itself can be separated.

CV-profiles of net-donor concentration, $N_D$, AS, DLTS and ODLTS spectra were measured on the Schottky-diodes preparing by evaporating of the gold contacts on the top of the structures in the temperature ranges between 80 and 350 K.

## 3 Results

The diodes without InAs ($Q = 0$) layer showed only a week step on CV-profiles correspondent to lowering of the net-donor density which is believed due to non-doped GaAs-layer. Introducing InAs leads to the appearance an apparent peak of the $N_D$ that at the room temperature increased with the increasing the depth of the InAs layer indicating the presence of the acceptor-like levels lying below the shallow donor level.

The samples with $Q = 0$ and $Q = 1$ do not show any signal during the measurements of AS, DLTS and ODLTS. AS measurements on the samples with $Q = 1.7$ reveal a peak of the HF-conductance and a step of the capacitance at a temperature of 85 K at the testing voltage frequency $\nu = 1$ MHz. The energy activation of the thermoemission of electrons from apparent level of about $80 \pm 20$ meV was estimated from the Arrenius-plot data obtained by the variation of $\nu$ from 1 to 10 MHz.

DLTS signal in a wide temperature region was detected in the samples with $Q = 4$. The shape of the spectrum changes dramatically when the applied bias changes. At at a forward or at a sufficiently low reverse voltage bias DLTS spectrum with a low temperature peak QD and high temperature peaks HT (Fig. 1) was registered. When the reverse bias voltage was increased the spectrum consisted of subsequential positive and negative peaks similar to the reported in [4] that should be ascribed to the emission from electron and hole traps respectively. It was found that QD-peak decreased with the decreasing filling pulse amplitude, $U_p$, with the appearance threshold of about 0.3–0.4 eV whereas HT peak remained constant up to, $U_p = 0.05$ V. That allows to separate the peaks by appropriate sequences of $U_p$ (Fig. 1) during DLTS experiment. The activation energies of the apparent emission proccess were found to be $0.33 \pm 0.02$ eV for QD peak and to be in the ranges from 0.4 to 0.6 eV for HT peak depending on the condition of the experiment. The amplitude of the QD does not whereas that of HT peak strongly depended on the temperature. Both peaks had similar logarithmic dependence on the refilling pulse duration that indicates the electron capture limiting with a occupancy dependent barrier.

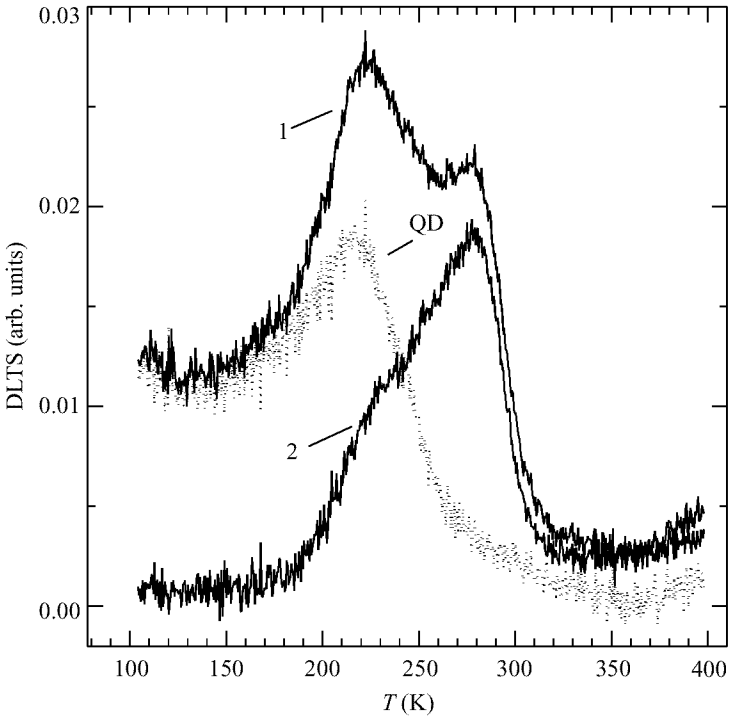


**Fig 1.** DLTS-Spectra on the sample QD-4ML as measured in a single tempreature scan. $U_p = 1-2.5$ V, $2-0.5$ V. $U_b = 0$ V. Dotted line is the difference bettween lines 1 and 2.

## 4 Discussion

The properties of the DLTS-peak QD are in accordance with the usual theory of the thermoemission from the traps except the low temperature tail of the signal, that was previously reported in [2] for the InP QD and may be due to the direct tunneling of the electrons from the QD states. That is why we ascribe QD-peak to the electron confined states of the InAs/GaAs quantum dots. The activation energy of the QD-peak agrees well with the theoretical calculations for the QD with a base diameter of 14 nm.

To explain other peculiarities of the DLTS signal in the samples with a high density of quantum dots we propose the model of the free carriers capture limited relaxation as follows. The plane with the QD when filled with electrons builds a large repulsive barrier for the electrons like the electronic states of grain boundaries in semiconductors [6]. During the filling voltage pulses not only the electron occupancy of the QD-levels but also the free electron density in the conduction band between the QD-plane and metallic contact increase because of the local minimum of the electrostatic potential. in between. In this way an electron "lake" will be created just after switching off the filling pulses. During the emission phase of the DLTS experiment the electron emission from the QD levels occurs in the presence of the electron current from the "lake" flowing through the QD plane. The rate of the QD states occupancy relaxation will be then defined as a sum of the electron emission and the electron capture rates and

will be sooner than the rate of the relaxation of the free electron density in the "lake". That is why the kinetic of the QD states occupancy will follow the kinetic of the time changes of the free electron density in the "lake". The latter is defined by the barrier that decreases with increasing of the voltage bias applied to the diode.

Detailed analysis of the model including mathematical treatment of the problem that will be presented at the conference allows to explain all properties of DLTS spectra observed.

## References

[1] N. N. Ledentsov, M. Grundmann, N. Kirstaedter, O. Schmidt, R. Heitz, J. Bohrer, D. Bimberg, V. M. Ustinov, V. A. Shchukin, A. Yu. Egorov, A. E. Zhukov, S. V. Zaitsev, P. S. Kop'ev, Zh. I. Alferov, S. S. Ruvimov, P. Werner, U. Gosele, and I. Heidenreich, *Solid State Electron.* **40** 785, (1996).

[2] S. Anand, N. Carlsson, M. E. Pistol, L. Samuelson, W. Seifert, *Appl. Phys. Lett.* **67** 3016 (1994).

[3] P. N. Brunkov, S. G. Konnikov, V. M. Ustinov, A. E. Zhukov. A. Yu. Egorov, M. V. Maximov, N. N. Ledentsov, P. S. Kop'ev, *Semiconductors* **30** 492 (1996).

[4] M. M. Sobolev, A. P. Kovsh, V. M. Ustinov, A. Yu. Egorov, A. E. Zhukov, M. V. Maximov, N. N. Ledentsov. *Semiconductors* **31** 1249 (1997).

[5] K. Schmalz, I. N. Yassievich, H. Ruecker, H. G. Grimmiss, H. Frankenfeld, W. Mehr, H. J. Osten, P. Schley, H. P. Zeindl, *Phys. Rev.* **50** 14287 (1994).

[6] A. Broniatowski, *Phys. Rev.* **36** 5895 (1987).

Ioffe Institute
6th Int. Symp. "Nanostructures: Physics and Technology"
St Petersburg, Russia, June 22–26, 1998.



# XPS study of Cu-clusters and atoms in $Cu/SiO_2$ composite films

Yu. S. Gordeev, S. A. Gurevich, T. A. Zaraiskaya, S. G. Konnikov, *V. M. Mikoushkin*, S. Yu. Nikonov, A. A. Sitnikova, S. E. Sysoev, V. V. Khorenko and V. V. Shnitov
Ioffe Physico-Technical Institute RAS, St. Petersburg, 194021, Russia

## Introduction

Investigation of optical and electrical properties of composite metal-insulator materials has been the topic of a considerable number of recent papers. For metallic particles in the size range of about 10 Å the phenomenon of macroscopic charge quantization is observed [1], which could make materials of this kind useful for creating single-electron devices. In order to produce these properties, it is necessary to know the chemical state of the cluster-forming atoms, the average cluster size and the average distance between them. One of the most effective ways to study the chemical state of elements is x-ray photoelectron spectroscopy, or XPS. Chemical states of atoms are determined by analyzing the chemical shifts of the photoelectron lines associated with changes in the binding energies $E_b$ of core electrons arising from changes in the interaction with neighbouring atoms. In this work we have attempted to obtain composite metal-insulator films of $Cu/SiO_2$ containing Cu-clusters and atoms in the unoxidized state. When an oxide is used as the insulator it is important to control the degree of oxidation of the metal introduced. We have aimed to develop the diagnostics for the chemical state identification of metal atoms and for obtaining parameters of ensemble of metal-clusters which are important for the single-electron tunneling processes.

## Methods

The composite thin films of $Cu/SiO_2$ were obtained by simultaneous sputtering of copper and quartz targets on a SEM-450 (Alcatel) setup after first pumping the chamber down to $10^{-5}$ Pa [2]. The deposition took place in an atmosphere of pure argon at a pressure of 0.3 Pa. The substrates temperature never exceeded 100°C. The films were deposited on a substrate made of Si that was first oxidised in dry oxygen, producing an oxide layer 500 Å thick. The sublayer of $SiO_2$ acted as a barrier to diffusion of copper into the substrate during the annealing of the composite films (see below). In this paper we discuss composite films with a thickness of 2000 Å in which the copper content was around 5 vol%, according to microanalysis data. A part of our films were annealed in an atmosphere of hydrogen at 850°C for 30 min. In the course of the annealing, clusters form, which are clearly visible in the transmission electron microscope (TEM). It is clear from TEM photograph that copper clusters with a characteristic size 50 Å form nonuniformly in the bulk of the film. There are no clusters with sizes larger than 10 Å in a subsurface layer of thickness about 150 Å (the resolution of the microscope was around 10 Å). The reason for this depletion of large clusters near the surface is unclear. This region has been a subject of our particular interest because it could be a promising material for single-electron devices if there are clusters there with sizes around or smaller then 10 Å. The concentration and chemical states of copper near the surfaces of the as-grown and annealed samples were measured by XPS using $AlK_\alpha$

x-rays (1486.6 eV). A Leybold-AG LHS-11 electron spectrometer was used. The films were cleaned with low energy ($E_i = 500$ eV) $Ar^+$ ions to reduced the possible influence of ion bombardment on the chemical state of the films under study to 1–2 atomic layers.

## Results

The relative content of main elements was determined from the intensity of the corresponding photoelectron lines using element sensitivity coefficients determined earlier. In this measurements, the ratio of the numbers of silicon and oxygen atoms turns out to be close to stoichiometric for $SiO_2$ in both the as-grown and the annealed films. The measured copper concentration in the subsurface region was $C_{Cu} = 5 \pm 1\%$ for the as-grown sample and $C_{Cu} = 4 \pm 1$ % for the annealed sample, in agreement with the average concentration obtained by x-ray microanalysis.

Analysis of chemical shifts of these photoelectron lines was complicated by static charging of the samples in the photoemission process. The amount of chemical shift due to charging was determined by comparing the position of the $Si_{2p}$ line with literature data for $SiO_2$ ($E_b = 103.4$ eV [3]). The average value of the shift due to charging of the as-grown sample was $\Delta E = 10.0$ eV, while $\Delta E = 3.0$ eV in the annealed sample. This increase in the line shift as a result of annealing is connected with a decrease in the conductivity of the material and is an additional evidence of segregation of copper of the as-grown sample into clusters. The spectra of $Cu2p_{3/2}$ photoelectrons and CuLVV Auger electrons shown in Fig. 1 and Fig. 2 were corrected for the value of static charge. Figure 1a shows $Cu2p_{3/2}$ spectra obtained before ionic cleaning of the sample surface. The intense low-energy satellites are present only in the oxide and hydroxide spectra of divalent copper (CuO, $Cu(OH)_2$). The satellite and the corresponding hydroxide shoulder of the fundamental line disappear almost completely when a layer of thickness 10–15 Å is etched from the surface (Fig. 1b). Hence, the photoelectron spectra leads us to conclude that copper at the surface was oxidized by atmosphere oxygen and it is not oxidized to its divalent state in the bulk region of either samples. A second conclusion that follows directly from Fig. 1 is that annealing changes the chemical state of copper

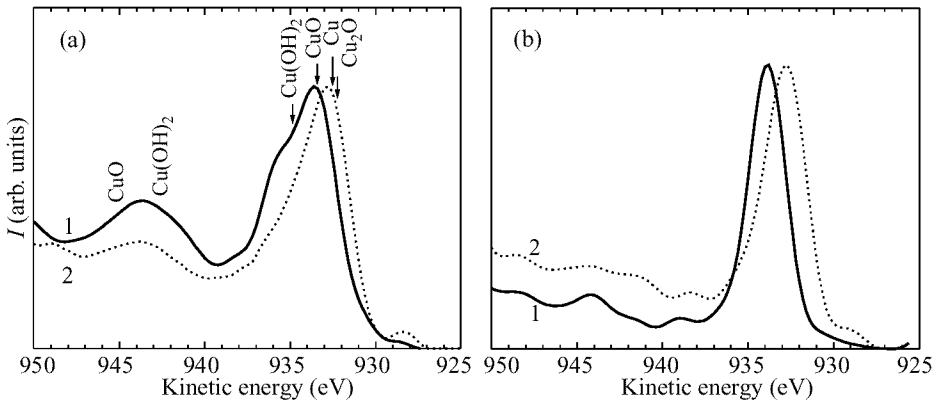


**Fig 1.** $Cu2p_{3/2}$ XPS spectra of as-grown (1) and annealed (2) samples measured on the original (a) and cleaned (b) surfaces.

**Table 1.** Binding energy $E_b$ ($Cu2p_{3/2}$) and value of Auger parameter $\alpha$ for samples under study and number of compounds.

| | $E_b$, eV | $\alpha$, eV |
|---|---|---|
| Cu | 939.7±0.2 [3] | 1851.3±0.2 [3] |
| $Cu_2O$ | 932.6±0.3 [3] | 1849.5±0.2 [3] |
| | 932.0±0.2 [4] | |
| CuO | 933.5±0.3 [3] | 1851.5±0.3 [3] |
| | 933.6±0.2 [4] | |
| $Cu(OH)_2$ | 935.0±0.2 [4] | — |
| $Cu \rightarrow SiO_2$ | 933.5 [5] | — |
| as-grown film | 933.7±0.1 | 1847.2±0.2 |
| annealed film | 932.8±0.1 | 1851.2±0.2 |

markedly, since the binding energy of the core 2p electron changes. Among the possible remaining states we can list univalent copper oxide $Cu_2O$, elemental copper in the $SiO_2$ matrix, and metallic copper segregated into clusters.

Since reliable identification of the oxide $Cu_2O$ and metallic copper based on core binding energy is hindered by the closeness of these energies, we extracted additional information from the Auger parameter $\alpha = E_b + E_A$, where $E_A$ is the kinetic energy of the corresponding Auger electron [3]. The physical meaning of the Auger parameter implies that its change when one chemical state converted to another is very close to the change in relaxation energy for the same chemical change. The states of copper for the films under study was identified from data of Table 1, in which we list values of the $\alpha$ and $E_b$ for various copper compounds averaged over the data compiled in Ref. [3] and also values of $E_b$ we obtained previously using one spectrometer under the same condition [4]. Comparison of the measured value of $E_b(Cu2p_{3/2})$ and of $\alpha$ for samples under study with literature one's for number of compounds allows us to conclude unambiguously that (i) a larger portion of copper is in the metallic state in the annealed sample, which can be true only if copper clusters form; (ii) practically all of copper is in the form of unoxidized atoms dispersed in the matrix of as-grown sample. The identification procedure is described in more details in our previous work [2].

Let us estimate the possible range of sizes of clusters. Based on the data from [6] for clusters of an element with similar electronic structure, silver, the values of $E_b$ and $\alpha$ approach the metallic values in particles that include decades or more atoms, i.e., with diameters of the order of 10 Å or more. It is the average size of our clusters because the TEM data reveals no clusters with sizes larger than 10 Å in the subsurface region.

To describe the cluster ensemble we have to know the percentage of copper atoms in clusters. For this we consider the CuLMM Auger spectra (Fig. 2) for the as-grown (curve 1) and annealed (curve 2) sample, and also the Auger spectrum of bulk metallic copper (curve 3) after subtracting the background formed by multiple scattering of the Auger electrons [2]. The complex shape of the spectrum of the annealed material allows to assume that it is a combination of spectra of metallic and elemental copper strongly shifted with respect to one another. A numerical simulation of the Auger spectrum of the annealed sample by the combination of spectra of metallic copper (curve 3 in Fig. 2) and elemental copper in a $SiO_2$ matrix (curve 1 in Fig. 2) showed that 70% of copper atoms are segregated into clusters. It is seen from the Fig. 2 (curve 1′) that 5% of all

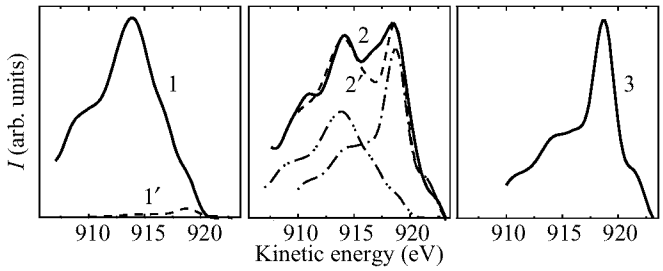


**Fig 2.** Spectra of CuLVV Auger electrons from the as-grown (1) and annealed (2) samples, and from metallic copper (3): 1′ — contribution of metallic copper, 2′ — model spectrum.

**Table 2.** The parameters of clusters in $Cu/SiO_2$ composite films.

| | ⟨N⟩, Å | $C_{cl}$, $cm^{-3}$ | ⟨l⟩, Å |
|---|---|---|---|
| as-grown film | 45 | $4.8 \cdot 10^{18}$ | 59 |
| annealed film | 45 | $6.7 \cdot 10^{19}$ | 25 |

copper segregates into clusters even during the deposition and before annealing. Taking into account the percentage of copper atoms in clusters, the full copper concentration measured and the average cluster size ⟨N⟩, we can estimate the concentration of clusters and atoms and the average distance between neighbour clusters and atoms ⟨l⟩ (Tabl. 2).

## Summary

Thus, the XPS-TEM study of $Cu/SiO_2$ composite metal-insulator films allowed us to develop the diagnostics of the chemical states of metal atoms and the parameters of the ensembles of metal-clusters and metal-atoms which are important for single-electron tunnelling processes.

This work was carried out with the financial support of MNTP, the "Physics of Solid-State Nanostructures" program (Projects 97-3005), the GNTR "Promising Micro- and Nanoelectronic Technologies" (Project 151/57/1), Grants No. 96-02-17966 and 96-02-18781 from the Russian Fund for Fundamental Research, and also with the help of St-Petersburg Joined Analytical Center.

## References

[1] E. Bart-Sadeh, Y. Goldstein, C. Zhang, H. Deng, B. Abeles, et.al.; *Phys. Rev. B* **50** 8961 (1994).
[2] S. A. Gurevich, et. al., *Phys. Solid State* **39** (10) 1691–1695 (1997).
[3] D. Briggs and M. P. Sikh (Eds.), "Surface Analysis by Auger and X-Ray Photoelectron Spectroscopy", (Russian translation, Mir, Moscow, 1987).
[4] V. V. Mamutin, et. al.; *Sverkhprovodimost* (KIAE) **6** 797 (1993).
[5] V. Y. Young, R. A. Gibbs, and N. Winograd; *J. Chem. Phys.* **70** 5714 (1979).
[6] Yu. S. Gordeev, et. al.; *Phys. Solid State* **36** 1298, (1994).

Ioffe Institute
6th Int. Symp. "Nanostructures: Physics and Technology"
St Petersburg, Russia, June 22–26, 1998.



# The formation of copper nanoclusters in $SiO_2$: an X-ray absorption study

*A. V. Kolobov*†§, H. Oyanagi‡, S. A. Gurevich§, V. V. Horenko§ and K. Tanaka†
† Joint Research Center for Atom Technology,
National Institute for Advanced Interdisciplinary Research,
1-1-4 Higashi, Tsukuba, Ibaraki 305, Japan
‡ Electrotechnical Laboratory, 1-1-4 Umezono, Tsukuba, Ibaraki 305, Japan
§ Ioffe Physico-Technical Institute, 194021 St Petersburg, Russia

**Abstract.** Results on Cu K-edge x-ray absorption study of copper dispersed in $SiO_2$ are reported. Randomly distributed in as-made samples at low concentration, copper atoms tends to form clusters at larger concentrations. The cluster size reaches a size of 20 to 50 Å after which the cluster growth stops. Only the first-neighbour peak is observed in as-made samples indicating either a very strong disorder in clusters or their low-dimensionality. Annealing results in the formation of copper clusters of the same size with fcc structure.

## 1 Introduction

Composite materials containing metallic particles of nanometer sizes embedded in insulating media have attracted wide interest because of their unique properties distinct from both metal and insulator. A new activity in this field was invoked by the suggestion that single-electron transport phenomena can be observed in metal-insulator composites at elevated temperatures [1]. For many such applications the detailed knowledge of structure parameters are of primary importance.

In this paper we report the results of Extended X-ray Absorption Fine Structure (EXAFS) measurements and present information on the structure of copper clusters embedded into $SiO_2$. In particular, it was shown that copper atoms randomly distributed in $SiO_2$ in as-made samples with low copper concentration form nanoclusters with fcc structure upon increase of copper content and/or upon annealing.

## 2 Experimental

Cu-$SiO_2$ samples were prepared by RF-magnetron co-sputtering of copper and silica in Ar gas atmosphere to obtain 0.1 $\mu$m thick films. By choosing the sputtering rates at each magnetron source the concentration of copper in silica was varied in a wide range from 8 to 40 volume %. The obtained films were annealed in hydrogen atmosphere, the temperature ranging from 700°C to 950°C, from 10 to 30 minutes.

The measurements were performed at BL13B station at the Photon Factory [2] using a 27-pole wiggler in a fluorescence mode. An array of 19-element high-purity Ge solid-state detectors was used to detect the fluorescence. Metallic bulk copper and $CuO_2$ have been used as standards in the data analysis.

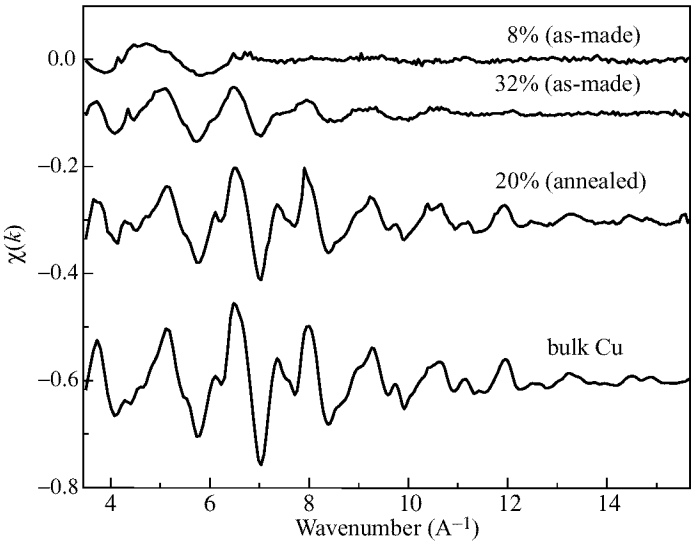


**Fig 1.** Raw EXAFS spectra of as-made samples with different Cu concentration measured at room temperature. Concentration of copper is marked in the figure. EXAFS spectra for annealed sample with intermediate Cu concentration as well as that for bulk copper are shown for comparison.

## 3 Results

Figure 1 shows raw Cu K-EXAFS oscillations measured at room temperature for as-prepared samples with copper concentration of 8 and 32% as a function of photoelectron wavenumber $k$ after subtracting the smooth background due to the atomic absorption. The background function given as a combination of the third and forth order polynomials, with tabulated coefficients (Victoreen Function) which smoothly interpolate EXAFS oscillations using a cubic spline method, was normalized to the edge jump and subtracted from the fluorescence spectrum. One can see that in the spectrum for the low concentration the signal intensity is lower and oscillations damp at lower $k$-values, which is characteristic of interaction with a light element. The spectrum for the sample with larger copper concentration clearly resembles that of bulk copper shown in the same figure for comparison.

The EXAFS oscillations multiplied by $k[k\chi(k)]$ were Fourier-transformed (Fig. 2) into the real space using the region extending from 4.5 to 15 $Å^{-1}$. It is seen that the sample with the lowest concentration does not have a peak at distances corresponding to Cu-Cu bond length. There is a small feature in that spectrum located at a somewhat smaller distances ($\sim$ 1.2 Å which may be indicative of dimer formation. As the concentration of copper increases, the Cu-Cu peak clearly appears.

The least-squares curve-fitting, based on the single-scattering theory [3] and FEFF [4] amplitudes, gives values of the average coordination numbers, bond lengths and disorder parameters (Debye-Waller factor) summarized in Table 1. One can see from the table that a small feature in the sample containing 8% Cu can, indeed, be attributed to dimers whose bond length is between that of a free dimer and a Cu-Cu bond length in bulk

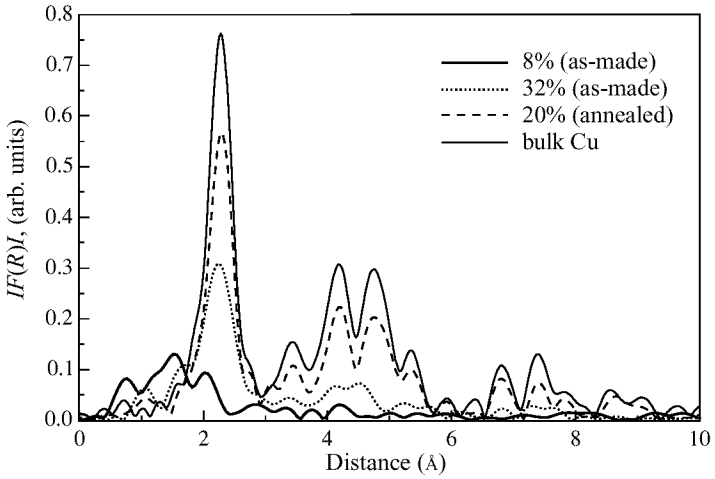


**Fig 2.** Fourier transforms of the spectra shown in figure 1.

**Table 1.** Coordination numbers, bond length and MSRD for Cu-Cu interaction in as-made samples with different Cu concentrations.

| Copper concentration, vol.% | Coordination number | Bondlength Å (±0.005) | DW factor Å |
|---|---|---|---|
| 8 | 0.9±0.2 | 2.45 | 0.042 |
| 16 | 2.7±0.5 | 2.54 | 0.073 |
| 20 | 5.6±0.8 | 2.54 | 0.092 |
| 25 | 8.1±1.0 | 2.55 | 0.096 |
| 32 | 8.0±1.0 | 2.56 | 0.080 |
| bulk Cu | 12.0 | 2.26 | 0.044 |

copper. As the concentration of copper increases, both the coordination number and bond length also increase. The Cu-Cu bond length in a cluster becomes equal to that in bulk metal at concentration more than 25 vol. % of copper, while the coordination number remains smaller.

## 4 Discussion

It is reasonable to assume that in an as-prepared samples with low copper concentration copper is randomly distributed throughout the $SiO_2$ matrix. In this case one should expect a very weak Cu-Cu correlation which agrees well with the obtained data for the as-prepared sample with the lowest concentration of copper. As the concentration of copper increases, Cu-Cu correlation becomes stronger and small Cu-clusters are formed which become larger in size as the copper concentration is further increased. Interestingly, after the coordination number reaches 8 no further increase in the coordination number is observed which implies that a certain portion of Cu atoms (about 25%) does not form dense clusters.

Another interesting feature is the absence of higher shells in the Fourier transforms

of the spectra for as-made samples. Given the size of the cluster of 50 Å [5] such peaks should have been observed. Their absence may be considered as an indication of strong disorder which agrees with the obtained values of mean-square relative displacement (MSRD) in as-made films being larger than in bulk copper. Upon annealing, the fcc structure is established as clearly evidenced by the Fourier transformed spectrum (Fig. 2).

*Acknowledgement*

This work, partly supported by NEDO, was performed in the Joint Research Center for Atom Technology (JRCAT) under the joint research agreement between the National Institute for Advanced Interdisciplinary Research (NAIR) and the Angstrom Technology Partnership (ATP). It was also supported in part by Russian Foundation for Basic Research under grant No. 98-02-18210, the Program of the Miinistry of Science of RF "Physics of Solid-State Nanostructures" grants No. 97-2014 and No. 97-1035, State Program "Micro- and Nanoelectronic Technology" grant No. 151/57/1.

## References

[1] Vishenski S,V., *Phys. Low-Dim. Struct.* **11/12**, 9 (1994).
[2] Oyanagi H., Haga K., and Kuwahara Y., *Rev. Sci. Instrum.* **67** 350 (1996).
[3] Stern E.A., *Phys. Rev.* **B10** 3027 (1974).
[4] Rehr J.J., Albers R.C., and Zabinsky S.I., *Phys. Rev. Lett.* **69** 3397 (1992).
[5] Gurevich S.A., et al. *Phys. Solid State*, **39** 1692 (1997).

Ioffe Institute
6th Int. Symp. "Nanostructures: Physics and Technology"
St Petersburg, Russia, June 22–26, 1998.



# Observation of a martensitic transition in the Raman spectra of ordered GaInP

A. M. Mintairov†§, J. L. Merz§, *A. S. Vlasov*†and D. V. Vinokurov†
† Ioffe Physico-Technical Institute RAS, St. Petersburg, Russia
§ Electrical engineering department, University of Notre Dame,
Notre Dame IN, US 46556

**Abstract.** We have observed a strong dependence of the intensity of the ordering-induced phonon bands on thermal treatment (rapid cooling and annealing) in Raman spectra (RS) of $CuPt_B$ ordered $Ga_{0.5}In_{0.5}P$ alloys. The changes of the Raman intensity occur only in diagonal backscattering configuration: $y' \parallel [\bar{1}10]$, where the polarization of light is parallel to the mirror planes of the ordered structure. We found that there are at least two different intensity distributions of the optical phonon bands the appearance of which is determined by thermal treatment and the alloy film thickness. The bond polarizability model analysis shows that the observed RS behaviour can be described in terms of the order-disorder martensitic transition on trigonal lattice sites.

## 1 Introduction

It is well known that microstructure of nearly all technologically important semiconductor alloys exhibit strong deviations from random atomic distribution [1]. These deviatioons appear as phase separation, short- and long-range order effects and are determined by thermodynamics and kinetics of the growth process. When the distribution of the atoms in alloy lattice sites is fixed, there exists degrees of freedom associated with crystal lattice-site rearrangement. The phase transformation in the alloys that can be treated only in terms of the displacements is known in classical metallurgy as diffusionless (martensitic) transformation [2]. Here we present results of the first observation of the martensitic transformation in epitaxial films of a semiconductor alloy. The alloy system is a $CuPt_B$-type long range ordered $Ga_{0.5}In_{0.5}P$ alloy [1], and the transition is revealed as a strong change of the Raman intensity of optical phonon modes on rapid cooling of the alloy. A bond polarizability model analysis shows the connection of the Raman intensities of the long-range ordered $Ga_{0.5}In_{0.5}P$ with trigonal lattice site rearrangement.

## 2 Experiment

Samples used were grown by MOVPE at temperature about 650 °C on (001) GaAs substrates. A substrate orientation of 6° miscut towards the $[111]_B$ direction was used to obtain a single orientation of the ordered $CuPt_B$-type structure ($[111]_B$-GaP/InP monolayer superlattice). We have investigated two samples with ordering degree about 0.5 and epilayer thickness 0.3 ("thin") and 3 $\mu$m ("thick"). The thermal treatment consisted of a rapid cooling down to 77 K, followed by annealing at $T = 400$°C for 30 minutes. After each treatment the backscattering Raman spectra (RS) were measured at 300 K in the $x'x'$ and $y'y'$ configurations, where $x' \parallel [110]$ and $y' \parallel [\bar{1}10]$. The intensities of the Raman bands were analysed using Lorentzian contour modeling [3, 4]. Lattice dynamical calculations of the perfectly ordered $GaInP_2$ $CuPt_B$ structure was performed using the Valence Overlap Shell model (VOSM).

## 3 Raman selection rules for perfectly ordered $GaInP_2$ $CuPt_B$ structure

We used the bond polarizability model (BPM) [5, 6] for deriving selection rules for optical phonons of the $GaInP_2$ $CuPt_B$ structure. The BPM unit of this structure consists of two trigonal $In_3GaP$ and $Ga_3InP$ tetrahedrons (eight non-equivalent bonds). Using approach described in [6] and assuming zinc-blende bond angles, a structure-dependent part of its Raman tensor can be written as follows:

$$\tilde{R}^Z = \begin{bmatrix} -1 & 0 & 0 \\ 0 & -1 & 0 \\ 0 & 0 & 2(1-\Delta^\nu) \end{bmatrix} \tilde{R}^Y = \begin{bmatrix} -\sqrt{2} & 0 & 0 \\ 0 & \sqrt{2} & -1 \\ 0 & -1 & 0 \end{bmatrix} \tilde{R}^X = \begin{bmatrix} 0 & \sqrt{2} & -1 \\ \sqrt{2} & 0 & 0 \\ -1 & 0 & 0 \end{bmatrix}$$

Here the term $\Delta$ reflects a trigonal distortion of the Raman polarizability of the zinc-blende lattice. In an assumption, that the bond polarizability is equal for four bonds of one sort (In-P and Ga-P), $\Delta$ depends only on phonon eigenvectors. The strong localization of GaP and InP-type phonons in the corresponding monolayers, found in the lattice dynamical calculations, allows to write $\Delta = (9/8)(1 - \Delta u_z)$, where $\Delta u_z = u_z^{\mathrm{PI}}/u_z^{\mathrm{PII}}$ is the ratio of the $Z$ component of the displacements of two basis P atoms.

For only the $R_{zz}^Z$ component contains the trigonal contribution, only the Raman configurations having $Z$ components of an incident and scattered electric field will be sensitive to it. In Table 1 we presented the corresponding selection rules for phonons with pure LO and TO polarizations. It is seen from Table 1, that only the $y'y'$ configuration includes $\Delta$ contribution. The TO phonons are allowed only in the $y'y'$ configuration and only for nonzero values of $\Delta$. Thus they can be activated in alloy only in the presence of $CuPt_B$ long-range order. These selection rules can fully explain the {110}-anizotropy of diagonal components observed in Raman spectra of spontaneously ordered $Ga_{0.5}In_{0.5}P$ alloys [4] and make an assignment of the ordering induced bands (see further discussion).

**Table 1.** Raman selection rules for the $\Gamma^{\sigma 211}$ phonons.

| Scattering | Scattering intensity | |
|---|---|---|
| geometry | LO | TO |
| $z(x'x')z$ | 1 | 0 |
| $z(y'y')z$ | $(1 - 4/9\Delta)^2$ | $32/82\Delta^2$ |

## 4 Raman spectra of thermally treated alloy and discussion

The experimental RS of thermally treated "thick" sample are presented in Fig. 1(a-c). Here the subscripts 1 and 2 are used for GaP and InP type vibrations and additional subscript e is used for the ordering-induced phonons.

The assignment of the ordering induced bands in Fig. 1(a) (initial state of the sample) was done using difference of the bands intensity in $x'x'$ and $y'y'$ configurations, rules from Table 1 and the results of the lattice dynamical calculations (see Table 2). The {110} intensity anisotropy of the $LO_{1e}$ and $LO_{2e}$ phonons was derived from the Lorentzian modeling. The appearance of the pure $y'y'$ line $TO_{1e}$ at 351 $cm^{-1}$ in Fig. 1(a), is well predicted from our calculations.

The spectra in Fig. 1(b) show that $x'x'/y'y'$ intensity anisortopy have significant changes after rapid cooling. The changes appear as a strong decrease of the intensity

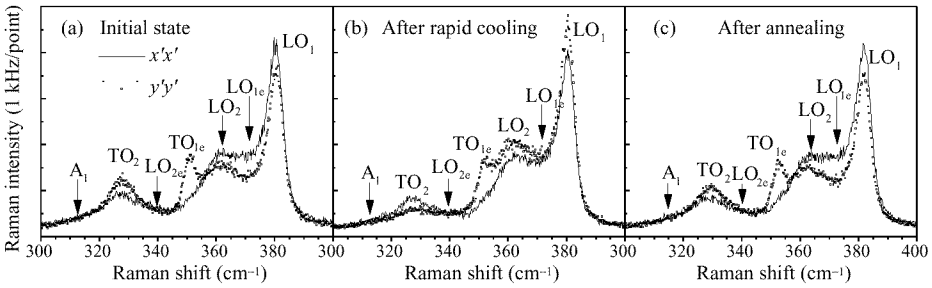


**Fig 1.** Raman spectra of the "thick" sample after different stages of thermal treatment: (a) initial state, (b) after rapid cooling, (c) after annealing. The spectra were measured in the backscattering $x'x'$ (solid curves) and $y'y'$ (dotted curves) configurations.

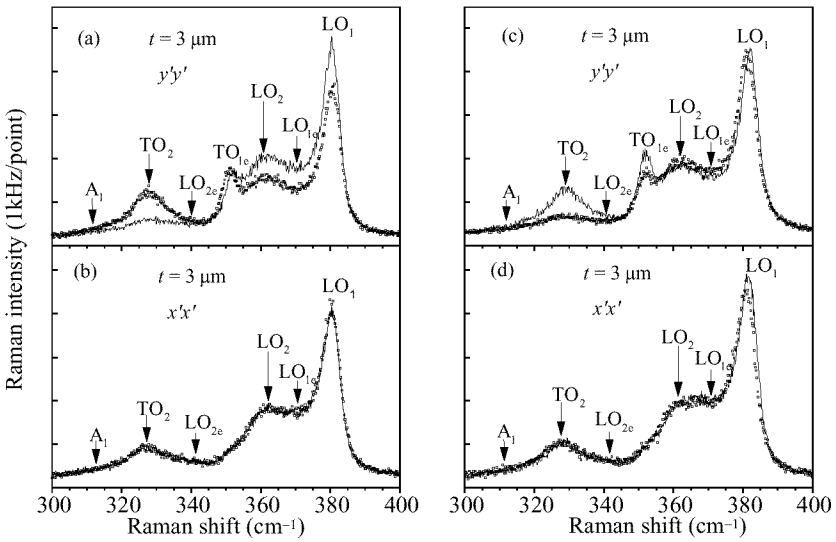


**Fig 2.** Thermal treatment dependence of the $y'y'$ (a, c) and $x'x'$ (b, d) RS of the "thick" and "thin" samples. Dotted curves: initial state, solid curves: after cooling.

of the $TO_{1e}$ and $TO_2$ bands and increasing of the intensity of the $LO_1$, $LO_{1e}$, $LO_2$ and $LO_{2e}$ bands in $y'y'$ configuration (see Fig. 2a,b). In Fig. 2(c-d) we also present $x'x'$ and $y'y'$ spectra for the thermally treated "thin" sample. One can see that the RS spectra of both samples are very similar, except the unusual fact that the intensity distribution of the bands in RS of the "thin" sample in its initial state is similar to the intensities of the "thick" sample after cooling, and spectra of the "thick" sample before cooling are similar to the "thin" sample after cooling. We have found, that annealing restores the initial band intensities (Fig. 1c). This can also be achieved by "annealing" the sample at room temperature for several weeks.

It is natural to connect the observed changes in the Raman band intensities with the changes of equilibrium atom positions, i.e. lattice state vector. Therefore, changing in the RS after thermal treatment is direct evidence of the martensitic transition in spontaneously ordered $Ga_{0.5}In_{0.5}P$. The difference in RS of the "thick" and "thin" samples shows, that a spontaneously ordered $Ga_{0.5}In_{0.5}P$ alloy film has at least two equilibrium

**Table 2.** Frequencies ($cm^{-1}$) of the $GaInP_2$ CuPt structure optical phonons, measured from Raman spectra and calculated using VOSM.

| Mode type | $TO_{o2}$ | $TO_{e2}$ | $LO_{e2}$ | $TO_{e1}$ | $TO_{o1}$ | $LO_{e1}$ |
|---|---|---|---|---|---|---|
| Calculation | 324.4 | 327.8 | 342.3 | 355.1 | 360.3 | 381.5 |
| Experiment | — | 328 | 340 | 351 | — | 370 |

lattice states, the energetic preference of which is determined by the elastic strain between the film and the substrate. In RS the difference between these two states appears as the difference in the $x'x'/y'y'$ intensity anisotropy for the ordering-induced phonons. From this point of view the ground lattice state of the "thick" sample is more "'ordered" (in relation of the CuPt*B* structure) at room temperature than that of the "thin" sample. The existence of differently "ordered" lattice states probably results from the different lattice symmetry of the substrate and alloy film. The resulting symmetry misfit strains will act to move the long-range ordered atoms from their exact trigonal lattice sites. For the "thin" sample such strains dominate, so that the ground state of "thin" sample is "disordered" at room temperature.

The observed changes in Raman intensities can be well described in terms of the changing of the parameter $\Delta$ only (see Table 1). Thus the fact, that we observed the changes in the Raman intensity of the long-range ordered $Ga_{0.5}In_{0.5}P$ only in the $y'y'$ configuration has clear connection with the rearrangements of the trigonal lattice sites.

The Raman intensities of the "disordered" lattice state correspond to a decrease of the parameter $\Delta$ for all ordering-induced phonons. This is naturally to connected with the shifting of the atoms situated in the ordered trigonal arrangement to new positions what in turn leads to the changing displacement amplitudes for phosphorus atoms. i.e. parameter $\Delta u_z$.

## 5 Conclusion

In conclusion, we have observed the martensitic transition in epitaxial layers of spontaneously ordered semiconductor alloys $Ga_{0.5}In_{0.5}P$. The transition is revealed as a strong dependence of the intensity of the order-induced Raman bands on the thermal treatment of the alloy. Our bond polarizability model analysis shows, that the observed Raman spectra behavior can be described in terms of the rearrangement of trigonally-ordered lattice sites, providing an excellent description of the RS of spontaneously ordered $Ga_{0.5}In_{0.5}P$ alloys and allowing to explain their changes due to thermal treatment.

## References

[1] A. Zunger and S. Mahajan, in: *Handbook on Semiconductors*, Vol. 3, Elsevier, Amsterdam, 1994.
[2] A. G. Khachaturyan, *Theory of structural transformations in solids*, Wiley, New York, 1983.
[3] A. M. Mintairov et al., *Phys. Solid Stat.* **37** 1985 (1995).
[4] A. M. Mintairov and V. G. Melechin, *Semicond. Sci. and Technol.* **11** 904 (1996).
[5] A. S. Barker, Jr., J. L. Merz, and A. C. Gossard, *Phys. Rev. B.* **17** 3181 (1978).
[6] A. M. Mintairov et al., *Phys. Rev. B* **56** 24 1527 (1997).

Ioffe Institute
6th Int. Symp. "Nanostructures: Physics and Technology"
St Petersburg, Russia, June 22–26, 1998.



# Atomic force microscopy and structural studies of MBE-grown $CdF_2$ layers on $CaF_2(111)$

*M. M. Moisseeva*†, N. S. Sokolov†, S. M. Suturin†, R. N. Kyutt†,
Yu. V. Shusterman‡ and L. J. Schowalter‡
† Ioffe Physico-Technical Institute RAS, St. Petersburg, Russia
‡ Rensselaer Polytechnic Institute, Troy, NY 12180 USA

The wide bandgap ($E_g$ = 8 eV) material $CdF_2$, doped with trivalent impurities, has well pronounced semiconducting properties. Bright electroluminescence (EL) has been observed in such crystals, with wavelength ranging from the IR to UV regions, depending on the dopant [1]. Recently, the feasibility of heteroepitaxial $CdF_2$ growth from a molecular beam on Si and $CaF_2$ surfaces has been demonstrated [2]. Therefore, fabrication of EL devices integrated with Si substrates would be very attractive. In our earlier studies [3], it was shown that, because of chemical interaction of $CdF_2$ molecules with Si surface at temperatures above 80–100°C, the crystalline quality of the layer quickly deteriorates with increase of the growth temperature. The post-growth annealing, usually employed to activate impurities in bulk $CdF_2$ [4], also presented problems for thin films on Si. There is , however, no the chemical interaction on $CaF_2$, so one can expect high quality growth at temperatures up to 600–700°C, when $CdF_2$ starts to sublime. Studies of doped $CdF_2$ growth at high temperatures are of interest for $CdF_2$ conversion in the semiconducting state without a postgrowth treatment.

In the present work, we apply Atomic Force Microscopy (AFM), Rutherford Backscattering Spectrometry/Channeling (RBS) and X-Ray Diffraction (XRD) to study the growth and structural perfection of Er-doped cadmium fluoride layers grown by Molecular Beam Epitaxy (MBE) on $CaF_2(111)$ substrates in a wide range growth temperatures range of 100–500°C.

## Epitaxial growth and surface morphology of $CdF_2$ layers

$CdF_2/CaF_2(111)$ heterostructures were grown at the Ioffe Institute in a small research MBE system equipped with RHEED apparatus. Two effusion cells were loaded with small pieces of $CaF_2$ and $CdF_2$ crystals sublimated at 1300°C and 850°C respectively to obtain fluoride molecular beams. Before $CdF_2$ growth, a 200–300 nm thick $CaF_2$ buffer layer was grown at 770°C on carefully polished $CaF_2(111)$ substrates. The growth rate of $CdF_2$ layers was about 2–3 nm/min and the growth temperature was maintained within the 100–500°C range. Er doping was performed by exposing the growing $CdF_2$ surface to Er or $ErF_3$ beams from two other effusion cells. Table 1 presents the list of studied structures, together with their parameters obtained from AFM, RBS and XRD studies.

The surface morphology measurements have been carried out in the contact mode using an P4-SPM-MDT atomic force microscope produced by NT-MDT (Zelenograd, Russia). We found in AFM images that the surface morphology of $CdF_2$ layers strongly depends on the growth temperature. On the surface of layers grown at 100°C (Fig. 1a), one can see relatively small mounds with a lateral size of 30–60 nm and 2–4 nm in

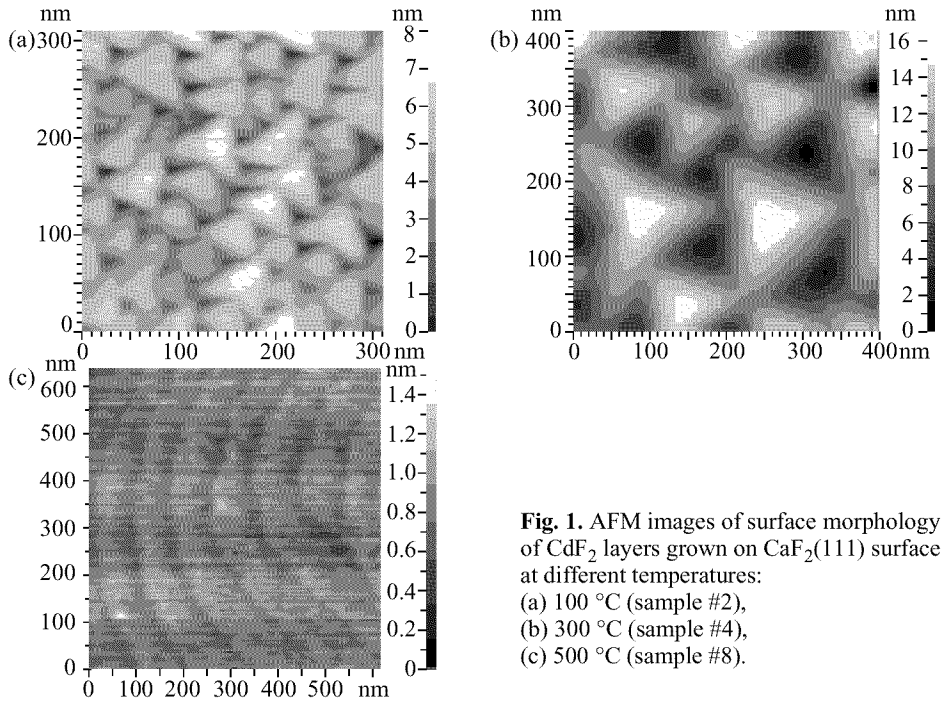


**Fig. 1.** AFM images of surface morphology of $CdF_2$ layers grown on $CaF_2$(111) surface at different temperatures:
(a) 100 °C (sample #2),
(b) 300 °C (sample #4),
(c) 500 °C (sample #8).

height. Some of them resemble triangular pyramids, others have no well-defined shape but still consist of the same type of facets. The surface of layers grown at 300°C has a similar but much more distinct morphology with noticeably larger facets (Fig. 1b). The average size of the pyramids increased to 150 nm and their height was about 10 nm. The angle between the facets and the (111) plane of the substrate was found to be about 10°, which corresponds to crystallographic planes (332) or is close to them. Similar low-angle mounds were observed during the epitaxial growth of Fe on Fe(100) [5] and numerous other studies. They are due to so-called Ehrlich-Schwoebel step barrier in interlayer diffusion [6, 7].

The surface morphology of $CdF_2$ layers grown at 400 and 500°C drastically changed. There were large round islands with lateral size of 1000–1500 nm and 4–12 nm in height. In general, the surface became much flatter and broad terraces (about 100 nm in width) between the monolayer (0.3 nm) steps were easily identifiable (Fig. 1c). Such 2D growth mode of fluorides on the (111) surface is expected at high temperatures because this surface has a minimum surface free energy in the fluorite-type structure [8].

## RBS/channeling measurements

The RBS backscattering/channeling measurements were carried out on the Dynamitron accelerator at SUNY, Albany (USA). The 2 MeV $^4He^+$ ions and backscattering angle of 164 degrees were used. After a random spectrum was taken and all angles were set up for channeling measurement, the sample was shifted to a new spot to avoid the beam damage, which proved to be significant for $CdF_2$. The energy resolution of the system was estimated to be about 20 keV.

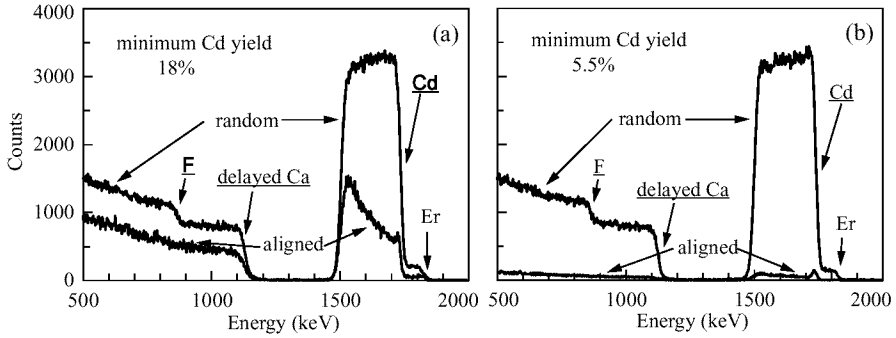


**Fig 2.** RBS random and aligned spectra for $CdF_2/CaF_2(111)$ heterostructures grown at different temperatures: (a) 100°C (sample #1), (b) 300°C (sample #5).

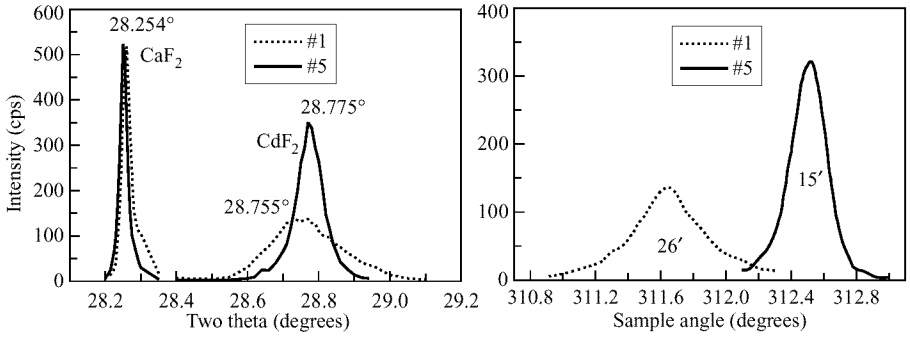


**Fig 3.** X-ray $\vartheta - 2\vartheta$ (a) and $\omega$ (b) diffraction curves from $CdF_2/CaF_2(111)$ heterostructures grown at 100°C (sample #1) and 300°C (sample #5).

Figure 2(a,b) presents the RBS/channeling data obtained for the $CdF_2/CaF_2(111)$ heterostructures grown at 100 and 300°C. As may be readily seen from the aligned to random signal ratio one, the $CdF_2$ layer in sample #5 is of much better crystalline quality, with the minimum Cd yield of only 5.5%. Another noteworthy feature is that the Er signal also decreases in the channeling orientation. This suggests that Er may occupy the substitutional rather than an interstitial position in the lattice, though a strict verification of this statement requires a channeling experiment along one more crystallographic direction. We plan to present these results at the conference.

## XRD studies

The structural perfection of $CdF_2$ layers was studied on a high resolution triplecrystal diffractometer with the use of CuK$\alpha$ radiation and 111 symmetrical Bragg's reflection. Figure 3 shows the diffraction curves measured for the samples grown at 100 and 300°C. One can find from the $\vartheta - 2\vartheta$ curves (see Fig. 3a) that the relative difference in the interplanar spacing of the $CdF_2$ layer and the $CaF_2$ substrate for these two structures is equal to $-1.71 \times 10^{-2}$ and $-1.79 \times 10^{-2}$, respectively. It is larger than expected from lattice mismatch for the bulk crystals ($\Delta a/a = -1.38 \times 10^{-2}$). This indicates the presence of residual strain. Both $\vartheta - 2\vartheta$ and $\omega$-curves are broadened, which is typical for most systems with large mismatch and film thickness about 1 $\mu$. The broadening

**Table 1.** Parameters of the studied $CdF_2$ layers.

| No. | growth $T$ (°C) | thick-ness (nm) | AFM type | AFM lateral size (nm) | AFM height (nm) | RBS $\chi_{min}$ (%) | XRD $\vartheta - 2\vartheta$ FWHM (arc.sec) | XRD $\omega$-scan FWHM (arc.sec) |
|---|---|---|---|---|---|---|---|---|
| 1(512) | 100 | 330 | M† | 30–60 | 2–4 | 18 | 430 | 1560 |
| 2(514) | 100 | 330 | M | 30–60 | 2–4 | – | – | – |
| 3(518) | 200 | 330 | M | 60–100 | 4–5 | – | 320 | 2170 |
| 4(510) | 300 | 370 | M | 100–150 | 8–10 | – | – | – |
| 5(513) | 300 | 300 | M | 100–170 | 8–10 | 5.5 | 150 | 900 |
| 6(515) | 300 | 330 | M | 100–150 | 8–10 | – | – | – |
| 7(519) | 400 | 330 | S‡ | 1000–1500 | 4–8 | 5.5 | 140 | 800 |
| 8(521) | 500 | 570 | S | 1000–1500 | 4–12 | – | 120 | 750 |

† pyramidal mounds; ‡ round shape islands with 1 ML steps

can be related to randomly distributed threading dislocations. Both curves show that the crystal quality of the structures grown at 300°C is considerably higher.

## Conclusions

The possibility of epitaxial $CdF_2$ growth on $CaF_2(111)$ substrates in a wide growth temperature range of 100–500°C has been demonstrated. It is found that there are pyramidal mounds on $CdF_2$ with a typical lateral size 30–60 nm at 100°C and 100–150 nm at 300°C. The angle between its facets and the growth plane is about 10°. At higher growth temperatures, the surface morphology drastically changes to large (1000–1500 nm) round islands formed by one-monolayer steps and 100 nm terraces. This indicates layer-by-layer growth. The RBS and XRD measurements show that the crystalline quality of the structures rapidly improves with the growth temperature.

The authors appreciate useful discussions with A. Yu. Khilko. This work was partially supported by grants of the Russian Foundation for Basic Research, the Russian Ministry of Science and the National Science Foundation.

## References

[1] J. M. Langer, T. Langer and B. Krukowska-Fulde, *J. Phys. D* **12** L95 (1979).
[2] N. S. Sokolov, N. N. Faleev, S. V. Gastev, N. L. Yakovlev, A. Izumi and K. Tsutsui, *J. Vac. Sci. Technol.* **A13** 2703 (1995).
[3] A. Yu. Khilko, R. N. Kyutt, Yu. V. Shusterman, L. J. Schowalter, N. S. Sokolov. *Abstracts of Int. Symp. Nanostructures: Physics and Technology*, St. Petersburg, Russia, 1996, p. 133–136.
[4] R. P. Khosla, *Phys. Rev.* **183** 695 (1969).
[5] J. A. Stroscio, D. T. Pierce, M. Stiles, A. Zangwill, and L. M. Sander, *Phys. Rev. Lett.* **75** 4246 (1995).
[6] G. Ehrlich and F. Hudda, *J. Chem. Phys.* **44** 1039 (1966).
[7] R. L. Schwoebel, *J. Appl. Phys.* **40** 614 (1969).
[8] L. J. Schowalter, R. W. Fathauer CRC Crit. Rev. Solid State Mater. Sci. **15** 367 (1989).

Ioffe Institute
6th Int. Symp. "Nanostructures: Physics and Technology"
St Petersburg, Russia, June 22–26, 1998.



# Raman study of optical vibrations in InAs/GaAs self-assembled quantum dots

*Yu. A. Pusep*†, G. Zanelatto†, J. C. Galzerani†, S. W. da Silva‡, P. P. Gonzalez-Borrero¶, P. Basmaji¶ and A. I. Toropov§

† Universidade Federal de São Carlos, 13565-905 São Carlos, SP, Brasil

‡ Universidade de Brasilia, 70910-900, Brasilia, DF, Brasil

¶ Instituto de Fisica de São Carlos, Universidade de São Paulo, 13560-970 São Carlos, SP, Brasil

§ Institute of Semiconductor Physics, 630090 Novosibirsk, Russia

The optical vibrational modes were studied in the strained InAs/GaAs heterostructures containing self-assembled quantum dots. The both, optical phonons in the InAs dots and in the GaAs barrier were detected by the resonance Raman scattering at the $E_0 + D_0$ gaps of InAs and GaAs correspondingly.

The LO and TO phonons in the InAs dots revealed strong shifts due to the strain. The observed strain induced frequency shifts were found in good agreement with the values calculated for the pyramidal InAs dots embedded in GaAs [1].

A number of Raman lines were observed in the frequency range of the GaAs optical phonons; the intensities of these lines significantly increased with increase of the density of the InAs dots measured by atomic force microscope. The theoretical analysis based on the calculation of the energy spectrum of the interface modes localised at sharp tips [2] and on the strain calculated for the pyramidal InAs/GaAs dots showed that the observed modes can be assigned to the GaAs-like interface modes localised at the apexes of the InAs pyramids, which are subjected to the strain. The Raman scattering measured with different excitation energies revealed the dispersion of these interface modes caused by both the spatial distribution of the strain in the InAs/GaAs heterostructure and the spatial dependence of the electrostatic potential of the interface modes.

## References

[1] M. Grundmann, O. Stier, D. Bimberg, *Phys. Rev. B* **52**, 11969 (1995).

[2] P. A. Knipp, T. L. Reinecke, *Phys. Rev. B* **46**, 10310 (1992).

Ioffe Institute
6th Int. Symp. "Nanostructures: Physics and Technology"
St Petersburg, Russia, June 22–26, 1998.



# Raman scattering in strained highly-doped p-type GaAs/GaAsP epitaxial layers

*A. V. Subashiev*†, V. Yu. Davydov, I. N. Goncharuk, A. N. Smirnov, O. V. Kovalenkov and D. A. Vinokurov
† State Technical University, St. Petersburg 195251, Russia
Ioffe Physical Technical Institute, St. Petersburg 194021, Russia
e-mail: arsen@tuexph.spb.neva.ru

Strained GaAs epitaxial layers and GaAs-based superlattices are known to be very effective as photoemitters of highly polarized electrons [1]. The efficiency of the polarized electron source is determined both by the maximum value of electron polarization and the quantum yield at the maximum, which depend on the thickness of the active semiconductor layer and the valence band splitting, induced by the layer strain. Therefore it is essential to have highly strained layers with sub-micron thicknesses. To produce high valence band splitting the value of the elastic strain in the GaAs active layer no less than 1% is needed. At such elastic strains the value of the critical thickness of a GaAs strained layer at which the misfit dislocations begin to introduce into the film and plastic relaxation occurs is about 10–20 nm, so that submicron layers are partially relaxed [2]. The relaxation causes inhomogeneous distribution of the dislocation density and the strain in the layer depth. Besides, to obtain negative electron affinity, the layers are highly doped with the acceptor impurities. The efficient control of the parameters of the layers becomes a difficult problem. Raman scattering is found to be effective to solve the problem.

We have studied GaAs strained quantum layers grown on relaxed [001] $GaAs_{1-x}P_x$ buffer layers using MOCVD. The incorporation of tensile strain was made possible by preparing a 1-$\mu$m-thick Ga $As_{0.3}P_{0.7}$/GaAs superlattice grown in its turn on [100] GaAs substrate which was followed by a $GaAs_{1-x}P_x$ buffer. The strain of the GaAs was measured using X-ray diffraction, Raman spectroscopy and photoluminescence.

The polarized Raman spectra of the samples with varying thickness and substrate composition were measured at room temperature with back-scattering geometry for several excitation lines of an Ar-ion laser. The Raman spectra of GaAs 0.15-$\mu$m-thick films at $GaAs_{1-x}P_x$ buffers with $x = 0.1$, 0.25, and 0.3 are presented in Fig. 1. The full width at half maximum (FWHM) of the LO line in the layers with $x \leq 0.2$ is found to be considerably larger than that of the undoped GaAs strained and unstrained reference layers. The frequency and the width of the LO-band depends strongly on the buffer composition: when the composition increases above $x = 0.2$ the full width at half maximum of the LO line decreases rapidly.

In Fig. 2 the Raman line shift and the FWHM are plotted as a function of the buffer P — content for 0.1-$\mu$m and 0.3-$\mu$m-thick layers. In both cases a narrowing of the Raman line accompanied by the low energy-shift is observed. Theoretical analysis showed that the evolution of the Raman spectrum is due to the self-energy effects in the LO phonon spectrum which originate from intersubband heavy-hole to light hole transitions caused by deformation potential-type interaction. The LO phonon line narrowing occurs when the strain-induced valence band splitting exceeds the LO phonon frequency. The

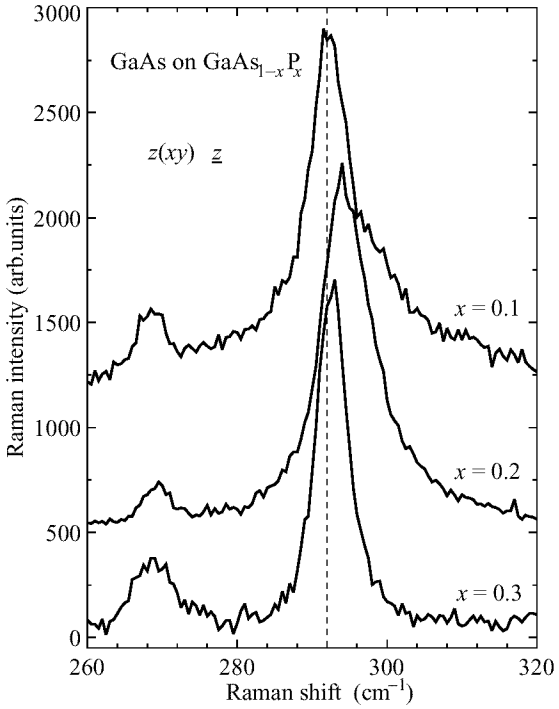


**Fig 1.** Raman spectra of the 0.15-$\mu$m-thick GaAs layers for several buffer (substrate) compositions changing the layer strain.

low-frequency shift observed with the narrowing is caused by the growth of the hole-transitions contribution to the LO phonon softening at the edge of the intersubband hole transitions.

The changes in the LO phonon Raman line are sensitive to the strain inhomogeneity in the sample in the light absorption depth. We used it to evaluate the strain relaxation. We have found the strain relaxation of about 80% even at small misfits ($x = 0.1$) and the layers thickness 0.1–0.2 $\mu$m while the narrowing at $x \geq 0.2$ observed for different excitation lines shows that the strain remains large and homogeneous even for $x = 30\%$ and 0.2 $\mu$m-thick layers. The estimates of the critical thickness $t_c$ for $x = 30\%$ (the lattice mismatch $\epsilon = \delta a/a = 1.02 \times 10^{-3}$, where $\delta a$ is the lattice constant's difference between the GaAs epilayer and GaAsP buffer substrate) according to relation of Ref. [3] gives $t_c \approx 9.8$ nm. Still the strain remains high even for the layers having the thickness 20 times larger than the critical. Our observation is consistent with previous findings [4] obtained from the polarized electron emission studies accompanied by the X-ray diffraction patterns analysis.

The asymmetry ($\Gamma_{low}/\Gamma_{high}$) of the GaAs LO line remains constant for $x \leq 0.2$, therefore it indicates the predominant contribution of the intersubband transitions to the LO line broadening.

This work is supported by CRDF Grant No. RPI-351. Partial support by the IN-

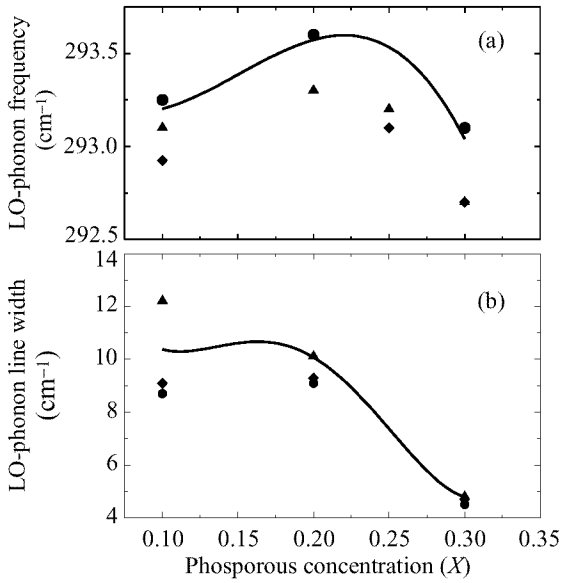


**Fig 2.** Raman LO-ponon line shift (a) and full width at half maximum (b) in GaAs epilayer on $GaAs_{1-x}P_x$ substrate as a functions of the phosphorous concentration $x$, points — layers of different thicknesses, lines — calculations.

TAS (project No. 94-1561) and by RFBR (Grant No. 96-02-19187a) is also gratefully acknowledged.

## References

[1] *Proc. of the Workshop on Photocathodes for Polarized Electron Sources for Accelerators,* SLAC-423, Jan., 1994.
[2] K. Mizoguchi, S. Nakashima and A. Takamori, *Applied Physics* **69** 8304 (1991).
[3] R. People and J. C. Beans, *Applied Physics Letters* **47** 322 (1985).
[4] H. Aoyagi, H. Horinaka, Y. Kamiya, et al. *Physics Letters A* **168** 415 (1992).

Ioffe Institute
6th Int. Symp. "Nanostructures: Physics and Technology"
St Petersburg, Russia, June 22–26, 1998.



# Optical transitions in quantum wells and quantum dots based on SiGe heterostructures

*Z. F. Krasil'nik*‡, V. Ya. Aleshkin‡, N. A. Bekin‡, N. G. Kalugin‡, A. V. Novikov‡, V. V. Postnikov‡, V. A. Markov†, A. I. Nikiforov†, O. P. Pchelyakov†, D. O. Filatov¶, and H. Seyringer§

‡ Institute for Physics of Microstructures RAS, Nizhny Novgorod
† Institute for Semiconductor Physics RAS, Novosibirsk
¶ The Nizhny Novgorod State University
§ Institute for Semiconductor Physics, Johanes Kepler University of Linz, Austria

**Abstract.** The growth of GeSi nanoislands and potoluminescence features in structures with localized states of electrons and holes are discussed.

## Introduction

Silicon and germanium are known to be indirect band semiconductors with a low photoluminence efficiency, especially at room temperature. The conduction and the valence bands of low-dimensional strained SiGe heterostructures largely differ from bulk materials, this difference depending on size quantization and deformation effects. The advances made in the past few years in the technologies for nanostructure growth on the basis of Si, Ge and their solid solution open new possibilities in terms of electron state engineering, including upgrading of photoluminescence effectiveness as one such target. The latter is what a potential application of these structures in the near-IR optoelectronic devices relies upon [1].

In this paper the photoluminescence features in SiGe structures with localized states of electrons and holes are discussed. A radiative recombination of electrons and holes in an indirect gap semiconductor is a three-particle process involving an electron, a photon and a third particle responsible for conservation of momentum in a recombination procedure. If an electron involved in recombination is well localized in space, its momentum is uncertain. The electron here may have the momentum value corresponding to a direct optical transition from the conduction to valence band. As a rule, the momentum-space-direct recombination transitions in SiGe heterostructures prove possible for electrons and holes that are located on different sides of a heterointerface [2]. The probability of such transitions is higher with a greater overlap of the electron/hole wave functions.

## 1 Energy band structure

Analysis of the energy bands for $Si/Ge_xSi_{1-x}$ and $Ge/Si_xGe_{1-x}$ heterojunctions shows that the potential well for holes is located on the heterointerface side with a smaller Si content [2]. The potential well for electrons may be on either side of the heterointerface, which depends on the character of elastic deformation, a alloy composition, etc. There are six electron valleys in the conduction band. It is important for modeling of structures

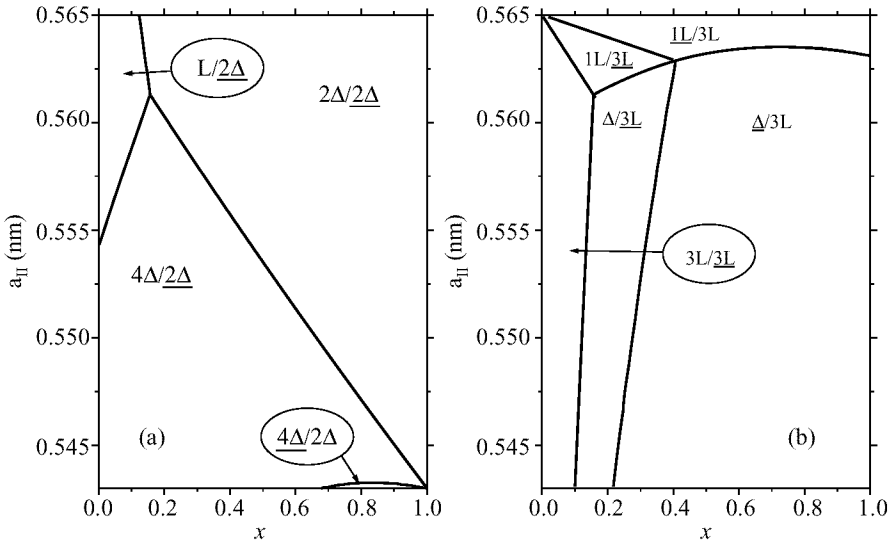


**Fig 1.** Regions of specific relative energy positions of the conduction-band-edge states in elementary semiconductors (Si or Ge) and in their alloys for (001) $Ge_{1-x}Si_x$/Si (Fig. 1(a)) and (111) $Ge_{1-x}Si_x$/Ge (Fig. 1(b)) heterostructures [2].

with allowed direct optical transitions which of the valleys form the conduction band bottom. A favourable situation is when the conduction band bottom is formed by a valley whose minimum in the momentum space is shifted relative to the valence band top in the direction perpendicular to the heterointerface. An electron confinement motion in this direction, i.e., near-heterointerface, which is quite likely for a number of reasons, leads to an uncertainty of the corresponding component of the electrons' momentum, so the direct transitions become allowed.

In Fig. 1 the calculation results are provided for two types of a heterointerface. The parameter regions corresponding to the above situation are such as to ensure that 2Δ-valleys will lie lowest in the conduction band for a Si/$Ge_xSi_{1-x}$ heterostructure grown on a Si(100) substrate and L-valleys for a Ge/$Si_xGe_{1-x}$ heterostructure grown on a Ge(111) substrate. The electron can be confined by forming a quantum well in the appropriate layer [3]. A detailed analysis of, for example, a Si/$Ge_xSi_{1-x}$ heterostructure on a Si substrate shows that the thickness of a 2D layer of solid solution towards this effect has to be tens of Angstrom and the Ge fraction in the alloy must exceed 30–40%. It is known that the growth process of such structures may facilitate self-organization of nanometer-scale GeSi islands, which are a major issue of the present work.

## 2 Technology

Basic features of self-organization of Ge islands in silicon in the MBE [4, 5] and CVD [6] growth of heterostructures have been established by now. The sizes and surface density of the islands largely depend on the growth conditions (substrate temperature, growth rate and Ge fraction in the deposited layer [4]).

The structures under investigation were grown on the "KATUN" and "BALZERS"

MBE systems. The residual gas pressure was of at $3 \times 10^{-10}$ Torr. The systems were equipment with e-gun for evaporation for Si and Ge. The growth process was controlled *in situ* by a spatial/temporal analysis of variations in the patterns of reflected high-energy electron diffraction (RHEED). Variations in the intensity profiles versus time were measured along the (00) streak in the [110] azimuth. The growth rate of Ge films was 0.005–0.1 nm/s, the substrate temperature varying in a $100 \div 700°C$ range. Silicon films were grown at $550 \div 950°C$ at the rate of 0.02–0.5 nm/s. For

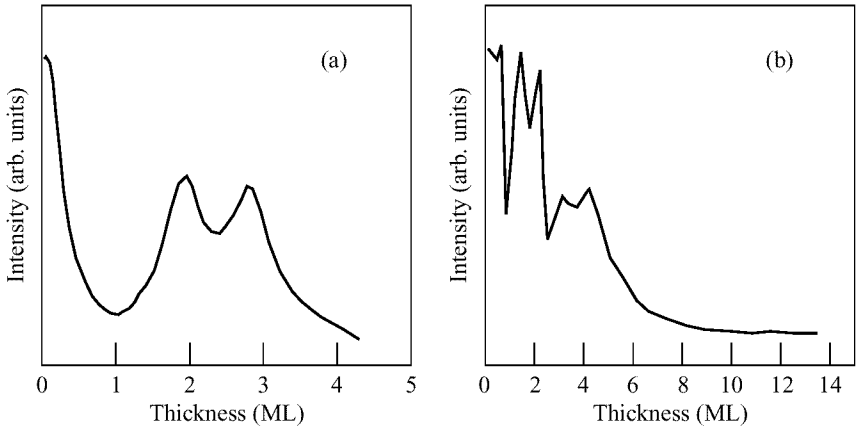


**Fig 2.** RHEED intensity oscillations of specular-beam observed from the surface of Ge films on Si (111) (a) and Si (100) (b).

the RHEED study of Ge islands formation it is important that this effect is associated with a 2D to 3D transition of the growth mode. This allows to precisely control the onset of a self-organization process. Figs. 2a and 2b demonstrate the typical intensity oscillations of a specular beam from the (111) and (001) surfaces of a Ge/Si film, respectively. It is clearly seen that the oscillation amplitude and average intensity start decreasing right after the onset of Ge growth. This decrease is caused by clustering and islands formation inherent in the growth by the Stranskii-Krastanov mode. The critical thickness for the 2D layer-by-layer mechanism to 3D mode transition ($h_c$ ) was found by measuring thickness values at which the oscillations vanish. In the Stranskii-Krastanov growth method, the less the elastic strain on a growing film, the larger $h_c$. In our case, elastic strains is reduced with a smaller Ge content in a $Ge_xSi_{1-x}$ alloy. We observed two oscillation periods throughout growth of a Ge film on Si at $T = 650°C$ (Fig. 1a) and six periods for a $Ge_{0.5}Si_{0.5}$ film. Another factor affecting growth of Ge islands is crystallographic orientation of substrate. One can see in Fig. 1 that the critical thickness for Ge growing on Si(111) and (001) surfaces is 2 monolayers (ML) and 5 ML, respectively.

## 3 Experimental results

Microprobe studies were carried out at room temperature on a Park Scientific Instrument atomic force microscope (AFM). The photoluminescence (PL) spectra from Ge/Si(001) structures excited by a $Kr^+$ laser ($\lambda = 647$ nm) were measured at 4.2 K with BOMEM

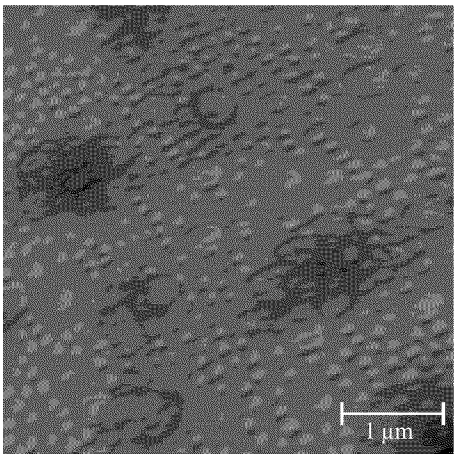


**Fig. 3.** AFM images of Ge film with a nominal thickness of 10 ML.

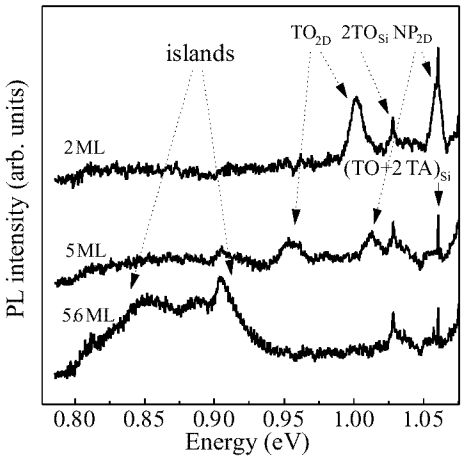


**Fig. 4.** PL spectra of Ge layers grown at 700°C with different thicknesses. The nominal thickness of Ge layers is given.

DA3-36 Fourier-transform spectrometer incorporating an InGaAs cooled photodetector.

Fig. 3 shows an AFM image of a sample comprising a Ge layer of thickness $d =$ 10 ML, grown on Si(100) at $T = 700°C$. According to the microprobe analysis data, the value of $h_c$ at our growth conditions was 5 ML, which is in good agreement with the RHEED results. As the Ge content was, the sizes and density of the islands increased. By their transverse sizes D, the islands can be divided into three groups: $D \leq 190$ nm, $200 \leq D \leq 300$ nm, and $D > 350$ nm. The sizes and shape of the islands in groups I and II suggest that they must be dislocation-free outgrowths in which partial relaxation of the elastic strain was caused by local deformation of the nearsurface layer of Si [5] and by relaxation of strain on the islands free surface. Group III includes the islands that have experienced relaxation of the elastic strain through plastic deformation and formation of misfit dislocations in them. The size of the islands in the growth plane, that allows formation of misfit dislocations is close to the critical size of the elastic-strained islands $D > 300$ nm, as measured in [6].

The surface density of islands, $N_s$, depends on a Ge layer thickness and varies for different contents of deposited Ge from $8 \times 10^7\,cm^{-2}$ to $2 \times 10^9\,cm^{-2}$ [7]. As the growth temperature goes down to 550°C, the distribution of islands becomes more homogeneous in size, the average size is getting smaller ($D \approx 190$ nm), and the surface density increases. The size and surface density data for self-assembled islands agree with the results in [4].

Fig. 4 is the PL spectra for Ge/Si(001) heterostructures. Besides the luminescence lines of a Si substrate (TO- and TA-phonons-assisted replicas (see Fig. 4)), the spectra observed from samples with an effective Ge layer less than 5 ML exhibit luminescence lines from the Ge (2D) wetting layer ($TO_{2D}$ for the TO-phonon-assisted replica and a no-phonon $NP_{2D}$ line). For the sample with $d_{Ge} = 2$ ML, the $NP_{2D}$ line falls within the phonon lines range $(TO + 2TA)_{Si}$ of substrate luminescence. With an increasing Ge

content the PL lines from the Ge layer are shifted to lower-frequencies due to a size quantization effect.

When a Ge layer thickness is above some critical value, there appears a wide peak in the region $0.8 \div 0.925$ eV, attributed to formation of Ge nanoislands.

## 4 Discussion

Typical sizes of islands in the growth plane are above 100 nm. Their height is by about an order smaller. Given such sizes the energy of the size quantization of holes in Ge islands would not exceed 20 meV, which leads us to a conclusion that the marked shift of the PL line $(80 \div 925)$ meV energies relative to Si cannot be treated unambiguously as being related to pure Ge islands on silicon. One may assume that the islands are a Ge-Si alloy [4] and then evaluate the molar fraction of Si in them. In Fig. 5 we provide

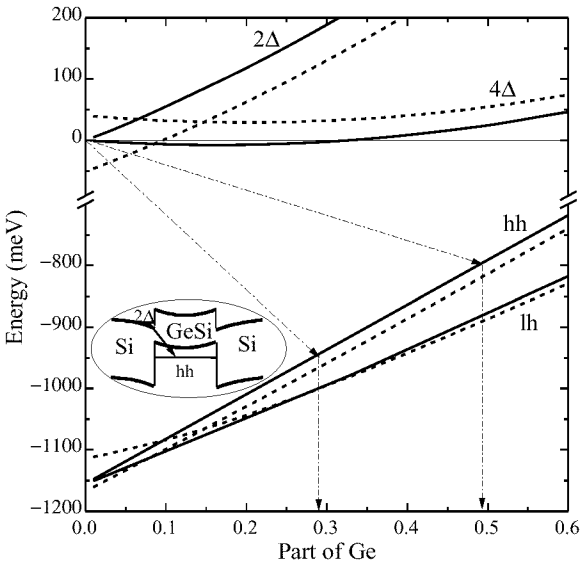


**Fig 5.** Conduction and valence bands of SiGe alloy, grown pseudomorphicaly on Si substrate (the lattice constant is equal to 5.43 Å– solid lines, the lattice constant is equal to 5.46 Å– dashed lines).

the band edge positions for a thin pseudomorphicaly alloy of $Si_{1-x}Ge_x$ on Si, calculated by the model in [2]. The symbols hh and lh are used to designate the heavy and the light hole subbands, respectively; $2\Delta$– is for two delta-valleys of the conduction band, in which the electron mass is maximum along the growth direction; $4\Delta$ – label the other four delta-valleys of the conduction band; L is the L-valley. The calculations testify to a possibility of photoluminescence in a $800 \div 925$ meV range for a pseudomorphicaly alloy grown on a Si substrate, provided the Ge fraction in the islands is 30–50%. The solution seems to form in the islands through segregation of Ge.

The structures feature a p-type conductivity, and the islands are potential wells for the holes which accumulate in the islands, giving them a positive charge. The surface density of holes in the islands given $\sim 10^{15}\,\mathrm{cm}^{-3}$ concentration of holes in Si, can be

evaluated as for a quantum well with the same energy level of the ground state for heavy holes: $\sim 4 \times 10^{10}\,\mathrm{cm}^{-2}$. Due to the Coulomb repulsion the holes inside the islands are expected to concentrate along the heterointerfaces. The positive charge of the island creates a quantum well for the photoelectrons in Si near the heterojunction (see the insert in Fig. 5). When the conduction band bottom in Si lies lower than in the islands (Fig.5 shows that this occurs at $x > 0.32$, the PL energy $E_{pl} < 960$ meV), the quantum confinement result in the fall of $2\Delta$–valleys energy with respect to $4\Delta$ ones, because of the larger electron masses along the (001) direction than in $4\Delta$–valleys. The focus here is on the electrons concentrated near the base and the tip of the islands, since it is them that provide the major contribution in photoluminescence because of a large difference in the areas of the lateral sides and the bases. Size quantization terminates the momentum conservation law (the Brillouin zone is two-dimensional), and the electron states of the $2\Delta$–valleys shift towards the center of 2D Brillouin zone. In this case, the interband optical transitions become direct in the momentum space ($p_{\mathrm{final}} - p_{\mathrm{initial}} = 0$), but in the real space the transitions are indirect, as the electrons and holes are localized on different sides of the heterointerface.

Assuming a partial relaxation of elastic strain in a solid solution through deformation of the surrounding silicon, the Ge fraction in islands whose PL lines fall within the $0.8 \div 0.925$ eV energy range must decrease, as follows from the calculations, compared to the islands that had no such relaxation. We can arrive at this conclusion by examining Fig. 5 in which the dotted lines show the positions of the band edges in a solid solution surrounded by deformed layers of silicon.

This work has been supported by the Russian Foundation for Basic Research, grants 96-02-16991, 97-02-18408 and the Russian Scientific Program "Physics ofsolid state nanostructures" grant 96-2011.

## References

[1] R. People, J. C. Bean, et al., *Appl. Phys. Lett.* **61** 1122 (1992).
[2] V. Aleshkin, N. A. Bekin, J. Phys.: *Condens. Matter.* **9** 4841 (1997).
[3] C. G. van de Walle, R. M. Martin, *Phys. Rev. B* **34** (8), 5622 (1986).
[4] G. Abstreiter, P. Schittenhelm, et al, *Semicon. Sci. Technol.* **11** 1525 (1996).
[5] D.J. Eaglesham and M. Cerullo, *Phys. Rev. Lett.* **64** 1944 (1990).
[6] G. Capellini, L. Di Gaspare et al., *Appl. Phys. Lett.* **70** 494 (1997).
[7] V. Aleshkin, N. Bekin, N. Kalugin et al., *Pis'ma ZhETF* **67(1)** 48 (1998).

Ioffe Institute
6th Int. Symp. "Nanostructures: Physics and Technology"
St Petersburg, Russia, June 22–26, 1998.



# Quantum bistability in a quasi bilayer hole system formed in wide potential wells of p-GeSi/Ge MQW heterostructure

*M. V. Yakunin*†, Yu. G. Arapov†, O. A. Kuznetsov‡, V. N. Neverov†, G. I. Harus† and N. G. Shelushinina†

† Institute of Metal Physics RAS, 620219, Ekaterinburg, GSP-170, Russia

‡ Scientific-Research Physicotechnical Institute, Nizhnii Novgorod State University, Russia

**Abstract.** Spontaneous switching between two stable states has been observed in the high field low temperature magnetotransport of wide potential well p-GeSi/Ge multilayered heterostructures in which the Fermi energy is comparable to the amplitude of the well bottom bending. These two states exist in broad ranges of temperatures and currents and look like the quantum Hall state for double layer system and the classical single layer state.

A system of two interacting 2D layers is an intriguing object for investigation of the quantum Hall regime magnetotransport in view of an additional degree of freedom arising here. On the other hand, such an object is closely connected with the problem of wide potential wells in selectively doped heterosystems since the well bottom bending that exist in these structures may lead to separation of the quasi-2D gas in the well into two gases located at the opposite potential walls. This may happen when the Fermi level lies lower than the bottom bending amplitude.

In our previous works [1] the quantum magnetotransport has been studied in the quasi 2D hole gas of wide potential well p-GeSi/Ge multilayered heterostructures and the quasi-two-dimensionality was manifested in that the second heavy hole confinement subband participated in kinetics leading to considerable changes in the structure of quantum Hall and magnetoresistivity curves. These heterostructures were selectively doped but there was a moderate value of the bottom bending so that the hole gas in the well could be treated as undivided. The latter manifested particularly in the existence of a wide quantum Hall plateau at $\rho_{xy} = 25.8$ K$\Omega$ corresponding to the filling factor $\nu = 1$ for the whole gas in the well. In this communication we describe the results obtained in a similar p-GeSi/Ge multi-quantum-well (MQW) heterostructure, but with wider wells, that we cannot explain in terms of a single hole gas.

We measured longitudinal $\rho_{xx}(B)$ and Hall $\rho_{xy}(B)$ magnetoresistances in a set of CVD grown multilayer samples with a following structure: substrate Ge(111)/buffer Ge $\sim 1.8\,\mu$/buffer $Ge_{1-y}Si_y$ $0 \div 1.6\,\mu$/N$\times$(Ge/$Ge_{1-x}Si_x$:B). Thickness' of Ge and GeSi layers in a multilayer region were approximately equal and varied from sample to sample in a range of $d = 100 \div 400$ Å. The GeSi layers were doped with boron in the central part with undoped spacers of $\sim 1/4$ the total layer thickness left on theirs both sides. In the range of $d = 100 \div 300$ Å, $y \approx 0.07$, $x = 0.07 \div 0.10$, hole densities $p_s = (2.8 \div 5) \cdot 10^{11}$ cm$^{-2}$ and mobilities $\mu = 10000 \div 15000$ cm$^2$/V·s a single stabile state was observed with distinct manifestations of integer quantum Hall effect (QHE) [1].

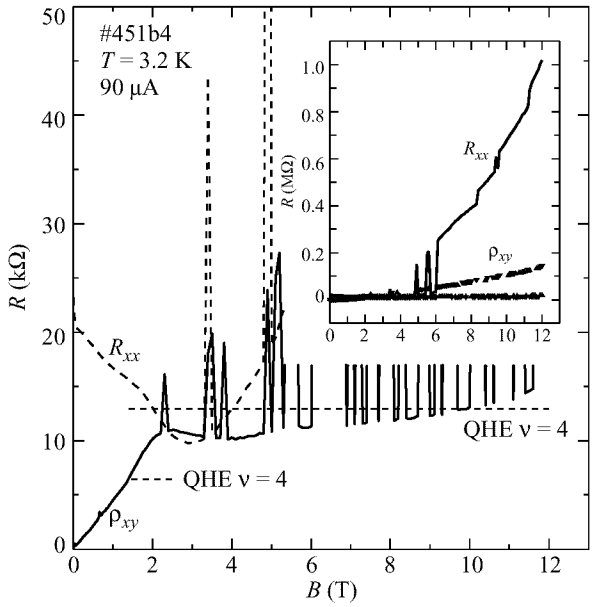


**Fig 1.**

Just another result was observed recently in a sample 451b4 with a wider well $d = 355$ Å and notably lower 2D hole density $p_s = 1.4 \cdot 10^{11}$ cm$^{-2}$ (other parameters: number of repetitions $N = 36$, $y \approx 0.087$, $x = 0.097$, and $\mu = 14000$ cm$^2$/V·s): Fig. 1. In the weak field region again the single state is observed with features of the QHE: weak plateau $\rho_{xy} \approx 6.5$ KΩ (close to the value for $\nu = 4$) and corresponding minimum in $\rho_{xx}(B)$ at $\sim 1.3$ T. Then in $B \gtrsim 2$ T the strong plateau shows up in $\rho_{xy}(B) \approx 11 \div 13$ KΩ (close to the value of 12.9 KΩ for $\nu = 2$) concomitant with the deep minimum in $\rho_{xx}$ at $B = 3$ T. At fields $B > 2 \div 3$ T the unstable behavior of experimental data begins. The most exiting feature (to our minds) is that the experimental points in this region are apparently grouped on two smooth curves: see Fig. 2. The first curve is the prolongation of the QH plateau that started at $\sim 2$ T with very weak magnetic field dependence slightly enhanced in the highest fields region. The second curve is the prolongation of the weak field curve, which extrapolates to zero with $B \to 0$ and monotonously depends on field with a slope much higher than that of the first curve. In the experiment the cause of the switching from one state to another is the change in polarity of dc current. Important is that data for both current polarities exist on each of the two split-of curves (see up and down triangles on the figure). Therefore the splitting of the data is not a manifestation of any asymmetry in the sample (e.g. in contacts) but switching the current polarity is simply an impact transforming the sample from one stable state to another one. Grouping of the points on the *smooth* curves means that the sample is in a stable state during measurements in a fixed field at a fixed current polarity. Then the current polarity is changed and the sample changes into another state or remains in the same state. In the field range where the intensive instabilities in $\rho_{xy}(B)$ exist the magnetoresistivity curve $\rho_{xx}(B)$ also reveals bistable behavior which transforms into sharp stepwise increase (see the insert in the Fig. 1) implying the break

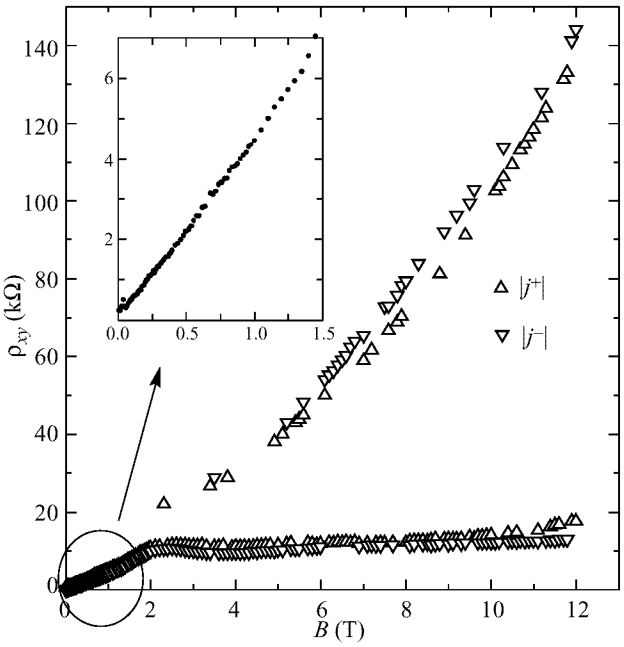


**Fig 2.**

up of the QHE. But we observed this bistable behavior at the current densities as low as $\sim$ 45 mA/m that seems too low for the break up effect. The effect was observed without considerable changes in the range of currents $0.1 \div 100\,\mu$A and temperatures $1.6 \div 4.2$ K.

Among the samples we investigated earlier [1] simple estimations predicted that for one of them, #1003, the Fermi level must be close to the well bottom bending amplitude $u_0$. Let's compare estimations for the sample #451b4 and those for #1003. For the simplest case of the uniform hole gas distribution in the infinite well: $u_0 \propto p_s d$. For #1003: $p_s = 4.8 \cdot 10^{11}$ cm$^{-2}$ and $d = 220$ Å. So in the sample #451b4 $u_0$ is approximately $(1.4/4.8)(355/220) \approx 0.5$ of the value for #1003. The first confinement level $E_1$ in the well in the energy range outside the band edge relief is roughly $\propto d^{-2}$ that is 0.4 and the Fermi level $E_F - E_1 \propto p_s$ is 0.3 of that for #1003. On the basis of these estimations we can anticipate that in the sample #451b4 the Fermi level drops lower than the bending amplitude does. Therefore probable becomes the situation that the Fermi level falls into the energy range corresponding to two potential wells in a single Ge layer and some quasi-double-layer behavior of the whole sample might be expected.

While the QH plateau for $\nu = 2$ is distinctly observed in #451b4 there is not a hint for the existence of the $\nu = 1$ peculiarity. Neither there is a minimum in $\rho_{xx}(B)$ at $B > 3$ T [in spite of instabilities the monotonous background in $\rho_{xx}(B)$ is still seen at $B \approx 6$ T where the minimum for $\nu = 1$ is expected] nor a plateau in $\rho_{xy}(B) > 13$ KΩ exist. On this basis we conclude that the plateau in $\rho_{xy}(B)$ and the minimum in $\rho_{xx}(B)$ at $B \approx 3$ T are the manifestations of the number one peculiarity of the Integer QHE (counting from the high field side). In other words, this is the manifestation of QHE for the filling factor $\nu = 1$ but for twice the number of 2D layers: not for 36 layers

(= the number of Ge layers in the sample), but for $2 \times 36 = 72$ layers. Another evidence that the plateau corresponds to $\nu = 1$ is its big length, that is an indication of the delayed transition into a high field insulating phase. The value of the hole density $p_s = 1.4 \cdot 10^{11}$ cm$^{-2}$ in a Ge layer was obtained from the slope of $\rho_{xy}(B)$ in extremely low fields (see the insert in the Fig. 2). The position of $\rho_{xx}$ minimum at 3 T yields the density of $\sim 0.7 \cdot 10^{11}$ cm$^{-2}$ in a single 2D layer (implying that it correspond to $\nu = 1$) indicating that there are two 2D sublayers in a Ge layer.

Some additional informational that may be useful in interpreting the phenomena observed. Investigations of the sample #399 of the same family as #451b4 but with narrow wells $d = 145$ Å and lower hole density in a Ge layer $p_s \approx 0.5 \cdot 10^{11}$ cm$^{-2}$ have revealed that it is in the insulating phase at low temperatures (although in conducting state at temperatures $T \gtrsim 15$ K). Therefore we can expect that separation of the hole gas inside the Ge layer of the sample #451b4 into two 2D sublayers may switch the sample into insulating phase since the effective thickness of a sublayer is less than a half the Ge layer thickness ($< 180$ Å) and a hole density in it is $\sim 0.7 \cdot 10^{11}$ cm$^{-2}$. We believe that transition into two-sublayer state when the Fermi level becomes lower than the band bending amplitude may be rather sharp for holes since their tunneling through the barrier will be weak due to big effective masses.

As it follows from our experiment, this transition as a matter of fact goes not into the insulating state but is limited by appearing of another conducting state. The monotonous, stemming from zero course of $\rho_{xy}(B)$ for this new state implies classical Hall effect and its slope in the weakest fields yields the hole density which is the double value obtained for the sublayer from the QHE in a first state. So we can establish that the sample in the fields $B \gtrsim 3$ T can exist in two states: (i) quantum Hall state with holes divided into two 2D sublayers in each Ge layer and (ii) classical state with undivided hole gas in a layer. As both of these states are metastable there must exist some self-stabilizing mechanism. Probably its essence is connected with the double sublayer potential structure itself. While the sublayers in a Ge layer are in balance with each other the first state exist. Going out of this balance drives the system into the state of a single conducting gas in a Ge layer and to destruction of the QH regime. This implies the change of the potential profile in the well probably due to the hole gas redistribution in the direction normal to the interface. The superlinear course of $\rho_{xy}(B)$ in the classical state indicates that some part of the hole gas is in the insulating phase and this part increase with field. The switching between two states must bear a collective character, i.e. to happen simultaneously in all the Ge layers otherwise the points would scatter far outside the smooth curves.

The work is supported in part by RFBR, project No. 98-02-17306, and by the program "Physics of Solid State Nanostructures".

## References

[1] Yu.G. Arapov et. al., *Proc. 11-th Internat. Conf. "High magnetic fields in the physics of semiconductors"*, Cambridge, USA, 1994, p. 632; *Semiconductors* (in press).

Ioffe Institute
6th Int. Symp. "Nanostructures: Physics and Technology"
St Petersburg, Russia, June 22–26, 1998.



# Hole levels in Ge self-assembled quantum dots probed with room temperature capacitance spectroscopy

*A. I. Yakimov*, A. V. Dvurechenskii, V. A. Markov,
A. I. Nikiforov and O. P. Pchelyakov
Institute of Semiconductor Physics, 630090 Novosibirsk, Russia

**Abstract.** Pyramidal Ge islands with the areal density $4 \times 10^{11}$ cm$^{-2}$ and the typical base length 12 nm have been grown on p-type Si (100) substrates at 300°C by molecular beam epitaxy. Capacitance spectroscopy was used to determined the allowed energy levels for holes in these quantum dots. At room temperature we observed the capacitance peaks with two types of spacings as a function of the gate voltage. The oscillations with largest period are attributed to the discrete quantum level structure while the peak splitting is a result of charging of dots by individual holes. The Coulomb charging energy is found to decrease with increasing of excited level number.

Self-assembled semiconductor islands created by epitaxial growth of lattice mismatched systems in the Stranski-Krastanow growth mode have the narrow size distribution and the extremely small lateral dimensions. Therefore, this approach is expected to produce quantum dots with superior electronic performance at room temperature. The most widely studied system so far is (InGa)As/GaAs (see [1] and references therein). The formation of three-dimensional islands after deposition of typically a few monolayers (ML) has also been observed for Ge/Si systems [2, 3]. The existence of single-electron phenomena in Ge/Si double-barrier heterostructures containing quantum dots at liquid hellium temperature has been demonstrated by conductance spectroscopy [4]. A powerful technique for probing low-dimensional structures is the measurement of capacitance [5-7]. In this paper we report the results of capacitance measurements on Ge self-assembled quantum dots grown by molecular beam epitaxy on Si (100). Our experiments reveal the structure in the capacitance at room temperature related to the presence of quantum hole levels in Ge islands as well as the Coulomb charging effects.

The layer sequence of the sample studied is as follows: a $p^+$-doped ($10^{19}$ cm$^{-3}$) Si(001) substrate; a 200 Å $Si_{0.75}Ge_{0.25}$ bottom electrode; a 80 Å undoped Si tunnel barrier; self-assembled Ge islands formed from a coverage of 10 ML at growth temperature 300°C and growth rate 0.35 Å/s; a 600 Å Si blocking barrier; and a circular Al Schottky gate (400 $\mu$m diam). The Ge clusters have a pyramid shape [2] with the typical base length of 120 Å, their areal density is $4 \times 10^{11}$ cm$^{-2}$ [4]. The capacitance was measured with a lock-in amplifier at 300 K. The data were taken only at voltages where the signal was purely capacitive. We worked at frequences below 100 kHz, where there was no frequency dependence. The ac bias used was 5 mV rms. The measurements were reproducible and did not show any hysteresis with changes of the gate voltage.

In capacitance-voltage curve we observe four well-resolved steps with period 0.23–0.33 V (Fig. 1).

These steps directly reflect the change in the density of hole states as the Fermi energy passes through successive discrete levels (labeled as $E_0$, $E_1$, $E_2$, and $E_3$, respectively)

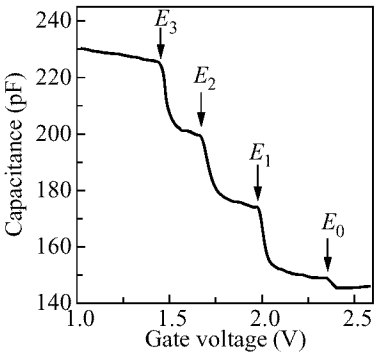


**Fig 1.** Capacitance-voltage characteristic.

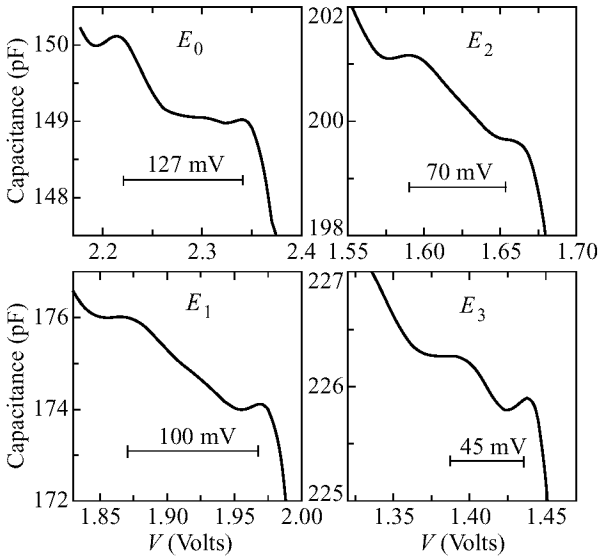


**Fig 2.** Expanded view of the four capacitance shoulders.

in quantum dots. An expanded view shows that each capacitance shoulder consists of two peaks (Fig. 2).

The gap between the split peaks gradually decreases from 127 mV for the ground hole state $E_0$ to 45 mV for the third excited state $E_3$. We suggest Coulomb charging may be the origin of the peak splitting. Usually the single-electron charging energy is calculated as $e^2/C$, where $C$ is the self-capacitance of the dot, independent on the quantum level structure. This approach is valid only for a system which contains a large number of electrons. In the opposite case, one must take into consideration the real shape of the particle wave functions in the dot. The electronic structure in pyramidal quantum dots was calculated by Grundmann et al [8]. They found that the hole ground state is squeezed at the bottom of the dot, the wave functions of the excited states are located along the opposite sides of the pyramide base or in the pyramide corners. The strength of the Coulomb interaction is determined by the wave-function overlap of the

holes in all occupied states. With increasing energy the overlap is reduced and hence the Coulomb energy gets smaller.

## References

[1] Nötzel R. *Semicond. Sci. Technol.* **11** 1365 (1996).
[2] Mo Y.-W., Savage D. E., Swartzentruber B. S., and Lagally M. G. *Phys. Rev. Lett.* **65** 1020 (1990).
[3] Abstreiter G., Schittenhelm P., Engel C., Silveira E., Zrenner A., Meertens D., and Jäger W. *Semicond. Sci. Technol.* **11** 1521 (1996).
[4] Yakimov A. I., Markov V. A., Dvurechenskii A. V., and Pchelyakov O. P. *J. Phys.: Condens. Matter* **6** 2573 (1994).
[5] Smith T. P. III, Lee K. Y., Knoedler C. M., Hong J. M., and Kern D. P. *Phys. Rev. B* **38** 2172 (1988).
[6] Ashoori R. C., Stormer H. L., Weiner J. S., Pfeiffer L. N., Baldwin K. W., and K. W. West. *Phys. Rev. Lett.* **71** 613 (1993).
[7] Medeiros-Ribeiro G., Leonard D., and Petroff P. M. *Appl. Phys. Lett.* **66** 1767 (1995).
[8] Grundmann M., Stier O., and Bimberg D. *Phys. Rev. B* **52** 11969 (1995).

Ioffe Institute
6th Int. Symp. "Nanostructures: Physics and Technology"
St Petersburg, Russia, June 22–26, 1998.



# Mechanism of photoluminescence from Si-nanocrystals fabricated in $SiO_2$-matrix

*K. S. Zhuravlev*, A. M. Gilinsky and A. Yu. Kobitsky
Institute of Semiconductor Physics, pr. Laverntieva 13
630090 Novosibirsk, Russia

## 1 Introduction

The observation of intense visible photoluminescence (PL) of porous silicon at room temperature by Canham [1] has stimulated extensive investigation of the emission properties of different kinds of nanocrystal structures, motivated by the need to integrate optical and electronic devices on silicon chip. Silicon nanocrystals fabricated by Si ion implantation into silicon oxide with subsequent thermal annealing are promising candidates as visible light emitters. In these nanocrystals the visible and near-infrared PL was observed [2, 3, 4]. However only the luminescence in the 1.5–1.7 eV range is considered to be connected with nanocrystals themselves [4].

Recently, two possible mechanisms of radiative recombination in silicon nanocrystals were discussed in the literature [3, 5]. These are the recombination between quantum confinement levels, and recombination via levels of defects localized either inside the nanocrystals or on the nanocrystal–amorphous silicon oxide interface.

In this work we report the results of an experimental investigation of Si-nanocrystals PL kinetics, excitation power and temperature dependencies. The goal of this study is to establish the mechanism of radiative recombination in Si-nanocrystals fabricated by thermal annealing of $SiO_2$ layers implanted with Si.

## 2 Experimental details

### *2.1 Sample preparation*

To prepare silicon nanoclusters, 500 nm-thick $SiO_2$ films thermally grown on (100) Si wafers were implanted with Si ions. Double implantation with energies of 100 keV and 200 keV at a target temperature of $-50°C$ was used (penetration depth 100–300 nm). The films were then subjected to transient heat treatment at 1200°C for 1 s in an Ar ambience, and finally annealed at 400°C for 0.5 h in an $N_2$ with 5% $H_2$ to improve the quality of the interfaces between the Si clusters and the surrounding oxide. The results of TEM and Raman scattering investigations evidenced the formation of crystalline silicon clusters with an average size of 3.5 nm [4].

### *2.2 Photoluminescence measurements*

Photoluminescence measurements were carried out using a double diffraction grating monochromator equipped with a cooled S-1 photomultiplier operated in photon counting mode. An $Ar^+$ laser operating at a wavelength $\lambda = 488$ nm was used for excitation of *cw* PL with a maximum power density of 2.5 kW/cm$^2$, while for transient PL excitation a frequency-doubled Q-switched Nd:YAG laser ($\lambda = 532$ nm, pulse duration 0.15 $\mu$s, peak power density 0.4 kW/cm$^2$) was used.

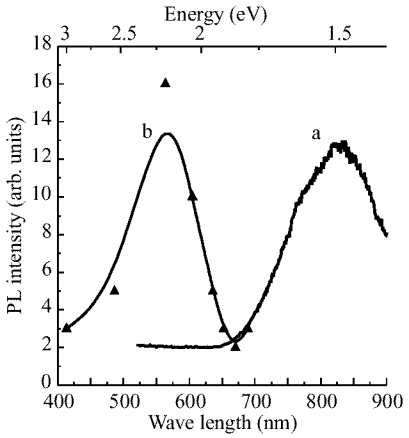


**Fig. 1.** The PL spectrum of the Si-nanocrystals (a) and the simulated PL spectrum (b).

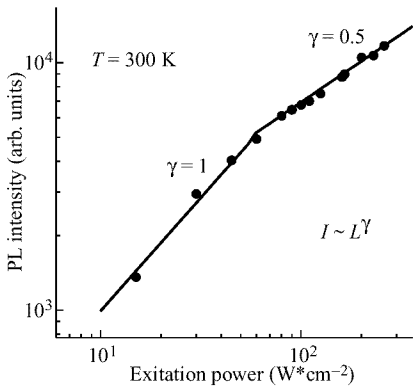


**Fig. 2.** The dependence of PL intensity of the Si-nanocrystals on the excitation power at room temperature.

## 3 Results

In Fig. 1 a typical room-temperature PL spectrum of silicon nanocrystals is shown. The spectrum comprises an asymmetrical wide band (width of about 300 meV) peaked at 1.5 eV. Also in this figure the distribution of sizes of silicon nanocrystals observed by TEM, and a simulated PL spectrum calculated on the basis of the distribution of sizes by the method suggested in [6] are shown. It is seen that the band in the simulated spectrum is shifted to shorter wavelengths in comparison with the experimental one and has its maximum at 2.1 eV, and also that the shapes of the simulated and experimental spectra are different.

In Fig. 2 the dependence of the PL intensity ($I_{PL}$) on excitation power ($L$) together with the approximation of this dependence by a power-law function $I_{PL} \sim L^{\gamma}$ is shown. Two parts with different slopes are observed in the dependence. At low excitation power the dependence is linear, while at high powers it becomes sublinear with $\gamma = 0.5$. It is necessary to note that the shape of the PL spectrum does not change with excitation power.

In Figs. 3,*a* and *b* the dependencies of the PL band position and intensity on temperature are shown, respectively. For comparison in Fig. 3,*a* the temperature dependence of the band gap of bulk silicon is shown. It is seen that the PL peak position changes only slightly with temperature as compared with the change of the bulk Si band gap. The PL intensity decreases by approximately 1.5 times with temperature increased from 80 to 300 K.

In Fig. 4,*a* transient PL spectra taken at room temperature are shown. It is seen that with increasing the delay time after the excitation pulse the shape of the spectrum does not change. In Fig. 4,*b* the decay curve of PL integrated over the spectrum is shown. The curve is approximated by a stretched exponential function $I_{PL} \sim \exp[-(t/\tau)^{\beta}]$ with a characteristic decay time $\tau = 20$ $\mu$s and a power $\beta = 0.43$.

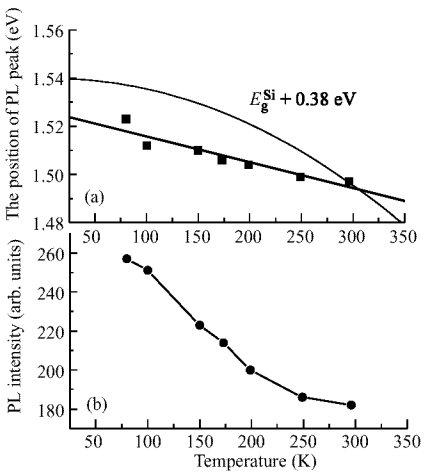


**Fig. 3.** (a) The temperature dependence of the maximum PL band from Si-nanocrystals and the band gap of the bulk Si. (b) The temperature dependence of PL intensity from Si-nanocrystals.

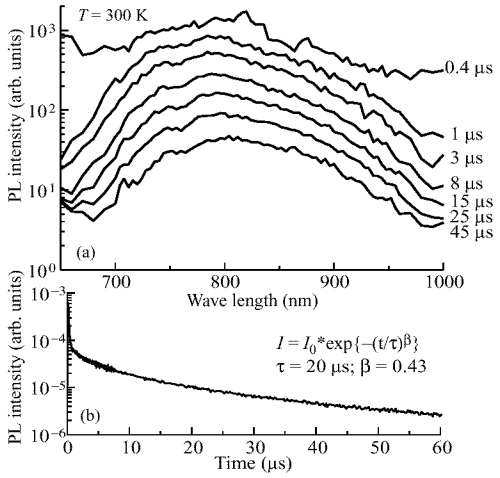


**Fig. 4.** (a) Time-resolved PL spectra of Si-nanocrystals. (b) The decay curve of integral PL intensity.

## 4 Discussion

The above results support the assumption that radiative recombination in silicon nanocrystals is governed by defect levels. The following observations point to this conclusion. Firstly, the energy of radiative recombination is less than the expected energy of optical transitions between the quantum-confined levels (see Fig. 1). Secondly, the sublinear dependence of PL intensity on the excitation power indicates that the recombination is mediated by some localized centers which saturate at high excitation powers [7] and thus let charge carriers recombine via competing nonradiative channels. In contrast, a sublinear dependence is not expected for the recombination between quantum-confined levels in nanocrystals.

Thirdly, the temperature dependence of the PL band position disagrees with that of the bulk silicon band gap, while the two dependencies should correlate in the case of recombination between quantum-confined levels in nanocrystals. Here, consideration of the effect of mechanical stress in silicon nanocrystals, which arises due to the difference of the thermal expansion coefficients of silicon and silicon dioxide, does not change the character of nanocrystal′s band gap temperature dependence and results only in a correction to the band gap of about 7 meV in the temperature range from 80 to 300 K.

For centers which are strongly bound with lattice the temperature dependence of their PL band energy is different from that of the band gap. The recombination via such centers, exhibiting usually a wide PL emission, is described using the configuration diagram model [8, 9]. In this model the direction of the PL band shift with temperature is determined by the ratio of the frequencies of vibration modes in the ground and excited states of the center. In our case, the ground state frequency is higher. The slight change of PL intensity with temperature points to a high value of the thermal activation energy of the centers.

Fourthly, the absence of spectral dependence of PL kinetics seen in Fig. 4 also

points to recombination via local centers. In the case of the quantum confinement recombination model the PL decay should proceed faster on the shorter wavelength side of the spectrum because of the strong dependencies of both the recombination probability and energy of optical transitions on nanocrystal radii. The calculated lifetime of transitions with 1.5 eV energy in the quantum confinement recombination model equals to 100 $\mu$s, which is greater than our experimental data. Moreover, the quantum confinement recombination mechanism should lead to an exponential PL decay [10].

The possible centers of radiative recombination can be localized either on the Si-$SiO_2$ boundary or in the $SiO_2$ matrix. The defects in $SiO_2$ are well investigated and there is no evidence for the existence of centers having their luminescence in the 1.5–1.7 eV range [11, 12].

The center of recombination on the Si nanocrystal-silicon dioxide boundary responsible for 1.5 eV luminescence was considered by G. Allan et al [5]. It was attributed to a single covalent bond, for example a Si–Si bond. The calculation shows that a metastable recombination state, separated by an energy barrier from the excited state, can exist on the boundary of small nanocrystals. The nonexponetial decay kinetics is possible in such centers if the barriers between excited and metastable states of the centers have a certain energy scatter and, consequently, the probability of carrier transition from the excited to recombination state differ. In our case, since the recombination centers are localized on the boundaries of nanocrystals, the barrier height can depend on the local environment.

## 5 Conclusion

The luminescence properties of silicon nanocrystals formed by Si ion implantation into $SiO_2$ matrix and a subsequent thermal annealing have been studied. For identification of PL mechanism the dependencies of *cw* PL on temperature and excitation power density, and time-resolved PL have been investigated. Experimental results point to the mechanism of recombination via the levels of centers which are localized on the silicon nanocrystal-silicon dioxide boundary.

We are grateful to G. A. Kachurin and I. E. Tyschenko for supplying us with the samples used in this study.

## References

[1] L. T. Canham, *Appl. Phys. Lett.* **57** 1046 (1990).
[2] H. Tamura et al., *Appl. Phys. Lett.* **65** (12) 1537 (1994).
[3] P. Mutti et al., *Appl. Phys. Lett.* **66** (7) 851 (1995).
[4] G. A. Kachurin et al., *Nucl. Instr. Meth.* **B 122** 571 (1997).
[5] G. Allan et al., *Phys. Rev. Lett.* **76** (16) 2961 (1996).
[6] J. B. Khurgin et al., *Appl. Phys. Lett.* **69** (9) 1241 (1996).
[7] W. Shockley and W.T. Read, *Phys. Rev.* **87** 835 (1952).
[8] R. C. O'Rourke, *Phys. Rev.* **91** (2) 265 (1953).
[9] K. K. Rebane, *Elementary theory of vibrational spectra structure of impurity centers in crystals.* M., p. 232 (1969) (in Russian).
[10] M. W. Carlen et al., *Phys. Rev.* **B 51** (4) 2173 (1995).
[11] V. A. Gritcenko, *Construction and electronical structure of amorphous dielectric and silicon MIS structures*, Novosibirsk, "Nauka", 1993 (in Russian).
[12] S. Bota et al., *Solid State Electronics* **39** (3) 355 (1996).

Ioffe Institute
6th Int. Symp. "Nanostructures: Physics and Technology"
St Petersburg, Russia, June 22–26, 1998.



# Shallow acceptors in strained Ge/GeSi heterostructures with wide quantum wells

V. Ya. Aleshkin†, V. I. Gavrilenko†, I. V. Erofeeva†, *D. V. Kozlov*†, O. A. Kuznetsov‡ and M. D. Moldavskaya†

† Institute for Physics of Microstructures, RAS, 603600 N. Novgorod, GSP-105, Russia, E-mail:dvkoz@ipm.sci-nnov.ru

‡ Physical-Technical Institute of N.Novgorod State University, Russia

**Abstract.** Energy spectra of shallow acceptors in uniaxially stretched Ge were calculated by variational technique. The results were used for the interpretation of the observed far infrared photoconductivity spectra of strained Ge/GeSi heterostructures with wide quantum wells.

## Introduction

The paper deals with shallow acceptors in wide quantum wells (QWs) in germanium layers in strained $Ge/Ge_{1-x}Si_x$ heterostructures grown on Ge(111) substrates. The deformation of Ge layers is equivalent to hydrostatic compression and uniaxial tension along the growth direction. The uniaxial part of the deformation splits the light and heavy hole subbands [1]. In wide QWs (with respect to a typical Bohr radius of acceptors) in Ge/GeSi heterostructures shallow acceptor are affected mainly by the strain rather than by the size quantization. Therefore at zero approximation the shallow acceptors in Ge/GeSi heterostructures can be treated as impurities in bulk Ge subjected to the uniaxial tension. Shallow acceptors in uniaxially compressed Ge were theoretically investigated in [1, 2]. It was shown that the compression results in the splitting of four-fold degenerated ground and excited states into pairs of two-fold degenerated states. In the present paper the variational calculations of shallow acceptors in uniaxially stretched along (111) direction Ge have been carried out using the effective mass approximation. The results are shown to be in a good agreement with the observed spectra of far IR (FIR) photoconductivity of p-type Ge/GeSi heterostructures.

## 1 Theory

In the case of uniaxial deformation the Hamiltonian in the envelope function equation for the valence band in Ge is the sum of $4\times4$ matrix Luttinger Hamiltonian [3] and the deformation term [1]. This Hamiltonian describes light and heavy hole subbands and the envelope wave function $F_j(r)$ $(j = 1-4)$ is four-dimensional vector. Eigenvalues of the envelope function equation with the Coulomb term in the Hamiltonian for the shallow acceptor in uniaxially stretched Ge were found by variational method in the manner similar to that used for the calculation of acceptor spectra in unstrained Ge [4]. Trial wave functions for variational calculation of acceptor spectra in strained Ge were

chose by similar [4] procedure. Trial wave functions were taken in the form

$$F_j(r,\theta,\varphi) = \sum_l r^l \exp\left(-\frac{r}{r_l}\sqrt{\sin^2\theta + q^2\cos^2\theta}\right)\sum_{m=-l}^{l} c_{lm}^j \sin^m\theta \frac{d^{|m|}P_l(q\cos\theta)e^{im\varphi}}{d(q\cos\theta)^{|m|}}$$

where $c_{l,m}^j$, $r_l$ and $q$ (parameter of anisotropy) are variational parameters, $P_l$ is the Legendre polynomials of $q\cos\theta$. Here $l = 0, 2$ for the ground state and $l = 1, 3$ for the lowest excited states, $z$ axis is chosen along the tension direction. The variational procedure can be simplified significantly by the reducing of the number of variational parameters taking into account the crystal symmetry. In uniaxially stretched Ge the double point symmetry group $D_{3d}$ corresponds to the center of Brillouin zone ($\Gamma$-point). The same group corresponds to the point $L$ in unstressed Ge. Therefore wave function of acceptor should be transformed by additional irreducible representations of double group in point L. There are six additional irreducible representation of group $D_{3d}$: $L_4^{\pm}$, $L_5^{\pm}$, $L_6^{\pm}$. One-dimensional representations $L_4^{\pm}$ and $L_5^{\pm}$ are complex conjugated; therefore they should be considered as one two-dimensional representation. Representation $L_6^{\pm}$ is two-dimensional. Wave function of the ground acceptor state transforms according to the irreducible representations which correspond to the top of valence band: $L_{4,5}^{+}$ (heavy holes) and $L_6^{+}$ (light holes). Dipole optical transitions from the ground state are allowed only into odd (respect to the inversion) excited states. The lowest odd excited states are $p$-like states. Therefore their wave functions should transform according to the irreducible representations $L_{4,5}^{-}$ and $L_6^{-}$.

The results of the calculations of the acceptor binding energies for the ground and the lowest excited states are plotted in Fig.1 as a function of the deformation. It is clearly seen that the deformation splits the ground state into $L_{4,5}^{+}$ and $L_6^{+}$ levels; the last one rapidly shifts to the continuum with the deformation. Binding energies of few

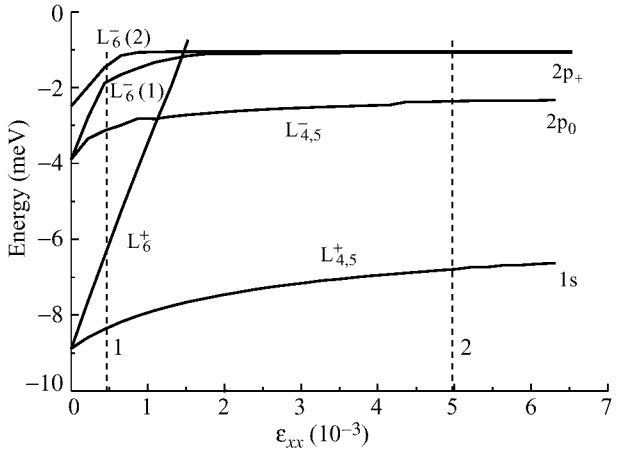


**Fig 1.** Binding energies of the ground and the lowest excited states of shallow acceptor in uniaxially stretched Ge versus the component $\varepsilon_{xx}$ of the deformation tensor (all other components are proportional to $\varepsilon_{xx}$). Vertical dashed line 1 and 2 indicate the deformation value for the sample # 309 and the "effective" deformation value for the sample #306.

lowest $p$-like excited states were calculated: $L^-_{4,5}$, $L^-_6(1,2)$. At high stress the influence of the split off light hole subband may be neglected and the acceptor spectra may be calculated as in the case of simple anisotropic band [5]. In Fig. 1 one can see that with the increase of the deformation the binding energies tend to the asymptotic values corresponding to $1s$, $2p_0$ and $2p_\pm$ levels of the simple anisotropic model [5]. In another limit $\varepsilon \to 0$ the results obtained are in a good agreement with those calculated for the unstressed Ge [3].

## 2 Experiment and discussion

The results of the calculations performed allow to interpret the experimental spectra of impurity FIR photoconductivity of Ge/GeSi heterostructures. The spectra were measured by using BOMEM DA3.36 FT spectrometer [6]. Fig. 2 represents photoconductivity spectra of two undoped sample # 306,# 309 (with residual acceptor impurities) and of the sample # 379 with boron doped QWs.

Photoconductivity spectrum of the sample #309 (Fig. 2a) with thick Ge layers consists of the line at $\hbar\omega \approx 5.3$ meV and the broad band at $\hbar\omega = 7-10$ meV. The line at $\hbar\omega \approx 5.3$ meV corresponds to the transition between ground state $L^+_{4,5}$ and the first excited state $L^-_{4,5}$ (Fig. 1). The energy separation between $L^+_{4,5}$ and $L^-_6(1)$ states corresponds to $\hbar\omega = 7$ meV that corresponds fairly well to beginning of short-wavelength photoconductivity band in the spectrum in Fig. 2a. At higher frequencies the photoconductivity may be explained by transitions to higher excited states and in the continuum.

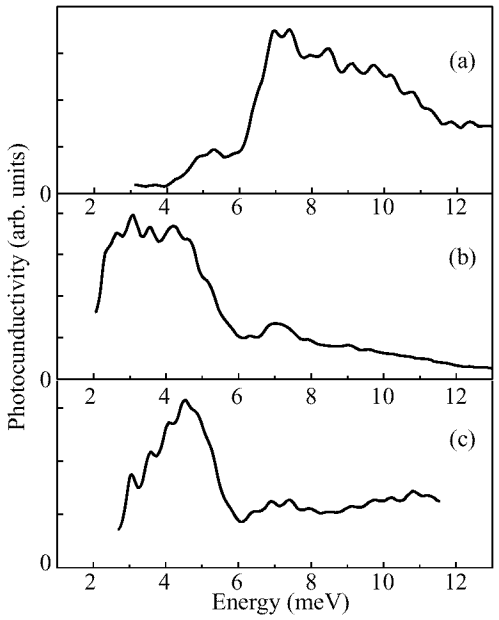


**Fig 2.** Impurity photoconductivity spectra of Ge/GeSi MQW heterostructures at $T = 4.2$ K; a: # 309 ($d_{QW} = 800$ Å), b: # 306 ($d_{QW} = 200$ Å), c: # 379 ($d_{QW} = 200$ Å).

According to the results of the calculations the typical wave function extension (Bohr radius) in direction of deformation is about 40 Å. Therefore the effect of size quantization on the acceptor spectrum is more pronounced in the samples # 306, 379 with narrower QWs. The energy gap between light and heavy hole subbands in these samples is 30–40 meV (cf. with 3 meV in # 309). This effect was taken into account by introducing the effective deformation which corresponds to the total splitting of the subbands (vertical line 2 in Fig. 1). This approach allows the qualitative description of the observed spectra (Fig. 2b,c). The position of the spectral line $\hbar\omega \approx 6.9$ meV is in a good agreement with the energy separation between the ground state $L_{4,5}^{+}$ and the continuum for the sample #306 (Fig. 1). The strongest line in the spectra in Fig. 2b,c should be naturally attributed to the transition between the ground state and excited state which turns into $2P_{\pm}$ level in the model of simple anisotropy band [5]. This transition should correspond to the frequency $\hbar\omega \approx 5.5$ meV. However the short-wavelength edge of the strongest photoconductivity band in Fig. 2b,c corresponds to a little bit lower frequency $\hbar\omega \approx 5$ meV. This indicates the necessity to consider the confinement effects on the excited impurity states more correctly.

**Acknowledgments**

This work was supported by RFBR (Grant # 97-02-16326), Russian Scientific Programs "Physics of Solid State Nanostructures" (Project "Physics of Microwaves" (Project #4.5), "Fundamental Spectroscopy," Project # 7.8), "Leading Science Schools" (Grant # 96-15-96719) and "Integration" (Projects #540,541).

**References**

[1] G. L. Bir and G. E. Pikus *Symmetry and strain-induced effects in semiconductors*, New York: Wiley, 1974.
[2] J. Brockx, P. Clsuws and J. Vennik. *Phys. Rev.* **35** 6165 (1986).
[3] J. M. Luttinger *J. Phys. Chem. Solids* **102** 1030 (1955).
[4] D. Schechter *J. Phys. Chem. Solids* **23** 237 (1962).
[5] R. A. Foulkner *Phys. Rev.* **184** 713 (1969).
[6] V. I. Gavrilenko et al. *JETP Lett.* **65** 209 (1997).

Ioffe Institute
6th Int. Symp. "Nanostructures: Physics and Technology"
St Petersburg, Russia, June 22–26, 1998.



# Negative magnetoresistance and hole-hole interaction in multilayer heterostructures p-Ge/$Ge_{1-x}Si_x$

Yu. G. Arapov†, O. A. Kuznetsov‡, V. N. Neverov† G. I. Harus†
and *N. G. Shelushinina*†
† Institute of Metal Physics RAS, 620219, Ekaterinburg, GSP-170, Russia
‡ Scientific-Research Physico-Technical Institute, Nizhnii Novgorod State University, Russia

**Abstract.** The quantum corrections to the conductivity of the high-mobility multilayer p-$Ge/Ge_{1-x}Si_x$ heterostructures are investigated at $T = (0.1 \div 20)$K in magnetic fields $B$ up to 1.5 T. The observed negative magnetoresistance with logarithmic dependencies both on temperature and magnetic field for $B > 0.1$ T is interpreted as the consequence of the particle-particle (hole-hole) attractive interaction in the Cooper channel. Out of the interaction constant value $g(T) = (\ln T_C/T)^{-1}$ the effective temperature of superconducting transition is estimated: $T_C \leq 0.03$ K.

## Introduction

The diffusive nature of electron motion in disordered conductors results in quantum corrections to the transport effects with nontrivial dependencies on temperature $T$ and magnetic field $B$ [1, 2]. These corrections are of the order of $(k_F l)^{-1}$ where $k_F$ is the Fermi quasimomentum and $l$ is the impurity scattering length. The total quantum correction consists of the single-particle weak localization part and the part due to disorder-modified electron-electron (e-e) interaction between particles with close momenta and energies (in diffusion channel) and between particles with small total momentum (in Cooper channel). All three quantum corrections, i.e., localization, e-e interaction in the diffusion channel and e-e interaction in the Cooper channel lead to the logarithmic low-temperature dependence for the conductivity at $B = 0$.

The different quantum corrections may be separated by the application of an external magnetic field as each quantum effect has its own range of characteristic magnetic fields. In the absence of spin scattering the magnetoresistance associated with the weak localization is negative. For this effect there exist two characteristic fields: the field $B_\varphi$ of crossover from parabolic to logarithmic $B$ — dependence of magnetoresistivity ($B_\varphi = \hbar c/4eL_\varphi^2$, $L_\varphi$ — being the inelastic scattering length) and the field $B_{tr} = \hbar c/2el^2$, where the magnetic length become less than the elastic scattering length. Beyond the diffusion approximation at $B \gg B_{tr}$ the effect of weak localization is suppressed in a great extent [3, 4].

For the correction $\Delta\sigma$ to the conductivity due to e-e interaction in the Cooper channel we have [5]

$$\Delta\sigma(B) - \Delta\sigma(0) = -\frac{e^2}{2\pi\hbar} g(T)\varphi_2(x) \qquad (1)$$

where $\varphi_2(x) = \ln x$ for $x \gg 1$ and $x = B/B_{\text{int}}$ for $B < B_s$, $x = B/B_s$ for $B > B_s$. Here $B_{\text{int}} = \pi\hbar c/2eL_T^2$ ($L_T^2 = \hbar D/kT$, $D$ being the diffusion constant) and $B_s = \pi kT/g\mu_B$ are the characteristic fields for orbital and spin effects, and $g(T)$ is the effective interaction constant of two particles with the opposite momenta: $g > 0$ for repulsive interaction and $g < 0$ for attractive interaction due to virtual phonon exchange. In the latter case $g(T) = (\ln T_C/T)^{-1}$ where $T_C$ is the superconducting transition temperature and expression (1) is valid for $T > T_C$. For the relation of the orbital and spin effects we have

$$B_s/B_{\text{int}} = 2(k_F l)(m_0/mg). \tag{2}$$

The interaction contribution in the diffusion channel is not sensitive to the magnetic field until the spin splitting become important at $B > B_s$ [2]. The corresponding magnetoresistance is proportional to the constant of direct Hartree interaction and should be positive.

## 1 Results and discussion

We have investigated the quantum corrections to the conductivity and magnetoconductivity of 2D hole gas in strained multilayer p-Ge/$Ge_{1-x}Si_x$ ($x = 0.03$) heterostructures at $T \geq 0.1$ K in magnetic fields up to 1.5 T. With the hole densities $p = (2.4 \div 2.6) \cdot 10^{11}$ cm$^{-2}$ and mobilities $\mu = (1.0 \div 1.7) \cdot 10^4$ cm$^2$/Vs we have a good metallic conductivity on Ge layers: $k_F l = (10 \div 20)$. For the Ge layer width $d = 200$ Å the motion of holes in transverse direction is quantized, only one confinement band to be occupied: $k_F d/\pi \approx 0.8$. The conductivity at $B = 0$ decreases with temperature decrease and varies as the logarithm of $T$ in a wide temperature range $(0.1 \div 20)$ K (Fig. 1).

Figure 2 shows the effect of negative magnetoresistance in a whole range of the classically weak magnetic fields $\omega_c\tau < 1$ ($B < B_c$, where $B_c = mc/e\tau$) at different temperatures. The magnitude and $T$ dependencies of the characteristic magnetic fields $B_\varphi$, $B_{\text{tr}}$, $B_{\text{int}}$, $B_s$ and $B_c$ for one of the investigated samples ($p = 2.4 \cdot 10^{11}$ cm$^{-2}$,

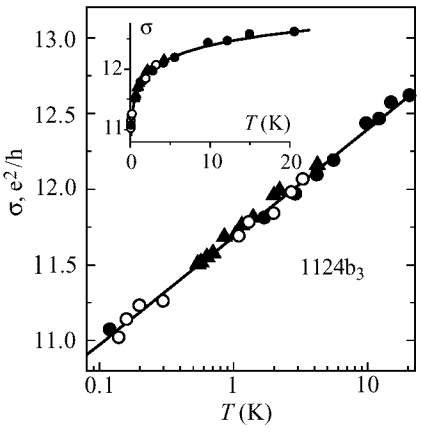


Fig 1.

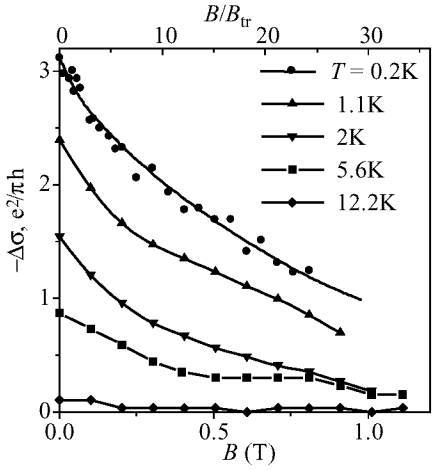


Fig 2.

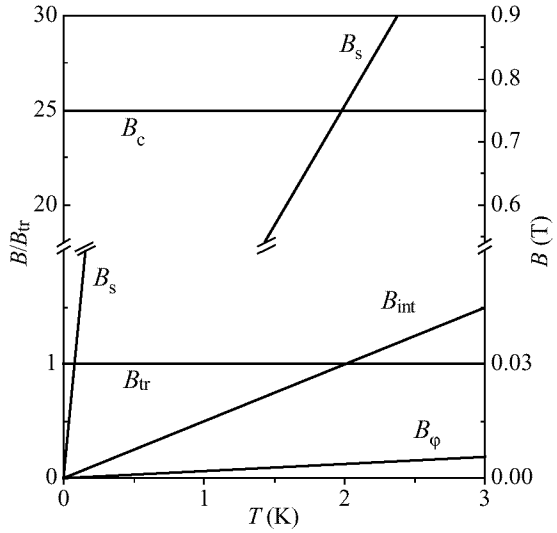


**Fig 3.**

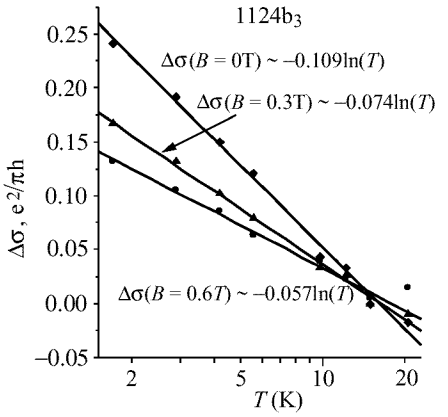


**Fig 4.**

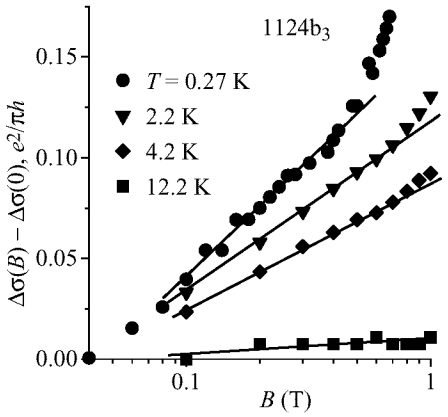


**Fig 5.**

$\mu = 1.0 \cdot 10^4$ cm$^2$/Vs, $k_F l = 12.4$, $l = 1 \cdot 10^{-5}$ cm, $B_{tr} = 0.03$ T) are presented on the diagram of Fig. 3. Here the relations $B_c = 2(k_F l)B_{tr}$ and $B_s = 2(k_F l)B_{int}$ are used (for the strained Ge valence band the spin splitting is about the half of the cyclotron one [6] and in Eq. (2) $m_0/mg \approx 1$).

Due to a high mobility of holes only a small magnetic field $B_{tr}$ is needed to suppress the effect of weak localization. The logarithmic dependence of $\Delta\sigma$ on $T$ at $B \gg B_{tr}$ (Fig. 4) unambiguously is the evidence of the quantum correction associated with e-e interaction. As the magnetoresistance observed at $B > 10B_{tr}$ is still negative we assume that this range of $B$ shows preferentially the effect of the particle-particle interaction in the Cooper channel (1) with $g(T) < 0$ (attraction of holes with opposite momenta). In accordance with Eq. (1) the logarithmic dependencies of $\Delta\sigma$ on magnetic field is

observed between 0.1 and 1 T (Fig. 5). On the $B - T$ diagram of Fig. 3 it may be seen that in this interval of $B$ ($3 \leq B/B_{tr} \leq 25$) for $T > 2$ K only the orbital effect in the Cooper channel is important ($B_{int} < B < B_s$). For $T < 2$ K both effects are actual and for sufficiently low temperature spin effect dominates ($B > B_s$). A fit of the magnetic field dependence gives $|g(T)| = 0.018\pi$ at $T = 0.27$ K which corresponds to superconducting temperature $T_c \approx 0.03$ K. It is only the upper limit for $T_c$ as, in principle, at $B > B_s$ the positive magnetoresistivity due to the spin splitting of the triplet state in the diffusion channel should also take place. In the presence of the latter contribution the true magnetoresistivity in the Cooper channel expected to be more negative than the observed one.

## 2 Conslusions

The observations of the magnetoresistance due to e-e interaction in the diffusion channel were reported for high mobility GaAs/AlGaAs heterostructures [7] and for MBE grown doped GaAs [8]. The positive part of the magnetoresistance for the electron gas in the short-period Si/SiGe superlattices was assigned both to the spin splitting in the diffusion channel and the e-e repulsion in the Cooper channel [9]. Moreover, due to the relatively short escape time from one well into another only anisotropic 3D (not 2D) version of theory was able the describe the experimental data. Our study of the negative magnetoresistance in p-Ge/$Ge_{1-x}Si_x$ heterostructures clearly demonstrates the wide intervals of temperature and magnetic fields where the quantum correction is dominated by the hole-hole attraction in the Cooper channel.

This work is supported in part by RFBR No. 98-0-02-17306 and Russian Program "Physics of Solid-State nanostructures".

## References

[1] Lee P. A. and Ramakrishnan T. V., *Rev. Mod. Phys.* **57** 287 (1985).
[2] Altshuler B. L. and Aronov A. G. in *Electron-Electron Interactions in Disorder Systems*, Amsterdam, 1985 p.1.
[3] Hikami S., Larkin A. I. and Nagaoka Y. *Progr. Theor. Phys.* **63** 707 (1980).
[4] Dyakonov M. I. *Sol. St. Commun.* **92** 711 (1994).
[5] Altshuler B. L., Aronov A. G., Larkin A. I. and Khmelnitskii D. E., *Zh. Eksp. Teor. Fiz.* **81** 768 (1981).
[6] Gorodilov N.A., et al. *Pis'ma Zh. Eksp. Theor. Fiz.* **56** 409 (1992).
[7] Choi K. K., Tsui D. C. and Palmaateer S. C., *Phys. Rev. B* **33** 8216 (1986).
[8] Poirier W., Mailly D. and Sanquer M. *Cond-mat/9706287.*
[9] Brunthaler G., Dietl T., Sawicki M., Stoger G., Jaroszynski J., Prinz A., Schaffler F. and Bauer G. *Semicond. Sci. and Technol.* **11** 1624 (1996).

Ioffe Institute
6th Int. Symp. "Nanostructures: Physics and Technology"
St Petersburg, Russia, June 22–26, 1998.



# Fabrication of SiGe quantum wires by self-accembled local molecular beam growth

V. S. Avrutin, *N. F. Izumskaya*, A. F. Vyatkin and V. A. Yunkin
Institute of Microelectronics Technology and High Purity Materials, RAS,
142432 Chernogolovka, Moscow district, Russia

**Abstract.** One-dimensional SiGe structures were grown by molecular beam epitaxy on mesa-patterned Si (100) and (111) substrates. The effect of temperature and deposition rate on faceting of local epitaxial Si and SiGe structures was studied in temperature range from 450°C to 900°C. Scanning electron microscopy revealed that the increase of growth temperature and/or the decrease of deposition rate result in faceting of the growing structures. Epitaxial structures with $Si_{0.75}Ge_{0.25}$ quantum wires 4 nm in thickness and 30–50 nm in width separated by 30-nm Si barriers were grown. Low-temperature luminescence spectra of these structures were obtained.

## Introduction

Common lithographic techniques are hardly suitable for fabrication of the quantum-size structures because of the limited spatial resolution of these methods. One of the possible ways to obtain the low-dimensional structures is a self-assembled growth. In recent years, a series of self-assembled growth techniques have been developed: growth on faceted substrates [1], growth on V-groove patterned substrates [2], and shadow-mask molecular beam epitaxy [3]. In this work, we studied the self-assembled molecular beam epitaxy of Si and SiGe layers on mesa-patterned Si (001) and (111) substrates under various growth conditions.

## 1 Experimental procedures

The samples were grown by molecular beam epitaxy on p-type Si (001) and (111) wafers patterned to form mesa stripes from 0.25 to 12 $\mu$m in width and 400 $\mu$m in length oriented along ⟨011⟩ direction. The mesa stripe pattern was formed by electron beam lithography and reactive ion etching with Al etch masks in $SF_6/O_2$ plasma. The grown structures were analyzed by scanning and transmission electron microscopy, secondary ion mass-spectrometry, and low-temperature photoluminescence.

## 2 Results and discussion

For (001) substrates, we found that {111} facets form on the lateral sides of the epitaxial layer during growth at a rate of 15 nm/min and the substrate temperature above 500°C (Fig. 1).

At the temperature below 500°C, the lateral faceting was not observed. The decrease in growth rate down to 3 nm/min leads to the facet formation at temperatures below 450°C. The bulges bounded by the {111} facets grow on the lateral sides of the epitaxial layer. We observed no appearance of {311} facet planes at the temperatures about 800°C, as was reported in [4].

In the case of the (111) substrates, the facets also form at the temperatures above 500°C. The epitaxial structures grown at 550°C with a rate of 20 nm/min are asymmetric. Within the accuracy of measurements (about 3°), the facets make the angles

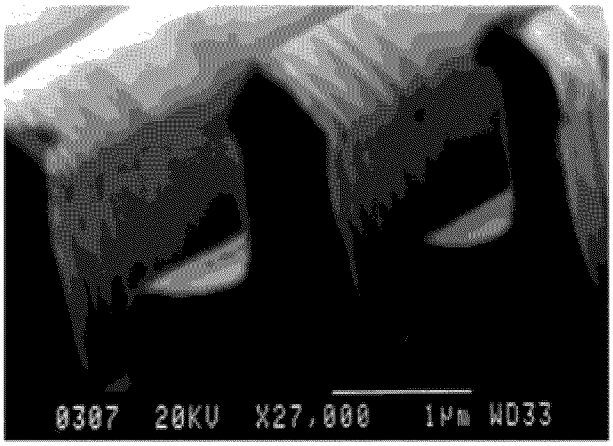


**Fig 1.** Typical epitaxial structure grown at 800°C.

of 48° and 74° with the substrate. Consequently, the structure may be bounded by the {331} and {115} or {001} and {111} planes, respectively, because the angles between these pairs of planes and the {111} substrate are almost the same. Since {111} and {100} are the most stable surfaces [5], most likely these facets are {001} and {111}. The epitaxial structures grown at 500–900°C with a rate of 5–20 nm/min are bounded by the same facets.

Doping of the growing layers with Ge up to 10 percents (i.e. introduction of strain to the growing film) has no influence on the faceting of the crystallization front.

Using the revealed regularities of the self-assembled epitaxial growth, structures with $Si_{0.75}Ge_{0.25}$ quantum wires 4 nm in thickness and 30–50 nm in width separated by 30-nm Si barriers were grown. Low-temperature luminescence spectra of these structures were obtained.

## 3 Conclusion

Thus, we have demonstrated the possibility to control the shape of the epitaxial structures by varying the growth conditions and to prepare one-dimensional structures down to several tens of nanometers in width on the top of the epitaxial layer using self-assembled epitaxy on relatively wide (about micrometer) mesa substrates.

## References

[1] Kop'ev P.S., Ledentsov N.N., Mel'tser B.Ya., Tabatadze I.G., and Ustinov V.M. *Fiz. Tekhn. Poluprovodn.* **28** 1046 (1996).
[2] Hartman A., Vescan L., Dieker C., and Luth H. *J. Appl. Phys.* **77** 1959 (1995).
[3] Hammerl E. and Eisele I., *Appl. Phys. Lett.* **62** 2221 (1993).
[4] Hobart K.D., Kub F.J., Gray H.F., Twigg M.E., Park D., and Thompson P.E. *J. Cryst. Growth.* **157** 338 (1995).
[5] Eaglesham D.J., White A.E., Feldman L.C., Moriya N., and Jacobson D.C. *Phys. Rev. Lett.* **70** 1643 (1993).

Ioffe Institute
6th Int. Symp. "Nanostructures: Physics and Technology"
St Petersburg, Russia, June 22–26, 1998.



# Acceptor states in boron doped SiGe quantum wells

*M. S. Kagan*, I. V. Altukhov, K. A. Korolev, D. V. Orlov, V. P. Sinis,
K. Schmalz†, S. G. Thomas‡, K. L. Wang‡, and I. N. Yassievich§
Institute of Radioengineering and Electronics RAS
11, Mokhovaya, 103907 Moscow, Russia
† Institute for Semiconductor Physics
Walter-Korsing str., 2, 15230, Frankfurt (Oder), Germany
‡ University of California, 66-147KK Engineering IV, Los Angeles, CA 90095, USA
§ Ioffe Physico-Technical Institute RAS
26, Politekhnicheskaya, 194021 St.Petersburg, Russia

**Abstract.** The temperature dependences of lateral conductivity and hole mobility in SiGe quantum well structures selectively doped with boron are presented. The boron $A^+$ centers are found to exist and determine the low-temperature conductivity. The activation energy of conductivity at higher temperatures is shown to be determined by the energy distance between strain-split boron $A^0$ levels. The model of two-stage excitation of free holes including the thermal activation of holes from the ground to split-off state and next tunneling into the valence band is proposed. The binding energy of $A^+$ centers and the energy splitting of boron ground states by strain are found.

Selectively doped SiGe quantum well structures (QWs) are of great interest for study of acceptor states which are degenerate in bulk material and should be split in two-dimensional (2D) systems due to space quantization and/or strain. The energy positions of ground and excited states of an acceptor can be controlled in a wide range by alloy composition, QW width, doping level and space position of an acceptor center. So-called $A^+$ states (acceptors binding an additional hole) [1,2] are of specific interest as they should exist in SiGe QWs in thermal equilibrium in contrast to bulk material where they can appear only due to excitation, e.g., by light. Similar $D^-$-states of donors have been investigated in GaAS/GaAlAs structures [3,4].

The *p*-type Si/SiGe/Si QWs MBE-grown pseudomorphically on the n-type Si substrate and selectively doped with boron were used for conductivity and magnetoconductivity measurements at the temperatures of 4 up to 300 K. The SiGe layer of 20 nm thickness was sandwiched between undoped Si buffer (130 nm wide) and cap (60 nm) layers. The SiGe QW was uniformly doped with boron; the B concentration was of $3 \times 10^{17}$ cm$^{-3}$. The content of Ge, $x$, in SiGe alloy was 0.1 and 0.15, respectively. Two boron $\delta$-layers with $B$ concentration of $2 \times 10^{11}$ cm$^{-2}$ positioned within the buffer and cap layers on the distance of 30 nm from each QW interface were used to obtain $A^+$ centers inside the QW. The buffer *delta*-layer should also supply holes to form the $p-n$ junction between the p-layers and the n-substrate. The contacts were deposited on the p-type side of structures so that the p-n junction prevented from a current along the substrate.

Figure 1 shows, in log-$1/T$ scale, the temperature dependence of conductivity, $\sigma$, along the SiGe layer for the samples with 0.1 and 0.15 Ge content, $x$. One can see two activation-law regions in the curves. The low-temperature activation energy is

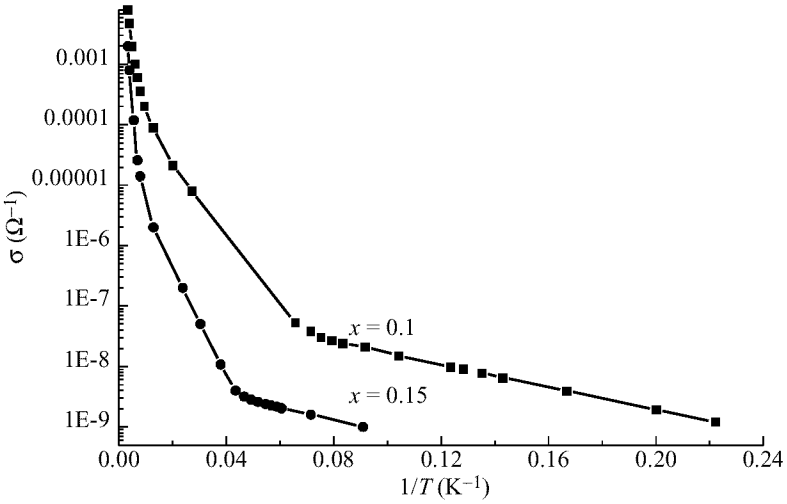


**Fig 1.** Temperature dependence of conductivity.

approximately 2 meV and practically coincides for the samples with different Ge content. The activation energy at higher temperatures ($T \geq 20$ K) is of $12 \pm 1$ meV for $x = 0.1$ and $18 \pm 1$ meV for $x = 0.15$. The hole mobility, $\mu$, determined from the measurements of transverse magnetoconductivity had the maximum value of 20000 cm$^2$/Vs at 28 K.

There are two possible explanations for $\sigma(T)$ dependence at low temperatures. First, the activation energy ($\approx 2$ meV) can be due to the thermally activated hopping conductivity. In dependence on the Fermi level ($\varepsilon_F$) position, the hopping can be over neutral ($A^0$) boron states if $\varepsilon_F \approx \varepsilon_0$, $\varepsilon_0$ is the $A^0$ binding energy, or positively charged $A^+$ states if $\varepsilon_F \approx \varepsilon^+$, it is $A^+$-centers binding energy. The main argument against the hopping is the low conductivity observed. Really, at the given doping level in QW, $3 \times 10^{17}$ cm$^{-3}$, the mean distance between impurities ($\approx 8$ nm) is of the order of the effective Bohr radius of impurity, which can be estimated by the expression $a_B \approx \hbar/\sqrt{2m\varepsilon_B}$. Using linear interpolation of GeSi parameters between Si and Ge, we get $a_B \approx 2.5$ nm for $A^0$ and $\approx 10$ nm for $A^+$ states [5]. Because of strong overlapping impurity states, the specific (on square) conductivity value can not be less than $10^{-3}$ to $10^{-4}$ $\Omega^{-1}$ (see, f.i., [6] for references). It is several orders of magnitude more than the experimental values.

The second possible origin of 2 meV activation energy can be the thermal hole emission from $A^+$ states. The calculation of the $A^+$ binding energy [7] gives just $\varepsilon^+ \approx 2$ meV, being weakly dependent on Ge content in SiGe alloy. The calculated temperature dependences of free hole concentration are shown in Fig. 2. The parameters for the best fit of calculate and experimental curves were found to be $\varepsilon_0 = 24$ meV and 36 meV for $x = 0.1$ and $x = 0.15$, respectively, $\varepsilon^+ = 2$ meV and $N^+ = 10^9$ cm$^{-2}$ for both structures ($N^+$—is the $A^+$-center concentration in the QW). Thus, the low-temperature activation energy is the binding energy of the boron $A^+$ centers in QW. However, the extra hole concentration supplied into QW turns out to be two orders less than the doping level of $\delta$-layers. The only reason for this seems to be Si surface states which can accumulate almost all holes from the $\delta$-layers.

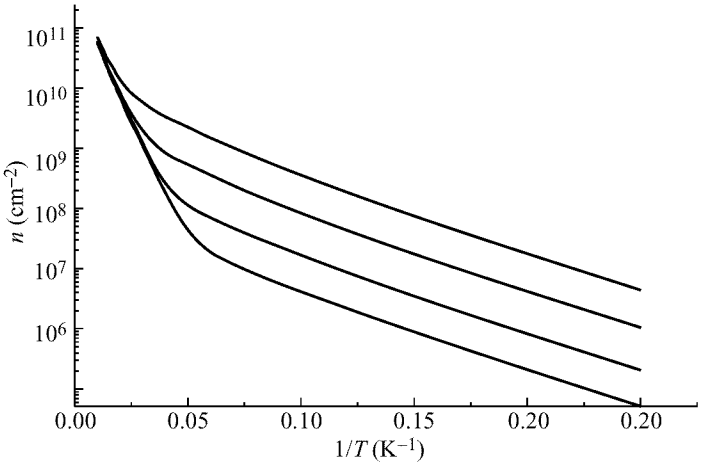


**Fig 2.** Calculated temperature dependence of hole concentration in QW at various $\delta$-layer doping level.

The origin of activation energy at higher temperatures is not so obvious. It should be one half of boron-$A^0$ binding energy because the Fermi level lies between the valence band edge and the $B^0$ ground state as it is filled. So, the observed high-temperature activation energies, 12 and 18 meV, should correspond to 24 and 36 meV $B^0$ binding energies. These values are, however, quite surprising. Indeed, the binding energy of shallow impurity should decrease with increasing both Ge content and strain, it is quite the contrary to the experiment. Moreover, the value of $\varepsilon_0 = 24$ meV seems not to be real for $x = 0.1$. The only energy which could agree with the above values of $\varepsilon_0$ is the energy difference between acceptor levels split by strain. Indeed, the splitting energy of the ground acceptor state found by means of linear interpolation between Si and Ge is $\approx$ 15 and 25 meV for $x = 0.1$ and $x = 0.15$, respectively. This is close to the experimental activation energies. (Note that the estimation of the energies by interpolation is very approximate.) The splitting energy can be as the activation one only if holes can pass from the split-off state into the valence band without activation, that is by tunneling. It is impossible in the scheme of flat bands. On the other hand, we have seen from the experiment that almost all holes from the $\delta$-layers accumulate in the surface states making the surface charged. So, the potential across the structure should appear inclining the valence bands. The scheme of potential distribution for this case is shown in Fig. 3. One can see from this scheme that the conductivity in this case can be controlled by two-stage process: first, the thermal activation of holes from the ground to split-off state takes place and then hole tunneling into free hole band creates the conductivity. To estimate the possible potential drop across the structure, let's remember an empirical law that for most homeopolar semiconductors the Fermi energy is fixed on the surface near 1/3 of the energy gap from the valence band. It is $\approx$ 0.4 eV for Si. The QW width is 5 times less than the structure width. So, the potential drop on the QW is of $\approx$ 80 meV. Of course, this estimation is too rough but it shows that the proposed model can be real. Thus, the arguments for the model are (i) the increasing activation energy of conductivity with Ge content, (ii) small additional

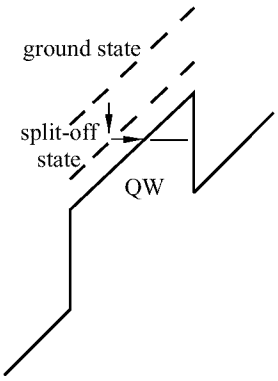


**Fig 3.** Scheme of conductivity activation by tunneling.

hole concentration supplied from $\delta$-layers into the QW, and (iii) charging the surface and arising the potential drop across the QW, as a consequence.

The experimental data presented give evidence for existence of $A^+$ centers in B doped SiGe QW structures in thermal equilibrium. The thermal emission of holes from these centers determines the conductivity along the QW at low temperatures. At higher temperatures, the conductivity is shown to be due to thermal activation of holes from the ground to strain-split B states following by hole tunneling into the QW valence band. The tunneling is possible due to a potential drop across the QW which arise due to hole capture at surface states of the Si cap layer making the surface charged. Note that in structures with doping profile and level investigated, it is possible to find the energy splitting of acceptor levels by strain from temperature dependence of conductivity.

This work was supported in part by Grants No. 96-02-17352 and 97-02-16820 from RFBR, No. 97-10-55 from Russian Ministry of Science and Technology and Volkswagen Stiftung Grant.

## References

[1] E. M. Gershenzon, Yu. P. Ladyzhenskii, and A. P. Mel'nikov, *JETP Lett.* **14** 380 (1971).
[2] E. E. Godik, Yu. A. Kuritsyn, and V. P. Sinis, *JETP Lett.* **14** 377 (1971).
[3] S. Huant, S. P. Najda, and B. Etienne, *Phys. Rev. Lett.* **65** 1486 (1990).
[4] D. M. Larsen, S. Y. McCann, *Phys. Rev. B* **46** 3966 (1992).
[5] K. Schmalz, I. N. Yassievich, K. L. Wang, and S. G. Thomas, *Phys. Rev. B* (1997), in print.
[6] B. I. Shklovskii and A. L. Efros, *Electronic Properties of Doped Semiconductors*, Springer, Heidelberg (1984).
[7] I. N. Yassievich, K. Schmalz, M. A. Odnobludov, and M. S. Kagan, *Solid State Electronics* **40** 97 (1996).

Ioffe Institute
6th Int. Symp. "Nanostructures: Physics and Technology"
St Petersburg, Russia, June 22–26, 1998.



# The growth kinetics of $Si_{1-x}Ge_x$ layers from germane and silane

*A. V. Potapov* and L. K. Orlov
Institute for Physics of Microstructures RAS
GSP-105, 603600, Nizhny Novgorod, Russia

**Abstract.** In the present paper we offer a model of the growth kinetics of $Si_{1-x}Ge_x$ layers from silane and germane molecular flows. The model considers disintegration of silane and germane molecules from chemisorption to formation of Si and Ge adatoms and their embedding in a crystal lattice. The numerical modeling of the epitaxial process has shown good agreement with the experimental data and has allowed to explain peculiarities of the experimental dependencies. The effective frequencies of $SiH_3$ and $SiH_2$ disintegration for the considered epitaxial method were estimated.

## Introduction

In the last decade the chemical vapour deposition from silicon and germanium hydrides at low pressures has been actively used for $Si_{1-x}Ge_x$ layer epitaxy. Despite the large number of experimental works the number of theoretical researches is insignificant, and the available models describe experimental data inadequately. Therefore, as remarked by L. T. Vinh with co-workers "improved models thus seem to be indispensable" [1]. The not good enough agreement of the theory and experiment is possible connected to an extremely simplified consideration of chemical processes on a growing surface. On the other hand, a detailed description of the kinetics of surface reactions inevitably will result in an increase of a number of parameters describing the rates of elementary processes. The task is complicated also by that the values of the majority of rate constants disintegration of $SiH_n$ and $GeH_n$ molecules, unfortunately, are unknown.

In the present paper we offer a model of the growth kinetics of $Si_{1-x}Ge_x$ layers from silane and germane molecular flows. The model considers disintegration of silane and germane molecules from chemisorption to formation of Si and Ge adatoms and their embedding in a crystal lattice. Using the published experimental data, on the basis of the model we have made estimations of rate constants of disintegration of $SiH_3$ and $SiH_2$ molecules.

## 1 Model

A comprehensive analysis of the process of disintegration of $SiH_n$ molecules on a surface Si(100) is made by S. M. Gates with co-workers [2]. They found out that the complete mechanism of silane disintegration is reactions:

$$SiH_4 + \underline{2} \overset{S_{SiH_4}}{\rightarrow} \underline{Si}H_3 + \underline{H}\ (1),\ SiH_3 + \underline{1} \overset{\nu_{MH_3}}{\rightarrow} \underline{Si}H_2 + \underline{H}\ (2),\ 2\underline{Si}H_2 \overset{\nu^{(1)}_{MH_2}}{\rightarrow} 2\underline{Si}H + H_2\ (3),$$
$$\underline{Si}H_2 \overset{\nu^{(2)}_{MH_2}}{\rightarrow} \underline{Si}H + \underline{H}\ (4),\ \underline{Si}H \overset{\nu_H}{\rightarrow} \underline{Si} + \tfrac{1}{2}H_2\ (5).$$

Taking into account a chemical similarity of $SiH_4$ and $GeH_4$ molecules it is possible to expect that the disintegration of germane will occur by an analogous way [3]. If on a growing surface there are $SiH_2$ and $GeH_2$ molecules, these molecules possibly can react by the reaction:

$$\underline{Si}H_2 + \underline{Ge}H_2 \overset{\nu^{(3)}_{MH_2}}{\rightarrow} \underline{Si}H + \underline{Ge}H + H_2 \quad (6).$$

An appropriate system of kinetic equations for dimensionless average concentrations of adsorbed particles is (M = Si, Ge):

$$\begin{gathered}
\frac{\partial \theta_{MH_3}}{\partial t} = 2\frac{{}^{S}MH_4\,{}^{F}MH_4}{N_s}\theta^2_{nbl} - 2\nu_{MH_3}\theta_{MH_3}\theta_v, \\
\frac{\partial \theta_{MH_2}}{\partial t} = 2\nu_{MH_3}\theta_{MH_3}\theta_v - 4\nu^{(1)}_{MH_2}\theta^2_{MH_2} - 2\nu^{(2)}_{MH_2}\theta_{MH_2}\theta_v - 2\nu^{(3)}_{MH_2}\theta_{SiH_2}\theta_{GeH_2}, \\
\frac{\partial \theta_{MH}}{\partial t} = 4\nu^{(1)}_{MH_2}\theta^2_{MH_2} + 2\nu^{(2)}_{MH_2}\theta_{MH_2}\theta_v + 2\nu^{(3)}_{MH_2}\theta_{SiH_2}\theta_{GeH_2} - \nu_{MH}\theta_{MH}, \\
\frac{\partial \theta_H}{\partial t} = \sum_{M=Si,Ge}\left(2\frac{{}^{S}MH_4\,{}^{F}MH_4}{N_s}\theta^2_{nbl} + 2\nu_{MH_3}\theta_{MH_3}\theta_v + 2\nu^{(2)}_{MH_2}\theta_{MH_2}\theta_v\right) - \nu_H(x)\,\theta_H, \quad (7) \\
\frac{\partial \theta_M}{\partial t} = \nu_M\theta_M - r\theta_M, \\
\theta_v + \theta_{MH_3} + \theta_{MH_2} + \theta_{MH} + \theta_M + \theta_H = 1, \\
\theta_v = \theta_{bl} + \theta_{nbl}, \\
\theta_{bl} = 3\left(\theta_{SiH_3} + \theta_{GeH_3}\right).
\end{gathered}$$

The system (7) is based on the following considerations. (a) Monomolecular adsorption takes place on a growing layer surface. (b) Lateral interactions between atoms and molecules on a growth surface are absent. (c) Chemisorption of silane and germane molecules requires two vacant not blocked adsorption sites. (d) The $GeH_3$ and $SiH_3$ molecules block 3 vacant adsorption sites. (e) The desorption rate of hydrogen atoms from an alloy surface linearly depends on Ge content. (f) The frequency of atom embedding into a lattice ($r$) depends on concentration of atoms Si and Ge as described in [4]. Growth rate and Ge content of an alloy layer can be calculated by the formulas

$$x = \frac{\theta_{Ge}}{\theta_{Ge} + \theta_{Si}}, \quad V = r\frac{N_s}{N_0}\left(\theta_{Si} + \theta_{Ge}\right).$$

## 2 Results and Discussion

Because the silane properties are investigated in more detail, we have focused the efforts on modeling of a growth from $SiH_4$. In order to define values of kinetic constants the experimental dependences of growth rate of layers on temperature [1, 5] and TPD spectra of hydrogen [2] have been used. As is visible from Fig. 1, the dependence $V(T)$ has a kink at the temperature about 620–630 °C. The $V(T)$ slope above this temperature is small and the activation energy approximately equals 0.1 eV. Such a value of the activation energy correlates well with the activation energy of disintegration of $SiH_3$ molecules [2]. Thus, the increase of the growth rate at $T > 620$–$630\,^{\circ}C$ is limited by the disintegration of $SiH_3$ molecules. The fitting of the theoretical dependencies $V(T)$ to experimental data has allowed to determine the disintegration frequency of $SiH_3$

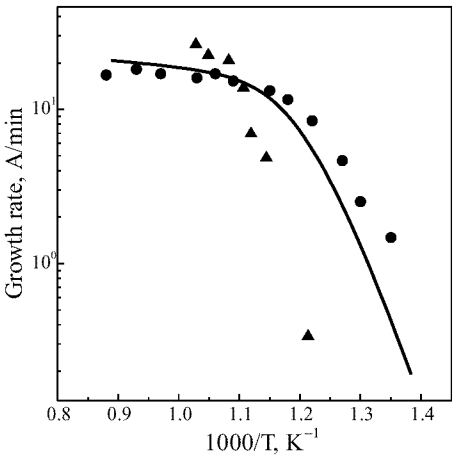


**Fig 1.** Experimental (curve) and theoretical (triangles — [1], circles — [5]) growth-temperature dependencies of the growth rate.

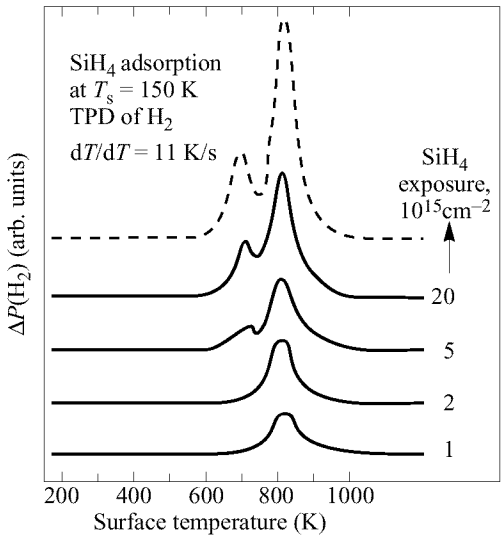


**Fig 2.** TPD data showing hydrogen desorption for silane adsorbed on the Si(100) [2].

molecules $\nu_{MH_3} \simeq 2.5 \times 10^0 e^{-0.087(\mathrm{eV})/kT}(\mathrm{s}^{-1})$. This result coincides with conclusions of S. M. Gates with co-workers [2].

The definition of disintegration frequencies of $SiH_2$ molecules is a more difficult task. The difficulty consists in the fact that the disintegration of these molecules proceeds by two ways simultaneously. In order to determine these parameters, we have used TPD spectra of hydrogen [2]. As is visible from Figs. 2 and 3, these spectra have two maxima at 700 and 800 °C. The occurrence of the first desorption maximum is caused by reaction between two $SiH_2$ molecules, the second maximum is connected with the simple hydrogen desorption from the Si(100) surface. Fitting the first peak we have

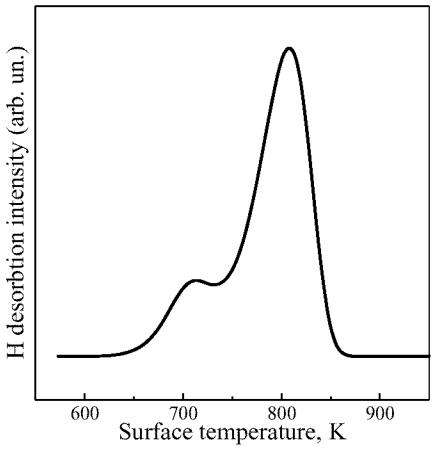


**Fig 3.** Calculated hydrogen TPD spectrum for silane adsorbed on the Si(100).

found $\nu^{(1)}_{MH_2} \simeq 5 \times 10^{17} e^{-2.5(eV)/kT}(s^{-1})$. The fitting of the second peak has allowed to specify the frequency of hydrogen desorption from the Si (100) surface ($\nu_H \simeq 8 \times 10^{12} e^{-2.13(eV)/kT}(s^{-1})$). The second peak has one feature: the low temperature half of the peak is narrower than the high-temperature one. The extension of this peak in the high temperature field is apparently connected with the monomolecular reaction (4). For the kinetic constant of this reaction we have found $\nu^{(2)}_{MH_2} \simeq 5 \times 10^2 e^{-0.6(eV)/kT}(s^{-1})$.

The authors thank the Russian Foundation for Basic Research (RFFI, grant No. 96-02-19278) and INTAS (grant No. 96-0580) for the rendered financial support.

## References

[1] L. T. Vinh, V. Aubry-Fortuna, Y. Zheng, et al. *Thin Solid Films.* **294** 59 (1997).
[2] S. M. Gates, C. M. Greenlief, and D. B. Beach. *J. Chem. Phys.* **93** 7493 (1990).
[3] B. Cunningham, J. O. Chu, and S. Akbar. *Appl. Phys. Lett.* **59** 3574 (1991).
[4] L. K. Orlov and A. V. Potapov. *Crystallography.* 1998 (to be published).
[5] Ki-J. Kim, M. Suemitsu, M. Yamanaka, et al. *Appl. Phys. Lett.* **62** 3461 (1993).

Ioffe Institute
6th Int. Symp. "Nanostructures: Physics and Technology"
St Petersburg, Russia, June 22–26, 1998.



# Quantum-dot cellular automata — experimental demonstration of a functional cell

*A. O. Orlov*, I. Amlani, G. L. Snider, G. H. Bernstein, C. S. Lent, J. L. Merz, and W. Porod

Department of Electrical Engineering, University of Notre Dame, Notre Dame, IN 46556 USA

**Abstract.** The experimental demonstration of a basic cell of Quantum-Dot Cellular Automata, a transistorless computation paradigm is presented. The device studied is a six-dot quantum-dot cellular system consisting of a four-dot QCA cell and two electrometer dots. The system is fabricated using metal dots, connected by capacitors and tunnel junctions. The operation of a basic cell is confirmed by the externally detected change of the cell polarization controlled by the input signal. The cell exhibits a bistable response, with more than 80% charge polarization within a cell.

In the last 30 years the microelectronics industry has made dramatic improvements in the speed and size of electronic devices, and the achievement of ever higher levels of integration requires a further increase in the number of devices fabricated on a chip. Since the early 1970s the device of choice for high levels of integration has been the field effect transistor (FET), and while the FET of today is a vast improvement over that of 1970, it is still a current switch like the mechanical relays first used to encode binary information. At gate lengths below 0.1 $\mu$m, FETs will begin to encounter fundamental effects which lead to performance degradation. One alternative approach which could allow the microelectronics industry to maintain continued growth in device density would be a the change from the FET-based paradigm to one based on nanostructures. Here, instead of fighting the effects that come with feature size reduction, these effects are used to advantage. One nanostructure paradigm, proposed by Lent et al. [1, 2], is Quantum-Dot Cellular Automata (QCA), which employs arrays of coupled quantum dots for binary computations [3, 4]. The advantage of QCA lies in the extremely high packing densities possible due to the small size of the dots, the simplified interconnection, and the extremely low power-delay product which can be arbitrarily reduced by adiabatic switching [5]. Using QCA cells with dots of 20 nm diameter, an entire full adder can be placed within 1 $\mu m^2$, approximately the area of a single 0.07 $\mu$m gate length FET.

A basic QCA cell consists of four quantum dots located at the corners of a square, coupled by tunnel barriers. If the cell is charged with two excess electrons among the four dots, Coulomb repulsion will force the electrons to opposite corners. There are thus two energetically equivalent "polarizations", as shown in Fig. 1a, which can be labeled logic "0" and "1". By properly arranging cells so that the polarization of one cell sets the polarization of a nearby cell, it is possible to implement all combinational logic functions. Since the cells communicate only with their nearest neighbors, there is no need for long interconnect lines. The inputs are applied to the cells at the edge of the system and the computation proceeds until the output appears at cells at the edge of the QCA array.

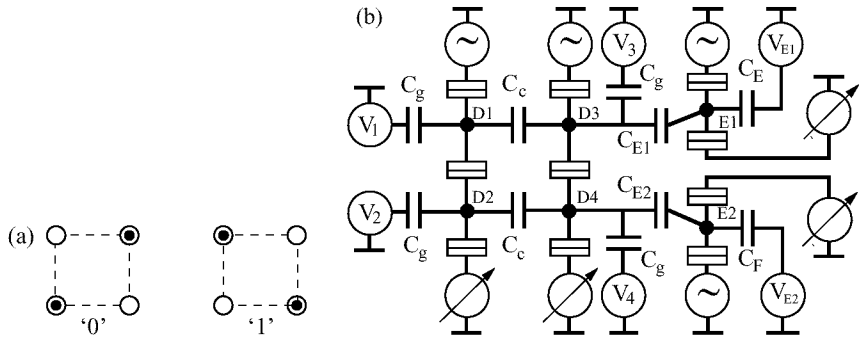


**Fig 1.** (a) Basic four-dot QCA cell showing the two possible polarizations. (b) Schematic diagram of the four-dot QCA cell with two electrometers.

We study a QCA cell fabricated using aluminum islands with aluminum-oxide tunnel junctions, grown on an oxidized silicon wafer. The fabrication used standard electron beam lithography and shadow evaporation to form the islands and tunnel junctions [6], with typical junction area of $50 \times 50\,\mathrm{nm}^2$. The first step in the development of QCA systems was recently demonstrated in [7] where we showed the possibility to switch the localization of an electron in a double-dot (DD) by swapping an electron in the input dots capacitively coupled to DD [7]. A schematic diagram of the improved device — the four-dot QCA cell with additional electrometers is shown in Fig. 1b. The four dots of the QCA cell consist of two DDs, where the dots are joined by a tunnel junction. This breaks the QCA cell into two half-cells, where electrons are allowed to tunnel "vertically" between dots, but not "horizontally". The input voltages $V_1$ and $V_2$ are connected to $D_1D_2$, which form the input half-cell. $D_1D_2$ is connected capacitively to the output half-cell $D_3D_4$, which is in turn capacitively coupled to the electrometers $E_1$ and $E_2$. Measurements were performed in a dilution refrigerator with a base temperature of 10 mK. Conductances of DDs and electrometers were measured simultaneously using a standard ac lock-in technique with 5 $\mu$V excitation, and a magnetic field of 1 T applied to suppress the superconductivity of Al. Capacitances of the circuit were determined from periods of Coulomb-blockade oscillations and IV-measurements [8].

The operation of a QCA cell is best understood by examining the conductance through the input half-cell as a function of the two gate voltages $V_1$ and $V_2$, as shown in the contour plot of Fig. 2. A peak in the conductance is observed each time the Coulomb blockade is lifted for the DD system, and due to the capacitive coupling between the dots each peak splits into a double peak. These peaks form the vertices of a hexagonal structure which we refer to as the "honeycomb", delineated by the dotted lines in Fig. 2 [9]. Within each hexagon the electron population of the dots is stable and changes when a border between cells is crossed. The excess electron population can thus be labeled, with the (0,0) hexagon centered at $V_1 = V_2 = 0$ V. A point in the honeycomb defined by a single setting of $V_1$ and $V_2$ is called the working point, which defines a particular configuration of electrons. Most important for QCA operation is motion of the working point in the direction shown by the direction $V_{\mathrm{diag}}$ in Fig. 2. This movement between the (1,0) and (0,1) hexagon represents the switching of an electron between the top and bottom dot. If working points for each half-cell are on the border between these

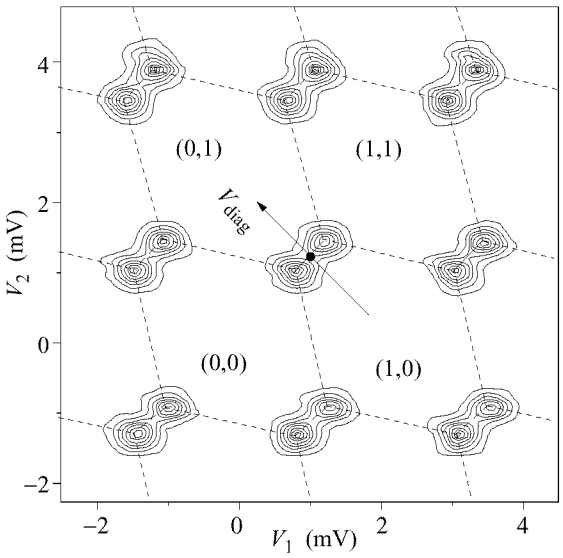


**Fig 2.** Contour plot of the measured conductance through the input half-cell as a function of $V_1$ and $V_2$. The excess electron population is noted as $(n_1, n_2)$.

states, the cell is non-polarized. If we than polarize input DD by applying the control signal to the input gates, the output DD will in turn be polarized to minimize the total energy of the system. The goal of our experiment is to demonstrate QCA operation by using electrodes to force this transition in the input half-cell and then have the potential changes on the input half-cell force an opposite transition in the output half-cell.

To demonstrate QCA operation, it is necessary therefore first to set both DDs in non-polarized state without the input signal. An input signal polarizes the input DD, which in turns polarizes the output DD. The external detectors then measure the position of an excess electron in the output DD.

To accomplish the first part of the task conductance of the DDs is measured as a function of corresponding gate biases, and the appropriate working points are thus chosen. To externally detect the charge state of each dot of $D_3D_4$ we use additional dots as electrometers [10], capacitively coupled to the output half-cell, as shown in the schematic of Fig. 2. The electrometer operates by detecting small potential changes in the dot being measured. Knowing the capacitance coupling the electrometer to the dot and the electrometer charge sensitivity, it is possible to calculate the potential on the measured dot.

QCA operation is demonstrated by applying a differential voltage to the input half-cell, a positive bias to $V_2$ and a negative bias to $V_1$. As this differential voltage is swept along $V_{diag}$, electrons tunneling one-by-one through $D_1D_2$ spend more time on $D_2$, and the electrostatic potential on $D_1$ and $D_2$ changes in response to the applied gate voltages and the position of electrons. The potential on $D_2$ increases with the positive voltage $V_2$, until an abrupt reset which occurs when an electron enters the dot. Likewise, the potential on dot $D_1$ also changes as a function of $V_1$, but with the opposite phase. Since the potentials on $D_1$ and $D_2$ act as additional gate voltages for $D_3$ and $D_4$, the

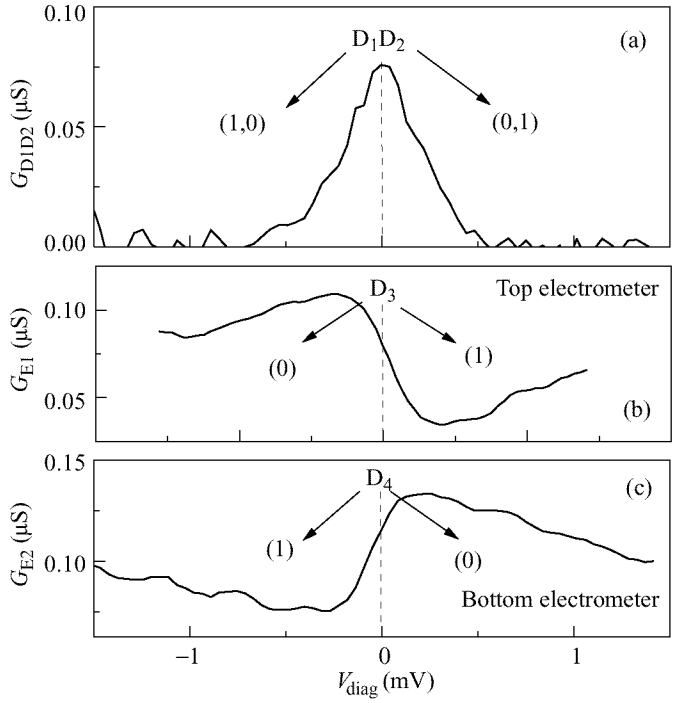


**Fig 3.** (a) Conductance through the input half-cell versus $V_{diag}$. The peak indicates the switch of an electron from $D_1$ to $D_2$. (b) Conductance through the electrometer $E_1$ indicating the addition of an electron to $D_3$. (c) Conductance through electrometer $E_2$ indicating the removal of an electron from $D_4$.

honeycomb of the output half-cell will shift in response to potential changes in the input half-cell. For QCA operation a shift must be sufficient to move the $D_3D_4$ honeycomb so that the working point of the $D_3D_4$ appears in (0,1) or (1,0) hexagons, depending on polarization of $D_1D_2$. This represents a switch of an electron in the output half-cell. The switching in the output half-cell will be detected by the two electrometers, where the current in one electrometer will increase as an electron leaves its adjacent dot, while the current in the other electrometer will decrease as an electron enters its adjacent dot. The experimental measurements confirm this behavior, as shown in Fig. 3, which plots the conductance through the input half-cell, along with the conductance through each electrometer as a function of the input voltage $V_{diag}$ ($V_2 = -V_1$). The peak in the conductance through the input half-cell, seen in Fig. 3a as $V_2$ increases, indicates that an electron has moved from $D_1$ to $D_2$. As the electron switches in the input half-cell the conductance of the top electrometer decreases (Fig. 3b), and rises for the bottom electrometer (Fig. 3c). This indicates that an electron has moved from $D_4$ to $D_3$ as expected due to the electron switch in the input half-cell. This confirms the polarization change required for QCA operation.

Using the electrometer signal of Fig. 3b we calculate the potential on $D_3$ as a function of the input differential voltage and compare it with theory. This is plotted in

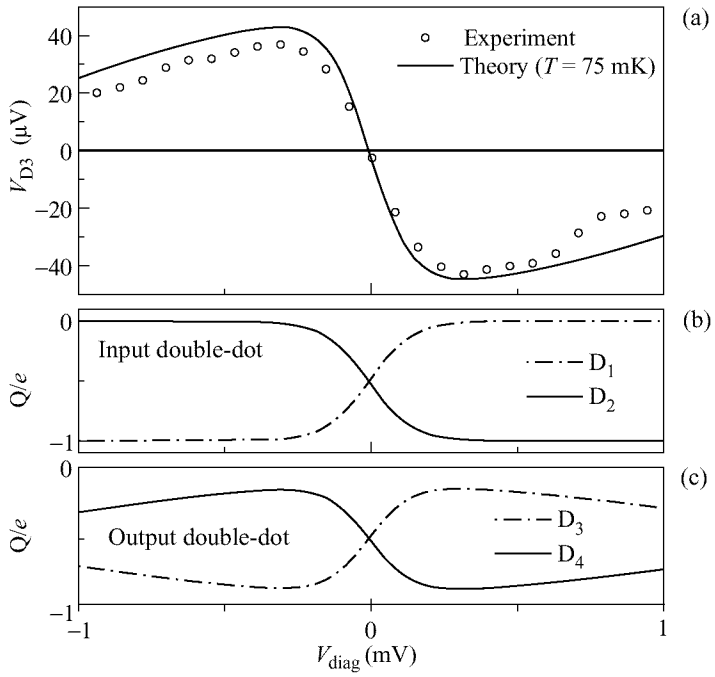


**Fig 4.** (a) Measured potential on dot $D_3$ as a function of $V_{diag}$, along with theory at 75 mK. Calculated excess electron population for (b), the input half-cell $D_1$ and $D_2$, and (c), the output half-cell $D_3$ and $D_4$, as a function of $V_{diag}$.

Fig. 4a, along with the theoretically calculated potential at a temperature of 75 mK. At a temperature of 0 K the potential changes are abrupt, while the observed potential shows the effects of thermal smearing, and theory at 75 mK shows good agreement with experiment. The heating of the electron system above the base temperature of the dilution refrigerator is likely due to the applied excitation voltage and noise voltages coupled into the sample by the leads. This effect is commonly seen in measurements of this type [11]. Figures 4b and 4c plot the theoretical excess charge on each of the dots in the input and output half-cells, at 75 mK.

This shows a 80% polarization switch of the QCA cell, and the polarization change can be further improved with an increase in the capacitances coupling input and output half-cells.

A device paradigm based on QCA cells offers the opportunity to break away from FET based logic, and to exploit the quantum effects that come with small size. In QCA approach, logic levels are no longer encoded as voltages but as the position of electrons within a quantum dot cell. QCA cells are scalable to molecular dimensions, and the performance improves as the size shrinks. A QCA cell with molecular dimensions should operate at room temperature since the energy spacings of the dot states will be larger than $kT$, even at 300 K.

Using metal island dots with oxide tunnel junctions, we have demonstrated the operation of a QCA cell. The cell exhibits a bistable distribution of electrons, and the

polarization of the cell can be switched by externally applied bias voltages.

This work was supported in part by the Defense Advanced Projects Agency, Office of Naval Research (contract No. N00014-95-1-1166), and the National Science Foundation.

## References

[1] C. S. Lent et al., *Nanotechnology* **4** 49 (1993).
[2] C. S. Lent and P. D. Tougaw, *Proceedings of the IEEE* **85** 541 (1997).
[3] C. S. Lent and P. D. Tougaw, *J. Appl. Phys.* **74** 6227 (1993).
[4] P. D. Tougaw and C. S. Lent, *J. Appl. Phys.* **75** 1818 (1994).
[5] P. D. Tougaw and C. S. Lent, *J. Appl. Phys.* **80** 4722 (1996).
[6] T. A. Fulton and G. H. Dolan, *Phys. Rev. Lett.* **59** 109 (1987).
[7] A. O. Orlov et al., *Science* **277** 928 (1997).
[8] K. K. Likharev, *IBM J. Res. Dev.* 114 (1988).
[9] H. Pothier et al, *Physica B* **169** 573 (1991).
[10] I. Amlani et al., *Appl. Phys. Lett.* **71** 1730 (1997).
[11] P. Lafarge et al., *Z. Phys. B* **85** 327 (1991).

Ioffe Institute
6th Int. Symp. "Nanostructures: Physics and Technology"
St Petersburg, Russia, June 22–26, 1998.



# Spectral response of quantum Hall effect far infrared detector

V. I. Gavrilenko‡, I. V. Erofeeva‡, N. G. Kalugin‡, *A. L. Korotkov*‡,
M. D. Moldavskaya‡, Y. Kawano† and S. Komiyama†
‡ Institute for Physics of Microstructures RAS, Nizhny Novgorod
† Graduate School of Arts and Sciences, University of Tokyo,Japan

**Abstract.** Cyclotron resonance photoconductivity of 2D electrons in GaAs/AlGaAs heterostructure in millimeter and submillimeter wavelength range in strong magnetic fields was investigated. Quantum Hall effect device was demonstrated as sensitive magnetically tunable narrow band ($2-5\ \mathrm{cm}^{-1}$) far infrared detector.

## Introduction

The magnetic field dependence of far infrared photoresponse of two-dimensional (2D) electrons has been the subject of several investigations [1-5]. In high magnetic fields the gap in the density of delocalized states occurs and quantum Hall effect (QHE) is observed. When the Fermi level $\varepsilon_F$ lies in localized states between two adjacent Landau levels the longitudinal resistance $R_{xx}$ vanishes and the Hall resistance $R_H$ is quantized to a multiple of $h/e^2$. Hence one can expect that the finite $R_{xx}$ emerges when electrons and holes are photoexcited in delocalized states near the level center above and below $\varepsilon_F$. This suggests that QHE device may serve as excellent cyclotron resonance (CR) detector in far infrared (FIR) range. In the work [5] high sensitive QHE FIR detector based on 2D electron gas in GaAs/AlGaAs heterostructures was realized. The photoresponse was studied using tunable by the magnetic field n-InSb emitter as a radiation source with rather broad emission line (about $20\,\mathrm{cm}^{-1}$). In the present work the high resolution study of the photoresponse in wavelength range $100\,\mu$m to 2 mm was carried out.

## 1 Experimental

The sample under study was fabricated from high mobility ($\mu_{4.2K} \approx 8 \cdot 10^5\,\mathrm{cm}^2/\mathrm{V} \cdot \mathrm{s}$) GaAs/AlGaAs heterostructure. The sample was a long Hall bar with a width $W = 50$ mm and a length $L = 170$ mm patterned in zig-zag shape and fitted into an area $4 \times 4\,\mathrm{mm}^2$ [5]. The sample was biased by dc current of $4\,\mu$A. In 2 mm wavelength range the response was studied as a function of the magnetic field using backward wave tube as a source of monochromatic radiation. At higher frequencies up to $100\,\mathrm{cm}^{-1}$ the spectra of the photoresponse were investigated using BOMEM DA3.36 Fourier-transform spectrometer. All measurements were made at $T = 4.2\,\mathrm{K}$.

## 2 Results and discussion

The dc measurements of the resistance $R_{xx}$ in magnetic fields are shown in Fig. 1. 2D electron concentration obtained from the period (in $1/B$ scale) of Shubnikov-de Haas oscillations is $n_s = 2.8 \cdot 10^{11}\,\mathrm{cm}^{-2}$. The observed minimums of $R_{xx}$ as a function of magnetic field correspond to the filling factors $\nu = hn_s/eB = 2$ (at $B = 5.6\,\mathrm{T}$), 4, 6, 8

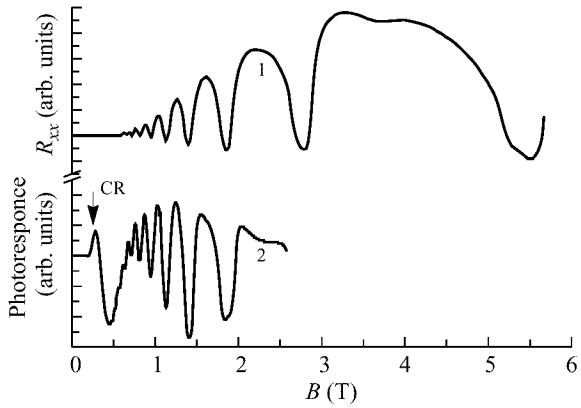


**Fig 1.** Longitudinal resistance $R_{xx}$ (curve 1) and photoresponse signal at $\lambda = 2.3$ mm (curve 2) of the sample versus magnetic field; $T = 4.2$ K.

etc. Fig. 1 presents also the magnetic field dependence of the sample photoresponse at $\lambda = 2.3$ mm. As it seen the CR signal (indicated by the arrow) is accompanied by distinct oscillations. The period of the photoresponse oscillations as well as the positions of maximums and minimums coincide with those for the Shubnikov–de Haas oscillations. The signal mechanism is tentatively considered as bolometric: the absorption results in heating of the electrons ($\Delta T_e$) and in the change in the electron mobility, the magnitude of the signal being proportional to $(\partial R_{xx}/\partial T) \cdot \Delta T_e$. It is seen that oscillations of the photoresponse are stretched rather far from the CR line and suppressed at $B \approx 3$ T that indicates the finite density of delocalized states between Landau levels [4]. The results of the detailed investigations of the photoresponse in the submillimeter wavelength range using backward wave tubes will also be presented in the report.

Fig. 2 represents the photoconductivity spectra of the sample in constant magnetic fields near integer filling factors $\nu = 8, 6, 4, 2$. The spectra were measured either "to the left" or "to the right" of $R_{xx}$ minimums. Sharp CR peaks with line width of few $cm^{-1}$ were observed in the spectra. CR line positions (from both Fig. 1 and Fig. 2) versus the magnetic field are plotted in Fig. 3a. The dependence is linear with the slope corresponding to the GaAs electron mass value $m = 0.068m_0$. The peak sensitivity was earlier shown to increase with the electron mobility and in this sample was estimated at $\nu = 2$ as $10^6$ to $10^7$ V/W [5]. The CR linewidth values (measured at 1/2 of the peak signal in Fig. 2) versus the magnetic field are shown in Fig. 3b. It is clearly seen that the linewidth undergoes rapid leaps near the integer values of the filling factors $\nu = 4$ and $\nu = 6$ that seems to result from the reduced screening due to density-of-states gaps [6]. At the filling factors $\nu \approx 2$ ($B = 5.5$ T) the linewidth increases 2 times that corresponds to the observed peculiarities of the linewidth oscillations in the transmission experiments [6].

Thus the QHE device was demonstrated as sensitive magnetically tunable narrow band FIR detector. The first results on the spectroscopic study of the FIR emission of hot carriers in MQW heterostructures obtained with QHE detector will be discussed in the report.

The research described in the publication was made possible in part Grants No. 7.8 from Russian Scientific Program "Physics of Quantum and Wave Phenomena/Funda-

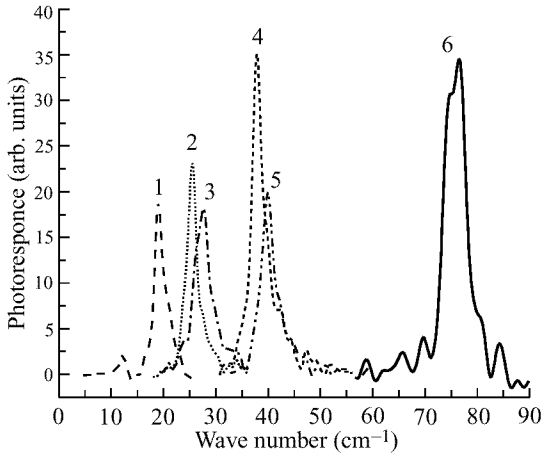


**Fig 2.** Spectra of the CR photoconductivity of the sample in constant magnetic fields near integer filling factor $\nu = 8$ ($B = 1.4$ T, curve 1); $\nu = 6$ ($B = 1.8$ T, curve 2 and $B = 1.9$ T, curve 3); $\nu = 4$ ($B = 2.8$ T, curve 4 and $B = 2.9$ T, curve 5); $\nu = 2$ ($B = 5.5$ T, curve 6); $T = 4.2$ K.

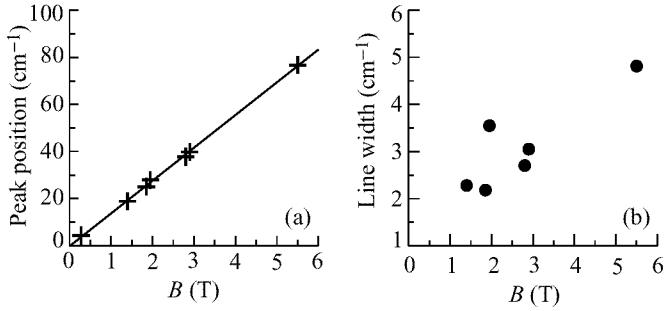


**Fig 3.** (a) the CR line positions from Fig. 1 and Fig. 2 versus magnetic field; (b) the CR linewidths (FWHM) from Fig. 2 versus magnetic field.

mental Spectroscopy", No. 97-2-14 from INCAS, #96-1023 from Russian Scientific Program "Physics of Solid State Nanostructures", No. 4.5 from Russian Scientific Program "Physics of Microwaves" and No. 97-02-16311 from RFBR.

## References

[1] D. Stein, G. Ebert, K. von Klitzing and G. Weimann. *Surf. Sci.* **142** 406 (1984).
[2] M. J. Chou, D. C. Tsui and Y. Cho.*Proc. 18th Int. Conf. on Physics of Semiconductors (World Scientific, Singapure, 1987)* 437.
[3] G. L. J. A. Rikken, P. Wyder, K. Ploog, et al. *Surf. Sci.* **196** 303 (1988).
[4] N. A. Varvanin, V. N. Gubankov, I. N. Kotel'nikov et al. *FTP* **24** 635 (1990).
[5] S. Komiayma, Y. Kawano and Y. Hisanaga. *Proc. 21st Int. Cohf. on Infrared and Millimeter Waves, Berlin, 1996)* Bt2.
[6] W. Sedenbusch, E. Gornik and G. Weimann. *Phys. Rev. B* **36** 9155 (1987).

Ioffe Institute
6th Int. Symp. "Nanostructures: Physics and Technology"
St Petersburg, Russia, June 22–26, 1998.



# Noise in metallic set transistors of the different contact area between their islands and a substrate

V. A. Krupenin†, *D. E. Presnov*†, M. N. Savvateev†, H. Scherer‡, A. B. Zorin‡ and J. Niemeyer‡

† Laboratory of Cryoelectronics, Moscow State University, 119899 Moscow, Russia
‡ Physikalisch-Technische Bundesanstalt, Bundesallee 100, D-38116 Braunschweig, Germany

The problem of background charge fluctuations in Single Electron Tunneling (SET) circuits is put in the forefront in recent investigations of SET devices. At low frequencies, these fluctuations substantially dominate over intrinsic fluctuations in SET devices and are usually characterized by a $1/f$ spectrum with a roll-off frequency of $0.1 \div 1$ kHz and intensity of $10^{-4} \div 10^{-3} e/\sqrt{Hz}$ at 10 Hz (see, for example, [1] and refs. therein). Such fluctuations can dramatically depress the performance of SET devices. For instance, they superimpose the limitation on sensitivity of an SET transistor used as an electrometer [2].

Although the intensity of background charge noise depends on many factors and widely varies from sample to sample, it was noticed a trend of its increase with the island size [3]. This might be qualitatively explained by the important role the substrate plays as a source of charge fluctuations. In particular, recent measurements using Al-based SET electrometers of stacked design [4] showed that the noise level can be decreased down to the value of $2.5 \cdot 10^{-5} e/\sqrt{Hz}$ at 10 Hz.

The aim of this work was to systematically examine SET transistors with different contacting areas between transistor islands and the substrate (keeping their electric parameters nominally similar). These areas varied from 50% to almost zero of the total island area (Fig. 1). The transistor 4 (Fig. 1) was practically insensitive to charge noise sources located in a substrate. Four chips (A-D), each comprising a series of four transistors (1-4), have been fabricated and studied.

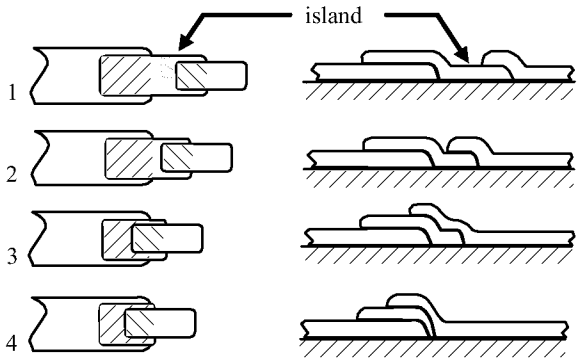


**Fig 1.** Four transistor structures with different island/substrate contact area.

The Al film structures (Fig. 2) with $Al/AlO_x/Al$ tunnel junctions were fabricated on a Si substrate buffered by sputtered $Al_2O_3$ layer 200 nm thick. The e-beam lithography

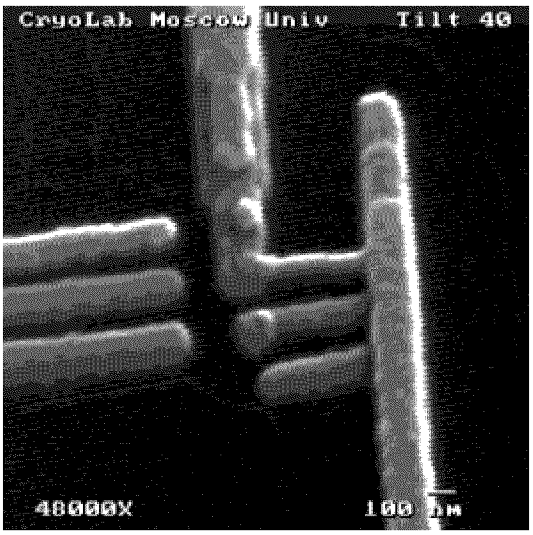


**Fig 2.** SEM image of the experimental structure.

**Table 1.** Noise level vs the island/substrate contact area for transistors on chip B at $I = 50$ pA.

| transistor number | 1 | 2 | 3 | 4 |
|---|---|---|---|---|
| Nominal contact area of an island to the substrate (% of total island area) | 50 | 40 | 20 | 0 |
| Charge noise at 10 Hz, $10^{-5}e/\sqrt{Hz}$ | 25 | 14 | 11 | 7 |

and traditional shadow evaporation technique were used for the fabrication process. There were three successive deposition cycles in-situ with different angles and two oxidation processes in between. The characteristics of the sample were measured in a dilution refrigerator at the bath temperature $T = 25$ mK. The samples were voltage biased and the current $I$ was measured. The noise floor of the setup was of the order of 20 fA/$\sqrt{Hz}$ at 10 Hz. SEM image of the experimental structure.

In all measured samples the noise level showed strong dependence on the contact area between the island and the substrate: the transistors with smaller contact area produce definitely less noise (see Table 1). At lower values of transport current I the equivalent charge noise of the transistors, which had no contact with the substrate (configuration 4 in Fig. 1), turned out to be suprisingly low for all the samples (see Table 2).

**Table 2.** The noise level of the samples of stacked design (transistor 4 in Fig. 1) at $I = 20 \div 30$ pA.

| chip | A | B | C | D |
|---|---|---|---|---|
| Charge noise at 10 Hz, $10^{-5}e/\sqrt{Hz}$ | 2.5 | 4 | 7 | 5 |
| Energy sensitivity | 230 | 500 | 1200 | 800 |

However, the measured noise levels are still higher than the fundamental noise floor, determined by shot noise [2] (and evaluated for our transistors as $3 \cdot 10^{-6} e/\sqrt{Hz}$. Thus, we attribute the observed noise to fluctuations of both the background charges inside the tunnel barriers and tunnel conductances [5]. The latter manifest themselves in an anomalous noise dependence on a polarization charge on the island.

This work is supported in part by the Russian Scientific Program "Physics of Solid State Nanostructures", the Russian Fund for Fundamental Research, the German BMBF and the EU (SMT Research Project SETamp).

## References

[1] A. B. Zorin, F.-J.Ahlers, J. Niemeyer, T. Weimann, H. Wolf, V. A. Krupenin and S. V. Lotkhov, *Phys. Rev. B* **53** 13682 (1996).

[2] A. N. Korotkov, D. V. Averin, K. K. Likharev and S. A. Vasenko, in: *Single Electron Tunneling and Mesoscopic Devices*, ed. by H. Koch and H. Lbbig (Springer-Verlag, Berlin, 1992), p. 45.

[3] S. M. Verbrugh, M. L. Benhamadi, E. H. Visscher and J.E. Mooij, *J. Appl. Phys.* **78** 2830 (1995).

[4] V. A. Krupenin, D. E. Presnov, M. N. Savvateev, H. Scherer, A. B. Zorin, J. Niemeyer, *IX Trilateral German-Russian-Ukrainian Seminar on High-Temperature Superconductivity*, Nizhny Novgorod, 11-15.09 1997, p. 64.

[5] V. A. Krupenin, D. E. Presnov, H. Scherer, A. B. Zorin and J. Niemeyer, Submitted to *Phys. Rev. Lett.* (1997).

Ioffe Institute
6th Int. Symp. "Nanostructures: Physics and Technology"
St Petersburg, Russia, June 22–26, 1998.



# Enhancement of the nonlinear response of the semiconductor tunnel structures in the skin-effect regime

*M. N. Feiginov* and V. A. Volkov
Institute of Radioengineering and Electronics, Russian Academy of Sciences,
Mokhovaya St., 11, Moscow, 103907, Russia.

**Abstract.** Nonlinear AC response of the semiconductor–barrier–semiconductor structures is considered. It is shown that in the vicinity of the barrier a low frequency plasma excitations–junction plasma polaritons (JPPs)—are excited on high frequencies. The excitation of JPPs has a substantial effect on the rectification properties of the structures in the skin-effect regime (on the frequency of 100 GHz and higher for the typical parameters of the structures). It leads to an essential increase in the rectified voltage. Its increase could be as large as one order of magnitude for the typical parameters of the structures.

## Introduction

As a rule, when one considers the AC response of the semiconductor–barrier–semiconductor (SBS) structures, the distribution of the electro-magnetic field and the electric charges, induced close to the barrier, are supposed to be homogeneous in the barrier plane. The assumption ceases to be true when the frequensies are sufficiently high. On those frequencies the AC electric current does not flow homogeneously to the barrier, but it is grouped in the skin-layer in the vicinity of the lateral surface of the structure. The inhomogeneity of the electric current is responsible for the excitation of peculiar plasma excitations close to the barrier–junction plasma polaritons (JPP). JPPs are propagating along the barrier and they are characterized by low speed of propagation. That are low-frequency excitations. Their excitation makes the distribution of the voltage drop on the barrier and the electric charges in its vicinity inhomogeneous in the plane of the barrier. The results concerning spectrum of JPPs and their influence on the linear AC response of the SBS structures were presented in [1]. Here we present the results concerning the influence of JPP excitation on the nonlinear AC response of the barrier structures. The conductivity mechanism through the barrier is irrelevant, it could be both tunnel and thermo-ionic. What is important for the practical applications is the nonlinearity of the conductance, the more it is the better.

In Section 1 we shall briefly review the results concerning JPP spectrum and the influence of JPP excitation on the linear AC impedance of the SBS structures. In Section 2 we shall discuss the new results concerning the influence of JPP excitation on the value of the rectified voltage in the SBS structures.

## 1 JPP spectrum and linear AC impedance of the barrier structures

We have found the spectrum of JPPs in the SBS structure. To describe the dependence of the electric current on the electro-magnetic field and the gradient of electron concentration we used the hydro-dynamic approximation. The following dispersion equation for JPPs has been derived [1]:

$$(\omega + i\nu)(\omega + i\nu_T)\kappa = \omega_p^2 \frac{d^*}{2}\left(\kappa^2 - \frac{\omega_p^2}{c^{*2}}\frac{\omega}{(\omega + i\nu)} - \frac{\omega(\omega + i\nu_T)}{c^{*2}}\right), Re(\kappa) > 0, \tag{1}$$

here $\omega_p^2 = 4\pi n_0 e^2/m^*\epsilon_l$ is the semiconductor bulk plasma frequency, $d^* = d + 2r_{TF}$ is the effective thickness of the barrier, $r_{TF}$ is the Thomas-Fermi screening radius, $\nu_T = 4\pi G d^*/\epsilon_l$ is the reciprocal $R_T C$ relaxation time due to the conductance of the barrier $(G)$, $\nu$ is the reciprocal momentum relaxation time in the semiconductor; $\kappa^2 = q^2 - \epsilon_s\omega^2/c^2$, $q$ is the 2D JPP wavevector in the plane of the barrier, $\epsilon_s = \epsilon_l\left[1 - \omega_p^2/\omega(\omega + i\nu)\right]$ is the dielectric function in the semiconductor allowing for the bulk plasma contribution, $c^* = c/\sqrt{\epsilon_l}$ is the effective light velocity in the barrier and $\epsilon_l$ is the lattice dielectric constant in the semiconductor and barrier (they are supposed to be the same). Eq. (1) have been derived in the low-frequency and long-wavelength approximations:

$$\max\{|\nu_T|,\ \omega,\ \nu\} \ll \omega_p,\quad q \ll \max\{1/d,\ 1/r_{TF}\}. \tag{2}$$

Further, we considered the linear response of the following structure: semiconductor with finite dimensions ($2W$ along $x$ axis, $\infty$ along $y$ axis, $L$ along $z$ axis)–barrier ($|z| < d/2$)–semiconductor ($2W \times \infty \times L$). The condition of the strong skin-effect is supposed to be fulfilled:

$$l_s(\omega) \ll W,\ L, \tag{3}$$

$l_s(\omega)$ is the skin-layer thickness. The following Eq. for the impedance of the pre-barrier region ($|z| < l_s(\omega) + d/2$) of the structure has been derived:

$$Z_j = \frac{i}{C(\omega + i\nu_T)}\frac{qW}{\tan(qW)}, \tag{4}$$

$C$ is the ordinary capacitance of the SBS structure. The first factor here is the ordinary impedance of the structure that one get if JPP excitation is not taken into account. The second factor appears due to JPP excitation by the current coming to the barrier region in the skin-layer along the lateral surface of the structure. In this case, the distribution of the current through the barrier ($j_T(x)$) has the form (we have been looking for a homogeneous solution in $y$ direction):

$$j_T(x) = j_T(W)\frac{\cos(qx)}{\cos(qW)}. \tag{5}$$

Eq. (4) is valid if the penetration length of the JPPs along the barrier ($1/q''$) from the lateral surface of the structure is large in comparison with the skin-layer thickness ($1/q'' \gg l_s$).

## 2 Nonlinear AC response of the barrier structure

Let us consider the small-signal nonlinear response. The problem is to calculate the DC rectified voltage in the SBS structure when a high-frequency voltage is applied to it. We consider the same structure as that used in the impedance calculations. We

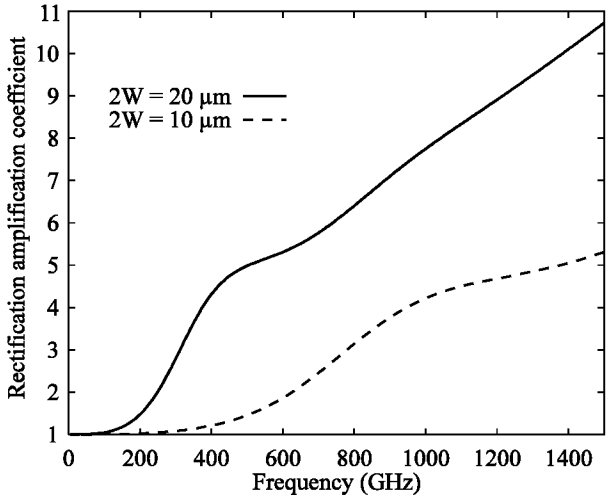


**Fig 1.** Rectification amplification coefficient at room temperature in the typical GaAs–barrier–GaAs structures with widths of 20 $\mu$m (upper curve) and 10 $\mu$m (lower curve).

suppose that the only nonlinear element in the structure is the barrier with nonlinear conductance. We suppose that the voltage drop on the barrier ($V(x)$) depends on the current through the barrier ($j_{\mathrm{T}}(x)$) as follows:

$$V(x) = \frac{1}{G} Re\left[j_{\mathrm{T}}(x)\right] + \alpha Re\left[j_{\mathrm{T}}(x)\right]^2, \tag{6}$$

where $\alpha$ is the nonlinearity parameter. We suppose that the second term in (6) is small as compared to the first one. In the case the following approach is applicable: at first, we find the linear solution for the $j_{\mathrm{T}}(x)$ (what in fact have been already made in the previous section), and further we are looking for a correction to $V(x)$ due to the nonlinearity, i.e. we substitute the linear solution for $j_{\mathrm{T}}(x)$ in (6) and average $V(x)$ over $x$ and $t$. In such a way we get the measurable rectified DC voltage $\langle V\rangle_{tx}$:

$$\langle V\rangle_{tx} = V_{\mathrm{rect}}^{\mathrm{classic}}(\omega) f(q(\omega)). \tag{7}$$

Here

$$V_{\mathrm{rect}}^{\mathrm{classic}}(\omega) = \frac{1}{2}\frac{\alpha}{(2W)^2}|I|\frac{1}{1+(\omega C/2WG)^2} \tag{8}$$

is the ordinary Eq. for the rectified voltage, if JPP excitation is not taken into account, $I$ is the net high-frequency current per unity of length in $y$ direction.

$$f(q) = \left|\frac{qW}{\sin(qW)}\right|^2 \left[\frac{\sin(2q'W)}{4q'W} + \frac{\sinh(2q''W)}{4q''W}\right] \tag{9}$$

is the amplification coefficient of the rectified voltage due to JPP excitation, $q(\omega) = q' + iq''$ is the solution of Eq. (1).

As it follows from (9), the amplification coefficient $f(q)$ is close to unity when the frequency is sufficiently low ($|q|W << 1$). On higher frequencies ($|q|W > 1$) $f(q)$ can increase significantly. The applicability area of Eqs. (7) and (9) coincides with that of the impedance Eq. (4).

For example, we calculated the frequency dependence of the $f(\omega)$ for the two identical $n$-GaAs structures of different widths, $2W = 20$ $\mu$m and $2W = 10$ $\mu$m (see Fig. 1). The other parameters are the following: the electron effective mass is $m^* = 0.07m$, the electron concentration in the semiconductor is $n_0 = 3 \cdot 10^{18}\,\mathrm{cm}^{-3}$, the barrier thickness is 30 nm, the electron mobility is $\mu = 2 \cdot 10^3\,\mathrm{cm}^2/\mathrm{Vs}$, the dielectric lattice constants in the semiconductor and barrier are equal to $\epsilon_l = 13.5$. One can see from Fig. 1 that the rectification amplification coefficient could be as large as one order of magnitude. In the structures with higher mobility the $f(\omega)$ plots are oscillating more significantly due to the resonant JPP excitation.

## Conclusions

We have shown that close to the barrier of the semiconductor–barrier (conducting, opaque, resonant tunneling one)–semiconductor structures low-frequency plasma excitations exist — junction plasma polaritons. They are excited by the high-frequency current coming to the barrier in the skin-layer along the lateral surface of the structures. JPP excitation leads to the build up of the AC voltage drop on the barrier or an effective change of the width of the barrier structure. Such effects are responsible for an amplification of the rectified voltage in the structures. The amplification becomes significant on the frequencies higher than 100 GHz for the typical parameters of the structures and it can be as large as one order of magnitude.

The work have been partially supported by the National programs “Physics of Solid State Nanostructures” (project 96-1019), “Surface Atomic Structures” (project 96-3.14), RFBR (grant 96-02-18811), INTAS-RFBR (95-0849) and CRDF (RC1-220).

## References

[1] Feiginov M. N. and Volkov V. A., *Proceedings of the 1997 International Semiconductor Device Research Symposium*, Charlottesville, USA, p. 155–158, 1997.

Ioffe Institute
6th Int. Symp. "Nanostructures: Physics and Technology"
St Petersburg, Russia, June 22–26, 1998.



# Numerical hydrodynamic modeling of non-linear plasma oscillations in the conduction channels of FETs and application to non-linear transformation of harmonic signals

*S. Rudin*† and G. Samsonidze‡§
† U.S. Army Research Laboratory, Adelphi, Maryland 20783, USA
‡ Ioffe Physico-Technical Institute, 194021 St. Petersburg, Russia
§ University of Maryland, College Park, Maryland 20742, USA

Plasma excitations have been of considerable interest in recent studies of semiconductor quantum wells and quasi-two-dimensional (2D) conduction channels in FETs and HEMTs. The intrasubband plasmons that are associated with a single electron subband can be studied as collective excitations in a two-dimensional electron fluid. When the electron-electron collision time is much smaller then the collision times with impurities and phonons the hydrodynamic model should be applicable to the carriers in MOSFET and HEMT channels. Various non-linear wave phenomena were predicted for the electron fluid [1]. Recently, Shur and Dyakonov [2] analyzed new effects related to plasma oscillations and proposed novel electronic devices operating in terahertz frequency range. The velocity of linear plasma waves $s_0$ is determined by the gate voltage swing $U_0$, $s_0 = (eU_0/m)^{1/2}$ where $m$ is the electron effective mass, $e$ is electron charge. In the case of GaAs HEMT for the gate lengths from 1 $\mu$m to 0.1 $\mu$m at $U_0 = 1$ V the fundamental plasma resonance frequency $\omega_0$ varies from 0.5 to 5 THz [2]. It was shown in ref. [1, 2] that under asymmetric boundary conditions on the source and drain contacts the linear plasmons become unstable and new non-linear effects in the device response appear.

In this work we consider a non-linear device response to harmonic signals applied as AC electric potentials at the source and drain contacts. We consider one dimensional fluctuation of 2D density along the channel ($x$ axis). Let $n_0$ be an equilibrium 2D density of electrons in the channel, determined by the gate voltages. We write the time and space dependent 2D density as $n(x,t) = n_0 + \delta n(x,t)$. The basic equations are [2]

$$\frac{\partial n}{\partial t} + \frac{\partial (nv)}{\partial x} = 0 \tag{1}$$

$$\frac{\partial v}{\partial t} + v\frac{\partial v}{\partial x} = -\frac{e}{m}\frac{\partial U}{\partial x} - \frac{v}{\tau} \tag{2}$$

where $\partial U/\partial x$ is the electric field component along the channel, $v(x,t)$ is local velocity of the electron fluid, $\tau$ is an electron collision time with phonons and impurities. If the distance $d$ from the channel to the gate is small compared to the channel length $L$ and the edge effects are neglected the Poisson equation which relates $U$ and $n$ can be treated in gradual channel approximation resulting in a linear local relation:

$$n(x,t) = \frac{C}{e}U(x,t) \tag{3}$$

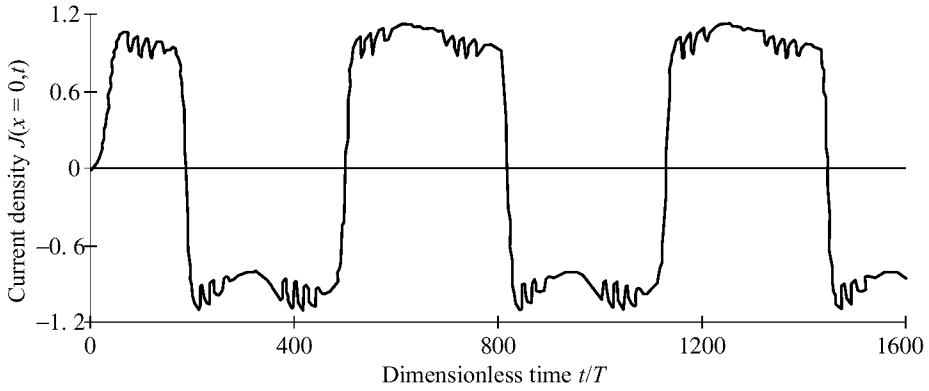


**Fig 1.** Dimensionless source current density.

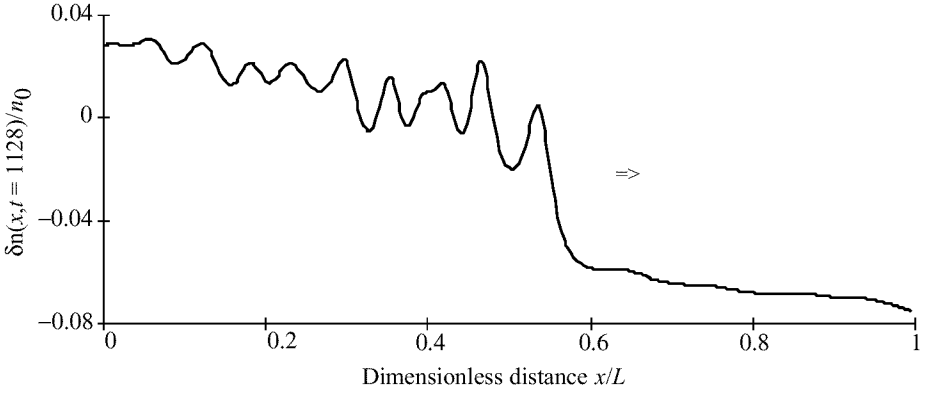


**Fig 2.** Electron density profile at $t/T = 1128$.

where $C$ is the gate capacitance per unit area. The deviations from this approximation in higher orders of $d/L$ lead to the non-linear dispersion effects in plasma waves [3] and are not included here.

In our numerical solution we introduce dimensionless variables: length $x/L$, time $t/T$ where $T = L/s_0$, density $n/n_0$, velocity $v/s_0$, frequency $\omega/\omega_0$. We also introduce a dimensionless friction coefficient $\gamma = L/s_0\tau$. The $\tau$ itself can be determined from a known mobility in the channel. We take boundary conditions corresponding to the application of harmonic signals at the source and the drain. We want to see how the high frequency plasma oscillations lead to a non-linear response when applied signals are of much lower frequency. From equation (3) the boundary conditions for applied electric potentials can be stated in terms of density variations: $\delta n(0,t)/n_0 = A_s \cos(\omega_s t)$, $\delta n(1,t)/n_0 = A_d \cos(\omega_d t)$. From the numerical solution of equations (1)–(3) we find the source (or drain) current density as $j_s(t) = n(0,t)v(0,t)$. It is shown in Fig. 1 as a function of time for $A_s = A_d = 0.1$, $\omega_s/\omega_0 = 0.01$, $\omega_d/\omega_0 = 0.03$, $g = 0.001$. We see that after a short transition a periodic regime is attained. In the Fourier analysis of $j(t)$ many harmonics besides those of the applied signals are generated. The form of $j(t)$ is found to be determined by the non-linear plasma waves in the channel. In particular during the time intervals corresponding to large drops and raises of the source current

a shock wave propagates in the channel, reflecting a few times between the contacts. The corresponding density profile is shown in Fig. 2.

We find that the non-linear wave propagation leads to the interesting non-linear response in the terminal current even though the applied signal is of much lower frequency then the fundamental plasma frequency. Similar response is found when the frequencies of applied signals are equal but their amplitudes are different or if there is a phase shift between applied signals. This may allow for the experimental demonstration of the non-linear plasma response and some novel device applications.

Acknowledgment: G.S. was supported by the U.S. Army European Research Office (London), contract No. N68171-97-M-5548.

## References

[1] M.I. Dyakonov and M.S. Shur, *Phys. Rev. Lett.* **71** 2465 (1993).
[2] M.I. Dyakonov and M.S. Shur, *IEEE Transactions on Electron Devices* **43** 380 (1996).
[3] S. Rudin and G. Samsonidze, in *Proceedings of ISDRS-97*, Charlottesville, Virginia, p. 583 (1997).

Ioffe Institute
6th Int. Symp. "Nanostructures: Physics and Technology"
St Petersburg, Russia, June 22–26, 1998.



# Transition from coherent to incoherent superlattices transport

*E. Gornik*, C. Rauch and G. Strasser
Institut für Festkörperelektronik, Technische Universität Wien, Austria

**Abstract.** Ballistic electron transport is used to study the transmittance of GaAs/GaAlAs superlattices. In a three terminal transistor type device an energy tunable electron beam is injected via a tunneling barrier into an undoped superlattice. The transmitted current is measured as a function of the injector energy. Resonances in the collector current are observed due to miniband conduction in the GaAs/AlGaAs superlattice. By analysing the transfer ratio of superlattices at various bias conditions miniband positions and miniband widths are determined. A significant decrease of the miniband transmission is observed with increasing electric field accross the superlattice, which is attributed to the the quenching of coherent transport. For longer superlattices an asymetry between positive and negative bias is found which is asigned to the transition between coherent and incoherent transport.

## Introduction

Electron transport in superlattice minibands was first considered by Esaki and Tsu [1]. In their model they calculate the dispersion relation of the miniband determined by classical transport. In the quantum mechanical picture a voltage drop over the superlattice causes the break up of the miniband into a Wannier-Stark ladder [2], which requires a different description in terms of tunneling [3-4]. The tunneling current decreases with increasing electric field as the wavefunctions become localized. In the calculation of the current through an infinite superlattice a phenomenological scattering time has to be introduced to reproduce the onset of the negative differential conductivity at $\omega_B$. $\tau = 1$, in order to mimic realistic current voltage characteristics [1, 5, 6] and thus the presence of incoherent transport.

A large number of studies of electrical transport in superlattices was done in the last decade [7–10]. In short period superlattices the formation of allowed and forbidden bands for resonant tunneling and band filling effects were confirmed experimentally [11-12]. The study of biased superlattices was severely hindered by space charge built up and domain formation [13]. So far there is no conclusive experiment which shows the occurrence of Esaki-Tsu type negative differential resistance (RTD) due to Bragg reflection at the zone boundary. Sybille et al. [14-15] performed the most extensive study in biased, doped superlattices and observed negative differential velocity. They were able to fit the drift velocity-voltage curves by using a modified Esaki-Tsu drift diffusion model.

Optical experiments led to a breakthrough by the observation of Bloch oscillations in the time domain of undoped superlattices [16]. In a previous experiment we have developed a three terminal technique which allowed the study of transport in undoped superlattices [17]. In this paper, we extend this technique of hot electron spectroscopy to biased superlattices [18].

## Experimental

We measured ballistic transport in GaAs/$Ga_{0.7}Al_{0.3}As$ superlattices, where the influence of electron-electron and electron-impurity scattering can be neglected due to extremely low current densities. Under flat band conditions the eigenstates of the periodic structure are extended over the entire length of the superlattice. To investigate the superlattice properties, a hot electron transistor structure is used. An energy tunable electron beam is generated by a tunneling emitter, passes the superlattice after traversing a thin highly doped GaAs region (base) and an undoped drift region. Electrons passing the superlattice are collected in a doped GaAs layer, reflected electrons are collected by the base contact.

Our samples, grown by molecular beam epitaxy, have the following common features: A highly doped $n^+$-GaAs collector contact layer is grown on a semi-insulating GaAs substrate. Followed by a superlattice and the drift regions which are slightly n-doped ($\sim 5 \times 10^{14}\,cm^{-3}$), in order to avoid undesired band bending. To reduce quantum mechanical confining effects originating from the quantum well formed by the emitter barrier and the superlattice the drift region is chosen to be at least 200 nm in width. This is followed by a highly doped ($2 \times 10^{18}\,cm^{-3}$) $n^+$-GaAs layer (base) of 13 nm width. As found in previous experiments [19], about 75% of the injected electrons traverse the base ballistically. On top of the base layer a 13 nm undoped $Ga_{0.7}Al_{0.3}As$ barrier is grown followed by a spacer and a $n^+$-GaAs layer, nominally doped to $n = 3 \times 10^{17}\,cm^{-3}$, in order to achieve an estimated normal energy distribution of injected electrons of about 20 meV [20]. Finally, a $n^+$-GaAs contact layer ($n = 1 \times 10^{18}\,cm^{-3}$) is grown on top of the heterostructure to form the emitter.

Standard photolithographic and wet etching techniques were employed in three terminal device processing. The emitter, base, and collector were contacted from above using a standard AuGe/Ni alloy. An emitter contact pad, which is connected to the $30 \times 30\,\mu m$ emitter mesa, is evaporated on top of a polyimid isolation layer.

## Results and discussion

Before we start to investigate the transmittance of the superlattice minibands, we want to have an exact knowledge of the energy distribution of the injected electrons. Thus, a three terminal device with a resonant tunneling diode instead of the superlattice was used to determine the shape of the injector. The energy diagram of the conduction band of this device is shown in Fig. 1. A resonant tunneling diode acts as an energy filter of the injected hot electrons. Electrons that have an energy which corresponds to the energy of the first resonant state can pass the energy filter, otherwise they are scattered back to the base and do not contribute to the measured collector current. The RTD (6 nm $Al_{0.3}Ga_{0.7}As$ barrier/12 nm GaAs well/8 nm $Al_{0.3}Ga_{0.7}As$ barrier) is designed in a way that the first state (23 meV) is well below the energy of an LO-phonon ($\hbar\omega_{LO} = 36$ meV) in order not be influenced by electrons that are scattered by LO-phonons. The measured ballistic current is in the order of 1 $\mu A/cm^2$.

The measured transfer ratio as a function of the injection energy, which is equivalent to the applied negative emitter bias, is shown in Fig. 2. Below the energy of the first resonant state $E_1$ of the RTD we observe no collector current, since no electrons are injected that have an energy which is high enough to cross the resonant tunneling barrier. The onset at about 21 meV determines the energy level of the first resonant state

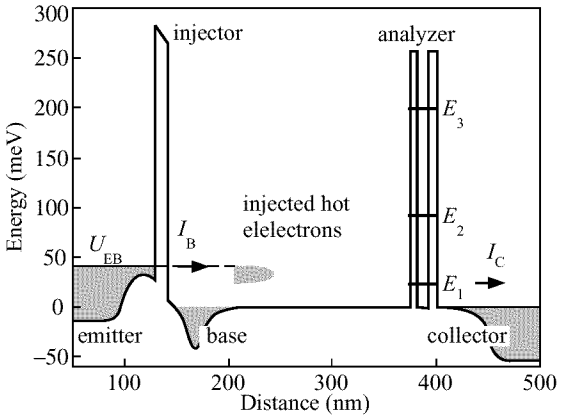


**Fig 1.** Schematic band diagram of a three terminal device with a resonant tunneling diode as a filter to measure the injected electron distribution.

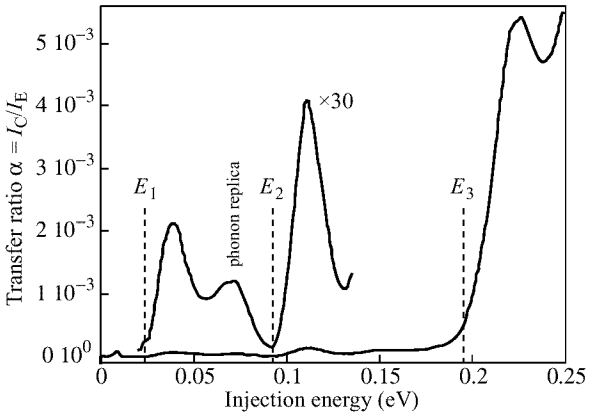


**Fig 2.** The transfer ratio $\alpha = I_C/I_E$ versus injection energy of the three terminal device with RTD. For injection energies up to 130 meV the transfer ratio is multiplied by a factor of thirty. The resonant states of the analyzer are indicated by dashed lines. LO-phonon replicas are observed for all levels.

$(E_1)$ of the analyzer RTD. By further increasing the emitter bias, we use the constant energy position of the first resonant state to perform spectroscopy of the injected hot electron distribution. Because the resonant linewidth of the double barrier structure is negligible compared to the width of the injector distribution, the measured transfer ratio is proportional to the hot electron distribution of the injector. The observed second peak at about 70 meV is due to electrons that are injected at higher energy and have lost 36 meV due to LO-phonon emission during transversing the base layer and the drift region. Since the k-vector in the current direction is conserved for LO-phonon scattering processes, these electrons are also collected efficiently at higher injection energies. The transfer ratio does not drop to zero in between these peaks due to the overlap of the injected electron distributions that traverse the drift region without scattering and those electrons that have lost the LO-phonon energy. Starting at about 90 meV we observe transport through the second resonant state $(E_2)$. This peak reproduces the shape of

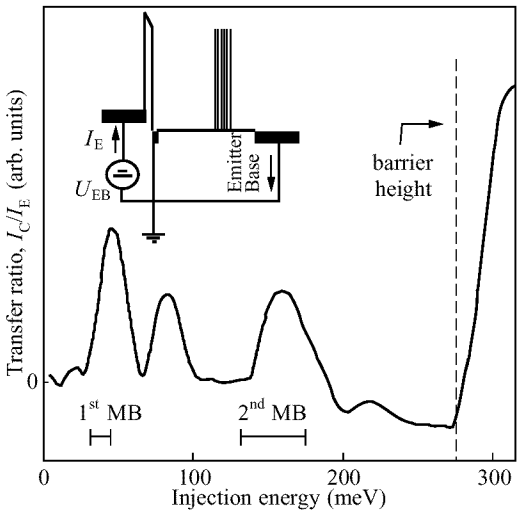


**Fig 3.** The transfer ratio $\alpha = I_C/I_E$ versus injection energy ($\approx e.U_{EB}$) of a sample with a 8.5 nm GaAs/2.5 nm AlGaAs superlattice. The calculated miniband positions are indicated by bars (|——|). The inset shows the measurement circuit in the common-base configuration.

the injected electron distribution for higher injection energies. At 187 meV we observe the third quantized level of the RTD. It should be noted that the measured onsets of the transfer ratio fits very well to the calculated positions of the position of the quantized states ($E_{1,\mathrm{calc}} = 23$ meV, $E_{2,\mathrm{calc}} = 87$ meV, and $E_{3,\mathrm{calc}} = 179$ meV). The calculated positions are indicated by dashed lines in Fig. 2.

Since the first peak of the transfer ratio is proportional to the injected hot electron energy distribution we can determine the full width at half maximum to be 20 meV. The shape of the distribution is slightly asymmetric with its maximum at the high energy side with respect to the GaAs conduction band edge. We observe no significant change of the shape of the energy distribution with higher injection energies up 200 meV.

The static transfer ratio $\alpha = I_C/I_E$, of a 8.5 nm/2.5 nm GaAs/AlGaAs five period superlattice is plotted in Fig. 3 as a function of the injection energy. Several maxima and a sharp rise at 280 meV are observed. The inset in Fig. 3 shows the measurement circuit used for the determination of the transfer ratio. All measurements are performed in common base configuration at 4.2 K. No current is observed below the energy of the first peak. The position of the first peak coincides very well with the first miniband. Thus, we conclude that the first peak is due to miniband transport through the lowest miniband. For energies higher than the first miniband the transfer ratio drops quite significantly since there is no transport possible through the forbidden minigap of the SL. The second observed peak is shifted 36 meV to higher injection energies and is attributed to the first LO-phonon emission replica ($\hbar\omega_{\mathrm{LO}} = 36$ meV) of the injected electron distribution. The relative position in energy and width are equal to that of the first peak. The energy range of electrons injected at voltages corresponding to these second peak is in the forbidden band and no contribution is expected from electrons which have not lost energy due to optical phonon emission. The peak at 150 meV represents transport through the second SL miniband. For an analysis of the observed features we compare the experimental data with the theoretically calculated miniband

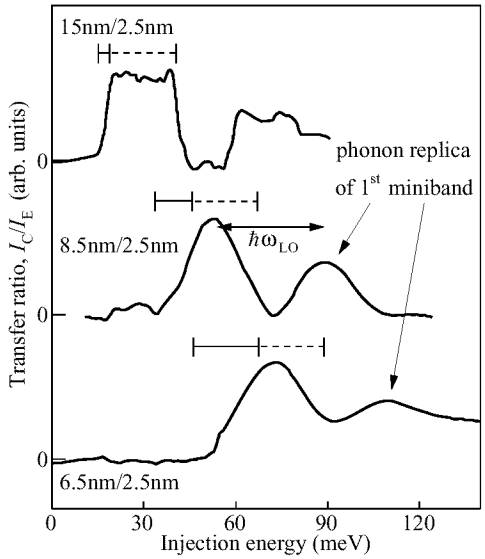


**Fig 4.** Transfer ratio a versus injection energy at lower injection energies for three samples with different superlattices (|—| indicates the calculated miniband position, |– – –| indicates the broadening due to the energy distribution of the injected electron beam). A double arrow represents the energy of a longitudinal optical phonon ($\hbar\omega_{LO} = 36$ meV).

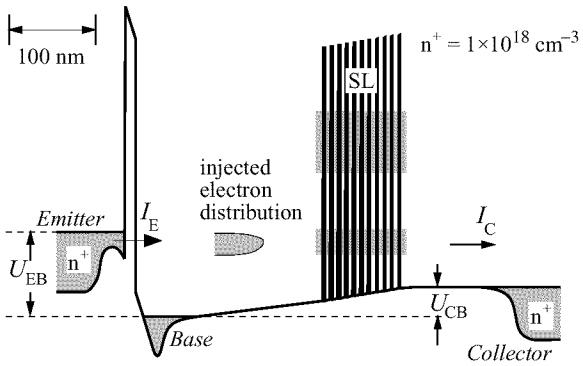


**Fig 5.** Schematic band diagram of a three terminal device with negative bias applied to the superlattice. The miniband positions are indicated by shaded areas. The base is grounded.

positions. The calculated positions and widths of the first and second miniband are indicated by bars. The sharp rise of the transfer ratio at 280 meV is due to the transition to continuum. This energy, which corresponds to the conduction band offset of the superlattice barriers, gives us a confirmation for the AlAs mole fraction of the AlGaAs compound.

In Fig. 4 we show the transfer ratio a as a function of the injection energy for three samples all have five periods with different well widths at low injection energies. There is a clear shift of the peaks to higher energies with decreasing superlattice well width. The calculated miniband positions are again indicated by bars as in Fig. 3. Since the calculated miniband width for the widest well is 3.5 meV and the observed peak

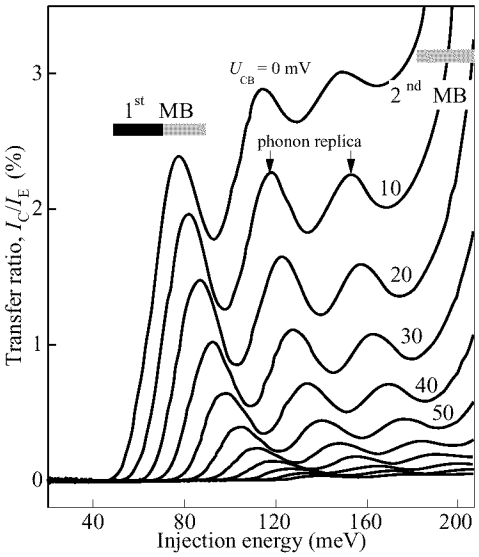


**Fig 6.** Transfer ratio $\alpha$ vs. injection energy at different collector base voltages. The dark bars indicate the calculated position of the minibands. The gray bars represents the full width at half maximum of the injected electron energy distribution.

corresponding to miniband transport through the first miniband has a width of about 24 meV, we can confirm the initial energy distribution of the injector to be about 20 meV wide, in agreement with the results shown in Fig. 2.

The measurements on biased superlattices are performed on a superlattice consisting of 5 and 10 periods of nominally 2.5 nm thick $Al_{0.3}Ga_{0.7}As$ barriers and 6.5 nm GaAs wells. For these parameters a simple Kronig-Penny calculation gives one miniband lying between 46 meV and 68 meV, and a second one between 182 meV and 276 meV. The calculated equilibrium Γ-point conduction energy diagram including band bending is shown in Fig. 5 for typical biasing conditions.

Fig. 6 shows a set of measured transfer ratios as a function of electron injection energy at different collector biases. As long as the injection energy is lower than the first miniband no ballistic current is observed. The sharp increase of the transfer ratio at about 45 meV coincides with the lower edge of the first miniband. The onset of the transfer ratio (miniband transport) shifts with the applied collector-base bias since the lower edge of the first miniband shifts with the applied bias. The value of the electric field in the superlattice is determined from a comparison of the measured miniband position (using the 3 dB criterium) with the miniband position derived from a self consistent Schrödinger calculation of the entire structure.

Longitudinal optical phonon replicas, shifted by 36 meV to higher injection energies, are observed at all biases and are used as an additional calibration for the applied bias. Due to these phonon replicas the transfer ratio does not vanish between the peaks since the full width at half maximum of the injected electron distribution (20 meV) plus the width of the first miniband (22 meV) is greater than the phonon energy. At zero bias the transmission through the superlattice should have a maximum, if we asume that the electronic wave functions of all superlattice states are extended over the total dimension

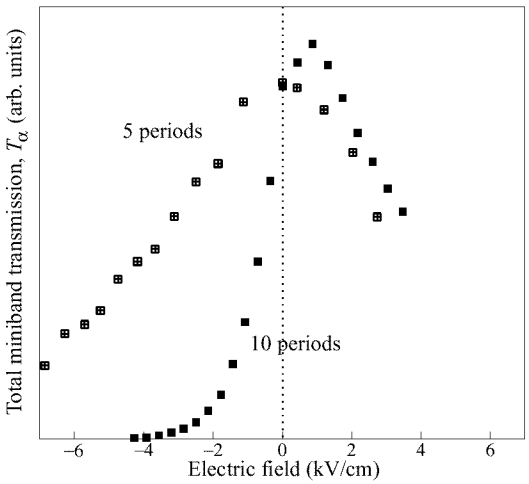


**Fig 7.** Measured total miniband transmission vs applied electric field.

of the superlattice.

The total miniband transmission, as a measure of the transmission, is defined as the integral over the first half of transfer ratio as a funtion of bias of the first peak. This represents the transport through the first miniband not taking into account electrons which have lost an LO phonon. Fig. 7 shows the total miniband transmission versus electric field for two different superlattices. It can be seen that the transmission vanishes for an applied electric field exceeding 4 kV/cm and 8 kV/cm. For low electric fields the superlattice states extend successively one after the other over the total superlattice dimension and become transparent which leads to an increase of current. At zero bias most of the superlattice states are extended, leading to a maximum of the measured transmission.

If we now compare the transmission for the five and ten period superlattice as a function of positive and negative bias we find clear differences: while the transmission for the five period superlattice is symetric and independent of the bias direction the ten period superlattice shows a clear asymetry. This asymetry we assigne to the onset of scattering in the ten period superlattice. This is also consisten with the asumtion that the mean free path is in the order of 800 nm in our samples which is just longer than the five period and shorter than the ten period superlattice.

## Summary

In summary direct experimental current spectroscopy of minibands in undoped superlattices is demonstrated using the technique of Hot Electron Spectroscopy. Miniband transport through the first and second miniband of superlattices with different well widths as a function of the hot electron injection energy is observed. We measured the injected electron distribution and are able to determine miniband widths and positions for flatband conditions. The obtained miniband widths and positions agree very well with theoretical calculations. The structure described in this paper gives the highest energy resolution reported so far.

Additionally we have shown the controlled decrease of superlattice conduction in a

superlattice with bias using the technique of hot electron spectroscopy. The experimental results are in good agreement with a calculation based on a transfer matrix method.

*Acknowledgement*

This work was partly supported by the Austrian Federal Ministry of Science, the Society for Microelectronics (GMe, Austria), and the U.S. Army European Research Office.

## References

[1] L. Esaki, and R. Tsu, *IBM J. Res. Dev.* **14** 61 (1970).
[2] G. H. Wannier, *Elements of Solid State Theory* (Cambridge University Press, London, 1959), pp. 190-193.
[3] R. Tsu and L. Esaki, *Appl. Phys. Lett.* **22** 562 (1973).
[4] J.B. Krieger and G.J. Iafrate, *Phys. Rev. B* **33** 5494 (1986).
[5] R.A. Suris and B.S. Shchamkhalova, *Sov. Phys. Semicond.* **18** 738 (1984).
[6] R. Tsu, and G. Döhler, *Phys. Rev. B* **12** 680 (1975).
[7] L. Esaki and L.L. Chang, *Phys. Rev. Lett.* **33** 495 (1974).
[8] F. Beltram, F. Capasso, D.L. Sivco, A.L. Hutchinson, S-N.G. Chu, and A.Y. Cho, *Phys. Rev. Lett.* **64** 3167 (1990).
[9] P. Voisin, J. Bleuse, C. Bouche, S. Gaillard, C. Alibert, and A. Regreny, *Phys. Rev. Lett.* **61** 1639 (1988); J. Bleuse, P. Voisin, M. Allovon, and M. Quillec, *Appl. Phys. Lett.* **53** 2632 (1988).
[10] E.E. Mendez, F. AgullIJ-Ruada, and J.M. Hong, *Phys. Rev. Lett.* **60** 2426 (1988).
[11] P. England, M. Helm, J.R. Hayes, J.P. Harbison, E. Colas, and L.T. Florez, *Appl. Phys. Lett.* **54** 647 (1989).
[12] G. Brozak, M. Helm, F. DeRosa, C.H. Perry, M. Koza, R. Bhat and S.J. Allen, *Phys. Rev. Lett.* **64** 3163 (1990).
[13] H.T. Grahn, R.J. Haug, W. MJIler, K. Ploog, *Phys. Rev. Lett.* **67** 1618 (1991).
[14] A. Sibille, J.F. Palmier, H. Wang, F. Mollot, *Phys. Rev. Lett.* **64** 52 (1990).
[15] A. Sibille, J.F. Palmier, F. Mollot, *Appl. Phys. Lett.* **60** 52 (1992).
[16] Ch. Waschke, H.G. Roskos, R. Schwedler, K. Leo, H. Kurz, and K. Köhler, *Phys. Rev. Lett.* **70** 3319 (1993).
[17] C. Rauch, G. Strasser, K. Unterrainer, B. Brill, and E. Gornik, *Appl. Phys. Lett.* **70** 649 (1997).
[18] C. Rauch, G. Strasser, K. Unterrainer, W. Boxleitner, E. Gornik, *phys. stat. sol. (b)* **204** 393 (1997).
[19] B. Brill, to be published (1996).
[20] S. Bending, A. Peck, J. Leo, K.v. Klitzing, P. Gueret, and H.P. Meier, *Solid-State Electronics* **32** 1161 (1989).

Ioffe Institute
6th Int. Symp. "Nanostructures: Physics and Technology"
St Petersburg, Russia, June 22–26, 1998.



# Single photon turnstile device

*Y. Yamamoto*†‡, J. Kim†, O. Benson† and H. Kan§

† ERATO Quantum Fluctuation Project, Edward L. Ginzton Laboratory, Stanford University, Stanford, CA 94305, USA

‡ NTT Basic Research Laboratories, 3-1 Morinosato-Wakamiya Atsugi, Kanagawa, 243-01, Japan

§ ERATO Quantum Fluctuation Project, Hamamatsu Photonics Inc., Hamamatsu, Shizuoka, Japan

**Abstract.** A single-photon turnstile device based on a simultaneous Coulomb blockade effect for electrons and holes was demonstrated in a mesoscopic double-barrier $p-n$ junction. The current-voltage characteristics at 50 mK featured three plateaus at $I = ef$, $2ef$, and $3ef$, where $f$ is an external modulation frequency. The emitted photon was detected by a Si solid-state photomultiplier with a quantum efficiency of $\geq 90\%$, multiplication gain of $\sim 30,000$, response time of $\sim 2$ ns, and absolutely no excess noise. The emitted photons at the first curent plateau were well localized at the rising edge of the driving pulse as expected.

## 1 Introduction

Quantum interference between indistinguishable quantum particles profoundly affects their arrival time and counting statistics. Photons from a thermal source tend to arrive together (bunching) and their counting distribution is broader than the classical limit (super-Poissonian or super-shot noise) [1]. Electrons from a thermal source, on the other hand, tend to arrive separately (anti-bunching) and their counting distribution is narrower than the classical limit (sub-Poissonian or sub-shot noise) [2, 3, 4]. Manipulation of quantum statistical properties of photons with various non-classical sources is at the heart of quantum optics: Fermionic features such as anti-bunching, sub-Poissonian and squeezing (sub-shot noise) behaviors were demonstrated for photons. While only one electron can occupy a single state due to the Pauli exclusion principle and thus the electrical conductance for a ballistic single-mode channel is quantized to $G_Q = 2e^2/h$, no similar effect for photons exists [5, 6, 7]. Here we report the first realization of such a quantized photon flux, i.e., a single-photon stream with a well-regulated time interval.

Recent mesoscopic physics experiments demonstrated that an ultra-small tunnel junction regulates the electron transport one-by-one due to the large single-charging energy compared to the thermal background energy [8, 9, 10]. This stimulated an interesting question of whether such single-electron control techniques can be extended to single-photon manipulation.

## 2 Principle of single-photon turnstile device

A single-photon turnstile device utilizes a simultaneous Coulomb blockade effect for electrons and holes in a mesoscopic double barrier p-n junction [Fig. 1(a)]. The structure consists of an intrinsic central quantum well (QW) in the middle of a p-n junction and the n-type and p-type side QWs isolated by tunnel barriers from the central QW. The

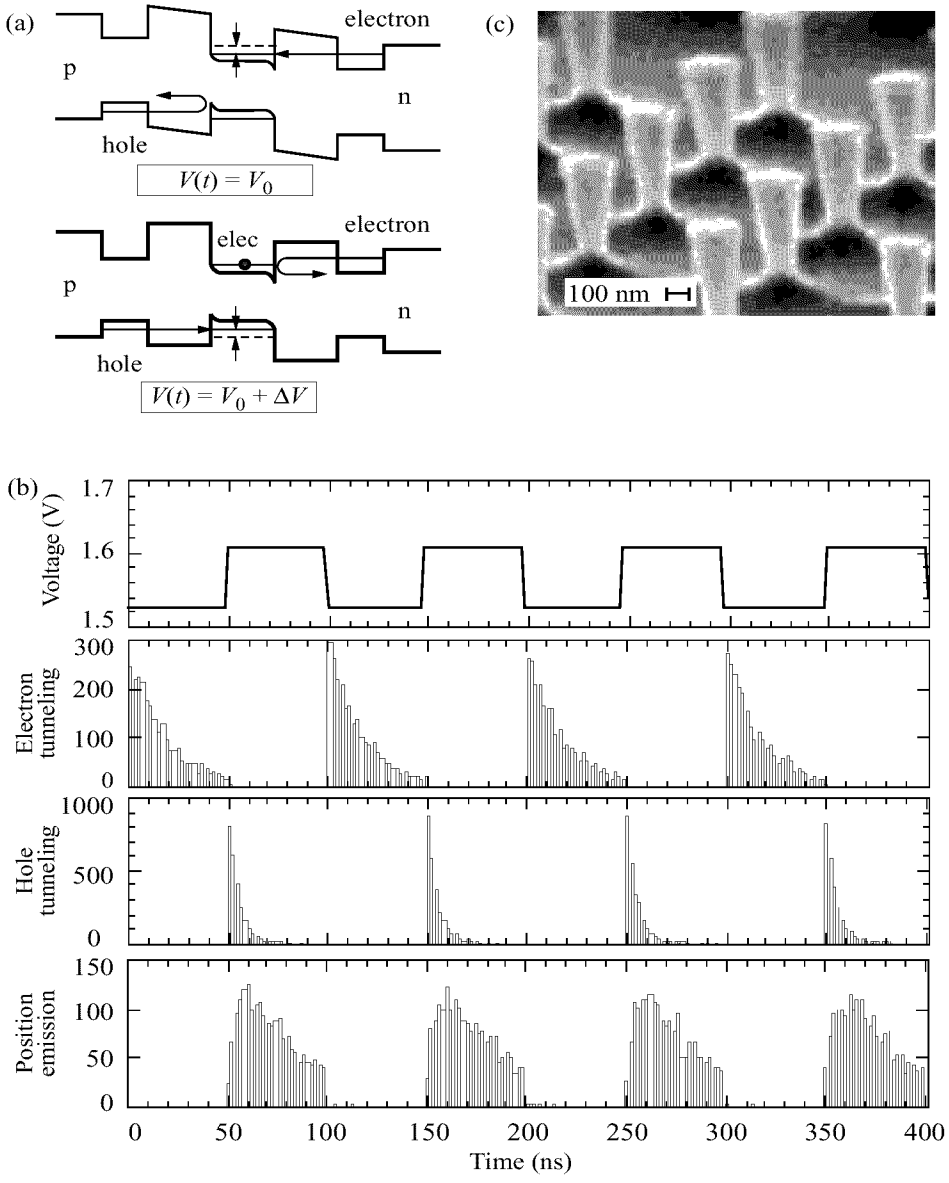


**Fig 1.** The principle of a single-photon turnstile device. (a) The energy band diagrams of the device at two bias voltages. (b) Monte-Carlo numerical simulation results for the statistical distribution of single-electron tunneling, single-hole tunneling, and single-photon emission. (c) Scanning electron microscope (SEM) photograph of typical etched post structures.

lateral size of the device is reduced to increase the single-charging energy $e^2/2C_i$, where $C_i$ ($i$ = n or p) is the capacitance between the central QW and the side QWs. The $n$-th electron resonant tunnel condition into an electron sub-band in the central QW is satisfied at a certain bias voltage $V_0$. When the $n$-th electron tunnels, the Coulomb blockade effect shifts the electron sub-band energy to off-resonance, so that the $(n+1)$-th electron tunneling is inhibited. In our single-photon turnstile device described later, the number of electrons in the central quantum well switches between $n-1$ and $n$, where $n$ is approximately 10. At this bias voltage, the hole resonant tunnel condition is not satisfied, so there is no hole in the central QW. Then the bias is increased to $V_0 + \Delta V$ to satisfy the hole resonant tunneling condition. If a single hole tunnels into the hole sub-band of the central QW, the subsequent hole tunneling is inhibited due to the Coulomb blockade effect for holes. By periodically modulating the bias voltage between the electron and the hole resonant tunneling conditions, we can periodically inject a single (n-th) electron and a single (first) hole into the central QW if the tunnel time is much shorter than the pulse duration. If the radiative recombination time of an electron-hole pair is also much shorter than the pulse duration, a single photon is always emitted per modulation cycle.

A Monte-Carlo numerical simulation of the device produces the statistics of subsequent photon emission events after a single photon is emitted at $t = 0$ [Fig. 1(b)]. Experimental parameters such as the electron tunnel time $\tau_e = 25$ ns, hole tunnel time $\tau_h = 4$ ns, radiative recombination lifetime $\tau_{ph} = 30$ ns, charging energy $e^2/2C_n = e^2/2C_p = 1.3$ meV and thermal energy $k_B\Theta = 4.3$ $\mu$eV are assumed. It is shown that a single-photon emission event is localized to a short time interval immediately after a single-hole tunneling event.

## 3 Experimental results

A GaAs/AlGaAs three-QW structure sandwiched by $n$-type and $p$-type AlGaAs bulk layers was grown using the MBE technique. Post structures with diameters of 200 nm–1.0 $\mu$m were made by electron-beam lithography followed by metal evaporation, lift-off, and $BCl_3/Cl_2$ ECR plasma etching. An SEM micrograph of typical etched posts is shown in Fig. 1(c). The surface of the device was passivated with sulfur in a $(NH_4)_2S$ solution and encapsulated by silicon nitride film. Finally, the structure was planarized with hard-baked photoresist and bonding pads were evaporated. The top semi-transparent metal served as the p-type contact from which an emitted photon is detected and the n-type contact was formed in the substrate.

The device was installed in a dilution refrigerator with a base temperature of 50 mK and was biased with a dc and ac voltage source. We applied a square wave ac voltage at a modulation frequency of 10 MHz and a modulation amplitude of 40 mV on top of the dc bias voltage and measured the current flowing through the device as a function of the bias voltage. A typical experimental result for a device with post diameter of 600 nm is shown in Fig. 2(a). The inset shows the current in a larger voltage scale. We observed a well-defined resonant tunneling current peak with very small background current even though the junction is so small, which indicates that a surface (leakage) current is well suppressed by the above-mentioned passivation process. Direct measurement of emitted photons from this device indicates that this resonant tunneling current produces photons with a very high internal quantum efficiency and, therefore, the non-radiative

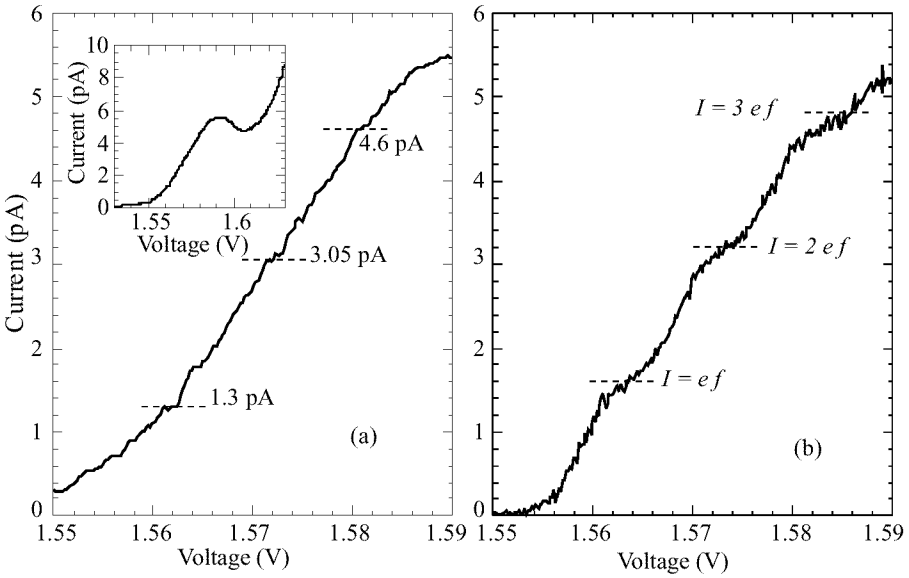


**Fig 2.** The current-voltage characteristics of the turnstile device. (a) Current vs. voltage characteristics of a 600 nm device. (b) Monte Carlo simulation result of current-voltage characteristics of the device.

recombination at the surface is negligible in our device. The tunnel current featured three plateaus near 1.4 pA, 3.1 pA, and 4.6 pA. These values correspond to $I = \eta_n nef$, where $e = 1.6\times10^{-19}$ C is the electron charge, $f = 10$ MHz is the modulation frequency, $n = 1, 2, 3$, and $\eta_n$ is the fidelity of the turnstile operation. The locking of the current at multiples of $I_0 = ef$ suggests that the charge transfer through the device is strongly correlated with the external driving signal [8, 9, 10]. A slightly smaller current compared to the expected values $I = nef$ is due to a finite missing rate of the n-th electron tunneling and the reverse tunneling rate of a hole. This is characterized by fidelity $\eta_n$, which is a measure of the accuracy of the turnstile operation. In our measurements, $\eta_1 = 81\%$, $\eta_2 = 95\%$, and $\eta_3 = 96\%$. Figure 2(b) shows the Monte-Carlo simulation result for the actual device parameters, which reproduces the measurement result well. At the first plateau, the single (n-th) electron and the single (first) hole are injected into the central QW per driving pulse, resulting in single-photon emission. At the second plateau ($n = 2$), two [n-th and (n+1)-th] electrons and two (first and second) holes are injected into the central QW per modulation cycle, resulting in two-photon emission. At the third plateau ($n = 3$), three electrons and three holes are injected per modulation cycle, resulting in three-photon emission. A non-unity fidelity $\eta_n$ is also evident from the numerical simulation.

The emitted photon from this device is detected by a Si solid-state photomultiplier (SSPM). This detector features a high quantum efficiency of $\sim$ 80%, high multiplication gain of $\sim$ 30, 000, fast response time of $\sim$ 2 nsec and absolutely no multiplication noise [11]. The detector was installed on the mixing chamber of the dilution refrigerator, but the temperature was held at 5.30 K with good thermal isolation. To observe the

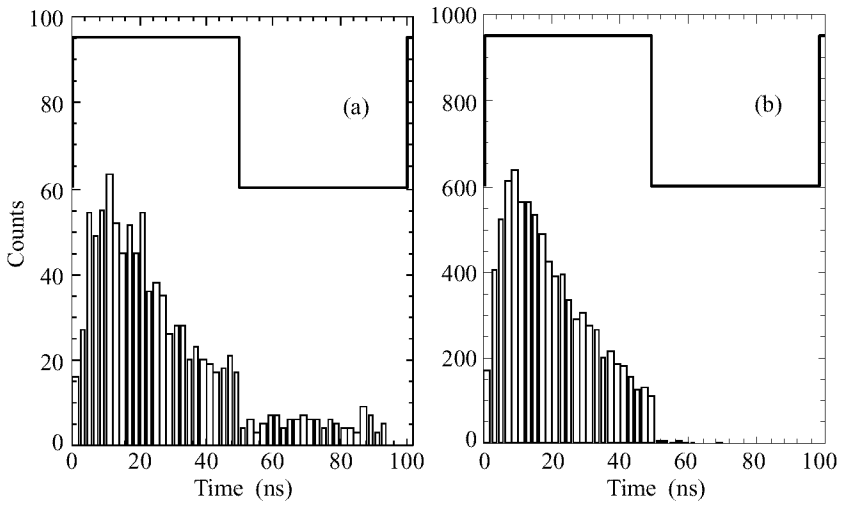


**Fig 3.** The photon emission characteristics of the turnstile device. (a) Histogram of the time interval between the rising edge of the driving ac modulation and the photon detection event on the first plateau, where a single electron and a single hole are injected per modulation cycle. (b) Monte-Carlo simulation result of the time interval for the first plateau.

correlation between the driving signal and photon emission, we measured the time interval between the rising edge of the driving pulse and the photon detection event at the first ($I = ef$) plateau of the current-voltage characteristics. As mentioned before, photons are expected to be emitted soon after the junction voltage is switched to the hole resonant tunneling condition. The histograms of the measured time interval are shown in Fig. 3(a) (first plateau). The data shows that the emitted photons follow the rising edge of the driving pulse, as expected. Two time constants can be identified from this data: The rapid increase of the histogram gives the finite hole tunneling time ($\tau_h \simeq 4$ ns), and the slow decay of the histogram gives the radiative recombination lifetime ($\tau_{ph} \simeq 30$ ns). The sharp cut-off of photon emission following the falling edge of the driving pulse in Fig. 3(a) is due to reverse hole tunneling and reduces the fidelity of turnstile operation. The experimental result, except for a small dark count (background), is well reproduced by the Monte-Carlo simulation using the same numerical parameters, as shown in Fig. 3(b).

## 4 Conclusion

The result reported here is the first generation of a heralded single photon, two photons, and three photons with a well-regulated time interval. Such a nonclassical photon source can provide an efficient source for future quantum information technology and a useful tool for fundamental tests of quantum mechanics.

## References

[1] R. Hanbury Brown and R. Q. Twiss *Nature* **177** 27 (1956).
[2] M. Reznikov, M. Heiblum, H. Shtrikman and D. Mahalu *Phys. Rev. Lett.* **75** 3340 (1995).

[3] A. Kumar, L. Saminadayar, D. C. Glattli, Y. Jin and B. Etienne *Phys. Rev. Lett.* **76** 2778 (1996).
[4] R. C. Liu, B. Odom, Y. Yamamoto and S. Tarucha *Nature* **391** 263 (1998).
[5] A. Imamoğlu and Y. Yamamoto *Phys. Rev. Lett.* **72** 210 (1994).
[6] A. Imamoğlu, H. Schmidt, G. Woods and M. Deutsch *Phys. Rev. Lett.* **79** 1467 (1997).
[7] Y. Yamamoto *Nature* **390** 17 (1997).
[8] P. Delsing, K. K. Likharev, L. S. Kuzmin and T. Claeson *Phys. Rev. Lett.* **63** 1861 (1989).
[9] L. J. Geerligs et al. *Phys. Rev. Lett.* **64** 2691 (1990).
[10] L. P. Kouwenhoven et al. *Phy. Rev. Lett.* **67** 1626 (1991).
[11] J. Kim, Y. Yamamoto and H. H. Hogue *Appl. Phys. Lett.* **70** 2852 (1997).

Ioffe Institute
6th Int. Symp. "Nanostructures: Physics and Technology"
St Petersburg, Russia, June 22–26, 1998.



# GaN-based two-dimensional electron devices

*M. S. Shur* and R. Gaska†
Rensselaer Polytechnic Institute, Troy, NY 12180-3590, shurm@rpi.edu
† APA Optics, Inc., 2950 N. E., 84th Lane, Blaine, MN 55449

**Abstract.** We discuss the properties of the two dimensional (2D) electron gas at AlGaN/GaN heterointerface. The density of the 2D gas is affected by piezoelectric effects and by doping levels in both AlGaN and GaN layers. The record values of the sheet carrier density have been achieved with sheet electron densities of the two-dimensional electron gas on the order of $1.5 \times 10^{13}\,cm^{-2}$ and the sheet carrier concentration in the surface heterostructure channel as high as $4 \times 10^{13}\,cm^{-2}$. At high electron concentration, electrons are divided between the 2D and 3D states, and this division affects the electron mobility in the channel. Optical polar scattering, impurity scattering, and piezoelectric scattering limit the mobility. The largest electron mobility was observed in AlGaN/GaN heterostructures grown on SiC. At room temperature, the mobility is over 2,000 $cm^2$/V-s; at cryogenic temperatures, the highest mobility is over 10,000 $cm^2$/V-s. These values are high enough for the observation of the Quantum Hall Effect. Multichannel 2D electron structures are being developed that will allow us to achieve a much higher current density and much higher power.

## 1 Introduction

The first evidence of the existence of the two-dimensional electron gas at the GaN/AlGaN heterointerface was provided by a large mobility enhancement at the heterointerface. In 1995, Khan et al. [1] observed a large mobility enhancement in the 2D-electron gas at the AlGaN/GaN interface. They measured the 2D electron gas Hall mobility around 5,000 $cm^2$/V-s at 80 K, compared to the maximum electron mobility of approximately 1,200 $cm^2$/V-s in their bulk doped GaN samples. Recently, Gaska et al. [2] reported on the electron mobility in the 2D-gas electron gas at the GaN/AlGaN interface exceeding 10,000 $cm^2$/V-s at cryogenic temperatures and exceeding 2000 $cm^2$/V-s at room temperature. These values were observed in the samples with very high sheet carrier concentration (on the order of $10^{13}\,cm^{-2}$).

Our estimates show that the maximum density of the two-dimensional electron gas at the GaN/AlGaN heterointerface or in GaN/AlGaN quantum well structures can reach $5 \times 10^{13}\,cm^{-2}$, which is more than an order of magnitude higher than for traditional GaAs/AlGaAs heterostructures. The mobility-sheet carrier concentration product for these two dimensional systems might also exceed that for GaAs/AlGaAs heterostructures and can be further enhanced by doping the conducting channels and by using "piezoelectric" doping [3, 4], which takes advantage of high piezoelectric constants of GaN and related materials.

The University of California, Santa Barbara group [5] reported record-breaking microwave power close to 3 W/mm achieved in GaN-based Heterostructure Field Effect Transistors. Their results (and similar, though not as spectacular results achieved by other groups [6]) show that these devices will compete with GaAs-based transistors in high power, high frequency applications.

In this paper, we review our recent results obtained for AlGaN/GaN heterostructures. We discuss the properties of the 2D-electron gas at AlGaN/GaN heterointerface with emphasis on the differences between these structures and their GaAs counterparts.

## 2 Band structure

Fig. 1 (from [7]) shows a typical band diagram of an AlGaN/GaN heterostructure. Notice the difference in the electric field slopes in GaN and AlGaN at the heterointerface. This difference is related to piezoelectric effect, and this band diagram is very different from a band diagram for a typical AlGaAs/GaAs heterostructure.

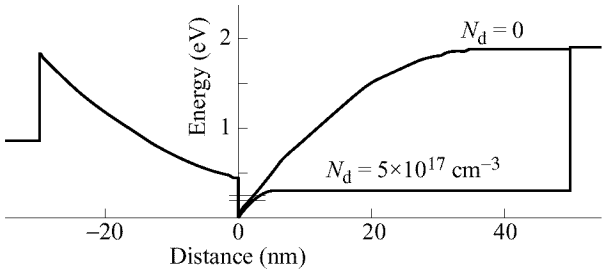


**Fig 1.** Band diagrams of the GaN heterostructures for doped and undoped GaN layers. The short horizontal lines show the position of the Fermi level (top line) and of the lowest subband (bottom line). Al mole fraction is $x = 0.2$. Schottky barrier height is 1 eV. Conduction band discontinuity, $\Delta E_c = 0.75\Delta E_g$. AlGaN doping, $5 \times 10^{18}\,\mathrm{cm}^{-3}$. 2D gas density is $5 \times 10^{12}\,\mathrm{cm}^{-2}$. $T = 300$. The electron effective mass is $0.23m_0$. The piezoelectric constants are $e_{31} = -0.58\,\mathrm{C/m}^2$, $e_{33} = 1.55\,\mathrm{C/m}^2$; $e_{31} = -0.36\,\mathrm{C/m}^2$, $e_{33} = 1\,\mathrm{C/m}^2$, for AlN and GaN, respectively. Material parameters of AlGaN were determined by taking a linear interpolation between GaN and AlN parameters as functions of the Al molar fraction. (From [7].)

Fig. 2 shows the position of the Fermi level, $E_F$, (counted from the bottom of the conduction band in GaN at the heterointerface) as a function of the sheet electron density, $n_s$ [7]. Also shown the Al molar fraction, which corresponds to the value of the conduction band discontinuity at the heterointerface. The effective mass of $0.24m_e$ (where $m_e$ is the free electron mass) was assumed in this calculation. The first seven subbands were accounted for. For $n_s$ higher than $1.5 \times 10^{12}\,\mathrm{cm}^{-2}$, the following approximation:

$$E_F = E_0 + n_s/D \tag{1}$$

is in good agreement with the computed dependence.

Fig. 2 shows that the values of $n_s$ close to $2 \times 10^{13}\,\mathrm{cm}^{-2}$ can be achieved for relatively low Al molar fractions. Such high concentrations are not achievable in AlGaAs/GaAs or even in AlInAs/InGaAs, which has a larger conduction band discontinuity than AlGaAs. Much higher values of $n_s$ in the AlGaN/GaN heterostructures can be achieved by doping the active layer so the total surface electron concentration in the channel

$$N_s = n_s + N_d d \tag{2}$$

This increase is related to the change in the band diagram caused by the channel doping illustrated by Fig. 1. As seen from Fig. 1, in the doped quantum well structures,

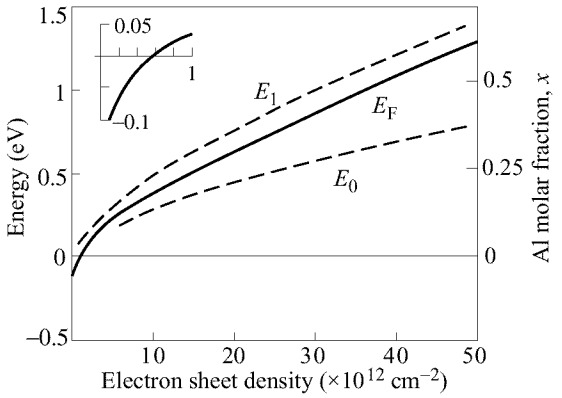


**Fig 2.** Fermi level (solid line) and the positions of the ground and first excited subbands for GaN/AlGaN heterostructure counted from the bottom of the conduction band in GaN at the heterointerface. The insert shows the position of the Fermi level at small values of $n_s$. Also shown the Al molar fraction, with corresponds to the value the conduction band discontinuity equal to the energy scale on the left [7].

electrons can go into bulk states, whose density is large enough to contain a very large electron sheet density.

Another important approach in increasing the electron sheet concentration, which is important for applications in power devices, is to use multichannel structures that have several parallel 2D-electron gas layers. Gaska et al. [8] report on the fabrication, characterization, and modeling of a double channel $Al_xGa_{1-x}N$/GaN Heterostructure Field Effect Transistors. The epilayer structure was grown by low pressure Metal Organic Vapor Pressure Epitaxy on sapphire substrates. In these structures, a 50 nm AlN layer growth on sapphire was followed by the deposition of a 0.8 $\mu$m nominally undoped GaN layer, 25 nm of $Al_{0.25}Ga_{0.75}N$, a second 0.1 $\mu$m nominally undoped GaN layer, and finally capped with 30 nm $Al_{0.25}Ga_{0.75}N$ barrier layer (see Fig. 3). Both AlGaN barrier layers were unintentionally doped with electron concentration of approximately $n = 10^{18}$ cm$^{-3}$. Devices with the source-drain spacing of 5 $\mu$m, the gate length of 2 $\mu$m and the gate width of 50 $\mu$m were fabricated. Ti/Al/Ti/Au of thickness 250/700/500/1000 angstroms was annealed at 900°C for 30 sec to make ohmic contacts; Pt/Au was used for the offset gate fabrication. The maximum source-drain current at zero gate bias was 0.5 A/mm, the maximum transconductance $g_m = 140$ mS/mm was measured at the gate bias of $-1.5$ V. The threshold voltage of these devices was $-4.5$ V.

Fig. 4 shows a qualitative band diagram of such a structure. The 25 nm AlGaN layer sandwiched between two GaN layers formed a Semiconductor-Insulator-Semiconductor structure. As was shown in [3, 9], strong piezoelectric effects cause the depletion at the top interface of this structure and accumulation at the bottom interface. This accumulation layer creates the second conducting channel in our devices. This conducting channel is separated from the ohmic source and drain contacts by the depleted region in GaN and by the thin AlGaN layer. Hence, this bottom conducting has very large series resistances at low drain biases. At high drain biases, the electron injection drastically decreases the series resistances for the bottom channel, and it starts contributing to the

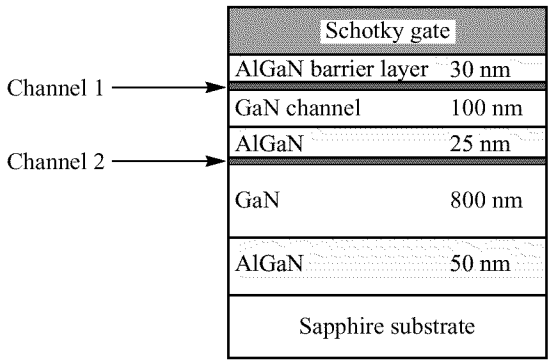


**Fig 3.** AlGaN/GaN epitaxial structure with two channels (after [8]).

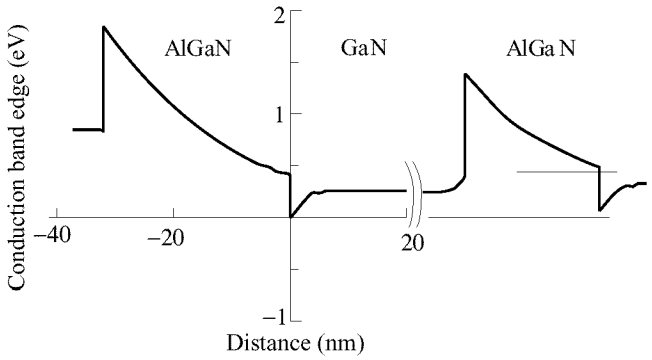


**Fig 4.** Qualitative band diagarm of two channel AlGaN/GaN heterostructure.

overall drain current. This contribution is responsible for a characteristic kink in the output characteristics at high drain biases.

Gaska et al. [8] also developed an analytical device model for a double channel HFET based on the Unified Charge Control Model. The model describes both subthreshold and above threshold regimes of operation and accounts for the drain-bias dependent series resistances for the bottom channel and accurately reproduces the measured current-voltage characteristics. The modeling results showed that such improved multichannel AlGaN-GaN heterostructures will be very promising for applications in power GaN-based HFETs.

The band diagrams shown above assume an abrupt AlGaN/GaN heterointerface. However, recent experimental and theoretical studies of the capacitance-voltage (C–V) characteristics and of the Hall mobility of the 2D-electron gas for strained $Al_{0.25}Ga_{0.75}N$-GaN heterostructures showed that the heterointerface might be graded. The heterostructures studied in [10] were grown on sapphire with the AlGaN barrier layer thickness varying from 10 nm to 100 nm. The measured C–V characteristics provided the strong experimental evidence that the piezoelectric effect causes an increase in the sheet electron concentration in heterostructures with $Al_{0.25}Ga_{0.75}N$ thickness up to 60 nm.

The strain-induced electric field changes the charge distribution in the heterostruc-

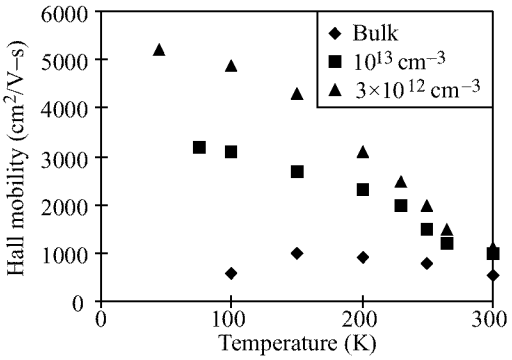


**Fig 5.** Hall 2D-electron gas mobility in bulk GaN and nominally undoped ($n_s = 3 \times 10^{12}\,cm^{-3}$) and doped ($n_s = 10^{13}\,cm^{-3}$) AlGaN/GaN heterostructures versus temperature [13].

tures. This, in turn, caused the shift of the C–V characteristics with respect to their unstrained positions while preserving their general shape. The magnitude of the shift depends on the strain and the strained layer thickness. The magnitude of strain was extracted from the comparison between the calculated and measured C–V characteristics. The results showed that relaxation increased gradually with the AlGaN thickness. The structure with a 100-nm thick barrier layer was fully relaxed. The conventional theory of strain relaxation for abrupt interfaces yields the critical thickness of unrelaxed $Al_{0.25}Ga_{0.75}N$ barrier at least 1.5 times smaller than the value extracted from these C–V measurements. In Reference [10], this difference was attributed to a gradual change in the Al mole fraction near the AlGaN-GaN heterointerface over approximately 5–6 nm.

## 3 Transport properties

A high electron sheet density in AlGaN/GaN heterostructures is very effective in screening the impurity scattering [11]. Recent measurements of the Quantum Hall and Shubnikov–de-Haas effect on similar AlGaN-GaN modulation doped structures with Si-doped channels clearly showed the existence of the two-dimensional (2D) electron gas in these structures with parallel conduction path provided by three-dimensional electrons [12]. The Hall mobility measurements and theoretical calculations reported in [11] showed that the 2D-electron gas mobility in doped channel structures at room temperature is nearly the same as in undoped structures. This is confirmed by our more detailed measurements shown in Fig. 5 [13].

Recent measurements of the Hall mobility and Quantum Hall Effect in the AlGaN/GaN HFETs grown on SiC substrates showed the electron mobility in these structures in considerably large than in similar structure grown on sapphire substrates, especially at cryogenic temperatures [2, 12]. This can be explained by a better material quality of GaN grown on SiC substrates because of much smaller lattice mismatch between AlGaN and SiC. A better material quality may manifest itself in a smaller dislocation density and/or in a less pronounced columnar structure. The dislocation density in GaN grown on sapphire is quite high (in the range $10^8 - 10^{10}\,cm^{-2}$ [14].) This material also has a pronounced columnar structure (called ordered polycrystalline microstructure [12].) The mobility limited by the dislocations is roughly proportional to

temperature [13]. The polycrystalline structure leads to the observation of the "mobility edge" [15] and may result in the exponential temperature dependence of the mobility with a very small, concentration-dependent activation energy [16]. Both scattering mechanisms related to the material imperfections should be much more pronounced at cryogenic temperatures. Hence, the data reported in [2] point out to a better material quality of GaN grown on SiC substrates.

Further studies [17] showed that at high electron densities, electrons occupy three-dimensional states in the doped channel near the GaN-AlGaN heterointerface, even at moderate doping levels, on the order of $10^{17}\,\mathrm{cm}^{-3}$. This model explains the observed decrease of room temperature electron Hall mobility with the channel doping. The mobility in $Al_{0.2}Ga_{0.8}N$-GaN heterostructures grown on sapphire and conducting 6H–SiC substrates decreases from 1,200 $\mathrm{cm}^2$/Vs (on sapphire) and 2,000 $\mathrm{cm}^2$/Vs (on 6H–SiC) at electron sheet density $n_s = 10^{13}\,\mathrm{cm}^{-2}$, to approximately 700–800 $\mathrm{cm}^2$/Vs at $n_s > 3 \times 10^{13}\,\mathrm{cm}^{-2}$ for both types of the substrates. The model also explains a non-monotonous electron mobility dependence on the gate bias in the "gated" Hall slab at temperature $T = 4.2$ K. The measured Hall mobility at 4.2 K first increases with the gate bias (from approximately 7,000 $\mathrm{cm}^2$/V-s at $V_g = -4$ V up to the record value of 11,000 $\mathrm{cm}^2$/V-s at $V_g = -0.5$ V). With a further increase in $V_g$, the mobility decreases down to 9,500 $\mathrm{cm}^2$/V-s at $V_g = 1.5$ V). With an increase in the gate bias from $-4$ V to 1.5 V, the sheet electron carrier concentration increases from approximately $3.5 \times 10^{12}\,\mathrm{cm}^{-2}$ to $1.1 \times 10^{13}\,\mathrm{cm}^{-3}$. At the gate bias $-0.5$ V, which corresponds to the maximum Hall mobility, the electron sheet concentration is $8 \times 10^{12}\,\mathrm{cm}^{-2}$ and is close to the maximum value of $n_s$ estimated for the 2D channel near $Al_{0.2}Ga_{0.8}N$-GaN heterointerface.

These results are important for choosing the optimum doping in AlGaN-GaN Doped Channel Heterostructure FETs, which should be dependent on the gate length.

*Acknowledgment*

I would like to thank my colleagues Drs. Bykhovski, Gelmont, Kaminski, Chen, Khan, Yang, Soloviov, Osinsky, Fjeldly, Knap, Contreras, Alause, Skiberbiszewski, Professors Camassel, Dyakonov, Robert, Dr. Sadowski, Huant, F. J. Yang, Goiran, and J. Leotin, who contributed to the research described in this paper. The work at Rensselaer Polytechnic Institute and at APA Optics has been supported by the Office of Naval Research and by the Cornell University (under the MURI subcontract).

## References

[1] M. A. Khan, Q. Chen, C. J. Sun, M. S. Shur, and B. L. Gelmont, *Appl. Phys. Lett.* **67** No. 10, Sep. 4, 1429–1431 (1995).

[2] R. Gaska, J. W. Yang, A. Osinsky, Q. Chen, M. Asif Khan, A. O. Orlov, G. L. Snider, and M. S. Shur, *Appl. Phys. Lett.* **72** No. 6, 707–709, Feb. 1998.

[3] A. Bykhovski, B. Gelmont, and M. S. Shur, *J. Appl. Phys.* Dec. **74** (11), 6734 (1993).

[4] P. M. Asbeck, G. J. Sullivan, E. T. Yu, S. S. Lau, and B. McDermott, *Device Research Conference Abstracts*, paper V-B-5, Fort Collins, Colorado (1997).

[5] B. J. Thibeault, B. P. Keller, Y.-F. Wu, P. Fini, U. K. Mishra, C. Nguyen, N. X. Nguyen, and M. Le, *IEDM-97 Technical Digest*, IEEE, December (1997).

[6] Q. Chen, R. Gaska, M. Asif Khan, Michael S. Shur, G. J. Sullivan, A. L. Saylor, and J. A. Higgins, *IEEE Electron Device Lett.* **19** No. 2, 44–46, Feb. (1998).

[7] M. S. Shur, *Symposium Proc. of Material Research Society*, Symposium E, Fall 1997, (to be published).
[8] R. Gaska, M. S. Shur, J. Yang, and T. A. Fjeldly, *MRS, Symposium D*, Spring, accepted (1998).
[9] A. D. Bykhovski, B. Gelmont, and M. S. Shur, *J. Appl. Phys.* **78** (6), 3691–3696, 15 September (1995).
[10] A. D. Bykhovski, R. Gaska, J. W. Yang, and M. S. Shur, submitted to *Electronic Materials Conference*, June 1998, Charlottesville, VA.
[11] M. S. Shur, B. Gelmont, and M. Asif Khan, *J. Electronic Materials* **25** No. 5, 777–785, May (1996).
[12] W. Knap, S. Contreras, H. Alause, C. Skiberbiszewski, J. Camassel, M. Dyakonov, J. L. Robert, J. Yang, Q. Chen, M. Asif Khan, M. Sadowski, S. Huant, F. J. Yang, M. Goiran, J. Leotin, and M. Shur, *Appl. Phys. Lett.* **70** (16), 2123–2125 (April (1997).
[13] M. S. Shur, Q. Chen, J. Yang, R. Gaska, M. Blasingame, M. Asif Khan, A. Ping, I. Idesida, V. P. Madangarli, and T. S. Sudarshan, *Proceedings of ISDRS-97*, pp. 377–380, Charlottesville, VA, Dec. (1997).
[14] S. D. Hersee, J. C. Ramer, and K. J. Malloy, *MRS Bulletin* **22** No. 7, 45–51, July (1996).
[15] B. P. Pödör, *Phys. status solidi*, **16**, K167 (1966); B. Heying, X. H. Wu, S. Keller, Y. Li, D. Kapolnek, B. P. Keller, S. P. Denbaars, and J. S. Speck, *Appl. Phys. Lett.* **68** 643 (1996).
[16] C. H. Seager, *Ann. Rev. Mater. Sci.* **15** 271 (1985).
[17] R. Gaska, J. W. Yang, M. S. Shur, A. O. Orlov, and G. L. Snider submitted to *Electronic Materials Conference*, June 1998, Charlottesville, VA.

# Author Index